12/5-96 JS ①
H

CONF-9510109--Vol.2

DOE/METC-96/1023, Vol. 2
(DE96000562)

Proceedings of the Advanced Turbine Systems Annual Program Review Meeting Volume II

Charles T. Alsup
Charles M. Zeh
Stanley Blazewicz

October 1995

U.S. Department of Energy
Office of Fossil Energy
Morgantown Energy Technology Center
Morgantown, West Virginia

Office of Energy Efficiency and Renewable Energy
Washington, D.C.

DISTRIBUTION OF THIS DOCUMENT IS UNLIMITED BS

Disclaimer

Available to DOE and DOE contractors from the Office of Scientific and Technical Information, 175 Oak Ridge Turnpike, Oak Ridge, TN 37831; prices available at (615) 576-8401.

Available to the public from the National Technical Information Service, U.S. Department of Commerce, 5285 Port Royal Road, Springfield, VA 22161; phone orders accepted at (703) 487-4650.

DOE/METC-96/1023, Vol. 2
(CONF-9510109--)
(DE96000562)
Distribution Category UC-103
UC-106
UC-111

Proceedings of the Advanced Turbine Systems Annual Program Review Meeting
Volume II

Technical Coordinators
Charles T. Alsup
Charles M. Zeh
Stanley Blazewicz

Sponsored by
U.S. Department of Energy
Office of Fossil Energy
Morgantown Energy Technology Center
P.O. Box 880
Morgantown, WV 26507-0880
(304) 285-4764
FAX (304) 285-4403/4469
http://www.metc.doe.gov/
and
Office of Energy Efficiency and Renewable Energy
Office of Industrial Technologies
1000 Independence Avenue SW
Washington, D.C. 20585
(202) 586-9220
FAX (202) 586-9260
http:///www.doe.gov/

MASTER

October 17-19, 1995

DISTRIBUTION OF THIS DOCUMENT IS UNLIMITED

Contents

Volume I

Session 2A — ATS Program Element Overviews

Session 2B — ATS Program Technical Reviews

Session 3 — ATS Related Activities

Session 4 — University/Industry Consortium Interactions

Session 5 — ATS Supportive Projects

Volume II

Poster Session

Appendices

Poster Session

P1

Lean Premixed Combustion Stabilized by Radiation Feedback and Heterogeneous Catalysis

Robert W. Dibble (rdibble@firebug.me.berkeley.edu; 510-642-4901)
Jyh-Yuan Chen (jychen@firebug.me.berkeley.edu; 510-642-3286)
Robert F. Sawyer (rsawyer@euler.me.berkeley.edu; 510-642-5573)
Department of Mechanical Engineering
50-B Hesse Hall
University of California
Berkeley, CA 94720-1740
http://www.me.berkeley.edu/~cal/

Introduction

Gas-turbine based systems are becoming the preferred approach to electric power generation from gaseous and liquid fossil-fuels and from biomass. As coal gasification becomes more prevalent, gas turbines will also become important in the generation of electricity from coal. In smaller, distributed installations, gas turbines offer the prospect of cogeneration of electricity and heat, with increased efficiency and reduced pollutant emissions.

One of the most important problems facing combustion-based power generation is the control of air pollutants, primarily nitrogen oxides (NO_x, consisting of NO and NO_2) and carbon monoxide (CO). Nitric oxide (NO) is formed during gas-phase combustion and is the precursor of nitrogen dioxide (NO_2), the principal component of photochemical smog. Recent research into the mechanisms and control of NO_x formation has been spurred by increasingly stringent emission standards.

Miller and Bowman (1989) and Bowman (1992) have reviewed research in NO_x production and control. There are four principal reaction mechanisms for the formation of NO_x in gas-phase combustion: the Fenimore ("prompt") NOx, which is initiated by CH radicals at the flame front of hydrocarbon flames; the Zel'dovich ("thermal") NO_x, which results from the presence of O radicals in the high temperatures of the post-flame zone; the N_2O mechanism, which is important at high pressures; and the fuel-bound nitrogen (FBN) mechanism, which occurs primarily in the combustion of coal and some liquid fuels.

NO_x emission in natural-gas fired turbines has traditionally been controlled either by lowering the temperature of the combustion products, or by removing NO_x from the products through some exhaust gas treatment method, such as selective catalytic reduction (SCR). Catalytic combustion over noble-metal catalysts offers a third method for controlling NO_x emissions, for a number of reasons. Most of the combustion reaction occurs on the catalyst surface; surface production of NO_x is low or nonexistent. Also, the catalyst permits low temperature combustion below the traditional lean limit, thus inhibiting NO_x formation routes

---

Research sponsored by the U.S. Department of Energy's Morgantown Energy Technology Center, under AGTSR Subcontract No. 93-01-SR007 with the South Carolina Energy Research and Development Center, Clemson, SC

in the gas phase. Furthermore, gas-phase chemistry may be inhibited by the catalyst due to adsorption of reactive intermediates.

The catalyst can also function as a preburner for a traditional combustor, permitting combustion at very lean overall equivalence ratios with low product temperatures (Dalla Betta, *et al.*, 1994, 1995; Schlegel, *et al.*, 1994). Since the catalyst produces little NO_x, an increase in fractional conversion of fuel within the catalyst will result in a decrease in overall NO_x emissions (Griffin, *et al.* 1994; Schlegel, *et al.* in press).

Objectives

Some of the unknowns in the current understanding of the catalytic combustion process are the detailed surface reaction mechanisms, the coupling of gas-phase and surface reactions through radical adsorption or desorption, and the effects of mass transport to the surface on the overall reaction rate. Since these processes interact, creating a complex modeling problem, researchers have often modeled the catalyst as a "black box" that produces a desired amount of fuel conversion (Schlegel, *et al.* in press). While this approach has been useful for proof-of-concept studies, we expect practical applications to emerge from a greater understanding of the details of the catalytic combustion process.

The catalytic combustion program at Berkeley is opening the "black box" by developing a numerical model that simulates both gas-phase and heterogeneous (surface) combustion in practical applications. The model will address questions regarding the interaction between mass transfer to the surface and surface reaction rate, the dependence of this relationship on pressure, the fuel conversion and pollutant formation rates in the catalyst bed, and the initiation of surface and gas-phase reactions.

Thus, the principal objective of this research project is thus the development of effective models for the simulation of catalytic combustion applications.

Approach

Our approach consists of two concurrent, complementary components. One of these is the development of a detailed numerical model of the catalytic combustion process that can be used to explore various physical processes occurring in the catalyst. The other is an experimental program utilizing an atmospheric pressure catalytic combustor. The laboratory experiments are designed and performed to obtain the data required to test the model, and the model is used to guide the efficient selection of experimental parameters for further experiments. This synergy between model and experiment is the guiding principle behind our catalytic combustion program.

The Experiments

In support of the model development, we have built an atmospheric-pressure research combustor for natural-gas combustion over noble-metal catalysts supported on ceramic honeycomb monoliths. In this reactor, the catalyst is segmented into wafers, with the gaps between each wafer permitting sampling access. Several researchers, including Sadamori *et al.* (1994) and Hayashi *et al.* (1994), have performed experiments using segmented catalysts, but the species concentrations and visual observations made possible by this segmentation are not reported in the literature. We present measured and modeled temperature and species (O_2, CO, CO_2, NO_x, and hydrocarbons) profiles at several axial locations

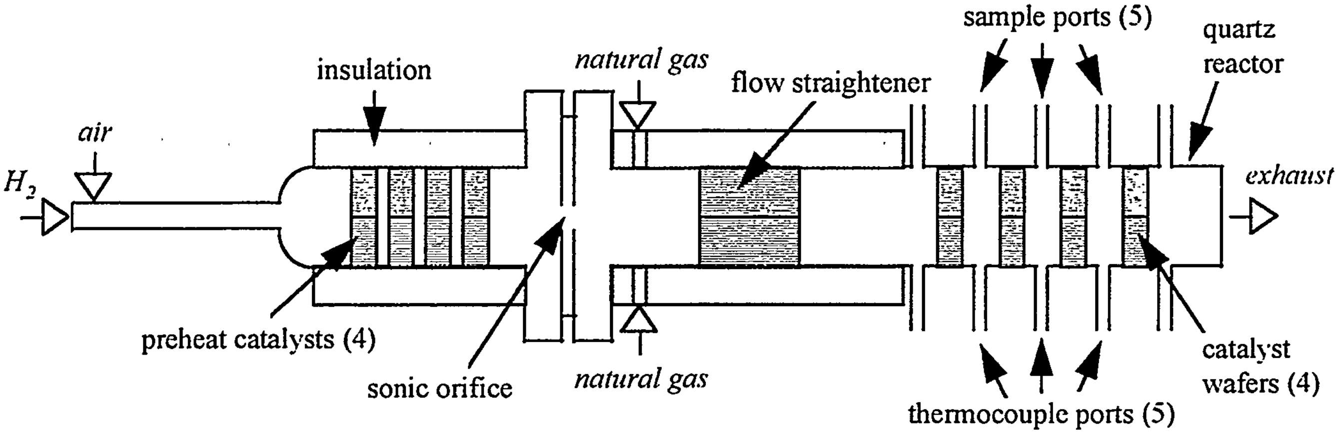

Figure 1: Schematic of U.C. Berkeley atmospheric-pressure catalytic combustor

within the catalyst. These measurements indicate the progress of combustion and pollutant formation and permit better validation of our numerical model than would measurements taken only at the catalytic combustor inlet and exit planes.

A schematic of the research reactor is shown in Fig. 1. For methane, catalytic reactions are negligible until the gas-phase temperature reaches 350°C over palladium catalysts or 600°C over platinum catalysts. Therefore, the fuel/air mixture must be heated upstream of the catalyst to at least this temperature. In a gas turbine, this preheating would be provided by the compressor; if necessary, a preburner or heat exchanger could provide further preheating (Sadamori, *et al.*, 1994; Beebe, *et al.* 1995; Dalla Betta, *et al.* 1995). However, since hydrogen will react on platinum catalysts at room temperature, a small amount of hydrogen burned in a separate upstream catalytic reactor provides this preheating in our reactor.

We chose platinum catalysts for our initial experiments because of the large body of literature available on the oxidation of methane over platinum. Modeling a platinum catalyst and comparing that model with experimental data allows us to assess the accuracy of the model before introducing further uncertainties in the less well-understood kinetics of catalytic combustion over palladium. The catalysts were prepared by Catalytica, Inc. The substrate is a 200-cpi (cells per square inch) honeycomb cordierite monolith with square channels. The wall thickness is 0.3 mm and the distance between walls is 1.5 mm; thus, the open area is 70% of the total. The washcoat (support material) is alumina, calcined at 850°C. The catalytic monolith contains 2% by weight of platinum particles. These catalysts are similar to those used in automobile three-way catalytic converters, and are typical of those used in catalytic combustion experiments.

We measured temperatures using Type K thermocouples. Species concentrations along the catalyst were measured using Horiba gas analyzers. Gas samples were extracted from the reactor through 1/8"-diameter, uncooled, stainless-steel suction probes, and the sample passed through a condenser prior to analysis. Natural gas flow rate was measured using a Sierra Instruments mass flow controller. The air flow rate was calculated by measuring the pressure drop across a calibrated orifice downstream of the preheater. This orifice also served to generate downstream turbulence, which aided the mixing of the incoming fuel with the preheated, vitiated air.

We refer to each set of temperature and species measurements taken at a single equivalence ratio under steady operating conditions as one "run." Over thirty runs have been completed. Four runs at different equivalence ratios were selected for detailed presentation. Inlet conditions for these four runs are given in Table 1. Flow velocities were varied within the range 5 to 10 m/s, with a mean of 7 m/s over the thirty runs. Although we used natural gas for the bulk of our experiments, substitution of bottled methane produced nearly identical results due to the very high methane content (>95%) of our natural gas supply.

Table 1: Typical reactor operating conditions

Equivalence ratio ϕ	0.18	0.25	0.30	0.39
Inlet temp (K)	846	848	852	850
Inlet velocity (m/s)	7.2	7.0	7.3	7.3

The Model

The model includes gas-phase and surface chemical kinetics as well as heat and mass transport between the gas and the surface. We used a combination of three computer codes to model the detailed gas-phase and surface kinetics: CHEMKIN for gas-phase chemical kinetics (Kee, *et al.* 1989), Surface CHEMKIN (Coltrin, *et al.* 1991) for heterogeneous chemical kinetics, and CRESLAF (Chemically Reacting Shear Layer Flow, Coltrin *et al.* 1993) for solution of the boundary-layer equations.

The gas-phase chemical reaction mechanism used with CHEMKIN was developed by the Gas Research Institute (version 1.2) and contains 32 species and 173 reactions; it can be obtained from http://www.gri.org/. The surface reaction mechanism, shown in Table 2, has been compiled from reactions published by Hickman and Schmidt (1993) and Deutschmann, *et al.* (1994). (N.B. Thermodynamic data are no less important to the modeling of chemical kinetics than the rate constant parameters.) The surface site density, a required model input, was estimated to be 2.7x10^{-9} moles/cm^2 as done by Deutschmann, *et al.* (1994) for Pt foils. The actual value could be smaller (since Pt occurs as particles on the catalyst surface), or larger (since the molecular-scale surface area of supported catalysts is larger than the macroscopic surface area), or these effects could cancel.

Table 2: Platinum surface mechanism used in CHEMKIN/CRESLAF model

Reactions in CHEMKIN form.: the numbers following each reaction are the preexponential factor (in cm-g-sec-mole units), preexponential temperature exponent, and the activation energy (in kJ/mole). For asterisked adsorption reactions, the first number is the sticking coefficient. Species of the form X(*) are adsorbed species; PT(*) is an open surface site; PT(B) is a bulk Pt atom; all other species are gas-phase.

```
adsorption/desorption reactions
H2+2PT(*)=>H(*)+H(*)+2PT(B)        0.05    0      0  *
2H(*)+2PT(B)=>H2+2PT(*)            1E+21   0   67.4
O2+2PT(*)=>O(*)+O(*)+2PT(B)        0.023   0      0  *
2O(*)+2PT(B)=>O2+2PT(*)            1E+21   0  220.0
H2O+PT(*)=>H2O(*)+PT(B)            0.50    0      0  *
H2O(*)+PT(B)=>H2O+PT(*)            1E+13   0   62.2
OH+PT(*)=>OH(*)+PT(B)              1.00    0      0  *
OH(*)+PT(B)=>OH+PT(*)              1E+13   0  192.8
H+PT(*)=>H(*)+PT(B)                1.00    0      0  *
O+PT(*)=>O(*)+PT(B)                1.00    0      0  *

Langmuir-Hinshelwood mechanism
CH4+2PT(*)=>CH3(*)+H(*)+2PT(B)     0.01    0      0  *
CH3(*)+PT(*)=>CH2(*)+H(*)+PT(B)    1E+21   0   20.0
CH2(*)+PT(*)=>CH(*)+H(*)+PT(B)     1E+21   0   20.0
CH(*)+PT(*)=>C(*)+H(*)+PT(B)       1E+21   0   20.0

Eley-Rideal mechanism
CH4+5O(*)=>CO(*)+4OH(*)            0.01    0   43.3*
CH3+PT(*)=>CH3(*)+PT(B)            1.00    0      0  *
CH3(*)+PT(B)=>CH3+PT(*)            1E+13   0  200.0
CO+PT(*)=>CO(*)+PT(B)              0.84    0      0  *
CO(*)+PT(B)=>CO+PT(*)              1E+13   0  126.0
CO(*)+O(*)+2PT(B)=>CO2+PT(*)       1E+21   0  100.8

Surface reactions
H(*)+O(*)+PT(B)=>OH(*)+PT(*)       1E+21   0   10.5
H(*)+OH(*)+PT(B)=>H2O(*)+PT(*)     9E+21   0   63.0
2OH(*)=>H2O(*)+O(*)                1E+21   0   51.7
C(*)+O(*)+PT(B)=>CO(*)+PT(*)       5E+19   0   63.0
CO(*)+PT(*)=>C(*)+O(*)+PT(B)      5.E+16   0  156.5
```

In its present form, the numerical model requires that the user specify catalyst surface temperatures; in doing so, we assumed that the surface temperature in each catalyst wafer was a linear function of axial distance. The surface temperature affects the gas-phase temperature through heat transfer from the surface. We selected entry and exit surface temperatures that allowed the model to reproduce the measured gas-phase temperatures.

We used the model to simulate the operation of the catalyst with the inlet conditions of each of the four runs presented in Table 1. Due to the low gas-phase temperatures, we assume that gas-phase reactions were negligible within the space between wafers and therefore model the set of four 2-cm wafers as a single 8-cm monolith. The axial profiles from the model are averages over the channel cross-section.

Results

Temperature Profiles

Measured and modeled gas-phase temperatures are presented in Fig. 2. The measured temperatures have been corrected for thermocouple radiation. Because of our choice of surface temperatures, the measured and modeled gas-phase temperatures match at the points between catalyst wafers. The measured temperatures agree well with the expected adiabatic temperature for the measured fractional conversion, indicating that heat losses from the catalyst are not significant.

Fuel Conversion Profiles

For measured data, the extent of reaction—the percentage of fuel conversion to products—is calculated using either the decrease in O_2 mole fraction or the increase in CO_2 mole fraction; both yielded similar results. Figure 3

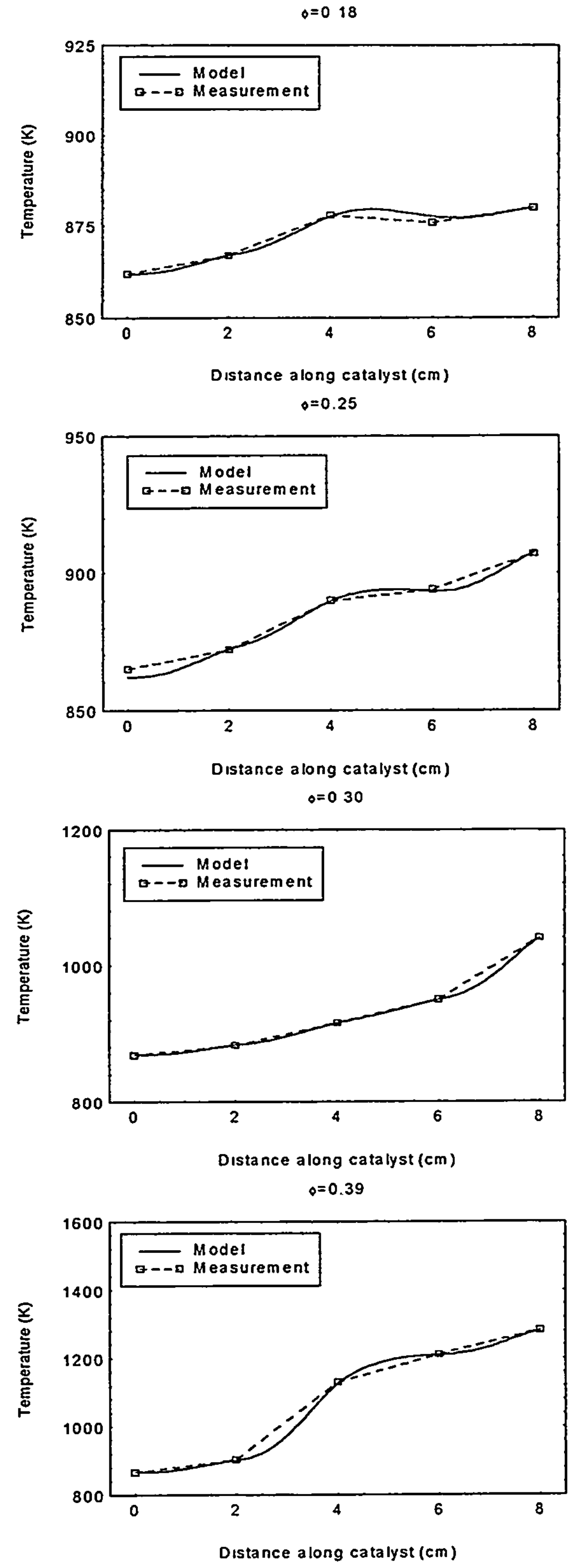

Figure 2: Measured and modeled gas-phase temperature profiles

shows measured and modeled conversion profiles for each run. The ratio of modeled and measured conversion is about unity for temperatures around 850 K. At higher temperatures, the ratio decreases to about 0.5. A comparison of Fig. 2 and Fig. 3 indicates that the model agrees very well with experiments at temperatures up to 900 K, but underpredicts conversion at higher temperatures.

Pollutant Measurements

In all cases, NO_x concentrations are below 1 ppm, the detection limit of the analyzer. Modeled and measured CO concentrations are presented in Fig. 4. At lower equivalence ratios, the measured CO concentrations are below 4 ppm. At the highest equivalence ratio, the CO measurements reach 20 ppm halfway through the catalyst before falling to the outlet value of 10 ppm. This decrease can be explained either by CO consumption on the catalyst or in the gas phase at the high temperatures resulting from the large fraction of fuel conversion, or possibly by conversion of the CO to CO_2 in the probe at the same high temperatures. Nguyen *et al.* (1995) have indicated that probe conversion becomes increasingly significant at gas temperatures above 1000 K.

In three of the cases, the CO predictions exceed the measurements by about 2 ppm. The model predicts that the CO concentration increases to about 2 ppm within the first wafer; this increase is not seen in the measurements. If the initial rise were eliminated, the model would agree well with the measurements.

In the first wafer of the ϕ=0.39 run, the initial rise to 2 ppm and the parallel slopes of the model and measurement are similar to those seen in the other runs. Measured CO at 4 cm is about 20 ppm, which is higher than the model prediction of 12 ppm. The model does not

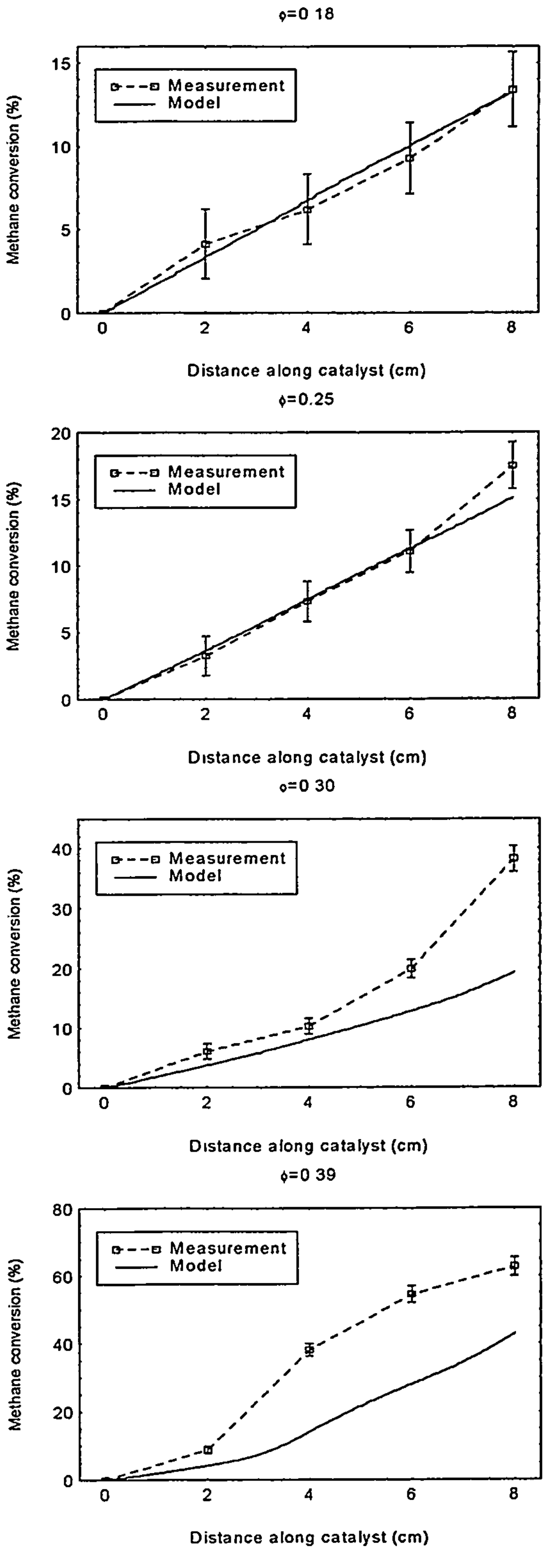

Figure 3: Measured and modeled fuel (natural gas) conversion profiles

predict the observed decrease in CO; again, that decrease may be due to intraprobe conversion.

Gas-Phase Reactions

We used the model without including the gas-phase mechanism to assess the effects of gas-phase reactions for the (higher temperature) runs with $\phi=0.30$ and $\phi=0.39$. The profiles of fuel conversion and CO concentration were indistinguishable from those from the model that included the gas-phase reactions. We conclude that, under these conditions and with this mechanism, the reactions take place entirely on the surface. Furthermore, this validates our assumption that gas-phase reactions are negligible between catalyst wafers.

Fuel Conversion Rate

The rate of fuel conversion is one of the most important outputs of a model of a catalytic combustor. As Fig. 3 shows, the percentage of fuel conversion in the catalyst increases with increasing equivalence ratio; if the fuel conversion rate was zero-order in fuel concentration, the curves would be identical, with no dependence on equivalence ratio.

Other researchers have found methane combustion over platinum catalysts to be first-order with respect to methane (Yao, 1980; Otto, 1989). Assuming a reaction that is first-order in fuel, the value of the global "rate constant" can be determined by the slope of the fractional conversion versus residence time in the catalyst. This rate is obtained by linear regression for all runs, since we find that the linear approximation produces good agreement with the results of the rigorous calculations.

Figure 5 depicts these fractional conversion rates (in percentage of fuel consumed per millisecond of residence time) versus the

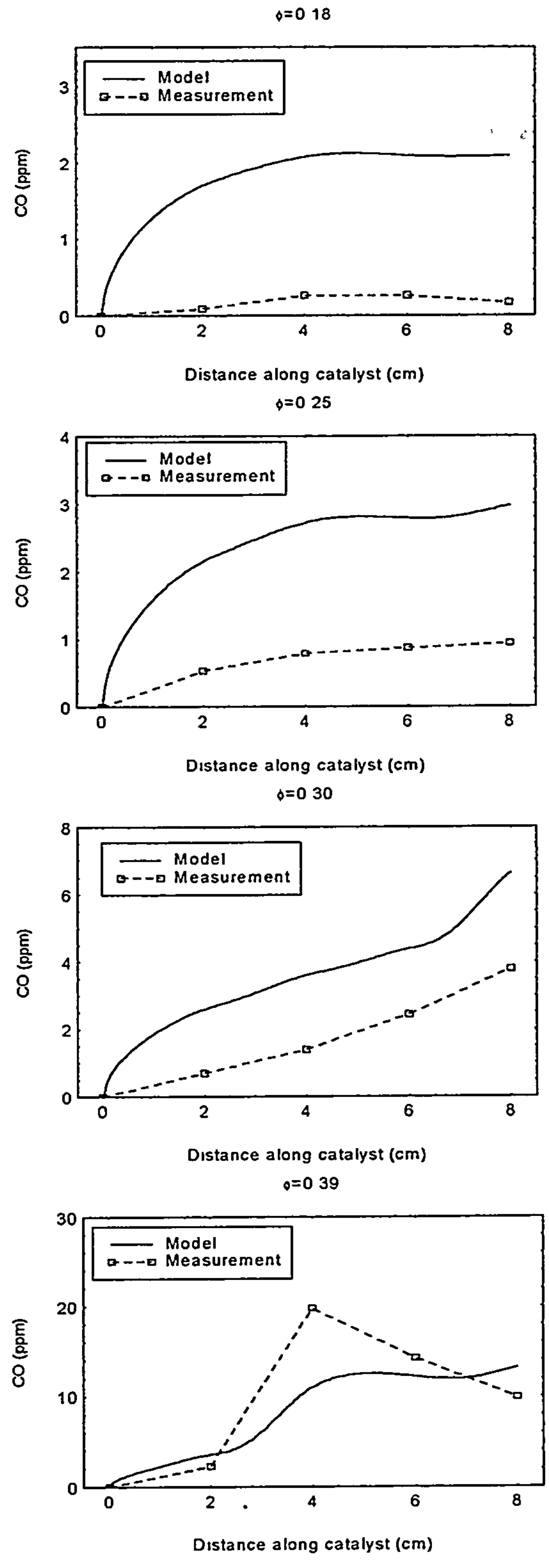

Figure 4: Measured and modeled CO mole fraction profiles

overall equivalence ratio. Each datum represents a net conversion rate for all four catalyst wafers during a single run. A positive correlation between fractional conversion rate and equivalence ratio is easily discernible despite the scatter present in the data. In contrast, a plot of fractional conversion rate versus local equivalence ratio exhibits no observable relationship. The graph exhibits two boundaries: a lower, non-zero boundary in which fractional conversion does not depend on equivalence ratio, and an upper boundary that is roughly linear in equivalence ratio. The lines drawn on the graph are not intended to imply linearity but exist merely to delineate the boundaries. Plots of individual wafer fractional conversion rate versus equivalence ratio appear very similar to Fig. 5, with both boundaries clearly discernible and all data bounded by the same boundaries appearing in Fig. 5.

Lower boundary. The lower boundary in Fig. 5 represents a process that is independent of equivalence ratio and therefore is independent of the composition of the fuel-air mixture near the surface. Since absolute conversion is equal to the product of fractional conversion and fuel concentration, this process is first-order in fuel concentration. We suggest that this process is indicative of the reaction on the catalytic surface and that this boundary represents the kinetic limitation.

The average inlet temperature for kinetically-limited data points (those below 7%/ms) is 877 K. The average of the measured conversion rates below 7%/ms is 2.4 ± 1.4 %/ms. A one-step rate given by Trimm and Lam (1980) predicts a conversion rate of 4.8%/ms at that temperature, a factor of two higher. However, the published rate is within two standard deviations of the average of our data, so we believe that ascribing the lower boundary to kinetically-limited conversion is justified.

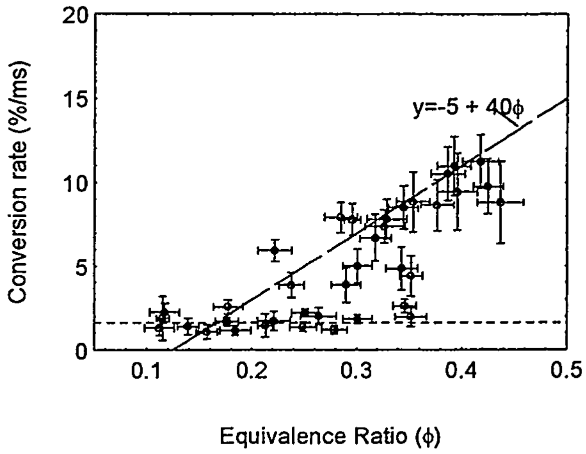

Figure 5: Fractional conversion rate vs. overall equivalence ratio

Upper boundary. A process that is first-order in fuel does not adequately explain the upper boundary in Fig. 5. An analysis of conversion rates for each wafer (rather than for the whole run) exhibit no discernible relationship with either the wafer inlet temperature or the local equivalence ratio. Only graphs of fractional conversion rate versus equivalence ratio or adiabatic flame temperature show the sloping boundary that appears in Fig. 5.

Our findings are as follows: When adiabatic flame temperature exceeds 1450 K (ϕ=0.34), the temperature dependence of the conversion rate is consistent with a diffusion limitation. However, due to the limited amount of data above this equivalence ratio, we hesitate to state that diffusion is the limiting process. When ϕ<0.34, the data are not consistent with diffusion limitation and we therefore hypothesize a surface-kinetic limitation. This hypothesis does not conform to the behavior predicted by a one-step reaction rate, namely that conversion occurs at a very low rate until a certain surface temperature, after which the reaction "jumps" to the higher, diffusion-controlled limitation.

We propose three explanations for this "blurring" of the transition. First, the behavior of supported platinum differs from that of the pure platinum foils used in many kinetic experiments. The reaction activation energy may depend on the platinum particle size (Otto, 1989; Briot, *et al.* 1990), catalyst pretreatment (Burch and Loader, 1994), or support material (Hicks, *et al.* 1990). Second, the oxidation mechanism on the surface is not a single-step reaction, and probably includes more than one pathway. Above some critical temperature, the reaction rate of one step may become fast enough that the step is no longer limiting, but the rates of other steps may still be relatively slow. Third, the significant amount of water in the inlet stream, produced in the hydrogen preburner stage, may partially deactivate the catalyst, as observed by Trimm and Lam (1980).

Surface Coverage

One of the limiting factors in the catalytic reaction is the number of available adsorption sites on the surface. The fraction of open sites depends on both pressure and surface temperature. At low temperatures, the surface is covered with oxygen atoms and appreciable reaction rates do not occur until the surface temperature increases to the point at which these O atoms can overcome the energy barrier necessary for desorption. At that point, open surface sites become available for the adsorption of fuel (Oh, *et al.*, 1991; Burch and Loader, 1994; Behrendt, *et al.* 1995).

Figure 6 shows the modeled fractional conversion rate as a function of open sites for each run. The model predicts a linear dependence of fuel fractional conversion rate on the fraction of open surface sites. The data for 1 atm, 5 atm and 12 atm lie on a single line; given a specified fraction of open sites, the fractional conversion rate is independent of pressure. Thus, pressure affects the conversion rate through a change in either the open site fraction or the diffusion rate of reactants to the surface.

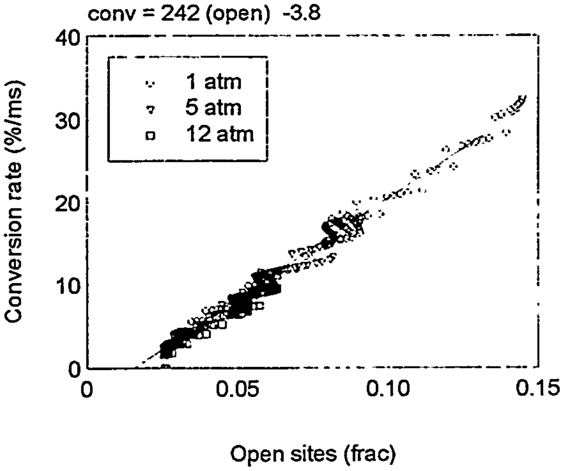

Figure 6: Effect of open surface sites on fractional conversion rate

Application

We anticipate that the models we develop under this research program will be useful by industry and researchers alike in the design of both experiments and practical gas turbine catalytic combustors. The model—which includes transport codes, mechanisms, and postprocessing routines—is portable and can be run on UNIX workstations. Intelligent design of experiments, guided by this model, can reduce unnecessary expenditures of time and money spent in the laboratory. Likewise, the development of low-NO_x gas turbine systems can be accelerated by using these models to test the effectiveness of combustor designs prior to engaging in time-consuming prototyping.

Future Activities

Our current work focuses on the extension of our surface chemistry models to conditions more useful to the gas turbine industry. This involves enhancements to both the experimental and the modeling components of our research program.

Work in Progress—Experimental

Since elevated pressures are more characteristic of gas turbine combustors, we are designing and building a high pressure catalytic combustor to supplant our previously used atmospheric pressure quartz combustor. It incorporates a number of improvements:

- Continuous operation at a rated pressure of up to 5 atmospheres in our laboratory at U.C. Berkeley and up to 30 atmospheres at the METC Combustion Research Facility
- Electrical preheating of inlet air for better control of catalyst inlet temperature and reduced effects of water in inlet stream.
- Measurements of surface temperature within catalyst monoliths
- Laser diagnostics access through the voids between catalyst sections
- Species and temperature measurements (both optical and conventional) in the post-catalyst homogeneous burn section

This new high pressure reactor will be used not only for our studies on palladium catalysis but also to test the effectiveness of our platinum model at high pressures.

Work in Progress—Modeling

Since palladium catalysts are a more suitable candidate for gas turbine combustor applications, we are concentrating our efforts on the development of a suitable model. The improvements to the reaction mechanism and transport codes are occurring concurrently with the upgrades to our experimental program.

We are currently working on a detailed surface reaction mechanism for methane catalytic combustion over supported palladium catalysts, using reaction rate parameters published in the literature wherever possible. In contrast to the case of platinum and rhodium, detailed reaction mechanisms have not yet been published for palladium.

The principal reason for this is the greater complexity of the reaction mechanism for palladium catalysts. Supported palladium undergoes a significant reduction in activity at 850°C due to reduction of the active species, PdO, to the unoxidized metal. Furthermore, support-metal interactions (including spillover) and absorption of adsorbed oxygen and other adatoms into the palladium bulk are likely to be more important than in the case of platinum.

In addition to continuing model development, we are upgrading our flow modeling code from CRESLAF to CURRENT, a newer code also developed at Sandia National Laboratories. This improved code is more versatile; unlike CRESLAF, which uses the boundary-layer approximation, CURRENT solves the full Navier-Stokes flow problem for two-dimensional configurations, using the well-known SIMPLER algorithm for the control volume formulation of the governing equations. As a result, CURRENT possesses better convergence properties than CRESLAF and is better able to model the flow conditions within the catalyst monolith.

We are also modifying a transient flame code for use in predicting flashback and startup, two very important processes that impact system performance.

References

Beebe, K. W., Cutrone, M. B., Matthews, R. N., Dalla Betta, R. A., Schlatter, J. C., Furuse, Y., and Tsuchiya, T., 1995, "Design and test of a catalytic combustor for a heavy duty industrial gas turbine," ASME Paper No. 95-GT-137.

Behrendt, F., Deutschmann, O., Maas, U., and Warnatz, J., 1995, "Simulation and sensitivity analysis of the heterogeneous oxidation of methane on a platinum foil," *Journal of Vacuum Science & Technology A*, Vol. 13, pp. 1373-1377.

Bowman, C. T., 1992, "Control of combustion-generated nitrogen oxide emissions," *Proceedings, 24th Symposium (International) on Combustion*, pp. 859-878.

Briot, P., Auroux, A., Jones, D., and Primet, M., 1990, "Effect of particle size on the reactivity of oxygen-adsorbed platinum supported on alumina," *Applied Catalysis*, Vol. 59, pp. 141-152.

Burch, R. and Loader, P. K., 1994, "Investigation of Pt/Al_2O_3 and Pd/Al_2O_3 catalysts for the combustion of methane at low concentrations," *Applied Catalysis B: Environmental*, Vol. 5, pp. 149-164.

Coltrin, M. E., Kee, R. J. and Rupley, F. M., 1991, "SURFACE CHEMKIN (Ver 4.0)," Sandia National Laboratories Report SAND90-8003C, Livermore, CA

Coltrin, M. E., Moffat, H. K., Kee, R. J. and Rupley, F. M., 1993, "CRESLAF (Ver 4.0)," Sandia National Laboratories Report SAND93-0478, Livermore, CA.

Dalla Betta, R. A., Schlatter, J. C., Nickolas, S. G., Razdan, M. K., and Smith, D. A., 1995, "Application of catalytic combustion technology to industrial gas turbines for ultra-low NO_x emissions," ASME Paper No. 95-GT-65.

Dalla Betta, R. A., Schlatter, J. C., Nickolas, S. G., Yee, D. K., and Shoji, T., 1994, "New catalytic combustion technology for very low emissions gas turbines," ASME Paper No. 94-GT-260.

Deutschmann, O., Behrendt, F., and Warnatz, J., 1994, "Modeling and simulation of heterogeneous oxidation of methane on a platinum foil," *Catalysis Today*, Vol. 21, pp. 461-470.

Griffin, T., Weisenstein, W., Schlegel, A., Buser, S., Benz, P., Bockhorn, H., and Mauss, F., 1994, "Investigation of the NO_x advantage of catalytic combustion," *Proceedings, 2nd International Workshop on Catalytic Combustion*, Tokyo, Japan, pp. 138-141.

Hayashi, S., Yamada, H. and Shimodaira, K., 1994, "High-pressure reaction characteristics of a catalytic combustor for gas turbines," *Proceedings, 2nd International Workshop on Catalytic Combustion*, Tokyo, Japan, pp. 148-153.

Hickman, D. A. and Schmidt, L. D., 1993, "Steps in CH_4 oxidation on Pt and Rh surfaces: High-temperature reactor simulations," *AIChE Journal*, Vol. 39, pp. 1164-1177.

Hicks, R. F., Haihua, Q., Young, M. L., and Lee, R. G., 1990, "Structure sensitivity of methane oxidation over platinum and palladium," *Journal of Catalysis*, Vol. 122, pp. 280-294.

Kee, R. J., Rupley, F. M., and Miller, J. A., 1989, "CHEMKIN-II," Sandia National

Laboratories Report SAND89-9009, Livermore, CA.

Miller, J. A. and Bowman, C. T., 1989, "Mechanism and modeling of nitrogen chemistry in combustion," *Progress in Energy and Combustion Science*, Vol. 15, pp. 287-338.

Nguyen, Q. V., Edgar, B. L., Dibble, R. W., and Gulati, A., 1995, "An experimental and numerical comparison of extractive and in-situ laser measurements of non-equilibrium carbon monoxide," *Combustion and Flame*, Vol. 100, pp. 395-406.

Otto, K., 1989, "Methane oxidation over Pt on γ-alumina: Kinetics and structure sensitivity," *Langmuir*, Vol. 5, pp. 1364-1369.

Sadamori, H., Tanioka, T., and Matsuhisa, T., 1994, "Development of a high temperature combustion catalyst system and prototype catalytic combustor turbine test results." *Proceedings, 2nd International Workshop on Catalytic Combustion*, Tokyo, Japan, pp. 158-161.

Schlegel, A., Benz, P., Griffin, T., Weisenstein, W., and Bockhorn, H., in press, "Catalytic stabilization of lean premixed combustion: method for improving NO_x emissions," *Combustion and Flame*.

Schlegel, A., Buser, S., Benz, P., Bockhorn, H., and Mauss, F., 1994, "NO_x formation in lean premixed noncatalytic and catalytically stabilized combustion of propane," *Proceedings, 25th Symposium (International) on Combustion*, pp. 1019-1026.

Trimm, D. L. and Lam, C. W., 1980, "The combustion of methane on platinum alumina fibre catalysts. I: Kinetics and mechanism," *Chemical Engineering Science*, Vol. 35, pp. 1405-1413.

Yao, Y.-F., 1980, "Oxidation of alkanes over noble metal catalysts," *Industrial and Engineering Chemistry Product Research and Development*, Vol. 19, pp. 293-298.

P2

Rayleigh/Raman/LIF Measurements in a Turbulent Lean Premixed Combustor

S. P. Nandula (nandulsp@ctrvax.vanderbilt.edu; 615-343-6162)
R. W. Pitz (pitzrw@vuse.vanderbilt.edu; 615-322-0209)
Vanderbilt University
Department of Mechanical Engineering
Nashville, TN 37212

R. S. Barlow (barlow@ca.sandia.gov; 510-294-2688)
G. J. Fiechtner (gjfiech@ca.sandia.gov; 510-294-2688)
Sandia National Laboratories
Combustion Research Facility
Livermore, CA 94566

Introduction

Much of the industrial electrical generation capability being added worldwide is gas-turbine engine based and is fueled by natural gas. These gas-turbine engines use lean premixed (LP) combustion to meet the strict NO_x emission standards, while maintaining acceptable levels of CO. In conventional, diffusion flame gas turbine combustors, large amount of NO_x forms in the hot stoichiometric zones via the Zeldovich (thermal) mechanism. Hence, lean premixed combustors are rapidly becoming the norm, since they are specifically designed to avoid these hot stoichiometric zones and the associated thermal NO_x. However, considerable research and development are still required to reduce the NO_x levels (25-40 ppmvd adjusted to 15% O_2 with the current technology), to the projected goal of under 10 ppmvd by the turn of the century. Achieving this objective would require extensive experiments in LP natural gas (or CH_4) flames for understanding the combustion phenomena underlying the formation of the exhaust pollutants. Although LP combustion is an effective way to control NO_x, the downside is that it increases the CO emissions. The formation and destruction of the pollutants (NO_x and CO) are strongly affected by the fluid mechanics, the finite-rate chemistry, and their (turbulence-chemistry) interactions. Hence, a thorough understanding of these interactions is vital for controlling and reducing the pollutant emissions. The present research is contributing to this goal by providing a detailed nonintrusive laser based data set with good spatial and temporal resolutions of the pollutants (NO and CO) along with the major species, temperature, and OH. The measurements reported in this work, along with the existing velocity data (Pan et al., 1991a) on a turbulent LP combustor burning CH_4, would provide insight into the turbulence-chemistry interactions and their effect on pollutant formation.

The literature on nonintrusive measurements of NO_x and CO is very limited, primarily due to the difficulty in measuring small concentrations (~ ppm) of CO and NO. Previous experimental studies of NO_x and CO formation have been based almost entirely on gas-sampling probe techniques (e.g., Drake

---

Research sponsored by the U.S. Department of Energy's Morgantown Energy Technology Center, under contract DE-FC21-92MC29061 with Clemson University Research Foundation, Box 345702, 300 Bracket Hall, Clemson, SC 29634-5702; telefax: 803-656-1429.

et al., 1987; Driscoll et al., 1992; Vranos et al., 1992). However, the instantaneous relationships between the pollutants and the other scalars which are crucial for evaluating the turbulence-chemistry interactions are lost, since the gas sampling probes provide only averaged measurements. Hence, the data from probes has limited applicability for evaluation and refinement of emissions models of emissions (e.g., characteristic time models, turbulence-chemistry models, and chemical reactor models).

Non-intrusive diagnostics based on Raman scattering has been used successfully by previous researchers (Dibble et al., 1987, 1990; Mansour et al., 1988, 1990, 1991; Masri et al., 1987a, b, c; Stårner et al., 1990) to obtain scalar (species and temperature) measurements in CH_4 flames. These measurements in CH_4 flames have provided a database for evaluation of combustion models and prediction of the turbulence-chemistry interactions (Pope, 1990; Mansour et al., 1989). However, there are no simultaneous laser based multiscalar measurements that include the exhaust pollutants (NO and CO). The clear need for such measurements in methane flames, which would point the way to the effects of turbulence-chemistry interactions in NO and CO formation and guide the development of emissions models and perhaps, reduced chemistry schemes, has prompted this research.

Objectives

The objectives of the research were (i) to obtain simultaneous and instantaneous quantitative nonintrusive laser based measurements with good spatial and temporal resolutions; (ii) to provide insights into the role of the turbulence-chemistry interactions on pollutant (NO and CO) formation in turbulent LP methane-air flames; and (iii) to provide a data base for evaluation and refinement of existing engineering models of emissions for gas-fired, lean premixed combustion turbines. The optical measurements include major species concentrations, temperature, and OH along with the pollutants NO and CO. The nonintrusive diagnostics program is a collaborative effort of Vanderbilt University, Sandia National Laboratories, and Wright Air Force laboratories.

In this paper, we present results of major species (CH_4, O_2, N_2, H_2O, CO_2), temperature, OH, and the pollutants (NO and CO) from a lean premixed bluff body stabilized turbulent combustor burning methane. Extensive measurements ranging from 0.1 diameters to 6 diameters downstream of the bluff body were performed to map the flow field of the combustor. The combustor and the flame parameters were chosen to match the conditions for which Pan and co-workers have reported velocity and temperature measurements using Laser Doppler Anemometry (LDA) and Coherent Anti-Stokes Raman Spectroscopy (CARS) respectively (Pan et al., 1991 a, b, 1992 a, b). These multiscalar measurements, along with the reported velocity measurements will provide insight into the NO_x and CO formation in the combustor.

Approach

The strategy for the Rayleigh/Raman/Laser Induced Fluorescence (LIF) measurements was as follows: spontaneous Raman scattering was used to obtain the quantitative single-pulse major species concentrations and the pollutant CO. In the present experiment (LP CH_4-air environment), the major species were the fuel (CH_4), the oxidizer (O_2 & N_2), and the products (H_2O & CO_2). Temperature was determined from the strong Rayleigh scattering signal which was monitored simultaneously. The Rayleigh signal was converted to temperature by a species weighted scattering cross-section (from the Raman measurements). The Rayleigh scattering cross-sections were calculated from the index of refraction data of Gardiner (Gardiner et al., 1981). The minor species, OH and NO, were measured by separate lasers using linear (or near-linear) laser induced fluorescence. The LIF signals from the minor species (NO and OH) were then corrected on a single-shot basis for quenching (which is species dependent) and population fraction (which is temperature dependent), to obtain their quantitative values. Temperature was also obtained for each laser shot from the measurements of species concentrations by invoking the perfect gas law.

Diagnostic System

A schematic of the experimental system is shown in Fig. 1. The lean premixed combustor was mounted at the exit of a vertical wind tunnel contraction which could be translated along the three axes. The beam from a Nd:YAG laser (532 nm, ~750 mJ/pulse, 5 Hz) was used for Raman (major species and CO) and Rayleigh (temperature) measurements. This laser has a pulse length of 5 ns which is stretched to 200 ns to avoid laser induced breakdown at the focal volume. The LIF measurements of minor species (NO and OH) were accomplished with two separate Nd:YAG-pumped dye laser systems. A fourth Nd:YAG laser system shown in the figure for measurements of CO by LIF (higher accuracy) will be incorporated in the next set of measurements (scheduled for May, 1996). The three laser beams were combined into a common axis, using two dichroic mirrors, and focused into

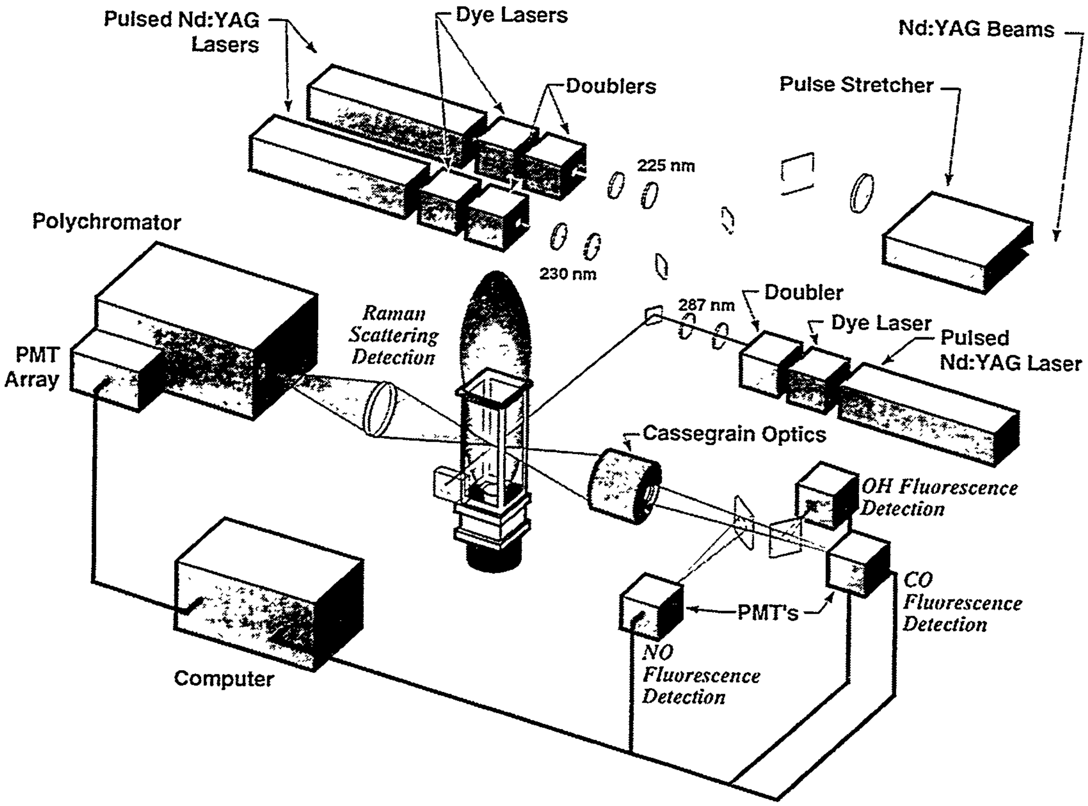

Fig. 1. Schematic of the Rayleigh/Raman/LIF diagnostic system.

the test section. The 532 nm beam was retroreflected into the measurement volume using a prism to effectively double the Rayleigh and Raman signals. The spatial resolution of the measurements was ~ 800 μm in each direction, and the delays between each of the three pulses were ~1 μs. The laser firing sequence was as follows: NO laser, followed by the OH laser and finally the 532 nm laser for Rayleigh/Raman measurements.

The scattered Raman and Rayleigh signals were collected using a six-element achromat and collimated using a conventional camera lens. The collimated light was relayed to photomultiplier tubes (PMT's) aligned at the exit plane of a 0.75-m spectrometer. Fluorescence signals from OH and NO were collected using Cassegrain optics located on the other side of the test section as shown in Fig. 1. A dichroic mirror separated and relayed the NO and OH fluorescence signals to separate detectors.

For OH excitation-detection, the frequency-doubled output for one of the dye lasers was tuned to the $O_{12}(8)$ transition in the $A^2\Sigma^+$ - $X^2\Pi$ (1, 0) band ($\lambda = 287.9$ nm). Colored glass filters were placed in front of the OH detector to capture much of the fluorescence from the dominant (1, 1), (1, 0), and (0, 0) bands, where the (0, 0) fluorescence is preceded by vibrational energy transfer. For NO excitation, the second dye laser was tuned to the $R_1(18)$ transition in the $A^2\Sigma^+$ - $X^2\Pi$ (0, 0) band. This state is reasonably isolated from the neighboring NO lines, and the ground state is populated over a wide range of temperatures, including room temperature. A solar-blind PMT (Hamamatsu R166) and Schott UG-5 colored glass filters were used for detection of NO signals. This arrangement allowed collection of fluorescence from the system of NO bands at 236, 247, 259, and 271 nm. The NO measurements were performed with a slight degree of saturation, which were accounted and corrected during data processing.

Wavelengths of the laser beams of NO and OH were each monitored indirectly by measuring fluorescence from two small premixed CH_4-air flames. The line widths and shifts of the two dyes lasers were constantly monitored during the course of the measurements and were adjusted as necessary to remain line-centered on the NO and OH transitions. Detailed descriptions of the experimental system have been reported previously (Barlow et al., 1990; Barlow and Carter, 1994).

Signal Calibration

The diagnostic system was calibrated for temperature dependent calibration factors and cross-talk between the Raman channels, to convert the raw signals to absolute species concentrations and temperature. This was accomplished by measuring signals in laminar adiabatic flames over a wide range of equivalence ratios. The O_2, N_2, H_2O, and H_2 Raman signals and the OH LIF signals were calibrated in H_2-air flames over an uncooled multi-element Hencken burner for equivalence ratios ranging from 0.2 (fuel lean) to 1.7 (fuel rich). The heat loss from the burner is negligible at sufficiently high flowrates and the flowfield at this location (~4 cm downstream) is uniform and at adiabatic equilibrium. The radiative heat losses in H_2-air flames for this burner are ~20-40 K. The calibration results are shown in Fig. 2. The lines in the figure show laminar adiabatic equilibrium calculations obtained using STANJAN (Reynolds, 1986). The calibrations show good agreement with the theoretical equilibrium curves. The single-pulse standard deviations of species concentrations, temperature, and mixture fraction are shown as error bars in Fig. 2.

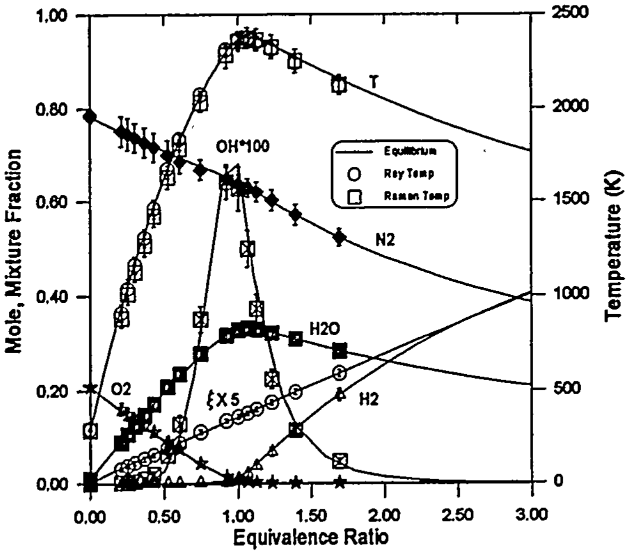

Fig. 2. Calibration results of the major species concentrations (O_2, N_2, H_2O, and H_2), OH, and temperature at various equivalence ratios in a laminar H_2-air flat flame. The lines show calculations for a laminar equilibrium flowfield. The error bars denote the single-shot uncertainty (± one standard deviation) in the measurements.

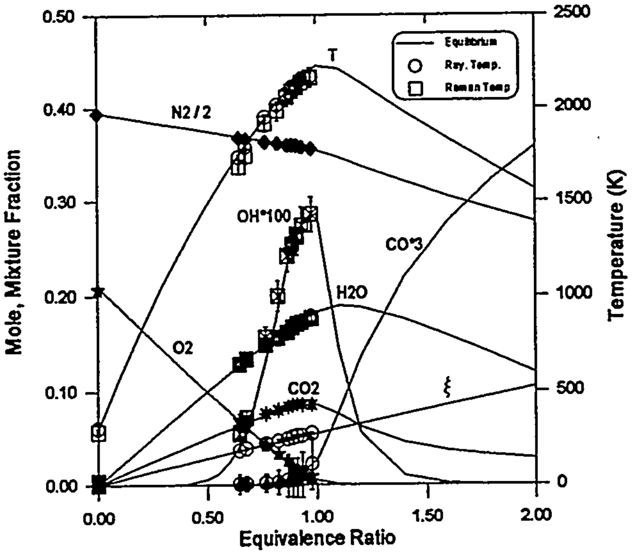

Fig. 3. Calibration results of the major species concentrations (O_2, N_2, H_2O, CO_2, and CO), OH, and temperature at various equivalence ratios in a laminar CH_4-air flat flame. The lines show calculations for a laminar equilibrium flowfield. The error bars denote the single-shot uncertainty (± one standard deviation) in the measurements.

Similar calibrations were performed in CH_4-air flames over the Hencken burner. The Raman signals from O_2, N_2, H_2O, CO_2, CO and the LIF signals from OH were calibrated in this flame. The radiative heat losses in CH_4 flames in the burner are slightly higher (~ 30-50 K) than those of the hydrogen flames due to the presence of CO_2. The calibration results in CH_4 flames are shown in Fig. 3. Thus temperature dependent calibration factors are derived for all the major species that are monitored except CH_4, since CH_4 decomposes readily even at moderate temperatures and no CH_4 is present even in rich CH_4 flames. Therefore, a constant calibration factor which was measured in CH_4 at ambient temperature was used.

The NO system was calibrated using laminar CH_4/N_2/O_2 flames over a McKenna burner. Naturally occurring NO concentrations in these flames are very small (~7 ppm) for reliable calibration of the diagnostic system. Hence, these flames are doped with known concentrations of NO (~ 30 ppm) for calibration of the NO LIF system. The flame was so chosen because the destruction of doped NO in these flames is small (Reisel et al., 1993). Detailed descriptions of calibration procedures have been documented in the literature (Barlow and Carter, 1994).

Measurement Uncertainty and Shot Noise

The single-shot uncertainties in the measurements were obtained from standard deviations of the measurements performed in the laminar adiabatic flame of the Hencken burner which was used for system calibration. Typical single-pulse uncertainties of species concentrations, temperature, and mixture fraction (ξ) are shown in Figs. 2 and 3 as error bars (± one standard deviation). The uncertainties are primarily due to the shot noise resulting from the photoelectron emission process of the photocathode. However, these uncertainties also include contributions from the instrument noise and fluctuations in the flame conditions.

In addition to these uncertainties, the LIF measurements (OH and NO) are subject to systematic errors due to the wavelength drift of the dye lasers from the line center. The maximum resulting uncertainties are estimated to be ~5% for OH and 10% for NO. The sensitivity of the NO LIF system is sufficient to obtain useful measurements below 10 ppm.

LP Combustor and Flame Parameters

Fig. 4 shows the combustor which was used for the experiments. Fuel (CH_4) and air are premixed upstream (~3 m) and the cold premixed fuel-air mixture is injected radially at the base of the combustor. Screens and honeycombs are placed in the combustor to make the flow uniform. A stainless steel conical bluff body of base diameter (d = 44.45 mm) and apex angle ($\theta = 45°$) served as the flame stabilizer. The bluff body was mounted coaxially in a 79 mm x 79 mm x 284 mm combustor test section. The blockage ratio with this configuration was 25%. The test section has rounded corners with four

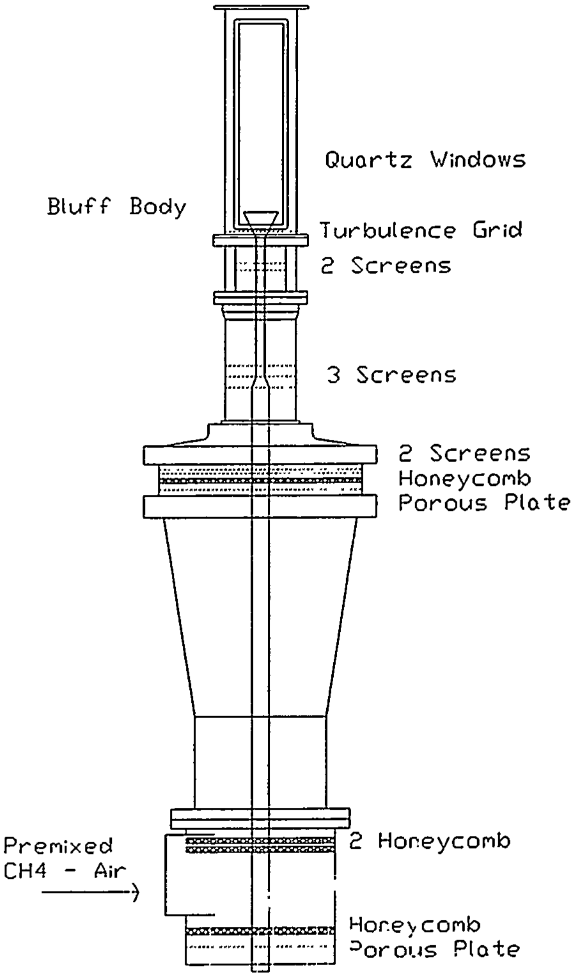

Fig. 4. Schematic of the bluff-body stabilized lean premixed CH_4-air turbulent combustor.

56.4 mm x 254 mm cutouts for mounting windows. Quartz windows were mounted on the signal receiving side of the diagnostic system. However, on the other side (where the laser beams pass through), the quartz windows were replaced by windows made of high temperature resistant (~2000° F) fiberfrax. This was primarily due to the fact that the energy density of the 532 nm YAG laser was higher than the damage threshold of the quartz windows. Small holes of 9.5 mm diameter were drilled through the fiberfrax to let the three laser (YAG and dye) beams to pass through. Small holes were chosen so that they would not significantly alter the flowfield in the combustor and still let the laser beams to pass through with sufficient clearance. A turbulence grid was placed at the entrance of the section at 58 mm upstream of the bluff body. The reference velocity at the entrance of the test section in this configuration was 15 m/s. The free stream turbulence and the velocity ratio (u_{rms}/S_L) are 24% and 30 respectively. The combustor is mounted on a vertical wind tunnel contraction which could be traversed along three axes.

The flame parameters in the present experiment correspond to an air flow rate of 3962 slpm (standard liters per minute) and fuel (CH_4) flow rate of 244 slpm, resulting in an equivalence ratio (ϕ) of 0.586 and an adiabatic flame temperature (T_{ad}) of 1641 K. The combustor produces a cone-stabilized premixed flame, which is shown in Fig. 5. The flame is stabilized by the bluff body (cone), with a recirculation zone which extends to about a diameter downstream, a shear layer or an annular flame zone, and a post flame zone. Rayleigh/Raman/LIF measurements were performed at various axial and radial locations on the combustor. In addition to the optical measurements, the pollutants (CO and NO_x) in the exhaust plane (x/d = 6.0) were measured with gas sampling probes. Table 1 summarizes the optical and gas sampling probe measurements. For brevity, only measurements at locations shown in bold (see Table 1) are presented in this paper.

Shadowing. Shadowing factors for the Raman, Rayleigh, and LIF signals were measured at each axial location, to account for the change in the solid angle of collection and obstruction of the signal due to the bluff body and/or the test section. Typical shadowing of the signals at 0.1 diameters downstream are

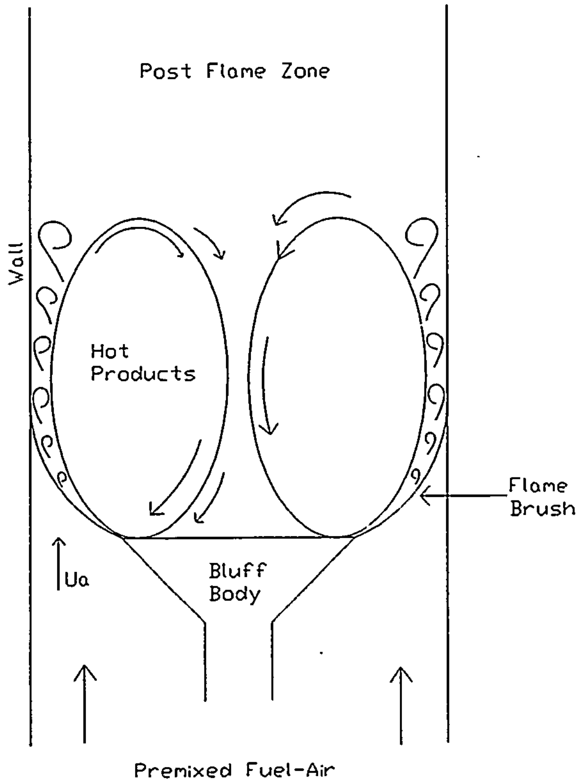

Fig. 5. Turbulent flame structure enveloping the recirculation zone of the bluff body stabilized combustor.

shown in Fig. 6. It is evident from the figure that at radial locations greater than 0.50 diameters, the signals decrease due to test section shadowing. A greater concern with shadowing was the increase in the Rayleigh background at large r/d. The Rayleigh background is almost seven-fold at x/d = 0.55 relative to x/d = 0 (see figure). This Rayleigh background signal is primarily due to the surface scatter from the location where the YAG laser clears the hole in the fiberfrax window. The 532 nm laser beam used for monitoring the Rayleigh signal is focused into the sample volume at a small angle, in order to accommodate retroreflection (see Fig. 1). Therefore, as the burner is traversed radially outward (which corresponds to moving the burner towards/away from the laser beam), the

Table 1. Summary of optical and gas sampling probe measurements.

Measurements	Streamwise location (x/d)	Comments
Optical Diagnostics (Major Species§, temperature, CO, OH, and NO)	**0.1**, 0.3, **0.6**, 0.8, 1.0, 1.2, 1.5, 2.0, **6.0** (exhaust plane)	Radial profiles at intervals of r/d = 0.05
Gas sampling probes (NO/NO_2 and CO)	**6.0** (exhaust plane)	Radial profiles at intervals of r/d = 0.1

§ Major species denote CO_2, CH_4, H_2, O_2, N_2, and H_2O.

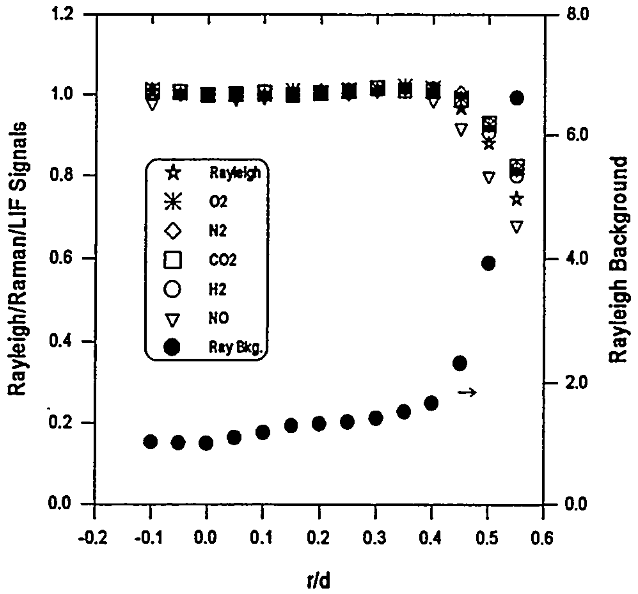

Fig. 6. Typical radial profiles of the Rayleigh/Raman/LIF shadowing factors and the Rayleigh background at x/d = 0.1.

laser beam does not clear the hole as it would at r/d = 0. Moreover, this shadowing of the Raman/LIF signals and the increase in the Rayleigh background were a function of the axial location. Therefore, the shadowing factors were quantified at each location and accounted for during data processing.

Results and Discussion

Radial profiles of the average major species mole fractions, temperature, mixture fraction, CO, OH, and NO at x/d = 0.1 are shown in Fig. 7. The bluff body and the quartz window (denoted as wall) are shown in the figure to facilitate the physical visualization of the combustor. The equilibrium values of the species concentrations, and temperature corresponding to the operating equivalence ratio (0.586) are also shown in the figure. Typically 600-1000 laser shots were registered at each radial location. In the recirculation zone (r/d < 0.5), the mean values of the species and temperature are fairly constant and close to their equilibrium values. The temperature in the recirculation zone (1540 K) is ~6% less than the adiabatic equilibrium temperature (1641 K). The results suggest that the recirculation zone loses about 6% of its heat to the environment, part of it to the bluff body.

Almost half a century back, Longwell proposed that the recirculation zone can be modeled as a "perfectly well stirred reactor" (Longwell et al., 1953). The results suggest that the recirculation zone is almost, but not "perfectly well stirred". More recently,

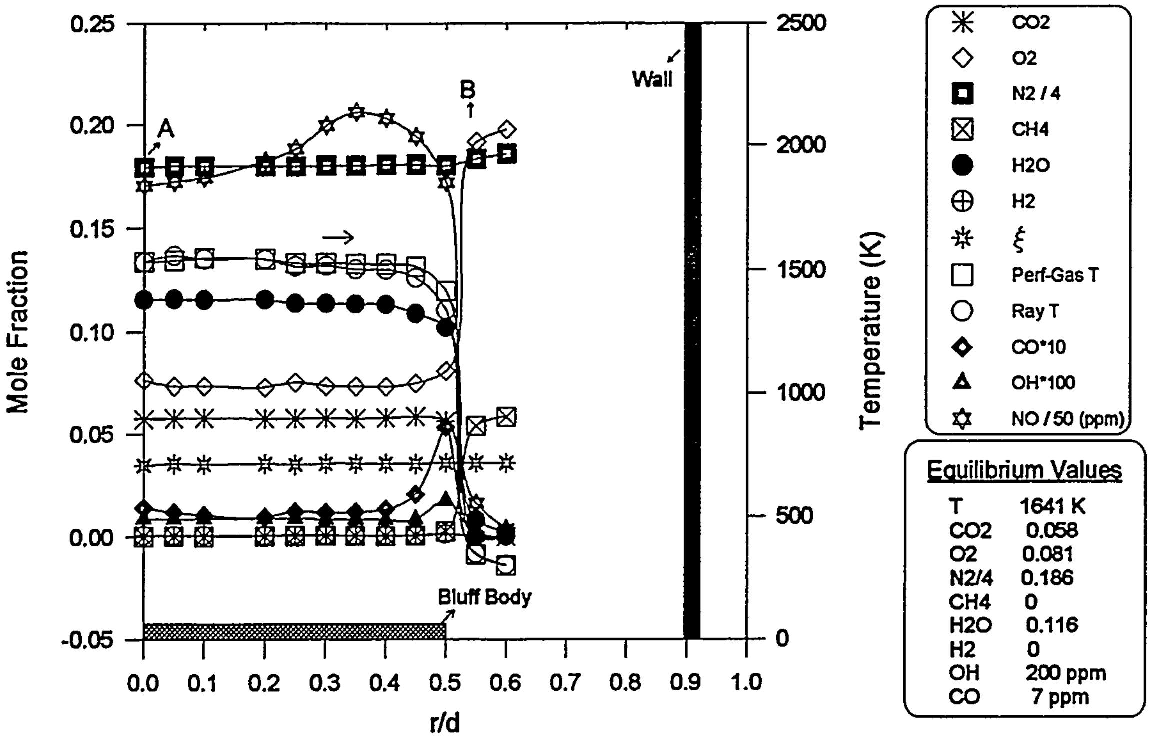

Fig. 7. Radial profiles of the mean species mole fractions, temperature, and mixture fraction at x/d = 0.1.

modellers (Swithenbank et al., 1980; Pratt, 1980) have proposed models of "partially stirred reactors (PSR)" and "imperfect micromixing". In these models the recirculation zone is modeled a PSR with a certain fuel-air recycle from the outside. Hitherto, due to the lack of measurements, modellers have assumed and modeled the recirculation zone with recycle ratios (1 - T/T_{ad}) of ~10-30%. However measurements from Fig. 7 show that the recycle ratio is 6% (1 - 1540/1641). This indicates that the breakthrough of fuel and air through the shear layer into the recirculation zone is much smaller than what the modellers believed. At r/d > 0.5, the temperature drops steeply from 1600 K to ambient (300 K). This cold reactant region is characterized by the unburnt fuel (X_{CH4} = 0.05), air (X_{N2} = 0.76, X_{O2} = 0.19), and the absence of products (H_2O and CO_2) and intermediate radicals (OH, CO, and NO). In the region between the recirculation zone and the cold premixed fuel/air lies a thin annular flame. The presence of this flame zone can be seen from the hydroxyl (OH) profile which peaks to 200 ppm at r/d = 0.5, which corresponds to the edge of the bluff body. The radial profile of CO also peaks at this point, with the peak CO values of 5000 ppmv. The CO concentrations based on equilibrium concentrations are very small (7 ppmv). This clearly points to the need of well refined engineering models that can accurately predict the pollutants in LP gas turbines. The NO concentrations in this region are relatively small, ~10 ppmv.

The radial profiles of the rms of the species and temperature are shown in Fig. 8. The profiles are fairly constant in the recirculation zone (r/d < 0.5). The rms profiles of fuel (CH_4), oxidizer (O_2, N_2), and temperature peak at r/d = 0.55, the region where the cold premixed fuel-air from regions of r/d > 0.55 exchanges heat and mass to the hot combustion products of the recirculation zone. Note that the rms of Rayleigh temperature is smaller

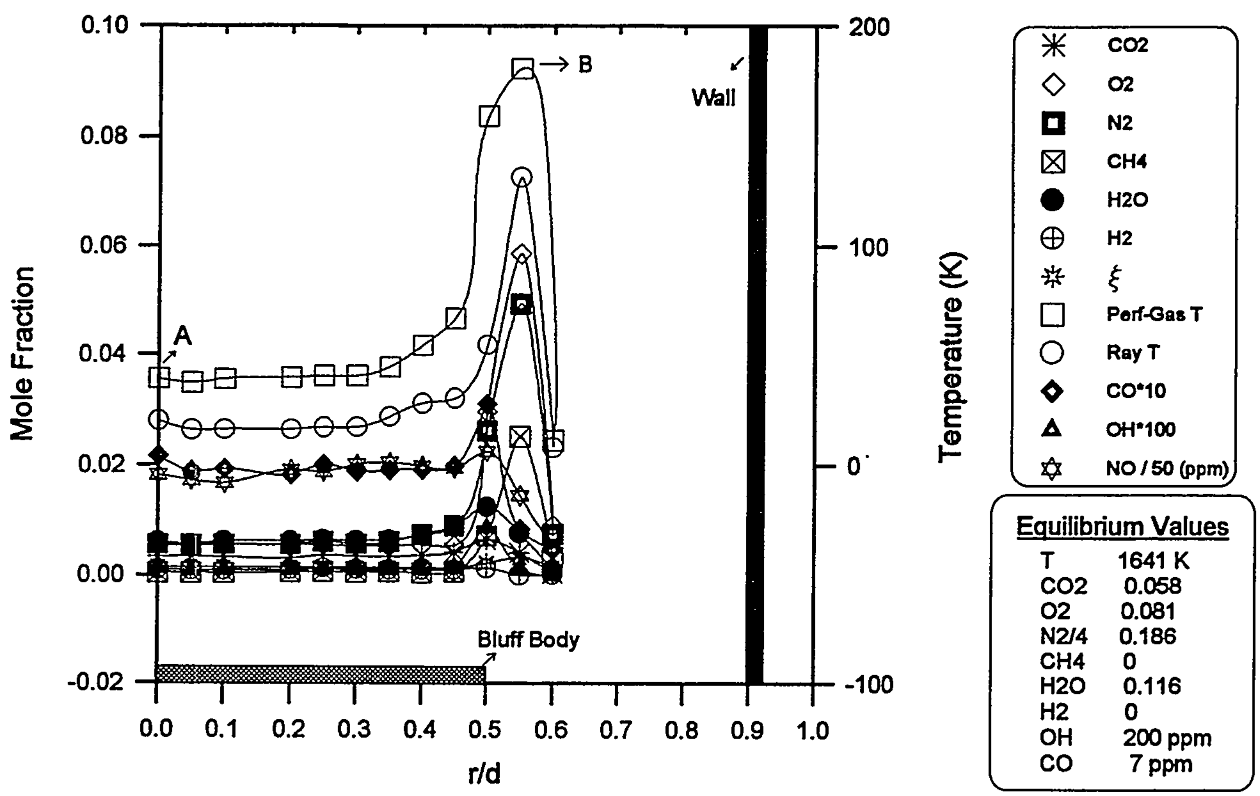

Fig. 8. Radial profiles of the rms species mole fractions, temperature, and mixture fraction at x/d = 0.1.

than that of the Raman perfect gas temperature (temperature calculated from the Raman species concentrations by invoking the perfect gas law). This is primarily due to reduced shot noise in the strong Rayleigh signals as opposed to the Raman signals. The rms profiles of the products (CO_2 and H_2O), the intermediate radical species (OH), and the pollutants (NO and CO) peak slightly inward at x/d = 0.5, the region of the annular flame zone (see OH profile of Fig. 7).

Scatter plots of the measured species mole fractions corresponding to points A and B in Fig. 7 (or 8) are plotted versus temperature in Figs. 9 and 10. Each scatter plot shown is an ensemble of 800 laser shots. Scatter plots such as these provide an overview of the chemistry as each point gives an instantaneous picture of the flame. The horizontal lines in the figures are the adiabatic equilibrium values of the major species (CH_4, O_2, CO_2, and H_2O) and OH corresponding to an equivalence ratio of 0.586. The data in the recirculation zone (Fig. 7) is confined to a narrow temperature band (~250 K). Moreover, the major species mole fractions are very close to their equilibrium values; the oxidizer (O_2) and N_2 (not shown here) are slightly below equilibrium and the products (H_2O and CO_2) are at superequilibrium. All the traits in the data are consistent with the well-stirred reactor concept of the recirculation zone. The CO, OH, and NO concentrations at this location are 740 ppm, 100 ppm, and 5 ppm respectively. In contrast to point A, which is in the recirculation zone, the data at point B (Fig. 10) lies over a broad range of temperature ranging from ambient (300 K) to adiabatic equilibrium temperature (1641 K), due to the turbulent mixing of the cold reactants with hot products. The residence times at this point are small,

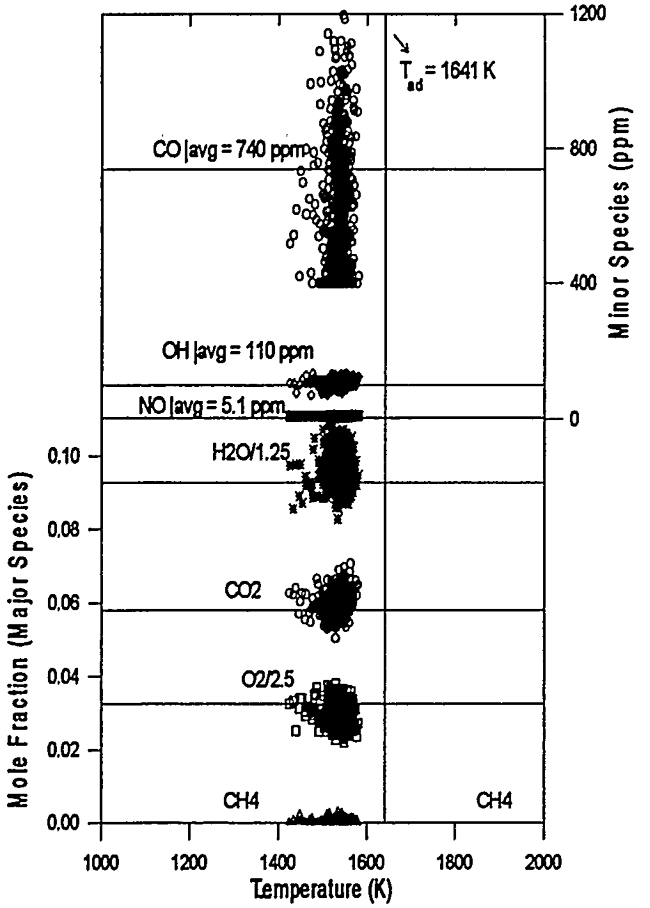

Fig. 9. Scatter plots of measured species mole fractions versus temperature in the combustor at x/d = 0.1 and r/d = 0 (Point A of Figs. 7 and 8). The equilibrium compositions of the major species and OH corresponding to an equivalence ratio of 0.586 are shown.

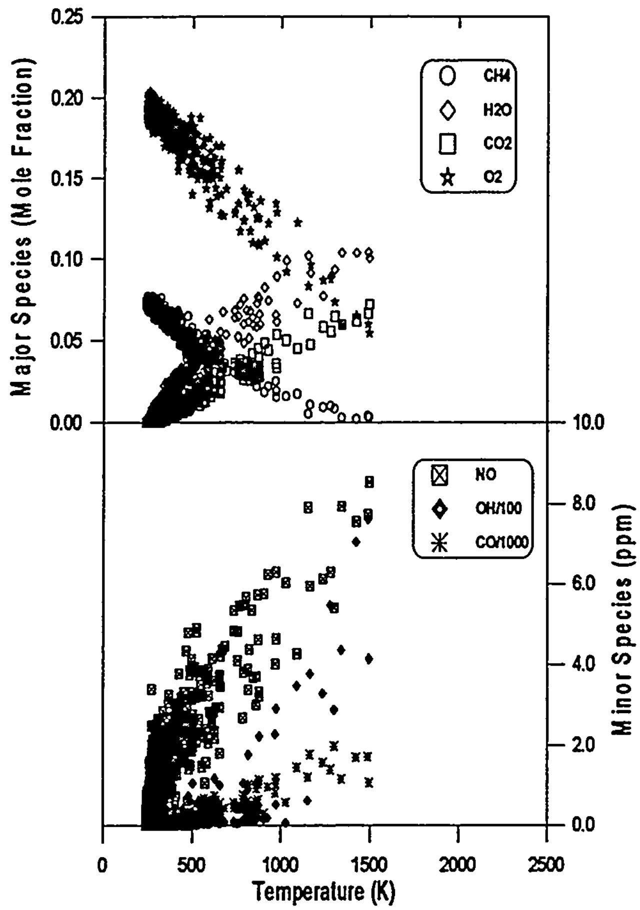

Fig. 10. Scatter plots of measured species mole fractions versus temperature in the combustor at x/d = 0.1 and r/d = 0.55 (Point B of Figs. 7 and 8). The equilibrium compositions of the major species and OH corresponding to an equivalence ratio of 0.586 are shown.

and this can be seen by the high intermediate radical concentrations. Superequilibrium OH values of 800 ppm, up to 4 times the equilibrium values (200 ppm) were recorded. The peak CO concentrations are ~2000 ppm, and the peak NO concentrations are ~10 ppm.

Mean and rms radial profiles of the species concentrations, and temperature at x/d = 0.6 are shown in Figs. 11 and 12. There are no significant differences in the mean and rms measurements of the major species and temperature, when compared to their counterparts at x/d = 0.1 (see Fig. 7). The results are consistent with the heat transfer arguments invoked earlier. However, the maximum NO concentrations at this location are ~8 ppm, slightly smaller from the peak values of 10 ppm at x/d = 0.1. The OH and CO profiles are broader than their corresponding counterparts at x/d = 0.1. This shows evidence of shear layer growth as we move downstream.

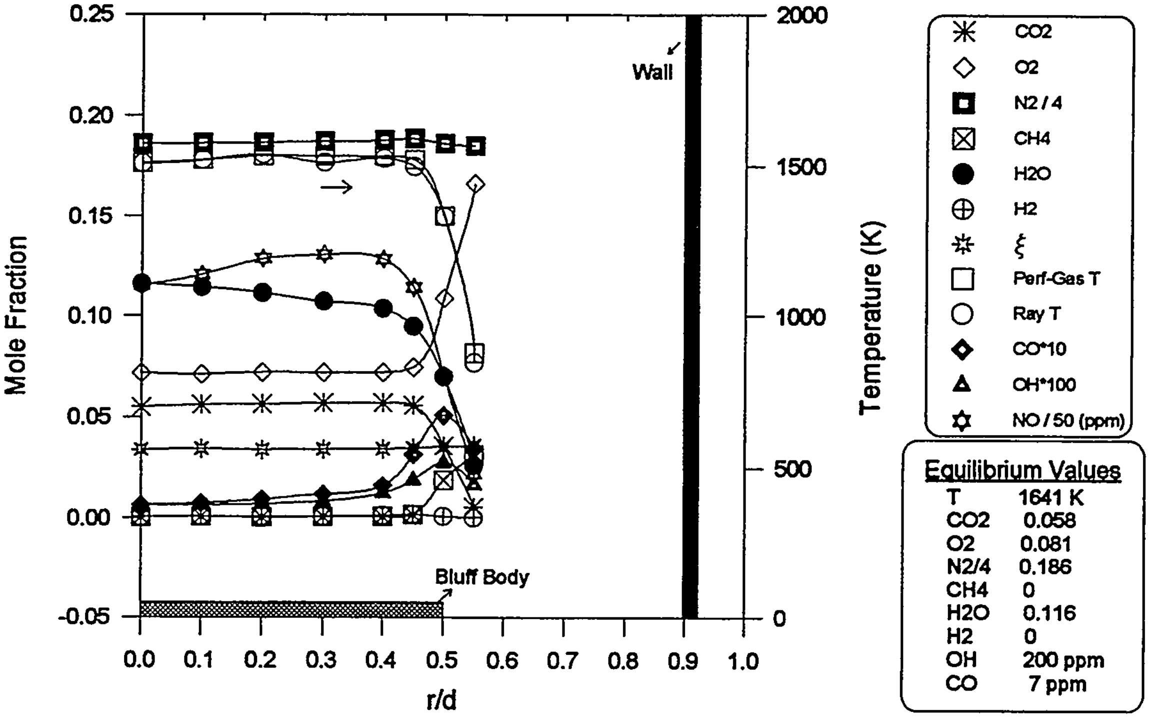

Fig. 11. Radial profiles of the mean species mole fractions, temperature, and mixture fraction at x/d = 0.6.

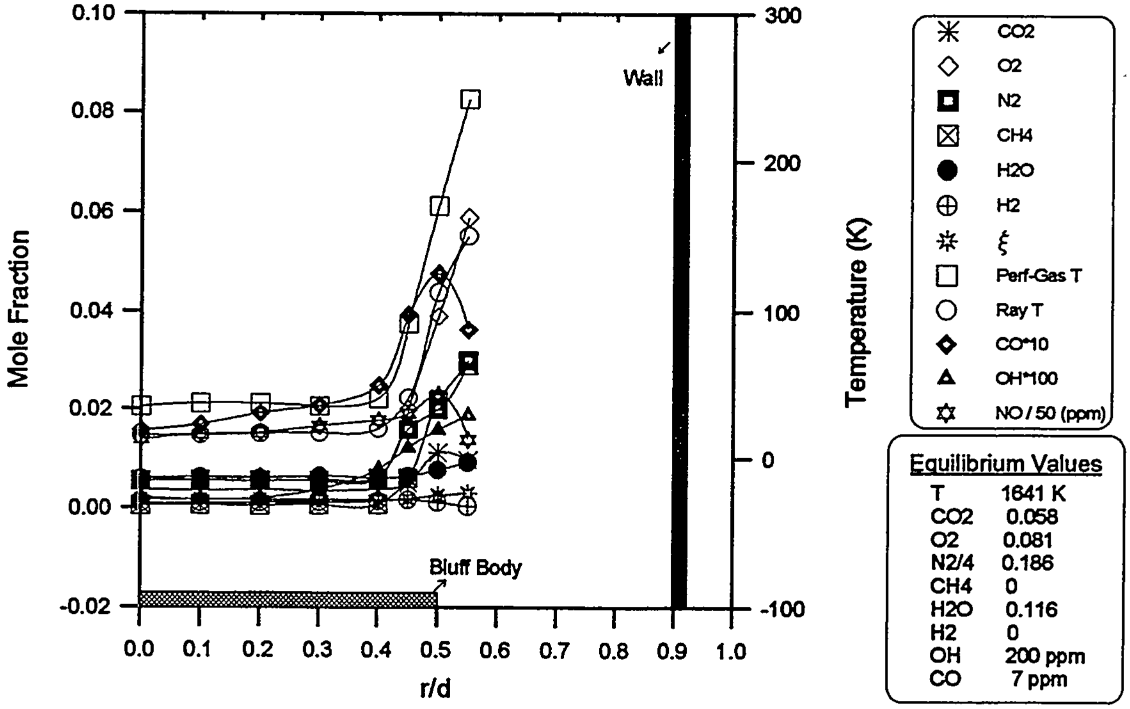

Fig. 12. Radial profiles of the rms species mole fractions, temperature, and mixture fraction at x/d = 0.6.

The shear layer growth is caused by the entertainment process, where isolated pockets of hot products (from the recirculation zone) and cold reactant gases (from the premixed fuel-air stream) are entrained into the shear layer (Pan et al., 1991b).

The mean and rms radial profiles at the exhaust plane of the LP combustor (x/d = 6.0) are shown in Figs. 13 and 14. At this downstream location where there has been sufficient time for the reactants to combine, the major species and temperature are fairly constant across the burner and correspond to adiabatic equilibrium values. The CO concentrations increase as we approach the wall. This increase in the CO concentrations is possibly due to quenching effects from the cold wall. The exhaust plane NO concentrations are about 6 ppm.

Probe Measurements. The exhaust pollutants (NO/NO_x and CO) were also measured with gas sampling probes. The NO/NO_x measurements were performed with a chemiluminescent gas analyzer, and CO was measured with a nondispersive infrared (NDIR) detector. Probe descriptions and calibration procedures have been reported previously in great detail (Mellor, 1994). Optical and gas sampling probe measurements of the exhaust pollutants (NO and CO) at x/d = 6 are shown in Fig. 15. The laser based (LIF) NO measurements agree with the gas sampling probe measurements within 2 ppm. However, the CO concentrations measured with the laser are about 10 times larger than the corresponding probe measurements. The reduced CO concentrations in the probe measurements are due to the oxidation of CO to CO_2 in the warmer sections of the probe via the reaction, CO + OH → CO_2 + H. The oxidation of CO to CO_2 in gas sampling probes have been reported in the literature (Kramlich and Malte, 1978; Nguyen et al., 1994). In lean premixed flames where there are considerable CO

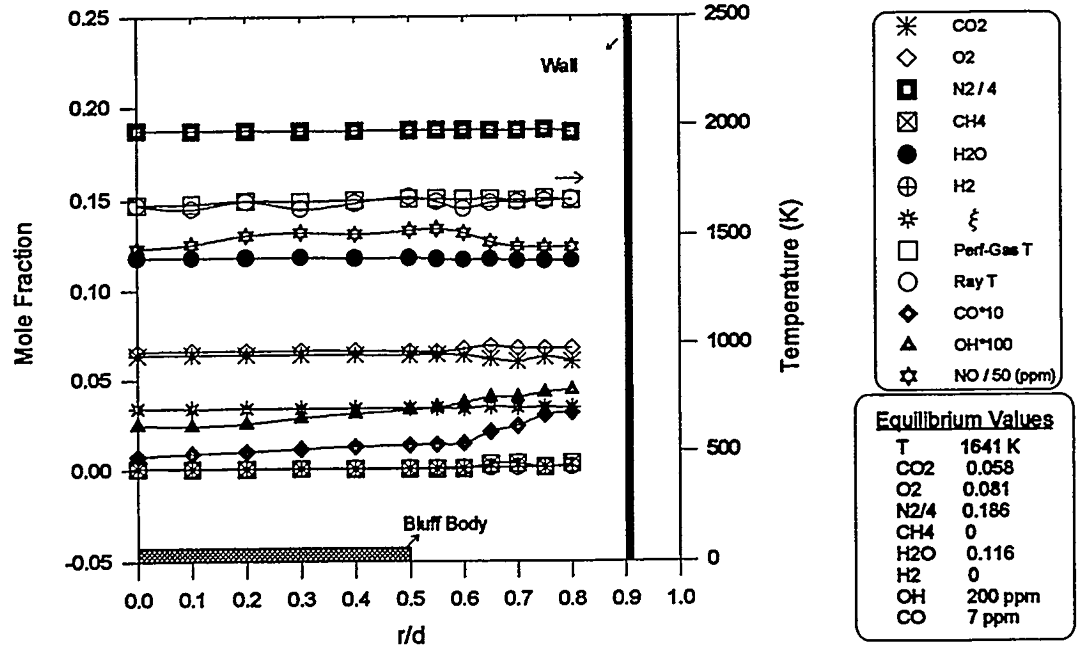

Fig. 13. Radial profiles of the mean species mole fractions, temperature, and mixture fraction at x/d = 6.0.

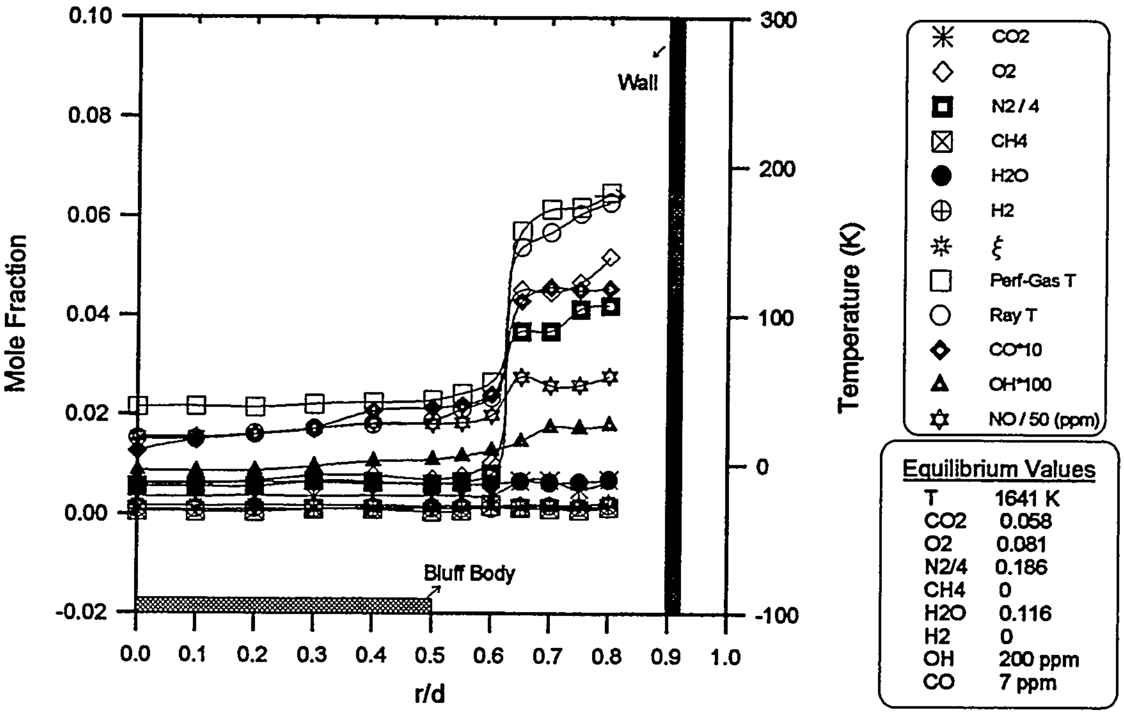

Fig. 14. Radial profiles of the rms species mole fractions, temperature, and mixture fraction at x/d = 6.0.

concentrations, the extraction gas sampling probes can be increasingly inaccurate.

Conclusions

Simultaneous and instantaneous time-resolved point measurements of major species (CO_2, CH_4, H_2, O_2, N_2, and H_2O) concentrations, temperature, and minor species (CO, NO and OH) concentrations were obtained using a combination of spontaneous Raman scattering, Rayleigh scattering, and laser-induced fluorescence in a turbulent lean premixed methane combustor. The fluorescence signals of NO and OH were corrected for Boltzman fraction and collisional quenching rates on a shot-to-shot basis. The detection limit of the NO measurements was ~4 ppm at 1550 K (Number density of 2 x 10^{13} cm^{-3}) in a calibration flame.

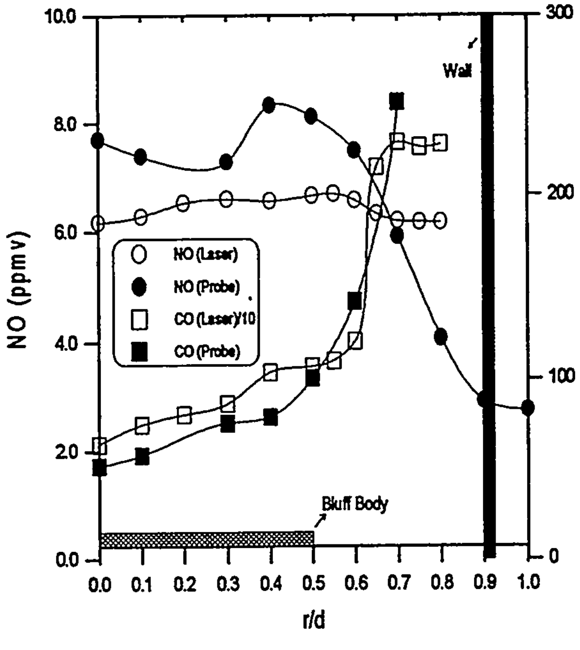

Fig. 15. Laser based and gas sampling probe measurements of exhaust pollutants (NO and CO) at x/d = 6.0.

The results of species concentrations and temperature in the recirculation zone show that the recirculation is not a perfectly stirred reactor. Measurements indicate that the recirculation resembles a partially stirred reactor. The measured recycle ratio in the recirculation is ~6%. This is quite different from the recycle ratios of 10-30% which the modellers are currently using to model LP gas turbines. This suggests that the breakthrough of the reactants into the recirculation quite small (~6%) as opposed to the nominal value of 25% used in the models. Annual shear layer growth by the edge of the recirculation zone was evident with downstream distance.

Measurements of NO in the exhaust plane (x/d = 6) of the combustor revealed relatively low concentrations of NO (~6 ppm). However, the CO concentrations in the exhaust were high ~1000 ppm. The laser based measurements of CO were about 10 times larger than the gas sampling probe measurements. This suggests that the catalytic reactions in the probe make extraction probe techniques for CO measurement quite inaccurate.

Currently, CO is measured by Raman scattering. However, the CO Raman signals are weak, resulting in poor measurement accuracy. In the next set of measurements, CO will be measured by LIF. Furthermore, the turbulence levels will be varied by varying the free-stream turbulence, and measurements of species, temperature, OH, NO, and CO will be performed. The effects of the variation in the blockage ratio and turbulence intensity on pollutant formation will be investigated.

Acknowledgments

This research was funded by the U.S. Department of Energy Technology Center under Contract No. DE-FC21-92MC29061, for the period of performance beginning September 1, 1993 and ending August 31, 1996. The work at Sandia National Laboratories was supported by the United States Department of Energy, Office of Basic Energy Sciences. The authors wish to acknowledge the METC Contracting Officer's Representative, Dr. Norman Holcombe. We also thank Dr. Mel Roquemore of Air Force Wright Laboratories, for lending the LP combustor.

References

Barlow, R. S., Dibble, R. W., Chen, J. Y., and Lucht, R. P. (1990), *Combustion and Flame* **82**, pp. 235-251.

Barlow, R. S., and Carter, C. D. (1994), *Combustion and Flame* **97**, pp. 261-280.

Dibble, R. W., Masri, A. R., and Bilger, R. W. (1987), *Combustion and Flame* **67**, pp. 189-206.

Dibble, R. W., Stårner, S. H., Masri, A. R., and Barlow, R. S. (1990), *Applied Physics B* **51**, pp. 39-43.

Drake, M. C., Correa, S. M., Pitz, R. W., Shyy, W., and Fenimore, C. P. (1987), *Combustion and Flame* **69**, pp. 347-365.

Driscoll, J. F., Chen, R. H., and Yoon, Y. (1992), *Combustion and Flame* **87**, pp. 37-49.

Gardiner, W. C., Hidaka, Y., and Tanzawa, T. (1981), *Combustion and Flame* **40**, pp. 213-219.

Kramlich, J. C., and Malte, P. C. (1978), *Combustion Science and Technology* **18**, pp. 91-104.

Longwell, J. P., Frost, E. E., and Weiss, M. A. (1953), *Industrial and Engineering Chemistry* **47**, No. 8, pp. 1634-1643.

Mansour, M. S., Bilger, R. W., and Dibble, R. W. (1988), *Twenty-Second Symposium (International) on Combustion*, The Combustion Institute, Pittsburgh, pp. 711-719.

Mansour, M. S., Bilger, R. W., and Stårner, S. H. (1989), *Combustion Science and Technology* **65**, pp. 83-101.

Mansour, M. S., Bilger, R. W., and Dibble, R. W. (1990), "Turbulent Premixed Flames of Methane near Extinction in a Reverse Flow reactor," *Second International Workshop on Turbulent Premixed Combustion*, CNRS, Paris.

Mansour, M. S., Bilger, R. W., and Dibble, R. W. (1991), *Combustion and Flame* **85**, p. 215.

Masri, A. R., Bilger, R. W., and Dibble, R. W. (1987a), *Combustion and Flame* **68**, pp. 109-119.

Masri, A. R., Bilger, R. W., and Dibble, R. W. (1987b), *Combustion and Flame* **71**, pp. 245-266.

Masri, A. R., Bilger, R. W., and Dibble, R. W. (1987c), *Combustion and Flame* **73**, pp. 261-285.

Mellor, A. M. (1994), "NO_x and CO Emissions Models for Gas-Fired, Lean, Premixed Combustion Turbines: AGTSR Semi-Annual Report 1," *Vanderbilt University.*

Nguyen, Q. V., Edgar, B. L., Dibble, R. W., and Gulati, A. (1995), *Combustion and Flame* **100**, pp. 395-406.

Pan, J. C., Vangsness, M. D., Heneghan, S. P., Schmoll, W. J., and Ballal, D. R. (1991a), "Laser diagnostic studies of confined turbulent premixed flames stabilized by conical bluff bodies: Data set", *University of Dayton Report*, UDR-TR-91-102, July.

Pan, J. C., Vangsness, M. D., Heneghan, S. P., and Ballal, D. R. (1991b), "Scalar measurements in bluff body stabilized flames using CARS diagnostics," *ASME Paper No. 91-GT-302.*

Pan, J. C., Schmoll, W. J., and Ballal, D. R. (1992a), Transactions of ASME, *Journal of Engineering for Gas Turbines and Power* **114**, pp. 33-38.

Pan, J. C., and Ballal, D. R. (1992b), "Chemistry and turbulence effects in bluff body stabilized flames," *AIAA Paper No. 92-0771.*

Pope, S. B. (1990), *Twenty-Third Symposium (International) on Combustion*, The Combustion Institute, Pittsburgh, p. 591.

Pratt, D. T. (1980), "Coalescence/Dispersion Modelling of Gas Turbine Combustors," *Gas-Turbine Combustor Problems*, Edt., A. H. Lefebvre, Hemisphere Publishing, New York, NY, pp. 315-334.

Reynolds, W. C. (1986), "The Element Potential Method for Chemical Equilibrium Analysis: Implementation in the Interactive Program STANJAN," *Stanford University.*

Reisel, J. R., Carter, C. D., Laurendeau, N. M. (1993), *Combustion Science and Technology* **91**, pp. 271-295.

Stårner, S. H., Bilger, R. W., Dibble, R. W., and Barlow, R. S. (1990), *Combustion Science and Technology* **21**, pp. 259-276.

Swithenbank, J., Turan, A., and Felton, P. G. (1980), "Three-Dimensional, Two-Phase Modelling Problems of Gas-Turbine Combustors," *Gas-Turbine Combustor Problems*, Edt., A. H. Lefebvre, Hemisphere Publishing, New York, NY, pp. 249-314.

Vranos, A., Knight, B. A., Procia, W. M., and Chiapetta, L. (1992), *Twenty-Fourth Symposium (International) on Combustion*, The Combustion Institute, Pittsburgh, pp. 377-384.

P3 Lean Premixed Flames for Low NO_x Combustors

P. Sojka, L. Tseng, J. Bryjak (sojka@ecn.purdue.edu; 317-494-1536)
J. Gore, Y. Sivathanu, A. Kelkar, C. Rama (gore@ecn.purdue.edu; 317-494-1452)
N. Laurendeau, M. Klassen, D. Thomsen (laurende@ecn.purdue.edu; 317-494-2713)
Thermal Sciences and Propulsion Center
School of Mechanical Engineering
Purdue University
West Lafayette, IN 47907

Introduction

Gas turbines are being used throughout the world to generate electricity. Due to increasing fuel costs and environmental concerns, gas turbines must meet stringent performance requirements, demonstrating high thermal efficiencies and low pollutant emissions. In order for U.S. manufactured gas turbines to stay competitive, their NO_x levels must be below 10 ppm and their thermal efficiencies should approach 60%. Current technology is being stretched to achieve these goals.

The twin goals of high efficiency and low NO_x emissions require extending the operating range of current gas turbines. Higher efficiency requires operation at higher pressures and temperatures. Lower NO_x emissions requires lower flame temperatures. Lower flame temperatures can be achieved through partially to fully premixed combustion. However, increased performance and lower emissions result in a set of competing goals.

In order to achieve a successful compromise between high efficiency and low NO_x emissions, advanced design tools must be developed. One key design tool is a computationally efficient, high pressure, turbulent flow, combustion model capable of predicting pollutant formation in an actual gas turbine. Its development is the goal of this program.

Achieving this goal requires completion of three tasks. The first task is to develop a reduced chemical kinetics model describing NO_x formation in natural gas-air systems. The second task is to develop a computationally efficient model that describes turbulence-chemistry interactions. The third task is to incorporate the reduced chemical kinetics and turbulence-chemistry interaction models into a commercially available flow solver and compare its predictions with experimental data obtained under carefully controlled conditions so that the accuracy of model predictions can be evaluated. The resulting design tool will be used by U.S. gas turbine manufacturers to design the next generation of lean premixed engines. Such lean premixed flame combustors will satisfy the low NO_x emission needs of the Advanced Turbine Systems (ATS) being developed by several industries under the sponsorship of the Fossil Energy (FE) program of the U.S. Department of Energy (DOE).

Objectives

The overall objectives of the research at Purdue are to:

Research sponsored by the U.S. Department of Energy's Morgantown Energy Technology Center, under contract DE-FC21-92MC29601 with South Carolina Energy Research and Development Center, 386-2 College Avenue, Clemson, SC 29634-5180, Dr. Daniel B. Fant, Telefax: 803-656-2267. Purdue University subcontract No. 93-01-SR009.

- obtain a reduced mechanism description of high pressure NO formation chemistry using experiments and calculations for laminar lean premixed methane air flames,

- develop a statistical model of turbulence - NO chemistry interactions using a Bunsen type jet flame, and

- utilize the high pressure chemistry and turbulence models in a commercial design code, then evaluate its predictions using data from an analog gas turbine combustor.

Work to date has resulted in the following achievements:

- spatially resolved measurements of NO in high-pressure high-temperature flat flames, plus evaluation of the influence of flame radiation on the measured temperature profile

- measurements of temperature and velocity PDFs for a turbulent methane/air flame were obtained for the first time, under operating conditions which allow their study in the distributed regimes, and the increase in $EINO_x$ with equivalence ratio predicted using a chemical kinetics model

- simulation of non-reacting combustor flow fields from ambient to elevated pressure and temperature conditions and comparison of those results with experimental velocity profiles.

Approach

Work is divided into three tasks: reduced chemical kinetics model, turbulence-chemistry interaction model, analog gas turbine modeling and experiments.

Reduced Kinetics Model

In order to determine optimal combustion parameters to minimize pollutants and maintain high efficiency in gas turbine engines, it is necessary to understand the chemical kinetics involved in the production of NO in high-pressure, natural-gas fired, premixed systems. In addition, accurate *in-situ* measurements of NO in these flames are required to verify any computer modeling scheme.

This paper describes recent work in improving both the accuracy of NO measurements in lean-high pressure $CH_4/O_2/N_2$ flames and the accuracy of kinetic modeling for these same conditions. Specifically, this portion of the research is involved in the validation and development of simplified kinetic models for predicting NO formation in these high-pressure lean conditions. To meet these objectives we are measuring NO concentrations in the post-flame zone of a flat, laminar, premixed $CH_4/O_2/N_2$ flame using laser-induced fluorescence. We are modeling NO production using the Sandia laminar premixed flame code. The flame code is being used not only to predict overall NO production in these flames, but to also help determine which NO production pathways are most important in the high-pressure, lean conditions relevant to this study. Knowledge of the pressure dependence of each pathway will be helpful in the later development of a reduced mechanism which may be included in turbulence models for determining NO formation in more realistic turbulent combustors.

In the last six months steps have been taken to improve the accuracy of both the LIF measurements and the modeling, as will be discussed later in this paper.

The laser system and optical layout used in performing the LIF measurements of NO are described elsewhere [Reisel *et al.*, 1993]; thus, only a brief summary will be presented here.

Excitation of NO is achieved through use of the $Q_2(26.5)$ transition of the NO molecule.

A pulsed ultraviolet laser beam is directed over a burner located inside the high-pressure combustion facility described by Carter *et al.* [Carter *et al.*, 1989]. The pressure vessel has four optical ports, two of which provide the optical access and exit for the laser beam through the combustion facility.

For fluorescence detection, we make use of an optical port perpendicular to the laser entrance and exit ports. The fluorescence is focused on the entrance slit of a 1/2-m monochromator. The broadband fluorescence signal encompasses a spectral width of 3 nm and is detected over a spectral region centered at 236 nm. This location and spectral width corresponds to the $\gamma(0,1)$ band of NO.

When performing a linear LIF measurement, one must consider the effects of both laser power fluctuations and quenching variations on the fluorescence signal. Corrections for laser power fluctuations can be made by normalizing the fluorescence signal using the measured laser power. Quenching variations could be handled in a similar manner; however, measurement of the quenching rate coefficient is not a trivial task. Comparisons of measurements obtained using both LIF and laser-saturated fluorescence (LSF) in atmospheric $CH_4/O_2/N_2$ flames demonstrate that the quenching variation is not significant. Additionally, the quenching rate coefficient has been modeled for each of the pressures used in this study. Results for each pressure predict less than a 15% change, with respect to the calibration flame, across our range of equivalence ratios.

Modeling of the chemical kinetics in these flames was performed using the Sandia, steady, laminar, one-dimensional, premixed flame code [Kee *et al.*, 1985]. The mechanism used as the chemical kinetics input into the computer model is based on the comprehensive mechanism assembled by Glarborg *et al.* [1986] as modified by Drake and Blint [1991]. This reaction mechanism considers 49 species and over 200 elementary reactions.

A burner surface temperature of 300 K is used as a boundary condition to simulate the heat loss to the water-cooled burner. A temperature profile generated via solution of the energy equation was used initially for modeling NO production trends. Well-resolved, experimentally measured temperature profiles are not easily obtained at high pressures owing to the close proximity of the flame front to the burner surface. While the calculated temperature profiles will not agree precisely with the actual temperature profiles (leading to some potential errors in quantitative agreement), the calculated post-flame temperatures appear to agree sufficiently with the measured post-flame temperatures so as to allow for an accurate assessment of the pressure trends. Steps taken to obtain more quantitative results are described later in this paper.

Turbulence-Chemistry Interaction Model

Practical gas turbine combustors involve turbulent flames and the residence times available are much smaller than those in the laminar flames studies by the above authors. Analytical studies on premixed turbulent flames have not provided complete insight into their structure. The analytical studies were based on assumptions that are hard to justify. A better study of the turbulent premixed flames can be done by using experimental data in the form of probability density functions (PDFs), length scales etc. of the dependent variables as input into the chemical kinetics models, thereby reducing the complexity of the modeling effort.

The conventional approaches to describing reacting flows in combustors such as gas turbine engines involve moment closure methods [Jones and Whitelaw, 1982], Monte-Carlo or stochastic methods [Ghoniem *et al.*, 1982, Kerstein, 1988], and PDF methods [Kollman, 1990; Pope, 1991].

The moment closure methods involve developing a hierarchy of equations for the different moments for the variables of interest (velocity, concentrations, temperature, etc.). Normally only the first two moments are considered since beyond this the number of modeling constants increases drastically without providing a correspondingly more accurate solution to the governing equations. However, for non-linear processes such as chemical kinetics, describing the temperature by two or even four moments leads to inaccuracies in the solutions for the chemical processes.

Monte-Carlo or stochastic methods include the Random Vortex methods of Ghoniem *et al.* [1982] and the Linear Eddy Model of Kerstein [1988]. These methods have been used with limited success to predict the scalar mixing of fluids. However, in application to reacting flows, they have problems with convergence, produce large errors due to the limited number of realizations and require extensive modeling efforts which are problem specific [Givi, 1987]. In addition, stochastic methods do not guarantee the conservation of mass, momentum and energy and require ad-hoc modeling for diffusion.

Conventional PDF methods [Kollman, 1990; Pope, 1991] are based on deriving transport equations for the PDFs of the variables of interest. The derivation results in an increase in dimension of the governing equations and the solution procedure requires Monte-Carlo simulations with the inherent problems discussed above. In addition, the turbulent convection and molecular diffusion terms have to be modeled, restricting their use to simple problems [Givi, 1987].

Recently, we developed a new approach called the Discrete Probability Function (DPF) method to solve statistical transport equations in the context of radiative heat transfer [Sivathanu and Gore, 1993]. The DPF method relies on the representation of the PDF transport equation using discrete parcels that are affected by convection and diffusion. The transport equations are solved for notional parcels representing realizable values of boundary conditions and source functions, while the probabilities of the solution so obtained are calculated from statistical laws. The DPF method, along with a model of the molecular diffusion process using spatial series analysis was subsequently used to successfully capture the scalar mixing in a shear layer [Sivathanu and Gore, 1994] and evaluated using data from Yoon and Warhaft [1990] and Bilger *et al.* [1991].

To apply the DPF method for calculating the pollutant production in a turbulent premixed flames, the statistics of temperature are required to take into account the non-linear dependence of the Arrhenius reaction rates on temperature. There have been relatively few measurements of the fluctuating temperature in premixed turbulent flames despite the importance of such information for modeling pollutant emission.

Yoshida [1981] studied the structure of hydrogen pilot stabilized premixed flames with equivalence ratios of 0.8 using compensated thin wire thermocouples. From their measurements, they found that the fluctuating temperature increases and reaches a maximum in the middle of the flame zone and decreases to zero outside the flame zone. The temperature fluctuations in the flame zone were found to be close to the predictions of a wrinkled laminar flame model, implying a bimodal PDF for temperature. Yanagi and Mimura [1981], who also studied pilot stabilized natural gas flames using thermocouples, came to the same conclusion.

However, Pita and Nina [1986] concluded that catalytic effects impose severe limitations on the accuracy of mean and fluctuating temperatures measured with coated or uncoated thermocouples. Accurate measurements of temperature are need to model the NO_x formation kinetics in turbulent premixed flames. Therefore, a thin filament pyrometer [Vilimpoc and Goss, 1988] was used to measure the fluctuating temperatures in the present work.

Based on the above observations, the objectives of the present work were to measure the fluctuating temperatures in turbulent premixed flames and to use the PDF of the temperature obtained from the measurement to predict the emission index of NO_x.

Temporally and spatially resolved measurements of velocity and temperature were obtained in a co-flow burner, whose sketch is shown in Fig. 1. Premixed fuel and air was sent through a 15 mm diameter inner tube, which is surrounded by a 100 mm diameter annulus for the co-flow air. Wire mesh and glass beads were used to straighten the flow. The premixed flame was stabilized by passing an annular co-flow of hydrogen through a pilot flame burner. The fuel-tube was cooled by passing water through a cooling coil surrounding the inner tube. The length of the fuel tube was 600 mm to ensure a completely developed pipe flow at the exit of the burner.

The mass flow rates of the fuel, the hydrogen used for the pilot flame and the co-flowing air were measured using calibrated rotameters. The mass flow rate of the air used to premix with the fuel was measured using a calibrated choked orifice. Two different heat release rates (4.2 kW and 8.4 kW) and two equivalence ratios (0.8 and 1.0) for each heat release rate were selected to obtain a total of four premixed turbulent flames. The co-flow of air for all flames was fixed at 0.5 g/s and the mass flow rate of the hydrogen used for the pilot flame was 2 mg/s. The Reynolds number based on cold gas properties at the fuel tube burner exit varied between 7000 and 17000.

The instantaneous temperatures were measured using a 15 mm SiC filament stretched inside the flame [Vilimpoc and Goss (1988]. A schematic of the experimental setup for the thin filament pyrometry technique is shown in Fig. 2. The radiation emitted by the SiC filament was imaged onto a cooled InSb detector (spectral window from 1200 to 5700 nm) through a chopper, aperture, and imaging lenses. The signal was amplified, phase locked, digitized and stored in a laboratory computer at 5000 Hz. The system was calibrated using the known temperatures from a laminar flame. The small size of the filament, low thermal conductivity and high emissivity offered good spatial and temporal response. The resulting data were used to obtain the PDFs of temperatures at all locations within the flames.

The radial and axial velocities were measured using a single component, dual beam Laser Doppler Velocimeter (LDV). Three pollutant species, NO_x, CO and UHC were measured by sampling the exhaust stream using Thermo Environmental Inc. chemiluminescent, gas correlation, and flame ionization analyzers respectively. CO_2 mole fraction was measured using a Rosemount Analytical NDIR CO_2 analyzer. The mole fractions of the pollutant species measured by the analyzers were converted to mass fractions. The mass fractions and CO_2 concentrations were used to find the emission index of the pollutant species.

The two dimensional conservation equation for the mass fraction of NO (Y_{NO}) in a turbulent reacting flow is:

$$\frac{\partial \rho Y_{NO}}{\partial t} + \frac{\partial \rho u Y_{NO}}{\partial x} + \frac{1}{r}\frac{\partial \rho r v Y_{NO}}{\partial y}$$

$$= \frac{\partial}{\partial x}\left(\rho D \frac{\partial Y_{NO}}{\partial x}\right) + \frac{1}{r}\frac{\partial}{\partial r}\left(\rho r D \frac{\partial Y_{NO}}{\partial r}\right) + \dot{\omega}''' \quad (1)$$

where, ρ is the density, u is the velocity in the axial (x) direction, v is the velocity in the radial (r) direction, D is the molecular diffusivity and $\dot{\omega}'''$ is the production rate of NO in kg/m^3-s.

Numerical simulations for calculating the PDF of Y_{NO} at all locations within the flame is computationally intensive. However, the emission index of NO_x can be calculated if the axial mass flux of NO is known at all locations. The total mass flux of NO$\left(\dot{m}_{NO}, \text{ in kg/s}\right)$ at any axial location can be calculated as:

$$\dot{m}_{NO} = \int_0^R 2\pi u r \rho Y_{NO} dr \qquad (2)$$

where R is the boundary of the computational domain beyond which the mass fraction of Y_{NO} is zero.

Neglecting axial diffusion the change in mass flux of NO for an axial spacing of Δx can be obtained from Eq. (1) and (2) as:

$$\Delta\dot{m}_{NO} = \Delta x \int_0^R 2\pi r \dot{\omega}''' dr \qquad (3)$$

The changes in the NO mass flux from the exit to the last axial location (where the production rate term goes to zero) are added together to give the overall mass flux of NO from the flame. This information along with the fuel flow rate is used to obtain the $EINO_x$ (NO_x emission index) for the flame.

The reaction rate term in Eq. (3) is obtained from Rokke *et al.* [1992], and includes the Zeldovich, prompt and nitrous oxide mechanisms. The concentrations of the major species are required to calculate the production of NO [Rokke *et al.*, 1992] and are obtained using state relationships as a function of temperature assuming the reaction rate progress variable for the major species is one.

The temperature at any location is fluctuating as a function of time. Therefore, to obtain the time averaged mass flux of NO, $\left\langle \Delta\dot{m}_{NO}\right\rangle$, Eq. (3) is multiplied by the PDF of T and integrated over the entire range of T as follows:

$$\left\langle \Delta\dot{m}_{NO}\right\rangle = \Delta x \int_{T_{min}}^{T_{max}} \int_0^R 2\pi r \dot{\omega}'''(T) PDF(T) dr dT \qquad (4)$$

where T_{min} and T_{max} are the minimum and maximum temperatures observed at any radial location r. For the four different flames, Eq. (4) was numerically integrated from x = 0 to x = 200 mm at which location the instantaneous peak temperatures were below 1100 K and NO production was negligible. 80 grids were used in the axial direction and the PDF of T was discretized by 50 bins. Doubling either the number of x-grids or the number of bins resulted in less than 1% change in $EINO_x$.

Analog Gas Turbine Modeling and Experiments

Non-reacting flow velocity measurements were made in an axisymmetric combustor at preheated and pressurized conditions. These measurements were used to evaluate the accuracy of non-reacting numerical simulations performed using FLUENT.

The experimental combustor is axisymmetric to facilitate modeling. A 2.54 cm diameter inlet feeds a 7.62 cm diameter dump zone that is fitted with quartz windows to allow optical access for LDV measurements, as well as access for gas sampling probe measurements to be performed during the next phase of work. A water cooling jacket surrounds the combustor casing.

Preheated, high pressure, unvitiated air is supplied from storage tanks to a non-contact heat exchanger and on to the combustor. The air flow rate is measured using a choked orifice.

Only non-reacting results are reported here, so no fuel is used. However, in future work fuel (methane) will be supplied by a bank of conventional high pressure gas cylinders. The fuel flow rate will be measured using a choked orifice.

Air and fuel are mixed upstream of the combustor via a radial "sting." The extent of mixing will be assessed using Mie scattering.

A honeycomb flow straightener and 2.25:1 area ratio contraction are located upstream of the combustor dump plane so that the velocity profile is sensibly flat at the dump plane. The flatness of that profile is checked using LDV.

Combustor pressure and inlet velocity are varied by controlling the rates of air and fuel supplied to the combustor and restricting the diameter of the combustor at its exit plane. The restriction consists of a stainless steel cap and one of a number of graphite nozzles which serve to choke the exit flow.

The combustor has been operated at pressures of 1, 2, 5, 10 and 15 atm. Inlet velocity is nominally 10 m/s.

The LDV system is that of Gould [1989]. It was operated in the forward scatter mode as a single component instrument. Frequency shifting was employed to allow unambiguous velocity measurement in regions of recirculation and to eliminate incomplete signal bias.

Seeding was accomplished by distributing Al_2O_3 particles into a secondary air stream via a high-pressure seeder. The seeded secondary stream was introduced to the main air flow upstream of the fuel injection sting. The secondary air mass flow rate was also measured using a choked orifice.

Experimental results are compared to numerical results generated using FLUENT. FLUENT uses the finite volume approach to discretize the equations of motion.

FLUENT has flexibility to allow inclusion of a number of submodels that describe various transport phenomena. These include the ideal gas equation of state, Fourier's Law of heat conduction, Fickian mass diffusion, and the assumption of Newtonian fluids.

There are three options for turbulence modeling: k-ε, renormalization group (RNG) k-ε, and the Reynolds' stress model (RSM). Previous work completed as part of this program indicated only slight differences in the level of agreement when comparing model simulations based on the three turbulence models with LDV data. Consequently, the "standard" k-ε model was chosen because it requires the least computational time to converge to a solution.

Results

Reduced Kinetics Model

Using the LIF apparatus described above, NO concentrations have previously been measured in high-pressure, premixed, laminar $CH_4/O_2/N_2$ flames. To enhance the accuracy of these measurements, we have improved the precision of our calibration system by installing a new high-pressure mass-flow controller system for delivery of the calibration gas. Of additional concern for the accuracy of these measurements is the effect of fluorescence interferences due to species other than NO. Specifically, O_2 fluorescence can cause a significant background offset which must be accounted for in LIF measurements of NO, especially at the lean, high-pressure conditions investigated here.

We studied the effect of O_2 interferences in nitrogen-air flames by obtaining fluorescence excitation and detection scans in the post-flame zone of a non-cooled 3.76 dilution ratio, 0.6 equivalence ratio, flat, premixed flame stabilized on a porous ceramic plug. The excitation scans show that the $Q_2(26.5)$ transition is not in the same region as any distinct interference feature, nor is it concurrent with any other NO feature. These traits, combined with this transition's relatively temperature-insensitive Boltzmann fraction make $Q_2(26.5)$ excitation a good choice for fluorescence measurements.

However, even though this excitation transition avoids major interference features, some fluorescence and Raman features will be excited at any wavelength in this region. To further avoid these interferences, it is necessary to choose a detection strategy that collects as much NO related signal as possible while rejecting non-NO interferences.

Thus, detection scans were obtained at 1 and 6 atm in both $CH_4/O_2/N_2$ and $CH_4/O_2/Ar$ flames. The argon diluted flames, shown in Figs. 3a and b, lack the NO signal and thus give a good indication of the location and magnitude of non-nitrogen related interferences. The nitrogen diluted scans of Figs. 3c and d contain the interference features as well as those due to N_2 and NO.

These detection scans are presented on a relative fluorescence basis by normalizing the peak signal to 1000. The $\gamma(0,1)$, $\gamma(0,2)$ and $\gamma(0,3)$ bands of NO are apparent in Figs. 3c and d at approximately 236, 246, and 258 nm, respectively. A strong N_2 Stokes Raman scattering signal is also seen at ~238 nm [Eckbreth, 1988] in the nitrogen-flame detection scans. An H_2O Raman line occurs within the $\gamma(0,2)$ band of NO, ~246 nm. Thus the $\gamma(0,2)$ band of NO would be a poor choice for NO detection. Also evident in these scans are the large interferences due to O_2 fluorescence seen as doublets before the $\gamma(0,1)$ band, between the $\gamma(0,1)$ and $\gamma(0,2)$ bands and in the middle of the $\gamma(0,3)$ band of NO. These interferences would also make the $\gamma(0,3)$ band of NO a poor choice for NO detection.

What these scans show us is that interferences can largely be avoided in LIF measurements of NO in lean methane-air flames, if the $Q_2(26.5)$ transition of NO is used for excitation in conjunction with detection of a 2 to 3 nm portion of the $\gamma(0,1)$ band of the NO molecule. However, at higher pressures and temperatures and in lower dilution ratio flames, the O_2 background can become significant even with the above excitation/detection scheme. To attain more accurate LIF measurements at these extreme conditions, correction procedures are currently being developed to experimentally measure the background and subtract it from the measured fluorescence signal.

In earlier reports, we have described the results of our extensive modeling effort using the Sandia 1-D premixed flame code to predict NO formation in the flames we have investigated experimentally. One issue which prevented accurate predictions of NO formation in high-pressure $CH_4/O_2/N_2$ flames was the inability of the flame code to adequately predict the temperature field above the burner surface, especially at high pressures. One cause for this deficiency was the failure of the model to account for radiative heat losses from the flame to the surroundings, which should become very significant at higher pressures. Our first step to alleviate this problem was the addition of a simple radiative heat loss model to the Sandia 1-D Premixed Flame Code. Assuming that these flames are in the optically-thin regime, a radiation source term was calculated using a Planck mean temperature coefficient. This coefficient was calculated from a narrow band model using the RADCAL program [Grosshandler, 1988]. Preliminary results for flames at atmospheric pressure are shown in Fig. 4.

Turbulence-Chemistry Interaction Model

The effect of the varying the amount of hydrogen used for the pilot flame on the emission indices of UHC, CO, NO and NO_x is shown in Fig. 5. All the flames used in the present study blow off if the hydrogen pilot is stopped. The amount of hydrogen required increases as the jet velocity increases. This is partly due to the higher velocities and also to the lower temperatures for the leaner flames. If the pilot flame is too small, UHC and CO levels increase very rapidly as the flame becomes unstable, and any further decrease of the hydrogen flow would blow off the flame.

The emission index for NO and NO_x increases with increasing hydrogen flow rate. The increase in adiabatic temperature produced due to combustion of hydrogen in the pilot flame is responsible for the increased levels of NO and NO_x. The higher temperature also promotes complete combustion, leading to lower emission indices for CO and UHC. All four flames used 2 mg/s of H_2 for the pilot flame. This low amount of hydrogen results in only about a 20% increase in $EINO_x$ allowing critical evaluation of the chemical kinetics model.

The PDFs of axial velocity, for five different radial locations and 60 mm above the burner, for the 4.2 kW lean premixed turbulent flame are shown in Fig. 6. The mean velocity decreases from the center line towards the edge of the flame, and the RMS velocity remains almost constant across the flame width. At locations close to the high temperature zone (r = 12 mm and r = 14 mm), the fluctuation in axial velocity is about 30 % of the mean. The PDF at the center is narrow and symmetric around the mean value. The effects of intermittency are evident for the PDF at r = 16 mm since the PDF has a long tail for positive velocities and is not symmetric around the mean value. Outside the flame zone, the mean and the fluctuations in velocity decrease rapidly. The shapes of the velocity PDFs are nearly Gaussian.

The PDFs of temperature at the same five radial locations for the 4.2 kW lean premixed turbulent flame are shown in Fig. 7. The mean temperature at the center is very low, rises to a maximum of 1755 at r = 12 mm and then decreases outside the flame. Interestingly, the fluctuations are minimum at the flame surface, indicating that the flame sheet is relatively stationary at this point despite the high level of axial velocity fluctuation. Close to the flame sheet, the peak temperatures reach close to adiabatic values. However, such high temperature excursions are not seen at the edge of the flow or at the center. In addition, the fluctuations increase towards the edge of the flow due to intermittency. At the center line of the jet and an axial location of 60 mm, the temperature is very low and below 900 K almost all the time.

There are a number of phase diagrams that define various combustion regimes in terms of length and velocity scales [Borghi, 1984; Williams, 1985; Peters, 1986]. In this work, we follow the analysis of Peters [1986] and plot the ratio of the RMS of velocity (u') to the laminar flame speed (S_L) as a function of the ratio of the integral length scale (l_t) to the laminar flame thickness (l_F), as shown in Fig. 8. The turbulent Reynolds (Re), Damkohler (Da) and Karlovitz (Ka) numbers are given by:

$$Re = u' l_t / \upsilon \tag{5}$$

$$Da = t_t / t_F = S_L l_t / u' l_F \tag{6}$$

and

$$Ka = t_F/t_k = l^2_F/l^2_F = \epsilon^{1/2} l_F/\upsilon^{1/2} S_L \qquad (7)$$

respectively where n is the kinematic viscosity, t_t is the integral time scale, and ε is the turbulent kinetic energy. Based on the above definitions, we can derive the following relationship for the three non-dimensional numbers, Re, Da and Ka, in terms of u'/S_L and l_t/l_F as [Peters, 1986]:

$$u'/S_L = Re \left(l_t/l_F\right)^{-1} \qquad (8)$$

$$u'/S_L = Da^{-1} \left(l_t/l_F\right) \qquad (9)$$

$$u'/S_L = Ka^{2/3} \left(l_t/l_F\right)^{1/3} \qquad (10)$$

The regimes of laminar flames ($Re < 1$) and well stirred reactor ($Da < 1$) are not of interest for the present work. Among the three remaining regimes, the wrinkled and corrugated flames belong to the flame regime which is characterized by the inequalities $Re > 1$ (turbulence), $Da > 1$ (fast chemistry) and $Ka < 1$ (sufficiently weak flame stretch). In the flamelet regime the Kolmogorov length scale is greater than the flame thickness, so the smallest eddies do not penetrate the flame sheet and we get thin laminar flamelets. u' is interpreted as the circumferential velocity of the largest eddies and when $u' < S_L$, these eddies can not convolute the flame front to form the multiply connected flame sheets. When $u' > S_L$, multiple flame sheets are formed giving rise to corrugated flamelets.

The boundary of the distributed reaction zone is given by $Ka = 1$ and can be expressed as the condition where the flame thickness is equal to the Kolmogorov scale. The distributed reaction zone is bounded by $Re > 1$; $Da > 1$ and $Ka > 1$. In the distributed reaction zone, $Ka > 1$, the Kolmogorov scale is smaller than the flame thickness and the smallest eddies can enter the flame structure thereby broadening the flame structure.

All previous measurements in the literature fall within either the wrinkled flamelet or corrugated flamelet regimes. The present work is the first time that flames stabilized (due to hydrogen pilot flame) in the distributed reaction regime are accessible.

The predictions and measurements of $EINO_x$ normalized by its value at equivalence ratio of 1 is shown in Fig. 9. The chemical kinetics model captures the change in $EINO_x$ with equivalence ratio quite well. However, the absolute values are about 330% higher for the 4.2 kW flame and 40% higher for the 8.4 kW flame. Two sets of predictions are also shown in Fig. 9. The open triangle represents predictions of $EINO_x$ obtained using the measured temperature PDF. The open circles represents predictions obtained using a Gaussian PDF, with the maximum temperature being limited to the adiabatic flame temperature. The data is represented by the solid circles. Both sets of predictions capture the increase in $EINO_x$ with equivalence ratio quite well. The predictions are shown only for two equivalence ratios since measurements of the temperature PDFs are available for only four flames.

Analog Gas Turbine Modeling and Experiments

Experimental data at pressures from 1 to 15 atm and temperatures from 295 to 480 K was obtained using our high pressure analog gas turbine combustor operating under non-reacting conditions. Table 1 illustrates the pressure-temperature combinations that have been investigated. Velocity data obtained at these conditions was used to evaluate the pressure and temperature scaling capabilities of FLUENT. Particular attention was paid to the influence of operating pressure and temperature on the flow field, and the agreement between experimental data and numerical simulations as these two parameters were varied.

Experimental data and model predictions for the cases listed in Table 1 are presented in Fig. 10 through 13. Experimental data were checked for symmetry by scanning the LDV probe volume across the combustor diameter. Velocity profiles from the two radii were then compared at a number of axial locations and the root-mean-square (rms) deviation, defined as

$$\frac{1}{N}\sqrt{\sum_{i=1}^{N}\frac{\left(u_{ir}-u_{il}\right)^2}{\left[\left(u_{ir}+u_{il}\right)/2\right]^2}}\ , \qquad (11)$$

computed. Here u_{ir} is the axial velocity at radial position i for the right hand radius, u_{il} is the axial velocity at radial position i for the left hand radius, and N is the number of radial positions at which data were acquired. The root mean square deviation between sides was less than 22%. The experimental data were also checked for repeatability by acquiring velocity fields on different days. The rms deviation between velocity fields acquired on different days, defined analogously to Eqn. (11), was 21%.

Table 1. Pressure-Temperature Conditions at Which LDV Data Were Obtained

Pressure, atm	Temp., K	Reynolds number, x10^{-4}	Dump velocity, m/s
1	295	1.8	9.8
2	295, 383	3.6, 2.1	11, 9.8
5	295, 439	9.0, 3.9	11, 9.8
10	295, 450	18, 7.5	11, 9.8
15	294, 477	27, 10	11, 10

Figure 10 illustrates agreement between model predictions and experimental data for a combustor pressure of 2 atm and an inlet temperature of 383 K. The results demonstrate that FLUENT accurately predicts the recirculation zone, present at x/H=2.1 and 4.7, and the decay of the central jet, between x/H=0.1 and x/H=8.3. Discrepancies between model predictions and experimental data exist at x/H=8.3, where FLUENT indicates the recirculation zone has ended and the experimental data shows it to persist, and at x/H=8.3 and 11.8, where FLUENT first under- and then over predicts the persistence of the central jet.

Figure 11 illustrates agreement between model predictions and experimental data for a combustor pressure of 5 atm and an inlet temperature of 439 K. The results demonstrate that FLUENT again predicts the recirculation zone, present at x/H=2.1 and 4.7, and the decay of the central jet. FLUENT simulations are most accurate at non-dimensional axial locations of 11.8 and 14.1. Discrepancies between model predictions and experimental data do exist, however, and are more prevalent than for the 2 atm case. In particular, at x/H=8.3 FLUENT indicates that the recirculation zone persists and the experimental data show it to have ended. Furthermore, at x/H=4.7 and 8.3 FLUENT consistently over predicts the persistence of the central jet.

Agreement between model predictions and experimental data improves as combustor pressure increases to 10 atm, as shown in Figure 12. Figure 12 results demonstrate that FLUENT accurately predicts the location of the recirculation zone and the breakdown of the core flow. A comparison of rms errors between the 5 and 10 atm cases (24 and 21%, respectively) clearly demonstrates the improved accuracy of the 10 atm simulations.

Agreement between model predictions and experimental data is as good for the 15 atm case as it is for the 10 atm case. Figure 13 presents the 15 atm results. Once again, FLUENT is able to accurately predict the location of the recirculation zone and the breakdown of the core flow. In addition, only minor discrepancies are present, as indicated by an rms error value of less than 21%.

In summary, Fig. 10 through 13 demonstrate that FLUENT is capable of predicting non-reacting, elevated pressure, preheated flow fields for our axisymmetric geometry. Comparison of the results in Fig. 10 through 13 demonstrates that pressure scaling effects on the flowfield are well described. Furthermore, the accuracy of the predictions are seen to improve with an increase in pressure.

Comparison of the results contained in Fig. 10 through 13 with results obtained at corresponding pressures and ambient temperature indicate that temperature scaling effects are also well described. The accuracy of the predictions are observed to improve with increasing inlet temperature.

Applications

Lean premixed flame combustors satisfy the low NO_x emission need of the Advanced Turbine Systems (ATS) being developed by several industries under the sponsorship of the Fossil Energy (FE) program of the U.S. Department of Energy (DOE). Computational tools for the design of lean premixed combustors are presently limited by the lack of understanding of the high pressure NO formation chemistry and turbulence chemistry interactions. The results of this study will improve the competitiveness of U.S. manufactured gas turbines by helping to provide a rational understanding of how engine design influences NO_x production.

Future Work

Our future work will be focused in three areas.

- We will continue to map NO concentrations in our preheated, high pressure flames and accelerate work on the development of a reduced NO kinetic mechanism for use with natural gas fired systems. The reduced kinetic mechanism will be supplied to the Analog Gas Turbine Group.

- We will simulate the energy equation to evaluate the DPF-based turbulence-chemistry interaction model further, make measurements of average major gas species concentration, and incorporate the DPF NO calculations into an industrial code for combustor design. Preliminary measurements of NO concentration statistics are being initiated in collaboration with the Reduced Kinetics Group.

- We will make major species measurements under elevated pressures conditions and simulate the profiles using FLUENT, while incorporating the reduced kinetic mechanism and turbulence - NO chemistry models being developed by the Reduced Kinetics and Turbulence-Chemistry Interaction Groups.

Acknowledgments

The authors gratefully acknowledge the efforts of Dr. Norman Holcombe, METC Project Manager, and Dr. Daniel Fant, Director, AGTSR. This work is supported by DOE contract DE-FC21-92MC29601, through the Morgantown Energy Technology Center. The South Carolina Energy Research and Development Center is the primary contractor, with Purdue University being a subcontractor. The period of performance is 1 September 1993 through 31 August 1996.

The authors also gratefully acknowledge the support of Purdue University's School of Mechanical Engineering, as well as helpful conversations with representatives from Allison

Engine Company, General Electric, Solar Turbines, Inc., United Technologies Research Center, and Westinghouse.

References

Bilger, R.W, Saetran, L.R. and Krishnamoorthy, L.V., 1991, Reaction in a Scalar Mixing Layer," J Fluid Mech., Vol. 233, p. 211.

Borghi R., 1985, "On the Structure and Morphology of Premixed Flames," Recent Advances in Aerospace Sciences, Ed. C. Casci, Plenum, p. 117.

Bowman C.T., 1992, "Control of Combustion-Generated Nitrogen Oxide Emissions: Technology Driven by Regulation," Twenty-Fourth Symposium (Int'l) on Combustion, The Combustion Institute Pittsburgh, PA, p. 859.

Carter, C.D., G.B. King, and N.M. Laurendeau, "A combustion facility for high-pressure flame studies by spectroscopic methods", *Rev. Sci. Instrum.* **60**, 2606 (1989).

Chew T.C., Bray K.N.C., Britter R.E., 1990, "Spatially Resolved Flamelet Statistics for Reaction Rate Modeling," Combust. Flame, Vol. 80, p. 65

Correa S.M., 1992, "A Review of NO_x Under Gas Turbine Conditions," Combust. Sci. Tech., Vol. 87, p. 329.

Drake M.C. and Blint R.J., 1991, "Calculations of NO_x Formation Pathways in Propagating Laminar, High Pressure Premixed CH_4/Air Flames," Combust Sci. Tech., Vol. 75, p. 261.

Eckbreth, A.C., *Laser Diagnostics for Combustion Temperature and Species,* Abacus Press, Cambridge, MA. (1988).

Ghoniem A.F., Chorin A.J., and Oppenheim A.K., 1982, "Numerical Modeling of Turbulent Flow in a Combustion Tunnel," Phil. Trans. R. Soc. Lond., Vol. A 304, p. 303.

Givi, P., 1989, "Model Free Simulations of Turbulent Reacting Flows," Prog. Energy Combust Sci, Vol. 15, p. 1.

Glarborg, P., J.A. Miller, and R.J. Kee, "Kinetic Modeling and Sensitivity Analysis of Nitrogen Oxide Formation in Well-Stirred Reactors", *Combust. Flame* **65**, 177 (1986).

Gould, R.D., "Turbulence Characteristics of an Axisymmetric Reacting Flow," Ph.D. Thesis, Purdue (1987).

Grosshandler, W.L., "Radiative Heat Transfer in Nonhomogeneous Gases: A Simplified Approach", *Int. J. Heat Mass Trans.* **23**, 1447 (1988).

Jones W.P. and Whitelaw J.H., 1982, "Calculation Methods for Reacting Turbulent Flows: A Review," Combust. Flame, Vol. 48, p. 1.

Kee, R.J., J.F. Grcar, M.D. Smooke, and J.D. Miller, A FORTRAN program for modeling steady laminar one-dimensional premixed flames. *Sandia Report SAND* 85-8240 (1985).

Kerstein A.R., 1988, "A Linear-Eddy Model of Scalar Transport and Mixing," Combust. Sci. Tech., Vol. 60, p. 391.

Kollman K.V., 1990, "The PDF approach to Turbulent Flow," Theoret. Comput. Fluid Dyn., Vol. 1, p. 249.

Michaud M.G., Westmoreland P.R. and Feitelberg A.S., 1992, "Chemical Mechanisms of NO_x Formation for Gas Turbine Conditions," Twenty-Fourth Symposium (International) on Combustion, The Combustion Institute Pittsburgh, PA, p. 879.

Moss J.B., 1980, "Simultaneous Measurements of Concentration and Velocity in an Open Premixed Turbulent Flame," Combust. Sci. Tech., Vol. 22, p. 119.

Peters N., 1986, "Laminar Flamelet Concepts in Turbulent Combustion," Twenty-First Symposium (Int'l) on Combustion, The Combustion Institute Pittsburgh, PA, p. 1231.

Pita G.P.A. and Nina M.N.R., 1989, "Errors Induced by Catalytic Effects in Premixed Flame Temperature Measurements," Int'l Conference on Instrumentation in Aerospace Simulation Facilities, IEEE, Piscataway, NJ, p. 179.

Pope S.B., 1991, "PDF method for turbulent reacting flows," Prog. Energy Combust. Sci., Vol. 11, p. 119.

Reisel, J.R., C.D. Carter, N.M. Laurendeau and M.C. Drake, "Laser-Saturated Fluorescence Measurements of Nitric Oxide in Laminar, Flat, $C_2H_6/O_2/N_2$ Flames at Atmospheric Pressure", *Combust. Sci. and Tech.* **91**, 271 (1993).

Rokke N.A., Hustad J.E., and Sonju O.K., 1992, "Scaling of Nitric Oxide Emissions from Buoyancy Dominated Hydrocarbon Turbulent-Jet Diffusion Flames," Twenty-Fourth Symposium (Int'l) on Combustion, The Combustion Institute Pittsburgh, PA, p. 385.

Sivathanu Y.R. and Gore, J.P., 1993, "A Discrete Probability Function Method for the Equation of Radiative Transfer," J. Quant. Spec. Radiat. Transfer, Vol. 49, pp. 269.

Sivathanu Y.R. and Gore J.P., 1994, "Discrete Probability Function Method for a Turbulence Mixing Layer," Fire, Combustion and Hazardous Waste Processing, ASME HTD- Vol. 296, p. 99.

Smallwod G.J., Gulder O.L., Shelling D.R., Deschamps B.M., and Gokalp I., 1995, "Characterization of Flame Front Surfaces in Turbulent Premixed Methane/Air Combustion," Combust. Flame, Vol. 101, p. 461.

Tanaka H. and Yanagi T., 1983, "Cross-Correlation of Velocity and Temperature in a Premixed Turbulent Flame," Combust. Flame, Vol. 51, p. 183.

Vilimpoc V. and Goss L.P., 1988, "SiC-Based Thin-Filament Pyrometry: Theory and Thermal Properties," Twenty-Second Symposium (Int'l) on Combustion, The Combustion Institute Pittsburgh, PA, p. 1907.

Williams F.A., 1985, Combustion Theory, Benjamin Cummins, Menlo Park, CA.

Wu W.S., Kwon S., Driscoll J.F., and Faeth G.M., 1991, "Preferential Diffusion Effects on the Surface Structure of Turbulent Premixed Hydrogen/Air Flames," Combust Sci. Tech., Vol. 78, p. 69

Yanagi T. and Mimura Y., 1981, "Velocity-Temperature Correlation in Premixed Flame," Eighteenth Symposium (Int'l) on Combustion, The Combustion Institute Pittsburgh, PA, p. 1031.

Yoon, K. and Warhaft, Z., 1990, "The Evolution of Grid-generated Turbulence under conditions of Stable Thermal Stratification," J. Fluid Mech., Vol. 215, p. 601.

Yoshida A., 1981, "An Experimental Study of Wrinkled Laminar Flame," Eighteenth Symposium (Int'l) on Combustion, The Combustion Institute Pittsburgh, PA, p. 931.

Yoshida A. and Tsuji H., 1979, Measurements of Fluctuating Temperature and Velocity in a Turbulent Premixed Flame," Seventeenth Symposium (International) on Combustion, The Combustion Institute Pittsburgh, PA, p. 931.

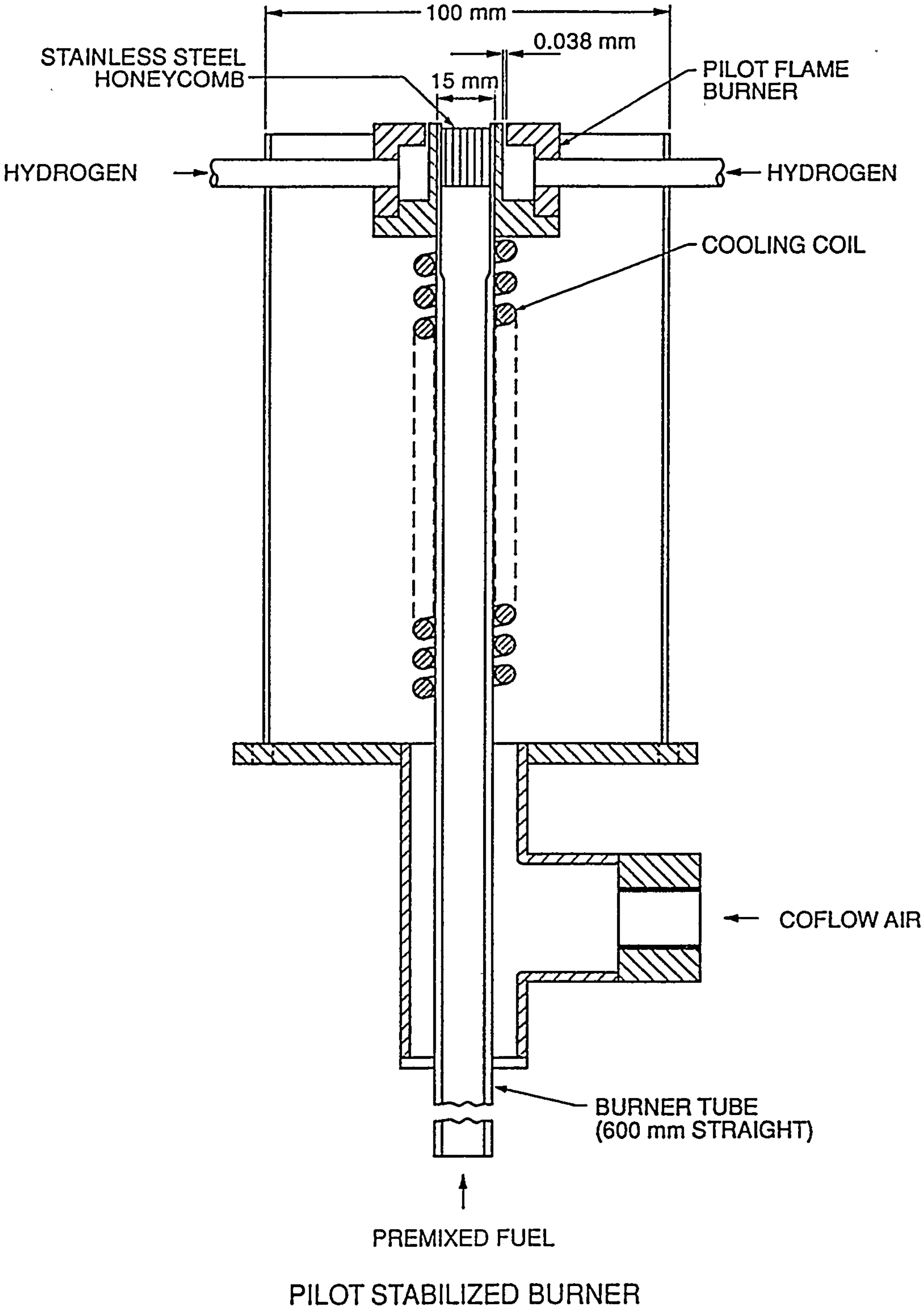

Figure 1. A Schematic of the Turbulent Premixed Burner

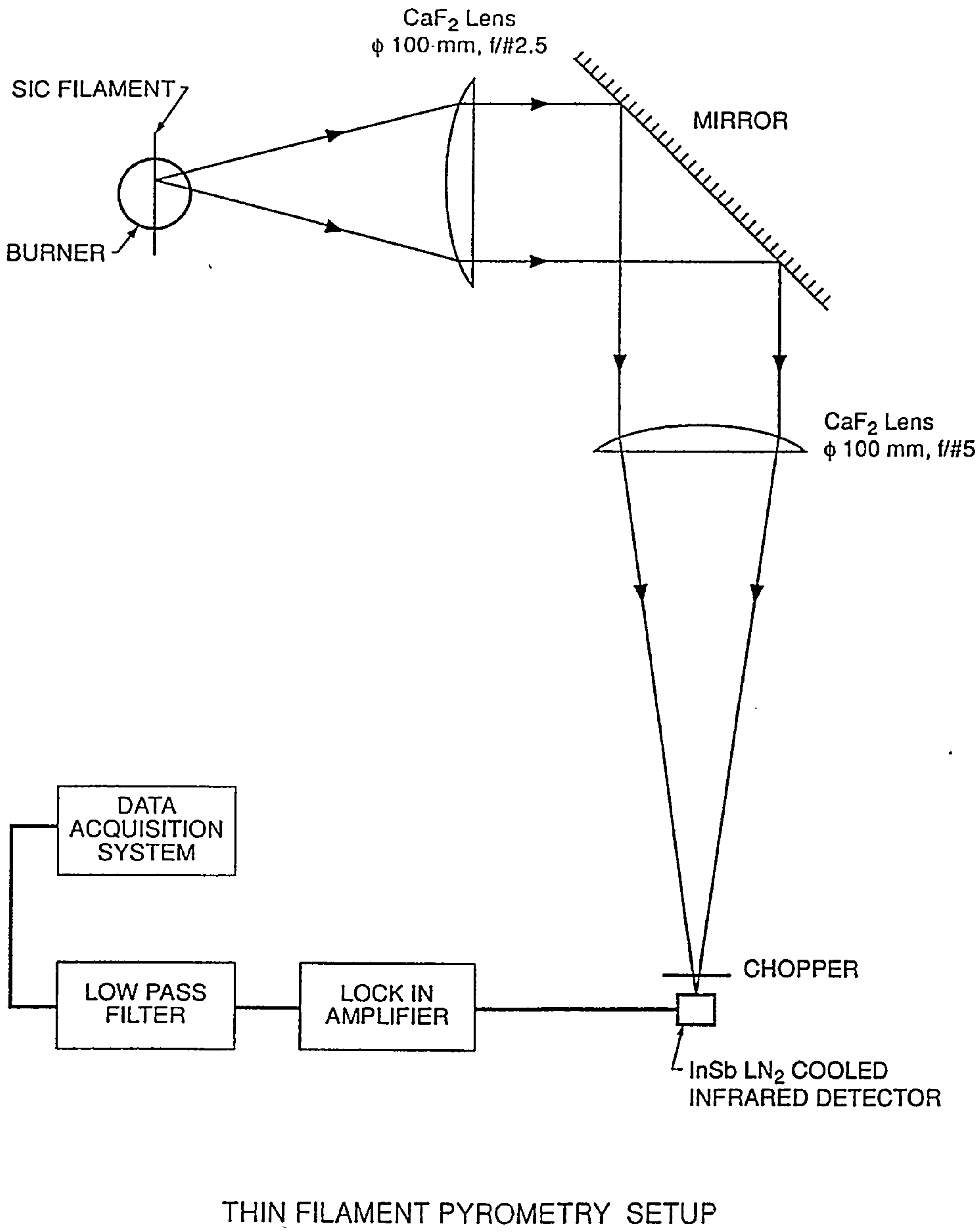

Figure 2. A Schematic of the Thin Filament Pyrometry System

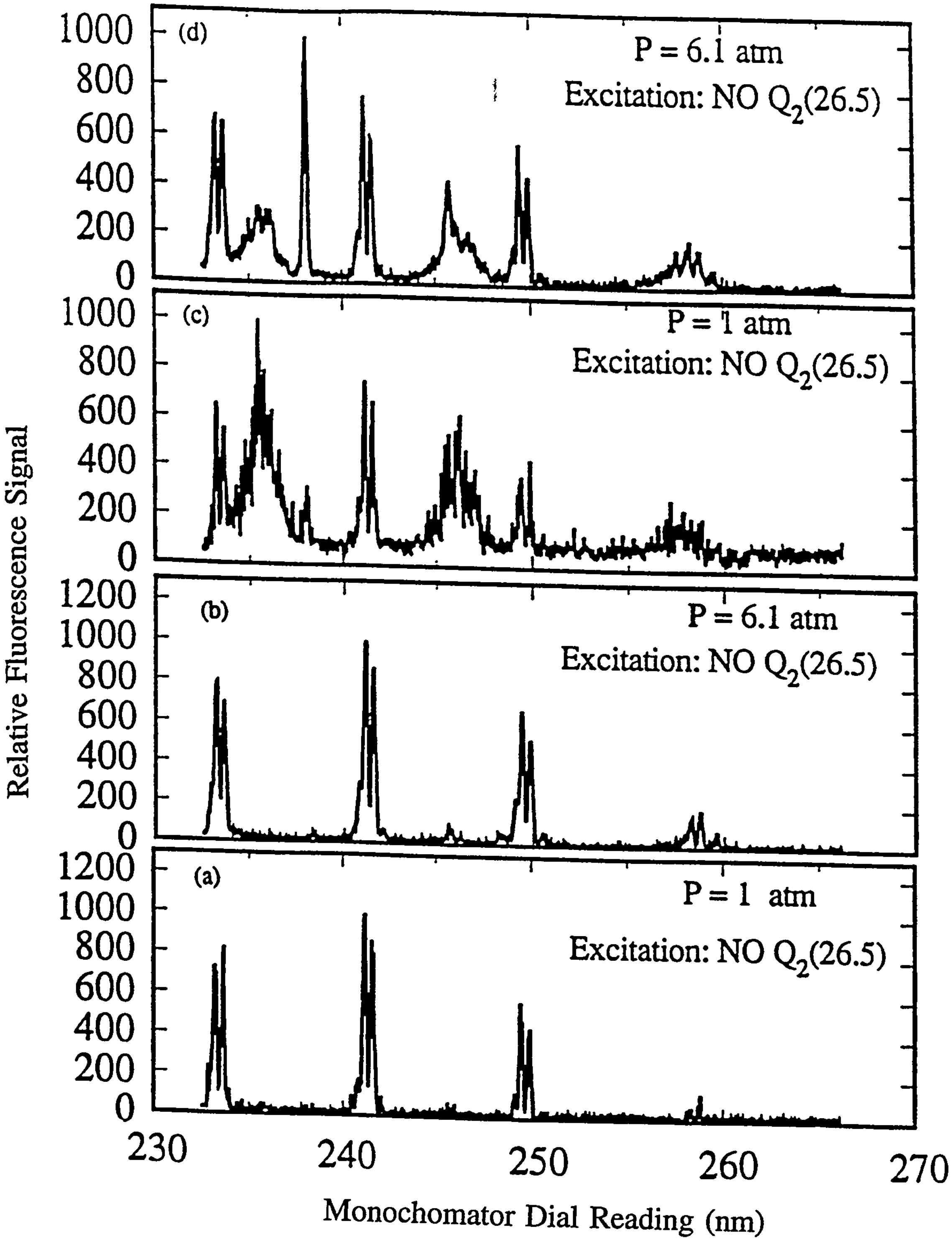

Figure 3. Relative Fluorescence Versus Wavelength for Two Flames at Elevated and Ambient Pressures: a) and b) Are Argon Diluted; c) and d) Contain Nitrogen

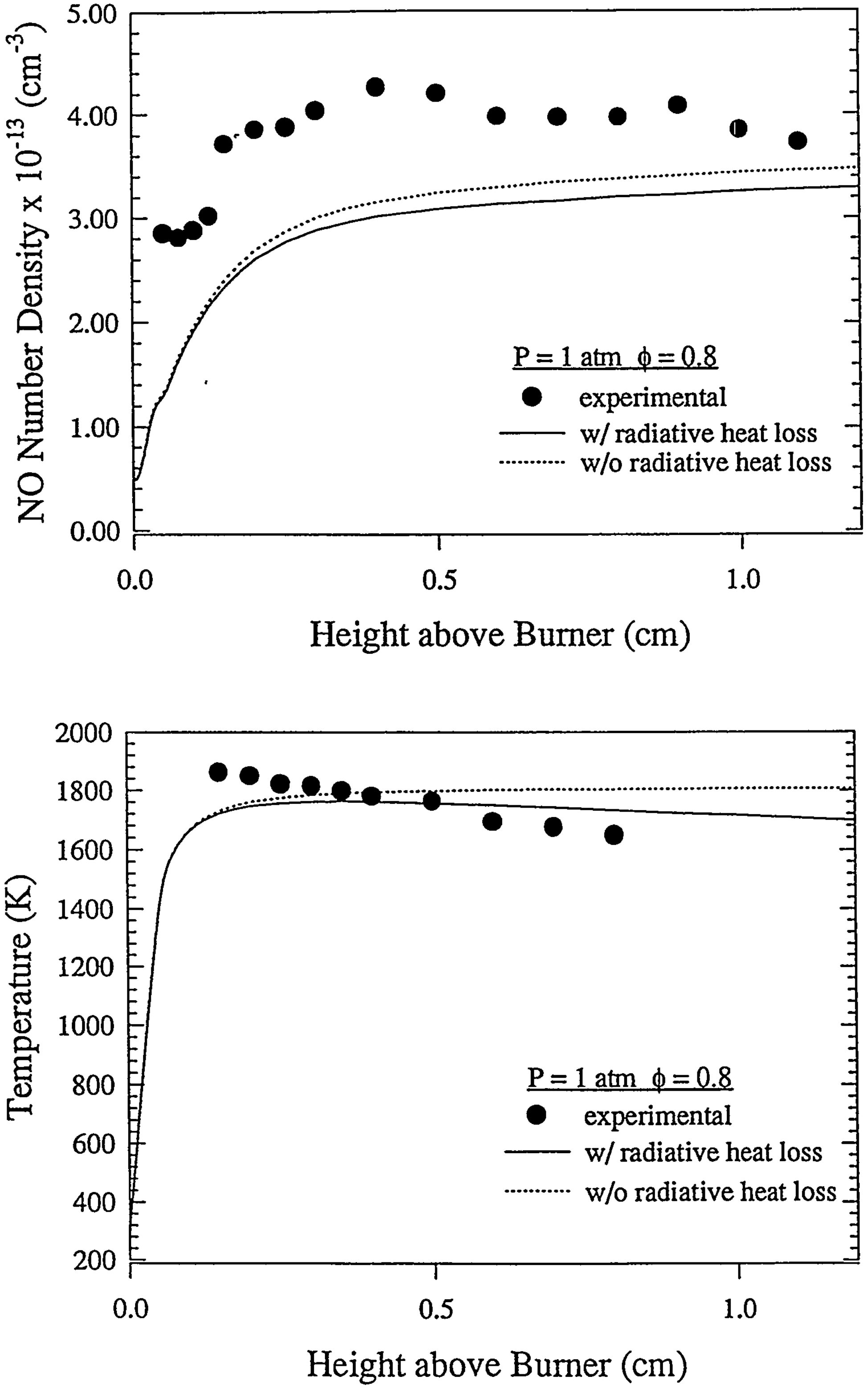

Figure 4. NO Number Density and Temperature Versus Axial Location Above the Burner Surface

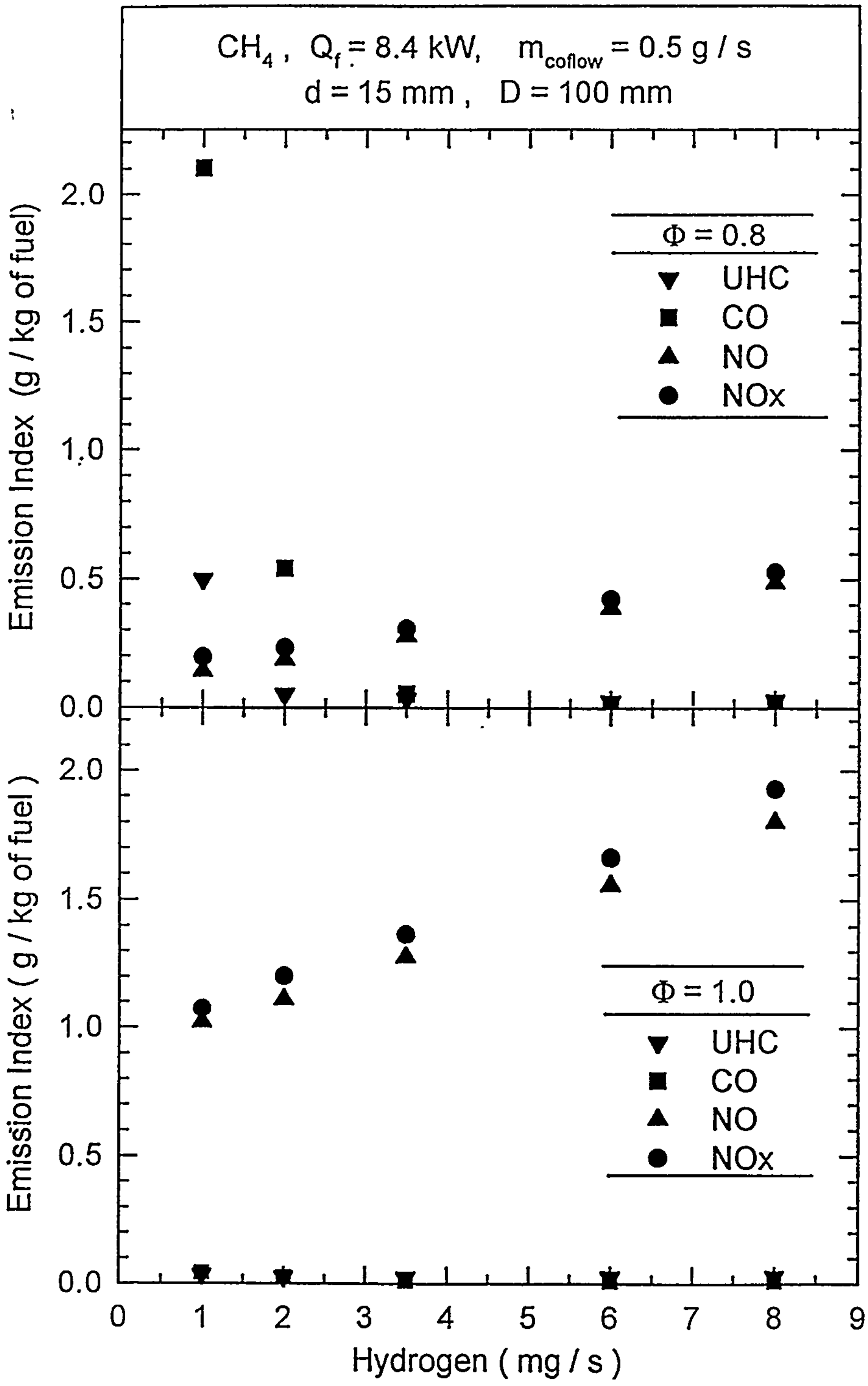

Figure 5. The Effect of Hydrogen Pilot Flame on the Emission Index

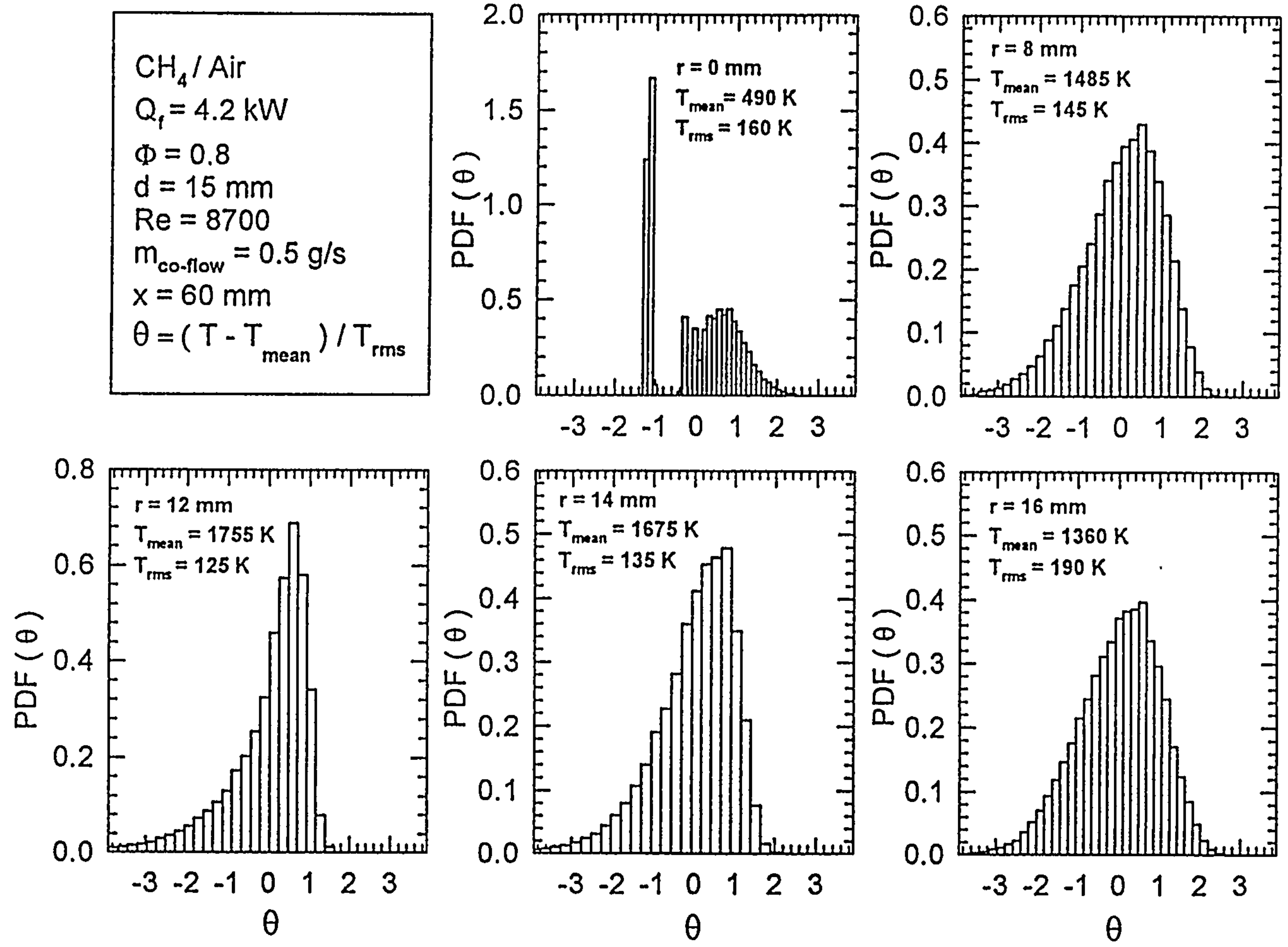

Figure 6. Probability Density Functions of Temperatures Measured in a Lean Premixed Flame

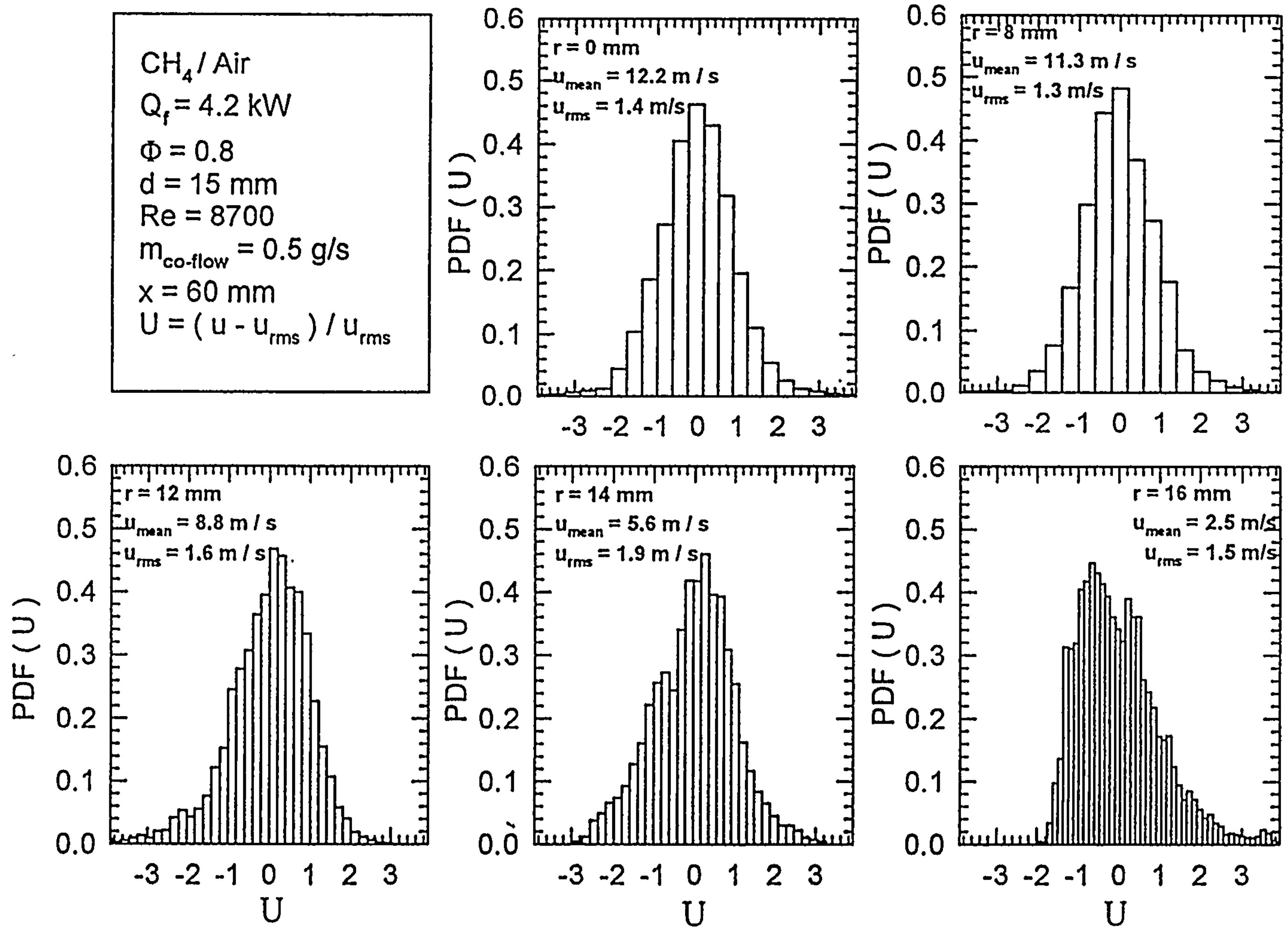

Figure 7. Probability Density Functions of Velocities Measured in a Lean Premixed Flame

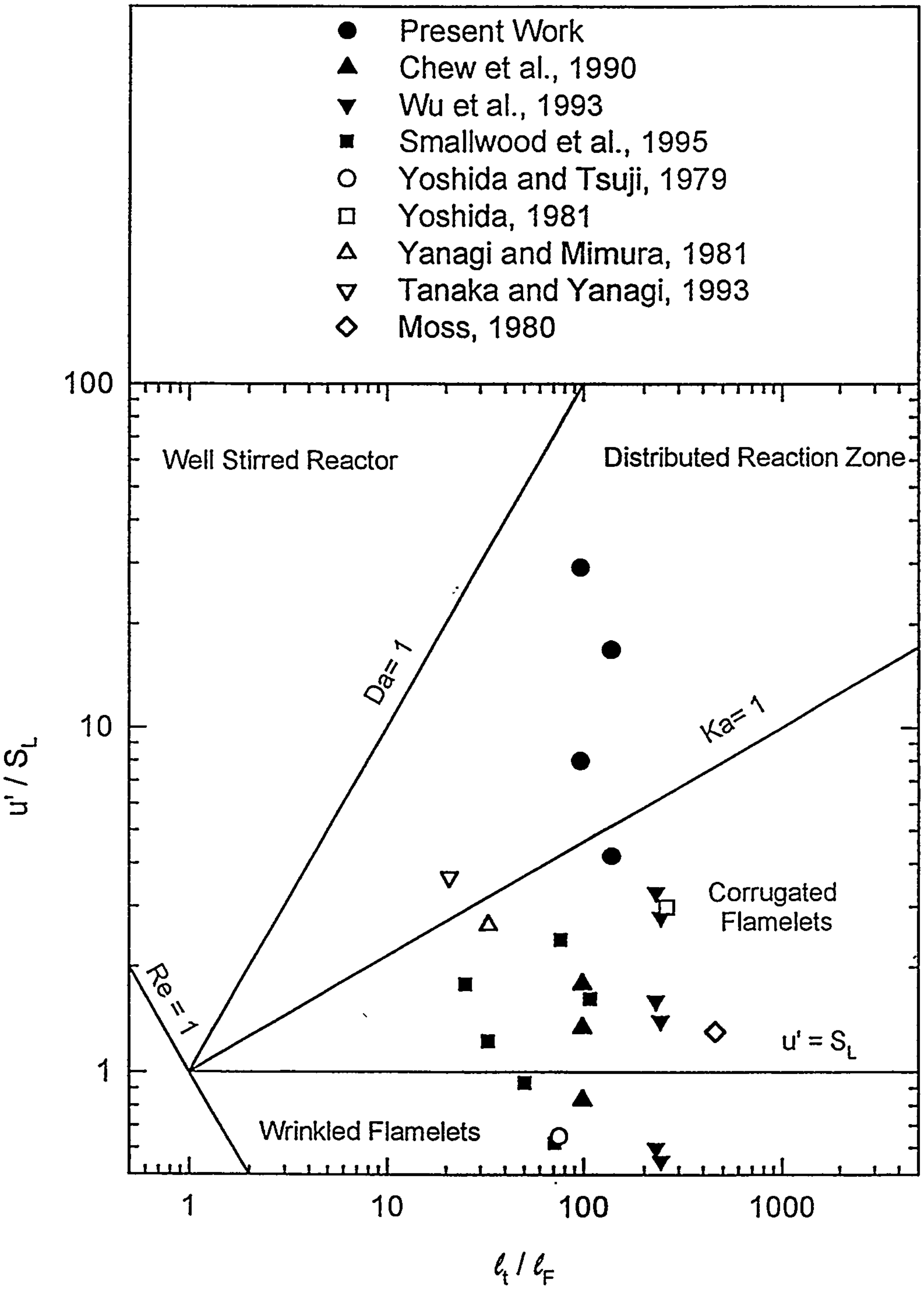

Figure 8. Phase Diagrams for Premixed Turbulent Flames

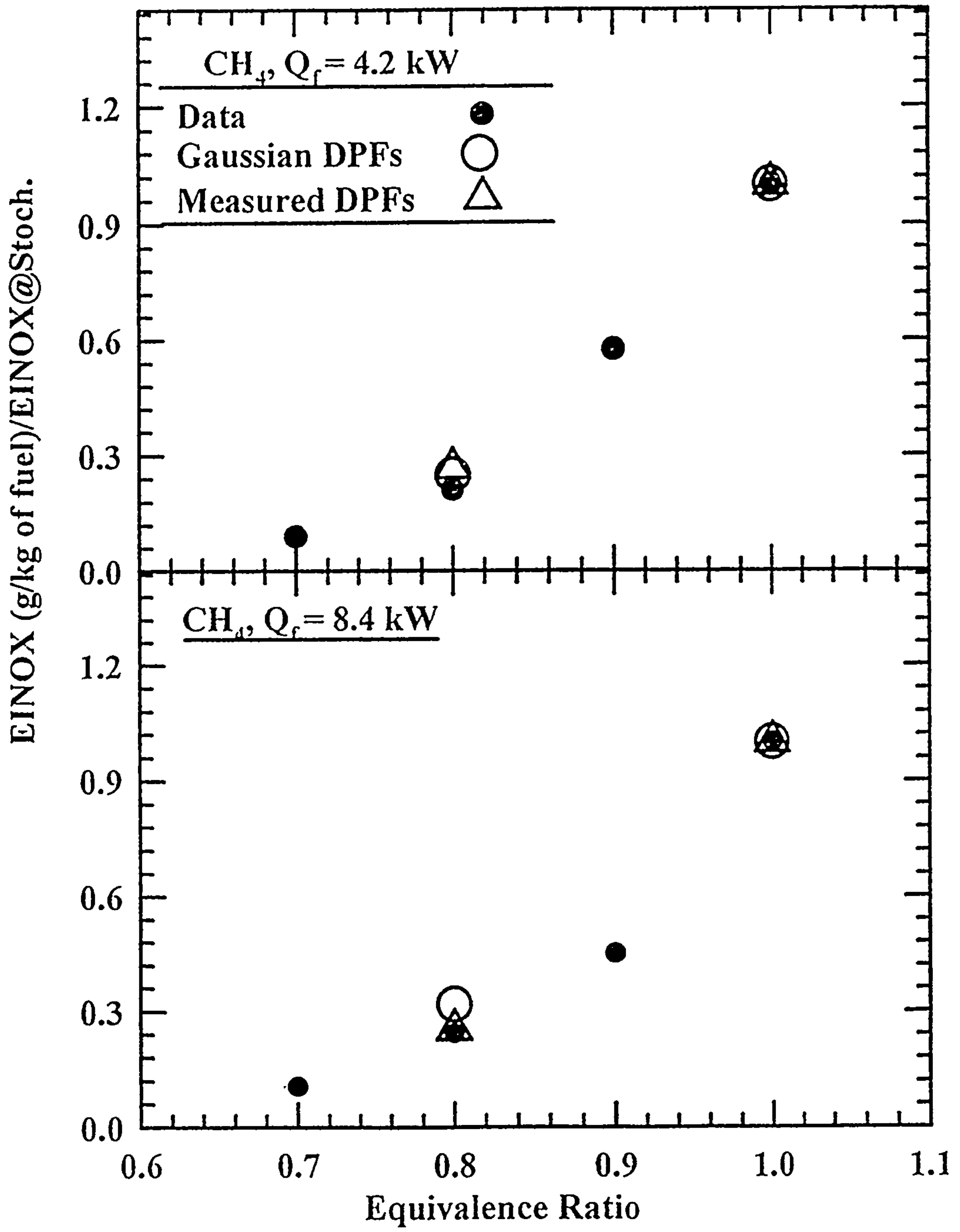

Figure 9. Measurements and Predictions of EINO$_X$ for the Premixed Turbulent Flames

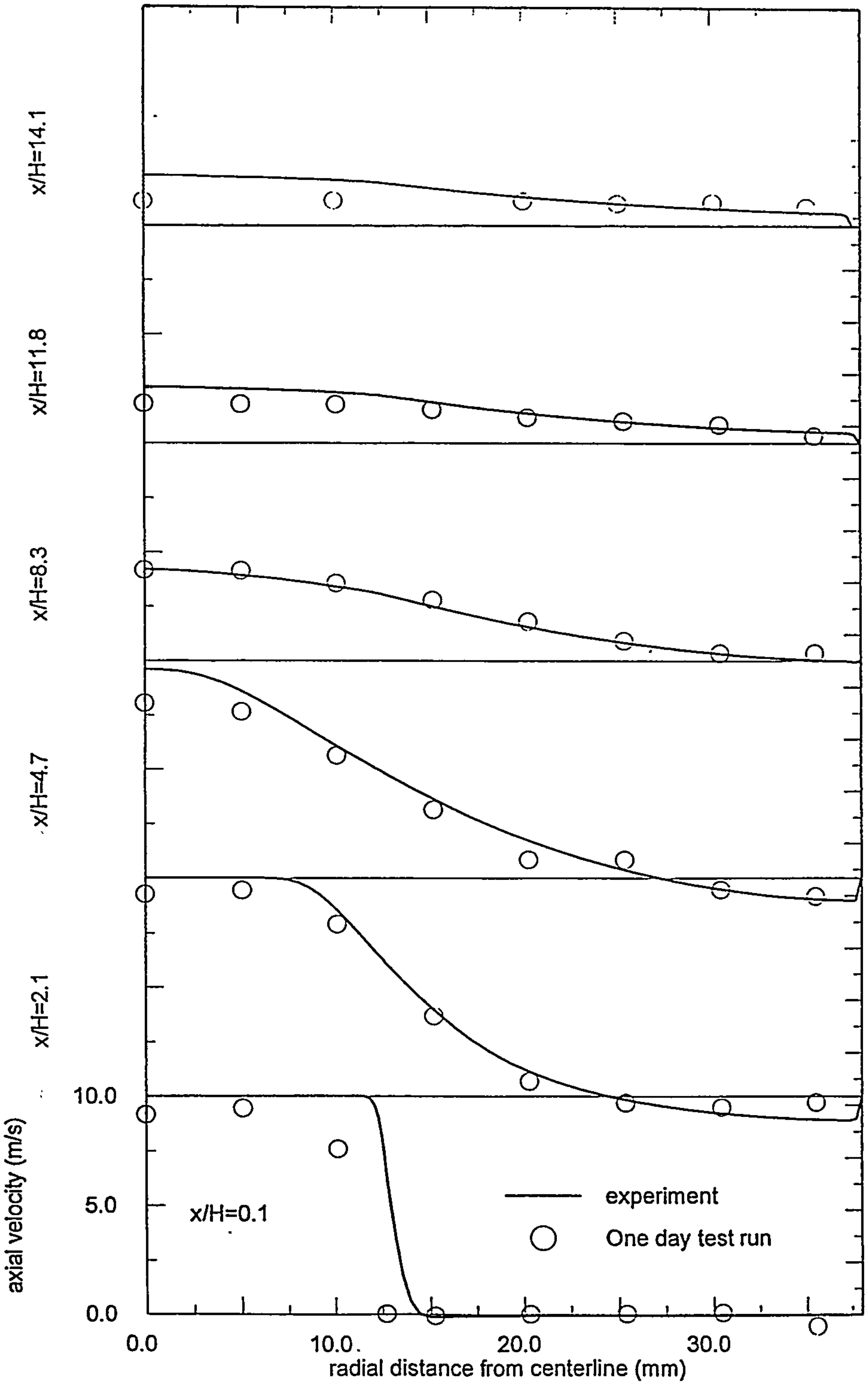

Figure 12. Axial Velocity Versus Radial Position at Six Axial Locations for the Combustor Operating at 10 atm and an Inlet Temperature of 450 K

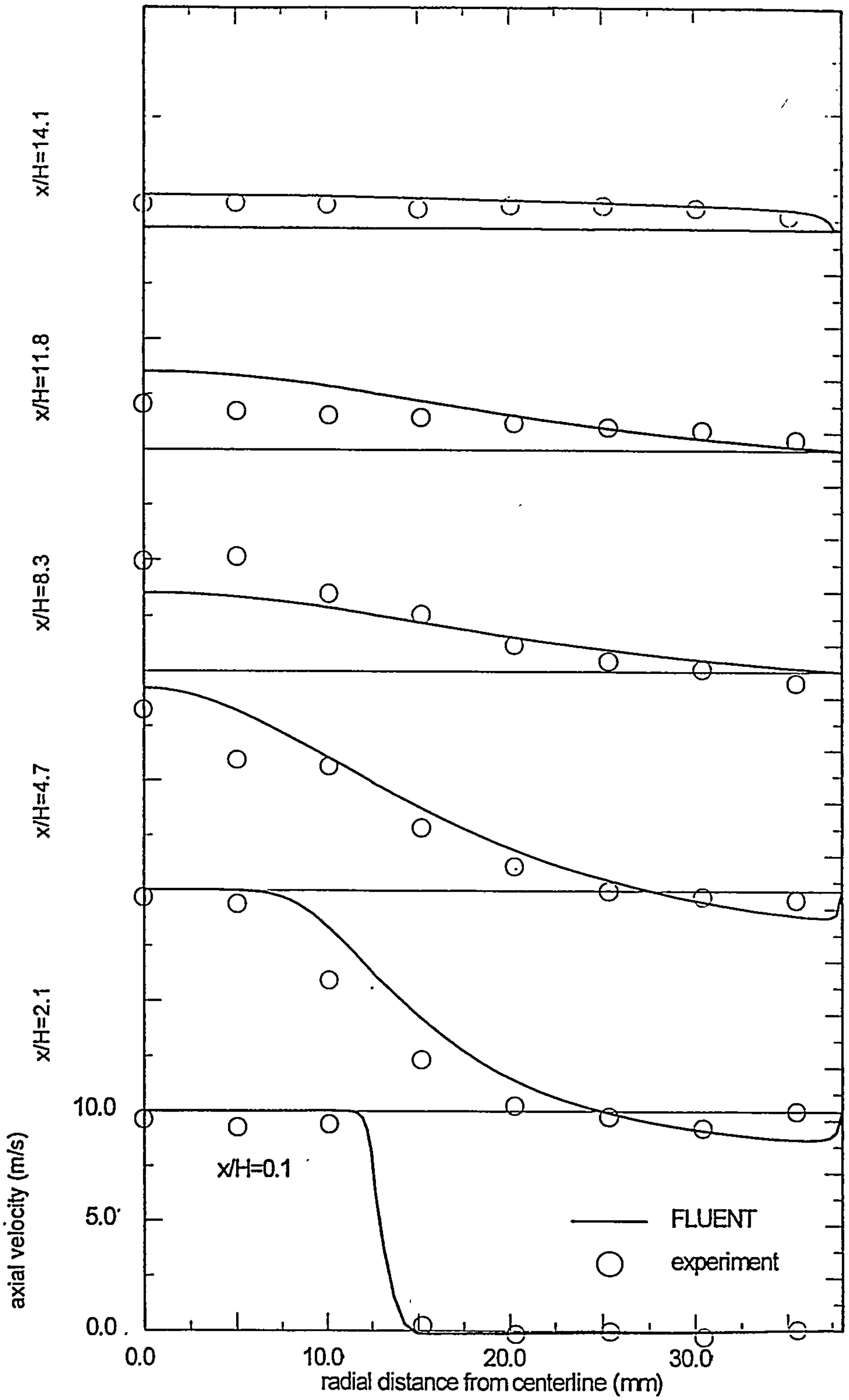

Figure 10. Axial Velocity Versus Radial Position at Six Axial Locations for the Combustor Operating at 2 atm and an Inlet Temperature of 383 K

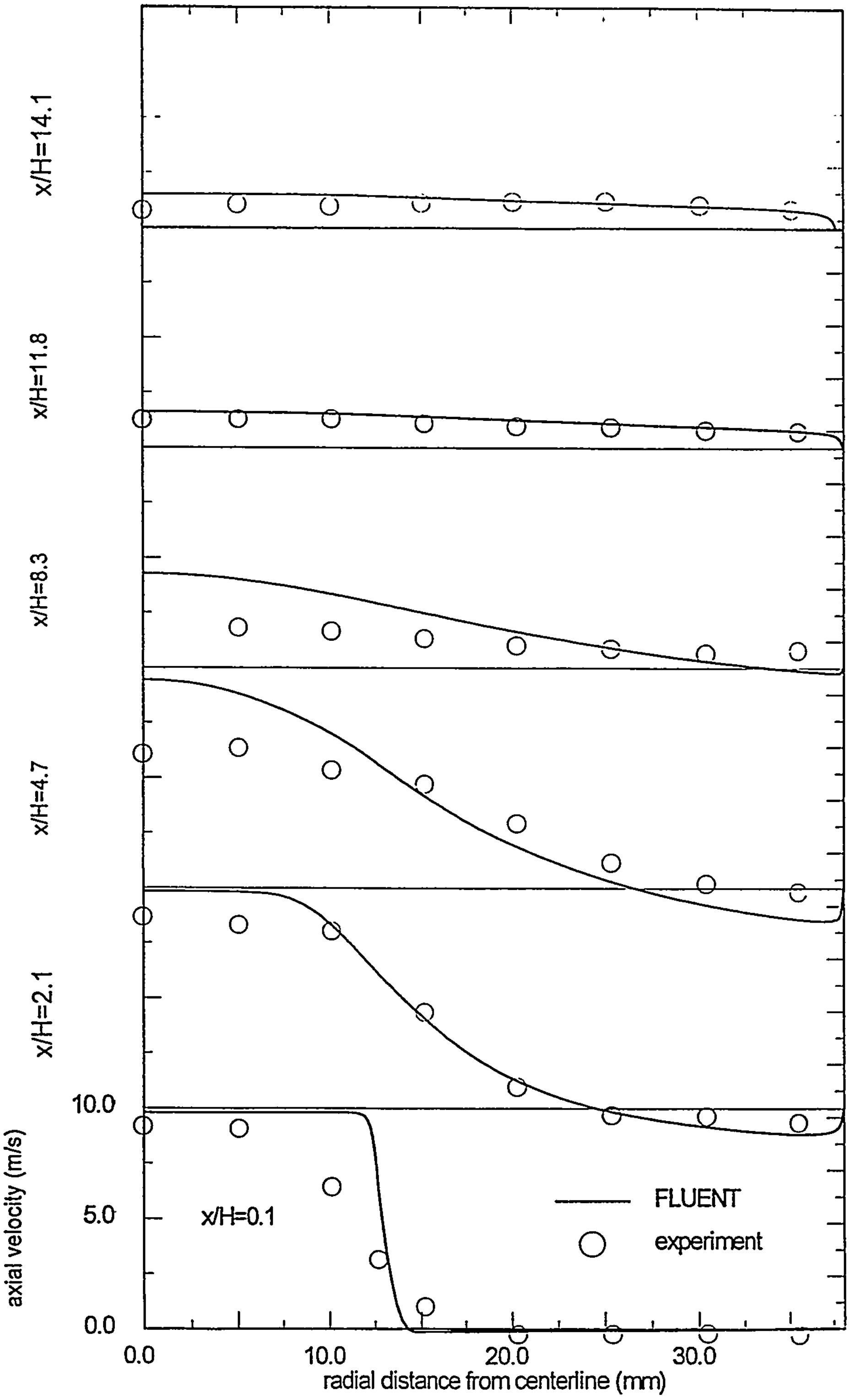

Figure 11. Axial Velocity Versus Radial Position at Six Axial Locations for the Combustor Operating at 5 atm and an Inlet Temperature of 439 K

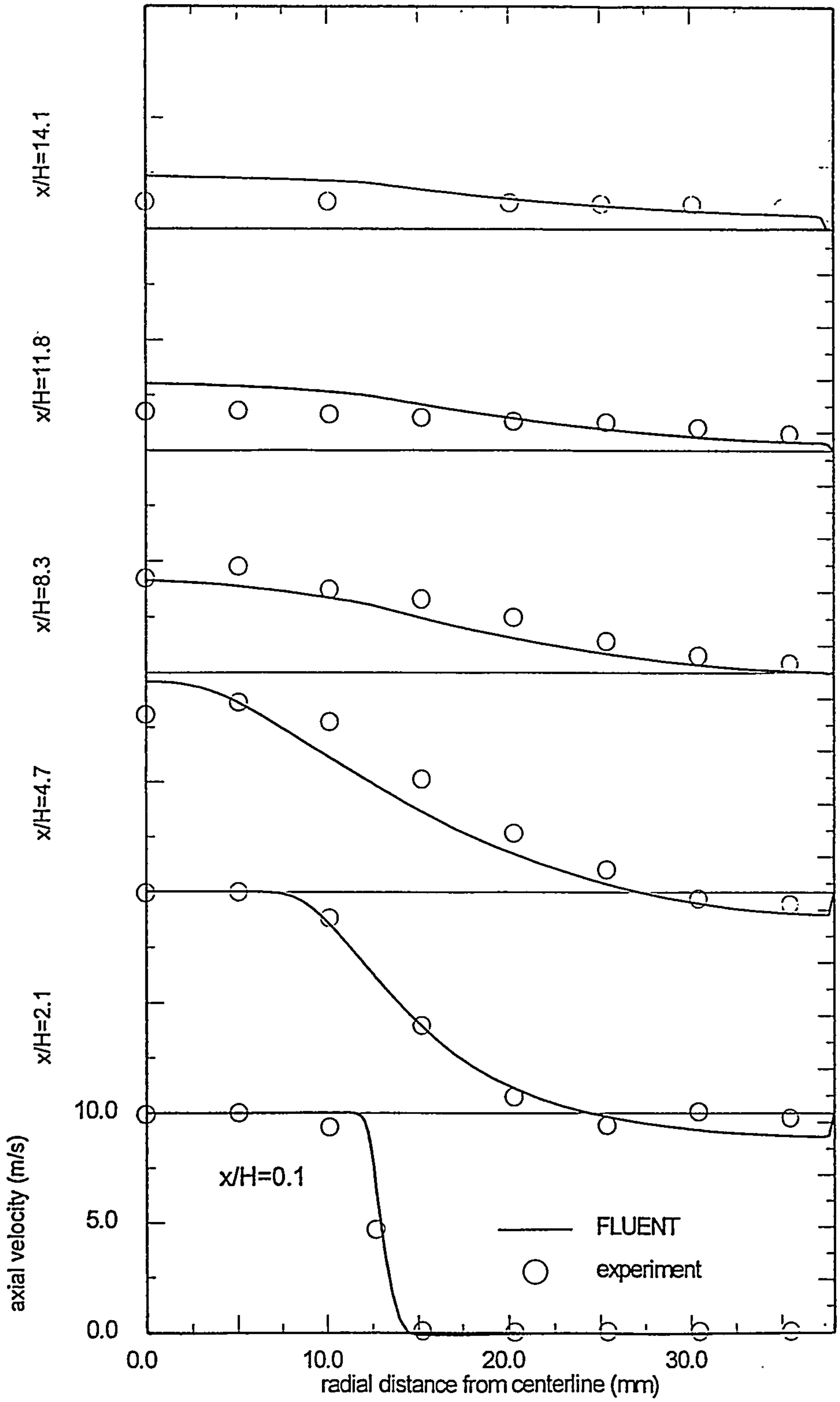

Figure 13. Axial Velocity Versus Radial Position at Six Axial Locations for the Combustor Operating at 15 atm and an Inlet Temperature of 477 K

P4

Functionally Gradient Materials for Thermal Barrier Coatings in Advanced Gas Turbine Systems

Stephen W. Banovic (swb0@lehigh.edu, 610-758-4270)
Katayun Barmak (kab6@lehigh.edu, 610-758-4218)
Helen M. Chan (hmc0@lehigh.edu, 610-758-5554)
Martin P. Harmer (mph2@lehigh.edu, 610-758-4227)
Arnold R. Marder (arm0@lehigh.edu, 610-758-4197)
Cindy M. Petronis (cmp4@lehigh.edu, 610-758-4701)
Douglas G. Puerta (dgp2@lehigh.edu, 610-758-5000)
Suxing Wu (suw2@lehigh.edu, 610-758-4216)
Materials Research Center and Energy Research Center
Lehigh University
5 E. Packer Avenue
Bethlehem, PA 18015

Introduction

New designs for advanced gas turbine engines for power production are required to have higher operating temperatures in order to increase efficiency [1]. However, elevated temperatures will increase the magnitude and severity of environmental degradation of critical turbine components (e.g. combustor parts, turbine blades,etc..). To offset this problem, the usage of thermal barrier coatings (TBCs) has become popular by allowing an increase in maximum inlet temperatures for an operating engine [2,3]. Although thermal barrier technology is over thirty years old, the principle failure mechanism is the spallation of the ceramic coating at or near the ceramic/bond coat interface [4,5]. Therefore, it is desirable to develop a coating that combines the thermal barrier qualities of the ceramic layer and the corrosion protection by the metallic bond coat without the detrimental effects associated with the localization of the ceramic/metal interface to a single plane.

Objectives

The concept for the delocalization of interfaces has led to the development of functionally, structurally, and chemically graded architectures and materials. Functionally Graded Materials (FGMs) for thermal barrier coatings are metal/ceramic composites that are discretely or continuously graded from 100% ceramic at the outer surface to 100% metal in the inner surface. It has been the focus of this research program to investigate novel techniques for producing FGMs that override present processing barriers of prevalently utilized methods. In an initial effort to produce FGMs, reaction-bonded metal oxide (RBMO) and electrodeposition processes have been studied on model systems.

Research sponsored by the U.S. Department of Energy's South Carolina Energy Research & Development Center, under contract DE-FC21-92MC29061 with the Materials Research Center and Energy Research Center at Lehigh University, 5 E. Packer Avenue, Bethlehem, PA, 18015; telefax: 610-758-4244.

Approach

Reaction-Bonded Metal Oxide (RBMO)

The reaction-bonded metal oxide (RBMO) process utilizes the oxidation reaction of attrition-milled and compacted metal/ceramic powder mixtures to make monolithic and composite ceramics. In the production of reaction-bonded Al_2O_3 (RBAO), the volume fraction of Al is usually in the range of 0.3-0.6, with the remainder of the powder mixture being predominantly Al_2O_3. The process offers significant advantages over conventional ceramic processing, such as low raw material costs, low processing temperatures, machinability of green bodies, and near-net-shape forming capability. Reaction-bonded ceramics and composites exhibit superior microstructures with sub-micron grain sizes and fracture strengths >800 MPa for the ZrO_2-containing RBAO bodies.

Electrodeposition

Electrodeposition is the application of a coating on a substrate by passing a current through an electrolytic solution. The electrolytic solution is a conducting fluid in which the flow of current is accompanied by the movement of ions from an anode to a cathode. As the M^+ ions are reduced at the cathode surface, an electroplated coating of M metal is produced. The advantages of electrodeposition is its low equipment costs and the ability to coat complex shapes. In order to fabricate an electro-composite, second phase particles are mechanically suspended in the electrolyte where they are incorporated into the metallic matrix due to physical and electrochemical means. The amount of co-deposited particles depends on many processing parameters such as the type of electrolyte bath, the current density, the amount of particles in the bath, and the size, shape, and nature of the particles.

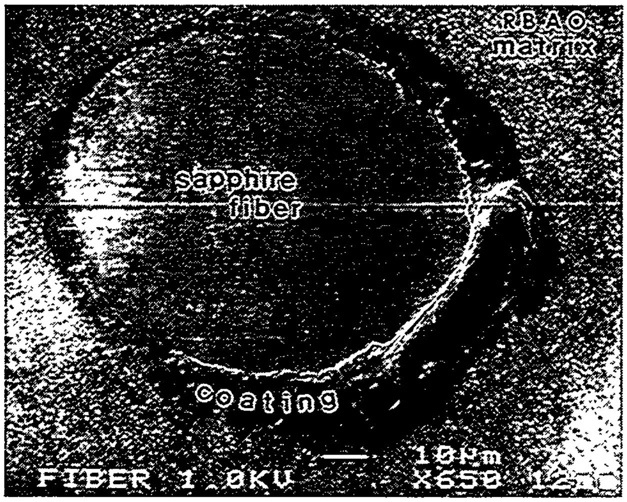

Figure 1: Microstructure of RBMO/sapphire-fiber composite. The fiber is coated with monazite.

Results

RBMO

In the present work, RBMO technology has been adapted to produce fiber reinforced ceramic matrix composites, as well as functionally graded structures for turbine components for use in advanced gas turbine systems. Large diameter ($>100\mu$m) continuous sapphire fibers coated with a thin layer of monazite ($LaPO_4$) were incorporated into a reaction-bonded mullite matrix which exhibits near zero shrinkage. The thickness of the coating layer can be controlled in the range of 2-20μm. Crack-free dense bodies consisting of 95 volume percent mullite and approximately 5 volume percent sapphire fibers were successfully produced by the reaction-bonding technique. The microstructure of the composites is shown in figure 1. Fracture studies have been conducted to determine the effectiveness of the fibers (and coatings) in enhancing toughness. Preliminary results (figure 2) showed that the monazite provides a weak interface to allow debonding of the fiber from the matrix, thus fulfilling one of the major requirements for promoting high toughness.

Figure 2: Fracture surface of the RBMO/sapphire-fiber composite.

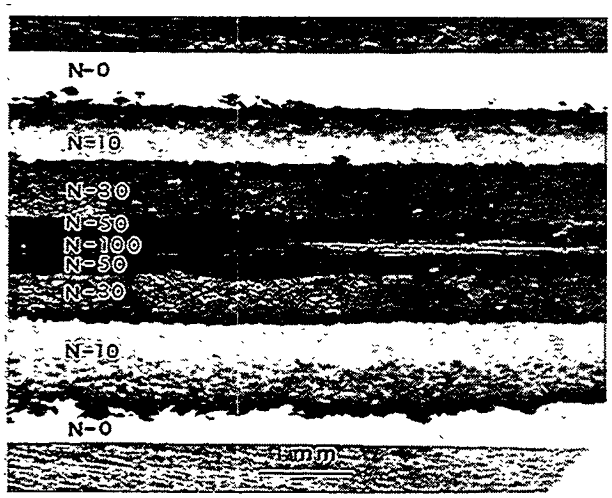

Figure 3: Cross-section of the FGM made by reaction-bonding.

The RBMO process was also used to fabricate layered structures (FGMs). The composition of each layer is given in Table I. All the powder mixtures except N-100 were attrition milled for 7 hours in acetone with TZP-balls. In forming the green body, layers of the precursor powders were symmetrically pressed together in the following sequence: Ni-0/Ni-10/Ni-30/Ni-50/Ni-100/Ni-50/Ni-30/ Ni-10/Ni-0. The samples were annealed in air at 750°C for 30 min,this heat-treatment was chosen so as to oxidize the Al, without oxidizing the Ni. Finally, sintering was conducted at 1300°C in an inert argon atmosphere to produce dense and crack-free samples. After reaction-bonding, the outermost layers consisted of Al_2O_3/ZrO_2, whereas the center layer was pure Ni metal. The compositions of the intermediate layers are graded so that they become Al_2O_3 rich going from the center to the outside. A cross-section of the FGM is shown in figure 3.

Table I: Powder composition (vol%) in each layer of the FGM material.

Sample	Ni-0	Ni-10	Ni-30	Ni-50	Ni-100
Ni	0	10	30	50	100
Al	45	45	40	35	0
Al_2O_3	35	35	20	5	0
ZrO_2	20	10	10	10	0

Electrodeposition

A model system of co-deposited metallic nickel matrix with second phase alumina (Al_2O_3) particles was used to investigate the effect of the processing parameters on the microstructure of the electrodeposits. It was found that a larger volume percent of incorporated alumina occurred when a nickel sulfamate bath was used compared to a Watts type bath. At higher current densities, a plateau occurred for the incorporation of particles, while decreasing the parameter resulted in a larger volume percent, figure 4. In addition, the particle characteristics played a large role in the incorporation. The volume percent increased when alpha alumina was deposited over gamma alumina, increasing the bath loading of particles (figure 4), decreasing the particle size, and having shapes nearer to that of spherical. Approximately 35 volume percent alumina has presently been

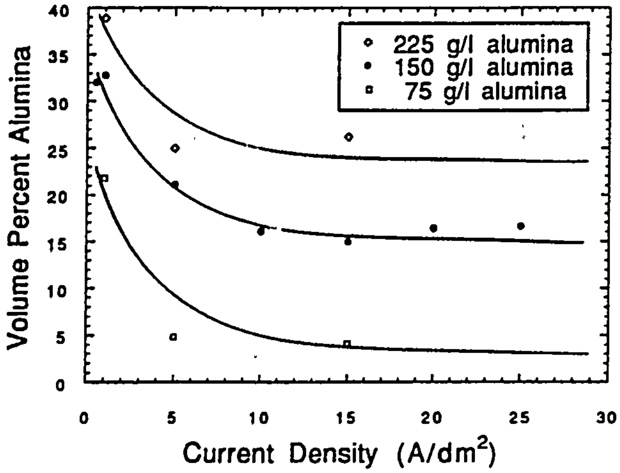

alumina
ent density

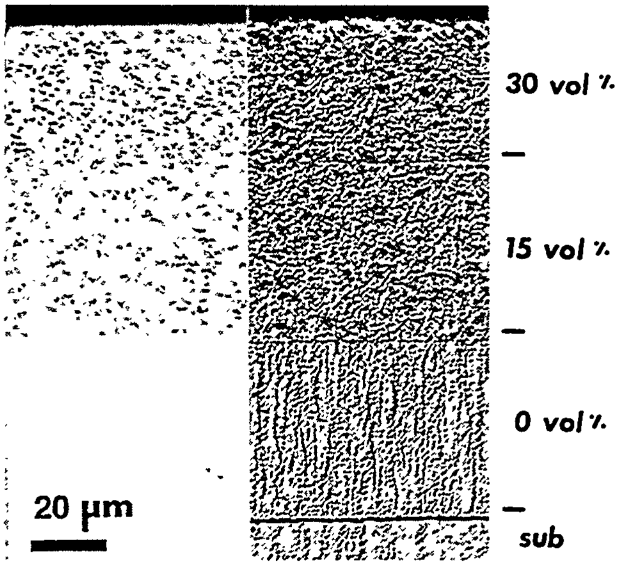

Figure 5: Cross-section a discretely layered FGM fabricated via electrodeposition.

incorporated. Through manipulation of the processing parameters, a trilayer graded structure has been produced, thus demonstrating the feasibility of electrodeposition in grading structures, as seen in figure 5. A microindentation hardness profile of the structure is displayed in figure 6. The increasing grade in microindentation hardness with increasing alumina volume percent is indicative of an increase in other mechanical properties, such as tensile strength, of the coating.

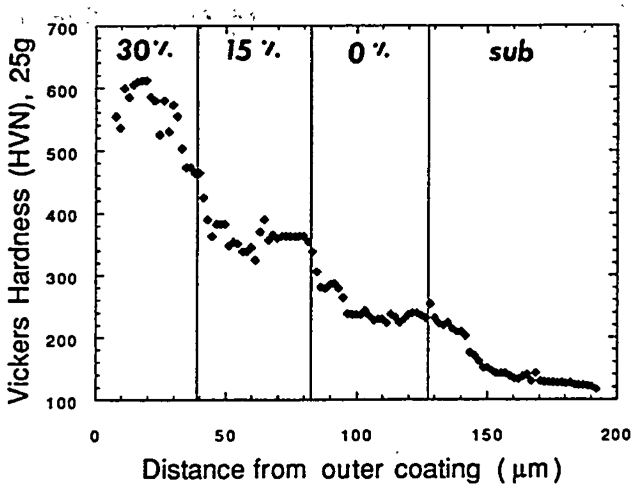

Figure 6: Characteristic microindentation hardness profile of a discretely graded structure.

Limitations in the amount of ceramic (inert) particles deposited has led to the expansion of this research to include electrophoretic deposition. This method is capable of depositing high volume percents of ceramic (inert) particles from a non-aqueous bath due to the attraction of the particles themselves. Coating thicknesses ranging from a few microns to a few millimeters can be produced within minutes. Initial efforts have led to the production of approximately 50μm crack-free ZrO_2 coatings.

Future Activities

RBMO

Future research will include the evaluation of the mechanical and thermo-mechanical properties of existing RBAO/FGM layered composites, as well as the production of composites with thinner layers. The mechanical properties of the fiber reinforced mullite matrix composites will also be assessed. Novel coatings produced by electrophoretic deposition of RBAO precursor powders is also being investigated.

Electrodeposition

Future research will focus on the production of finer graded architectures using electrodeposition. In conjunction with the electrophoresis process, the fabrication of a thermal barrier FGM will be studied. The characterization of these FGMs will be investigated before and after thermal cycling, as well as their mechanical and thermo-mechanical properties.

Acknowledgements

The authors would like to acknowledge our contract officers Dr. Paul Micheli, Dr. Norm Holocombe, and Dr. Daniel Fant. This work was performed during the period of September 1, 1994, through August 31, 1995.

References

1. Meetham, G.W. 1985. *J of Vac. Sci. and Tech*, A3 (6): 2509-15.
2. Sheffler, K.D. and Gupta, D.K. 1988. *J of Engr. for Gas Turbines and Power*, 110:605-9.
3. Reardon, J.D. and Dorfman, M.R. 1987. *J of Matl for Energy Systems*, 8 (4): 414-9.
4. Wu, B.C. et al. 1989. *Thin Solid Films*, 172:185-96.
5. Miller, R.A. 1987. *Trans. Of ASME*, 109: 448-51.

P5

Advanced Turbine Cooling, Heat Transfer, and Aerodynamic Studies

Je-Chin Han (JCH2187@ACS.TAMU.EDU; 409-845-3738)
Meinhard T. Schobeiri (TMS1885@ACS.TAMU.EDU; 409-845-0819)
Department of Mechanical Engineering
Texas A&M University
College Station, TX 77843-3123

Introduction

The contractual work is in three parts: **Part I** - Effect of rotation on enhanced cooling passage heat transfer, **Part II** - Effect of Thermal Barrier Coating (TBC) spallation on surface heat transfer, and **Part III** - Effect of surface roughness and trailing edge ejection on turbine efficiency under unsteady flow conditions. Each section of this paper has been divided into three parts to individually accommodate each part. Part III is further divided into Parts IIIa and IIIb.

Part I

In modern gas turbine engines, as turbine inlet temperature increases the engine thermal efficiency increases. However, the heat transferred to the blades in the turbine also increases. Still, the level and variation of temperature within the blade material (which cause thermal stresses) must be limited to achieve reasonable blade durability goals. The blades are cooled by air extracted from the compressor of the engine. Since this extraction incurs a penalty to the thermal efficiency it is necessary to understand and to optimize for the engine and turbine operating conditions, the cooling method used, and the turbine blade geometry. This investigation studies jet impingement cooling which is a very effective cooling method. Jet impingement cooling uses cool jets of air, produced by pressure differences across nozzles in a nozzle array, to impinge on and cool a heated target surface (the interior surface of a turbine blade).

Numerous studies on jet impingement cooling (i.e. reviewed by Downs and James (1987)) have concentrated on designs for turbine blades. For example Kercher and Tabakoff (1970) and Florschuetz and Su (1987) varied geometric and operating parameters on stationary test models to determine optimum passage designs. For rotating turbine blades however, rotation creates additional forces (centrifugal and Coriolis) on the air and thus alters air motion and target surface heat transfer when compared with those results for stationary conditions. Only Epstein et al. (1985) studied the effect of rotation on jet impingement heat transfer (for jet flow perpendicular to the direction of rotation) in the concave leading edge region of a turbine blade. They showed heat transfer decreased up to 30% with significant jet deflection near the blade root when compared with stationary results. Therefore, this investigation expands on the limited information for the effects of rotation

---

Research sponsored by the U.S. Department of Energy's Morgantown Energy Technology Center, under Contract DE-FC21-92MC9061 with Texas A&M University, College Station, TX 77843-3123.
Telefax: 409-862-2418

on jet impingement cooling for use in the internal cooling passage design of rotating turbine blades.

Part II

Advanced gas turbine engine components are covered by thermal barrier coatings (TBC) to protect the surface from hot post-combustion gases. Spallation of TBC (coating loss) occurs due to thermal stresses, or erosion and corrosion caused by using coal derived fuels. TBC spallation exposes the metal surfaces to hot gases and increases local and downstream heat transfer coefficients. Ekkad and Han (1995) studied the effect of depth, size, and shape of spallation on a flat surface. They reported that the heat transfer coefficient with spallation is enhanced up to two times compared with that for a smooth surface. The present study simulates the effect of TBC spallation on surface heat transfer on a cylindrical leading edge. The cylindrical leading edge simulates the turbine blade leading edge region. Ekkad et al. (1995) presented detailed heat transfer and film effectiveness measurements for film cooling on a cylindrical leading edge model. They presented results at five blowing ratios under two free-stream turbulence conditions. The present study investigates the effects of free-stream turbulence and film cooling on surface heat transfer coefficients and film effectiveness with spallation. Detailed distributions within and around the spallation are measured using a transient liquid crystal technique.

Part III

Part IIIa. The improvement of efficiency and performance of turbine and compressor stages has been a key issue in turbomachinery research and development for several decades. Considerable efforts have been made to develop blade profiles with optimum efficiency for a variety of specific stage-load and flow coefficients encountered in turbine engine design technology. The optimization of blade geometry regarding the profile loss/efficiency, incidence and deviation range by the industry and research institutions was performed utilizing steady flow cascade experiments. As a rule, the implementation of these profiles into the turbine component was associated with discrepancies in efficiency behavior that are partially attributed to the unsteady nature of the turbomachinery stage flow. Realizing the impact of unsteady flow on turbomachines, many researchers have investigated the effect of unsteady inlet flow on flat plates, cascades and on turbine stages using different types of wake generators. Refer to Schobeiri et al. (1995) for a detailed review of the relevant literature.

Part IIIb. The improvement of thermal efficiency of power generation gas turbines has been a major goal in turbomachinery research over the last decades. Accordingly, considerable efforts have been made to increase the turbine inlet temperature. For conventional turbine blade material, the increased inlet temperature requires cooling of the front stages. The cooling mass flow is injected partially or entirely through the trailing-edge slots into the downstream axial gap, where the cooling and the main mass flows are mixed. The ejection process is associated with losses that can be minimized by optimizing the relevant ejection parameters. These parameters include, among others, the ejection velocity ratio, ejection mass flow ratio, slot-width/trailing-edge-thickness ratio, and the boundary layer parameters on the suction and the pressure surface. Improper selection of these parameters results in higher mixing losses that reduce the efficiency of the cooled gas turbine blade.

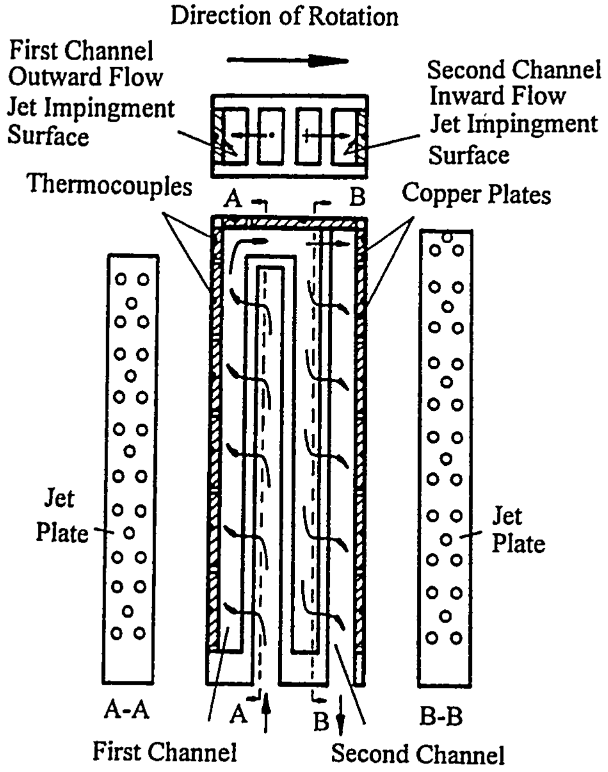

Figure 1.1 Test Model Schematic

Objectives

Part I

This investigation's goal is to measure flow distributions in and local convective heat transfer on smooth target surfaces in rectangular cross sectioned, orthogonally rotating, channels with jet impingement cooling under rotating conditions. Figure 1.1 shows sketches of cross sections for the test model. This model's design permits simultaneous testing for two jet impingement arrays. Air first enters a supply channel in the test model. Then in the first channel air jets created by one jet plate (see section A-A) flow opposite to the direction of rotation (forward rotation indicated in Figure 1) and impinge on the jet impingement surface in the first channel. The air then flows radially outward in the first channel inducing cross flow on other jets in the first channel array. The air then turns 180° (without impinging jets), flows radially inward and becomes the supply air for jets in the second channel. In the second channel, air jets created by the other jet plate (see section B-B) flow in the direction of rotation and impinge on the jet impingement surface in the second channel. Air exits the second channel radially inward and again induces cross flow on other jets in the second channel array. The test model will rotate in the forward and reverse directions. Also, non-rotating data will be taken for a baseline and compared with previous investigations.

Part II

The objective of this study is to investigate the effects of TBC spallation on a cylindrical leading edge model using a transient liquid crystal technique. Detailed heat transfer coefficient distributions are obtained for four spallation locations on the leading edge of the cylinder under varying free-stream turbulence conditions. Film cooling holes were placed at 15° from the leading edge. Film cooling was combined with two downstream spallation locations to study the effect of spallation on film cooling. Two different depths of spallation were tested at each location to investigate the heat transfer enhancement caused by the spallation depth.

Part III

Part IIIa. The published research works on turbine cascade aerodynamics including the boundary layer studies, have largely concentrated on the measurements of the profile losses and the boundary layer development under steady flow conditions. The few available boundary layer measurements are not comprehensive enough to provide any conclusive evidence for the interpretation of the boundary layer transition and separation process and its direct impact on profile loss and efficiency. A research program has been initiated to address the effects of the unsteady wake flow on the turbine efficiency. The objectives of this research are to: (1) provide a detailed unsteady boundary layer information essential for understanding the turbomachinery wake flow physics and its impact on efficiency and heat transfer; and (2) establish an unsteady boundary layer transition model. The data are analyzed using the conventional and wavelet-based methods.

Part IIIb. The first objective of this research is to experimentally investigate the effect of the relevant ejection parameters such as the ejection velocity ratio, ejection mass flow ratio, the slot-width/trailing edge thickness ratio, and the suction and pressure surface boundary layer parameters on the cascade aerodynamics and particularly on the mixing losses downstream of a cooled gas turbine blade. The second objective is to compare the experimental results with an extended theory developed by Schobeiri (1989). Based on the results, criteria will be established that allow an optimum aerodynamic design of the trailing edge ejection.

Approach

Part I

This experimental study uses the steady state method to measure convective surface heat transfer coefficients. For this method, heated surfaces (copper plates) in the test model are cooled by air flowing across the surfaces and temperatures are measured by thermocouples. The local heat transfer coefficient, Nusselt number Nu, is:

$$\begin{aligned} Nu &= h\,d_{jet}/k \\ &= d_{jet}\,q_{net}/[k A_{plate}(T_{wall}-T_{bulk\,air})] \end{aligned} \qquad \textbf{(1.1)}$$

where d_{jet} is the jet hole (nozzle) diameter, k is the air thermal conductivity, A_{plate} is the heated plate exposed surface area, T_{wall} is a plate temperature, $T_{bulk\ air}$ is bulk air temperature adjacent to the plate, and q_{net} is the heat (energy) transferred from the plate to the air. To determine flow distribution throughout the test model, channel air temperatures and pressures are measured to calculate individual jet and channel flow rates.

Part II

The detailed heat transfer coefficient and film effectiveness distributions are obtained using a transient liquid crystal technique. The technique uses a real time image processing system. The image processing system consists of an RGB camera, a monitor, and a PC with a CFG frame grabber board. The surface is heated to a constant temperature and suddenly cooled by a room temperature free-stream. The color change time of the liquid crystal is captured for each pixel location on the surface. The time required for each pixel to change color to red from the initiation of the transient test is stored. The surface temperature response of the test surface is based on a semi-infinite solid assumption. The solution for a semi-infinite solid with 1-D transient conduction and a convective boundary condition at the surface is given by

$$\frac{T_w - T_i}{T_\infty - T_i} = 1 - \exp\left(\frac{h^2 \alpha t}{k^2}\right) erfc\left(\frac{h\sqrt{\alpha t}}{k}\right) \qquad \textbf{(2.1)}$$

where T_w is the color change temperature obtained from calibration, T_i is the initial temperature of the test surface, T_∞ is the free-stream temperature, t is the time of color change from the start of the transient test, and α and k are the thermal diffusivity and conductivity of the test surface material. The heat transfer coefficient (h) is obtained at each pixel using the above equation (Ekkad and Han, 1995). For the film cooling case, the free-stream temperature (T_∞) is replaced by a film temperature (T_f) which is a mixture of both the free-stream and coolant (T_c) temperatures. Film cooling effectiveness is defined as

$$\eta = \frac{T_f - T_\infty}{T_c - T_\infty}; \quad or \quad T_f = \eta T_c + (1-\eta) T_\infty \qquad \textbf{(2.2)}$$

Replacing T_∞ with T_f in Eq. (2.1) and then replacing T_f in terms of η from Eq. (2.2), the following equation with two unknowns of h and η is obtained

$$T_w - T_i = [1 - \exp(\frac{h^2 \alpha t}{k^2}) erfc(\frac{h\sqrt{\alpha t}}{k})] \qquad \textbf{(2.3)}$$
$$[\eta T_c + (1-\eta) T_\infty - T_i]$$

Two similar tests are run to obtain both h and η. In the first test, both the coolant and free-stream are at room temperature and the heat transfer coefficient is calculated using Eq.(2.1). The coolant is heated to a temperature close to the initial temperature for the second test. Since the local heat transfer coefficient is known, the film effectiveness can be calculated by rearranging Eq.(2.3) as

$$\eta = \frac{T_w - T_i}{T_c - T_\infty}\frac{1}{F(h)} + \frac{T_i - T_\infty}{T_c - T_\infty} \qquad \textbf{(2.4)}$$
$$where \quad F(h) = 1 - \exp(\frac{h^2 \alpha t}{k^2}) erfc(\frac{h\sqrt{\alpha t}}{k})$$

Detailed heat transfer coefficient and film effectiveness distributions are obtained by applying Eqs. (2.1) and (2.4) at each pixel location (Ekkad et al., 1995).

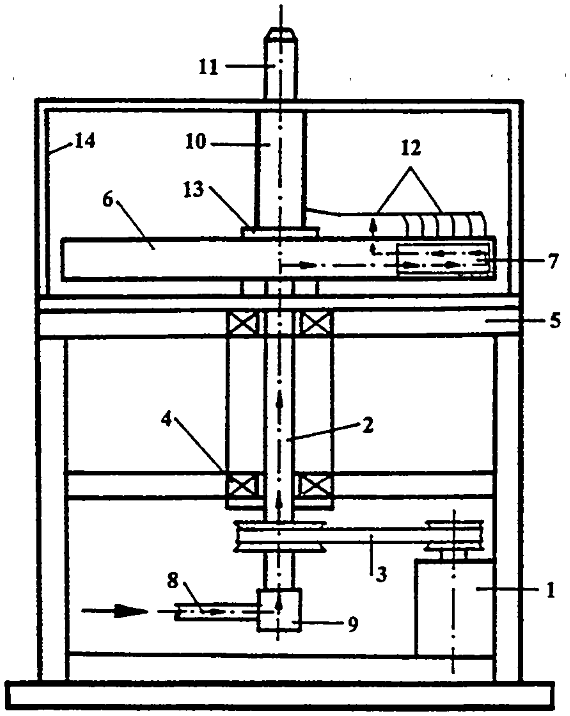

1. Electric Motor
2. Rotating Shaft
3. Belt Drive-Pulley System
4. Bearing Support System
5. Steel Table
6. Rotating Arm
7. Two-Pass Test Model
8. Compressed, Regulated Air
9. Rotating Union
10. Slip Ring Unit
11. Scanivalve Unit
12. Pressure Taps & Tubing
13. Hub
14. Safety-Guard

Figure 1.2 Test Stand Schematic

Project Description

Part I

Figure 1.2 shows a test stand schematic. Compressed air (coolant) is regulated by a flow control valve, flows through a sharp edge orifice flowmeter, through tubing, and through a rotating union at the bottom of a rotating shaft. The air then passes through the hollow rotating shaft and an aluminum, hollow rotating arm mounted perpendicularly onto the shaft. Finally the air passes through the test model and exits through a hole in the arm into the lab. An electric motor with an adjustable frequency controller turns the shaft, arm, test model, a slip ring unit and a scanivalve unit via a toothed belt. A digital photo tachometer measures the shaft speed.

Figure 1.1 also shows a schematic of the test model (223.5mm long) located at one end of the rotating arm, which is designed to simulate jet impingement cooling in a rotating turbine blade. The supply and heated rectangular cross section channels are 9.5 x 19.0mm. Air enters a supply channel and then flows through the first channel jet plate (1.59mm thick) with 25 holes (nozzles) in a repeating staggered (2-1-2) arrangement. The hole diameters are 3.175mm and are spaced 3 diameters (9.5mm) away from the heated target jet impingement surface in the first channel. Air impinges on this surface and then flows radially outward creating cross flow on other jets. There are no holes (jets) in the 180° turn region but the outside wall is heated. The air, then enters a second supply channel, flows through the 28 holes of the second channel jet plate, impinges on the heated target jet impingement surface in the second channel, and exits the test model radially inward which creates cross flow on other jets. The hole diameters, arrangement and spacing to target surface are the same as for the first channel.

To obtain regionally averaged (local) heat transfer measurements, the heated target surfaces are made of isolated copper plates. Thin (1.59mm) strips of teflon separate and insulate these plates. The two target walls consist of 6 plates each (5 plates 38.1 x 19.1 x 3.2mm, 1 plate 25.4 x 19.1 x 3.2mm) with an additional two plates (25.4 x 19.1 x 3.2mm each) for the turn region. The plates are heated by electrical resistance heaters (one per wall) in grooves on the back sides of the plates and contain an imbedded thermocouple to measure local wall temperature. Thermocouples in the channel centers measure the bulk air temperature adjacent to each plate and at the inlet and outlet to the test model. The remainder of the test model is teflon for insulation. A slip ring unit mounted atop a hub connects the shaft to the arm. This unit transfers thermocouple outputs to a data logger interfaced to a personal computer and variable electric transformer outputs to the heaters.

Two tests are conducted to obtain local Nusselt number. The parameter q_{net} equals q_{total} - q_{loss} where q_{total} is the heat generated at a plate for heat transfer tests and q_{loss} is the heat loss for a plate. For heat transfer tests, the rotating speed and overall air flow rate are set and the transformers adjusted until the desired heated wall temperatures are reached. The plate and air temperatures, voltages and currents for each heater, and overall flow rate are recorded at steady state conditions. Then q_{total} is the heater power (voltage x current) times the proportion of exposed plate area to total exposed plate area for the wall (heater). The heat loss per plate (q_{loss}) is the amount of heat flowing into the test model and test stand but not convecting directly to the air. Separate tests for heat loss are performed at the same rotating speed, with no air flow, and with the exit covered with tape to prevent forced convection induced by rotation. Several input power levels are used to determine heat loss as a function of plate temperature. Using the method of Kline and McClintock (1953) the maximum uncertainty for Nusselt number is estimated to be less than 7%.

To obtain flow distribution measurements, there are wall static pressure taps in all of the channels. These taps measure the local pressure difference and permit the local jet air flow rate through holes and thus the local channel flow rate for the two jet arrays to be determined. Tubes from the taps are connected to the scanivalve unit. This unit measures the pressure at each tap using a pressure transducer and a multiport fluid switch. The unit transfers its output via the slip ring unit.

The flow distribution tests are conducted adiabatically (without heat). This investigation assumes the flow distribution is relatively unchanged by heat addition during heat transfer tests. For flow tests, the rotation speed and desired total flow rate are set at desired levels. The static pressure readings in the channels are then recorded using the scanivalve unit. The pressure transducer is also calibrated. Calculations for individual jet flow rates assume one-dimensional flow and use an ideal gas equation of state, continuity, discharge coefficients and incompressible flow relations.

Part II

Image Processing Setup. The image processing system is described above. The RGB camera is focused on the liquid crystal coated test surface and the test program is activated. The test surface is heated to a temperature above the color range of the liquid crystals. Once a steady surface temperature is achieved, the transient test is initiated by switching on the mainstream air. The time of color change at each location on the test surface is measured by the PC. The heat transfer coefficient and film effectiveness are calculated using the equations above.

Cylindrical Leading Edge Test Setup. The test setup consists of a low speed suction-type wind tunnel facility. The flow enters through a contracting nozzle followed by the test tunnel (76.2 cm wide, 25.4 cm high, and 183 cm long) and is discharged through a blower. The cylindrical test model is placed 77.5 cm downstream of the nozzle exit in the middle of the test tunnel. The cylinder, 7.62 cm in diameter and 25.4 cm long, is hollow with six cartridge heaters hidden inside to heat the outside surface. The cartridge heaters conduct to a copper cylinder that in turn conducts to the polycarbonate exterior, which is 0.64 cm thick and has low thermal conductivity and diffusivity. Figure 2.1 shows the entire test setup.

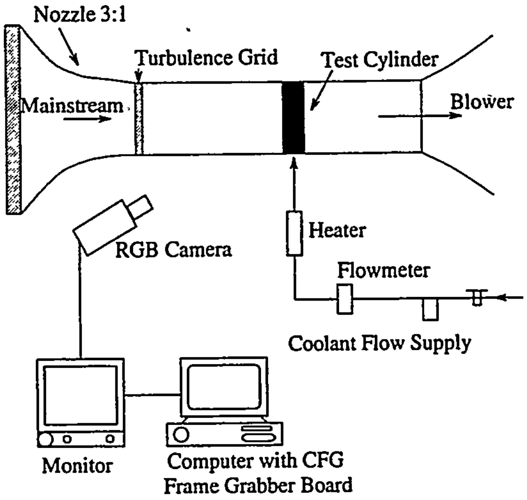

Figure 2.1 Experimental Setup

The front half of the polycarbonate exterior is replaceable. Spallations are machined on each piece at a different location. A spallation occupies about a 20° width on the cylinder. Spallations are placed 0°-20° (S1), 10°-30° (S2), 20°-40° (S3), and 35°-55° (S4). All the spallations are of the same size and are 3.81 cm long (L) and 1.27 cm wide (W). Two different spallation depths of 0.25 cm and 0.51 cm are tested for each spallation location. For the film holes case, film holes are placed at ±15° from the leading edge and are 0.475 cm in diameter and incline 30° and 90° in the spanwise and streamwise directions, respectively. Ten holes in each row are spaced four-hole diameters apart (P/d=4.0). The film hole-to-leading edge diameter

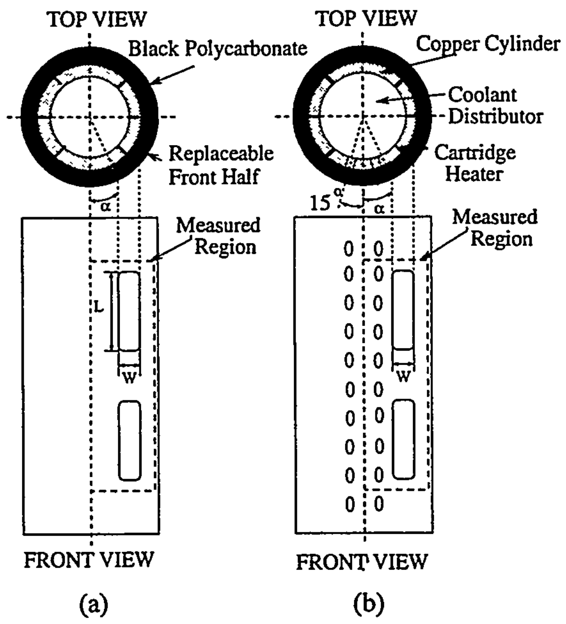

α = 0°, 10°, 20°, 35°
W = 1.27 cm
L = 3.81 cm

Figure 2.2 Leading Edge Test Models (a) Spallation (b) Film Cooling with Spallation

ratio (d/D) was 0.063 and the film hole length-to-hole diameter ratio (L/d) was 3.1. Figure 2.2 illustrates a typical spallation test section and a spallation with film cooling test section.

For the film holes with spallation case, spallations are placed at S3 (20°-40°) and S4 (35°-55°) from the leading edge with film holes at the same location as that for only film cooling case.

Part III

Part IIIa. To study the unsteady cascade flow aerodynamics, a large-scale, high-subsonic research facility is developed (see Fig. 3.1). The facility is capable of sequentially generating up

(a) Test section

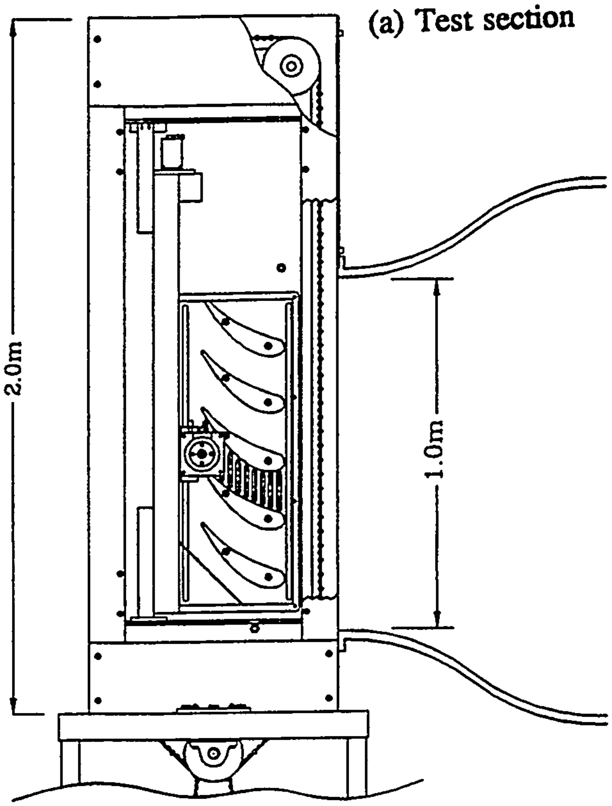

(b) Pressure tap blade

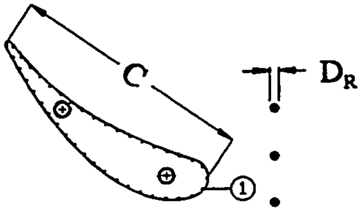

(c) Boundary layer measurement channel

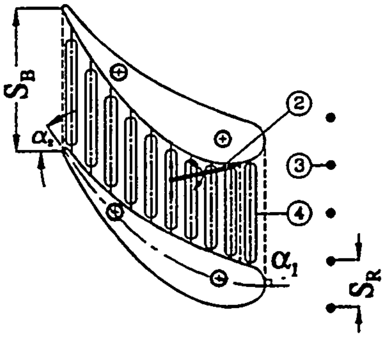

Figure 3.1 Test Section: 1-Static Pressure Taps, 2-Boundary Layer Probe, 3-Wake Generating Rods, 4-Slots for Streamwise Movement of the Probe

to four different unsteady inlet flow conditions that lead to four different unsteady wake structures, passing frequencies, and free-stream turbulence intensities.

A large centrifugal fan with a volume flow rate of 15 m^3 supplies air with a possible maximum mean velocity of approximately 100 m/s at the test section inlet. The flow entering the fan passes through a fiber-glass filter capable of filtering particles of up to 5 μm. A diffuser of length 1500 mm and an area ratio of 1:4.75 is located downstream of a straight pipe that connects the diffuser with the fan. A settling chamber consisting of five screens and one honeycomb flow straightener controls the flow uniformity. Downstream of the settling chamber is a nozzle with an area ratio of 6.75:1 that accelerates the flow to the required velocity before it enters the wake generator. With this tunnel configuration, it is possible to achieve a constant mean fluctuation velocity over a wide velocity range at the nozzle exit. For a nozzle exit velocity of 30 m/s, a turbulent intensity of $Tu = 0.75\%$ was measured. Two-dimensional periodic unsteady inlet flow is simulated by the translational motion of a wake generator (see Fig. 3.1) with a series of cylindrical rods attached to two parallel operating timing belts driven by an electric motor. The belts, having a length of 5000 mm, span over five shaft-pulleys arranged around the cascade test section. The diameter and number of rods can be varied to simulate the wake width and spacing that stem from the trailing edge of rotor blades. The belt-pulley system is driven by a 10kW motor. A frequency controller controls the belt speed to a maximum of 25 m/s. The wake-passing frequency is monitored by a fiber-optic sensor. The sensor also serves as the triggering mechanism for data transfer and its initialization, which is required for ensemble-averaging. The belt is attached with three clusters of rods with constant diameter and spacing (see Table 3.1). As a result, the effect of three different wake passing frequencies at one boundary layer point can be measured sequentially. This cluster configuration considerably reduces the time required for a systematic boundary layer measurement. The data analysis program separates the buffer zones between data clusters and evaluates the data pertaining to each zone. The cascade test section, located downstream of the wake generator, integrates five turbine blades whose geometry is described in the NASA Report by Schobeiri et al. (1991). One blade was specially manufactured and equipped with 40 static pressure taps distributed uniformly around the blade. This blade is connected to a scanivalve to obtain the pressure distribution. A computer controlled traversing system with an encoder feedback is used for accurate positioning of the probes. A single hot-wire probe measures the boundary layer flow.

The data acquisition system is controlled by a 486-personal computer that includes a 16 channel, 12-bit analog-digital (A/D) board with 8-channel simultaneous sample and hold. Mean velocities and turbulent fluctuations are obtained using a commercial 3-channel (TSI), constant temperature hot-wire anemometer system. The wake generator speed and the passing frequency signals of the rods are transmitted by a fiber-optic trigger sensor. The passage signals of the rods are detected by the sensor using a silver-coated reflective paint on one of the belts. This sensor gives an accurate readout of the speed of the wake generator and the passing frequency of the rods. To ensure a high level of accuracy, the calibration method and the facility described in John and Schobeiri (1993) was used for all hot-wire calibrations. The instantaneous velocity components are calculated from the temperature compensated instantaneous voltages by using the calibration coefficients. For steady flow

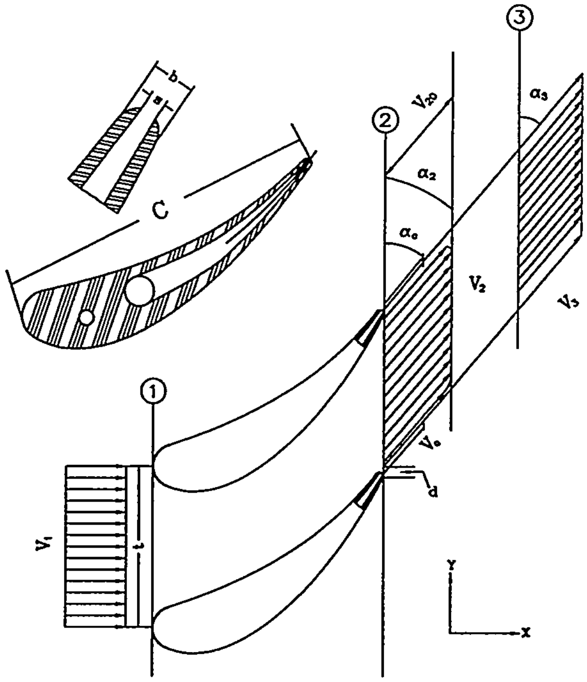

s	b	C	t	α_2
2.6 mm	7.4 mm	281.8 mm	164.0 mm	28.2°

Figure 3.2 Control Surface for Calculating the Pressure Loss Coefficient

investigation, 16384 samples are taken at a sampling rate of 1000 Hz for each point in the boundary layer traverse. For unsteady flow, 2048 samples are taken for each of 100 revolutions of the wake generator, rotating at 7 m/s. The above number of samples per revolution and total number of revolutions were obtained by a preliminary investigation.

Part IIIb. The research facility discussed in Part III-A of this paper was used for the experimental investigations. Since the major components have already been discussed in Part III-A, only a brief description of the trailing edge ejection system is presented. A special blade with an internal cavity and a fixed external ejection slot was designed and integrated into the turbine cascade facility. The blade, which has the same geometry as the one discussed in Part III-A, was mounted in the middle of the turbine cascade. The dimensions of the blade and the trailing edge are given in Fig. 3.2. Filtered air drawn from a medium pressure air line enters a rotameter with an inlet pressure of 1.3 bars and is injected into the blade internal cavity. During the experiments, the temperature difference between primary air flow and ejection air was less than 2°C. Total pressure, flow angles, turbulent intensity, turbulent normal, and shear stresses were measured at the inlet plane and at the trailing edge plane using pneumatic and x-wire probes. For pneumatic measurements, a miniature five hole probe was provided and thoroughly calibrated. For the calibration of the five-hole probe, the non-nulling algorithm developed by Wendt and Reichert (1993) was used that helped automate the calibration procedure. The new method developed by John and Schobeiri (1993) was used for x-wire calibration. A computer controlled traversing system with an encoder feedback was used for the vertical traverse of the five-hole and x-wire probes. The data acquisition system was controlled by a 486-personal computer that includes a 16 channel, 12-bit analog-digital (A/D) board with 8-channel simultaneous sample and hold. Mean velocities and turbulent fluctuations were obtained using a commercial 3-channel (TSI) constant temperature, hot-wire anemometer system. At each point, pressure from each hole of the five-hole probe was sampled sequentially by a rotary scanner and measured with a high precision differential pressure transducer connected to the A/D board. The instantaneous velocity components from the x-probe were calculated from the temperature compensated instantaneous voltages by using the calibration coefficients. A sampling rate of 1000 Hz was used for investigating the steady flow. A comprehensive data reduction system was also generated to reduce the data and evaluate the ejection effect.

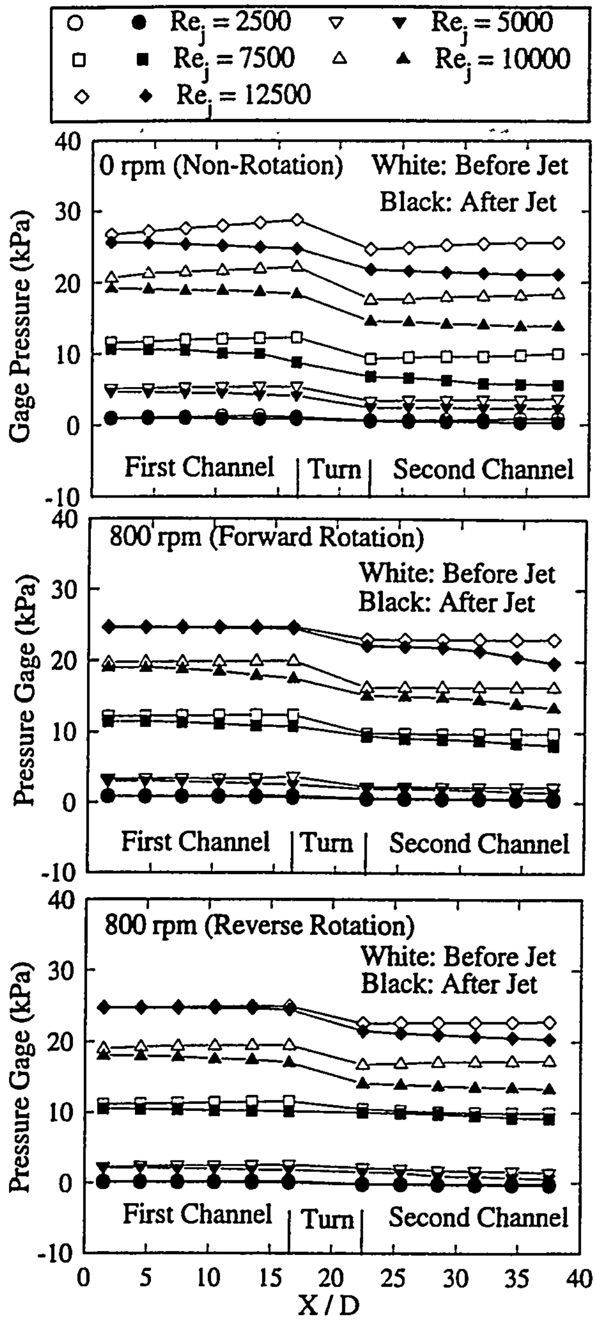

Figure 1.3 Pressure Distributions for Stationary and Rotating Tests

Results

Part I

When considering test model geometry, Nusselt numbers for jet impingement cooling in rotating channels depends on: (1) the ratio of the test model's mean radius to jet diameter, $r_m / d_{jet} = 647.7 / 3.175$; (2) the ratio of channel distance to channel hydraulic diameter, X / D; (3) average jet Reynolds number, Re_j ($\rho_j V_j d_{jet} / \mu$); (4) Prandtl number, 0.72 for air; (5) jet rotation number, Ro ($\Omega d_{jet} / V_j$); (6) wall to jet density (temperature) difference ratio, $(\rho_j - \rho_{wall})/\rho_j = (T_{wall} - T_j)/T_{wall} = 0.129$ ($T_{wall} - T_j = 45°C$); (7) arm rotation direction; and (8) channel geometry (cross section and orientation). Operating conditions are: Re_j = 2500, 5000, 7500, 10000 and 12500, and Ω = 0, 400 and 800 rpm, combining to produce Ro = 0.0023, 0.0028, 0.0038, 0.0057, 0.0075, 0.0113 and 0.0226. The ranges for operating parameters Re_j, Ω, Ro, and $(\rho_j - \rho_{wall})/\rho_j$ are chosen to model actual turbine operating conditions.

For low speed flows in stationary geometries local velocity changes depend on pressure differences or gradients. Figure 1.3 shows channel static pressures versus channel location for the five jet Reynolds numbers under stationary (top) and rotating, 800 rpm in the forward direction (middle) and 800 rpm in the reverse direction (bottom), conditions. By observation the sense and trend of relative pressure differences across the jet nozzles (= before jet pressures - after jet pressures) are the same regardless of channel, Reynolds number, and rotation speed and direction. For all channels, as channel location increases (from X / D = 0 in the first channel and from X / D = 22.5 in the second channel) so do the nozzle pressure differences and so do the jet velocities. From continuity considerations and as indicated by decreasing after jet pressure curves, the first and second channel velocities increase from zero as channel location increases. As expected, the magnitudes of the nozzle pressure differences (jet velocities) and channel gradients (channel

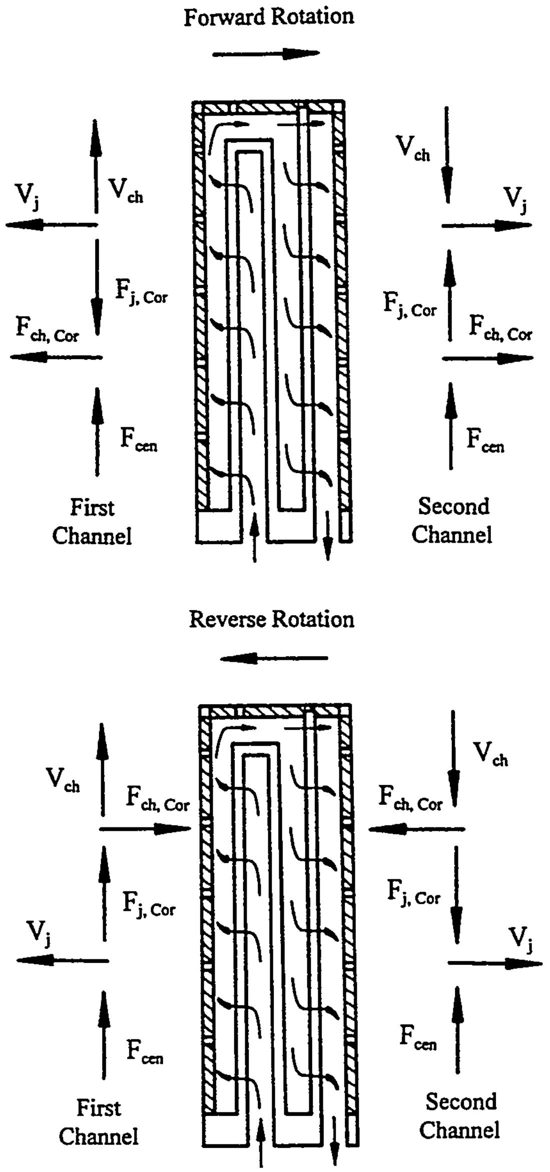

Figure 1.4 Air Velocity and Force Diagrams for Rotating Conditions

velocities) increase as Re_j increases. The static pressures decrease significantly in the turn region due to irreversible mixing losses from relatively high fluid shear stresses.

However, as Figure 1.4 shows, rotation produces centrifugal forces (radially outward) and Coriolis forces (in various directions depending on local velocity direction) altering air flow. For the channel flow directions, the centrifugal forces and Coriolis forces for jet velocities only slightly add to or reduce the air channel velocities. This is because the channel velocities are driven by relatively large forces (i.e., pressure differences or gradients). In addition, rotation creates Coriolis forces acting on fluid moving in the channel flow directions. These Coriolis forces for channel velocities are directed towards the target walls for forward rotation and away from the target walls for reverse rotation.

Figure 1.5 shows the Nusselt number versus channel location for stationary (top), 800 rpm in the forward direction (middle), and 800 rpm in the reverse direction (bottom) operating conditions. As expected for stationary results at a jet Reynolds number, the Nusselt numbers for the first channel are the same as those for the second channel and decrease as channel location increases. However, the Nusselt numbers in the turn region are larger than those for either channel. For the channels, local convection at the point of impingement is high and decreases as distance from this point increases. As channel location increases, however, the magnitude of channel cross flow velocity increases and bends jets away from the target surfaces towards the channel flow direction. This reduces locally high heat transfer at the point of impingement. Also, as channel cross flow develops the heat transfer initially decreases with increasing channel location (for each channel) as for developing flow at a channel entrance. Unlike channel flow alone (without jet impingement), the heat transfer increases further downstream since the amount of channel cross flow increases as the result of added jet flow. This produces increasing velocity gradients at the target surfaces, which increase heat transfer. Thus, for both channels as channel location increases,

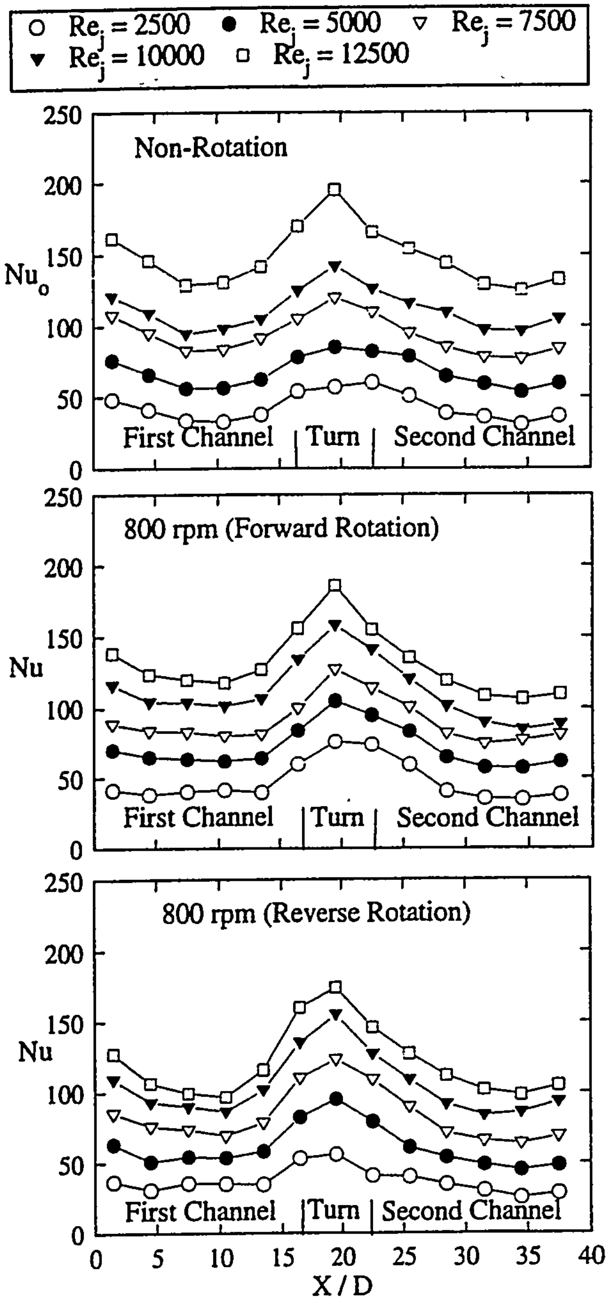

Figure 1.5 Nusselt Number Versus Channel Location for Stationary and Rotating Tests

regional heat transfer starts relatively high due to jet impingement, then decreases due to developing channel cross flow conditions and jet deflection, and finally increases slightly at the channel end due to added channel cross flow. The high heat transfer in the turn region is because all of the first channel flow is directed at the heated turn surfaces, thinning their boundary layers and increasing heat transfer. Finally, as Re_j increases so do Nusselt numbers.

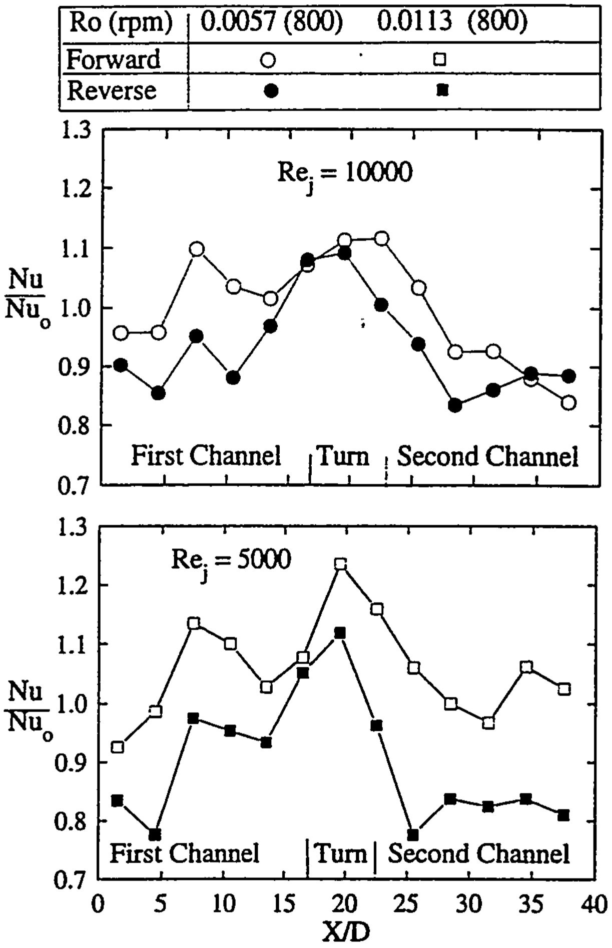

Figure 1.6 Nusselt Number Ratio Versus Channel Location for Ro=0.0057 and 0.0113

Figure 1.5 also shows the rotating heat transfer results. Since rotation does not significantly alter the jet and channel flow velocities (see Figure 1.3), the target surface velocity profiles and thus, the rotating Nusselt numbers follow the same trends but at different levels from those for stationary conditions. These differences are mainly caused by channel Coriolis forces and are explained below.

Figure 1.6 shows the effect of rotation on the local Nusselt number ratio (Nu / Nu_o) versus channel location. The Nusselt number ratio is the local Nusselt number for rotation divided by the corresponding measured local Nusselt number for non-rotation. For rotation number Ro = 0.0057 (Re_j = 10000) the Nusselt number ratios for forward rotation are larger (and mostly above 1.0) than those for reverse rotation (and mostly below 1.0). This is because the channel Coriolis forces for forward rotation are directed at the target surfaces in both channels, which thin their boundary layers and increase their heat transfer (see Figure 1.4). However, for reverse rotation channel, Coriolis forces are directed away from the target surfaces and decrease heat transfer. Finally, as Ro increases to 0.0113 (Re_j = 5000), the effect due to rotation increases (the Coriolis force increases). The forward rotation Nusselt number ratios increase above 1.0 while the reverse Nusselt number ratios decrease below 1.0 as compared to those for Ro = 0.0057.

Part II

Tests were conducted for a mainstream Reynolds number (Re) of 100,900 based on the cylinder diameter. The mainstream velocity (U) was 21.5 m/s. Two grids were used to generate higher turbulence intensities of 4.1% and 7.1%. Film effectiveness and heat transfer coefficient measurements with film cooling were measured at a coolant-to-mainstream blowing ratios of 0.4 and 0.8. Results are presented in terms of Nusselt number (Nu=hD/k). The local Nusselt number is normalized by the mainstream Reynolds number to obtain $Nu/Re^{0.5}$. Results in the present study are limited to the one side of the front half of the cylinder and are presented from the true leading edge (0°) to about 72° from the leading edge.

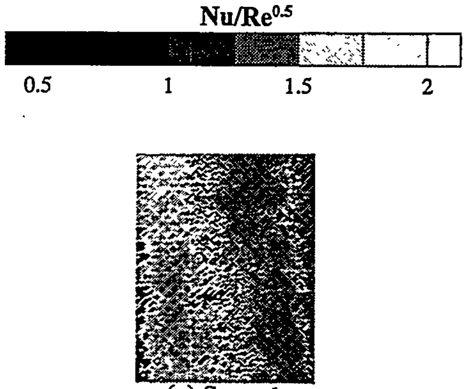

(a) Smooth

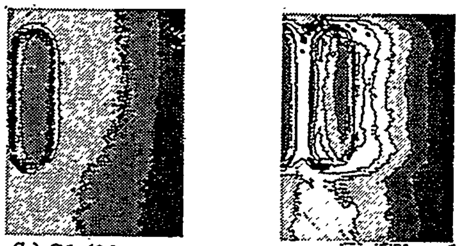

(b) S1 (0°-20°)
(c) S2 (10°-30°)

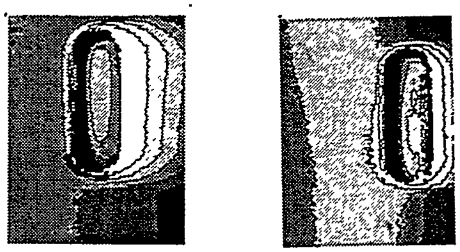

(d) S3 (20°-40°)
(e) S4 (35°-55°)

Figure 2.3 Detailed $Nu/Re^{0.5}$ Distributions for Various Spallation Locations

Figure 2.3 presents detailed $Nu/Re^{0.5}$ results for smooth surface and all four spallation locations for a spallation depth of 0.51 cm and a free-stream turbulence intensity of 7.1%. The direction of flow is from left to right. The $Nu/Re^{0.5}$ values decrease along the surface of the cylinder from 0° to 72° from leading edge for the smooth surface. The highest $Nu/Re^{0.5}$ values near the leading edge are around 1.5 and decrease downstream. The four spallation locations are presented in the order of location from the leading edge. The spallation S1 (0°-20°) produces very little enhancement compared to the smooth surface. Typically, local heat transfer coefficients downstream of the spallation are enhanced and heat transfer coefficients inside the spallation decrease compared to the smooth surface. The level of enhancement, as seen in Figure 2.3, depends on the spallation location. The highest enhancement is obtained for S3 (20°-40°) where the $Nu/Re^{0.5}$ values are as high as 2.5 immediately downstream of the spallation.

Figures 2.4-2.5 show the spanwise-averaged Nu/Nu_0 distributions for each of the four spallation locations under the three free-stream turbulence conditions where Nu_0 is the local Nusselt number for a smooth surface with no spallation. The $\overline{Nu}/Nu_0$ distributions show the local enhancement due to spallation compared to a smooth surface. Figure 2.4 presents the $\overline{Nu}/Nu_0$ values for a spallation depth of 0.25 cm. By normalizing the Nusselt number with spallation with the Nusselt number without spallation, the effect of free-stream turbulence becomes small. Comparing the effect of the spallation location, the highest enhancement is obtained for the spallation S3 (20°-40°). Spallation S4 (35°-55°) also produces high Nusselt number enhancement immediately downstream. There is little effect of the spallation on the upstream Nusselt number ratio values as can be seen for the cases of S3 and S4.

Figure 2.5 presents similar results for a depth of 0.51 cm. An increase in spallation depth increases downstream Nusselt numbers and decreases Nusselt number values inside the spallation. The trend in the distributions shows a significant change inside the spallation for all the locations.

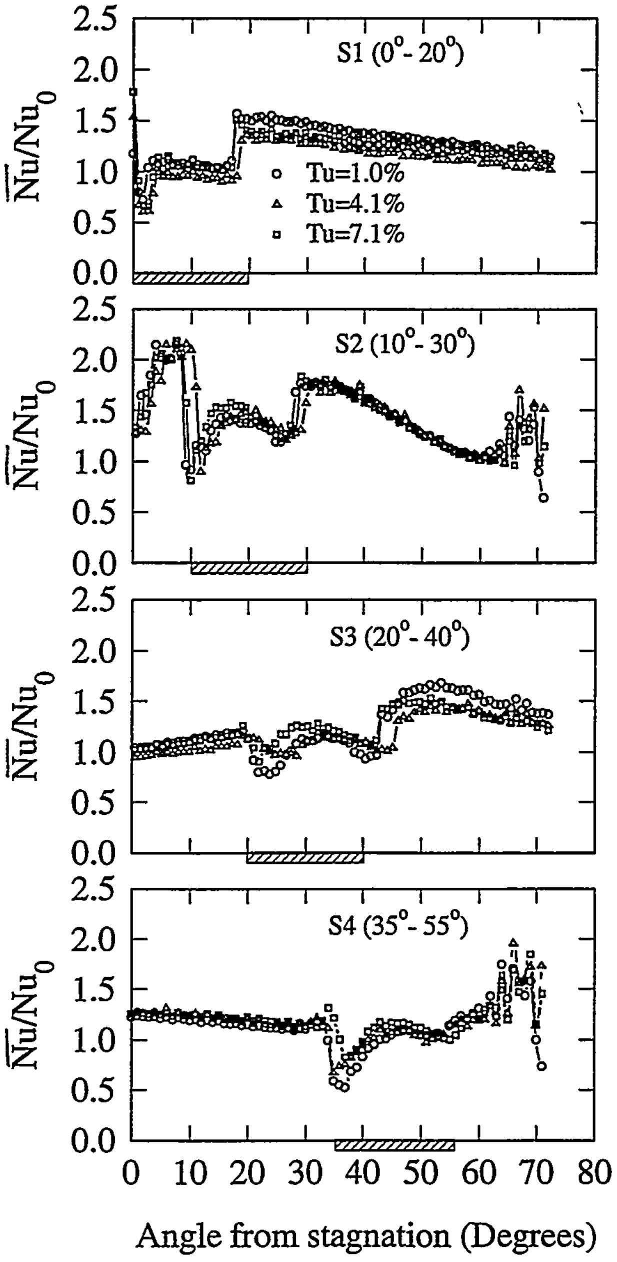

Figure 2.4 Spanwise Averaged Nu/Nu_0 Distributions for Various Spallation Locations Under Three Free-Stream Turbulence Conditions for a Spallation Depth = 0.25 cm

Figure 2.6 presents the effect of spallation location on detailed $Nu/Re^{0.5}$ distributions with film cooling at a blowing ratio of M=0.4. The film

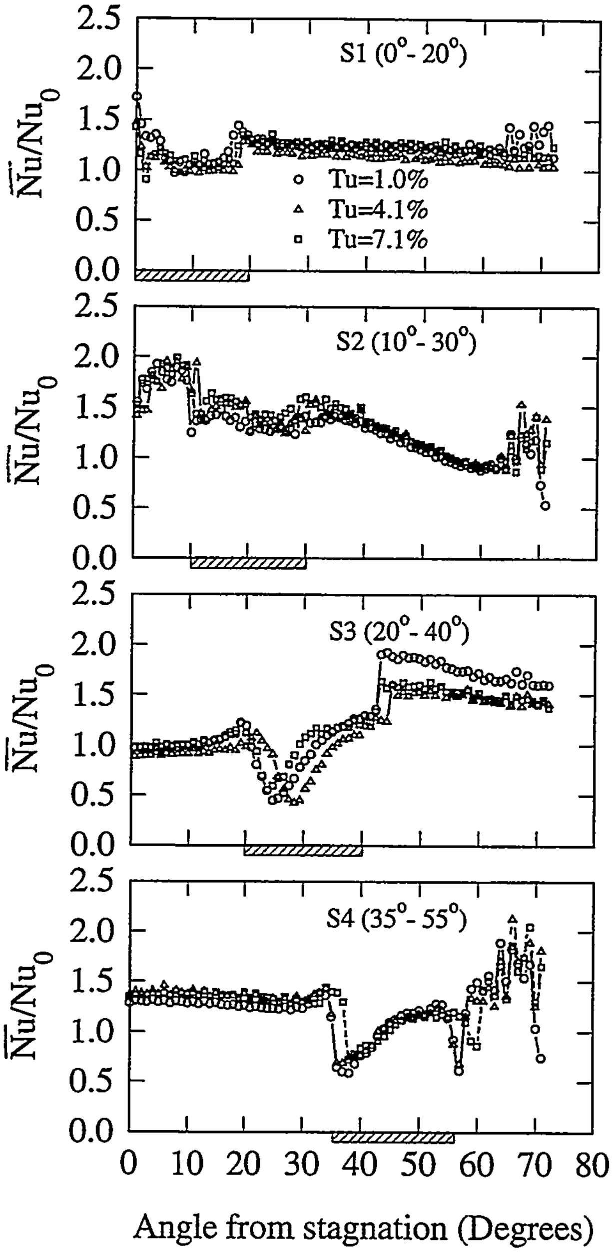

Figure 2.5 Spanwise Averaged Nu/Nu_0 Distributions for Various Spallation Locations Under Three Free-Stream Turbulence Conditions for a Spallation Depth = 0.51 cm

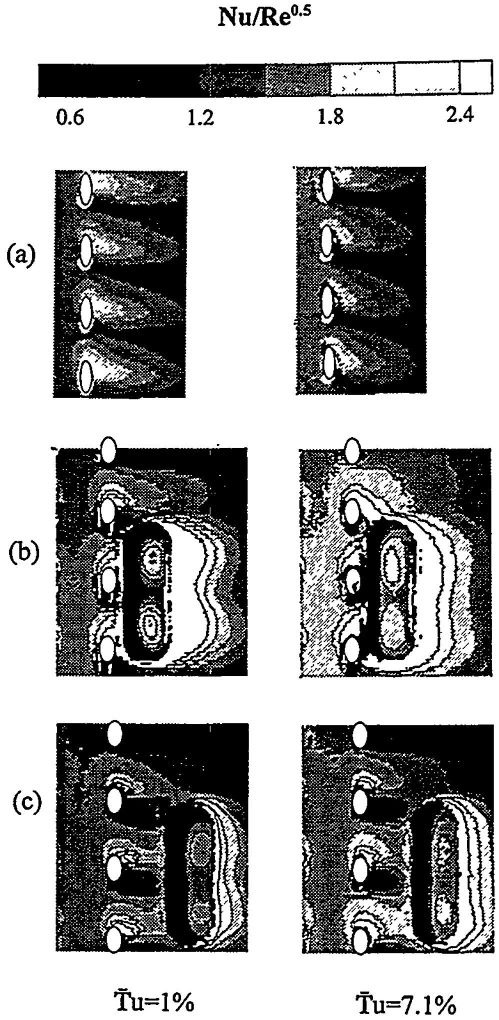

Figure 2.6 Effect of Spallation Location on Detailed $Nu/Re^{0.5}$ Distributions with Film Injection (a) No Spallation (b) S3 (20°-40°) (c) S4 (35°-55°)

holes are located at 15° from the leading edge. Two spallation locations are tested in conjunction with the film cooling holes. Spallation locations were S3 (20°-40°) and S4 (35°-55°). Results at two free-stream turbulence intensities of 1% and 7.1% are presented. Film cooling results without spallation are presented from Ekkad et al. (1995c). From the figure, it can be observed that the film cooling jets are more disturbed by the spallation S3 than for the spallation S4, which is farther downstream. The spallation S3 enhances local $Nu/Re^{0.5}$ greatly downstream of spallation .

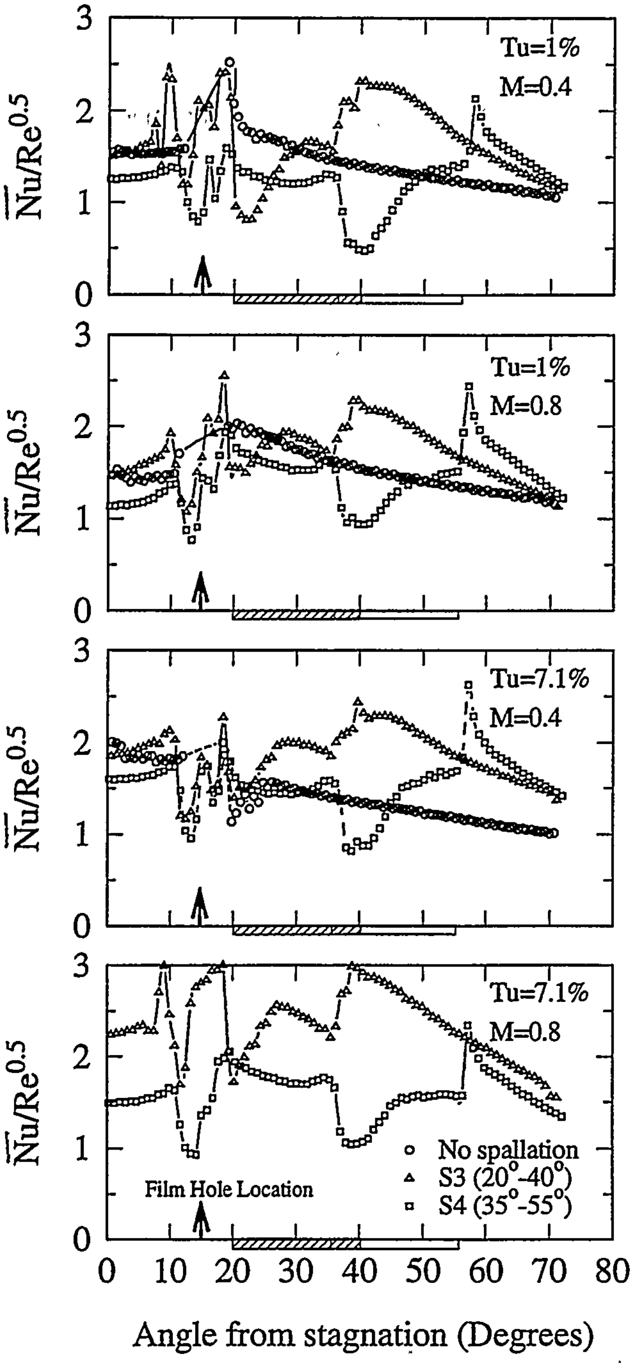

Figure 2.7 Spanwise Averaged $Nu/Re^{0.5}$ Distributions for Film Injection with Various Spallation Locations for M=0.4 and M=0.8

However, the $Nu/Re^{0.5}$ values inside the spallation are lower compared to the smooth surface. The film cooling jets appear to separate at the upstream edge of the spallation S3 and reattach immediately downstream of the spallation. The coolant jets are already weaker when they reach S4, which is about 20° downstream compared to S3, which is only 5° downstream of the film holes. For the higher free-stream turbulence case of 7.1%, the $Nu/Re^{0.5}$ values are higher compared to the Tu=1% case. Higher free-stream turbulence increases local flow disturbances thus enhancing $Nu/Re^{0.5}$ values. For the S3 case, the effect appears stronger compared to the S4 case. Higher free-stream turbulence also increases local $Nu/Re^{0.5}$ values inside the spallation. This may be due to the lesser protection provided by the jets, which are weaker under higher free-stream turbulence condition.

Figure 2.7 compares the spanwise-averaged $Nu/Re^{0.5}$ results for film cooling with and without spallation for blowing ratios of M=0.4 and M=0.8. The effect of spallation location and free-stream turbulence are presented. In each case, the $\overline{Nu}/Re^{0.5}$ values for film cooling only are compared with film cooling and spallation locations S3 and S4. Results for film cooling only are presented from Ekkad et al. (1995c). The spallation increases downstream $\overline{Nu}/Re^{0.5}$ values and decreases $\overline{Nu}/Re^{0.5}$ values inside the spallation. The film cooling without spallation case for each turbulence intensity and blowing ratio is shown to indicate the enhancement caused by spallation with film injection.

Figure 2.8 presents the effect of spallation on detailed film effectiveness distributions with film cooling at a blowing ratio of M=0.4. The effectiveness distributions are jet-like along the hole for no spallation case at the Tu=1% case. When a spallation is placed immediately downstream of injection (S3), the jet-like effectiveness patterns disappear and the jets appear to coalesce immediately downstream of the

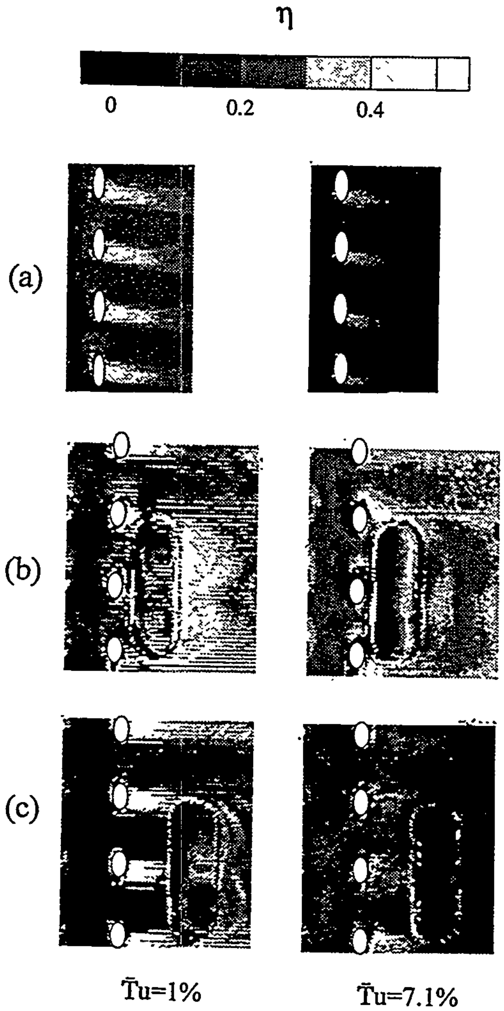

Figure 2.8 Effect of Spallation Location on Detailed Film Effectiveness Distributions with Film Injection (a) No Spallation (b) S3 (20°-40°) (c) S4 (35°-55°)

spallation cavity. A high effectiveness region is obtained along the spallation downstream edge. Effectiveness decreases further downstream. When a spallation is placed farther downstream of injection (S4), the effectiveness distribution is not disturbed although the effectiveness downstream of the spallation increases compared to no spallation case. This may be due to jet separation and reattachment at the edges of the spallation. For a higher free-stream turbulence, effectiveness reduces for all three cases. For the S3 spallation case, the effectiveness is still much higher than for

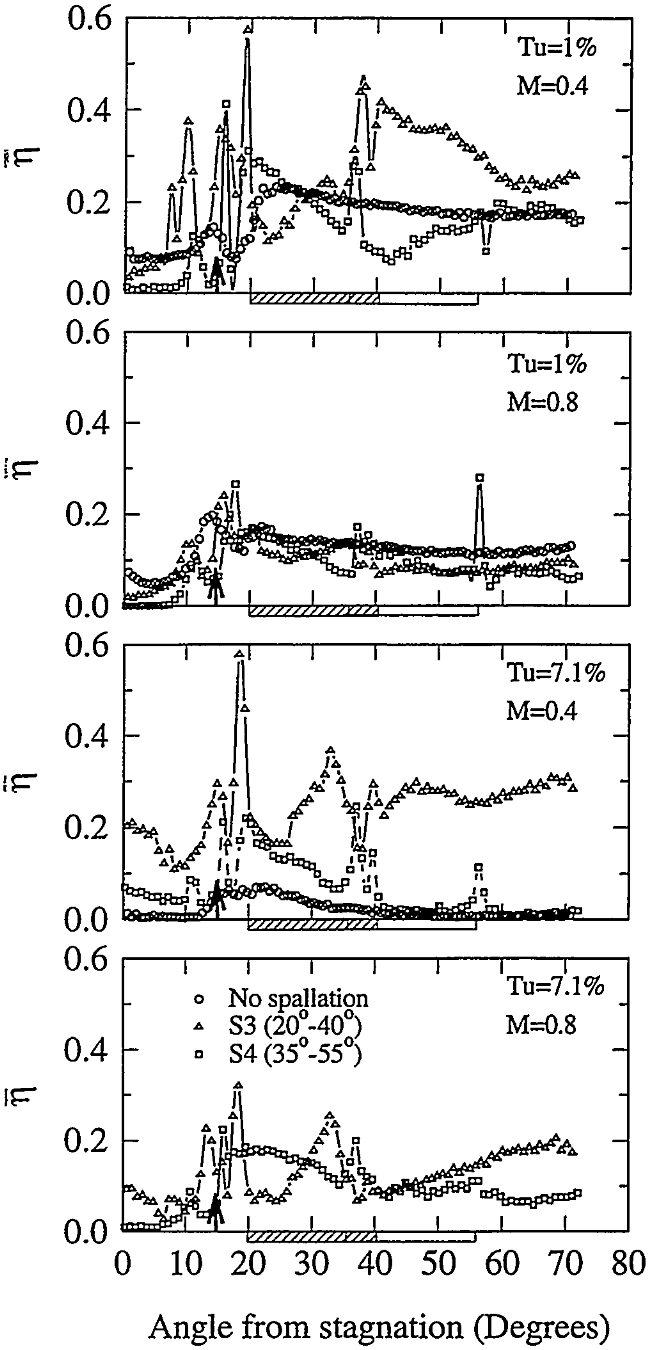

Figure 2.9 Spanwise Averaged η Distributions for Film Injection with Various Spallation Locations for M=0.4 and M=0.8

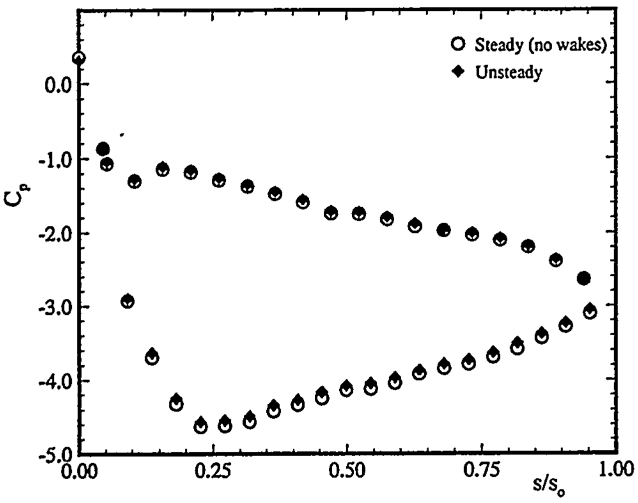

Figure 3.3 Pressure Distribution at Re_c= 264,187

the no spallation and S4 spallation cases. Effectiveness is very low inside the spallation for both S3 and S4.

Figure 2.9 compares the spanwise averaged film effectiveness ($\bar{\eta}$) for film cooling without spallation to film cooling with spallation. The presence of a spallation S3 increases film effectiveness downstream and decreases film effectiveness inside the spallation. Film effectiveness for a case with spallation S3 is in general higher than that for the case with spallation S4. Effectiveness decreases as blowing ratio increases from M=0.4 to M=0.8. The film cooling without spallation data is shown for comparison to see the effect of the spallation location on film effectiveness distribution.

Part III

Part IIIa. The time-averaged pressure distribution, shown in Fig. 3.3, was taken by a multi-channel scanivalve for a steady and an unsteady case, where rods with one uniform spacing of S_R = 160 mm, were attached to whole length of the belt. The noticeable deviation in pressure distribution between the steady and unsteady cases, especially on the suction surface, is due to the drag of the bars adding transverse momentum to the flow. On the suction surface (lower portion) the flow first accelerates sharply, reaches a minimum pressure coefficient at $s/s_0 \approx 0.25$ and then continuously decelerates at a moderate rate until the trailing edge is reached. On the pressure surface, the flow accelerates, reaches a minimum pressure coefficient at $s/s_0 \approx 0.1$, and experiences a short deceleration and then accelerates almost continuously at a slower rate. This pressure distribution indicates that the flow on both surfaces, except for a short distance around $s/s_0 \approx 0.1$, is subjected to a negative pressure gradient until $s/s_0 \approx 0.25$ is reached. Beyond this point, the pressure gradient on the pressure surface remains negative, while on the suction surface, positive pressure gradient prevails.

Table 3.1 Specifications of Inlet Flow, Blade, Cascade, and Wake Generator Characteristics

Parameters	Values	Parameters	Values
Inlet velocity	V_1 = 15 m/s	Inlet turbulence intensity	Tu = 0.8 %
Blade inlet metal angle	α_1= 0°	Blade exit metal angle	α_2= 61.8°
Blade height	L = 200 mm	Blade spacing	S_B = 160 mm
Blade chord	C = 281.8 mm	Blade Re-number	Re_c = 563600
Cascade solidity	σ = 1.76	Cascade flow coefficient	φ = 2.14
Steady flow spacing	$S_R = \infty$ mm	Ω - parameter steady case	Ω = 0.000
Cluster 1 rod spacing	S_R = 160 mm	Ω - parameter for cluster 1	Ω = 0.822
Cluster 2 rod spacing	S_R = 80 mm	Ω - parameter for cluster 2	Ω = 1.644
Cluster 3 rod spacing	S_R = 40 mm	Ω - parameter for cluster 3	Ω = 3.288
Rod diameter	D_R = 5 mm	No. of rods in cluster 2	n_R = 19
No. of rods in cluster 1	n_R = 11	No. of rods in cluster 3	n_R = 38

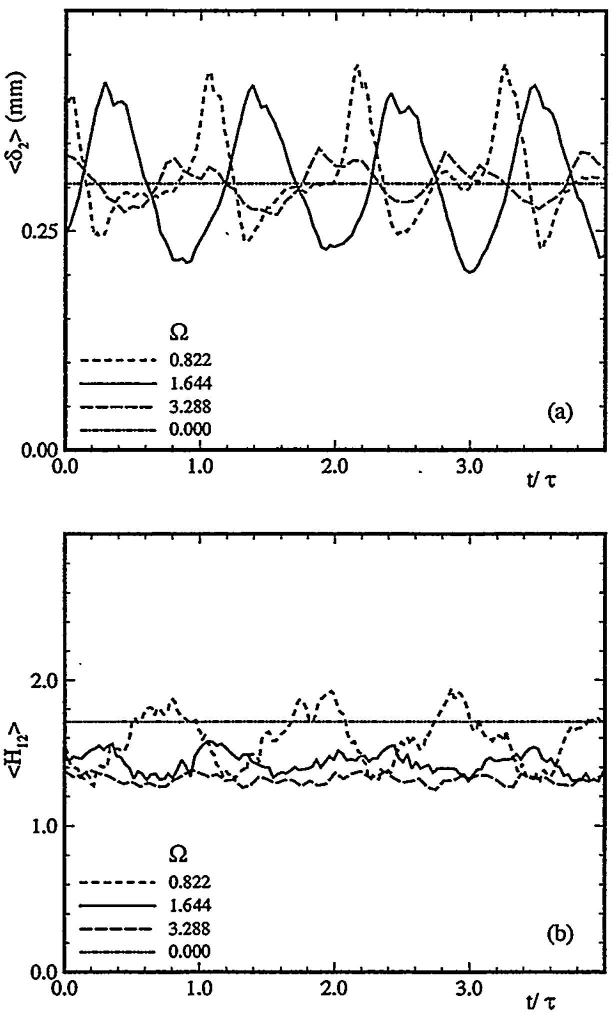

Figure 3.4 Ensemble-Averaged (a) Momentum Thickness and (b) Shape Factor on Pressure Surface at $S/S_0 = 0.719$

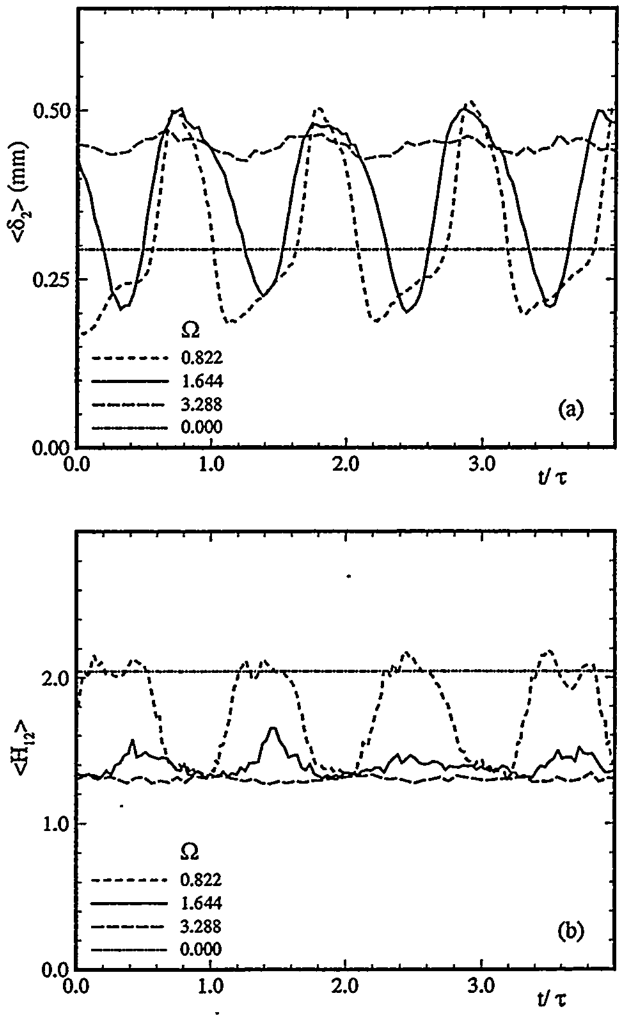

Figure 3.5 Ensemble-Averaged (a) Momentum Thickness and (b) Shape Factor on Suction Surface at $S/S_0 = 0.509$

Boundary layer profiles under the influence of three different wake-passing frequencies and a steady inlet condition were taken on the suction surface at 13 streamwise positions and on the pressure surface at 11 streamwise positions. The steady case results serve as the reference case for comparison with the unsteady cases. To account for the unsteadiness caused by the frequency of the individual wake generating clusters and their spacing, the flow velocity, and the cascade parameters, we define an unsteady flow parameter $\Omega = (c/S_R)(U/V_{ax}) = (\sigma S_B)/(\varphi S_R)$ that includes the cascade solidity σ, the flow coefficient φ, the blade spacing S_B, and the rod spacing S_R. The individual cluster configurations with the corresponding Ω-parameter are specified in Table 3.1.

The integral parameters such as momentum thickness and shape factor are of particular interest to a turbine designer, since

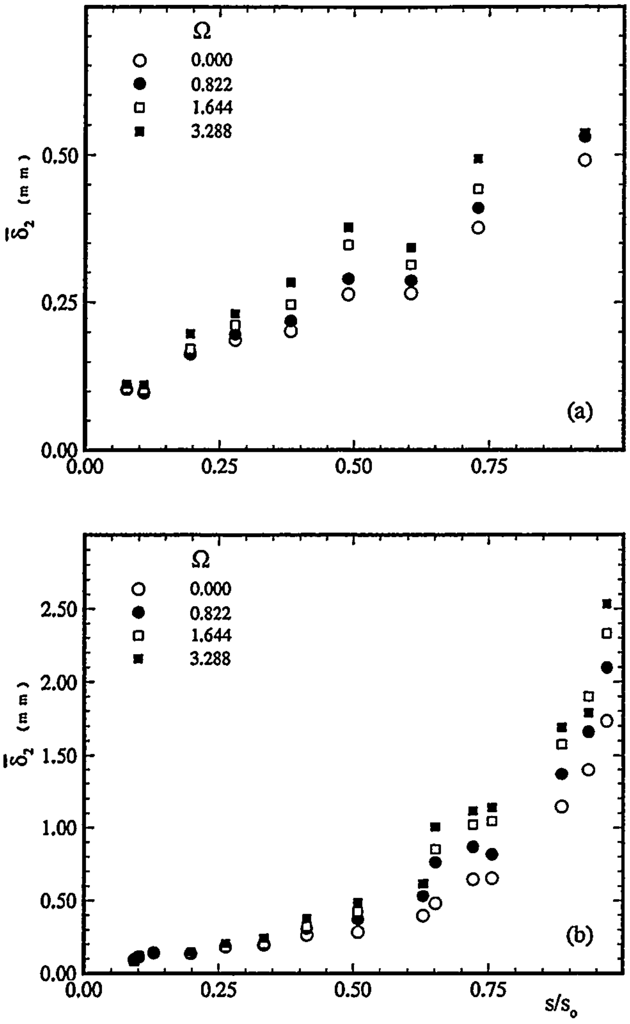

Figure 3.6 Time-Averaged Momentum Thickness Distribution on (a) Pressure and (b) Suction Surfaces

they provide an accurate first estimation of the quality of the designed blade. The ensemble-averaged distributions of the momentum deficiency thickness and shape factor on the pressure and suction surfaces at one streamwise location are presented in Figs. 3.4 and 3.5 for four different Ω-values. Here, the period τ represents the wake-passing period specific to the individual wake generating cluster, which is characterized by the Ω-value under investigation. The periodic behavior of the ensemble-averaged momentum thickness as a result of the embedded periodic wake flow is clearly visible for both pressure and suction surfaces. It is observed that by convecting downstream, $<\delta_2>$ experiences a continuous increase, where its time-averaged value approaches the steady case ($\Omega = 0$) value. The shape factor $<H_{12}>$ experiences a similar periodic change with an average below the steady case as shown in Figs. 3.4b and 3.5b. Other information regarding the overall evaluation of turbine blade is provided by the time-averaged momentum thickness as shown in Fig. 3.6 for pressure and suction surfaces. The time-averaged momentum thickness indicates that for the particular blade under investigation, an increase of unsteady parameter Ω results in a consistent augmentation of the momentum thickness over the entire pressure and suction surfaces. Although a general conclusion cannot be drawn from these results, they evidence the impact of unsteady wake flow on the boundary layer parameters and thus the profile loss coefficient and efficiency. This clearly shows that the steady state data cannot be transferred to the unsteady turbine design technology without modifications.

The analysis of the data from a wavelet-based perspective is presented below. Intermittency calculations are made according to the recommendations by Hedley and Keffer (1974). The procedure utilized for the analysis of instantaneous time traces is summarized in Schobeiri et al. (1995). Ensemble averages of intermittency factor for the first two passing periods are plotted in Figs. 3.7 and 3.8 for pressure and suction surfaces. Figure 3.7 shows the results on pressure surface at y = 1.0 mm for the rod spacings of 160, 80 and 40 mm respectively. Figure 3.7a shows a virtual absence of turbulence between the wakes, showing the minimal interaction between them. The wakes are distinct through major portion of the blade

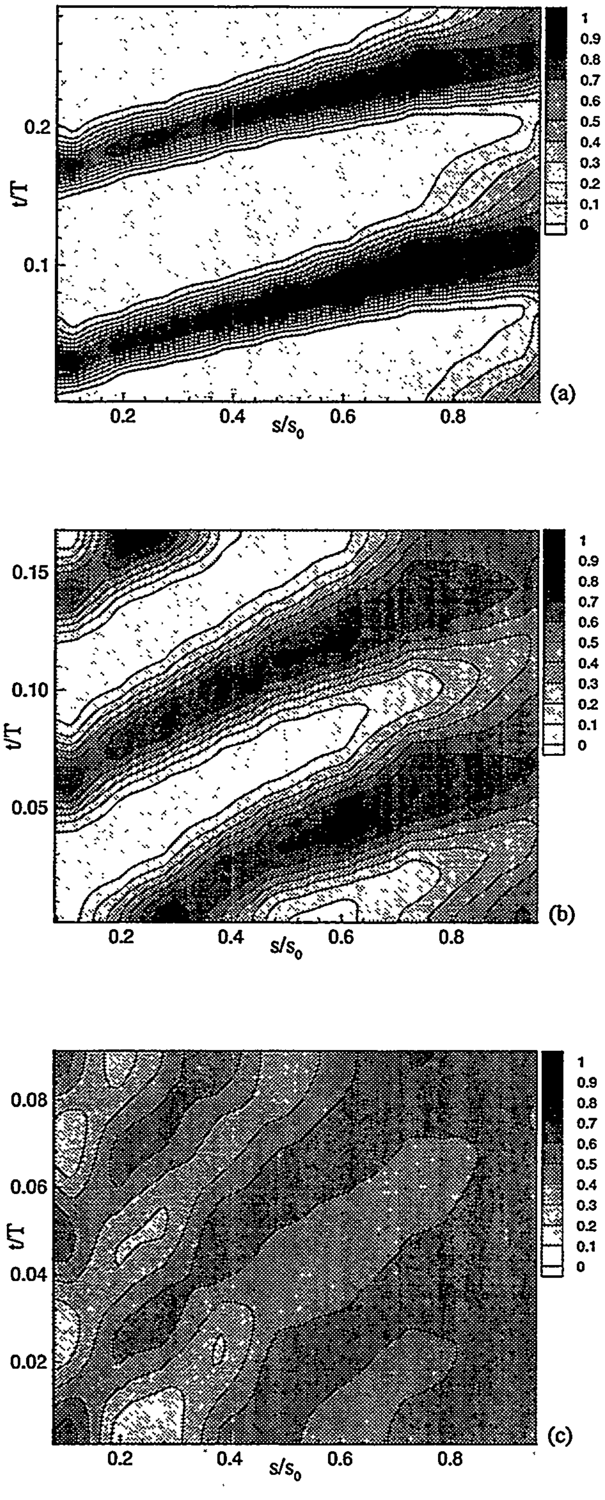

Figure 3.7 Ensembe-Averaged Intermittency Factor in the Spatial-Temporal Domain at y=1 mm for Rod Spacings of (a) 160, (b) 80, and (c) 40 mm for the Pressure Surface

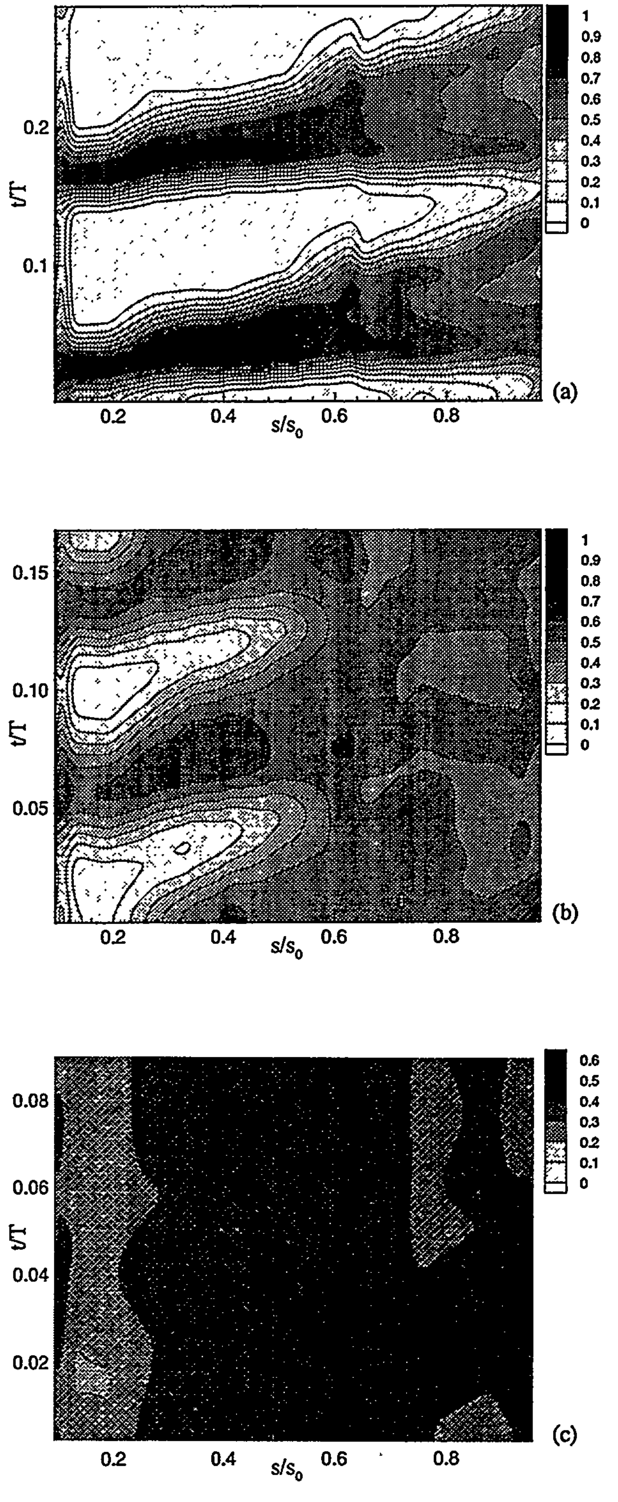

Figure 3.8 Ensembe-Averaged Intermittency Factor in the Spatial-Temporal Domain at y=1 mm for Rod Spacings of (a) 160, (b) 80, and (c) 40 mm for the Suction Surface

and at about s/s_0 of 0.75, the change of slope makes the wakes to merge near the trailing edge of the blade. This merging is caused by the change in the flow dominated by the convection of free-stream wakes to the propagation of boundary layer spots traveling at lower speed. The increase in the wake frequency (low rod spacing) causes the wakes to merge earlier resulting in the region being highly turbulent due to the spot-dominated wall layer empowering the wake-dominated freestream. The results in the case of suction surface show the merging of wakes taking place much earlier compared with pressure surface with higher intermittency values observed throughout the surface (Figs. 3.8(b,c)).

The emerging complexity of the flow makes it imperative to quantify the active scales so that modeling can include more of the relevant physics. The classical method of Fourier power spectrum analysis is effective in recognizing the wake passing frequency, but ill-suited for analyzing the turbulence within the wakes. Wavelet tools allow quantitative measurement of both duration and time of occurrence of the small scale disturbances inside the wake region. The instantaneous velocity time traces are analyzed using a Mexican hat wavelet. The method for analysis of the data is described in Schobeiri et al. (1995). The dominant time scales on pressure and suction surfaces are plotted in Figs. 3.9 and 3.10, respectively, for the rod spacings of 160, 80 and 40 mm. Figure 3.9a shows similar pattern compared to the intermittency distribution with small time scales inside the wake region. In the case of Fig. 3.9b, the merging of the wakes is seen with the time scales approaching the sampling interval beyond s/s_0 of 0.8. This small scale activity is dominant through the half span of the blade for 40 mm rod spacing (Fig. 3.9c). The suction side shows similar results with the flow being fully turbulent for 40 mm rod spacing case as shown in Fig.

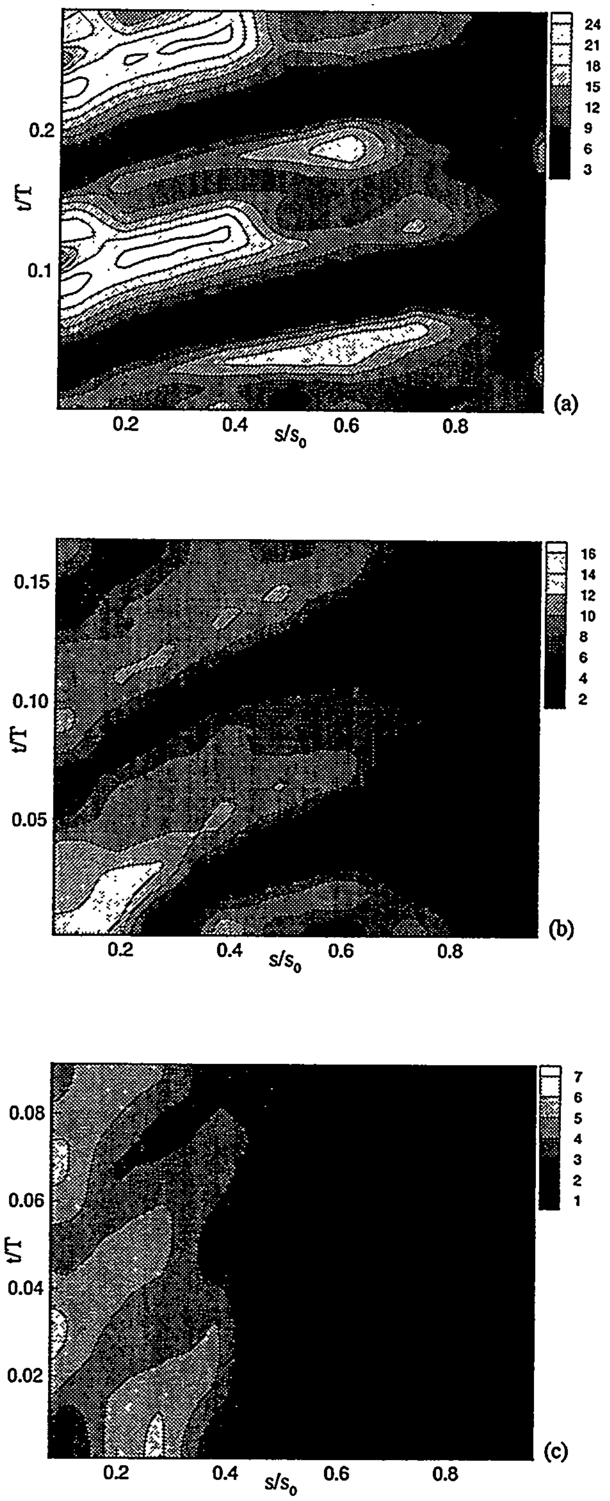

Figure 3.9 Ensembe-Averaged Dominant Time-Scale (msec) in the Spatial-Temporal Domain at y=1 mm for Rod Spacings of (a) 160, (b) 80, and (c) 40 mm for the Pressure Surface

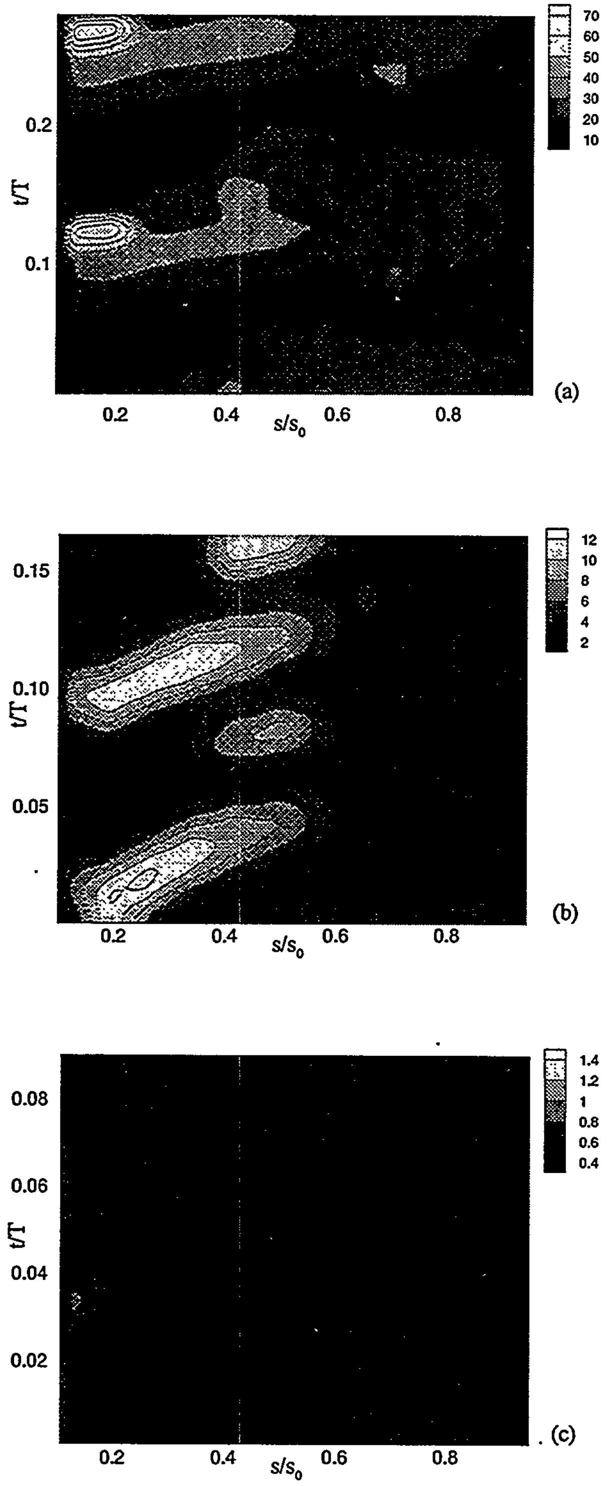

Figure 3.10 Ensembe-Averaged Dominant Time-Scale (msec) in the Spatial-Temporal Domain at y=1 mm for Rod Spacings of (a) 160, (b) 80, and (c) 40 mm for the Suction Surface

3.10c.

Part IIIb. All the measurements were taken over two full blade spacings with the ejection blade in the middle. It was not possible to position the probe tips exactly in the trailing edge plane. As a result, the distance between the pneumatic probe tip and trailing edge is 14 mm. The results are presented as a function of the probe position along y axis. The trailing-edge of the investigated blade has a y-coordinate of 163.2 mm. The positions, $y < 163.2$ mm are on the suction side of the trailing edge ejection blade while the positions, $y > 163.2$ mm are on its pressure side. The measurements were performed for 14 different ejection mass flow ratios $\dot{m}_c/\dot{m}_2$ ($\dot{m}_c$ = ejection mass flow, $\dot{m}_2$ = primary mass flow at station 2) ranging from $\dot{m}_c/\dot{m}_2 = 0.0 - 0.042$. Figure 3.2 shows the control surface required for performing the integration necessary for calculating the total pressure loss coefficient. The experimental measurements were carried out at station 2 (Fig. 3.2) and the properties at station 3 are calculated from the relations given in Schobeiri (1989).

The five-hole probe measurements are plotted in Figs. 3.11 and 3.12. Figure 3.11 shows the ejection velocity profiles for three representative non-dimensional ejection velocities, $\mu = V_c/V_{20} = 0.$, 0.3, and 1.0. The wake region represents the trailing edge ejection region. The z-component of velocity is very close to zero in all the cases indicating that the flow is two-dimensional. Comparing the case of $\mu = 0.3$ (Fig. 3.11b) with no ejection case of $\mu = 0.0$ (Fig. 3.11a), the wake appears to be deeper for $\mu = 0.3$ case due to a stronger dissipation for small ejection velocities as predicted by Schobeiri (1989). For the case where the ejection velocity is very close to the main flow velocity ($\mu = 1$), the velocity profile (Fig. 3.11c) shows a valley on the suction side

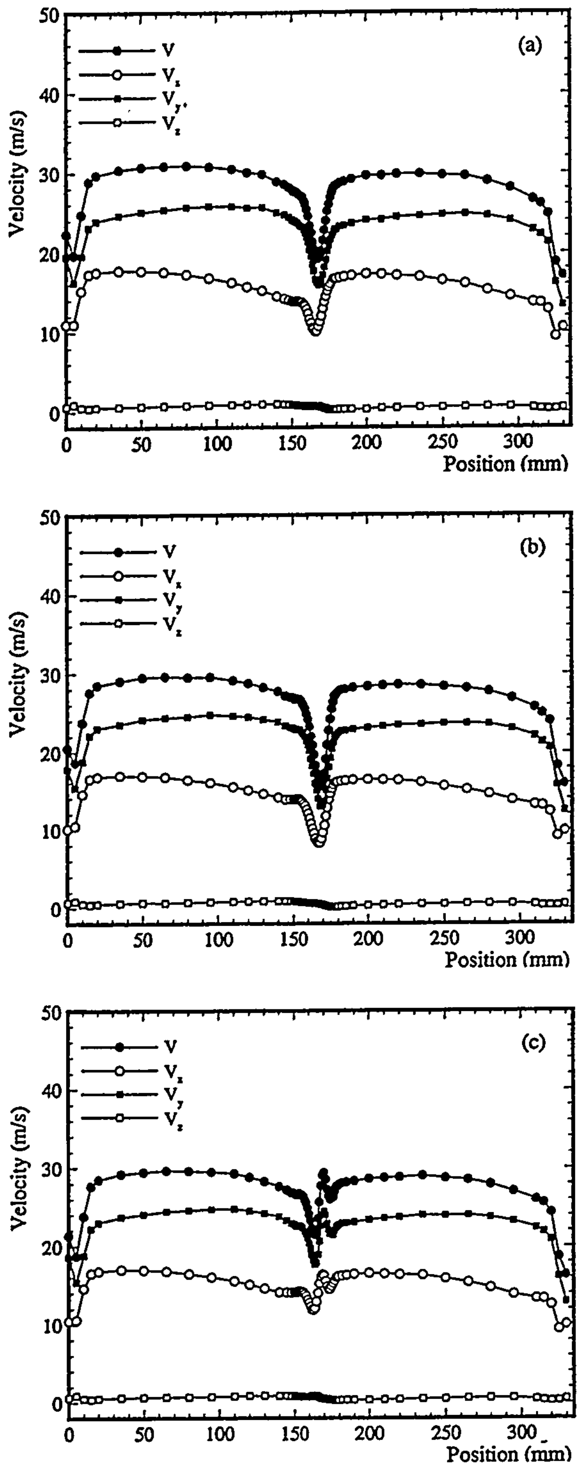

Figure 3.11 Ejection Velocity Profiles with Five-Hole Probe at x=14 mm from the Trailing Edge for μ of (a) 0.0, (b) 0.3, and (c) 1.0

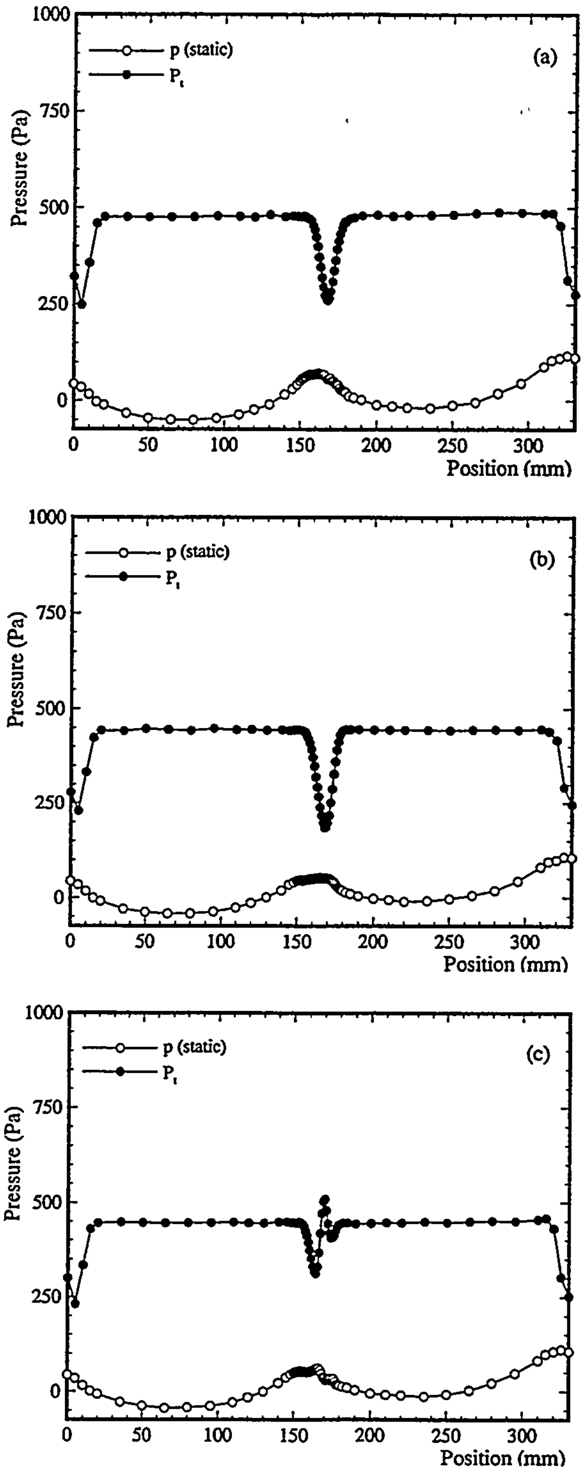

Figure 3.12 Pressure Distribution with Five-Hole Probe at x=14 mm from the Trailing Edge for μ of (a) 0.0, (b) 0.3, and (c) 1.0

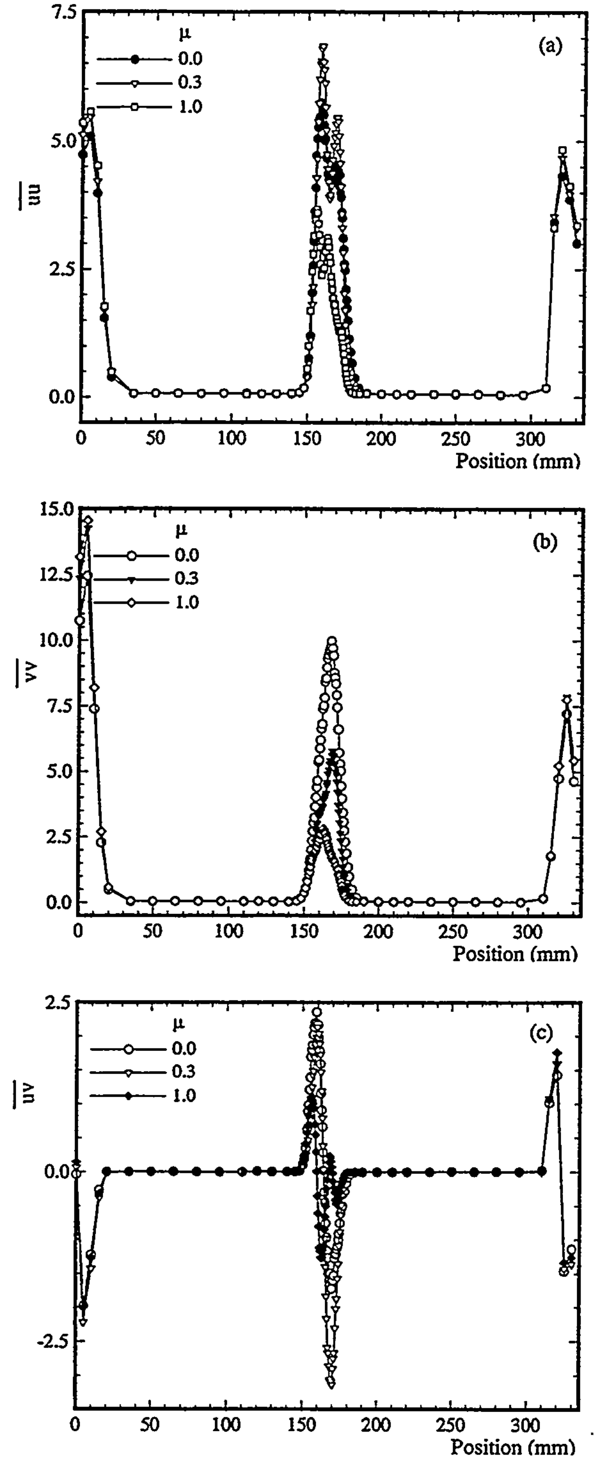

Figure 3.13 (a) Longitudinal, (b) Lateral Reynolds Normal Stresses, and (c) Reynolds Shear Stress

and a peak on the pressure side. From the analysis, this appears to be the case with minimum pressure loss coefficient. Figure 3.12 shows the total and static pressure distributions for $\mu = 0.0$, 0.3, and 1.0. The total pressure shows tendencies similar to the velocity distribution (Fig. 3.11), discussed earlier.

The x-wire measurements are presented in Fig. 3.13. Since the velocity components are similar to those measured by the five hole probe, only the Reynolds stresses are presented. Longitudinal Reynolds stress and Reynolds shear stress components (Fig. 3.13a,c) have the highest peak at $\mu = 0.3$ and the smallest at $\mu = 1.0$. This confirms the theory by Schobeiri (1989) that ejection velocity ratios $\mu < 1.0$ result in stronger dissipation and thus higher mixing losses. The peaks in lateral Reynolds stress (Fig. 3.13b) decrease continuously with increasing μ. Of all the Reynolds stresses, shear stress (Fig. 3.13c) shows the strongest asymmetry. The case with $\mu = 0.3$ shows a very strong negative peak towards the pressure side. Of all the mass flow cases investigated, this case has the highest dissipation and accordingly results in maximum pressure loss coefficient. A double peak can be observed for the case of $\mu = 1.0$. This case is found to be around the optimum pressure loss coefficient range. To obtain the trailing edge mixing losses, it is necessary to carry out some further analysis of the data. Figures 3.14(a,b,c) show the integrated static pressures, total pressures, and energy at stations 2 and 3 (Fig. 3.2) as a function of μ. The difference of the energies at stations 2 and 3 represents the dissipation due to the mixing of the cooling jet with the main flow.

Figure 3.15 shows the pressure loss

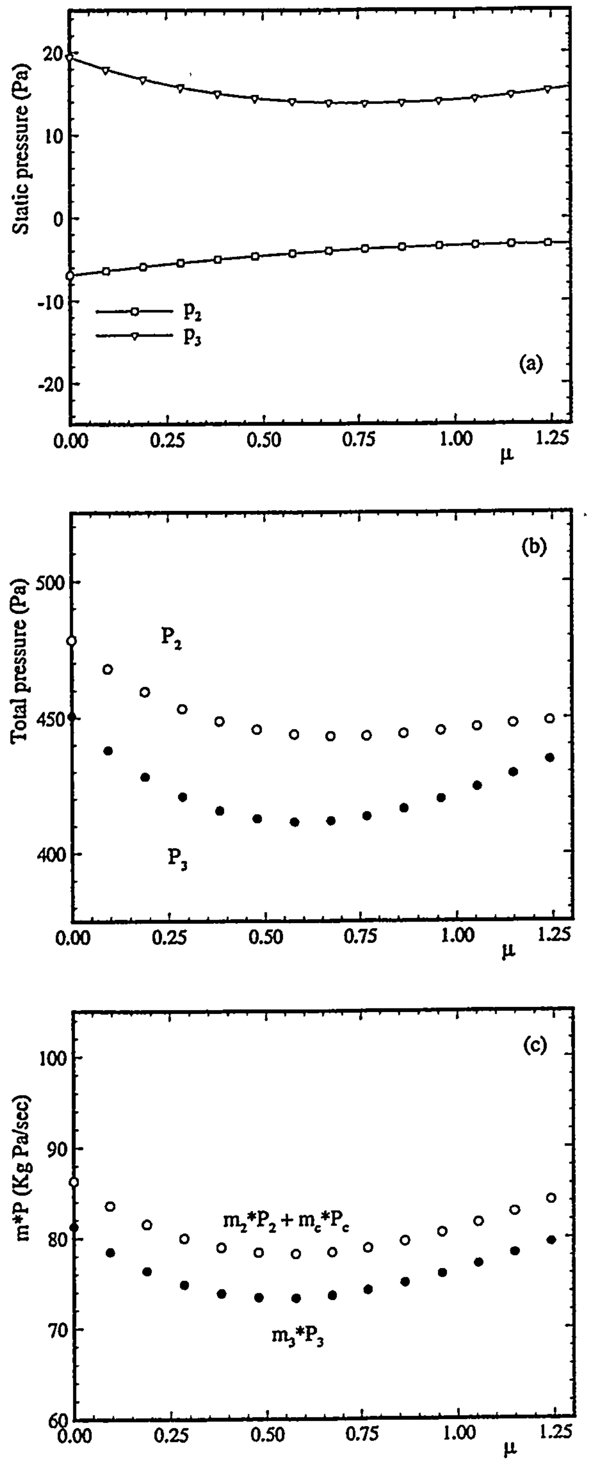

Figure 3.14 (a) Static, (b) Total Pressures, and (c) m*P at the Inlet and Exit of the Control Surface

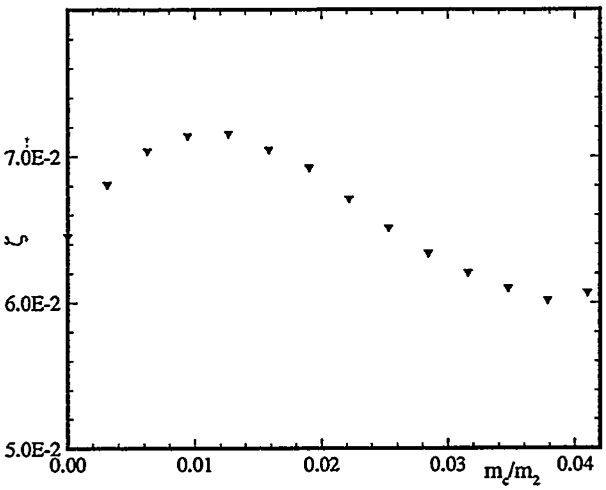

Figure 3.15 Pressure Loss Coefficient

coefficient,
$$\zeta = \frac{(\dot{m}_2 * P_2 + \dot{m}_c * P_c) - (\dot{m}_3 * P_3)}{\frac{1}{2}\dot{m}_3 V_3^2}$$
as a function of the non-dimensional ejection mass flow ratio. In the above equation, $\dot{m}_3$ is the mass flow at station 3 given by $\dot{m}_3 = \dot{m}_2 + \dot{m}_c$. As can be seen from Fig. 3.15, the peak loss due to dissipation occurs at $\dot{m}_c/\dot{m}_2 = 0.011$ which corresponds to $\mu = 0.3$. The minimum loss appears to be around $\dot{m}_c/\dot{m}_2 = 0.036$, that corresponds to $\mu = 1.0$. Further analysis of the data and comparison with the theory is still in progress.

Applications

Part I

The results above are useful for the design of coolant passages with jet impingement for rotating turbine blades. While differences between stationary and rotating jet impingement data are within 25% for turbine operating conditions, the effects due to the relationship between channel flow direction and the direction of rotation are still important.

Part II

The results presented in this study are very useful to the gas turbine designer. Modern gas turbine blades are protected from high temperature inlet gases by covering the blade with a thermal barrier coating. The protective coating chips off due to erosion or corrosion and exposes the blade metal surface to the hot gases. This is detrimental to the turbine blade. This spalding of the TBC coating enhances local and downstream heat transfer coefficients and causes further damage to the blade. This study investigates the level of heat transfer enhancement caused by the spallation of TBC coating. The results from the present study can help the designer predict the blade life when TBC spalding occurs.

Part III

Modeling the transition process is one of the key issues in turbine aerodynamics and heat transfer design. The goal of the boundary layer research is to provide an unsteady boundary layer transition model. Optimization of trailing edge ejection losses reduce the turbine blade losses, thus improving the turbine blade efficiency.

Future Activities

Part I

It is well known that adding ribs to coolant passages with channel flow increases surface heat transfer for stationary and rotating conditions. Therefore, future tests will investigate the effect of rotation on jet impingement heat transfer for ribbed target surfaces.

Part II

The effect of spallation on surface heat transfer enhancement will be studied for an actual turbine blade under various free-stream turbulence conditions. The effects of mainstream Reynolds numbers and upstream unsteady wakes will also be studied. The results will be correlated to provide a useful data base for turbine designers. Also, the effect of spallation on a turbine blade with film cooling will also be studied.

Part III

Further experimental and theoretical boundary layer and trailing edge ejection investigations are under completion. The development of an unsteady boundary layer transition model is underway. For optimization of the trailing edge ejection aerodynamics, the comparison of the experimental results with an already existing and extended theory (developed by Schobeiri, 1989) will be the basis for establishing necessary criteria that allows a turbine aerodynamicist to optimize the design of the trailing edge ejection.

Acknowledgments

Acknowledgments are due to Dr. Norman Holcombe who is the METC Contracting Officer's Representative (COR). The period of performance for this part of the project was September 1, 1994 to August 31, 1995.

References

Downs, S. J., and James, E. H., 1987, "Jet Impingement Heat Transfer - A Literature Survey," ASME Paper No. 87-HT-35.

Ekkad, S.V. and Han, J.C., 1995, "Local Heat Transfer Coefficients In and Around Cavities

On a Flat Surface Using a Transient Liquid Crystal Image Method," submitted to *AIAA Journal of Thermophysics and Heat Transfer*.

Ekkad, S.V., Du, H., and Han, J.C., 1995, "Local Heat Transfer Coefficient and Film Effectiveness Distributions on a Cylindrical Leading Edge Model Using a Transient Liquid Crystal Image Method," accept for presentation at the *1995 International Mechanical Engineering Congress & Exposition*, San Francisco, CA. Also submitted to *ASME Journal of Heat Transfer*.

Epstein, A. H., Kerrebrock, J. L., Koo, J. J., and Preiser, U. X., 1985, "Rotational Effects on Impingement Cooling," Symposium on Transport Phenomena in Rotating Machinery," April 28-May 3, Honolulu, HI.

Florschuetz, L. W., and Su, C. C., 1987, "Effects of Crossflow Temperature on Heat Transfer Within an Array of Impinging Jets," ASME *Journal of Heat Transfer,* Vol. 109, pp. 74-82.

Hedley, T. B., Keffer, J. F., 1974, "Turbulent/Non-turbulent Decisions in an Intermittent Flow," *Journal of Fluid Mechanics*, Vol. 64, pp. 625-644.

John, J., Schobeiri, T., 1993, "A Simple and Accurate Method for Calibrating X-probes," ASME *Journal of Fluids Engineering*, Vol. 115, pp. 148-152.

Kercher, D. M., and Tabakoff, W., 1970, "Heat Transfer by a Square Array of Round Air Jets Impinging Perpendicular to a Flat Surface Including the Effect of Spent Air," ASME *Journal of Engineering for Power,* Vol. 92, No. 1,, pp.73-82.

Schobeiri, M. T., 1989, "Optimum Trailing Edge Ejection for Cooled Gas Turbine Blades," ASME *Journal of Turbomachinery*, Vol. 111, pp. 510-514.

Schobeiri, M. T., Radke, R. E., 1994, "Effects of Periodic Unsteady Wake Flow and Pressure Gradient on Boundary Layer Transition along Concave Surface of a Curved Plate," Presented at the International Gas Turbine and Aeroengine Congress and Exposition, The Hague, Netherlands, 94-GT-327.

Schobeiri, M. T., K. Pappu, L. Wright, 1995, "Experimental Study of the Unsteady Boundary Layer Behavior on a Turbine Cascade," Presented at the International Gas Turbine and Aeroengine Congress and Exposition, Houston, Texas.

Schobeiri, M. T., K. Read, J. Lewalle, 1995, "Effect of Unsteady Wake Passing Frequency on Boundary Layer Transition, Experimental Investigation and Wavelet Analysis," Presented at the International Gas Turbine and Aeroengine Congress and Exposition, Houston, Texas, 95-GT-437.

P6

Life Prediction of Advanced Materials for Gas Turbine Application

Dr. Sam Y. Zamrik (SYZESM@engr.psu.edu; 814-865-5241)
Dr. Asok Ray (A2R@ecl.psu.edu; 814-865-6377)
Dr. Donald A. Koss (Koss@ems.psu.edu ; 814-865-5447)
The Pennsylvania State University
121 Hammond Bldg.
University Park, Pa 16802

Introduction

Most of the studies on the low cycle fatigue life prediction have been reported under isothermal conditions where the deformation of the material is strain dependent. In the development of gas turbines, components such as blades and vanes are exposed to temperature variations in addition to strain cycling. As a result, the deformation process becomes temperature and strain dependent. Therefore, the life of the component becomes sensitive to temperature-strain cycling which produces a process known as "thermomechanical fatigue, or TMF". The TMF fatigue failure phenomenon has been modeled using conventional fatigue life prediction methods, which are not sufficiently accurate to quantitatively establish an allowable design procedure. To add to the complexity of TMF life prediction, blade and vane substrates are normally coated with aluminide, overlay or thermal barrier type coatings (TBC) where the durability of the component is dominated by the coating/substrate constitutive response and by the fatigue behavior of the coating. A number of issues arise from TMF depending on the type of temperature/strain phase cycle:

1- time-dependent inelastic behavior can significantly affect the stress response. For example, creep relaxation during a tensile or compressive loading at elevated temperatures leads to a progressive increase in the mean stress level under cyclic loading.

2- the mismatch in elastic and thermal expansion properties between the coating and the substrate can lead to significant deviations in the coating stress levels due to changes in the elastic modulii.

3- the "dry" corrosion resistance coatings applied to the substrate may act as primary crack initiation sites.

Crack initiation in the coating is a function of the coating composition, its mechanical properties, creep relaxation behavior, thermal strain range and the strain/temperature phase relationship. Of particular importance are the coating ductility and the coefficient of thermal expansion mismatch between the coating and substrate, which can cause thermally induced strains causing cracking at the surface and creep relaxation.

As a result of the complex constitutive behavior of the coating/substrate system, TMF life prediction methodology has yet to be developed to explicitly describe the fatigue response of the coating/substrate systems.

Objectives

The main focus of the research program is directed towards life prediction modeling of coated advanced gas turbine materials. Emphasis is placed on life characterization which is based on low cycle

---

Research sponsored by U.S Department of Energy's Morgantown Energy Technology Center, under cooperative agreement DE-FC21-92MC29061 with the South Carolina Energy Research and Development Center, subcontract AGTSR 9301SR012D

fatigue (LCF) under isothermal conditions and also on thermo-mechanical fatigue (TMF). The microstructure of failed coated and uncoated specimens is being analyzed to assess the deformation response, the fracture mechanism, and the environmental effect. IN 738 LC has been selected as a basic material which will be followed in the future by directionally solidified (DS) and single crystal (SC) materials..

Project Description

The project is divided into two parts: experimental and analytical. The TMF experimental part is not as simple as the isothermal fatigue testing and becomes very sensitive to temperature/strain programming. Software programs for TMF and heating were developed to cover the following loading schemes:

-Strain-temperature out-of-phase cycling where the strain is in compression at the maximum temperature.

-Strain-temperature out-of-phase cycling where the strain is held in compression for a period of 90 seconds at the maximum temperature. This type of cycling simulates the creep and relaxation effects and introduces the mean stress.

The experimental facility consists of servo-hydraulic MTS system designed for axial-torsion strain cycling at high temperatures. Only the axial load component was used. The specimen was heated by induction with three adjustable coils to maintain uniform temperature distribution over the gage length with five thermocouples equally spaced and wrapped around the gage length measuring the temperature distribution. Strain was measured by an axial high temperature air cooled MTS extensometer with wedge probes placed over one inch gage length. The strain and temperature input were computer controlled. The TMF test system is shown in Fig. 1. Thermocouples and coils placement on the specimen are shown in Fig. 2.

Analytical And Experimental Approach

a- Analytical Solution:

Life Prediction Model Development:

In developing a life prediction model, the specimens are subjected to mechanical and thermal loads in addition to the environmental effect which has to be incorporated in the analysis. Most of the current life models under constant temperature (isothermal) conditions utilize a simple approach using total or plastic strain range-cycle relation such as the Coffin-Manson relation. The plastic strain range is selected at the mid-life cycle range which describes the average deformation process in fatigue cycling. However, this type of approach is not adequate to describe the life under the variable temperature and strain since the damage process is dependent on strain, mean stress, thermal effect, creep and ductility. The life prediction model has to incorporate all these variables and since cyclic strain is the primary mechanical driving mechanism, the mid-life strain-cycle as represented by the hysteresis loop is incorporated in a proposed damage model based on the concept of "non-linear continuum damage mechanics". The continuum damage model is a strain base and to accurately predict the mid-life strain-cycle hysteresis loop, a viscoplastic model proposed by A. Freed (1) is used. The viscoplastic model can also accounts for the material response to kinematic or isotropic hardening. These two processes effects the yield phenomenon . During kinematic hardening the center of the yield surface moves gradually while the radius of the yield surface remains constant in a stress space, as a result a mean stress develops. For the isotropic hardening case, the center of the yield surface remains fixed in the stress space while the radius of the yield surface progressively increases resulting in a decrease in the hysteresis loop width. The two types of hardening mechanisms are shown in Figs. 3 and 4.

Viscoplastic Model

The life prediction model under development has two components: a viscoplastic component and a non-linear continuum damage component. The vsicoplastic component has been completed and is presented in a simplified form. The model accounts for the nonlinear kinematic hardening process observed in IN 738 LC material under a TMF compressive and hold-time strain cycling. The two type of cycle produces a significant mean stress.

The basic components of the model is strain, strain rate, stress, temperature, and creep rate. For an isothermal uniaxial LCF strain cycle, the total strain is:

$$\varepsilon = \varepsilon_e + \varepsilon_{in}$$

and the rate:

$$\dot{\varepsilon} = \dot{\varepsilon}_e + \dot{\varepsilon}_{in}$$

the inelastic strain rate is also a function of deviatoric stress S, internal stress variables κ and temperature T:

$$\dot{\varepsilon}_{in} = f(S, \kappa, T)$$

Three internal stress variables, which are represented by κ, characterize the inelastic deformation of the material : the time dependent back stress B which takes into account the kinematic hardening; the time dependent drag stress D, a scalar quantity, which measures the isotropic hardening; and the time dependent limiting stress L, which is also a scalar quantity, accounts for the radius of the yield surface. The model is a rate process and uses the concept of an effective stress Σ, sometimes referred to as "overstress", which is responsible for the yield process.

The deviatoric stress S for uniaxial stress is defined as:

$$S = \frac{2}{3}\sigma_x$$

and the effective stress for the uniaxial case is defined as:

$$\Sigma_x = S_x - B_x$$

For steady state conditions under varying temperatures when the hysteresis loop is saturated, the internal stresses are written for the uniaxial case as a rate in the form of :

$$\dot{B}_x = H_b\left(\dot{\varepsilon}^p_x - \frac{B_x}{L}\dot{\varepsilon}^p_x\right) + \frac{B_x}{H_b}\frac{\partial H_b}{\partial T}\dot{T}$$

and

$$\dot{L} = \frac{L}{H_L}\frac{\partial H_L}{\partial T}\dot{T}$$

$$\dot{D} = \frac{D}{H_d}\frac{\partial H_d}{\partial T}\dot{T}$$

where H_b is the kinematic modulus and H_L, H_d are the isotropic hardening modulii. At the steady state condition, the back stress saturates, i.e. $\dot{B}_x = 0$. In addition, if the temperature T is constant, i.e., $\dot{T} = 0$, the scalar variables L and D become constants.

The inelastic strain rate is expressed as:

$$\dot{\varepsilon}_{in} = \theta\, Z(\zeta)\,\frac{\Sigma_x}{\Sigma_2}$$

where the thermal diffusivity, θ , is defined as:

$$\theta = \left\{\exp\left[\frac{-Q}{kT}\right]\right\} \quad \text{for } T \geq T_m/2$$

$$\theta = \left\{\exp\left[\frac{-2Q}{kT_m}\left\{\ln\left(\frac{T_m}{2T}\right) + 1\right\}\right]\right\}$$

for $T \leq T_m/2$

and

$$\Sigma_2 = \sqrt{\frac{2}{3}\Sigma_{ij}\Sigma_{ij}}$$

and for the uniaxial case, becomes $\Sigma_2 = |\Sigma_x|$

The Zener Holloman parameter Z is defined as:

$$Z(\zeta) = A\,\zeta^{\,n} \qquad \text{if } \zeta \le 1$$

$$Z(\zeta) = A\,e^{\,n(\zeta - 1)} \qquad \text{if } \zeta > 1$$

where A and n are material constants and ζ is defined at the steady state condition and at mid-life as:

$$\zeta = \frac{|\Sigma_x|}{D}$$

$\Sigma_x = S_x - B_x$ and D becomes a constant for the isothermal case but varies for TMF conditions.

Under steady state or during a stabilized cycle, the inelastic strain rate can be assumed to approach the steady state creep rate $\dot{\varepsilon}_{ss}$. Having steady state creep rate data at several temperatures and stress levels, the Zener-Holloman stress function $Z(\zeta) = \frac{\dot{\varepsilon}_{ss}}{\theta}$ is plotted vs. the deviatoric stress S as shown in Fig. 5. From Fig. 5, C is the point where the curve deviates from a linear relation, n is the slope of the linear section and A is the intercept or for a better accuracy, a least square curve fit can be used.

The kinematic hardening modulus H_b and the isotropic hardening modulii H_L, H_d are determined by an optimization process using stabilized LCF hysteresis loop generated at three constant temperatures (mid-life loops). Once these parameters are determined, the TMF inelastic strain-cycles are predicted from isothermal inelastic-strain cycles for any cyclic strain range with or without hold-time (creep) as shown in Figs. 6-8.

b- Experimental Approach:

Material And Test Results

- Material, Specimen and Coatings:

The nickel base superalloy IN 738 LC material, solution-treated condition (1120°C for 2 hrs, air cooled), was received in the as-cast bars having one inch (25.4mm) in diameter by six and quarter inches (16 cm) in length. Tubular test specimens machined by a low stress grind process were aged in a dynamic vacuum of ~ 2.7×10^{-4} pa. for 24 hrs at 843°C (1550°F) followed by an air cool. The microstructure of the cast material consists of dentritic structure with a high volume fraction of fine-scale gamma-prime particles as well as large second phase particles, mostly primary gamma prime and/or carbides, in the interdendritic regions. No evidence of large-scale (>1mm) porosity was seen. The chemical composition of the material is presented in Table 1. Fatigue specimens were overlay coated (NiCoCrAly) over either three quarter or full length of the gage length where the gage length was one inch. The overlay coating thickness was 5.8 mil (147 µm) and was deposited on the specimen using a low pressure plasma spraying process. The N_iAl-based aluminide coating was deposited using a pack cementation process and had a thickness of 1.3 mil (33 µm) with a 0.4 mil (10 µm) deep diffusion zone.

- Tests Results:

1- Isothermal Fatigue Tests (Uncoated Specimens)

A total of six isothermal fatigue tests were conducted at 1500°F under different strain range amplitudes: three of these were LCF with two under a compressive hold-time and one under a tensile-hold time of 90 seconds. The difference between the tension and compression 90 seconds hold-time tests is the apparent response of the mean stress. In the tension test, the mean stress became compressive, while in the compression test, it became tensile. A comparison of lives between the two types of tests at 0.5% strain range showed that the compressive hold test reduced the life by a factor of 5 as a result of the tensile mean stress which develops.

At 1600°F, one 90-second hold-time compressive test was completed at a strain range of 0.5%. The fatigue life (N_i) was 303 cycles as compared to a similar hold-time test at 1500°F where the fatigue life was 517 cycles. The 100°F temperature increase reduced the life by 41%. N_i is defined as the cycle at which the peak tensile stress begins to decrease rapidly during strain cycling.

2- Isothermal Fatigue Tests (Overlay Coated Specimens)

At 1600°F, one 90-second hold-time compressive test was conducted at a strain range of 0.5%. The fatigue life ($N_i = 613$) for the coated specimen was longer when compared to a similar uncoated hold-time test at the same strain range and temperature ($N_i = 135$).

3- Thermomechanical Fatigue Tests (TMF) (Uncoated Specimens)

At 1600°-900°F, a total of five TMF tests were completed. The first two TMF tests were conducted at strain ranges of 0.5% and 0.8% and the next three TMF tests with compressive hold-time of 90 seconds at the same strain ranges. A comparison of life, at strain range of 0.5%, between the TMF (zero hold-time) tests at 1600°-900°F and TMF with 90 seconds hold time in compression, showed a significant reduction in life. For example, at a strain range of 0.5%, the N_i life of 790 cycles was reduced by the hold time test to 563 cycles while at 0.8% strain range the life was reduced from 282 cycles to 112 cycles.

4- Thermomechanical Fatigue Tests (TMF) (Overlay Coated Specimens)

The one in. gauge lengths of the IN 738LC specimens were either partially coated to 3/4 in. or to full length of the specimen. The overlay coating thickness was 5.8 mil (147 µm). Two - 3/4 in gauge length coated specimens were tested at 1600°-900°F without creep effect (zero hold time) at strain ranges of 0.5% and 0.8% and one test was at 0.8% strain range with compressive hold-time of 90 seconds at the maximum temperature. Specimen failure occurred by cracking either outside the coated section or at the transition region between coated and uncoated sections of the specimen. As a result, fatigue lives are not reported here.

The fully coated specimens were tested at a strain range of 0.5% without and with 90 seconds compression hold-time. For the TMF tests (zero hold-time), the overlay coating improved the life of the uncoated substrate from 790 cycles to 2058 cycles. However, introducing hold-time, the overlay life was reduced substantially from 2058 cycle to 643 cycles .

5- Thermomechanical Fatigue Tests (TMF) (Aluminide Coated Specimens)

Four TMF fatigue tests were conducted on aluminide coated specimens. Three tests with zero hold-time at strain ranges of 0.3%, 0.5% and 0.8% and one test with 90-seconds compressive hold-time at 0.5% strain range. The aluminide coating reduced the fatigue life as compared to uncoated specimens by a factor of 2.2 for the 0.5% strain range tests and by 3.6 for the hold-time test. TMF test data for the two types of coatings are shown in Fig. 9 and Table 2 is a summary of all fatigue tests completed to date.

Microstructure Failure Observations of Tested Specimens:

i- Uncoated Specimens: Crack Initiation Behavior

Crack initiation and propagation was transgranular under all test conditions. Optical and scanning electron microscopy revealed that crack initiation occurred at both the outer and inner walls as shown in Fig. 10. The fracture surfaces near the crack initiation sites were flat, semi-circular and oxidized.

The isothermal fatigue test specimens all exhibited fatigue crack initiation predominantly from the outer surface. In contrast, the TMF specimens often contained both an outer initiation along with numerous small cracks initiating on the interior of the specimen.

ii- Overlay Coated Specimen: Crack Initiation Behavior

Three overlay coated specimens have been tested in fatigue under both isothermal and TMF conditions (see Table 2). The isothermal test at the strain range of 0.5%, that included a hold time of 90-seconds in compression, had multiple crack initiations on the uncoated interior surface of the specimen. However, the TMF cycling initiated many small surface cracks in the coating as shown in Fig. 11. A few cracks propagated through the coating and penetrated the substrate (Fig. 12) but most were confined to the coating (Fig. 13). Also debonding of the overlay coating was observed in the TMF type tests which was absent in isothermal tests.

iii- Aluminide Coated Specimen: Crack Initiation Behavior

Four fatigue specimens were aluminide coated over three quarter of one inch gauge length. Three specimens were tested with no hold-time and one where the compressive strain was held for 90 seconds at maximum temperature. TMF test results showed that the cracks initiated in the coating, propagated through the inter-diffusion zone and penetrated the substrate as shown in Figs. 14 and 15. The aluminide coating showed both intergranular and transgranular fracture features. Fig. 16 shows the aluminide coating structure.

Future Work

TMF tests of coated specimens will continue to compliment the analytical approach. The effect of coating on life will be characterized by microstructural analysis which will describe the deformation and fracture mechanisms. Other types of material's structures such as DS and SC materials and other types of coatings will be investigated in the future where life is affected by the material durability and resistance to creep damage.

Industrial Partners Participation

The PI of the research program is in direct consultation with our industrial partners: Westinghouse Electric, Power Generation Division in Orlando, Fl., Allied Signal Aerospace Co. of Phoenix, AZ and Solar Turbine of San Diego, California..

Acknowledgment

The authors would like to acknowledge the research support by U.S Department of Energy's Morgantown Energy Technology Center, under cooperative agreement DE-FC21-92MC29061 with the South Carolina Energy Research and Development Center. The program is under subcontract AGTSR 9301SR012D. The research program is supporting two doctoral candidates: Messrs. Ravindra Annigeri and Mark Renauld.

Also our gratitude to Mr John Junkin of Westinghouse, Power Division, Orlando, Florida, for his support in providing the overlay coating on the specimens and to Dr Graham Webb of Allied Signal Aerospace Co. of Phoenix, Arizona, for his contribution in coating specimens with aluminide coating.

References

1- Freed, A., "Thermoviscoplastic Model with Application to Copper," NASA Technical Paper 2845,1988.

2- Kuwabara, Nitta, A., and T. Kitamura, "Thermal-Mechanical Fatigue Life Prediction In High Temperature Component Materials For Power Plant," ASME Int. Conf. on Advances in Life Prediction Methods, Materials Conference, N.Y., 1983, pp. 131-141.

3- Au, P., and R. V. Dainty, "Isothermal Low Cycle Fatigue Properties of Diffusion Aluminide Coated Nickel and Cobalt Based Superalloys," Surface Modification Technologies III, Eds., T.S.Sudarshan and D. G. Bhat, TMS, 1990, pp.729-747.

4- Ostergren, N., J., " A Damage Function and Associated Failure Equations for Predicting Hold-Time and Frequency Effects in Elevated Temperature, Low Cycle Fatigue," Journal of Testing and Evaluation, Vol. 4, No. 5, Sept. 1976, pp. 327-339.

5- Jiao, F. " Low Cycle Fatigue Behavior of IN 738 LC at 1223K," Proc. of Third Int. Conf. on Low Cycle Fatigue and Elasto-Plastic Behavior of Materials," 1992, pp.298-303.

6- Strang, S., "High Temperature Properties of Coated Superalloys," Behavior of High Temperature Alloys in Aggressive Environment, Proc. of Petten Int. Conf., The Metal Society of London, 1979, pp.595-611.

7- Castillo, R.and A. K. Koul, "Effects of Microstructure Instability on the Creep and Fracture Behavior of Cast IN 738 LC Ni-base Superalloy," High Temperature Alloys for Gas Turbines and Applications," Betz, W., eds, D. Reidel Publishing Co., Dordrecht, 1986, pp.1395-1409.

8- Castillo, R.and A. K. Koul, "Factors Influencing the Residual Creep Life Prediction of Service Exposed Ni-base Superalloys Components," Life Assessment and Repair Technology for Combustion Turbine Hot Section Components, ASM Int., Metal Park, 1990, pp 19-34.

9- Tipler, H., R., "Regeneration of the Creep Properties of a Cast Ni-Cr-base Alloy," AGARD-CP-317, Paper #12.

10- Castillo, R., A. K. Koul and E. H. Toscano, "Lifetime Prediction under Constant Load Creep Conditions for a Cast Ni-base Superalloy," Journal of Engineering for Gas Turbines and Power, vol. 109, 1987, pp.99-106.

11- Kloos, K., H., J. Granacher, and H. Demus, "Creep Rupture Strength of Cast Turbine Blades under Hot Gas Corrosion," Corrosion and Mechanical Stress at High Temperature, Guttmann, V. and Merz, M. eds., Applied Science Publishers, London, 1981, pp. 243-255

12- Hartnagel, W., R. Bauer and H. W. Grunling, "Constant Strain Rate Creep Tests with Gas Turbine Blade Material under Hot Corrosion Environmental Conditions," Corrosion and Mechanical Stress at High Temperature, Guttmann, V. and Merz, M. eds., Applied Science Publishers, London, 1981, pp. 257-272.

13- Villat, M., P. Felix., "High Temperature Corrosion Protective Coating for Gas Turbines," Sulzer Technical Review, Vol. 3, 1976, pp. 97-104.

14- Nazmi, M. Y., "High Temperature Low Cycle Fatigue of IN 738 and Application of Strain Range Partitioning," Metallurgical Trans. A, ASM, Vol. 14A, March 1983, pp. 449-461.

15- Zamrik, S. Y.," An Interpretation of Axial Creep-Fatigue Damage Interaction in Type 316 Stainless Steel," ASME Trans., Journal of Pressure Vessel Technology, Vol.112, Feb. 1990, pp. 4-19.

16 Gabrielli, F, M. Marchionni and G. Onofrio, "Time Dependent Effect on High Temperature Low Cycle Fatigue and Fatigue Crack Growth Propagation of Nickel Base Superalloys," Advances in Fracture Research, Proc., of the 7th Int. Conf. on Fracture (ICF7), March 1989, pp. 1149-1163.

TABLE 1: CHEMICAL COMPOSITION OF ALLOY IN 738 - LC

Heat Treatmeant	Element	Percentage
Solutionize at 2050 °F(1120 °C) for 2 hr followed by aging at 1550 °F (843 °C) for 24 hr.	Cr	15.7 - 16.3
	Co	8.0 - 9.0
	Ti	3.2 - 3.7
	Al	3.2 - 3.7
	W	2.4 - 2.8
	Mo	1.5 - 2.0
	Ta	1.5 - 2.0
	Nb	0.6 - 1.1
	Ni	Balance

Table 2. Penn State IN-738LC Fatigue Test Summary

Specimen #	Coating	Emech	ISO/TMF	Temp Range F (C)	Hold Time Seconds	Cycles Ni	Cycles N90	Cycles N70	Cycles N50	Mid-Cycle	Peak Stress (MPa)	Valley Stress (MPa)	Mean Stress (MPa)
20	-	0.3%	ISO	1500 (816)	0		86759 (runout)			43561	247	-184	31.5
11	-	0.5%	ISO	1500 (816)	0	2494	3189	3476	3807	1500	420	-343	38.5
17	-	2.0%	ISO	1500 (816)	0		Spec Separation, N=5			3	757	-820	-32
16	-	0.5%	ISO	1500 (816)	90 s (T)	4611	4959	5128		2467	220	-483	-132
22	-	0.3%	ISO	1500 (816)	90 s (C)	8312	8542	8648	8731	4239	362	-80	141
21	-	0.5%	ISO	1500 (816)	90 s (C)	517	622	649	670	225	487	-224	132
25	-	0.5%	OP TMF	900-1500 (482-816)	0	5177	5427	5444	5458	2661	507	-209	149
27	-	0.7%	OP TMF	900-1500 (482-816)	0	847	1253	1361	1497	582	656	-371	143
28	-	0.5%	IP TMF	900-1500 (482-816)	0		10012 (runout)			5052	199	-530	-166
31*	-	0.5%	ISO	1600 (871)	90 s (C)	135	250	285	324	146	397	-200	98.5
36	-	0.5%	ISO	1600 (871)	90 s (C)	303	481	508	526	250	448	-204	122
29	-	0.5%	OP TMF	900-1600 (482-871)	0	790	1139	1147	1154	562	623	-189	217
32	-	0.8%	OP TMF	900-1600 (482-871)	0	282	Spec Separation, N=329			175	716	-400	158
35	-	0.3%	OP TMF	900-1600 (482-871)	90 s (C)	6387	6924	7371			456	9	233
33	-	0.5%	OP TMF	900-1600 (482-871)	90 s (C)	563	Spec Separation, N=642			258	608	-194	207
38	-	0.5%	OP TMF	900-1600 (482-871)	90 s (C)	785	1113	1165	1226	405	565	-170	198
34	-	0.8%	OP TMF	900-1600 (482-871)	90 s (C)	112	Spec Separation, N=117			39	720	-398	161
13	Overlay	0.5%	ISO	1600 (871)	90 s (C)	613	786	817	835	420	430	-210	110
12	Overlay	0.5%	OP TMF	900-1600 (482-871)	0	1171	1543	(fractured)		789	636	-201	218
14	Overlay	0.8%	OP TMF	900-1600 (482-871)	0	172	Spec Separation, N=173			92	797	-412	193
15	Overlay	0.8%	OP TMF	900-1600 (482-871)	90 s (C)	55	Spec Separation, N=66			22	794	-392	201
41	Overlay	0.5%	OP TMF	900-1600 (482-871)	0	2058	2371	2373	2376	1102	581	-160	211
50	Overlay	0.5%	OP TMF	900-1600 (482-871)	90 s (C)	643	1010	1078	1126	350	578	-160	209
2	Aluminide	0.3%	OP TMF	900-1600 (482-871)	0	6540	7876	8161	8598	3958	432	-26	203
4	Aluminide	0.4%	OP TMF	900-1600 (482-871)	0	1356	1754	1826	1880	753	451	-149	151
1	Aluminide	0.5%	OP TMF	900-1600 (482-871)	0	360	547	609	678	245	523	-271	126
7	Aluminide	0.8%	OP TMF	900-1600 (482-871)	0	190	Spec Separation, N=239			113	555	-393	81
8	Aluminide	0.5%	OP TMF	900-1600 (482-871)	90 s (C)	218	456	472	483	100	529	-235	147

Ni=Cycle for which a deviation from maximum linear tensile stress was first detected

N90=Number of cycles to 90% of maximum linear tensile stress; 10% load drop

N70=Number of cycles to 70% of maximum linear tensile stress; 30% load drop

N50=Number of cycles to 50% of maximum linear tensile stress; 50% load drop

Figure 1. Computer controlled test system for thermomechanical fatigue test

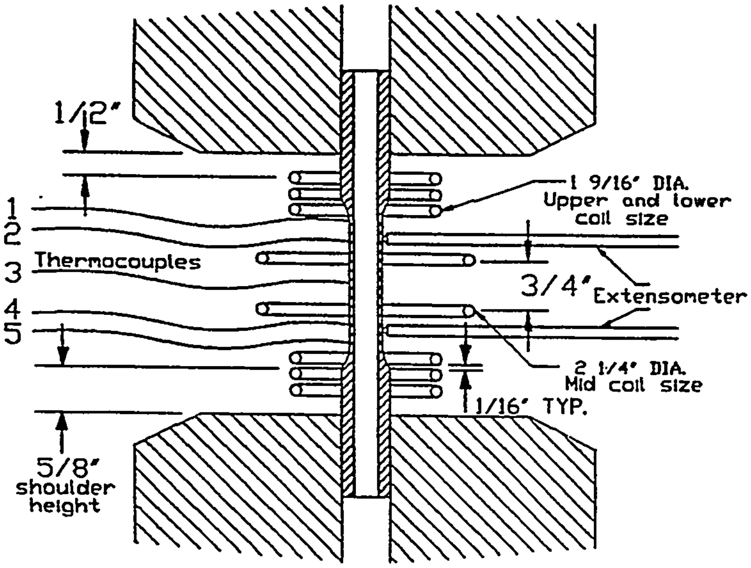

Figure 2. Cross-section of specimen, induction coils and thermocouples

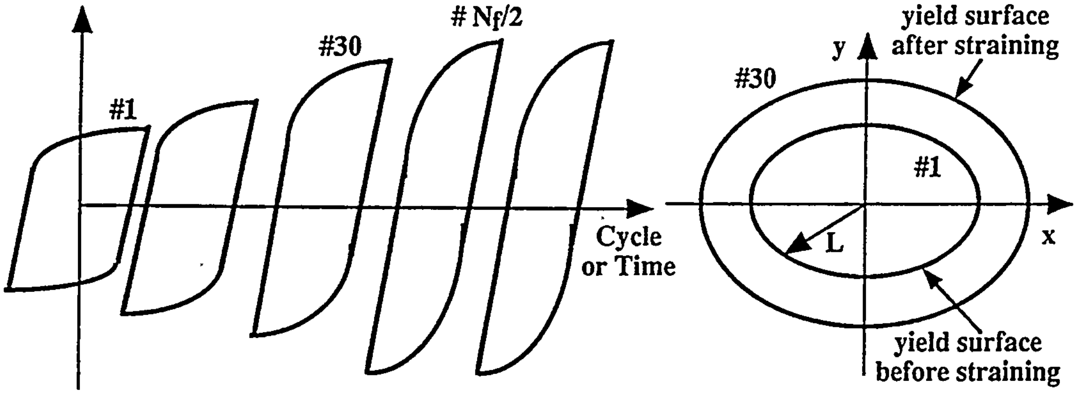

Figure 3. Isotropic hardening behavior in polycrystalline materials

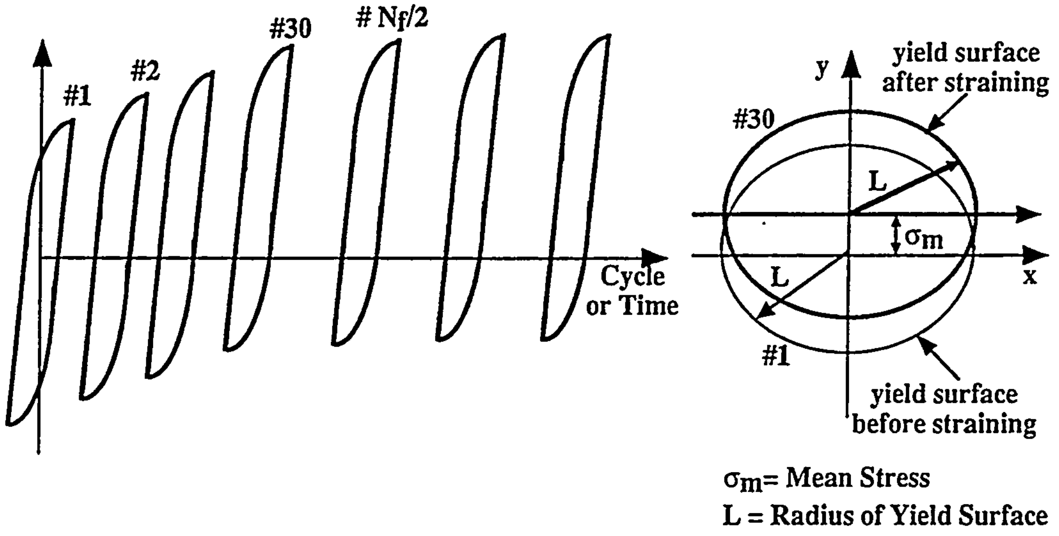

Figure 4. Kinematic hardening behavior in polycrystalline materials

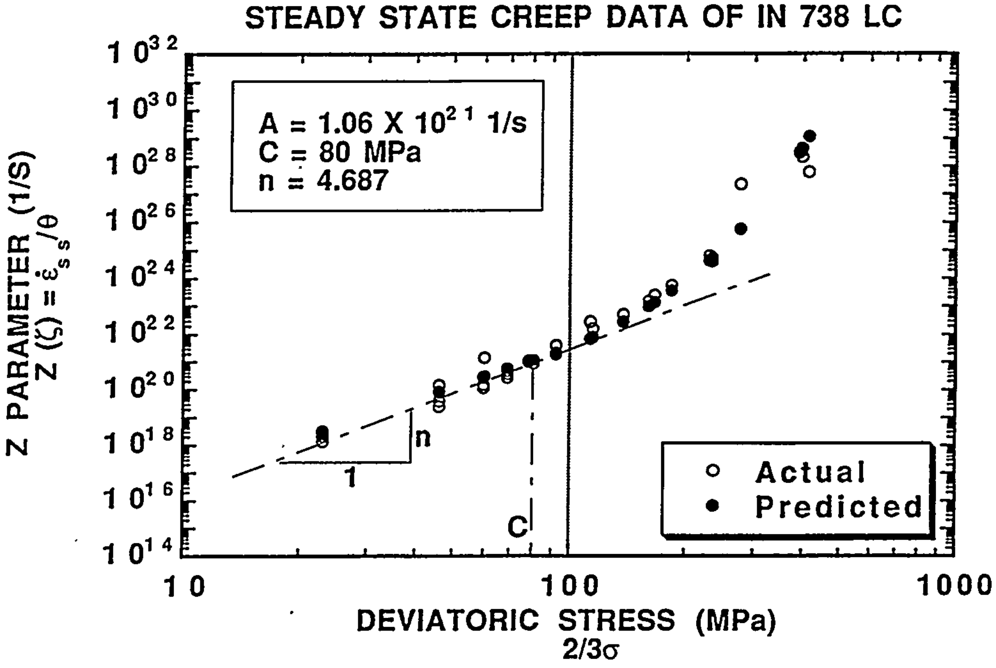

Figure 5. Zener-Hollomon plot of stress dependence of steady state creep rate illustrating determination of material parameter C

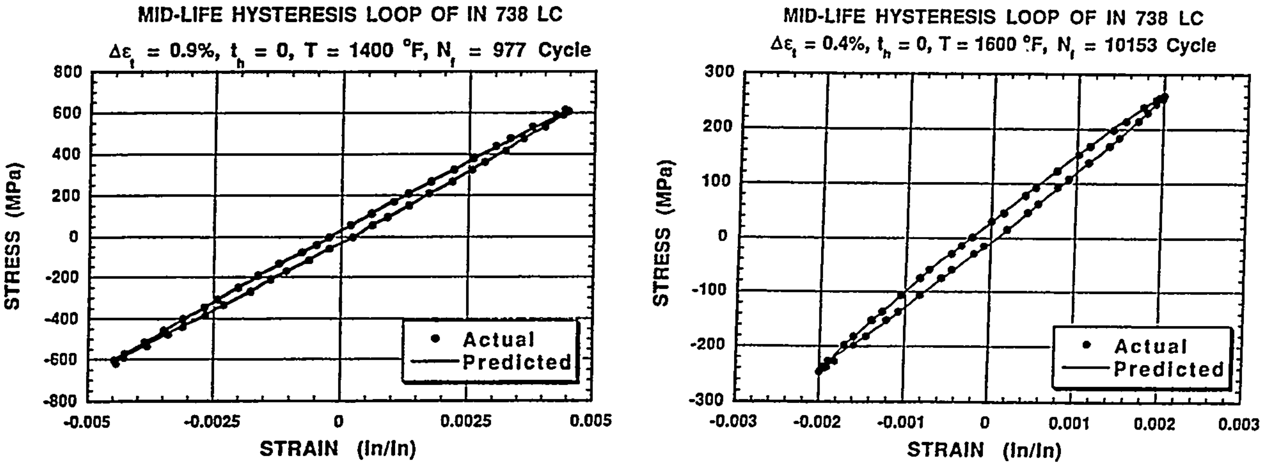

Figure 6. Predicted mid-life isothermal LCF hysteresis loops without hold time

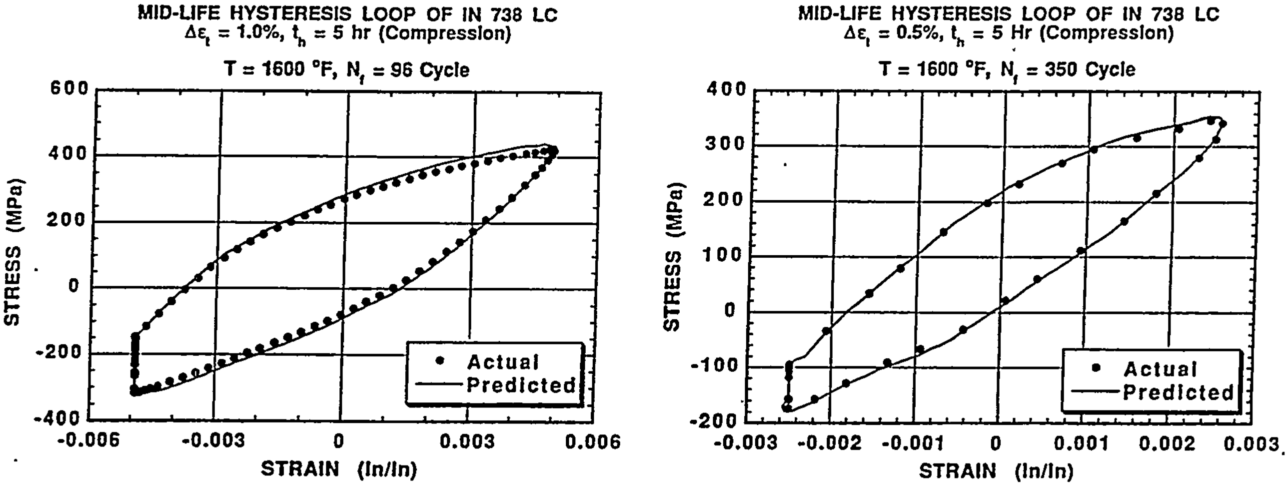

Figure 7. Predicted mid-life isothermal LCF hysteresis loops with hold time

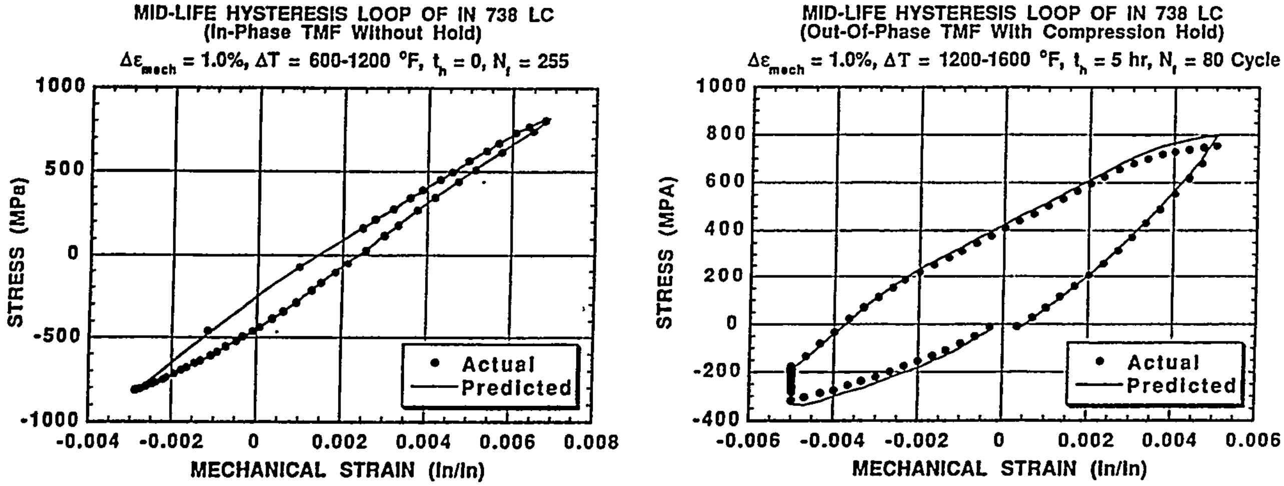

Figure 8. Predicted mid-life thermomechanical fatigue hysteresis loops

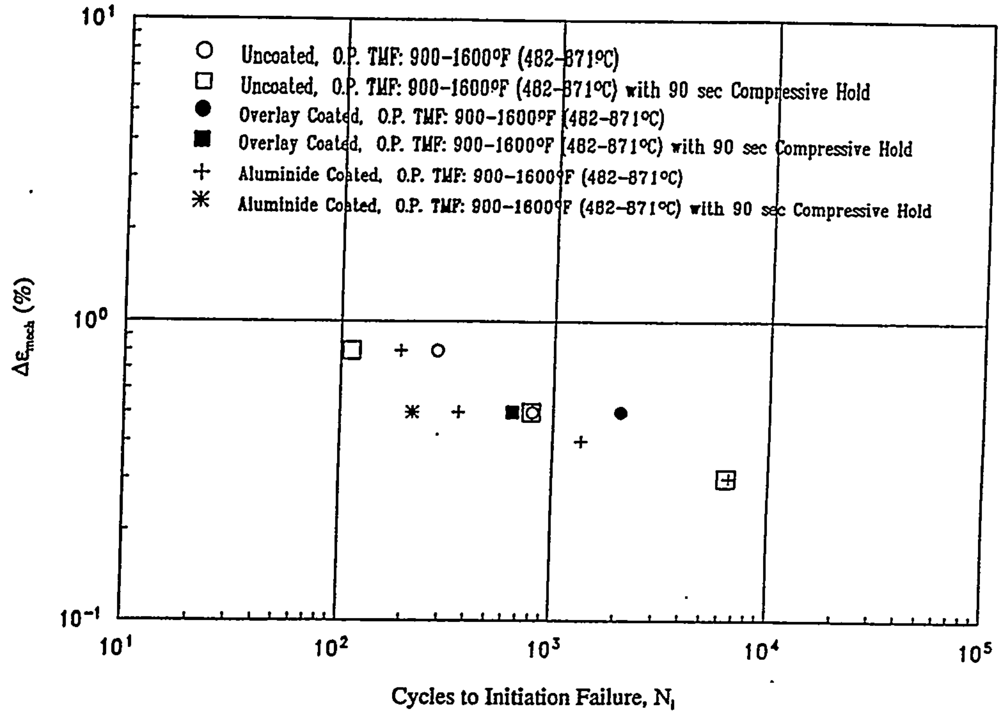

Figure 9. Penn State O.P. TMF Results

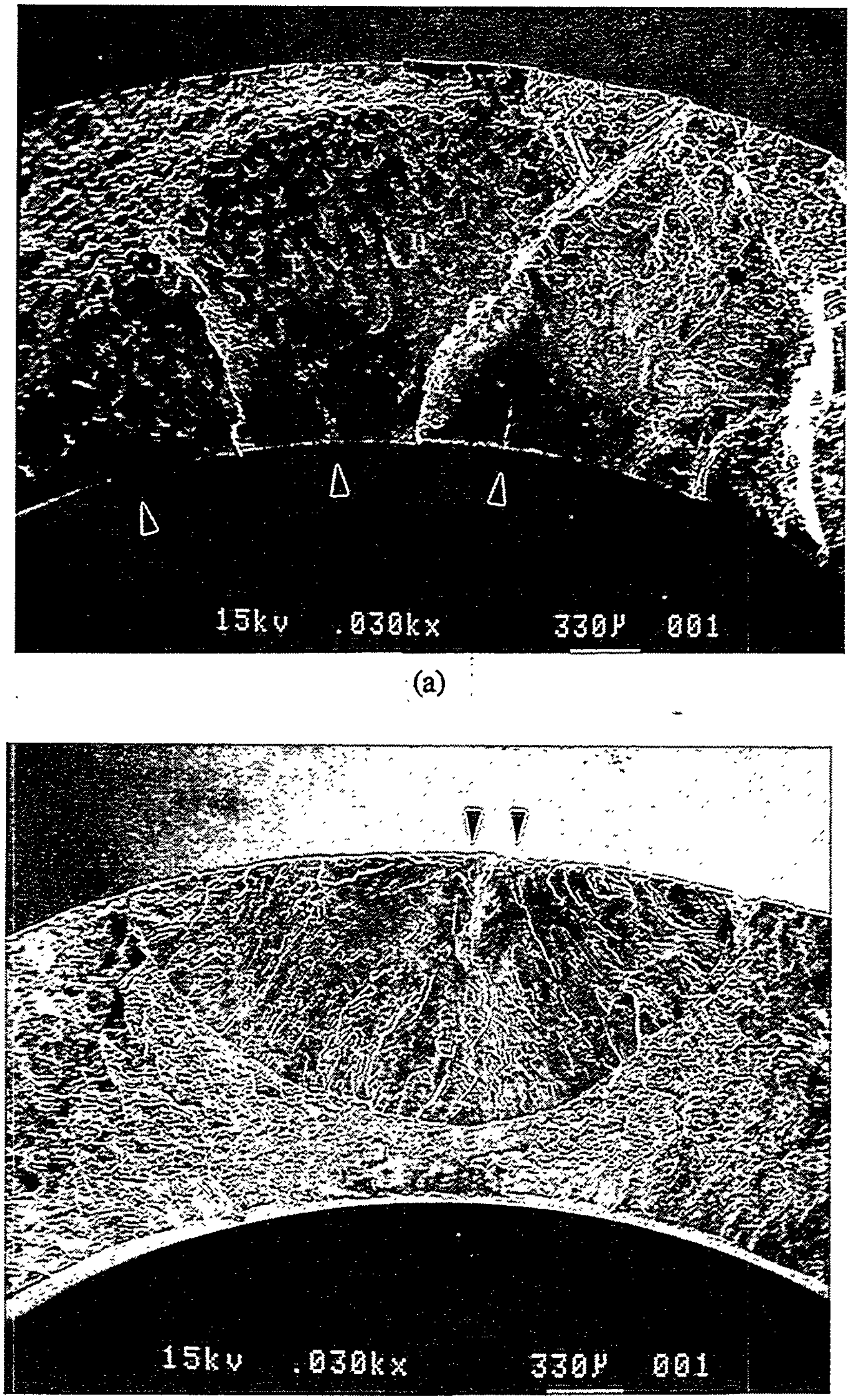

(a)

(b)

Figure 10. SEM fractographs of uncoated specimens showing: (a) interior wall fatigue crack initiations, $\Delta\varepsilon_{mech}$=0.5%, O.P. TMF, ΔT=900-500°F, N_i=5177 and (b) exterior wall fatigue crack initiation, $\Delta\varepsilon_{tot}$=0.5%, isothermal, T=1500°F, N_i=2494.

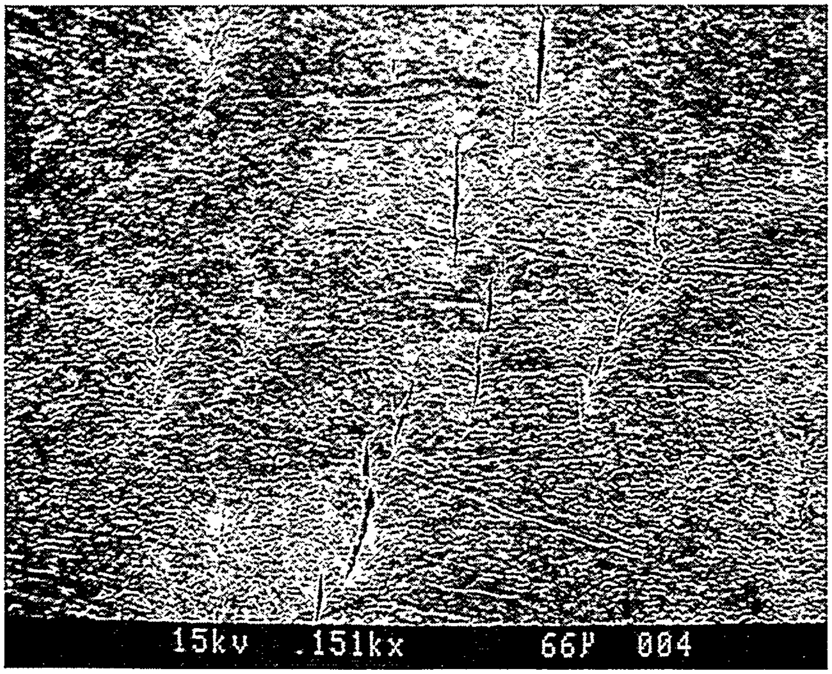

Figure 11. SEM micrograph showing surface fatigue cracks in overlay coating. $\Delta\varepsilon_{mech}$=0.5%, O.P. TMF, ΔT=900-1600°F, N_i=1171.

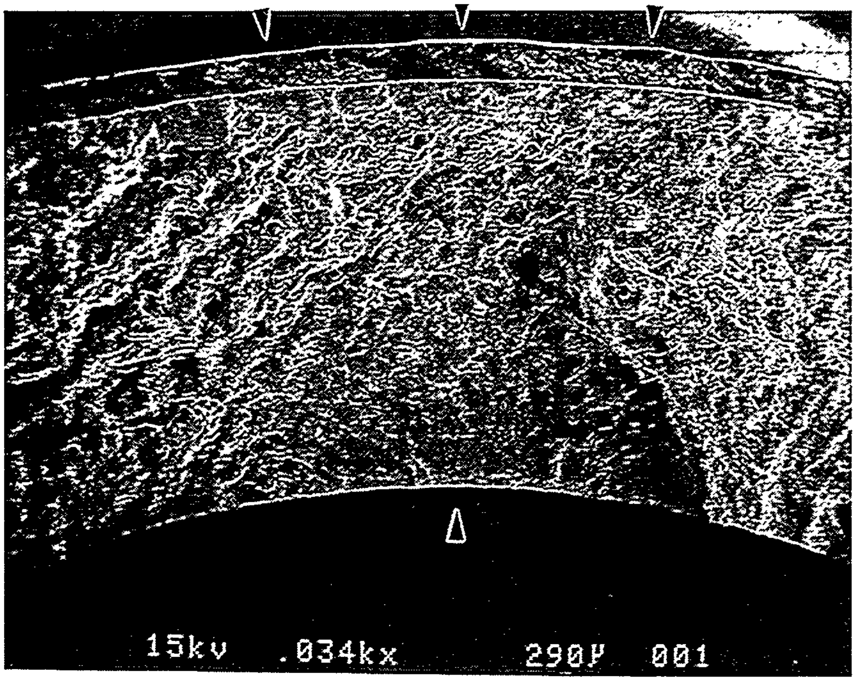

Figure 12. SEM fractograph showing fatal inner wall fatigue crack initiation and outer wall crack penetration through overlay coating and into substrate. $\Delta\varepsilon_{mech}$=0.5%, O.P. TMF, t_h=90 sec (comp), ΔT=900-600°F, N_i=643.

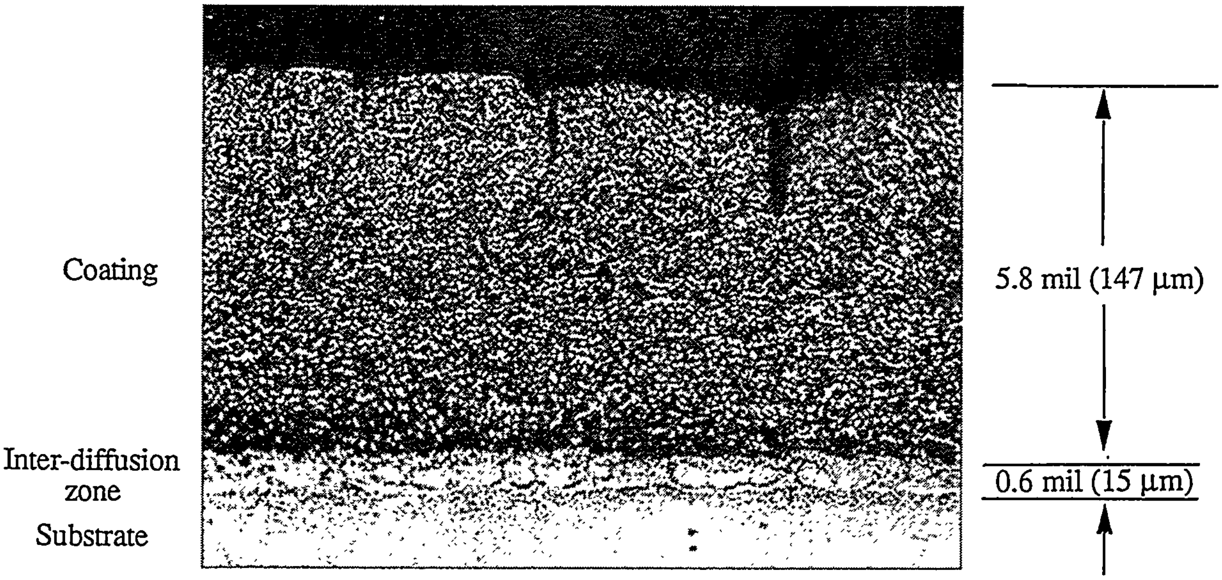

Figure 13. Crack initiation and blunting in overlay coating. $\Delta\varepsilon_{mech}$=0.5%, O.P. TMF, ΔT=900-1600°F, N_i=1171. (330X)

Figure 14. Light micrograph showing crack penetration through aluminide coating, inter-diffusion zone and substrate. $\Delta\varepsilon_{mech}$=0.5%, O.P. TMF, ΔT=900-1600°F, N_i=360. Crack length=7.6 mil (193 µm). (170 X)

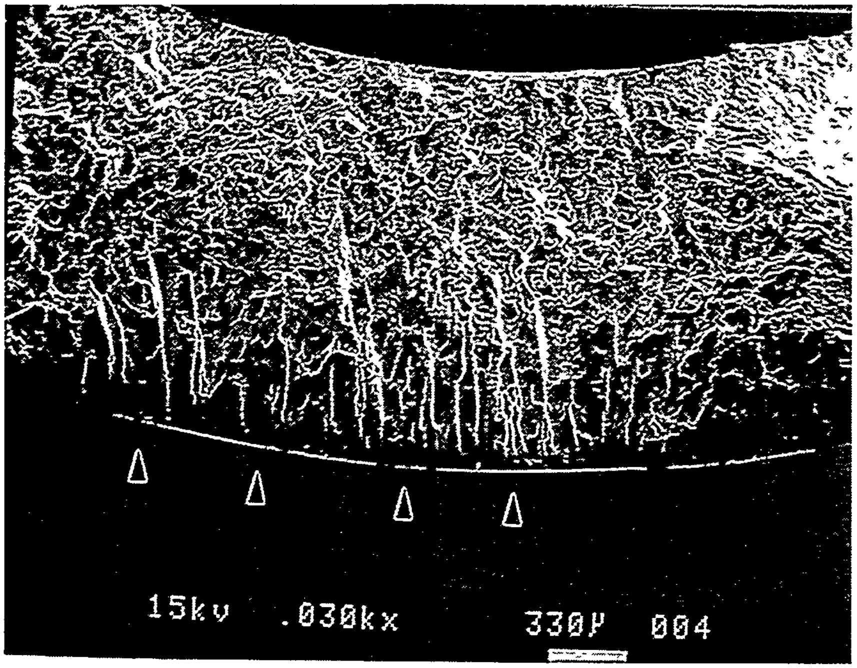

Figure 15. SEM fractograph showing numerous aluminide coating crack initiations. $\Delta\varepsilon_{mech}$=0.5%, O.P. TMF, ΔT=900-1600°F, N_i=360.

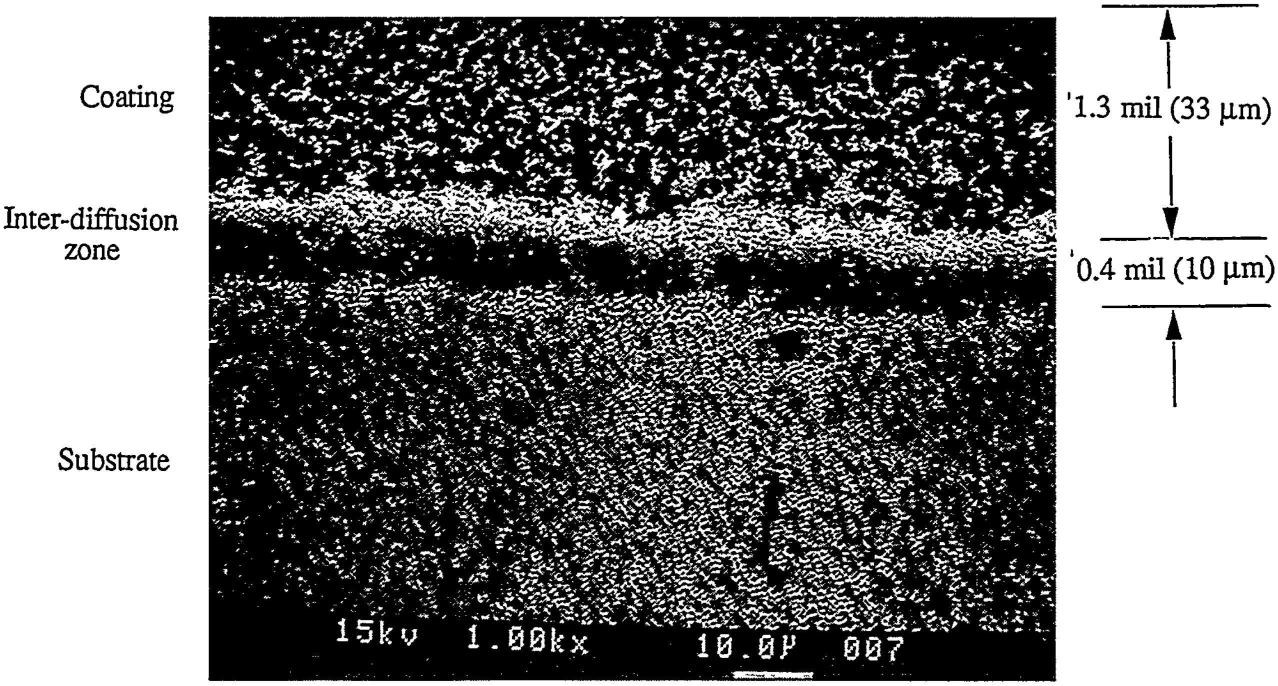

Figure 16. SEM micrograph showing etched coating and substrate microstructure after testing. $\Delta\varepsilon_{mech}$=0.5%, O.P. TMF, ΔT=900-600°F, N_i=360.

P7

Advanced Combustion Technologies for Gas Turbine Power Plants

Uri Vandsburger (uri@stnick.me.vt.edu; (540)-231-4459)
Randolph Hall, 0238
Department of Mechanical Engineering
Virginia Tech
Blacksburg, VA 24061

Larry A. Roe (lar@engr.uark.edu; (501) 575-3750)
Department of Mechanical Engineering
University of Arkansas

S. B. Desu (desu@vt.edu; (540) 231-6640)
Department of Materials Science and Engineering
Virginia Tech
Blacksburg, VA 24061

1. Introduction

During the second half of fiscal year 1995 progress was made in all three funded subject areas of the project as well as in a new area. Work in the area of mixing and combustion management through flow actuation was transferred into an enclosed facility. Jet mixing in a ducted co-flow was examined. The same jets were also subjected to a strong acoustic field established in the duct. Excitation of the jet with static spatial modes was shown to be effective even in the presence of co-flow and the acoustic field. Only when a (reflective) wall is placed at the jet exit plane did the acoustic field dominate the jet dispersion (as expected due to reflective boundary conditions and the jet shear layer receptivity). This case is, however, not the most relevant to gas turbine combustors since it precludes co-flow. In the area of combustor testing, the design, fabrication, and assembly of a mudular combustor test rig for the project has been completed at the University of Arkansas. In the area of high temperature piezoceramic actuator materials development, $Sr_2(Nb_xTa_{1-x})_20_7$ powders have been synthesized, and bulk samples and thick films sintered. These materials have a curie temperature of about 1400 °C compared wtih 300 °C for the commercially available PZT. While at room temperature the new materials show a piezoelectric constant (d_{33}) which is a factor of 100 lower than PZT, at high temperatures they can exhibit significant action. A new area of non-linear, neural-net based, controllers for mixing and combustion control has been added during the second contract year. This work is not funded by the contract. Significant progress was made in this area. Neural nets with up to 15 neurons in the hiden layer were trained with experimental data and

---

Research sponsored by the U.S. Department of Energy's Morgantown Energy Technology Center, under subcontract 93-01-SR013 (through South Carolina Energy R&D Center) with Virginia Tech, Blacksburg VA 24061-0238; fax: 540-231-9100

also with data generated using linear stability theory. System ID was performed successfully. The network was then used to predict the behavior of jets excited at other modes not used for the training. Work plans for the first half of the third year call for:

- development of improved passive and active schemes for rapid mixing,
- testing of the new piezoceramic materials in a high temperature environment, including the University of Arkansas combustor,
- fabrication of thick and thin films, and
- make progress towards a Neural Net mixing and combustion controller.

2. Objectives

The overall stated objectives for this project can be grouped into two categories:

- Development of actuation methodologies for enhancement of mixing between gas streams, and the increase of combustion stability.
- Development of high temperature materials for use as actuators and sensors in combustor environments.

For the second year, the specific goals set were:

- Examination of the utility of spatial mode excitation in ducted jets subject to an acoustic field.
- Synthesis of high temperature piezo-ceramic powders, and sintering of bulk materials and thick films.

Both goals have been fulfilled in a satisfactory manner.

The objectives for the third year include:

- Combustor testing of high temperature piezoelectric
- Development of new passive-active mixing enhancement methodologies based on simple concepts.
- Development of Neural Network based controllers for mixing and combustion stability.

3. Project Description

3.1 Non-Reacting Jets with Co-Flow in a Noisy Enclosure

3.1.1 Introduction. After the successful demonstration of spatial mode actuation, static and dynamic, on free jets, the next step was the examination of these methods on jets with co-flow in an enclosure. Since gas turbine combustors typically also exhibit a lively acoustic environment it was decided to examine the robustness of the spatial mode actuation scheme in the presence of an acoustic field generated by a pair of loudspeakers exciting the first transverse mode.

3.1.2 Experimental Equipment and Setup. Since the last report, additional hot-wire measurements have been performed to obtain information concerning the effect of various acoustic fields on the developing jet flow. The experimental setup is shown in Figure 1. Depending on the different test conditions, time-averaged and phase-locked velocity and turbulence data have been acquired and processed. The turbulent kinetic energy maps presented in this report are an axisymmetric cut of the x=0 plane which can be used for scaling the mixing characteristics in the mixing layer.

To verify the credibility of the data from previous hot-wire measurements, smoke flow visualization with a laser sheet was carried out. A schematic of the flow visualization system is shown in Figure 2. The smoke was generated by electrically heating mineral oil. Flow field pictures were taken with a Stanford Computer Optics 4 Quik 05 intensified CCD camera. A PC

486 computer was used to control the camera for image acquisition and image processing.

The flow conditions for the visualization tests were identical to those of the hot-wire tests, i.e. jet velocity $U_j = 15$ m/s, with a corresponding Reynolds number of 10,000, co-flow velocity U_{coflow} 3 m/s, and a simulated overall equivalence ratio $\phi = 0.45$. In the case of the excited jet, a spatial mode excitation has been applied with m=+-1 and excitation frequency of 70 Hz.

Both longitudinal and transverse acoustic modes have been introduced into the duct to examine their effects on the jet flow. The longitudinal acoustic mode was the preferred mode of the jet shear layer, with a frequency of 210 Hz and a sound pressure level of 105 dB at the anti-node. Since the jet flow field appeared to be more sensitive to the transverse acoustic mode than to the longitudinal mode, emphasis was placed on the investigation of the effect of the transverse resonance mode on the flow field. The first transverse mode of the duct has a frequency of 1335 Hz and a SPL of 125 ~ 136 dB at the anti-node).

3.2 Development of Neural Network Based Controllers

3.2.1 Motivation and Objectives. A new aspect of the program was initiated this year addressing the development of non-linear control strategies for mixing and reacting shear flows. This effort involves an additional faculty member from the department of mechanical engineering, Dr. William Saunders, and a graduate student, both not supported by the project. Due to the inherent non-linear nature of fluid flow systems, neural network based systems seem very attractive.

Research at Virginia Tech has already investigated and identified actuation schemes which are highly beneficial for the mixing of initially separate fluids (Vandsburger and Ding, 1994). The main objective of this research is to explore the possibilities of applying nonlinear control methodologies, e.g., neural networks, as part of a complete control system for jet flows, both non-reacting and reacting.

To fully realize the potential of these control techniques in shear flows and practical combustion devices, the research has been divided into three distinct stages:

I. Construct a neural network model of the near and far field structure of spatially excited jets.
II. Develop a neural network adaptive controller to optimize air/fuel mixing.
III. Apply the concepts developed in stages I and II to reacting shear flows in order to optimize combustion.

Thus, the research is focused around increasing volumetric heat release rate by maximizing air/fuel mixing.

3.2.2 Neural Network Modeling of Spatially Excited Jets. Traditional control strategies are able to predict cause and effect relationships upon a particular system with the use of a mathematical model that describes the physics of the process involved. Most often a differential equation is the underlying model used to describe the dynamics of such a system. For example, in the conventional spring/mass/damper system, the differential equation is ordinary, linear, and of closed form. However, the equations governing the dynamics of fluid flow (Navier-Stokes), are not as easily solved, even when gross assumptions are made. However, by choosing an artificial neural network (ANN) as the mathematical model for the control scheme, the difficult and often futile task of identifying the exact physics involved in a complicated reacting flow is surpassed. Neural networks can be highly nonlinear by design and are able to establish complex relationships between multiple inputs and outputs by learning from experimental data. Essentially, the differential equation describing the physics of the problem is replaced by the experimentally-based ANN model. A simple example of such system identification using neural networks is illustrated in Figure 3. In Figure 3, the teacher represents the actual system based upon an experimental data set of input (x(t)) and output (f[x(t)]) examples, and the object of the neural network is to emulate the teacher by minimizing the error signal, e(t), between the two models.

The question now becomes whether experimental data can be used to emulate a jet undergoing spatial mode manipulation, as shown in Figure 4. The experimental actuation technique which was used to generate such iso-velocity contours involved the use of acoustic actuators placed around the exit of a jet. This arrangement allowed the excitation of various azimuthal (spatial) modes which affect the cross-sectional size and shape of the iso-velocity profile downstream from the nozzle exit. Here, the inputs to the system identification diagram are the actuation signals to the loudspeakers, and the outputs are the iso-velocity contour data. Once the ANN is trained to emulate the jet, the neural network could then be given an untrained actuator signal for which it would anticipate the flow field evolution. Figure 5 illustrates an example of this, where the ANN models a jet undergoing +/-2 mode excitation. Both linear and non-linear neural networks were used to generate the velocity profiles for a normalized velocity contour of 0.3 at three distances downstream of the jet exit (x/D = 3.5, 4.5, 5.5).

Spreading rates for different spatial mode excitations can also be approximated by the ANN as shown in Figure 6. In Figure 6, the ANN was not trained on experimental data for modes +0.5 and +0.75, yet it still generalizes well to give a reasonable estimate of spreading. By anticipating such aspects of the flow field from specified actuator control signals, the ANN-generated flowfield model will ultimately serve as the foundation upon which to build an adaptive control system.

3.3 Medium Scale Combustor at University of Arkansas

As part of the ATS project, a medium scale combustor test rig was to be constructed at the university of Arkansas, department of mechanical engineering. The test system is to be capable of evaluating actuated combustor methodologies at realistic scales, temperatures, and acoustic environments. The fuel is natural gas; either premixed of non-premixed operation is available. The first series of experiments will evaluate flame stabilization and will operate in the premixed mode. The acoustic environment is provided by external acoustic drivers, with controlled amplitude and spectral content. Intrinsic background noise levels in the air supply system are minimized to provide controlled conditions in the combustor section. A 500 CFM Gardener-Denver Cycloblower was chosen for the primary air supply because of the very low pressure fluctuations associated with this helical screw design. During this reporting period, the air supply system was designed, the blower was specified, purchased (with non-contract funds) and installed, and acoustic analyses of the air supply ducting, fuel/air mixer, flow straiteners, and flashback arrestor were conducted. The analyses show a predicted background noise level of 85 dB, well below the level capable of being produced in the test section by external drivers. Assembly of the air supply system is approximately 80 percent complete.

For premixed operation, a fuel injection and mixing section ensures complete mixing of the fuel and air with a minimum reactive volume and a minimum residence time. Using a simplified Fluent CFD model, a radial spoke, multipoint fuel injector scheme and a cross-flow (cone) mixer were designed. The model is currently being refined to more accurately predict the fuel-air mixing.

A preliminary design of the test section and combustor has been completed. The initial testing will be of an axisymmetric, centerbody-stabilized, premixed combustor, which models many of the stabilization characteristics of proposed ATS designs. The centerbody will incorporate piezoceramic shear layer actuators and will be similar in design to the nozzles used for actuated jet mixing studies at Virginia Tech, although the actuators themselves will be manufactured from the new materials being developed under the materials portion of this contract at Virginia Tech. This will provide for the evaluation of the actuators under full temperature conditions. The quartz test section will provide full optical access for shadowgraph and emission photography.

During this period, existing gas analyzers were evaluated and checked for proper operation. The analyzers available are a Thermo Electron Model 10A chemiluminescent analyzer for NO_x, two Beckman Model 315A(S) NDIR analyzers for CO and CO_2, and a Beckman Model 400 FID hydrocarbon analyzer. The NO_x analyzer has been fully checked out and is in working condition. The CO and CO_2 analyzers passed the initial tests but are currently missing calibration curves for some ranges. The hydrocarbon analyzer is considered a low-priority diagnostic device and has not yet been evaluated.

3.4 Fabrication and Property Measurement of High Temperature Piezoelectric Materials

3.4.1 Overview. Due to the high temperatures encountered in a reacting flow, the piezoelectric materials to be used in a combustor must possess high Curie-temperatures. $A_2B_2O_7$ materials like $Sr_2(Nb_xTa_{1-x})_2O_7$ and $La_2Ti_2O_7$ were chosen to satisfy the high Curie-temperature requirements. Compared to conventional actuator materials, for example PZT, [$Pb(Zr_xTi_{1-x})O_3$], the new piezoelectric materials have lower dielectric constants and piezoelectric coefficients at room temperature, but exhibit extremely high Curie-temperatures. Conventional piezoelectric materials are not suitable for high temperature applications due to their lower Curie temperature (e.g. PZT, Curie temperature≈ 300°C). Table 1 shows a comparison between the new material, $Sr_2(Nb_xTa_{1-x})_2O_7$ and the conventional material, $Pb(Zr_xTi_{1-x})O_3$.

During this reporting period, $Sr_2(Nb_xTa_{1-x})_2O_7$ thick films were prepared by the tape-casting method. X-ray diffraction patterns were used to identify the single phase formation, and their piezoelectric properties were measured by a d_{33} meter.

There are three possible types of piezoelectric ceramic actuator designs: multilayers, bimorphs, and the Moonie structure. The characteristics of the different ceramic actuators are summarized in Table 2. The multilayer actuator exhibits large forces and small displacements, whereas the bimorph actuator generates small forces and large displacements. The Moonie structure actuator, shown in Figure 7, is a reasonable compromise capable of sizable forces and appreciable strains. The piezoelectric coefficient for the Moonie structure actuator was found to be larger than without the Moonie structure.

3.4.2 Experimental Approach and Technique. A flow chart outlining the preparation of the thick film is shown in Figure 8. Reagent-grade (purity 99.9%) component oxides in their respective mole ratios were mixed for 24 hours in a crucible including alumina media and alcohol. The resulting slurry was dried at 150°C and calcined at various temperatures for 3 hours to obtain the single-phase. The calcined powders were ball-milled again in an organic binder solution for 24 hours. The amount of binder and solvent was adjusted by viscosity of the mixed slurry. The binder contains polyvinyl butyral (PVB) polymer, a plasticizer, a surfactant, and an ethanol+toluene solvent. Samples were prepared by casting the slurry using a scalpel. The thick films were formed on silicone coated mylar sheets for easy peel-off. The process of drying the films was followed by a binder removal procedure: heating up to 500°C for 3 hours and holding at 500°C for 2.4 hours. Then, the thick films were sintered at various temperatures ranging from 1200°C to 1500°C.

3.4.3 Moonie Actuator. The composite actuators consist of piezoelectric ceramics and brass-end caps. A shallow cavity, as shown in Figure 7, was made in the center of the brass cap. The brass-end caps were attached to the piezoelectric ceramic using silver paste. Special care was taken not to fill up the cavity, or short circuit the ceramic electrodes. The stacked composite was heated at 150°C under stress to solidify the bond. An epoxy resin was pasted around the circumference to encapsulate the actuator.

Because the polarization inside the ceramics is randomly oriented, the piezoelectric ceramics do not exhibit their piezoelectric properties until a high DC voltage is applied to the sample. The polarization is forced to be aligned in the direction of the applied DC voltage. This process is called poling.

When a sample is poled, an insulating material is needed because of the very high applied voltage (more than 2MV/m). Silicon oil is typically used as the insulating material. By increasing the temperature of the silicon oil bath, the polarization can be more easily switched to the direction of the applied voltage. However, the elevated temperature must be kept below the Curie temperature or the samples lose their piezoelectric properties. In the present experiments, the samples were poled at 3MV/m for 15 min. in a silicon oil bath held at 200°C. The direct piezoelectric coefficient was measured at a frequency of 60 Hz using a d_{33} meter.

4. Results

4.1 Non-Reacting Jets with C0-Flow in a Noisy Enclosure

The turbulent kinetic energy maps of an excited jet with co-flow in a cavity with a partially closed exhaust end are shown in Figure 9 and Figure 10 for cases with and without the imposition of a longitudinal acoustic field, respectively. The results show very little change in the flow field, which implies that any coupling from the longitudinal acoustic field is unable to compete with the perturbation from the actuators. Other explanations could be the protective effect of the co-flow layer or the relatively low sound pressure levels due to the unrestricted co-flow inlet, the absence of a reflective boundary condition at the jet exit (no end plate).

A time-averaged turbulent kinetic energy map of an unexcited jet in a cavity with a closed co-flow inlet and a partially closed exhaust end is shown in Figure 11 while the phase-mean data of the same jet subject to an imposed transverse acoustic field in the same cavity is shown in 12. It is seen that under the imposition of the acoustic field, the shear layer thickness increases and the potential core length decreases.

Similar results can be found in Figure 13 and Figure 14, which are the phase-mean turbulent kinetic energy maps of an excited jet in a cavity with a closed co-flow inlet and a partially closed exhaust end, with and without an imposed transverse acoustic field, respectively. Although the turbulent kinetic energy distribution is affected by the acoustic field both in space and time, the basic flow features resulting from spatial modulation obviously remains unchanged.

The test duct inlet condition became a major focus of these experiments since it strongly influences the response of the jet flow to the imposed acoustic field. The effects of the co-flow and duct exit cross sectional area were also investigated.

The flow visualization images of ducted jet flow for different inlet conditions are shown in Figure 15. When exposed to the acoustic field, the jet seems to expand relatively faster when the co-flow is stabilized by a wall. In comparison, the jet expansion does not change in an obvious manner in the absence of that wall. This result implies that the acoustic boundary conditions near the jet shear layer strongly influence the impact of an imposed acoustic field. The effect of an acoustic field in a combustor on the fuel mixing will therefore depend on the design of the fuel injection region.

The influence of the end nozzle on the coupling between the acoustic field and the developing flow field looks minimal as shown in Figure 15. The reason appears to be that the end nozzle was located at the opposite side of the loudspeakers with respect to the examined jet and thus the existence or not of the end nozzle had only a negligible influence on the sound pressure level near the jet shear layer.

The images of an unexcited jet subject to a imposed transverse acoustic field in the cases of with and without co-flow are shown in Figure 17. Similar to what was found in previous studies, the co-flow tended to attenuate the effect of acoustic field on the jet flow. The small effect may also be attributed to unrestricted co-flow inlet.

4.2 Medium Scale Combustor: University of Arkansas

At this time, the blower is mounted in place and a delivery date for the 25-hp drive motor and variable speed controller has been set. The duct supports, flow straiteners, and flashback arrestor are complete. The pipe sections and miscellaneous components (interconnects, fittings, gaskets, etc.) are on hand. The mixing cone has been received and is ready to be machined and installed.

Installation of a 5 psig natural gas supply line (with non-contract funds) was recently completed. Work is in progress on the remainder of the fuel supply system; the fuel injection ring fabrication is awaiting final results from the fluent analysis. All necessary gas analysis and optical instrumentation is in place.

4.3 High Temperature Piezoelectric Materials

The $Sr_2(Nb_xTa_{1-x})_2O_7$ (x=1.0) ceramics prepared by the chemical coprecipitation method (CCP) were cut along a-axis, b-axis, and c-axis as shown in Figure 18 to investigate the anisotropy in electrical properties. The dielectric properties were measured at a frequency of 10 kHz for a $Sr_2(Nb_xTa_{1-x})_2O_7$ sample sintered at 1500°C. The results of the electrical properties of $Sr_2(Nb_xTa_{1-x})_2O_7$ (x=1.0) ceramics prepared by the CCP method and the conventional method (CON) are summarized in Table 3. The dielectric constant of the a-cut sample is higher than that of the single crystal. The microstructures of the samples cut along the three axes are presented in Figure 19. The orientation of grains can be clearly observed in the a-cut and b-cut samples, whereas the grains in the c-cut sample seem to be randomly oriented.

Dielectric constants of $Sr_2(Nb_xTa_{1-x})_2O_7$ ceramics were plotted as a function of temperature as shown in Figure 20. The Curie temperature increased with the composition, x. Relative permitivity at Curie temperature and grain orientation are shown in Figure 21. The value of grain orientation is proportional to the composition.

The d_{33} coefficient expresses the ratio of the strain developed in a piezoelectric ceramic to the applied field: $\varepsilon_{ij} = d_{ijk}E_k$, where ε_{ij}, d_{ijk}, and E_k represent mechanical strain, piezoelectric coefficient effect, and electric field, respectively. It is also related to the ratio of the voltage developed by a ceramic for an applied stress. As such, it determines the "sending" and "receiving" characteristics of a ceramic, and is one of the most important coefficients to know when evaluating piezoelectric materials. The d_{33} coefficients were measured at room temperature for $Sr_2(Nb_xTa_{1-x})_2O_7$ ceramics, and were plotted as a function of composition, x, in Figure 22. The $Sr_2(Nb_xTa_{1-x})_2O_7$ ceramics (x=0.2 and 0.4) with relatively low Curie-temperatures showed larger d_{33} values than the ceramics with the compositions x=0.8 and 1.0. The value of d_{33} coefficient is inversely proportional to the composition. It has to be stressed again that the d_{33} values were measured at room temperature. They are expected to increase by close to 100 at higher temperatures.

The d_{33} piezoelectric coefficient was measured by using a d_{33} meter on various samples: the bulk ceramics prepared by conventional method (CON), molten salt method (MSS), and chemical coprecipitation method (CCP), and the thick films. Generally, the d_{33} value of the thick films is higher than that of the bulk samples. Among the bulk ceramics, the sample prepared by the CCP method exhibited a little larger d_{33} coefficient than the sample prepared by CON and MSS methods.

Moonie structure actuators were fabricated by using $Sr_2(Nb_xTa_{1-x})_2O_7$ (x=1.0) ceramics prepared by MSS method, and their piezoelectric coefficients were measured, again at room temperature. The value of the d_{33} coefficient increased from 1.4 pC/N to 1.9 pC/N by using the Moonie-structure design. The Moonie structure actuator improves the d_{33} coefficient by adding the d_{31} coefficient to the d_{33} coefficient. When an electric field is applied to a sample, the piezoelectric ceramic extends longitudinally through d_{33}, and contracts transversely through d_{31}. In the Moonie structure actuator, the radial motion of the ceramic is transformed to the flextensional motion of the brass caps. Therefore, the axial displacement comes from two different sources. One is the longitudinal displacement of the ceramic itself through d_{33}, and the other is the flextensional motion of the metal arising from the transverse contraction through d_{31}. The two contributions add together to give overall larger displacements.

5. Activities Planned for Year 3

5.1 Flow Control Area

After the proven success of spatial mode excitation of free and enclosed jets the realization of these methods in practical devices has to be considered. The practical realization of piezoceramic-based jet flow actuation has to overcome two hurdles, one the proof or reliability of moving/vibrating parts, and the availability of appropriate materials. The second part has been addressed through the development of high curie temperature piezoceramic materials discussed in section 3.4.

For practical reasons industry will be skeptical of mixing control relying on moving parts, even if it is the only scheme offering real control. For this reason a compromise solution will be sought during the coming period. The solution will be based on two approaches.

1) Combine passive mixing regulation with a minimum of active elements.
2) Develop an active mixing control system where the number of actuators is minimized.

Both approaches will be tested on experimental hardware which has already been set up in the Reacting Flow Lab at Virginia Tech. Both schemes will be developed and tested for open/free and enclosed/ducted jets, including the subjection to a noisy environment.

5.2 Neural Network Controller for Optimization of Air/Fuel Mixing

Once the jet is modeled correctly, a second neural network can be implemented to serve as a controller which adaptively optimizes air/fuel mixing. In addition to the ANN control algorithm, the proposed control system also includes actuators, sensors and actuation techniques developed at Virginia Tech. The loudspeakers and/or piezoelectric materials will serve as the actuators, and optical techniques will be employed as the sensors in order to feed-back the effectiveness of a particular actuation scheme on the mixing process. Using flow visualization will allow fast, quantitative analysis of two and three-dimensional iso-concentration contours in the flow field.

5.3 Combustion

At the University of Arkansas, the Fluent model results for the fuel injection and mixing section will be incorporated into the final fuel injector design. Machining of the fuel injector and mixer will be completed. The blower motor and speed controller, all remaining ductwork, and fuel supply lines will be installed and instrumented. Combustor design will be finalized and fabrication started. Initial hot testing with a generic, non-actuated combustor will be conducted to validate the operation of the air supply, fuel supply, and instrumentation.

New actuator materials will be tested in the combustor in early 1996. The setup will be one of an actuated bluff body stabilizer for lean, premixed, combustion.

5.4 Work in the Materials Area

The future work in materials development will focus on improving d_{33} coefficients of bulk ceramics and thick films. Large piezoelectric coefficient will be obtained by fabricating more dense and compositional homogeneous samples, increasing the temperature of oil bath, and applying higher electrical voltage. The following tasks will be carried out:

- fabricate thick films as a function of composition x,
- apply Moonie-structure design to the thick film,
- measure d_{33} coefficient at higher temperature,
- test several actuator geometries in high temperature environments at Virginia Tech and the University of Arkansas.

6. References

Gutmark , E., Parr, T.P., Parr, D.M., Schadow, K.C.,"Evolution of vortical structures in flames," Twenty-Second Symposium (International) on Combustion, 1988, p. 523-529.

Vandsburger, U., and Ding, C., "Spatial modulation of a forced triangular jet", Experiments in Fluids v 18 n 4 Feb 1995. p239-247.

7. Acknowledgement

The authors would like to acknowledge the continuous support of the SCERD staff, in particular Mr. Dan Fant and Larry Golan. Special thanks for enabling one of the students, S. D. Lepera, to spend a summer internship at Allison Turbine in 1995.

Table 1. The structural and electrical properties of $Pb(Zr_xTi_{1-x})O_3$ and $Sr_2(Nb_xTa_{1-x})_2O_7$.

	$Pb(Zr_xTi_{1-x})O_3$	$Sr_2(Nb_xTa_{1-x})_2O_7$
Structure family	Perovskite	Pyroniobate
Dielectric constant at room temperature	High	Low
Piezoelectric constant at room temperature	High	Low
Curie temperature	Low (≈ 300°C)	High (≈ 1400°C)

Table. 2. Types of piezoelectric actuators and their characteristics.

	Advantages	Disadvantages
Multilayer actuator	Low driving voltage Quick response High generative force	Low displacement
Bimorph actuator	Large displacement	Slow response Low generative force
Moonie-structure actuator	Sizable force and displacement	

Table 3. Electrical properties of $Sr_2(Nb_xTa_{1-x})_2O_7$ (x=1.0) sample sintered at 1500°C.

Method	**Sample**	**Dielectric constant,ε (10 kHz)**	**Dielectric loss, tanδ (10 kHz)**
CCP	a-cut	86 (75*)	0.0077
	b-cut	44 (46*)	0.0102
	c-cut	35 (43*)	0.0047
	disk type	49	0.0291
CON	disk type	52	0.0684

* indicates data from *Ferroelectric Properties of* $Sr_2Nb_2O_7$ *Single Crystal*

Table 4. d_{33} coefficients of $Sr_2(Nb_xTa_{1-x})_2O_7$ (x=1.0) ceramics and thick films at room temperature.

samples	method	d33 coefficient (pC/N)
Bulk ceramics	CON	1.0
	MSS	1.4
	CCP	1.7
Thick film		2.0

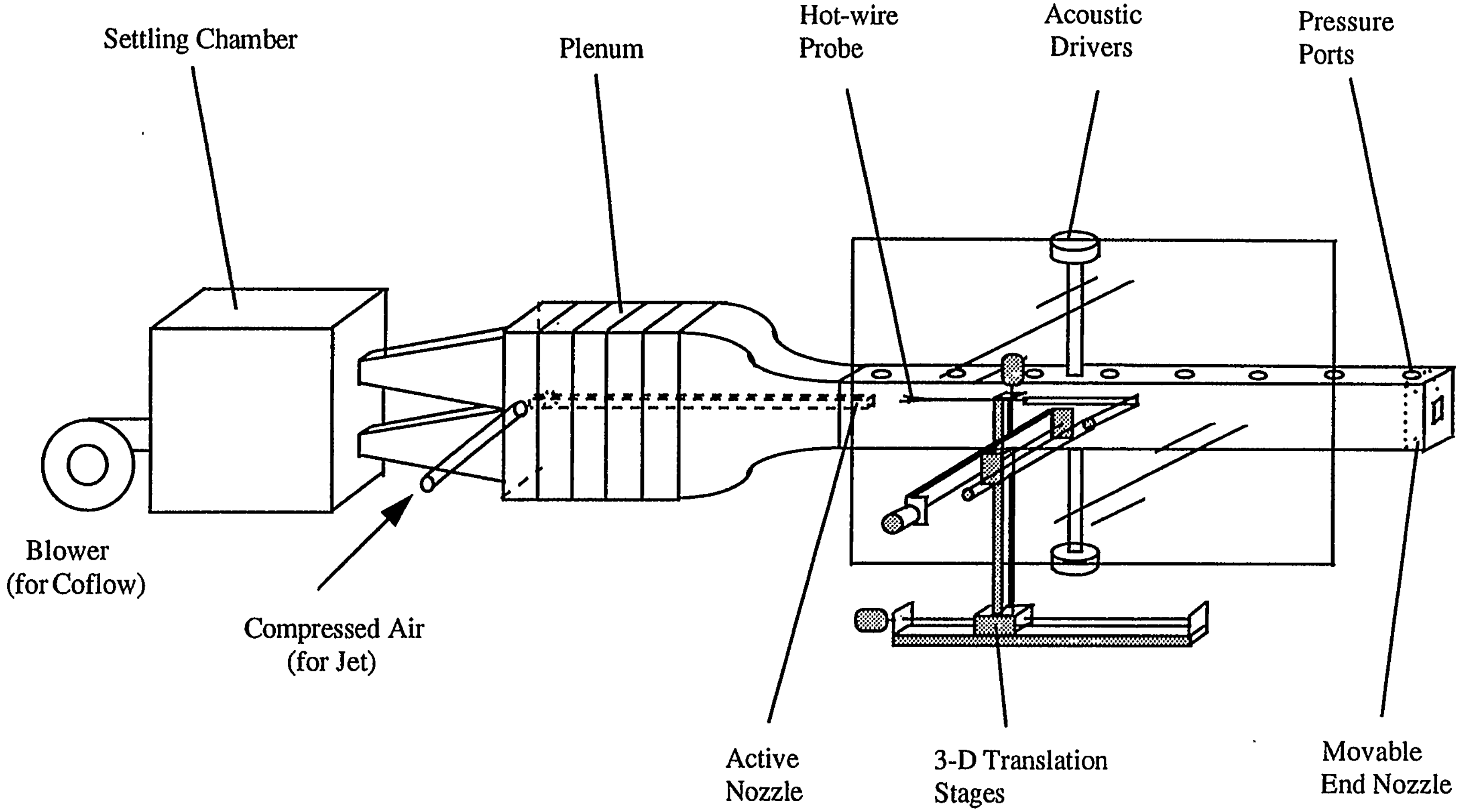

Figure 1. System setup for hot wire measurement

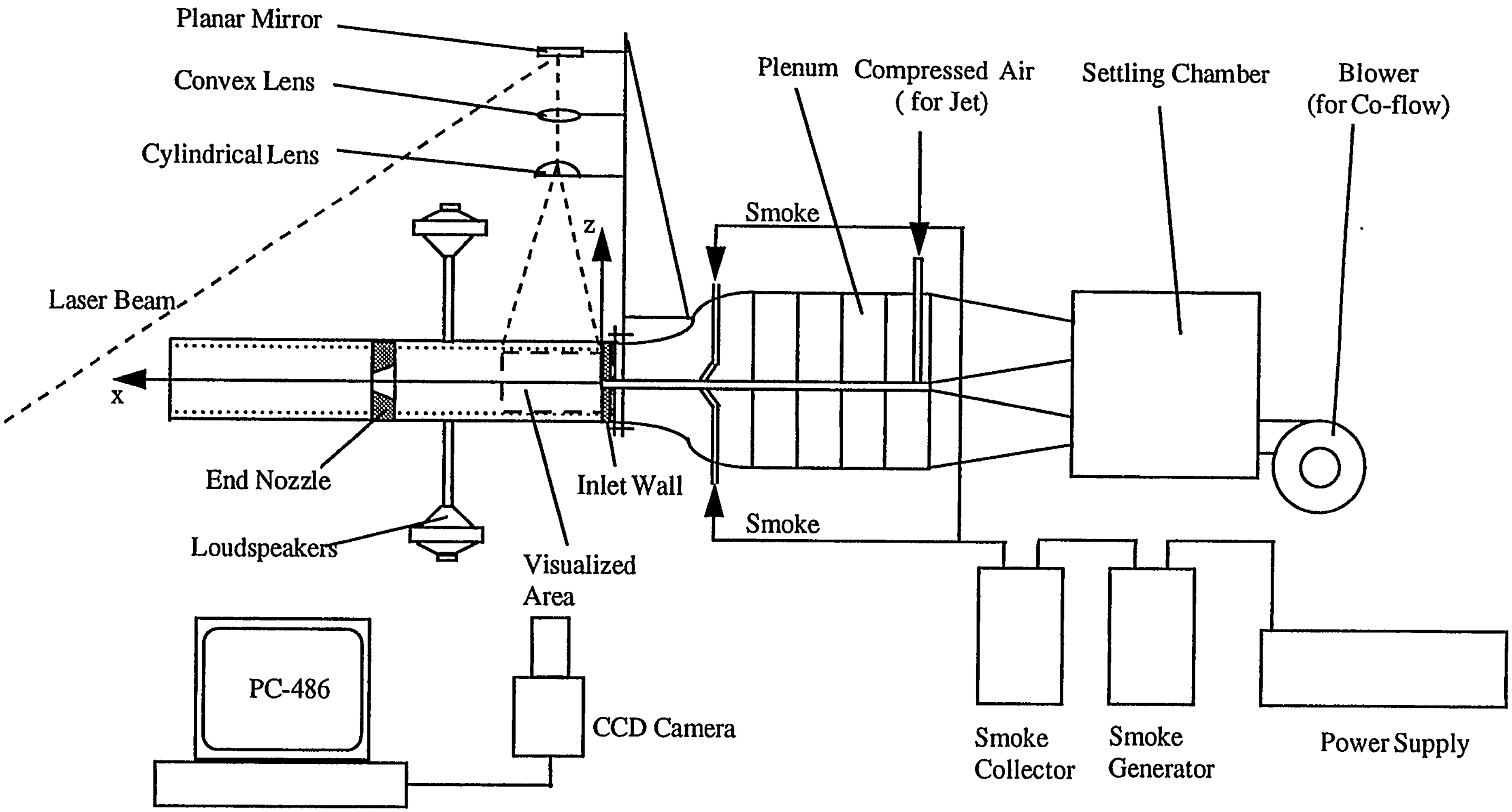

Figure 2. System setup for flow visualization

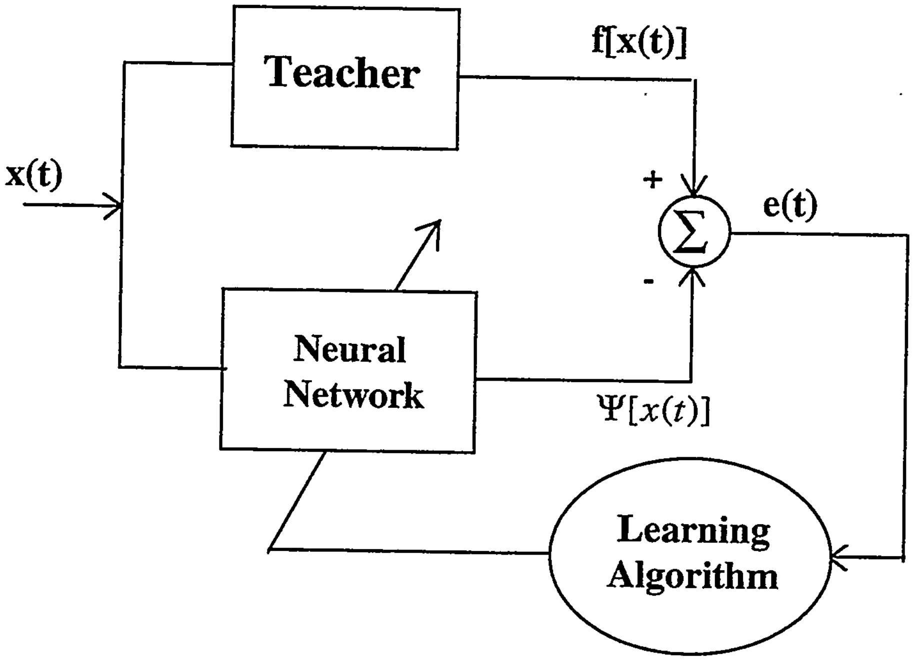

Figure 3. Modeling a system with Neural Networks

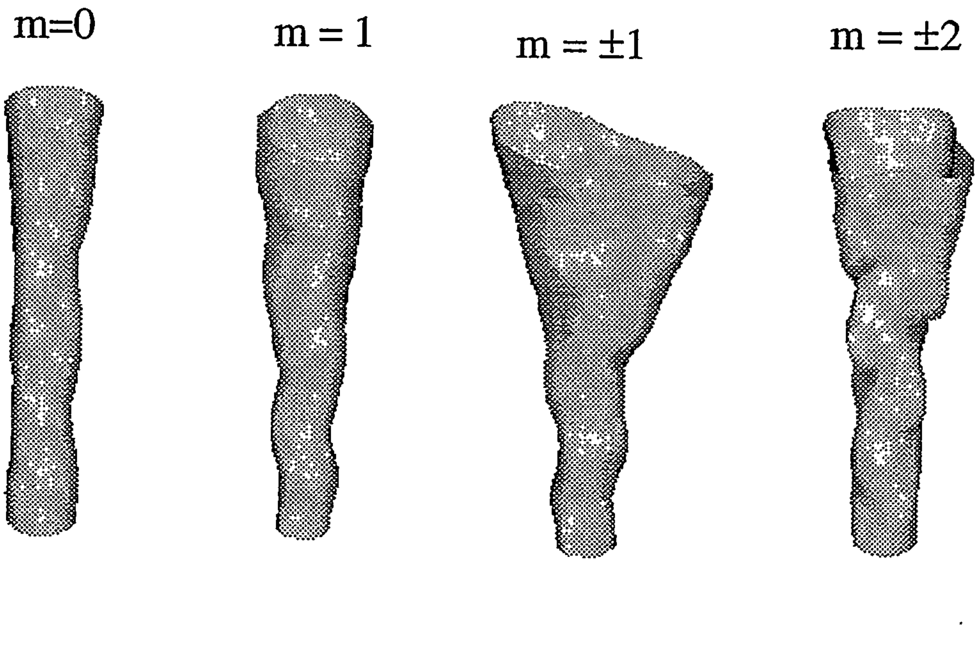

Figure 4. Iso-Velocity Contours of a Jet Undergoing Spatial Mode Manipulation

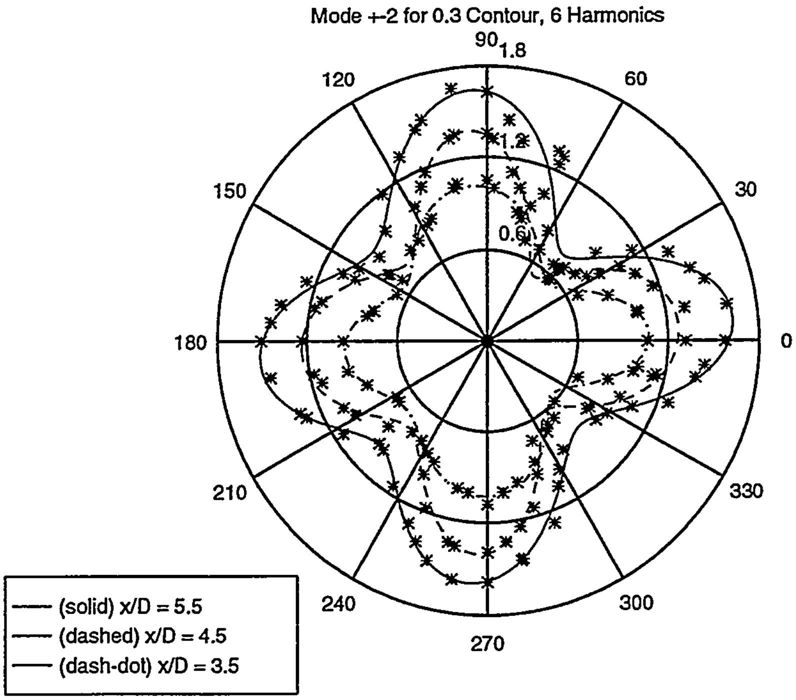

Figure 5. Approximation of velocity profiles for different distances (x/D) downstream of the jet exit

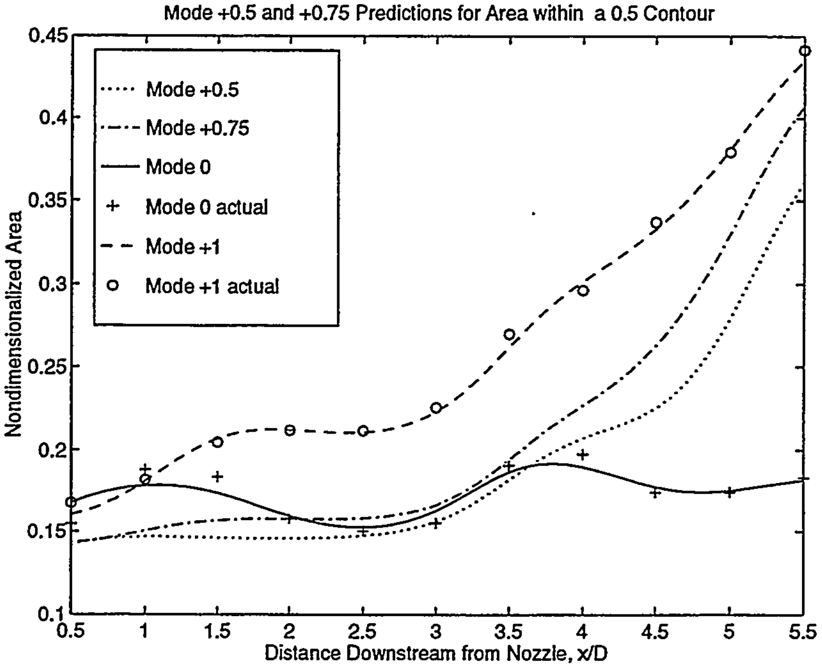

Figure 6. ANN Predictions for Jet Spreading Rates

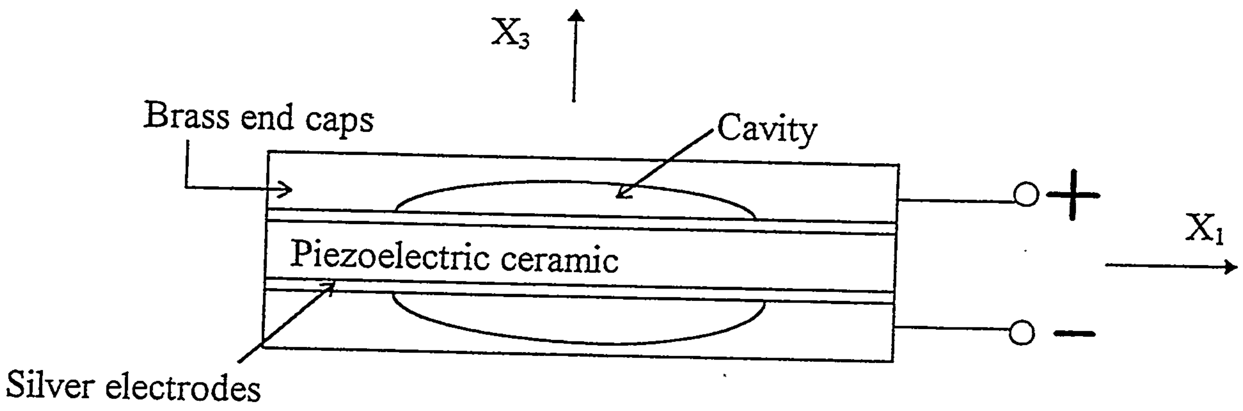

Figure 7. Design of Moonie structure actuator

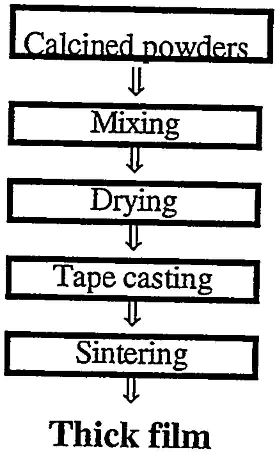

Figure 8. Schematic outline of tape-casting method for synthesizing piezoelectric thick film

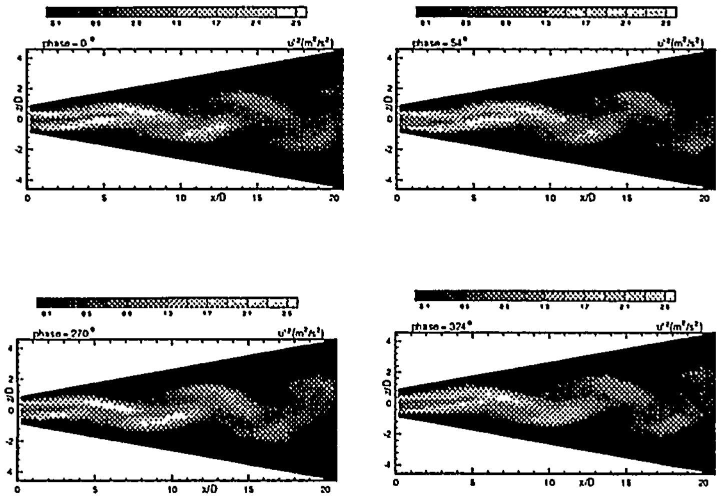

Figure 9. Phase-mean turbulent kinetic energy map of an excited jet with co-flow in a cavity with a partially closed exhaust end.
U_j = 15 m/s, U_{coflow} = 3 m/s
Jet excitation mode = +-1

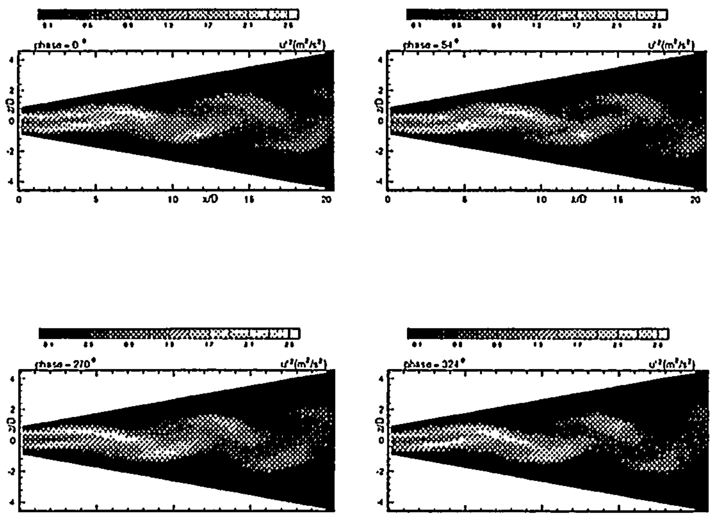

Figure 10. Phase-mean turbulent kinetic energy map of an excited jet with co-flow subject to imposed acoustic field in a cavity with a parially closed exhaust end
U_j = 15 m/s, U_{coflow} = 3 m/s
Jet excitation mode = +-1
Acoustic disturbance: first longitudinal resonance, f = 210 Hz
SPL = 105 dB at antinode

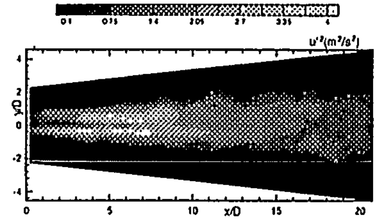

Figure 11. Time-mean turbulent kinetic energy map
unexcited jet
closed co-flow inlet
partially closed outlet
U_{jet} = 15 m/s

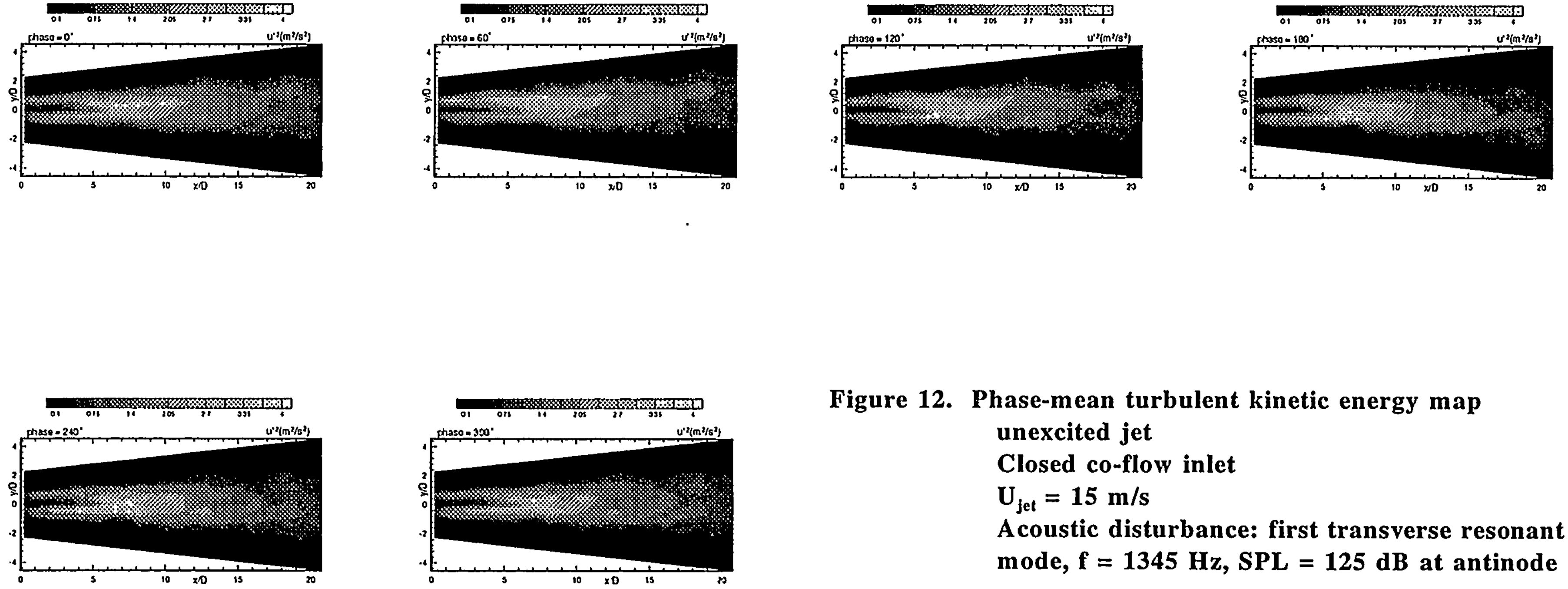

Figure 12. Phase-mean turbulent kinetic energy map
unexcited jet
Closed co-flow inlet
U_{jet} = 15 m/s
Acoustic disturbance: first transverse resonant
mode, f = 1345 Hz, SPL = 125 dB at antinode

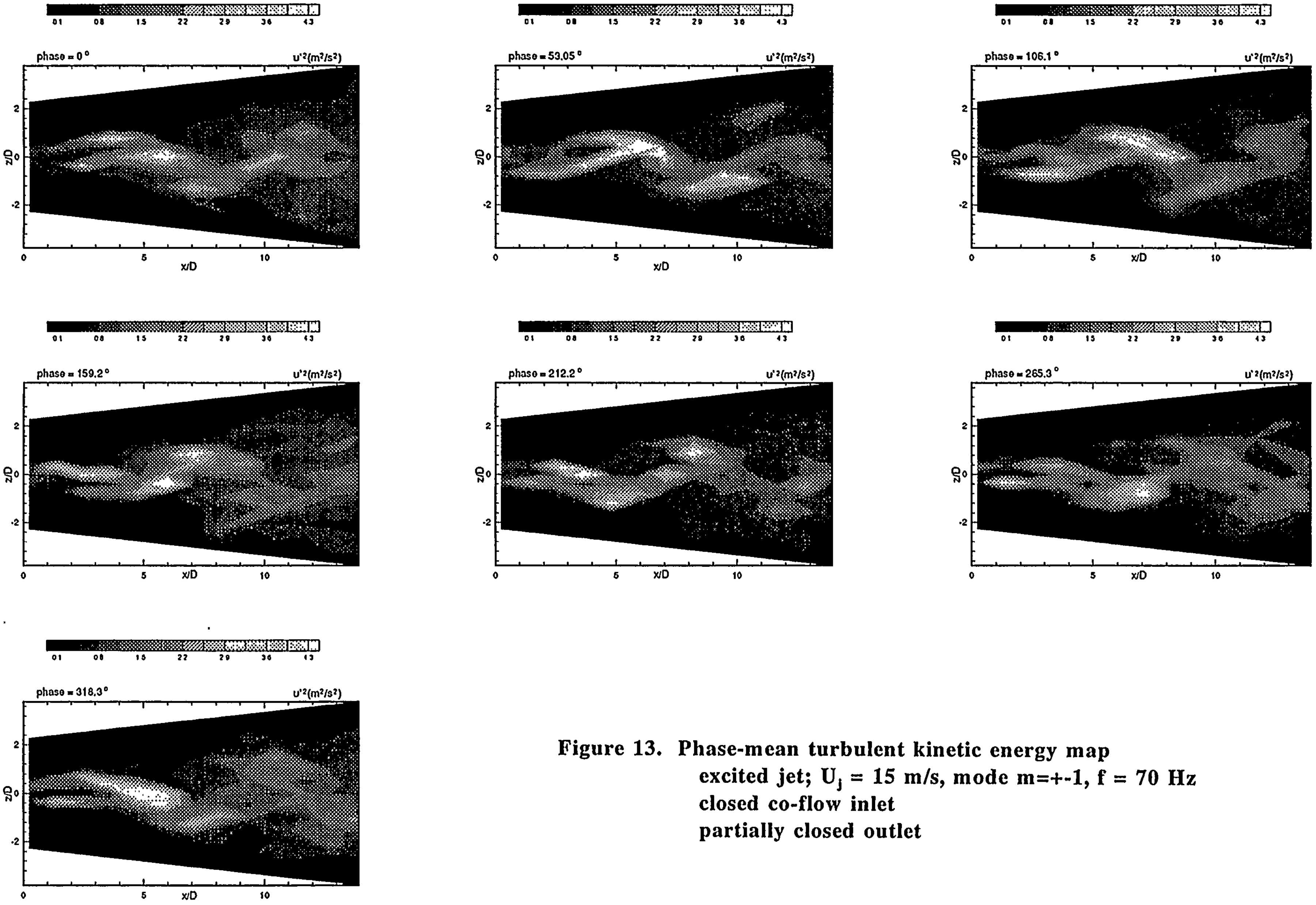

Figure 13. Phase-mean turbulent kinetic energy map
excited jet; U_j = 15 m/s, mode m=+-1, f = 70 Hz
closed co-flow inlet
partially closed outlet

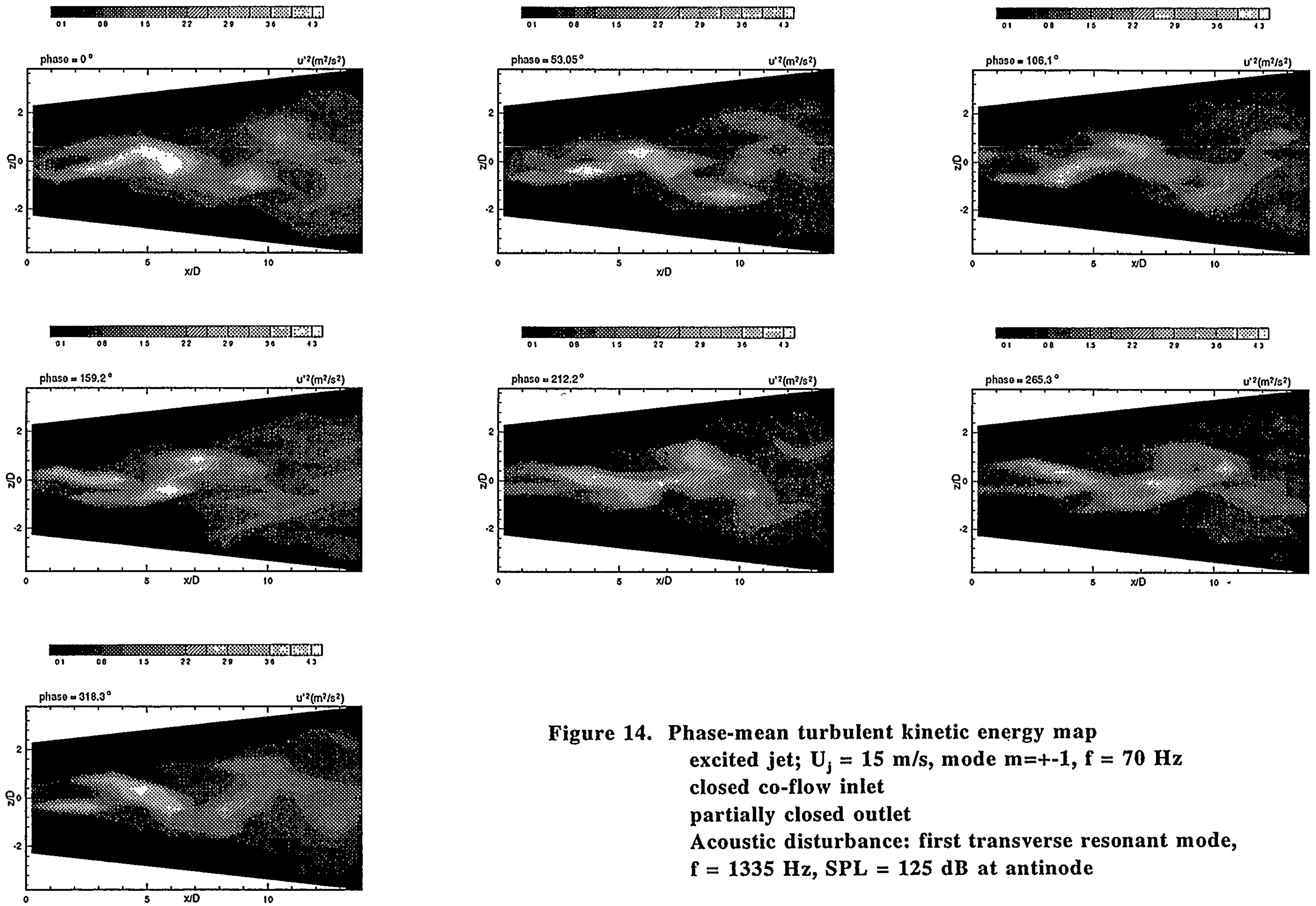

Figure 14. Phase-mean turbulent kinetic energy map
excited jet; U_j = 15 m/s, mode m=+-1, f = 70 Hz
closed co-flow inlet
partially closed outlet
Acoustic disturbance: first transverse resonant mode,
f = 1335 Hz, SPL = 125 dB at antinode

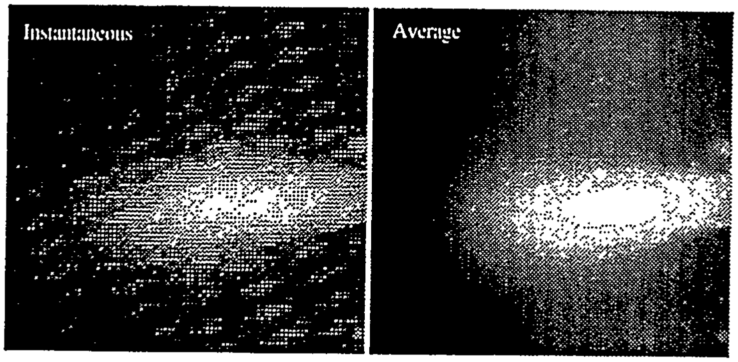

(a). No imposed acoustic field

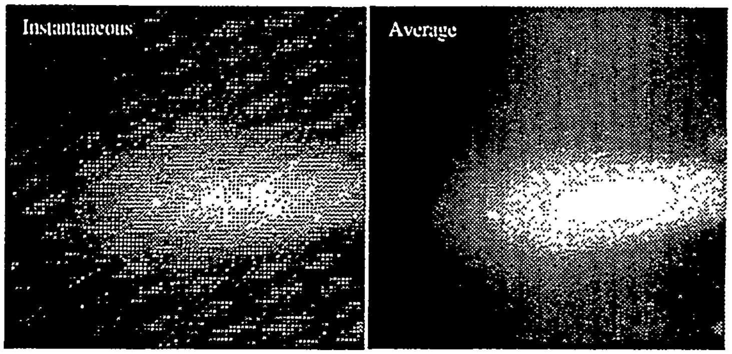

(b). With imposed acoustic field

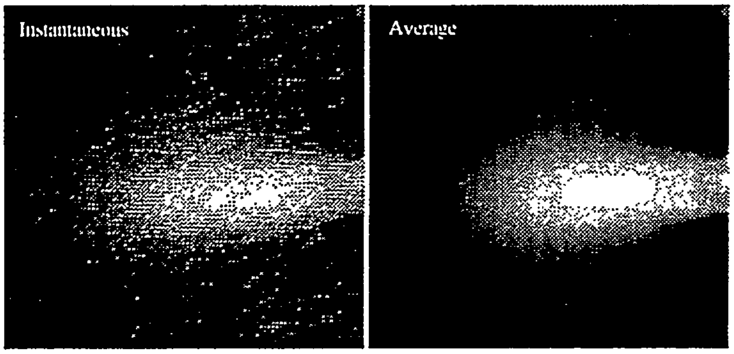

(c). No imposed acoustic field

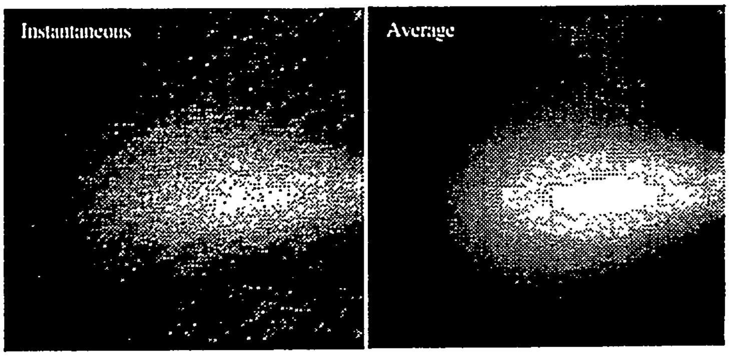

(d). With imposed acoustic field

Figure 15. Jet into cavity with partially closed exhaust end with no co-flow
(a), (b) With unrestricted co-flow inlet
(c), (d) With closed co-flow inlet

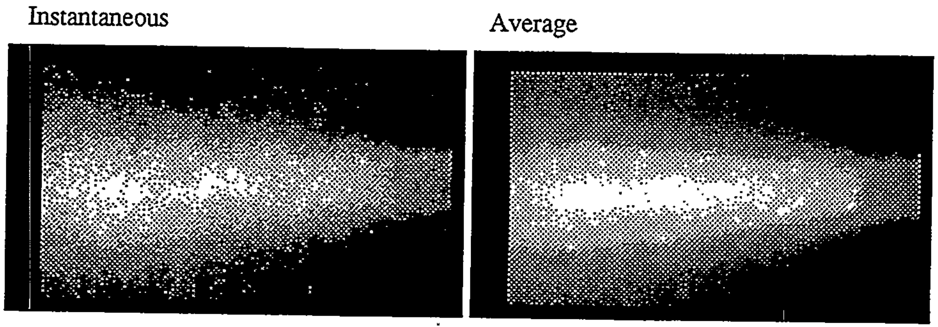

(a) No imposed acoustic field

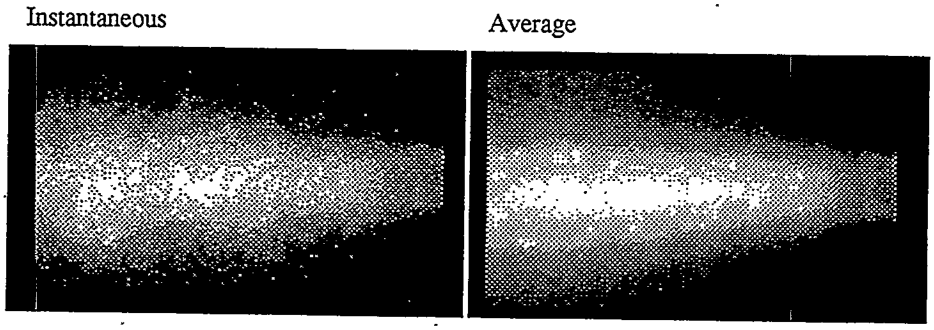

(b) With imposed acoustic field

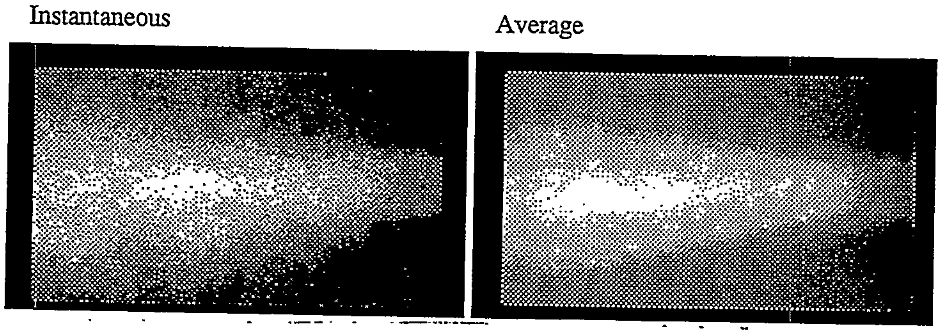

(c) No imposed acoustic field

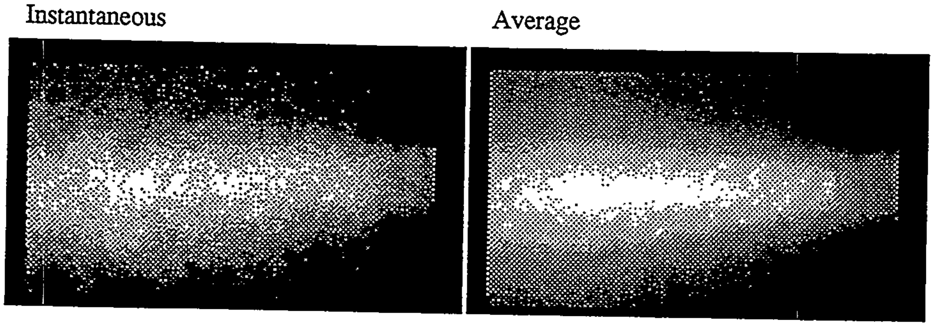

(d) With imposed acoustic field

Figure 16. Jet into cavity with unrestricted co-flow inlet with no co-flow
(a), (b) With no end nozzle
(c), (d) With end nozzle

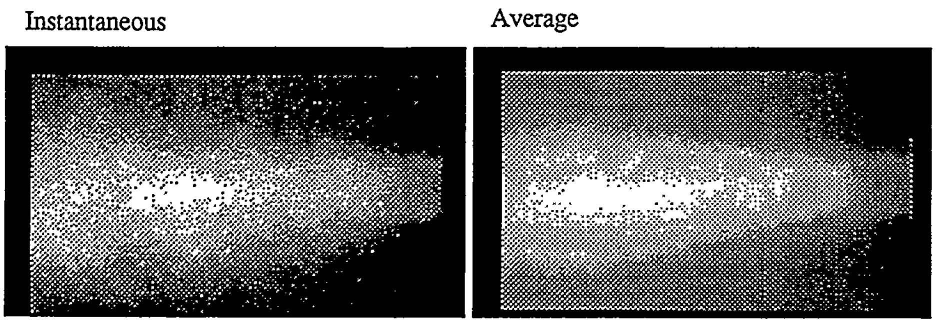

(a). No imposed acoustic field

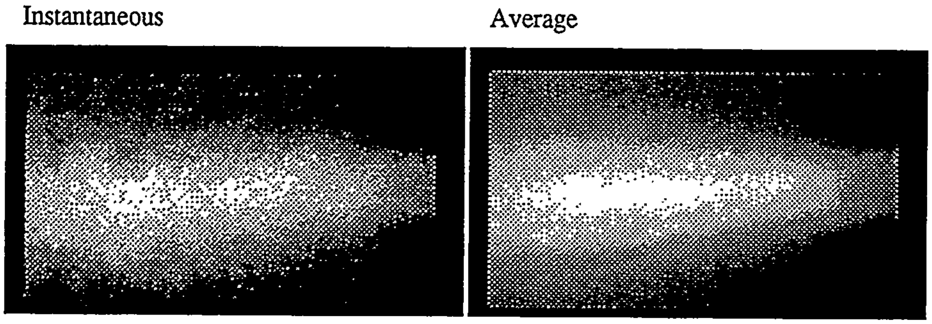

(b). With imposed acoustic field

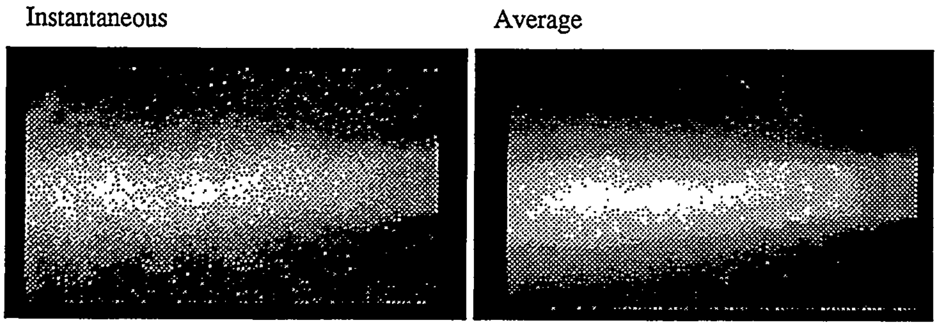

(c). No imposed acoustic field

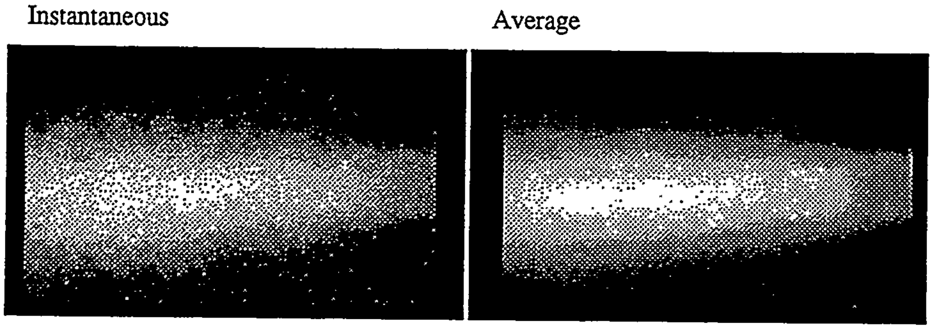

(d). With imposed acoustic field

Figure 17. Jet into cavity with unrestricted co-flow inlet with end nozzle
(a), (b) With no co-flow
(c), (d) With co-flow

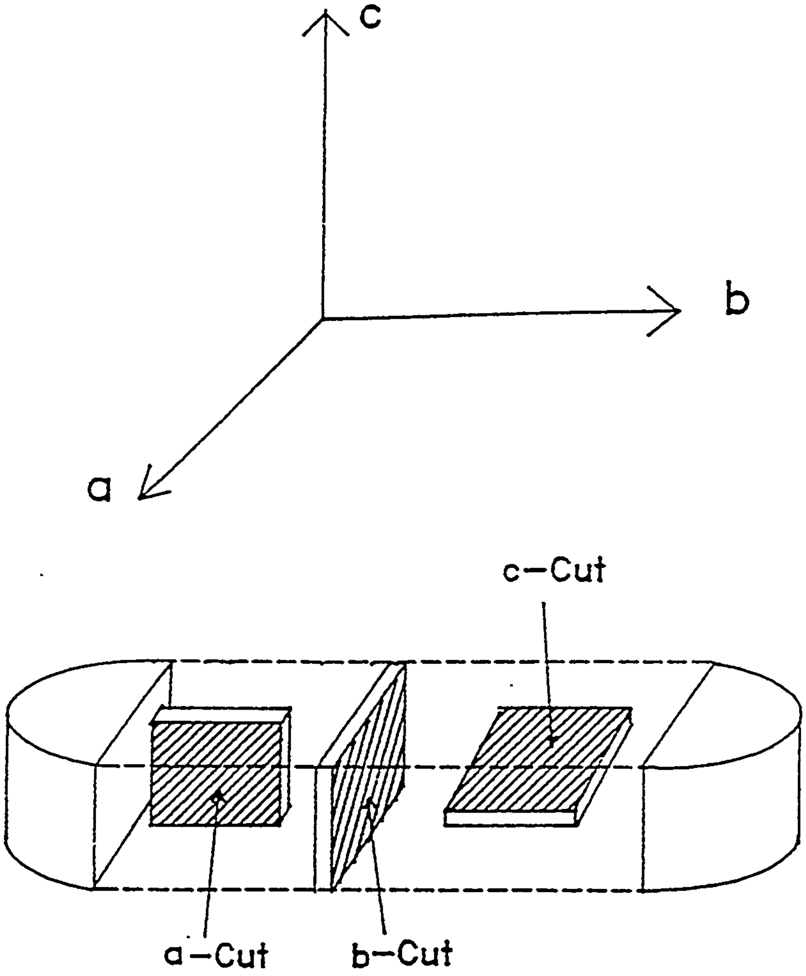

Figure 18. Cutting of grain oriented $Sr_2(Nb_xTa_{1-x})_2O_7$ ceramics (x = 1.0) fabricated by chemical coprecipitation method

a-cut

b-cut

c-cut

Figure 19. SEM micrographs for sintered $Sr_2(Nb_xTa_{1-x})_2O_7$ ceramics (x = 1.0) cut along a-axis, b-axis, c-axis

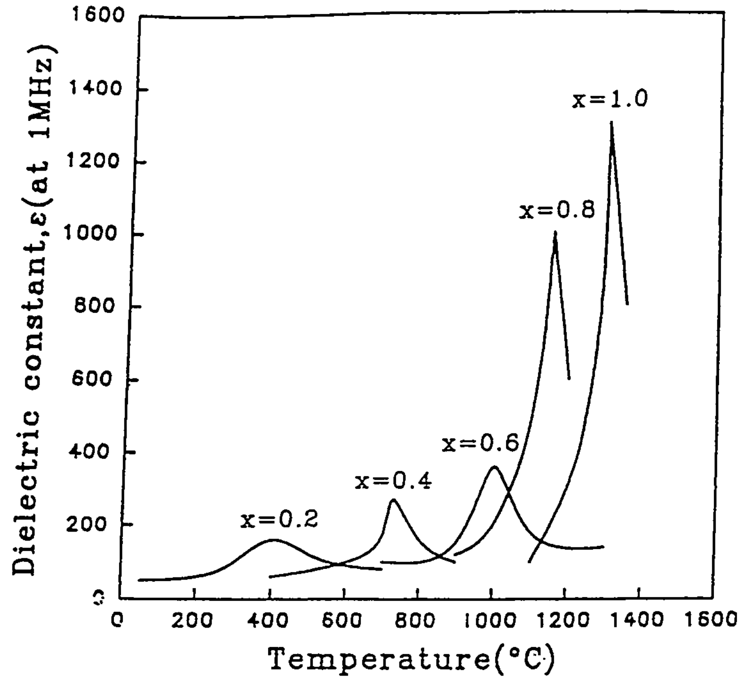

Figure 20. Temperature dependence of dielectric constant for $Sr_2(Nb_xTa_{1-x})_2O_7$ ceramics sintered at 1500 °C

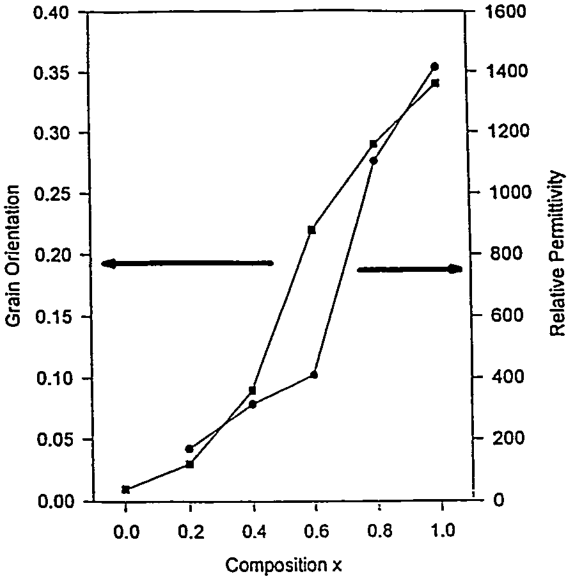

Figure 21. Relative permittivity at Curie temperature and grain orientation vs. composition x for $Sr_2(Nb_xTa_{1-x})_2O_7$ ceramics

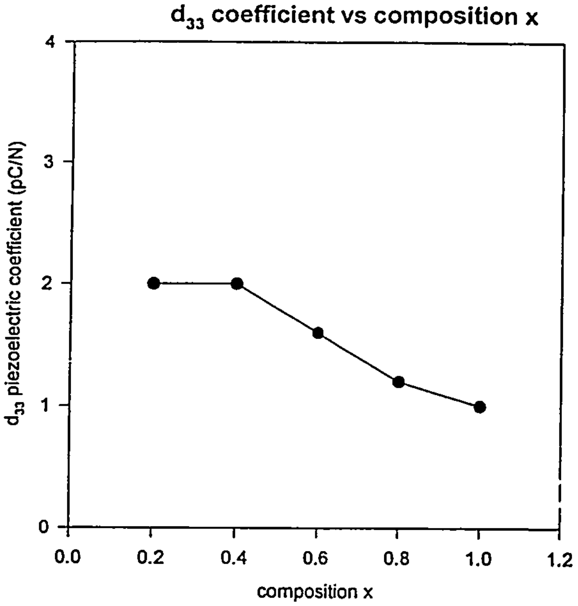

Figure 22. Compositional dependence of the d33 coefficient for $Sr_2(Nb_xTa_{1-x})_2O_7$ ceramics sintered at 1500 °C

P8 Combustion Modeling in Advanced Gas Turbine Systems

L. Douglas Smoot (lds@byu.edu; 801-378-8930)
Paul O. Hedman (hedman@byu.edu; 801-378-6238)
Thomas H. Fletcher (tom@harvey.et.byu.edu; 801-378-6236)
B. Scott Brewster (brewster@guitar.et.byu.edu; 801-378-6240)
Stephen K. Kramer (kramer@bones.et.byu.edu; 801-378-4548)
Advanced Combustion Engineering Research Center
45 Crabtree Building, Brigham Young University
Provo, UT 84602

Introduction

The goal of the U.S. Department of Energy's Advanced Turbine Systems (ATS) program is to help develop and commercialize ultra-high efficiency, environmentally superior, and cost competitive gas turbine systems for base-load applications in the utility, independent power producer, and industrial markets. Combustion modeling, including emission characteristics, has been identified as a needed, high-priority technology by key professionals in the gas turbine industry.

Objective

The primary objective of the four year ATS program at this center is to develop a comprehensive combustion model for advanced gas turbine combustion systems using natural gas fuel with consideration of coal gasification or biomass fuels.

Approach

Three tasks have been undertaken to achieve the overall objective of this program. The first task is to improve and validate various submodels needed to accurately predict various aspects of the gas turbine combustion process. Of particular emphasis are submodels for predicting carbon monoxide and nitrogen oxides, particularly at the higher temperatures and pressures proposed for advanced turbine systems. Ongoing improvements in existing submodels such as turbulence, finite-rate chemistry, and pollutant emissions are also being considered for addition to the 3-D code. These submodels will be validated by data obtained with advanced diagnostic systems from the LSGTC.

The second task is to refine the BYU/ACERC 3-D code (PCGC-3) for application to gas turbine combustors and implement proven submodels into the gas turbine model. Refinements and submodels will also be available for incorporation into other prominent computational fluid dynamics (CFD) platforms such as those from Fluent, a commercial developer of CFD codes.

The third task is to interact extensively with industrial and university organizations with strong gas turbine interest. An ACERC/ATS technical advisory committee (TAC) composed of prominent industrial organizations with specific interest in utility and industrial gas turbine manufacture and application has been formed. The TAC provides direction and support of this research program. Concerns particular to the industry are being addressed, and results will be provided to participating industrial members.

Research sponsored by the U.S. Department of Energy's Morgantown Energy Technology Center, under cooperative agreement No. DE-FC21-92MC29061 with South Carolina Energy Research and Development Center, 386-2 College Avenue, Clemson University, Clemson, SC 29634-5181; telefax: 803-656-1429, subcontract 93-01-SR014 with Advanced Combustion Engineering Research Center, Brigham Young University, 45 CTB, BYU, Provo, UT 84602; telefax: 801-378-3831.

Results

Key accomplishments of the past year are described below.

Task 1 - Submodel Development

The first task is to improve and validate various submodels needed to accurately predict various aspects of the gas turbine combustion process.

1.1 - Code Evaluation. The objective of this subtask was to evaluate the existing PCGC-3 code by comparing model results to local measurements from the BYU/ACERC laboratory-scale gas turbine combustor (LSGTC). Variables of interest included local gas velocities and temperatures. Key model needs were identified through this effort. Work on this subtask was completed during the first year of the study.

1.2 - Fundamental Experiments. The objective of this subtask is to conduct key experiments in the LSGTC to provide needed data for PCGC-3 and submodel evaluation. Measurements include: 1) gas temperatures and concentrations of CO, CO_2, O_2, and N_2 using coherent anti-Stokes Raman spectroscopy (CARS), 2) velocity components using laser Doppler anemometry (LDA), 3) presence of OH, CH, CO, NO, NO_2 and possibly N_2O using planar, laser-induced fluorescence (PLIF), and 4) flame and flow structure using digitized images from film or video cameras.

Dual-Stokes CARS Measurements. The dual-Stokes CARS system which is designed to simultaneously measure near-instantaneous concentrations of CO, CO_2, N_2, and O_2, was reduced in size to accommodate the setup of other laser-based diagnostic techniques. The CARS optical system has been optimized and a full gas temperature map of the LSGTC was measured. Example spectra at two locations are presented in Figure 1.

Figure 1a is near the burner exit ($z = 1.0$ cm, $r = 0.9$ cm) and has an estimated mean temperature of 800 K. The mean spectrum at this location shows that small amounts of O_2 are present along with CO_2. At this location at the onset of the reaction zone, unburned fuel and products will co-exist. Five centimeters further along the reaction zone, the smaller O_2 signal and a relatively larger CO_2 signal indicate the progress of the reaction (Figure 1b, $z = 6.0$ cm and $r = 3.3$ cm). The mean temperature for this location is approximately 1400 K.

A program (CARS.F) was obtained from Sandia National Laboratories in order to extract temperature and specie concentrations from these spectra. However, this program only reduces one spectrum at a time. Accurate representation of the statistical properties of the turbulent flame being studied used five hundred laser shots from each location. Therefore, an additional program was written and linked to CARS.F to extract and reduce single laser shots sequentially obtained from the file containing all five hundred. This shell program also subtracts out the background signal and normalizes the spectrum against the non-resident signal. The shell program was validated with signals obtained in known temperature environments. Problems that have been found with the manner the Sandia CARS.F program handles data are being resolved.

LDA Measurements. Laser Doppler Anemometry measurements of axial, radial, and tangential velocities were obtained on the LSGTC for an air flow of 500 slpm at $\phi = 1.1$, $\phi = 1.0$, $\phi = 0.8$, and $\phi = 0.65$ with the medium swirl (MS) configuration. Recirculation zones were identified as well as other flow features. Mean flow velocities and root-mean-square velocities were determined.

Figure 2 presents some example velocity PDFs generated from the LDA data obtained during this study. These PDFs are important to code development and verification. Currently, PCGC-3 assumes a scalar PDF shape, such as Gaussian, for the entire flow field. Figure 2 shows velocity PDFs for the ATS-MS burner at $\phi = 0.65$. The PDFs presented in this figure were calculated from velocity measurements taken at an axial location of 5 mm above the injector and at radial locations of 12 mm, 15 mm and 18 mm. Each column of axial, radial and tangential velocity PDFs corresponds to the

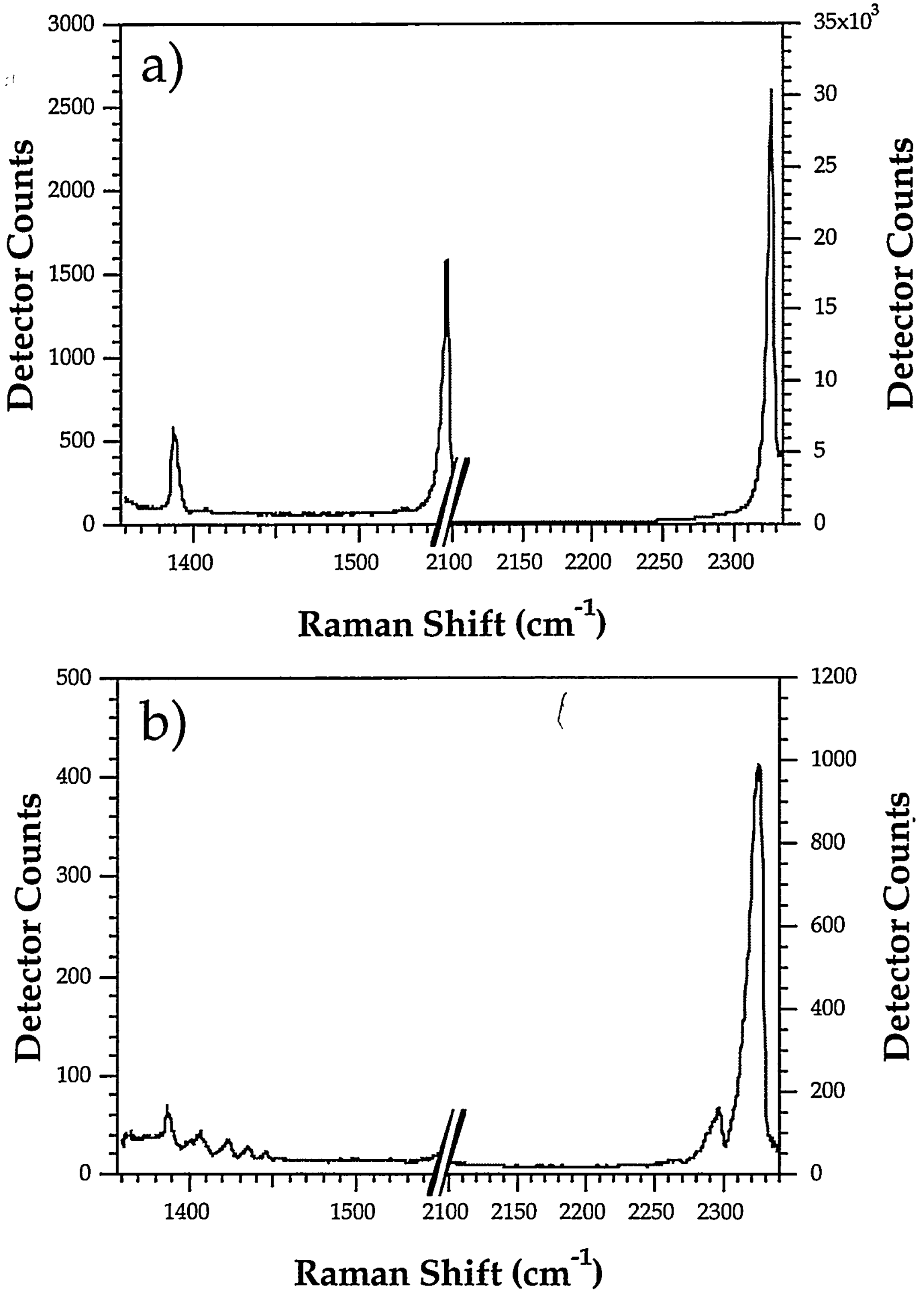

Figure 1. Sample averaged spectra in the LSGTC at a) z= 1.0 cm, r = 0.9 cm and b) z = 6.0 cm and r = 3.3 cm.

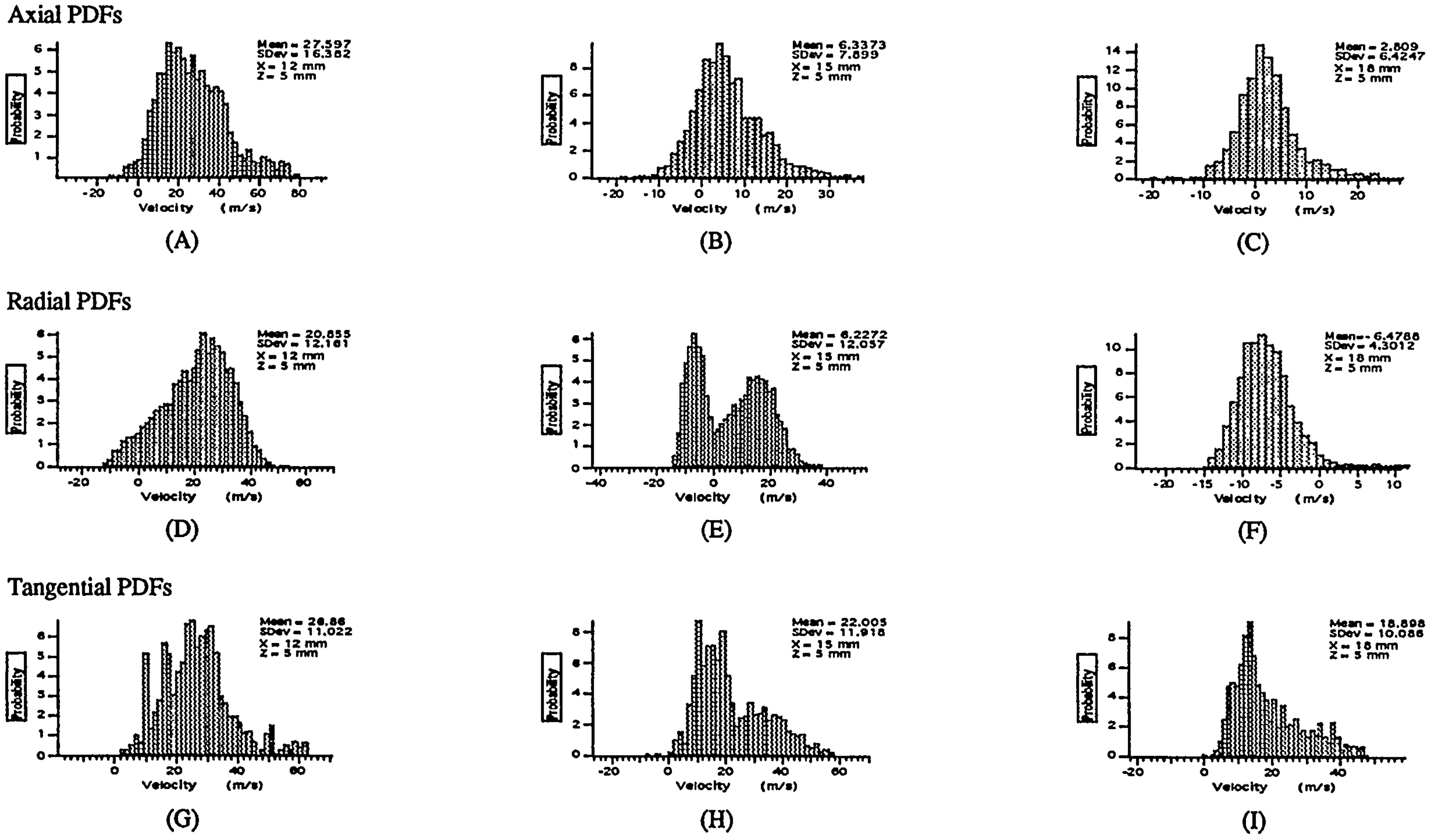

Figure 2. Axial, radial and tangential velocity pdfs at radial locations of 12 mm, 15 mm, and 18 mm, and an axial location of 5 mm downstream of the injector. ATS-MS burner, premixed natural gas/air, air flow rate of 500 slpm, $\phi = 0.65$.

same radial location in the burner. The axial velocity distribution, Figures 2A-2C, remained fairly Gaussian as one moved from inside the vortex, through the shear zone and into the surrounding outside gases. The large decrease in mean velocity caused by momentum dissipation in the shear zone is readily observed. The radial velocity PDFs, Figures 2D-2F, show the interaction of the gases forced out by the vortex and those being recirculated in the lower corners of the combustor. Figure 2E, which shows the velocity PDF at the shear layer, has a bimodal distribution with one peak occurring near the radial velocity value inside the vortex, and the other peak being near the velocity value found in the recirculation zone. The tangential velocity PDFs , Figures 2G-2I, show a similar trend to the radial velocity PDFs . The velocity PDF in the shear zone, Figure 2H, has a bimodal distribution with peaks near the tangential velocity values measured to either side of the shear zone.

Figure 3 shows an example of an axial-radial $\overline{u'v'}$ and axial-tangential $\overline{u'w'}$ Reynolds stress contour map of the ATS-MS burner at $\phi = 0.65$. Many modeling approaches assume that the Reynolds stress is isotropic. From Figure 3, it is apparent that the Reynolds stresses are not isotropic for this system. The contour shapes, locations, and magnitudes differ significantly for the axial-radial (Figure 3A) and the axial-tangential (Figure 3B) Reynolds stresses. The Reynolds stress magnitudes for $\overline{u'v'}$ range from -5 to 50 m^2/s^2, while those for $\overline{u'w'}$ range only from -5 to 25 m^2/s^2. The largest Reynolds stresses occur in the region along the vortex wall, which indicates that there are high turbulence levels and large momentum transport at the boundary between the vortex and the gases in the burner. This observation is consistent with the conclusions drawn from the mean and RMS velocity contours, which showed high RMS velocity values and rapid decay of the mean velocity at the vortex wall due to shearing between the high velocity swirling gases from the injector and the lower velocity gases in the burner.

Planar Laser Induced Fluorescence (PLIF) of CH radicals. PLIF images of CH have been successfully acquired in a natural gas, premixed Bunsen burner flame. CH is an excellent marker of the flame zone and can actually be observed by the eye as part of the bright, inner blue chemiluminescent cone. Previous fluorescent studies used OH to mark the flame zone; however, OH is known to persist longer in the flame. CH is a better flame zone marker due to its very high reactivity and because it is also implicated in the formation of prompt NO_X.

Excitation of CH occurs at a wavelength near 387 nm. This light is generated by wave mixing the fundamental of a Nd:YAG DCR-2A laser(1064 nm) with the output of a tunable dye laser using Rhodamine 640 dye. The Nd:YAG pumps the tunable dye laser with frequency doubled 1064 nm light, and the residual is used for mixing in the WEX (Wave Length Extender). The total power of the 387 nm laser light is 14 mJ/pulse with a 10 ns pulse width. The laser light is optically formed into a sheet and passed through the flame as shown in Figure 4. Fluorescence at 431 nm is captured by an Intensified Charge Coupled Device (ICCD) using a Nikon 50 mm/f 1.2 lens and a GG-420 long-pass filter. The images are downloaded to a computer for further analysis. Figure 4 also shows four instantaneous images of the fluorescence emitted from the CH radical.

1.3 - Submodel Improvements. The objective of this subtask is to improve the submodels in the code using available technology and advances from this study, from other ACERC researchers under independent funding, and from the literature, in order to provide increased agreement with the key experiments identified in Subtask 1.2. Specific submodels being considered include finite-rate chemistry, NO_X formation at high pressures in fuel-lean systems, and CO/CO_2 non-equilibrium.

Evaluation of Reduced Mechanisms. A comprehensive study was conducted to select and evaluate potential reduced mechanisms of methane combustion for use in comprehensive premixed turbulent combustion codes. The two most promising mechanisms were by Seshadri and Peters (Chen and Dibble, 1991) and by

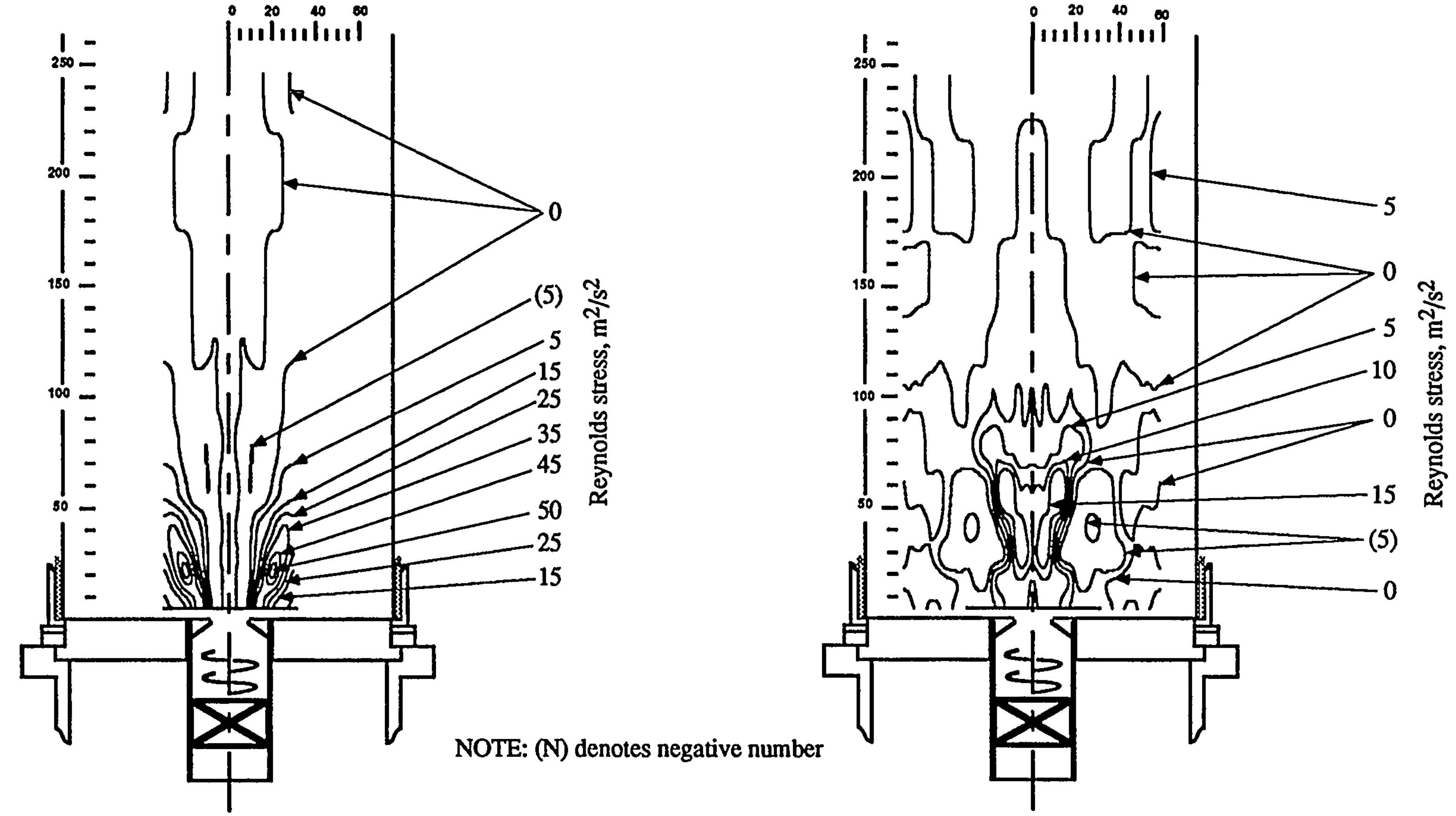

NOTE: (N) denotes negative number

A) Axial-radial Reynolds stress $\phi = 0.65$

B) Axial-tangential Reynolds stress $\phi = 0.65$

Figure 3. Sample axial-radial $\overline{u'v'}$ and axial-tangential $\overline{u'w'}$ Reynolds stress contours for the ATS-MS burner at $\phi = 0.65$.

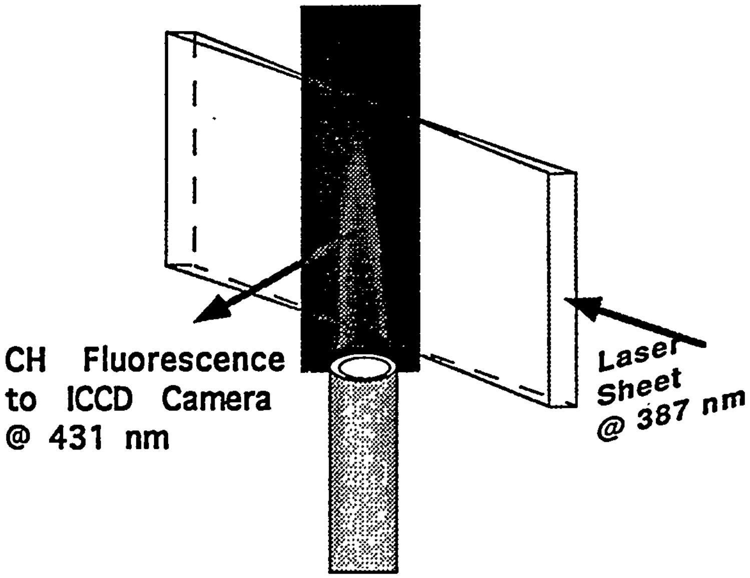

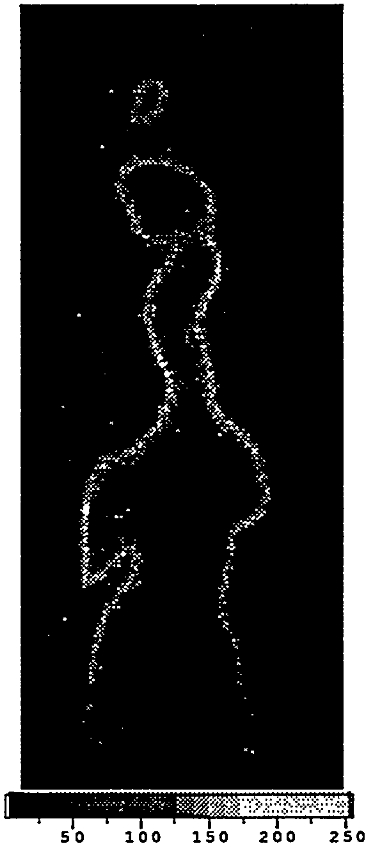

Figure 4

Above: Natural flame emission taken from video of natural gas bunsen burner.

Right/Below: Instantaneous bunsen burner CH fluorescence (F @ 1.0).

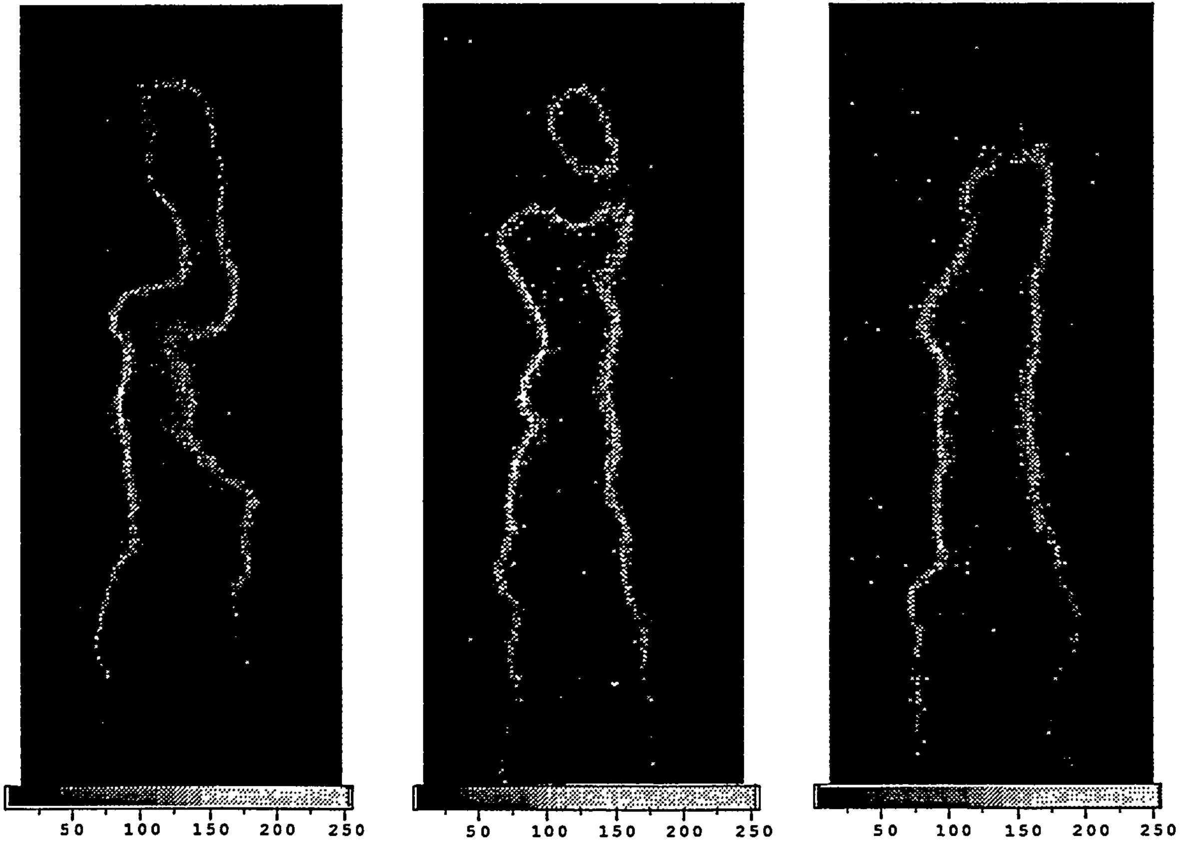

Bilger (Chen and Dibble, 1991). The reduced mechanisms were tested and compared against a full mechanism (GRI Mech. 1.2) for different conditions such as varying equivalence ratios, inlet temperatures, residence times, and pressures. A Perfectly-Stirred Reactor code (PSR) (Glarborg, et al., 1992) and a Premixed code (Kee, et al. 1992) were used to perform the evaluations. Efforts are also being made to acquire additional reduced mechanisms of methane combustion and the NOx mechanism which is in the being developed by GRI.

PSR code calculations: A total of 243 test calculations were performed using the PSR code in conjunction with the full mechanism and both reduced mechanisms, varying such parameters as pressure, equivalence ratios, inlet temperature, and residence time. In order to do these runs, the CHEMKIN package, which handles finite rate elementary reactions, had to be modified so that it could treat global reaction rates. The CKWYP subroutine in the package was replaced by a new subroutine which allowed calculation of global reaction rates.

The net rate constants for each of these global reactions are computed from algebraic expressions involving rate constants for about 25 elementary reaction steps. Figure 5 shows the variation of temperature with equivalence ratio for pressures of 1.0 and 30 atmospheres. The inlet temperature for the PSR reactor was taken as 600 K and the residence time was taken as 2 x 10^{-3} seconds. It is seen from Figure 5 that the Seshadri-Peters mechanism shows fairly good agreement with the full mechanism (GRI) at both pressures. The Bilger mechanism seems to show slight disagreement with the full mechanism (GRI) at high pressures for low equivalence ratios.

Figure 6 shows the CH_4 predictions for pressures of one and 30 atmospheres using the PSR code. It is seen that, although the Seshadri-Peters mechanism gives good predictions at 1 and 30 atm pressures, the Bilger mechanism gives poor predictions at both pressures for fuel-lean mixtures. Figure 7 shows the PSR CO predictions for the Peters-Seshadri, Bilger, and GRI full mechanism for pressures of 1 and 30 atm. It is seen that at both pressures, the two reduced mechanisms give almost identical predictions but differ from the full GRI mechanism predictions. It is postulated that the reduced mechanism predictions are more accurate at high pressure than at atmospheric pressure because C_2 chemistry is not included.

Premixed code calculations: The premixed code also runs in conjunction with the CHEMKIN package like the PSR, but is used to model burner-stabilized or freely propagating, steady-state, premixed laminar flames. Predictions of premixed laminar methane-air flames were performed using the full and reduced mechanisms as a function of pressure and equivalence ratio, using an inlet temperature of 300 K. Figure 8 shows the variation of temperature along the length of the premixed flow reactor for pressures of 1 and 30 atm (ϕ = 0.85). The Seshadri-Peters mechanism gives good agreement with the full mechanism at all pressures. Figure 9 shows CH_4 predictions using the premixed code for an inlet temperature of 300 K and an equivalence ratio of 0.85. The figure shows that at all pressures the combustion rate predicted by the full GRI mechanism is similar to the Seshadri and Peters reduced mechanism. Figure 10 shows the variation of predicted CO concentration with distance along the reactor for both 1 and 30 atm. The predictions show that the peak CO concentration in the Seshadri-Peters mechanism is slightly different compared to the full GRI mechanism (compare scales on the y axis).

Task 2 - Code Development

The objective of Task 2 is to develop an advanced, 3-dimensional gas turbine combustor model from the foundation of ACERC's existing 3-D code, PCGC-3. Task 2 is closely coordinated with an independently funded DOE/METC (DE-AC21-93MC30040) study being jointly conducted by Advanced Fuel Research, Inc. (AFR), and BYU/ACERC, which has a task for conducting gaseous combustion modeling.

2.1 - CFD Improvements. The objective of this subtask is to investigate improvements to the PCGC-3 fluid mechanics platform in order to better model the conditions and geometries associated with gas turbine

(a) 1 atm (b) 30 atm

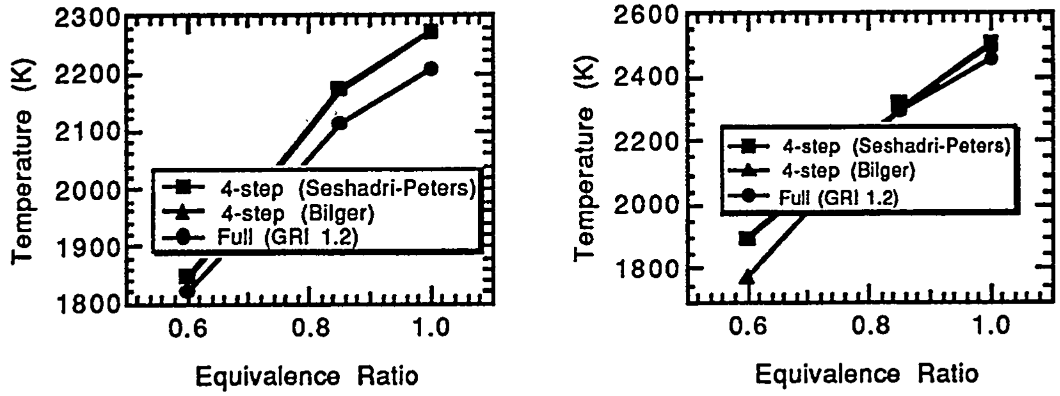

Figure 5. PSR calculations as a function of temperature and equivalence ratio (T_{inlet} = 600 K; τ = 2 ms)

(a) 1 atm (b) 30 atm

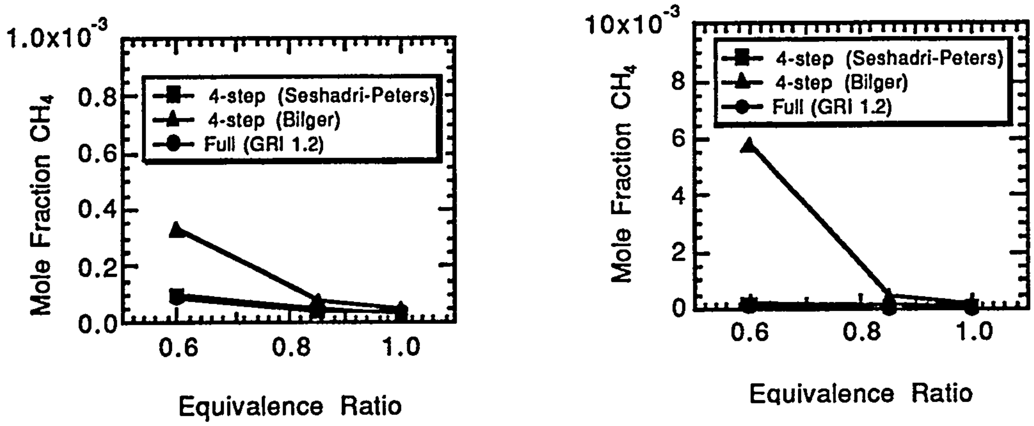

Figure 6. PSR calculations of mole fraction CH_4 as a function of equivalence ratio at two pressures (T_{inlet} =600 K; τ = 2 ms).

(a) 1 atm (b) 30 atm

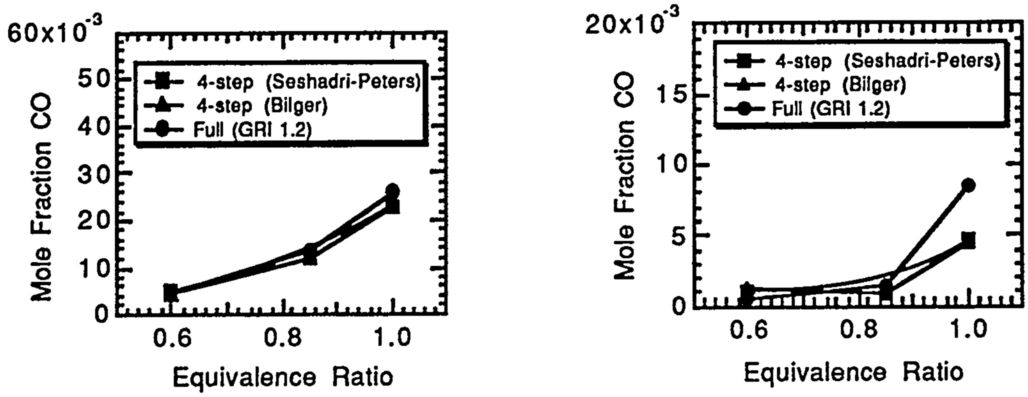

Figure 7. PSR calculations of mol fraction CO as a function of equivalence ratio at 1 and 30 atm (T_{inlet} =600 K; τ = 2 ms)

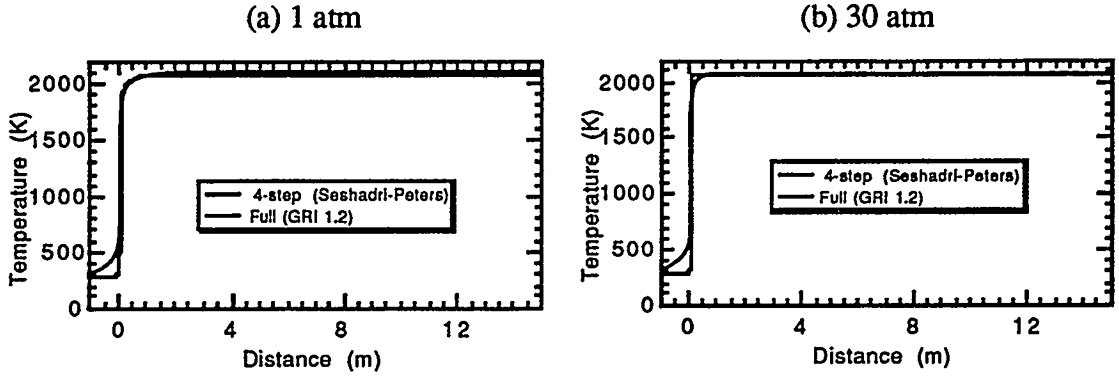
(a) 1 atm

(b) 30 atm

Figure 8. Premixed calculations of temperature ($T_{inlet} = 300$ K and $\phi = 0.85$)

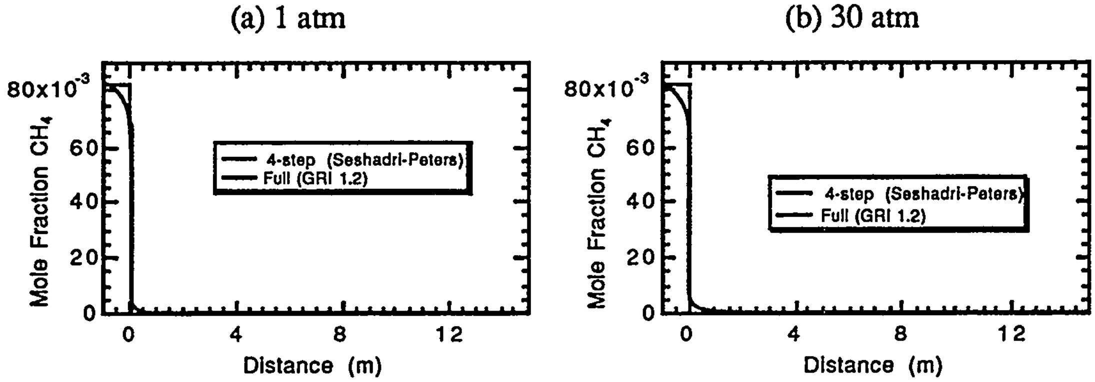
(a) 1 atm

(b) 30 atm

Figure 9. Premixed calculations of mole fraction CH_4 ($T_{inlet} = 300$ K, and $\phi = 0.85$)

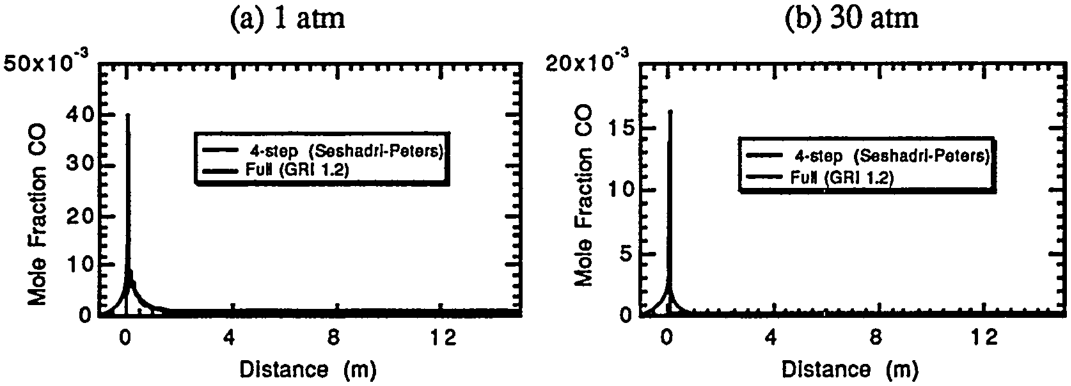
(a) 1 atm

(b) 30 atm

Figure 10. Premixed calculations of mole fraction CO ($T_{inlet} = 300$ K, $\phi = 0.85$)

combustors. During the last year, the foundations of a new unstructured-grid flow solver were developed, under independent funding from the National Science Foundation (NSF), and the resulting code is being used as a basis for developing the gas turbine combustor model. The code uses the Control Volume Finite Element Method (CVFEM) of Baliga and Patankar (1983). Both collocated (Prakash, 1986) and staggered (Meng, 1994) schemes are employed. However, only the collocated scheme is operational at present. The skewed, mass-weighted upwind interpolation function for the dependent variables is used in the convection discretization, and linear interpolation functions are used for the diffusion, pressure gradient and source term discretization.

The new code was tested by simulating 1) developing laminar flow through a straight channel, 2) two-dimensional, laminar flow over a backward-facing step, and 3) turbulent flow over a backward-facing step. Calculations were also performed with FLUENT/UNS (Fluent Inc.'s unstructured-grid code) for comparison, and results were compared with experimental data or, in the case of laminar flow through the straight channel, with an analytical solution. Agreement was excellent for all of the laminar predictions. Geometry and predictions for turbulent flow over a backward-facing step are shown in Figure 11. Flat profiles were assumed at the inlet (x=-0.254 m), and the inlet turbulence intensity was assumed to be 5 percent. The grids were generated by GEOMESH (Fluent Inc.'s unstructured grid generator). The profiles have been normalized by the maximum velocity at each axial position. Experimental profiles were normalized by the maximum experimental velocity, and predicted profiles were normalized by the maximum predicted velocity. Raw data, without normalization, were not plotted because the experimental values were only available in normalized form. The predictions with two grid densities are similar, indicating that the solution is fairly grid-independent. The recirculation zone is significantly underpredicted, and the predicted velocity does not approach zero at the walls. Nodes that reside on the wall do not satisfy the no-slip condition. The manner of implementing the law-of-the-wall boundary condition is therefore being investigated to remedy this problem. Except for the near-wall regions, the shapes of the experimental and predicted profiles seem to be in reasonable agreement.

2.2 - Incorporation of Submodels. The objectives of this subtask are: 1) to incorporate the best-available, proven, advanced code submodels from the broad, on-going ACERC research program, from the literature, from known developers of submodels, and those developed in Task 1, and 2) to perform systematic checks of the code to verify accuracy of code programming, and appropriateness of newly installed improved submodels.

Implementation of PDF2DS into PCGC-3. An advanced gas-phase combustion submodel applicable to lean, premixed combustion (LPC) of natural gas in gas turbines is being developed under the independently funded DOE/METC project (DE-AC21-93MC30040). Such combustion is of significant commercial interest and yet there are no generally available combustion codes for predicting LPC flames. The submodel is intended for use in the comprehensive combustion code being developed under this study. The foundation of the submodel is PDF2DS, a 2-dimensional (2-D), velocity-scalar probability density function (PDF) code developed by Dr. Stephen Pope at Cornell University (Correa and Pope, 1992). Details of the velocity-scalar PDF method are given in Pope (1985). The submodel is being implemented under the independently funded study in PCGC-3.

The PDF2DS code has been implemented as a submodel in the 2-D, axisymmetric option of PCGC-3, and it has been tested for variable density, non-reacting flow. PCGC-3 calculates the flowfield, based on the k-e turbulence model, and PDF2DS calculates the density field. The two codes are coupled, as shown in Figure 12, and must be solved iteratively until the density field is no longer changing significantly in PDF2DS. The combined code seems to function reasonably well, except there is an inconsistency between

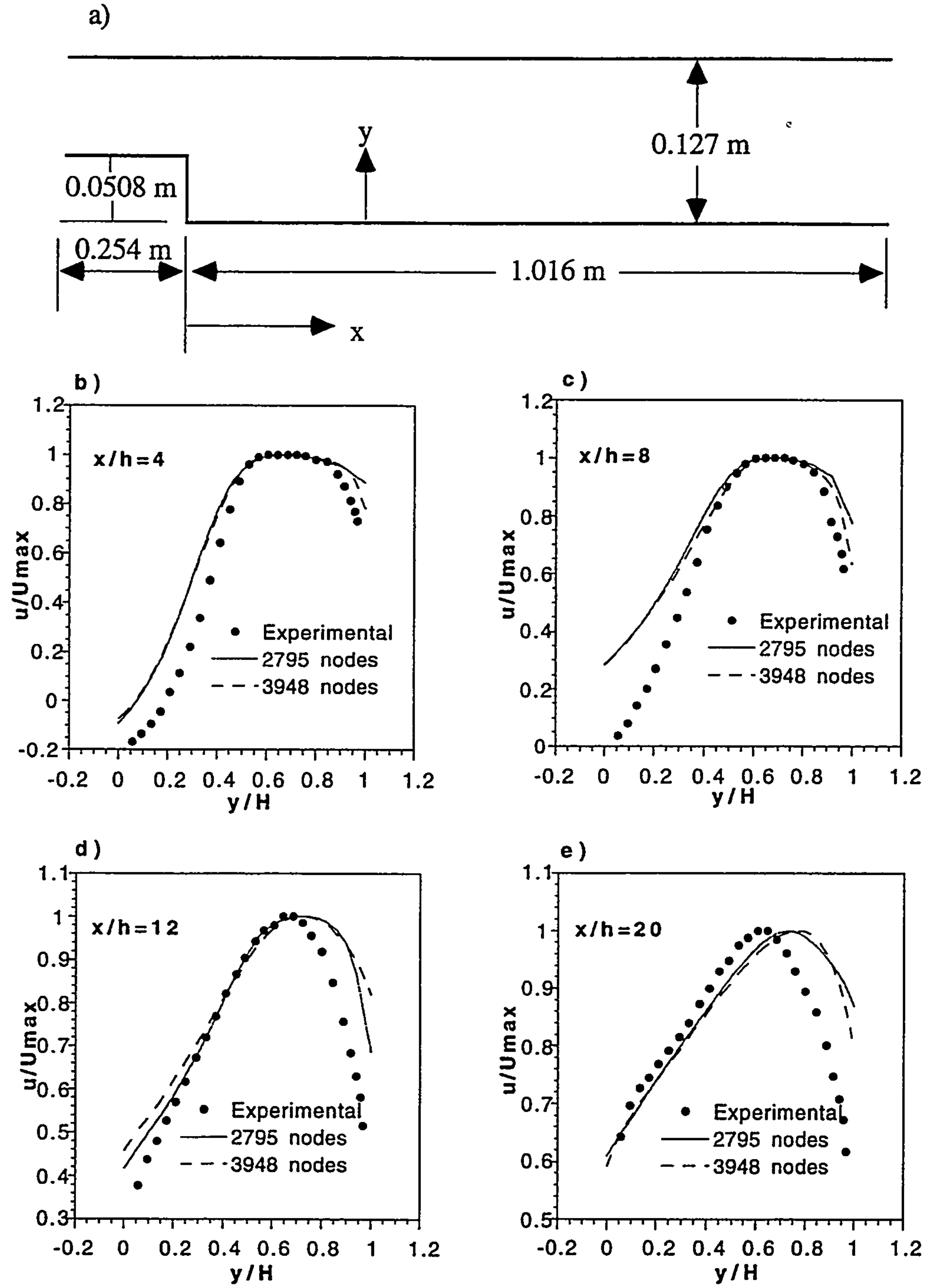

Figure 11. Geometry and predictions of axial velocity profiles for turbulent flow over a backward-facing step. (Experimental data from Westphal et al., 1984)

the computational grids of the two codes that seems to be causing problems. PCGC-3 uses a staggered grid, with velocities stored at cell faces and all other properties stored at cell centers, while PDF2DS uses a collocated grid with all properties stored at cell corners. Currently, PCGC-3 values are interpolated to the cell corners for use in PDF2DS and density is interpolated to the cell centers for use in PCGC-3. Consistency in grid definition is needed for the two codes to work compatibly.

Since PDF2DS provides no chemistry for reacting flow, the submodel is being extended to include chemistry applicable to LPC of methane, and table look-up procedures are being investigated to increase computational efficiency. A two-step mechanism (Westbrook and Dryer, 1981) is being implemented first. Later, a four-step mechanism (Seshadri and Peters, 1990) will be implemented.

Figure 13 shows a scatterplot of PDF particles for LPC of a methane-air jet with the two-step mechanism. Particle temperature is indicated by the shading, with the darkest particles at 300 K and the lightest (almost white) particles at 2012 K. The diameter of the jet was 2 cm, the equivalence ratio was 0.8, the inlet temperature was 300 K, and the jet Reynolds number was 36,140. The jet issued into a large cylindrical enclosure (1 m length, 0.4 m diameter). Radiation and heat losses were neglected. Approximately 100,000 PDF particles were used. Chemistry was implemented with the look-up tables described above.

Figure 14 shows a plot of CO mole fraction for particles residing in the first row of computational cells along the reactor centerline. Mole fractions exceeding equilibrium values were obtained at axial locations up to half the reactor length. Beyond this location, only equilibrium values were obtained.

Incorporation of PDF methods into the ACERC Unstructured-Grid Flow Solver. During the last year, integration of the advanced submodel applicable to LPC in gas turbines into the new unstructured-grid flow solver was performed and testing was initiated. An axisymmetric, constant-density, turbulent, non-premixed, non-reacting, test problem was solved as follows: First, the flowfield was converged by the flow solver (314 nodes, 550 cells). This step required approximately 500 iterations, starting from scratch (less than 30 CPU-min on an HP-735 workstation). Second, the PDF particles (91,146 total) were randomly distributed throughout the flow domain and initialized by linearly interpolating the velocity, pressure and turbulent kinetic energy from the unstructured mesh nodes onto the particle positions. Third, velocity-scalar PDF transport calculations were performed for the particles for 923 time steps (108 μsec/step), which is equivalent to approximately 10 reactor residence times. The PDF submodel calculations required approximately 14 CPU-hr (~1 CPU-min/time step). And finally, the mean mixture fraction field was calculated from the PDF particle mixture fractions using spline interpolation. Since the fluid mass density was uniform, there was no feedback from the PDF submodel to the flow solver. The predicted scalar mixing shows some unusual structural features (e.g., waviness) that are probably not realistic. This is probably due to the procedures that are used to interpolate grid properties on to the particles and/or visa versa. This issue is being investigated.

Incorporation of LPDF2D into PCGC-3. An updated version of a two-dimensional, node-based, scalar-only version of a probability density function (PDF) submodel, called LPDF2D, available from the NASA/Lewis Research Center, and which allows for the incorporation of gas-phase chemistry necessary for premixed combustion with turbulence interactions, was also obtained and incorporated into the axisymmetric option of PCGC-3 and tested. The advantage of the scalar-only PDF method is that it is simpler than the velocity-scalar method. The disadvantage is that it assumes gradient diffusion with a turbulent diffusivity. In LPDF2D, there is randomness in the implementation of both convection and diffusion. In PDF2DS, on the other hand, there is no randomness in the transport (by the mean and fluctuating velocity), i.e., the randomness is one level removed—in the fluid particle acceleration. Hence, the PDF method implemented in PDF2DS is more accurate than

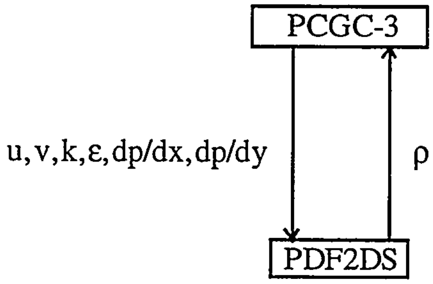

Figure 12. Coupling between PCGC-3 and PDF2DS.

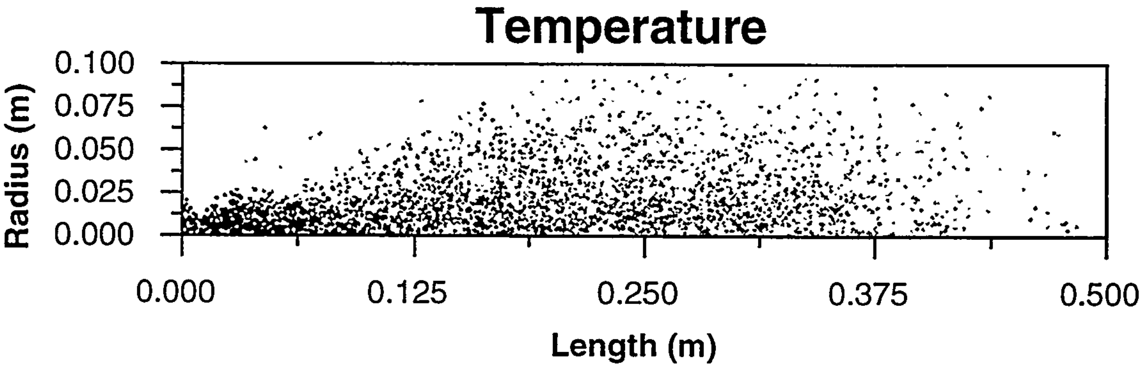

Figure 13. Scatterplot of PDF particle temperature in LPC of a methane-air jet.

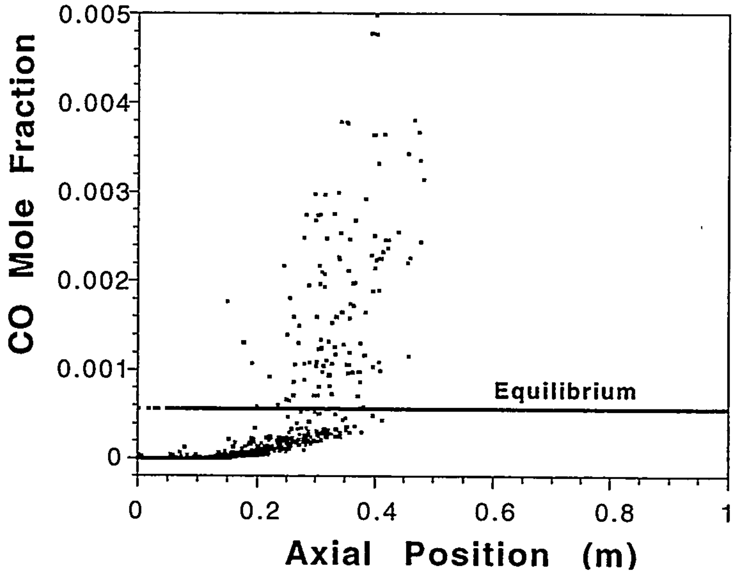

Figure 14. Predicted mole fraction of CO for PDF particles near the centerline of a premixed, methane-air jet.

that implemented in LPDF2D. Unfortunately, acceptable results were not obtained with LPDF2D, even for non-reacting flow. Several technical limitations were identified in the submodel and conveyed to researchers at NASA/LeRC. However, an improved version of the submodel, incorporating changes to address these limitations, is not yet available.

Subtask 2.3 - Parametric Predictions. The code is being used to make parametric predictions on advanced gas turbine designs obtained from the affiliated industrial manufacturers of gas turbine systems. Two practical gas turbine geometries were obtained from Westinghouse Electric Corp. Both are for premixers. The files for these geometries were created at Westinghouse by Computer Vision, a computer-aided design program, and transferred over the Internet in standard IGES format. The files were read at BYU by Fluent Inc.'s GEOMESH program, and boundary-fitted coordinate (BFC) grids were generated. Preliminary simulations with the FLUENT program (version 4.31) were then carried out to establish a methodology of generating computational grids based on solid modeling databases generated by design groups in industry. Simulation of the premixer shown in Figure 15a was then performed with the new ACERC code. Inlet conditions consisted of a low-velocity secondary inlet (air) and a high-velocity primary inlet (CH_4 at the small hole). Figure 15b shows the predicted scalar mixing (primary = 1, secondary = 0), on a cutting plane which sits perpendicular to the plane of the secondary inlet. The simulation results predict extensive, but not complete mixing of the fuel and oxidizer streams at the outlet.

Task 3 - Industry and AGTSR Interaction

The third task is to interact with industrial and university organizations with gas turbine interest. An ACERC/ATS technical advisory committee (TAC), composed of sixteen prominent industrial organizations with specific interest in utility and industrial gas turbine manufacture and application, was formed previously. The TAC provides direction for this research program. Concerns particular to industry are being addressed, and results are being provided to participating industrial members.

Members of the TAC have been contacted by telephone and mail, and have been sent copies of the annual report. The ASME Cogen Turbo Power conference was attended and the issues that were thought to be of most interest to the end user were discussed, such as combustor can burnout, restricted levels of turndown, combustion stability problems, and NOx attainment when other fuels. There has been extensive interaction with Westinghouse and NASA-Lewis on geometries and modeling approaches. BYU investigators presented their work at the annual ATS program review at the ATS combustion workshop in Indianapolis. Visits to BYU have been made by Dr. J. Y. Chen (University of California, Berkeley) and Dr. Phillip C. Malte (University of Washington) to interact with the ATS program. A letter detailing the status of the project and asking for input from the members of the Technical Advisory Committee was recently sent.

In addition to the work being performed under this contract, research at BYU on advanced gas combustion models is being supported by other funding. The Department of Energy, through the Morgantown Energy Technology Center, is funding a collaborative project by Advanced Fuel Research (AFR) of East Hartford, CT, and BYU (contract number DE-AC21-93MC30040) which focuses specifically on the development of advanced submodels for turbulent, gaseous combustion. This study is referred to in this report as the AFR study. Further, ACERC is supporting several initiatives in adapting PCGC-3 to complex geometries and turbulence that complement work on this project. Other work has also been performed by ACERC researchers that can be applied to this project.

Future Activities

Task 1. Further velocity data will be acquired with natural gas as fuel for the MS configuration at $\phi = 1.2$, as noted above, and at $\phi = 0.65$, $\phi = 0.80$ $\phi = 1.0$, and $\phi = 1.2$ for the HS and LS configurations. In addition, LDA measurements will be taken for all three

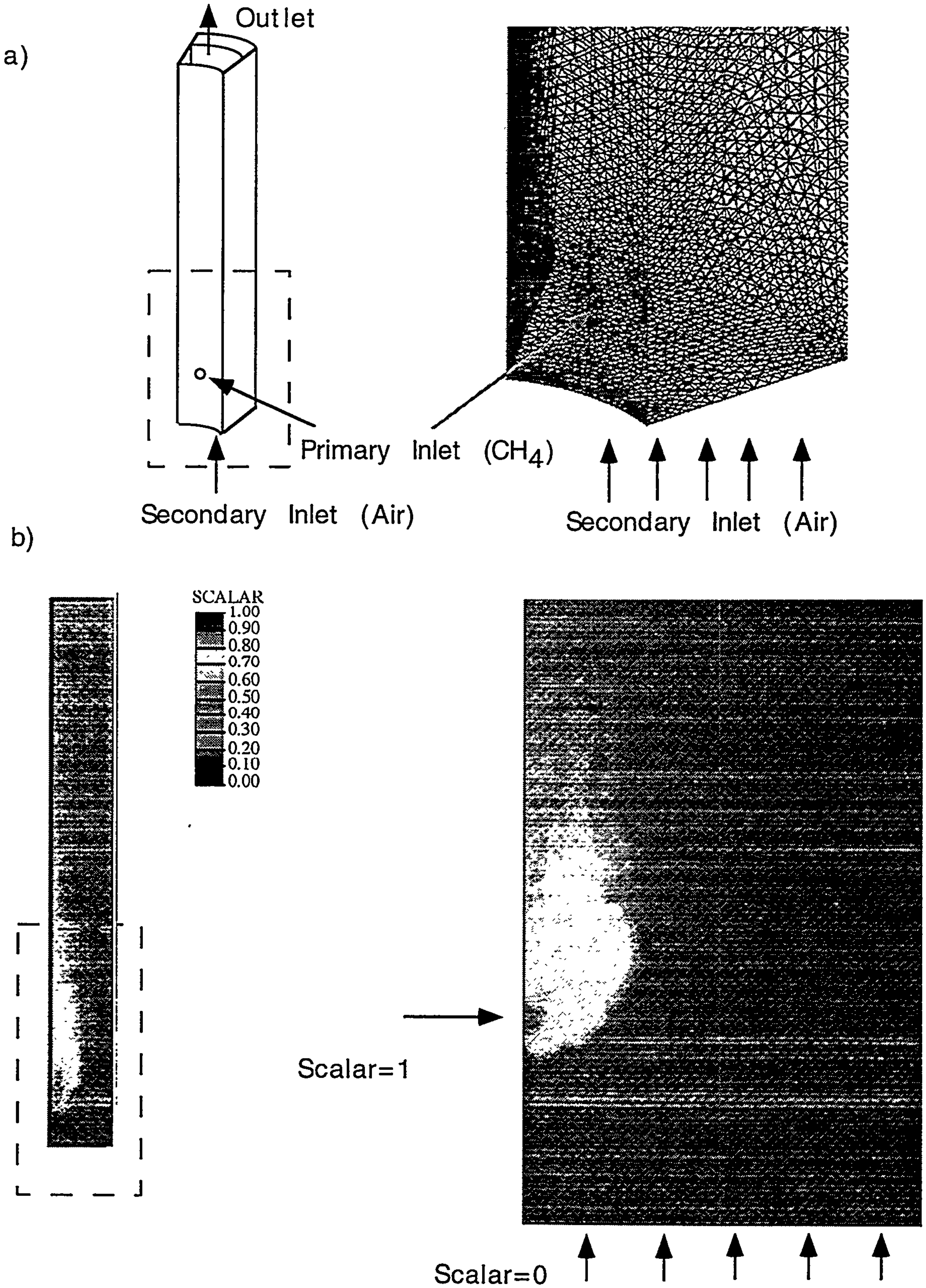

Figure 15. Geometry, computational grid and predicted scalar mixing for Westinghouse gas turbine premixer.

configurations (HS, MS, LS) with liquid ethanol as fuel. Again fuel equivalence ratios of $\phi = 0.80$, $\phi = 1.0$, and $\phi = 1.2$ will be studied but $\phi = 0.65$ will be replaced with a lean blowout condition, probably around $\phi = 0.50$. Mapping of velocity, temperature, and N_2, O_2, CO, and CO_2 species concentrations for various configurations of the ATS premixed natural gas/air burner using LDA and CARS will be completed. In addition, PLIF images of OH and CH in the burner will be obtained.

Task 2. The ACERC unstructured code will be extensively revised and rewritten to improve accuracy, computational efficiency, and robustness. The unstructured-grid PDF submodel will be extended to variable-density, reacting flow and interfaced with a chemistry submodel for LPC being developed by an independently funded project. Both submodels will be incorporated in the unstructured-grid flow solver. Simulation of practical gas turbine combustor geometries will continue. One or more practical combustor "basket" geometries will be obtained from Westinghouse and simulated.

Future simulation efforts with the unstructured-grid code will focus on combustor "basket" geometries with chemical reaction. Because the inlet conditions and degree of premixing are so critical to predicting pollutant formation in LPC, non-reacting simulations of the premixer will be used to provide the inlet conditions for the combustor simulations. It is anticipated that the first reacting, combustor simulation for a practical geometry will be completed with the new unstructured-grid code and PDF submodel with kinetics for LPC on or around January 1, 1996.

Acknowledgments

This report was prepared with the support of the U.S. Department of Energy, Morgantown Energy Technology Center, Cooperative Agreement No. DE-FC21-92MC29061 (Dr. Paul Mitchell and Dr. Norm Holcombe, project managers). This financial support through the South Carolina Energy Research and Development Center, subcontract 93-01-SR014 (Mr. Daniel Fant, Program Director, and Dr. Lawrence P. Golan, SCERDC Director) is greatly appreciated. References are made in this report to work performed under separate funding agreements with the Advanced Combustion Engineering Research Center (with the principal grant from the National Science Foundation's Engineering Centers Division), Brigham Young University, the Air Force, and the DOE/METC with Advanced Fuel Research, Inc. Their support is appreciated. Students who participate on this project include Steven Cannon, Robert Dawson, Jason Haslam, Kyle Kinghorn, Hemant Mallampalli, Robert Murray, and Craig Phillips. Post-doctoral associates who have contributed include Fanli Meng and James Farmer. Also, the participation on the Technical Advisory Committee for this project of Allison Engine Company, General Electric, Solar Turbine, United Technologies Research Center, Westinghouse Electric Corp., Babcock and Wilcox, Foster Wheeler, Electric Power Research Institute, Gas Research Institute, Los Angeles Department of Water and Power, and Sacramento Municipal Utility District is greatly appreciated.

References

Baliga, B. R., and Patankar, S. V., "A Control Volume Finite-Element Method for Two-Dimensional Fluid Flow and Heat Transfer," Numerical Heat Transfer, 6, pp. 245-261 (1983).

Chen, J.Y. and Dibble, R.W., "Applications of Reduced Chemical Mechanisms for Prediction of Turbulent Non-Premixed Methane Jet Flames," in Reduced Kinetic Mechanisms and Asymptotic Approximations for Methane-Air Flames, M.D. Smooke (Ed.), Springer-Verlag, pp. 193-226 (1991).

Glarborg, P., Kee, R.J., and Miller, J.A., "PSR: A Fortran Program for Modeling Well Stirred Reactors," Sandia Report, (1992).

Kee, R.J., Grcar, J.F., Smooke, M.D., and Miller, J.A., "A Fortran Program for Modeling Steady Laminar One-Dimensional Premixed Flames," Sandia Report, (1992).

Meng, F., "A Staggered Control Volume Finite Element Method for Turbulent Reacting Flows Coupled with Radiation," Ph.D. dissertation, University of Montreal, CA (1994).

Peters, N., "Reducing Mechanisms," in Reduced Kinetic Mechanisms and Asymptotic Approximations for Methane-Air Flames, M.D. Smooke (Ed.), Springer-Verlag, pp. 48-67 (1991).

Prakash, C., "An Improved Control Volume Finite-Element Method for Heat and Mass Transfer, and for Fluid Flow using Equal-Order Velocity-Pressure Interpolation," Numerical Heat Transfer, 9, pp. 253-276 (1986).

Seshadri, K., and Peters, N., "The Inner Structure of Methane-Air Flames." Comb. Flame., 81, pp. 96-118 (1990).

Smooke, M.D. and Giovangigli, V., "Formulation of the Premixed and Nonpremixed Test Problems," in Reduced Kinetic Mechanisms and Asymptotic Approximations for Methane-Air Flames, M.D. Smooke (Ed.), Springer-Verlag, pp. 1-28 (1991).

Westbrook, C.K., and Dryer, F., "Simplified Reaction Mechanisms for the Oxidation of Hydrocarbon Fuels in Flames," Comb. Sci. Tech., 27, pp. 31-43 (1981).

Westphal, R. V., Johnston, J. P., and Eaton, J. K., "Experimental Study of Flow Reattachment in a Single-Sided Sudden Expansion," NASA Contractor Report 3765, Stanford University, Report MD-41 (1984).

P9 Heat Transfer in a Two-Pass Internally Ribbed Turbine Blade Coolant Channel With Cylindrical Vortex Generators

R. Hibbs
S. Acharya[1] (ACHARYA@ME.LSU.EDU; 504-388-5809)
Y. Chen
D. Nikitopoulos
T. A. Myrum
Mechanical Engineering Department
Louisiana State University
Baton Rouge, LA 70803

Abstract

The effect of vortex generators on the mass (heat) transfer from the ribbed passage of a two pass turbine blade coolant channel is investigated with the intent of optimizing the vortex generator geometry so that significant enhancements in mass/heat transfer can be achieved. In the experimental configuration considered, ribs are mounted on two opposite walls; all four walls along each pass are active and have mass transfer from their surfaces but the ribs are non-participating. Mass transfer measurements, in the form of Sherwood number ratios, are made along the centerline and in selected inter-rib modules. Results are presented for Reynolds number in the range of 5,000 to 40,000, pitch to rib height ratios of 10.5 and 21, and vortex generator-rib spacing to rib height ratios of 0.55, and 1.5. Centerline and spanwise averaged Sherwood number ratios are presented along with contours of the Sherwood number ratios. Results indicate that the vortex generators induce substantial increases in the local mass transfer rates, particularly along the side walls, and modest increases in the average mass transfer rates. The vortex generators have the effect of making the inter-rib profiles along the ribbed walls more uniform. Along the side walls, horseshoe vortices that characterize the vortex generator wake are associated with significant mass transfer enhancements. The wake effects and the levels of enhancement decrease somewhat with increasing Reynolds number and decreasing pitch.

Introduction

Since the efficiency of a gas turbine engine depends on the turbine inlet temperature, one of the primary goals in the development of advanced turbine systems is to explore more effective methods of heat removal from the turbine blades. This paper deals with the flow and heat transfer in the internally ribbed coolant channels of a gas turbine blade and aims to examine heat transfer enhancement brought about by placing vortex generators above the ribs in the coolant passages. This expected enhancement is based on observations made in flow past ribs (Acharya et al., 1991) in which it was shown that the separated shear layer behind the rib was characterized by

---

Research sponsored by the U.S. Department of Energy's Morgantown Energy Technology Center, under Contract DE-FC21-92MC20961 with South Carolina Energy Research and Development Center, 386-2 College Avenue, Clemson, South Carolina, 29634-5181.

[1] Author to whom all correspondence must be addressed.

large scale vortical structures, and that these structures could be manipulated by introducing an external perturbation into the flow in order to promote mixing behind the rib. Greater mixing and shear layer growth behind the ribs is expected to lead to enhancement in surface heat transfer. In this paper the vortex street behind a cylindrical vortex generator mounted above the rib will be used as the external perturbation, and its effect on the heat transfer from the ribbed surface will be examined. The long term goal of the study is to examine the heat transfer behavior for the above geometry under rotating conditions. However, in this paper, only stationary coolant channel results are reported.

Numerous experimental investigations reporting the local and average heat transfer behavior in ribbed channels are available in the literature (e.g. Sparrow and Tao, 1983; Han and Zhang, 1991; Acharya et al., 1993; Acharya et al., 1995a, 1995b). In general, these studies consistently report significant heat transfer enhancement due to the ribs, with peak heat transfer values in the vicinity of reattachment and just upstream of the rib. A number of studies have also reported flow measurements in ribbed channels in order to explain the observed heat transfer behavior. Humphrey and Whitelaw (1979) have shown that the ribs induce a strong generation of turbulent kinetic energy as well as gradients in Reynolds stresses which result in a normal-stress-driven secondary flow. Developing flow characteristics in a ribbed duct show that the interaction of shear layers formed by consecutive ribs results in an increase in turbulent kinetic energy (Liou, Chang, and Hwang, 1990). Karniadakis, Mikic, and Patera (1988) performed a numerical study, and using the Reynold's Analogy of momentum and heat transfer, showed that heat transfer rate increases with flow instability. Acharya et al. (1994) have reported measurements of velocity and heat transfer past a surface mounted rib, and have shown the correlation between the surface heat transfer and near wall turbulence levels.

In recent years, more effective heat removal techniques have been explored. A half delta wing geometry has been shown to generate longitudinal vortices embedded in the boundary layer in such a way that heat transfer dominates over momentum transfer (Wroblewski and Eibeck, 1991). With this vortex generator geometry, it was shown that the maximum heat transfer occurred at low Reynolds numbers (Garimella and Eibeck, 1991). A small fence-like geometry placed opposite a ribbed wall was shown to reduce the occurrence of local hot spots in the fully-developed region by inducing a more uniform heat transfer distribution (Hung and Lin, 1992). A cylindrical vortex generator placed above and parallel to the ribs in a duct has been shown to significantly increase heat transfer at low Reynolds numbers (Myrum et al., 1992). Further investigations with the cylindrical vortex generators have shown that the local streamwise distributions of heat transfer are more uniform, but are restricted to the inter-rib region immediately downstream of the generator (Myrum, Qiu, and Acharya, 1993). A later, more extensive study of the effects of cylindrical vortex generators has shown that heat transfer enhancement can be attributed to the enhancement of near-wall turbulence (Myrum et al., 1995). It is believed that this increased turbulence is the result of the interaction of the wake downstream of the cylinder and the separated shear layer downstream of the rib (Myrum and Acharya, 1994).

The above studies of Acharya, Myrum and co-workers with cylindrical vortex generators have shown significant heat transfer enhancement at low Reynolds numbers. These studies have, however, been performed in a two dimensional rectangular geometry. The present investigation will study the effect of this vortex generator geometry in a square-sectioned, ribbed duct over a range of Reynolds numbers. The flow in this geometry is three dimensional with secondary flows expected to have some effect on the flow structure. To the authors' knowledge, no studies on the effect of cylindrical vortex generators in a square-sectioned duct have been made.

The Experiments

The experiments are performed in a test apparatus designed for the study of mass transfer (sublimation of naphthalene) in a rotating duct that simulates the coolant channels of a turbine blade. Mass transfer measurements permit the acquisition of detailed local distributions of the Sherwood number which can then be converted to Nusselt numbers using the heat-mass transfer analogy.

An overall schematic of the experimental setup is shown in Figure 1. Compressed air is used as the working fluid for all experiments in order to more closely simulate the operational parameters in a turbine engine. The air is taken from large, exterior reservoirs in order to minimize flow disturbances caused by the compressor. A concentric bore orifice plate is used to measure the mass flow rate in the meter run. A regulator is used to maintain a constant supply pressure in the meter run. Test section and meter run pressures are measured using mechanical pressure gauges that have a 2.5 psi resolution, and are controlled independently with gate valves located downstream of both the meter run and test section. Naphthalene laden exhaust air is directed through flexible tubing to a fume hood.

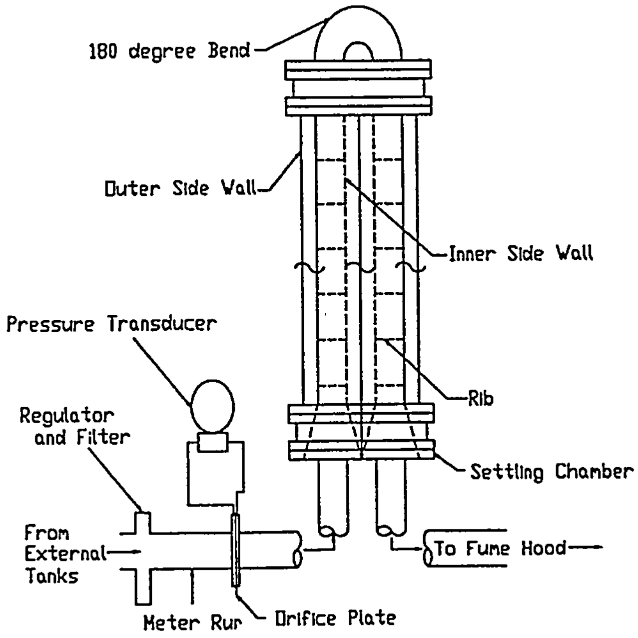

Figure 1. Schematic of Experimental Apparatus

Apparatus

The aluminum alloy test section consists of a 2.75 in. tapered settling chamber; a frame that supports eight removable, hollow plates; and a removable 180 degree bend. These major components are secured in a flange-like manner, using O-rings between all parts to prevent air leakage. When assembled, the test section forms 1 x 1 x 12 in. long inlet and outlet sections 1.5 in. apart that are connected by the 180 degree, 1 x 1 in. square cross-section bend. The aluminum ribs are 0.1 x 0.1 x 1.0 in. long and have holes on either end for mounting (Figure 2). Steel, 0.025 in. diameter music wire is inserted into these holes to secure them to the side walls of the test section. The ribs are mounted only on opposite walls and are not coated with naphthalene. The vortex generators (rods) are made from 0.078 in. diameter steel music wire. The rods are positioned in the test

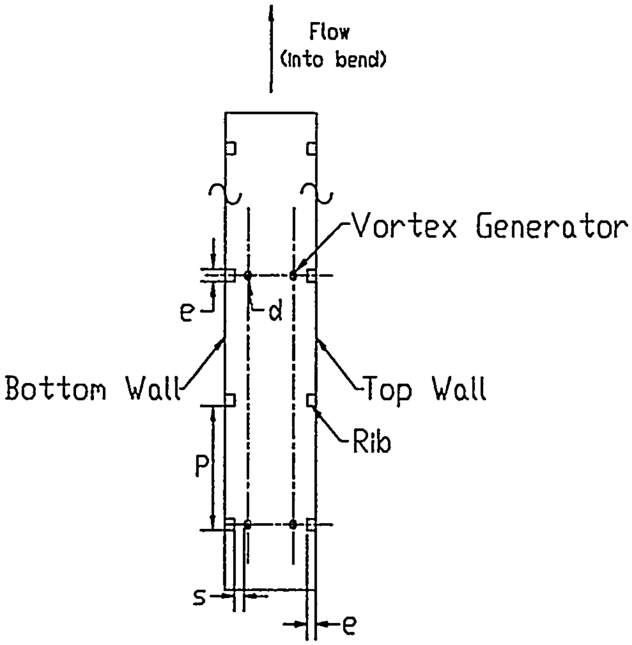

Figure 2. Schematic of Test Section Showing Geometrical Notation

section by means of small aluminum brackets that allow for variation of rib-rod spacing.

Detailed surface profiles of the cast surfaces are required for local mass transfer results. These profiles are obtained by moving the walls under a fixed, linear variable differential transducer (LVDT) type profilometer. A bi-directional traversing table is securely mounted to the platform of a milling machine. The plates are secured to a 0.625 in. thick tooling aluminum plate which is fixed to the traversing table. This mounting plate has been machined with an assortment of pin supports and machine screw taps to ensure the walls not only lie flat on the plate, but also are mounted in the same location for all scans. A custom written program run on a personal computer is used to control the motion of the traversing table through micro-step drive motors with a 0.00005 in. step size.

Procedure

Fresh, 99% pure naphthalene crystals are melted in a heavy-walled glass beaker with an electric heating element. The clean test section walls are clamped to stainless steel plates which have been polished to a mirror-like finish. Molten naphthalene is quickly poured into the hollow cavity of the plate frame to fill completely the region between the walls. The cast plates stand for at least eight hours in a fume hood to attain thermal equilibrium with the laboratory.

Each wall is then separated from the casting plate and mounted to the mounting plate for scanning. After scanning, the plates are stored in an air-tight container, saturated with naphthalene vapor, to hinder natural sublimation until the test section is assembled.

Test section assembly is begun by first inserting the two inner side walls and then attaching the bend. Any ribs or vortex generators are then attached to these walls and the two outer side walls are mounted. The alignment of all ribs and vortex generators is checked before the four top and bottom walls are assembled. After the experiment is over, the test section is disassembled and the walls are placed in the storage container until they are scanned again.

Data Reduction

Mass flow rate in the meter run is calculated from measurements of temperature, pressure, and differential pressure using standard equations for concentric bore orifice meters (Stearns, et al., 1951 and Miller, 1989).

Naphthalene sublimation depth is calculated from the two surface profiles for each wall. Each profile is normalized with respect to a reference plane computed from three points scanned on the aluminum surface of the walls. The difference between the normalized profiles gives the local sublimation depth.

The local mass flux $\dot{m}''$ at each location is calculated from the following expression:

$$\dot{m}'' = \rho_s \delta / \Delta t \qquad (1)$$

where ρ_s is the density of solid naphthalene, δ is the local sublimation depth, and Δt is the duration of the experiment. Vapor pressure at the wall p_w is calculated from the following equation (Sogin, 1958):

$$\log_{10}(p_w) = A - B/T_w \qquad (2)$$

where A and B are constants and T_w is the absolute wall temperature. Wall vapor density ρ_w is then calculated using the perfect gas law. Bulk vapor density of naphthalene $\rho_b(x)$ is obtained by mass conservation balances of naphthalene from the inlet ($x = 0$) to the streamwise location (x).

The local mass transfer convection coefficient h_m is then calculated as follows.

$$h_m = \dot{m}''/(\rho_w - \rho_b(x)) \qquad (3)$$

The binary diffusion coefficient $D_{n\text{-}a}$ for naphthalene sublimation in air is taken as the ratio of the kinematic viscosity of air ν to the Schmidt number for naphthalene-air ($Sc = 2.5$). The local Sherwood number Sh is then calculated by:

$$Sh = h_m D / D_{n\text{-}a} = h_m D Sc/\nu \qquad (4)$$

where D is the hydraulic diameter of the test section. Sherwood number results presented in this study have been scaled with a correlation adapted from McAdams for fully developed smooth wall pipe flow.

$$Sh_o = 0.023 Re^{0.8} Sc^{0.4} \qquad (5)$$

where Re is the duct Reynolds number.

Comparison of heat transfer and mass transfer results is done through the use of the heat-mass transfer analogy (Sogin, 1958).

$$Nu = Sh(Pr/Sc)^{0.4} \qquad (6)$$

where Nu is the Nusselt number and Pr is the Prandtl number of air. An augmentation number N is used to compare mass transfer augmentation for tests involving vortex generators. It is defined as follows:

$$N = Sh_{rib\text{-}rod}/Sh_{rib} \qquad (7)$$

where $Sh_{rib\text{-}rod}$ is the Sherwood number with the vortex generators installed and Sh_{rib} is the Sherwood number for the baseline. Both local and area-averaged results are compared in this manner. Area-averaging is performed over the cross stream width of the wall.

Uncertainty

Uncertainties for all computed values are estimated using the second-power equation method (Kline and McClintock, 1953). The estimates for these experiments are comparable to previously reported values for both heat transfer and mass transfer studies, but are believed to be conservative.

Volume flow rate and duct Reynolds number (Re) uncertainties are estimated to be less than 10 percent for Re > 6000. The reported resolution of the LVDT is 0.00005 in. while the A/D board is reported to have an accuracy of 0.000078 in. in a 12 kHz acquisition rate, 16 bit resolution mode.

Experimental tests of accuracy and repeatability for the entire acquisition system indicate a sublimation depth uncertainty of 0.00015 in. Sublimation depths are maintained at about 0.006 in. by varying the duration of the experiment. This target depth was selected to minimize uncertainties in both depth measurement and changes in duct cross section area. These uncertainties were found to be 1 and 3 percent, respectively. The resulting experimental duration was between 90 minutes for Re=30,000 and 180 minutes for Re=5,000.

Vapor density uncertainty based on measured quantities is negligible for both wall and bulk values. Overall uncertainty in Sherwood number calculation is about 8 percent and varies slightly with Reynolds number (<1 percent).

Experimental Results

The experiments reported in this paper were performed with ribbed top and bottom walls and smooth side walls. Measurements were made for the following parameters (see Figure 2 for notation): rib height-to-hydraulic diameter ratio, $e/D = 0.1$ and vortex generator (rod) diameter-to-rib height ratio, $d/e = 0.78$. Rods are placed above all the ribs for $P/e = 21$, and over every other rib, beginning with the first one in the duct, for rib pitch-to-rib height ratio, $P/e = 10.5$. For $s/e=0.55$, rods are placed in both the inlet and outlet sections, but for $s/e = 1.0$ and 1.5, rods are placed only in the inlet section. Three different Reynolds numbers: 5,000, 10,000, and 30,000 were investigated for the rib only baseline and each of the three rod clearance ratios.

Along the centerline of each plate, 120 points are measured and these are used for the calculation of the bulk naphthalene vapor density. To obtain more detailed measurements in both the developing and fully developed regions of the walls, profile measurements on a 30 x 28 (streamwise x transverse) uniform grid are made in selected inter-rib modules.

Rib-Only Baseline Measurements

Figure 3 shows the centerline Sherwood number ratio in the inlet (radially inward leg) and the outlet (radially outward leg) sections for the rib-only baseline case at a Reynolds number of 30,000. Along the ribbed top and bottom walls (Figure 3a) periodic fully developed profiles are obtained after only a few inter-rib modules. Asymmetry between the top and bottom walls is present for most of the inlet, and is due to the asymmetry in the inlet flow profile. The asymmetry diminishes significantly in the last three inter-rib modules of the inlet duct and essentially vanishes in the outlet section. Peak Sherwood number ratios are typically between 3.0 and 3.25 in the inlet and between 2.75 and 3.0 in the outlet. These values remain nearly constant throughout the length of the section. The profiles typically have two peaks, one that occurs nearly 5-6 rib heights downstream of the rib and corresponds to reattachment, and the other that occurs just upstream of each rib and corresponds to a corner eddy upstream of the rib. These observations are consistent with those reported in the literature (e.g. Acharya et al., 1995a).

The centerline profiles for the smooth side walls qualitatively resemble the asymptotically decaying profiles (to fully developed values) observed for a smooth surface. However, a careful inspection shows small periodic undulations in the profile with the peaks in the vicinity of the ribs. These peaks appear to correlate directly with the peaks in the turbulence intensity profiles reported by Acharya et al. (1994). Sherwood number ratios for the

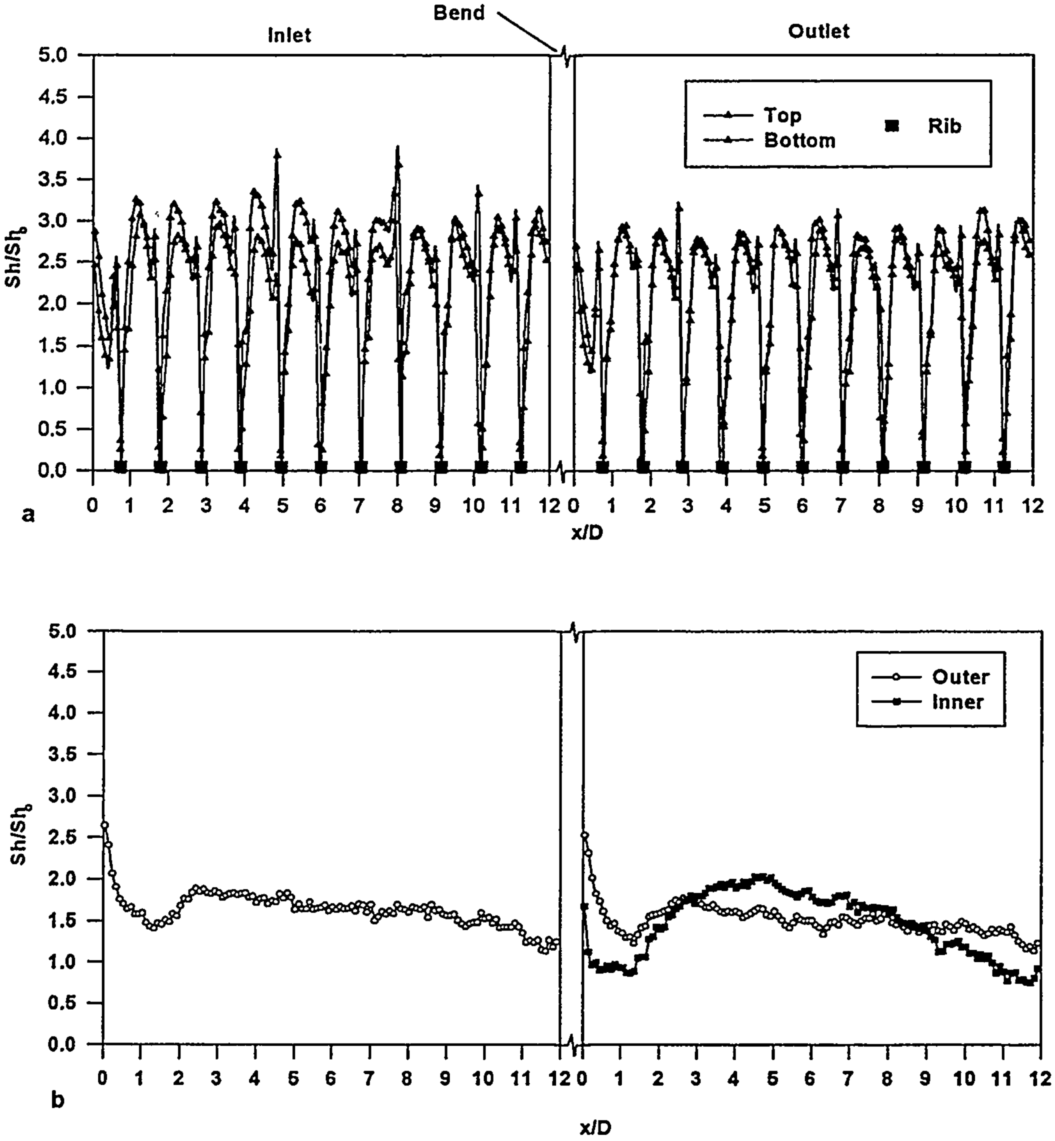

Figure 3. Centerline Sherwood Number Ratio Distribution for the Rib-only Baseline Case: Re = 30,000, P/e = 10.5

inlet are in the range of 1.5 - 2.0 over most of the plate. This nearly two-fold enhancement of centerline mass transfer over the purely smooth walls can be attributed to an increase in the turbulence levels caused by the ribs. The profiles in the outlet section show that immediately past the bend the Sherwood numbers along the outer wall are higher than those along the inner wall. This is presumably due to the effect of secondary flows induced by the bend and leads to a noticeable asymmetry between opposing walls in the first inter-rib module past the bend.

Detailed contours of Sherwood number ratio in the inlet section of the duct for the baseline case are shown in Figure 4. The developing region is depicted by the first two inter-rib spaces and the fully developed region is depicted by the last four inter-rib spaces. The asymmetry between opposing walls in the developing region, noted earlier in the centerline profiles, is quite evident in the contours. Asymmetry is dampened downstream indicating that the flow field induced in a rib-roughened duct quickly overwhelms the history of the inlet field. The fully developed mass transfer on the top and bottom walls clearly shows regions of separation, reattachment, redevelopment, and recirculation that, as noted earlier, have been previously reported in the literature based on centerline values. Sherwood number ratio in most of the separated region downstream of a rib is in the range of 1.0 to 2.0. A peak value in the vicinity of 3.0 occurs near the point of flow reattachment, and in the fully developed region, this peak is relatively uniform in the spanwise direction. Sherwood number ratios expectedly decrease downstream of reattachment. Just upstream of the rib appears to be a small but energetic eddy that, in the transverse direction, spans most of the rib and extends about one rib height upstream of the rib. Sherwood number ratios as high as 4 are noted in this region.

The Sherwood number ratios for the smooth side walls show similar asymmetry in the developing region, but this asymmetry persists throughout the duct. Contours in the fully developed region clearly show a periodically fully developed distribution on the outer wall. Local mass transfer near the ends of the ribs is very high ($Sh/Sh_o = 4$), but is restricted to the near vicinity of the rib. These localized regions of high mass transfer near the ribs correlate spatially with the peaks in the streamwise turbulence intensity measured in the vicinity of the ribs (Acharya et al., 1993, Acharya et al., 1994, Acharya et al., 1995a). Sherwood number ratios in the mid-span regions of the smooth walls are of the order of 2. This mass transfer enhancement on the side walls extends up to nearly 4 rib heights toward the mid-span of the plate, and is believed to result from an increase in turbulence levels caused by the ribs.

Local mass transfer for the baseline case in the outlet section is shown in Figure 5. As was suggested from centerline values, overall mass transfer is lower in the outlet section than in the inlet section. Top and bottom wall symmetry is excellent. Comparison of the inner and outer walls clearly shows the effects of the bend. Higher Sherwood numbers are observed on the outer surface relative to the values on the inner wall. Secondary flows induced by the bend are expected to drive the flow toward the outer wall resulting in higher Sherwood numbers along these walls as observed here.

Mass transfer distributions in the fully developed region of the outlet duct resemble those from the inlet duct, except that the peak values along the ribbed walls are 15-25%

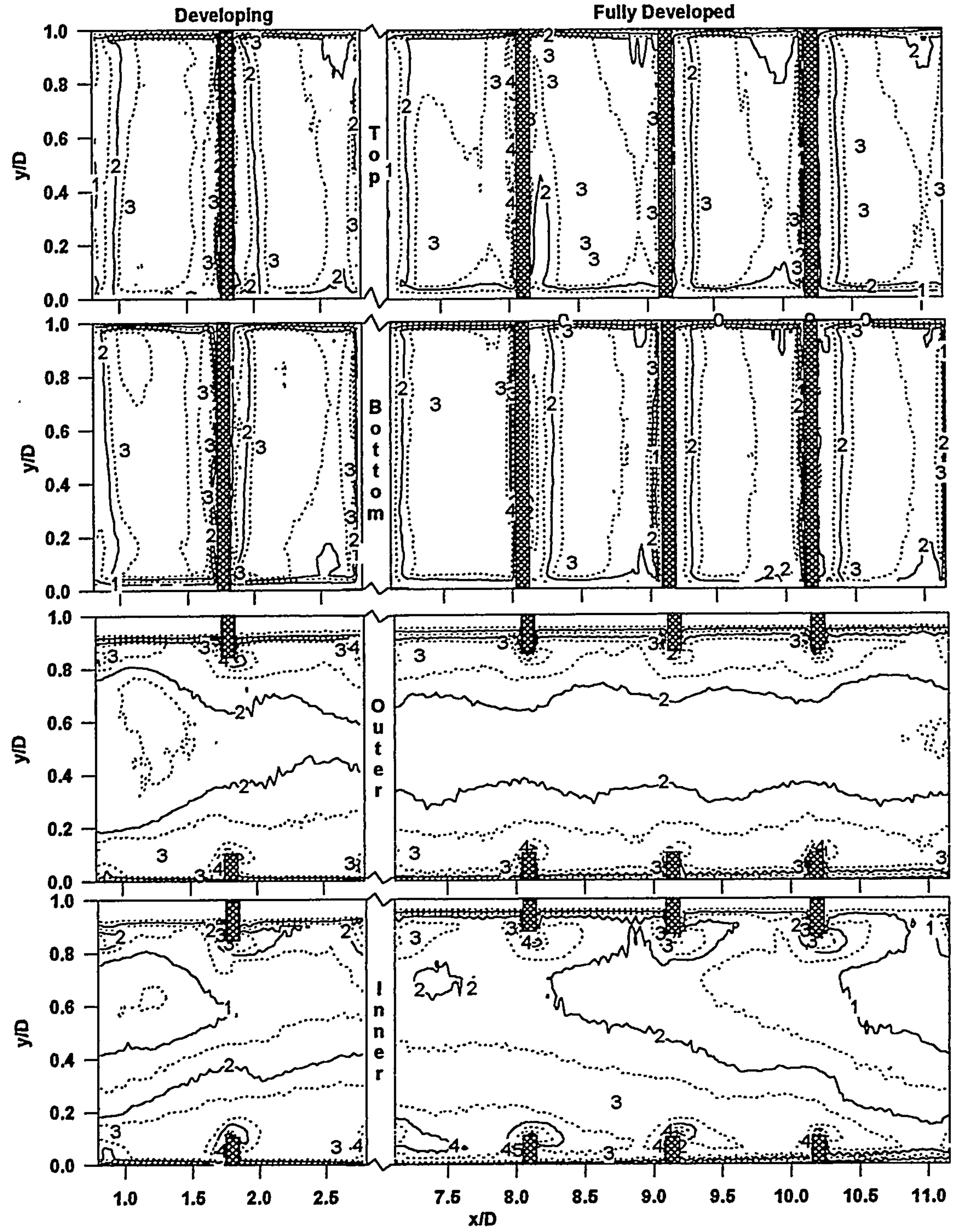

Figure 4. Detailed Sherwood Number Ratio Contours in the Inlet Section for the Baseline Case: Re = 30,000, P/e = 10.5

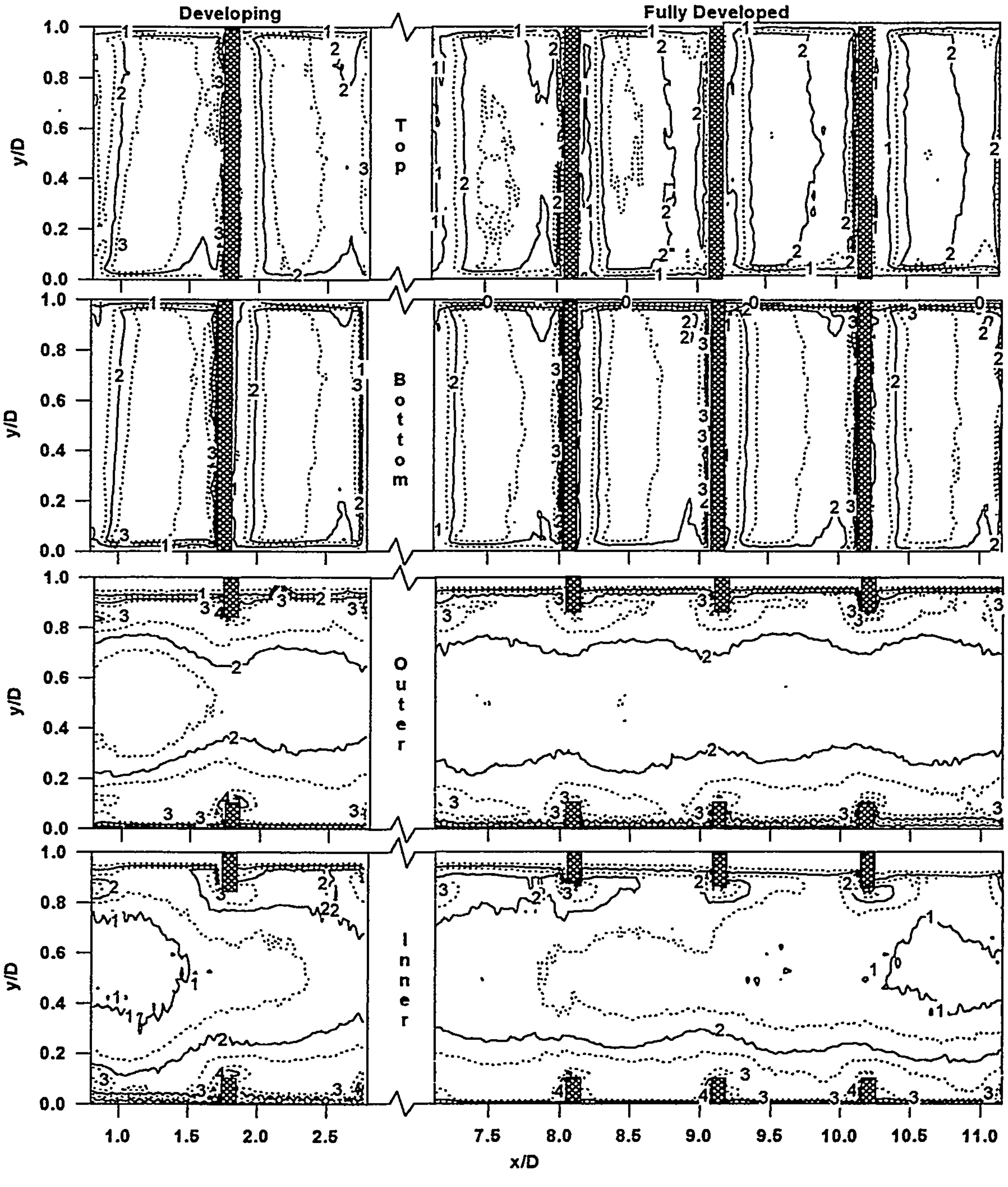

Figure 5. Detailed Sherwood Number Ratio Contours in the Outlet Section for the Baseline Case: Re = 30,000, P/e = 10.5

lower. The mass transfer distribution on the side walls is also similar to that in the inlet, but the region of augmentation ($Sh/Sh_o > 1$) is restricted to only about two rib heights.

Rib-Vortex Generator (Rod) Measurements

Centerline mass transfer distribution for both the rib only baseline and the s/e=0.55 rib-vortex generator spacing at P/e = 21 and Re=5,000 is shown in Figure 6. Mass transfer in the inlet duct is noticeably enhanced by the presence of vortex generators. In particular, the peak value upstream of each rib is consistently 1.5-2 times greater than the baseline rib-only values. In the first two inter-rib spaces, the profiles are similar in shape to the baseline profile, with the reattachment location appearing to be roughly at the same location (5-6 rib heights downstream of the rib). From the third inter-rib module onwards, the inter-rib Sherwood number profiles for the rib-rod cases appear to be more uniform, and suggests a delayed reattachment (10-15 rib heights downstream of the rib). However, these more uniform Sherwood numbers are generally higher than the rib-only values, and particularly so in the later regions of the inter-rib module. Presumably the rods enhance the inter-rib turbulence intensities and provide an overall increase in the mass (heat) transfer from the ribbed surface.

The outlet centerline Sherwood number distribution indicates that the enhancement of local mass transfer is not as pronounced as in the inlet. However, the same trends of generating a more uniform Sherwood number distribution in the inter-rib modules can be observed.

Centerline mass transfer distribution along the side walls in both the inlet and outlet sections show that vortex generators induce considerable enhancement (nearly 2-2.5 the rib-only value). It is believed that this enhancement is due to the horseshoe vortices shed behind the base of the rods and the associated increases in the turbulence levels. Overall, the presence of the rods seems to merely shift the mass transfer distribution upward, without altering the trends. Similar mass transfer behavior is seen in the outlet section.

Figure 7 presents the results at the lowest and highest Reynolds numbers studied (Re=5,000 and 40,000) and for the same P/e and s/e values in Figure 6. Only the fully developed region (the last inter-rib module in each section) is shown. The results, in the form of a mass transfer augmentation number, $N=Sh_{rib-rod}/Sh_{rib}$, are presented for each of the four walls in the inlet and outlet sections. At the lower Re value, mass transfer enhancement of the order of 50% is obtained along the smooth walls with peak enhancement as high as 80%. Along the ribbed top wall, there is an initial degradation for up to six rib heights followed by a substantial increase in mass transfer with peak N-values reaching 1.75. For Re=40,000, the behavior is similar, with centerline mass transfer along the smooth side walls enhanced by nearly 50% due to the presence of the vortex generators. Along the ribbed bottom wall of the inlet passage, the centerline N-values show about a 20% average increase in mass transfer, with a peak increase of nearly 40%. It is worth noting that these increases are primarily downstream of 8 rib heights from the rib, and that the maximum enhancement generally occurs just ahead of the rod-rib pair downstream. Along the top ribbed wall enhancement levels are similar to those along the bottom ribbed wall. In the outlet passage, enhancement in the ribbed wall mass transfer is observed over most of the streamwise extent of the inter-rib module, with a peak enhancement of nearly 50% for the bottom ribbed wall.

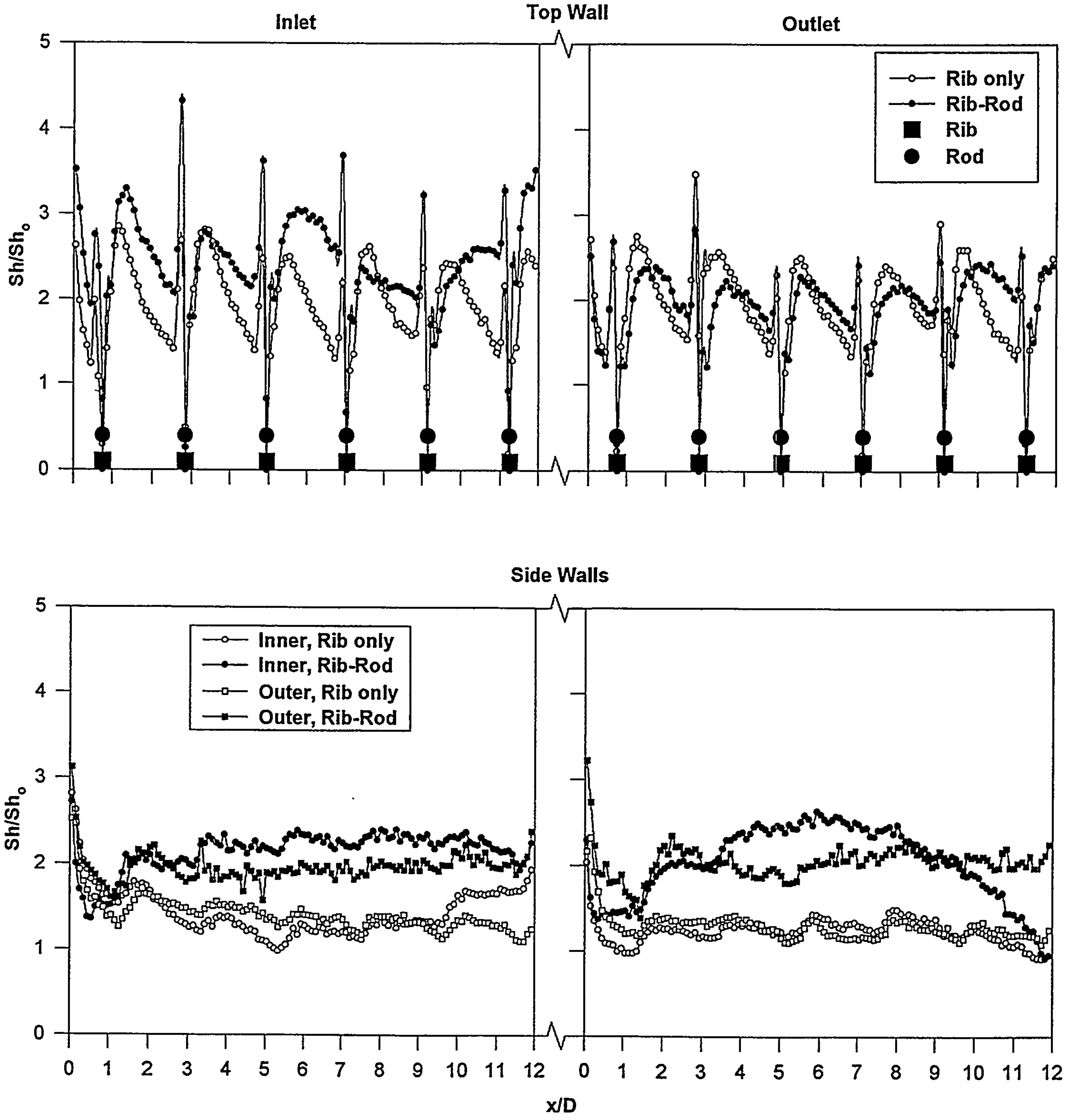

Figure 6. Comparison of Centerline Sherwood Number Ratio:
Re = 5,000, P/e = 21, s/e = 0.55

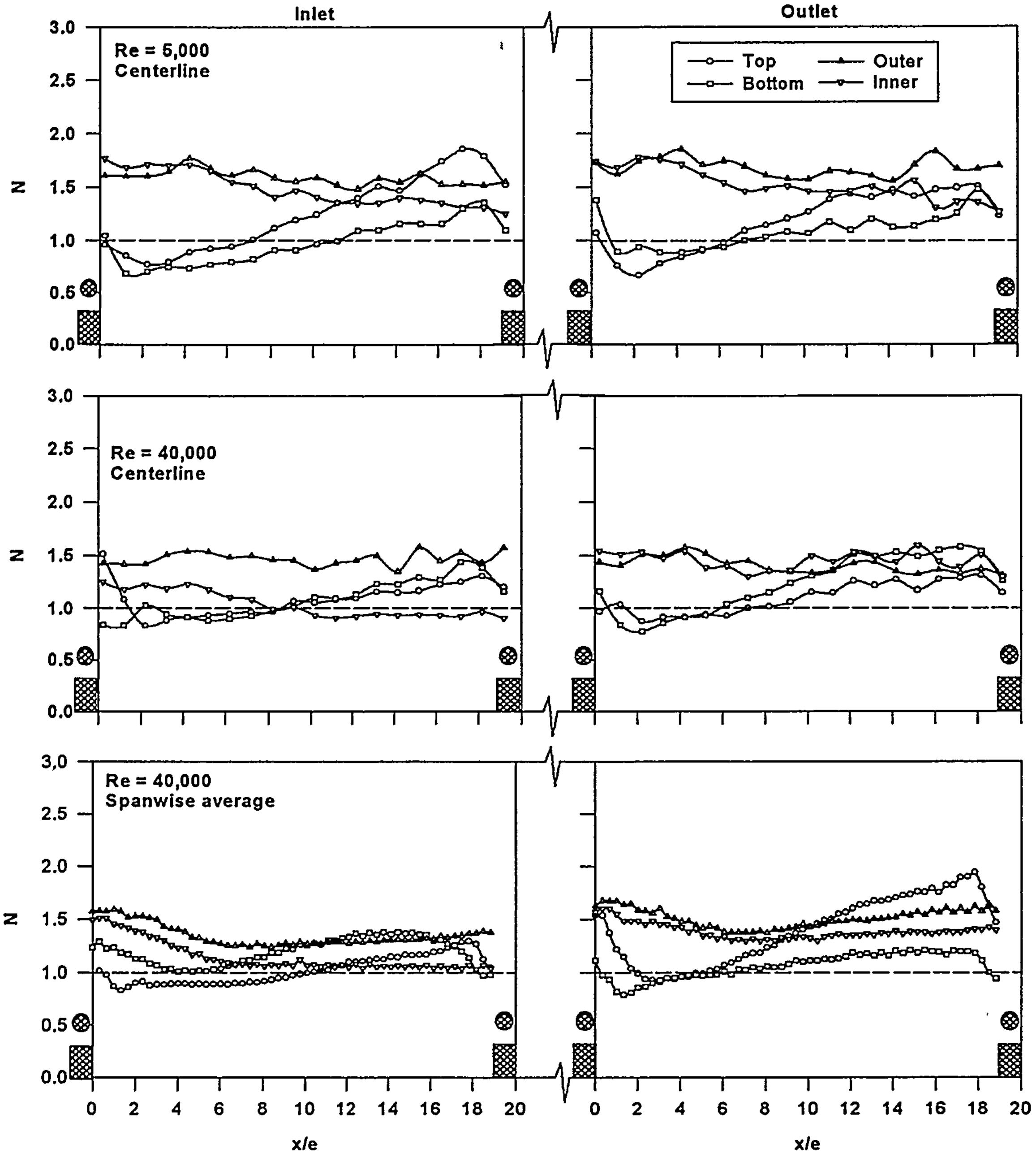

Figure 7. Fully Developed Centerline Mass Transfer Augmentation Number: P/e = 21, s/e = 0.55

To highlight the effects of the spanwise variations in the enhancements induced by the vortex generator, spanwise-averaged augmentation numbers are also presented for Re= 40,000. Spanwise averaged profiles of the mass transfer augmentation number expectedly have a smoother appearance than the centerline profiles. Spanwise averaged values for the side walls are consistent with the centerline, with average enhancements along the side walls that are typically of the order of 50% except for the inner wall of the inlet duct where the enhancements are somewhat lower. For the ribbed walls, the enhancement levels are somewhat lower in the outflow passage.

Contours of the local mass transfer augmentation numbers in a fully developed inter-rib module for all the walls is shown in Figure 8 for Re = 5,000, P/e = 21, and s/e = 0.55. As seen in Figure 6, there is enhancement in the second half of the inter-rib module, and degradation in the first half. It is clear from Figure 8, that on the top wall the enhancement (peak value of N is nearly 2) is greater than the degradation (minimum value is around 0.6), and that the spanwise profile is fairly uniform. Near the outer and inner walls, high values of N are noted. Along the bottom ribbed wall, the enhancement levels are lower. The side walls show significant enhancements (values of N as high as 2.75 can be seen) with the peak values centered in the wake of the vortex generator. The traces of N in the two wakes behind the vortex generators show that they are deflected away from the rib as the flow emerges from the rib-rod inter-space. The two wakes appear to merge downstream (at approximately 10 rib heights downstream of the rod); the wake effect on the mass transfer can be seen to persist through the entire inter-rib module.

Figure 9 shows the behavior at the lower P/e=10.5. Observations similar to those noted above can be made. Along the ribbed walls local regions of mass transfer degradation and enhancement can be seen, but overall the enhancement levels and coverage exceed the degradation. Mass transfer degradation levels are typically 20% while enhancements levels are typically in the 20-40% range.

Mass transfer contours for the side walls again clearly show the effect of vortex shedding behind the rods. In the wake region behind the rods, significant mass transfer enhancement is present. The inner wall seems to benefit more from the rods than the outer wall. This behavior may be explained by the scaling of local Sherwood numbers by those for the baseline. The “distinct” wake regions behind the rods on the outer wall seem to extend to about five rib heights and show enhancement of up to 100% before the two wake regions combine. In the region after the two wakes have combined, mass transfer enhancement is about 20 - 40%. The contours for the inner wall indicate that the wakes combine later and that enhancement is much greater--up to over 300%. Mass transfer near the centerline of both side walls is enhanced, even in the region between the wakes. Average enhancement for the side walls is approximately 40% over the entire inter-rib space.

Local mass transfer contours for s/e = 1.5 and Re = 10,000 and 30,000 are shown in Figure 10. Enhancement at higher Reynolds numbers is somewhat smaller than the enhancement at the lower Reynolds numbers. It is believed that the shear layers formed by the ribs and rods are much thinner at higher Reynolds numbers and thus do not influence the flow as much as they do at lower Reynolds numbers. For the ribbed walls, degradation up to 20% is observed while enhancement levels up to 40% are noted. The surface area with enhancement is again much larger than the area where degradation occurs. Along the side

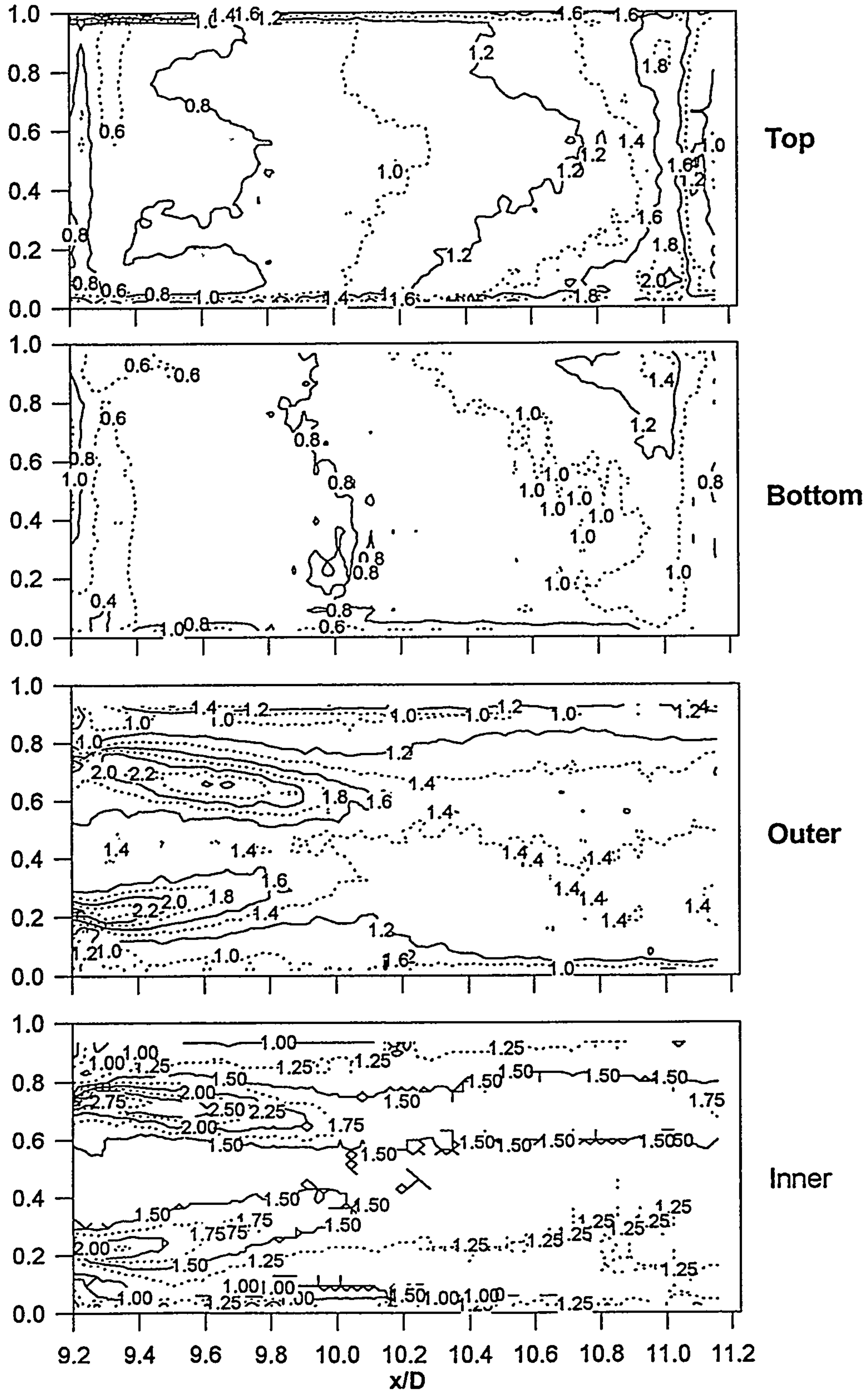

Figure 8. Detailed Mass Transfer Augmentation Numbers in the Fully Developed Inlet Section: Re = 5,000, P/e = 21, s/e = 0.55

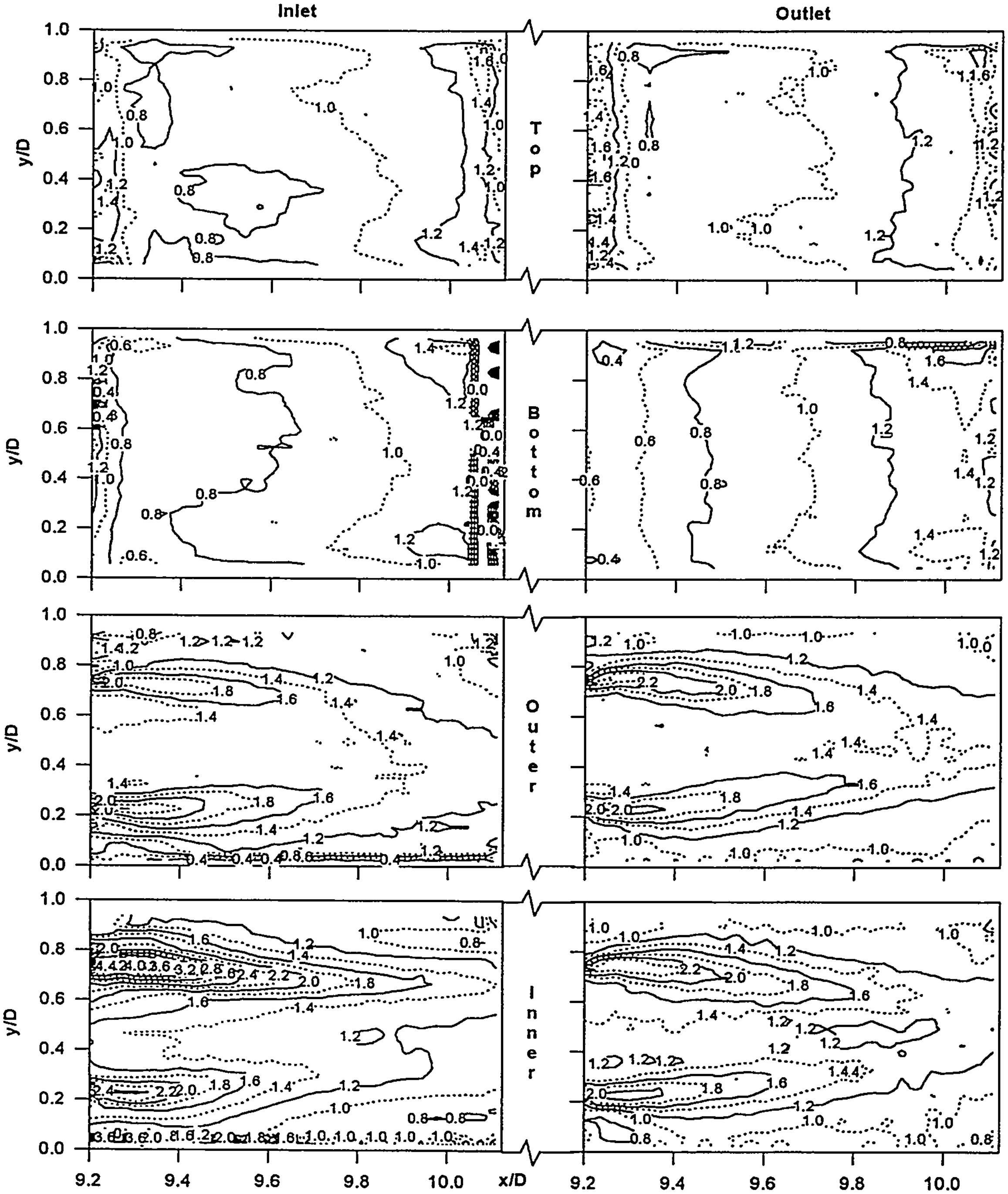

Figure 9. Detailed Fully Developed Mass Transfer Augmentation: Re = 5,000, s/e = 0.55

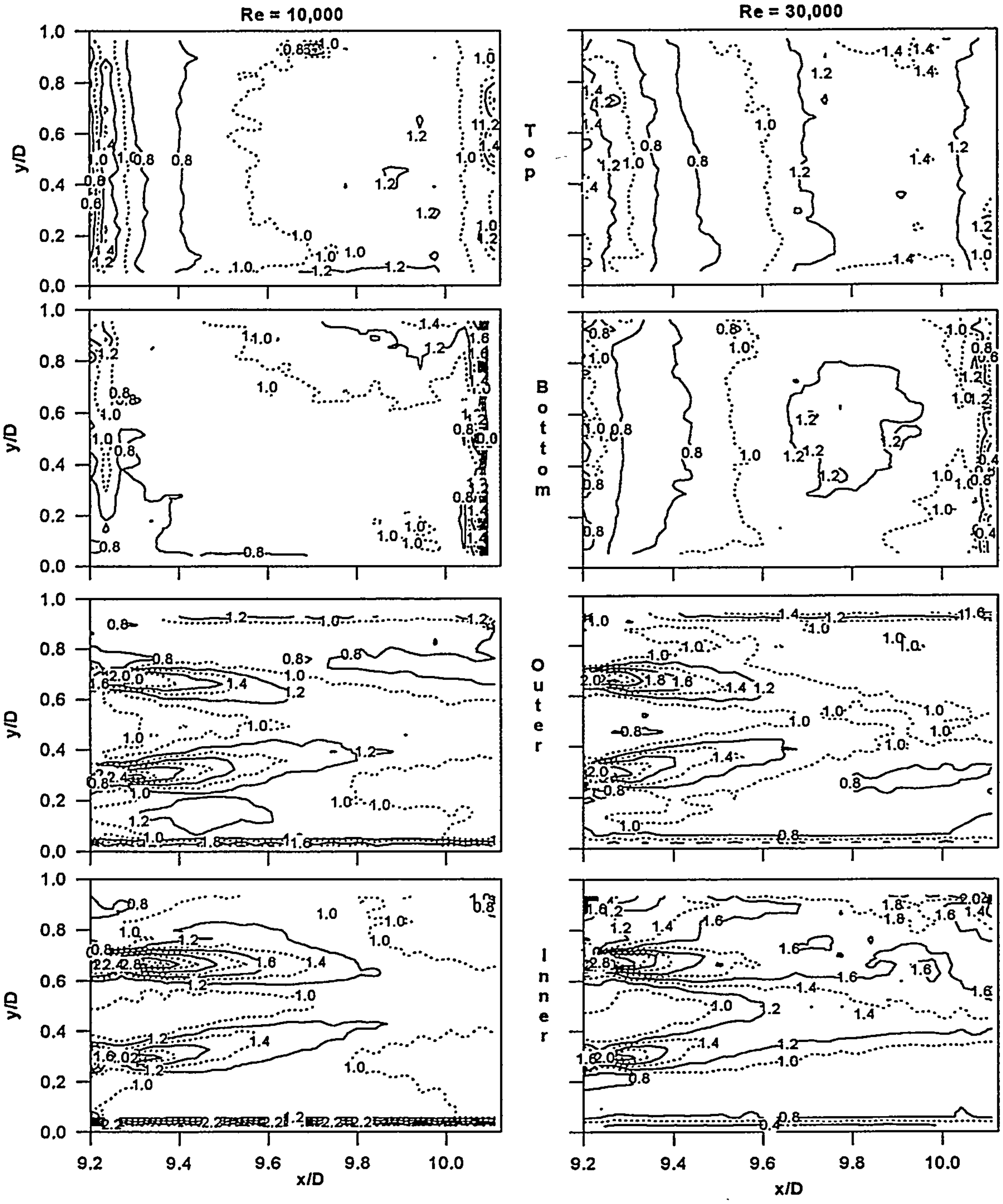

Figure 10. Effect of Reynolds Number on Fully Developed Mass Transfer Augmentation: s/e = 1.5

walls maximum enhancement levels are in the range of 2-2.8, but they are much more localized. Unlike the flow at lower Reynolds numbers, the merging of the two wakes is not apparent along the smooth walls of the inlet passage. In fact, in the midspan regions the augmentation number is typically 1, indicating no enhancement. Along the inner wall of the outflow passage, some wake interference can, however, be observed.

Concluding Remarks

An experimental study is made to measure the local Sherwood numbers in the internally ribbed passages of a square turbine blade coolant channel with a radially outward flow leg and a radially inward flow leg. The primary objective of the study is to examine if cylindrical vortex generators placed above the ribs can be used to enhance mass transfer from the surfaces. Measurements of the mass transfer include centerline and spanwise averaged profiles of Sherwood number ratios and corresponding contours in the developing and periodically developed regions. The following main conclusions are obtained.

1. Baseline rib-only results confirm the reported peaks in the Sherwood number in the vicinity of reattachment and just upstream of the rib where a strong corner vortex is formed. Along the smooth side walls, significant enhancement is obtained with the peak occurring in the vicinity of the rib. This peak correlates with the measured location of maximum turbulence intensity.

2. For the higher pitch case (P/e=21), significant enhancement due to the vortex generators is obtained along the ribbed walls in the developing region of the inflow passage. In the periodically developed region, the profile is more uniform, with degradation in the initial separated region and enhancement in the later regions of the inter-rib module. The enhancement levels and coverage substantially exceed the corresponding degradation quantities. Along the smooth walls, the horseshoe vortices in the wake of the vortex generator are associated with high levels of mass transfer enhancement. The wakes from each vortex generator are deflected away from the rib, and appear to merge downstream. The wake effect is seen to decrease somewhat with Reynolds number.

3. Spanwise average profiles in the developed regions indicate an average 50% increase in the mass transfer from the side walls due to the vortex-generators. Along the ribbed walls the average enhancement levels are lower. Local enhancement levels can be substantially higher--reaching values in the vicinity of 300% along the side walls.

4. For the lower pitch (P/e=10.5), the general behavior is the same as that for P/e=21. Enhancement levels are somewhat lower and the wake interference and merging effects along the side walls are weaker.

5. Future studies are directed at optimizing the vortex generator geometry and making measurements under rotating conditions.

Acknowledgment

This research was performed under a subcontract from the South Carolina Energy Research and Development Center to Louisiana State University (93-01-SR015). The contract monitors were Dr. Daniel Fant and Dr. Larry Golan. Their help is gratefully acknowledged.

References

1. Acharya, S., Myrum, T., and Inamdar, S., 1991, "The Effect of Subharmonic Flow Pulsation in a Ribbed Pipe: Flow Visualization and Pressure Measurements," AIAA Journal, Vol. 29, No. 9, pp. 1390-140.

2. Acharya, S., Dutta, S., Myrum, T., and Baker, R.S., 1993, "Periodically Developed Flow and Heat Transfer in a Ribbed Duct," Int. J. Heat and Mass Transfer, Vol. 36, No. 8, pp.2069-2082.

3. Acharya, S., Dutta, S., Myrum, T., and Baker, R.S., 1994, "Turbulent Flow Past a Surface Mounted Rib," J. Fluids Engng., Vol. 116, No. 2, pp. 238-246.

4. Acharya, S., Myrum, T., Sinha, S., and Qiu, X., 1995a, "Developing and Periodically Developed Flow, Temperature and Heat Transfer in a Ribbed Duct," ASME/JSME Thermal Engg. Conf., March 1995, Maui, Vol. 1, pp. 303-312; also Int. J. Heat Mass Transfer (accepted).

5. Acharya, S., Myrum, T.A., and Dutta, S., 1995b, "Heat Transfer in Turbulent Flow Past a Surface Mounted Two-Dimensional Rib," ASME Intl. Mech. Engg. Conf. and Expo., San Francisco, November 1995.

6. Durst, F., Founti, M., and Obi, S., 1988, "Experimental and Computational Investigation of the Two-dimensional Channel Flow over Two Fences in Tandem," *J. Fluids Engineering*, Vol. 110, pp. 48-54.

7. Garimela, S.V., and Eibeck, P.A., 1991, "Enhancement of Single Phase Convective Heat Transfer from Protruding Elements Using Vortex Generators," *Int. J. Heat Mass Transfer*, Vol. 34, No. 9, pp. 2431-2433.

8. Han, J.C., and Zhang, P., 1991, "Effect of Rib-Angle Orientation on Local Mass Transfer Distribution in a Three-pass Rib-roughened Channel," *J. Turbomachinery,* Vol. 113, pp. 123-130.

9. Humphrey, J.A.C, and Whitelaw, J.H., 1979, "Turbulent Flow in a Duct with Roughness," In *Turbulent Shear Flows 2*, (Ed. Bradbury et al.), Berlin, Springer-Verlag, pp. 174-188.

10. Hung, Y. H., and Lin, H.H., 1992, "An Effective Installation of Turbulence Promoters for Heat Transfer Augmentation in a Vertical Rib-heated Channel," *Int. J. Heat Mass Transfer*, Vol. 35, No. 1, pp. 29-42.

11. Karniadakis, G.E., Mikic, B.B., and Patera, A.T., 1988, "Minimum-Dissipation Transport Enhancement by Flow Destabilization: Reynolds' Analogy Revisited," *J. Fluid Mech.*, Vol. 192, pp. 365-391.

12. Kline, S.J., and McClintock, F.A., 1953, "Describing Uncertainties in Single-sample Experiments," *Mech. Engineering*, Vol. 75, No. 1, pp. 3-8.

13. Liou, T.M., Chang, Y., and Hwang, D.W., 1990, "Experimental and Computational Study of Turbulent Flows in a Channel with Two Pairs of Turbulence Promoters in Tandem," *J. Fluids Engineering*, Vol. 112, pp. 302-310.

14. Miller, R.W., 1989, *Flow Measurement Engineering Handbook*, 2nd. Ed., New York, McGraw-Hill Publishing Co.

15. Myrum, T.A., Acharya, S., Inamdar, S., and Mehrotra, A., 1992, "Vortex Generator Induced Heat Transfer Augmentation Past a Rib in a Heated Duct Air Flow," *J. Heat Transfer*, Vol. 114., pp. 280-284.

16. Myrum, T.A., Qiu, X., and Acharya, S., 1993, "Heat Transfer Enhancement in a Ribbed Duct Using Vortex Generators," *Int. J. Heat Mass Transfer,* Vol. 36, No. 14, pp. 3497-3508.

17. Myrum, T.A., and Acharya, S., 1994, "Enhanced Heat Transfer in Ribbed Ducts Using Vortex Generators," Final Report, GRI-94/0256.

18. Myrum, T.A., Acharya, S., Sinha, S., and Qiu, X., 1995, "The Effect of Placing Vortex Generators Above Ribs in Ribbed Ducts on the Flow, Flow-Temperature and Heat Transfer Behavior," J. Heat Transfer (in review).

19. Sogin, H.H., and Providence, R.I., 1958, "Sublimation from Disks to Air Streams Flowing Normal to Their Surfaces," *Transactions of the ASME*, Vol. 80, pp. 61-69.

20. Sparrow, E.M., and Tao, W.Q., 1983, "Enhanced Heat Transfer in a Flat Rectangular Duct with Streamwise-periodic Disturbances at One Principal Wall," *J. Heat Transfer*, Vol. 105, pp. 851-861.

21. Stearns, R.F., Johnson, R.R., Jackson, R.M., and Larson, C.A., 1951, *Flow Measurement with Orifice Meters*, Toronto, D. van Nostrand Co., Inc.

22. Wroblewski, D.E., and Eibeck, P.A., 1991, "Measurements of Turbulent Heat Transport in a Boundary Layer with an Embedded Streamwise Vortex," *Int. J. Heat Mass Transfer*, Vol. 34, No. 7, pp. 1617-1631.

23. Zukauskas, A., 1994, "Enhancement of Forced Convection Heat Transfer in Viscous Fluid Flows," *Int. J. Heat Mass Transfer*, Vol. 37, Suppl. 1., pp. 207-212.

P11 Rotational Effects on Turbine Blade Cooling

George J. Govatzidakis (617-253-3764)
Gerald R. Guenette (617-253-3764)
Jack L. Kerrebrock (617-253-3764)
Massachusetts Institute of Technology
Department of Aeronautics and Astronautics
77 Massachusetts Avenue
Cambridge, MA 02139

Abstract

An experimental investigation of the influence of rotation on the heat transfer in a smooth, rectangular passage rotating in the orthogonal mode is presented. The passage simulates one of the cooling channels found in gas turbine blades. A constant heat flux is imposed on the model with either inward or outward flow. The effects of rotation and buoyancy on the Nusselt number were quantified by systematically varying the Rotation number, Density Ratio, Reynolds number, and Buoyancy parameter. The experiment utilizes a high resolution infrared temperature measurement technique in order to measure the wall temperature distribution. The experimental results show that the rotational effects on the Nusselt number are significant and proper turbine blade design must take into account the effects of rotation, buoyancy, and flow direction.

The behavior of the Nusselt number distribution depends strongly on the particular side, axial position, flow direction, and the specific range of the scaling parameters. The results show a strong coupling between buoyancy and Corollas effects throughout the passage. For outward flow, the trailing side Nusselt numbers increase with Rotation number relative to stationary values. On the leading side, the Nusselt numbers tended to decrease with rotation near the inlet and subsequently increased farther downstream in the passage. The Nusselt numbers on the side walls generally increased with rotation. For inward flow, the Nusselt numbers generally improved relative to stationary results, but increases in the Nusselt number were relatively smaller than in the case of outward flow. For outward and inward flows, increasing the density ratio generally tended to decrease Nusselt numbers on the leading and trailing sides, but the exact behavior and magnitude depended on the local axial position and specific range of Buoyancy parameters. Similar trends of rotation were noted at a higher Reynolds number, although the Reynolds number effect was secondary compared to the rotational effects.

A momentum integral model of the flow in a heated rotating duct was also developed. It assumes a core flow with boundary layers along the duct walls. The Coriolis and buoyancy terms are maintained in the equations of motion, profiles are assumed for velocity and temperature and the resulting

---

Research supported by the U.S. Department of Energy, Morgantown Energy Technology Center, under AGTSR Subcontract No. 94-01-SR017 with Massachusetts Institute of Technology, Department of Aeronautics and Astronautics, 77 Massachusetts Avenue, Cambridge, MA, 02139; Fax: 617-258-6093.

differential equations are solved to give the variation of Nusselt number in the radial direction. A parametric study with the model shows that the model predicts the correct behavior of Nusselt number with rotation up to a Rotation number of 0.20 on both the leading and trailing sides.

P12 Manifold Methods for Methane Combustion

B. Yang (byang@mae.cornell.edu, 607-255-8270)
S. B. Pope (pope@mae.cornell.edu, 607-255-4314)
Upson Hall
Cornell University
Ithaca, NY 14853

1. Introduction

Great progresses have been made in combustion research, especially, the computation of laminar flames [1,2,3,4] and the probability density function (PDF) method in turbulent combustion [5,6,7]. For one-dimensional laminar flames, by considering the transport mechanism, the detailed chemical kinetic mechanism and the interactions between these two basic processes, today it is a routine matter to calculate flame velocities, extinction, ignition, temperature, and species distributions from the governing equations. Results are in good agreement with those obtained from experiments [8,9]. However, for turbulent combustion, because of the complexities of turbulent flow, chemical reactions, and the interaction between them, in the foreseeable future, it is impossible to calculate the combustion flow field by directly integrating the basic governing equations. So averaging and modeling are necessary in turbulent combustion studies. Averaging, on one hand, simplifies turbulent combustion calculations, on the other hand, it introduces the infamous closure problems, especially the closure problem with chemical reaction terms. Since in PDF calculations of turbulent combustion, the averages of the chemical reaction terms can be calculated, PDF methods overcome the closure problem with the reaction terms. It has been shown that the PDF method is a most promising method to calculate turbulent combustion [6]. PDF methods have been successfully employed to calculate laboratory turbulent flames: they can predict phenomena such as super equilibrium radical levels, and local extinction [7]. Because of these advantages, PDF methods are becoming used increasingly in industry combustor codes.

Although PDF methods have shown great promise in studying turbulent combustion, there is still a challenge to be overcome - coupling the detailed description of the turbulent combustion flow field provided by PDF methods with detailed chemical kinetic mechanisms. Suppose that $\phi(t)$ represents the composition of a particle in a PDF calculation of turbulent combustion. Then we need to calculate the increment in composition $\Delta\phi(t)$ over a time step Δt. In principal, this can be done by directly integrating the ordinary differential equations stemming from the detailed kinetic mechanism. But in practice, since a typical combustion system involves dozens of chemical species and hundreds of chemical reactions, and we need to do such integrations on the order of 10^9 times, the direct numerical integration of the equations would require huge amount of supercomputer time (several hundred days) and thus make it impossible in practical use. So simplifications of detailed kinetic mechanisms have been made in the

---

This work is supported by AGTSR Subcontract number 94-01-SR018 from the South Carolina Energy Research and Development Center, Research Manager Dr. Daniel B. Fant.

past in order to reduce the demand of computer time. Results from the calculations of simplified chemistry are tabulated as functions of a few variables. Then these tables are used in turbulent combustion calculations.

There are basically two different ways of doing the simplification of detailed chemistry: the reduced mechanism method [10,11,12] and the intrinsic low-dimensional manifold (ILDM) method [13]. For the reduced mechanism method, the simplification made to the detailed chemistry is achieved by the introducing steady-state assumptions for some species, usually the intermediate species, and the partial equilibrium assumptions for particular reactions. The reduced mechanism method has been employed in laminar flame calculations and in turbulent combustion calculations [7,14]. It has several disadvantages because of it's fundamental philosophy. For the reduced mechanism method, one needs to know in advance what species are in steady-state, and what reactions are in partial equilibrium. Reduced mechanism systems are derived manually from the given detailed chemistry. For different fuel/oxidizer systems, or even for the same fuel/oxidizer system under different conditions, different reduced mechanisms should be used. Thus it requires a considerable amount of human time and labor to develop such systems. Assumptions of partial-equilibrium and steady-state used in the reduced mechanism method are only valid in particular reaction ranges. Also the accuracy cannot be given and controlled.

The manifold method is based on a more intrinsic study of the chemical reaction process happening in combustion [13]. As it is observed, there is a wide range of time scales for chemical reactions, from 10^{-9} second to seconds. Fast reactions, or reactions with small time scales, quickly bring composition points down to attracting manifolds. Then composition points move along on manifolds. By assuming that the movement of the composition point away from manifolds to be zero, detailed chemistry can be simplified. The manifold method overcomes the drawbacks of the reduced mechanism method. It requires no preliminary knowledge of which chemical species are in steady-state and which chemical reactions are in partial equilibrium. The only given assumption is the dimension of the manifold. The manifold method has been successfully used in both laminar flames and turbulent combustion studies [7,14]. In these studies, a manifold with fixed dimension, for example, two dimensions, has been considered. The results from manifold calculations are tabulated in a pre-processing stage. Then the method of table-look-up is used in PDF calculations. There are still some difficulties and inconveniences:

- In general, it is not straightforward to parametrize the manifold.
- In different regions of the composition space, manifolds of different dimension are appropriate.
- The table generation (which is not fully automated) must be performed for each set of conditions of interest (fuel, pressure, equivalence ratio, etc.).
- The whole of the manifold is (wastefully) tabulated since it is not known *a priori* which regions are needed.

So a more efficient way is needed which can preserve the virtues of the manifold method and overcome these difficulties and inconveniences.

2. Objectives

Our objective is to develop a new method which can be used to study realistic chemistry in methane combustion with NO_x mechanism. The realistic chemistry used is a simplification to a more detailed chemistry based on the manifold method. The accuracy of the simplified chemistry can be controlled, and it is determined by the interaction between the transport process and the chemical reaction process, and the phenomena we are interested in.

3. Approaches

The new method developed here is called the "tree method." The basic idea of it is quite simple. It is shown in the following picture. As the PDF or partially stirred reactor (PaSR) calculations are performed, an unstructured table is generated, containing N pairs of compositions and their corresponding increments, $\{\phi^{(n)}, \Delta\phi^{(n)}, n = 1, 2, ..., N\}$. The table is stored in a tree structure that is initially empty (N=0). For each particle on each time step in the PDF or PaSR calculations, the increment $\Delta\phi$ is sought based on the particle's composition ϕ. The tree is searched for an entry $\phi^{(n)}$ close to ϕ. If one exists, then $\Delta\phi^{(n)}$ is used to approximate $\Delta\phi$. If a sufficiently close table entry does not exist, then $\Delta\phi$ is computed by the direct integration of equations from detailed chemistry, and the result is added to the table.

There are several key problems needed to be solved in the development of this new method. First, in the beginning stage, a partially stirred reactor needed to be constructed to provide composition particles and a tool for testing the new method. Second, for a complex chemistry like that of methane flames, the number of the pairs in the unstructured table may be very large for a required accuracy. So the way to search for a close entry $\phi^{(n)}$ to ϕ should be efficient. Third, we need to develop a method to couple reaction and mixing.

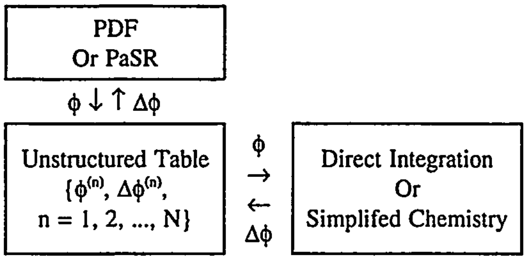

Figure 1. A Schematic Illustration of the Method

3.1 Partially Stirred Reactor

A partially stirred reactor, as shown in the following picture, has M particles, or L = M/2 pairs of particles. For convenience, all particles in the PaSR are initialized to the complete combustion condition (for methane-air combustion, only N_2, H_2O, and CO_2 exist under the complete combustion condition) at the beginning. After time step Δt, there are $m_{out} = L\Delta t/\tau_{res}$ pairs of particles flow out of the reactor, where τ_{res} is the residence time. Randomly choose $m_{pair} = L\Delta t/\tau_{pair}$ pairs of particle and put them in the candidate pile. Here τ_{pair} is a time scale of pairing. There are $m_{in} = m_{out}$ pairs of particles flowing into the PaSR, and they pair randomly with the particles in the candidate pile. Then mixing occurs between pairs of particles.

3.2 The Method for Generating An Unstructured Table

The ideas of the method for generating an unstructured table are the followings. The composition space is covered by cells. There are two kinds of cells - the coarse cells (of different sizes) and the fine cells (of different sizes). There is a single composition point

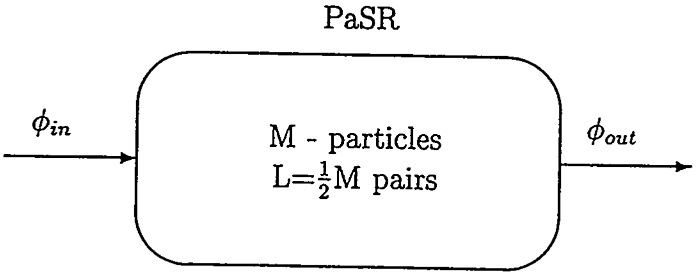

Figure 2. A Partially Stirred Reactor

that represents a cell. For a fine cell, all increments of compositions of points in the cell are accurately represented by the increment of the representative cell point. For a given composition point, the cells are searched based on the indexes of the components of the composition. These indexes are determined by the expected accuracy. If the indexes match the indexes of a composition point in the unstructured table, then the value of the increment of this point is returned. Otherwise, the given composition point is added to the table and the increment is calculated.

3.3 Coupling Mixing and Reaction in Intrinsic Low-Dimensional Manifolds

As it will be shown in the section of accomplishments and applications, particles away from manifolds quickly relax to manifolds due to the fast chemical reactions. So we base our calculations on the particles on manifolds. The following section describes the method, for a given particle, how to find the closest manifold point of it.

3.3.1 The Closest Manifold Point

Let the composition of a particle be $\phi = \{Y_1, Y_2, ..., Y_{ns}, h\}^T$, where Y_i, i = 1, 2, ..., n_s, is the mass fraction of species i, n_s is the number of species, and h is the specific enthalpy. Let $n = n_s + 1$ be the dimension of ϕ. The evolution of ϕ is determined by the equation:

$$\frac{d\phi}{dt} = S \ , \qquad (1)$$

where S is the source term due to chemical reactions. For a given particle $\phi^{(0)}$, the closest manifold point $\phi^{(m)}$ is defined as follows. At the manifold point $\phi^{(m)}$, let

$$W = \begin{bmatrix} W^s \\ W^f \end{bmatrix}$$

be the matrix such that, $\hat{\phi}^s = W^s\phi$ is in the slow subspace, and $\hat{\phi}^f = W^f\phi$ is in the fast subspace [13,14] (these subspaces are defined in terms of the eigenvalues λ_i and the eigenvectors of the Jacobian matrix J, $J_{\alpha,\beta} = \partial S_\alpha(\phi)/\partial\phi_\beta$). The dimension of the slow subspace, m_s, is determined by the given flow time scale τ^*, which means that the eigenvalues of the slow subspace, $\lambda_i > -1/\tau^*$, i = 1, 2, ..., m_s. The dimension of the fast subspace is $m_f = n - m_s$. Suppose that W^e is a matrix determining the element conservation, then the closest manifold point $\phi^{(m)}$ is determined by solving the following problem:

Minimize the 2-norm of $\phi^{(m)} - \phi^{(0)}$, subject to the following conditions:

$$W^e(\phi^{(m)} - \phi^{(0)}) = 0, \qquad (2)$$

$$W^f S(\phi^{(m)}) = 0, \qquad (3)$$

$$\phi_i \geq 0, \ i = 1, 2, ..., n_s. \qquad (4)$$

These equations are solved by the iteration method. Let $\phi^{(i)}$ be the estimate of $\phi^{(m)}$ after the i-th iteration, the next iteration is

$$\phi^{(m)} \simeq \phi^{(i+1)} = \phi^{(i)} + \delta\phi^{(i)} \equiv \phi^{(0)} + \Delta\phi^{(i)}.$$

With W evaluated at $\phi^{(i)}$, linearize Eq. 3 around $\phi^{(i)}$, write the equations in terms of $\Delta\phi^{(i)}$, Eqs. 2 and 3 become

$$W^{c}\Delta\phi^{(i)} = 0, \tag{5}$$

$$[W^{f}J]\Delta\phi^{(i)} = W^{f}\{J(\phi^{(i)} - \phi^{(0)}) - S(\phi^{(i)})\}. \tag{6}$$

Eqs. 5 and 6 are underdetermined. Generally, they are solved by the singular value decomposition method to get a minimum norm solution [15]. If a solution with negative mass fractions is found (in violation of conditions Eq. 4) then, we use the quadratic programming method [16,17] to get the minimum norm solution for Eqs. 5 and 6 under constraints (4).

3.3.2 Coupling Mixing and Reaction in Manifolds

This section describes how the coupling of mixing and reactions are treated to get the value of $\phi^{(0)}(t + \Delta t)$ for a given particle, $\phi^{(0)}(t)$. For ease of exposition, we use eigenvector basis vectors, in practical calculations, orthonormal bases for the subspaces are used.

At the beginning of the time step (from $t = 0$ to $t = \Delta t$), $\phi^{(0)}$ is close to the manifold: any departure of $\phi^{(0)}$ from the manifold is due to manifold curvature and the non-zero time step Δt. Denote the pairing particle of $\phi^{(0)}$ by $\phi_p^{(0)}$, perform the mixing:

$$\frac{d\phi^{(0)}}{dt} = (\phi_p^{(0)})/\tau_{mix}, \tag{7}$$

$$\frac{d\phi_p^{(0)}}{dt} = (\phi^{(0)} - \phi_p^{(0)})/\tau_{mix}, \tag{8}$$

where τ_{mix} is the mixing time scale. Solving Eqs. 7 and 8, we can get $\phi_{mix}^{(0)}(t+\Delta t)$ due to the mixing. This value is used to define the "mixing vector," F:

$$F \equiv \left[\phi_{mix}^{(0)}(t + \Delta t) - \phi^{(0)}\right] / \Delta t. \tag{9}$$

Let $\phi^{(m)}$ represent the closest manifold point to $\phi^{(0)}$. At $\phi^{(m)}$, calculate the projection matrix P,

$$P = \begin{bmatrix} P^{s} \\ P^{c} \\ P^{f} \end{bmatrix} \tag{10}$$

such that for any vector x

$$Px = \begin{bmatrix} \hat{x}^{s} \\ \hat{x}^{c} \\ \hat{x}^{f} \end{bmatrix} \tag{11}$$

where $\hat{x}^{s}$, $\hat{x}^{c}$, $\hat{x}^{f}$ are the components of x in the eigenvector bases of the "slow reactive," "conserved," and "fast reactive" subspaces. The equation coupling reaction and mixing is,

$$\frac{d\phi}{dt} = S(\phi) + F. \tag{12}$$

Linearize it about $\phi^{(m)}$,

$$\frac{d}{dt}\delta\phi = S^{(m)} + J\delta\phi + F, \tag{13}$$

where

$$\delta\phi \equiv \phi - \phi^{(m)}, \tag{14}$$

$$S^{(m)} = S(\phi^{(m)}), \tag{15}$$

and J is the Jacobian matrix,

$$J_{\alpha\beta} = \left[\frac{\partial S_\alpha(\phi)}{\partial \phi_\beta}\right]_{\phi^{(m)}}. \tag{16}$$

Transform Eq. 12 by premultiplying it by P:

$$P\frac{d}{dt}\delta\phi = \frac{d}{dt}P\delta\phi =$$

$$\frac{d}{dt}\begin{bmatrix}\delta\hat{\phi}^s\\ \delta\hat{\phi}^c\\ \delta\hat{\phi}^f\end{bmatrix} = \begin{bmatrix}\hat{S}^m\\ 0\\ 0\end{bmatrix} + \begin{bmatrix}\Lambda^s\\ 0\\ \Lambda^f\end{bmatrix}\begin{bmatrix}\delta\hat{\phi}^s\\ \delta\hat{\phi}^c\\ \delta\hat{\phi}^f\end{bmatrix} + \begin{bmatrix}\hat{F}^s\\ \hat{F}^c\\ \hat{F}^f\end{bmatrix}. \tag{17}$$

Note that the "conserved" components of $S^{(m)}$ and Λ are zero, by virtue of the conservation properties. The "fast" component of $S^{(m)}$ is zero by definition of the manifold.

For the "slow" and "conserved" components, Eq. 17 is to be integrated for a time step Δt from the initial condition,

$$\delta\phi(0) = \phi^{(0)} - \phi^{(m)}. \tag{18}$$

The "fast" components are set to

$$\delta\hat{\phi}^f(\Delta t) = 0, \tag{19}$$

so that the final result $\phi(\Delta t)$ is close to the manifold (i.e., it has no component in the fast subspace at $\phi^{(m)}$).

For the conserved component we have,

$$\frac{d}{dt}\delta\hat{\phi}^c = F^c, \tag{20}$$

and so the solution is

$$\begin{aligned}\delta\hat{\phi}^c(\Delta t) &= \delta\hat{\phi}^c(0) + \hat{F}^c\Delta t\\ &= P^c\{(\phi^{(0)} - \phi^{(m)}) + (\phi^{(1)} - \phi^{(0)})\}\\ &= P^c\{\phi^{(1)} - \phi^{(0)}\}.\end{aligned} \tag{21}$$

The second step follows from the definition of F, and the third from the constraint that $P\phi^{(m)} = P\phi^{(0)}$. Thus, as expected, the conserved components in mixing are unaffected by reactions.

For a slow reactive component α, Eq. 17 is

$$\frac{d}{dt}\delta\hat{\phi}^s_\alpha = \hat{S}^{(m)}_\alpha + \hat{F}^s_\alpha + \lambda^s_\alpha\delta\hat{\phi}^s_\alpha. \tag{22}$$

This has the analytic solution

$$\delta\hat{\phi}^s_\alpha(\Delta t) = a_\alpha\delta\hat{\phi}^s_\alpha(0) + b_\alpha\left[\hat{S}^m_\alpha + \hat{F}^s_\alpha\right], \tag{23}$$

where

$$a_\alpha = e^{\lambda^s_\alpha\Delta t}, \tag{24}$$

$$b_\alpha = (e^{\lambda^s_\alpha\Delta t} - 1)/\lambda^s_\alpha, \tag{25}$$

For positive λ^s_α, the approximate solution,

$$\delta\hat{\phi}^s_\alpha(\Delta t) = \delta\hat{\phi}^s_\alpha(0) + \Delta t\left[\hat{S}^m_\alpha + \hat{F}^s_\alpha\right], \qquad (26)$$

is used. This is corresponding to $a_\alpha = 1$, $b_\alpha = \Delta t$.

For a given Δt, whatever basis is used for the slow subspace, because Eq. 13 is linear, the solution can be written as,

$$\delta\hat{\phi}^s_\alpha(\Delta t) = A\delta\hat{\phi}^s_\alpha(0) + B\left[\hat{S}^m_\alpha + \hat{F}^s_\alpha\right], \qquad (27)$$

In the eigenvector basis, $A = \mathrm{diag}\{a_\alpha\}$, $B = \mathrm{diag}\{b_\alpha\}$.

Let ϕ^R be the exact solution to

$$\frac{d\phi}{dt} = S(\phi), \qquad (28)$$

from initial condition $\phi^{(m)}$, integrated for a time Δt, and define

$$\Delta\phi^R = \phi^{(R)} - \phi^{(m)}, \quad \Delta\hat{\phi}^R = P^s\Delta\phi^R. \qquad (29)$$

Observe that the solution to the linearized system Eq. 27 for the same case is

$$(\Delta\hat{\phi}^R)_{\mathrm{linearized}} = B\hat{S}^{(m)}, \qquad (30)$$

(see Eq. 27). It is preferable to use the exact result. Hence Eq. 27 can be replaced by

$$\delta\hat{\phi}^s(\Delta t) = \Delta\hat{\phi}^R + A\delta\hat{\phi}^s(0) + B\hat{F}^s. \qquad (31)$$

Let

$$P^{-1} = Q = \left[Q^s\ Q^c\ Q^f\right]. \qquad (32)$$

Then the final result is

$$\phi(t+\Delta t) = \phi^{(m)} + \delta\phi(\Delta t) = \phi^{(m)} + P^{-1}\begin{bmatrix}\delta\hat{\phi}^s(\Delta t)\\ \delta\hat{\phi}^c(\Delta t)\\ 0\end{bmatrix}$$

$$= \phi^{(m)} + Q^s\delta\hat{\phi}^s(\Delta t) + Q^c\delta\hat{\phi}^c(\Delta t). \qquad (33)$$

4. Project Description

The work of this 2-year project is divided into the following parts:

1. Design a partially stirred reactor to provide sample points and integrate the governing equations of mixing and reaction simultaneously,
2. Introduce a method to treat chemical reactions and perform the coupling of mixing and reaction,
3. Find an efficient way of tabulation,
4. Perform tests to determine the accuracies and parameters used by the method,
5. Apply the new method to PDF calculations of turbulent methane combustions.

At the present stage, as discussed in Part 3, most work on Parts 1-3 has been done. We have a partially stirred reactor and a code to do the direct integration of the governing equations of mixing and reactions. The method to treat chemical reactions and perform the coupling of mixing and reaction was discussed in Section 3.3.2. The method is based on the manifold method, and the closest manifold point is used to do the mixing and reaction. The tabulation method is described in Section 3.2. In order to determine the accuracies and parameters, we need to do some tests: PaSR tests - both for single particle and multiple particles (say 100 particles), using direct numerical integration; tests of the coupling model of mixing and reaction to measure errors and determine quantities used in tabulation; tests of tabulation, given a required accuracy, determine the cell-size criterion.

5. Accomplishments and Applications

The chemical kinetic mechanism used in calculations is shown in Table 1. It does not include the NO_x chemistry at the present.

In PaSR calculations, the incoming particles to the PaSR are methane/air mixtures at stoichiometric condition. The particles in the PaSR are initialized to the complete combustion - only CO_2, H_2O, and N_2 exist. Particles in the partially stirred reactor are arranged in pairs. Suppose that i'th and (i+1)'th particles are of a pair, the evolution of the particles are determined according to the following governing equations:

$$\frac{d\phi^{(i)}}{dt} = S + (\phi^{(i+1)} - \phi^{(i)})/\tau_{mix}, \qquad (34)$$

$$\frac{d\phi^{(i+1)}}{dt} = S + (\phi^{(i)} - \phi^{(i+1)})/\tau_{mix}, \qquad (35)$$

here S is the source term due to chemical reactions. In calculations, the mixing time scale $\tau_{mix} = 10^{-4}$ second, the pairing time scale $\tau_{pair} = 10^{-4}$ second, the residence time scale $\tau_{res} = 10^{-3}$ second. There are 100 particles in the partially stirred reactor, the time step $\Delta t = 6 \times 10^{-5}$ second, the pressure is 1 atmosphere.

From direct integrations of Eqs. 34 and 35, the changes of the average mass fractions as functions of time are shown in Figs. 3-6. It can be seen that after about four residence times, the particles in the PaSR reach a statistically steady condition. For the first particle in the PaSR, the change of the mass fraction of water is plotted in Fig. 7. One interesting thing to note is that it reaches zero at time step 72, which means that this particle flow out of the PaSR at time step 72, corresponding to time = 4.32×10^{-3} second.

From the PaSR calculations, we have an ensemble of particles. Investigations have been done to study the chemical process which relaxes the particles to manifolds. Randomly choose particles from the PaSR calculations, plot the distances of particles from the corresponding manifold points, d, and the dimensions of the manifolds, m. They are illustrated in Figs. 8-13. In these figures, the solid lines represent the distances, and the dashed lines represent the dimensions. The figures show that the particles quickly relax to the corresponding manifolds. The typical time scale of such a relaxation process is on the order of 10^{-4} second, which is much smaller than a typical mixing process which has a time scale on the order of 10^{-3} second. So it would be a good assumption to assume that processes occur on manifolds.

The closest manifold points are calculated for the particles of the ensemble from calculations of the partially stirred reactor. The time scale τ^* equals 10^{-4} second. Fig. 14 shows the number of particles as a function of the dimensions of manifolds. One can see that most points are concentrated on low dimensional manifolds.

Table 1. Chemical Kinetic Mechanism*

No.	Reaction	A_n	n	E_n
1	H + 02 = OH + O	1.59E+17	-0.927	16874.
2	O + H2 = OH + H	3.87E+04	2.70	6262.
3	OH + H2 = H2O + H	2.16E+08	1.51	3430.
4	OH + OH = O + H2O	2.10E+08	1.40	-397.
5	H + H + M = H2 + M	6.40E+17	-1.0	0.
6	H + OH + M = H2O + M	8.40E+21	-2.00	0.
7	H + 02 + M = HO2 + M	7.00E+17	-0.80	0.
8	HO2 + H = OH + OH	1.50E+14	0.0	1004.
9	HO2 + H = H2 + 02	2.50E+13	0.0	693.
10	HO2 + O = 02 + OH	2.00E+13	0.0	0.
11	HO2 + OH = H2O + 02	6.02E+13	0.0	0.
12	H2O2 + M = OH + OH + M	1.00E+17	0.0	45411.
13	CO + OH = CO2 + H	1.51E+07	1.3	-758.
14	CO + O + M = CO2 + M	3.01E+14	0.0	3011.
15	HCO + H = H2 + CO	7.23E+13	0.0	0.
16	HCO + O = OH + CO	3.00E+13	0.0	0.
17	HCO + OH = H2O + CO	1.00E+14	0.0	0.
18	HCO + 02 = HO2 + CO	4.20E+12	0.0	0.
19	HCO + M = H + CO + M	1.86E+17	-1.0	16993.
20	CH2O + H = HCO + H2	1.26E+08	1.62	2175.
22	CH2O + O = HCO + OH	3.50E+13	0.0	3513.
23	CH20 + OH = HCO + H2O	7.23E+05	2.46	-970.
24	CH20 + 02 = HCO + HO2	1.00E+14	0.0	39914.
25	CH20 + CH3 = HCO + CH4	8.91E-13	7.40	-956.
26	CH20 + M = HCO + H + M	5.00E+16	0.0	76482.
27	CH3 + O = CH20 + H	8.43E+13	0.0	0.
28	CH3 + OH = CH20 + H2	8.00E+12	0.0	0.
29	CH3 + 02 = CH3O + O	4.30E+13	0.0	30808.
30	CH3 + 02 = CH2O + OH	5.20E+13	0.0	34895.
31	CH3 + HO2 = CH3O + OH	2.28E+13	0.0	0.
32	CH3 + HCO = CH4 + CO	3.20E+11	0.50	0.
33	CH4 + H = CH3 + H2	7.80E+06	2.11	7744.
34	CH4 + O = CH3 + OH	1.90E+09	1.44	8676.
35	CH4 + 02 = CH3 + HO2	5.60E+12	0.0	55999.
36	CH4 + OH = CH3 + H2O	1.50E+06	2.13	2438.
37	CH4 + HO2 = CH3 + H2O2	4.60E+12	0.0	17997.
38	CH3O + H = CH2O + H2	2.00E+13	0.0	0.
39	CH3O + OH = CH2O + H2O	5.00E+12	0.0	0.
40	CH3O + 02 = CH2O + HO2	4.28E-13	7.60	-3528.
41	CH30 + M = CH20 + H + M	1.00E+14	0.0	25096.

* Rate constants are in the form $k_n = A_nT^n\exp[-E_n/(\hat{R}T)]$, here $\hat{R}$ is the universal gas constant. Units are moles, cubic centimeters, seconds, Kelvins, and kJ/mole.

The complex tabulation method was tested for a simple function on a domain. This method was also used to tabulate the particles from the ensemble of PaSR calculations. It worked well for both cases. Further tests are needed.

Compared with the reduced mechanism method, the manifold method, and the tabulation method used before, the new method overcomes the drawbacks of the reduced mechanism method and preserves the advantages of the manifold method. The difficulties and inconveniences with the manifold method no longer exist in the new method because the dimensions of manifolds can be changed, the table is unstructured so that the manifolds do not have to be parametrized, the table is generated in situ as the PDF calculations is in progress so only the required regions are tabulated. Accuracy is achieved by specifying the size of the cell, which can be controlled. With all these advantages and it's high flexibilities, the new method will be a valuable toll for turbulent combustion calculations under various conditions.

6. Future Activities

In the future, we will test the method of coupling mixing and reaction against direct numerical integrations, determine the errors and the quantities that will be used in tabulation. Single particle calculation will be used to determine the effect of cell size on accuracy and storage in calculations using the tabulation method. The chemical kinetic mechanism will include NO_x chemistry.

Once we have all the information about accuracies, and control quantities, the new method will be applied to PaSR calculations to determine the overall performance. Finally, it will be implemented it to PDF calculations of turbulent methane combustion.

References

1. Smooke, M. D., Solution of Boundary-Stabilized Premixed Laminar Flames by Boundary Value Methods. *Journal of Computational Physics*, 48: 72-105, 1982.
2. Smooke, M. D., Error Estimate for the Modified Newton Method With Applications to the Solution of Nonlinear, Two-Point Boundary Value Problems. *Journal of Optimization Theory and Application*, Vol. 39, No. 4, pp. 489-511, 1983.
3. Smooke, M. D., Miller, J. A., and Kee, R. J., Solution of Premixed and Counterflow Diffusion Flame Problems by Adaptive Boundary Value Method. In *Numerical Boundary Value ODEs*, U. M. Ascher and R. D. Russell Eds., Birkhauser, Basel, 1985.
4. Dixon-Lewis, G., David, T., Gaskell, P. H., Fukutani, S., Jinno, H., Miller, J. A., Kee, R. J., Smooke, M. D., Peters, N., Effelsberg, E., Warnatz, J., and Behrendt, F., Calculation of the Structure and Extinction Limit of a Methane-Air Counterflow Diffusion Flame in the Forward Stagnation Region of a Porous Cylinder. *Twentieth Symposium (International) on Combustion*, The Combustion Institute, 1984, pp. 1893-1904.
5. Pope, S. B., PDF Methods for Turbulent Reactive Flows, *Progress in Energy and Combustion Science*, 11, 119-192, 1985.

6. Pope, S. B., Computations of Turbulent Combustion: Progress and Challenges. *Twenty-Third Symposium (International) on Combustion*, The Combustion Institute, 1990, pp. 591-612.

7. Norris, A. T., Pope, S. B., Modeling of Extinction in Turbulent Diffusion Flames by the Velocity-Dissipation-Composition PDF Method, *Combustion and Flame*, 100, 211-220 (1995).

8. Smooke, M. D., Crump, J., Seshadri, K., Giovangigli, V., Comparison Between Experimental Measurements and Numerical Calculations of the Structure of Counterflow, Diluted, Methane-Air, Premixed Flames. *Twenty-Third Symposium (International) on Combustion*, The Combustion Institute, 1990, pp. 463-470.

9. Smooke, M. D., Puri, I. K., Seshadri, K., A Comparison Between Numerical Calculations and Experimental Measurements of the Structure of a Counterflow Diffusion Flame Burning Diluted Methane in Diluted Air. *Twenty-First Symposium (International) on Combustion*, The Combustion Institute, 1986, pp. 1783-1792.

10. Peters, N., Numerical and Asymptotic Analysis of Systematically Reduced Reaction Schemes for Hydrocarbon Flames. In *Numerical Simulation of Combustion Phenomena*, Lecture Notes in Physics, 241, pp. 90-109, 1985.

11. Smooke, M. D. (Ed.), *Reduced Kinetic Mechanisms and Asymptotic Approximations for Methane-Air Flames*, Lecture Notes in Physics, Springer-Verlag, 1991, Vol. 384.

12. Peters, N., Rogg, B. (Eds.), *Reduced Kinetic Mechanisms for Applications in Combustion Systems*, Lecture Notes in Physics, Springer-Verlag, 1993.

13. Maas, U., Pope, S. B., Simplifying Chemical Kinetics: Intrinsic Low-Dimensional Manifold in Composition Space, *Combustion and Flame*, 88, 239-264 (1992).

14. Maas, U., Pope, S. B., Laminar Flame Calculations Using Simplified Chemical Kinetics Based on Intrinsic Low-Dimensional Manifolds, *Twenty-Fifth Symposium (International) on Combustion*, The Combustion Institute, Pittsburgh, 1994, pp. 1349-1356.

15. Golub, G. H., Van Loan, C. F., *Matrix Computations*, 2nd ed., John Hopkins University Press, Baltimore, 1989.

16. Coleman, T. F., A Reflective Newton Method for Minimizing a Quadratic Function Subject to Bounds on Some of the Variables. Cornell Theory Center, Cornell University, 1992.

17. Land, A. H., Fortran Codes for Mathematical Programming: Linear, Quadratic and Discrete. John Wiley & Sons, New York, 1972.

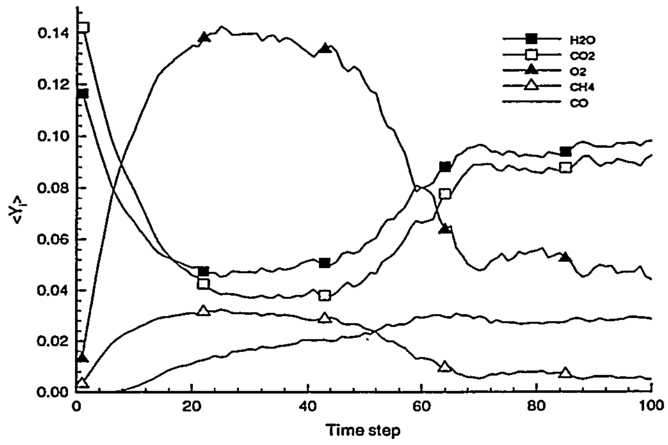

Figure 3. Average Mass Fractions of H_2O, CO_2, CH_4, CO as Functions of Time

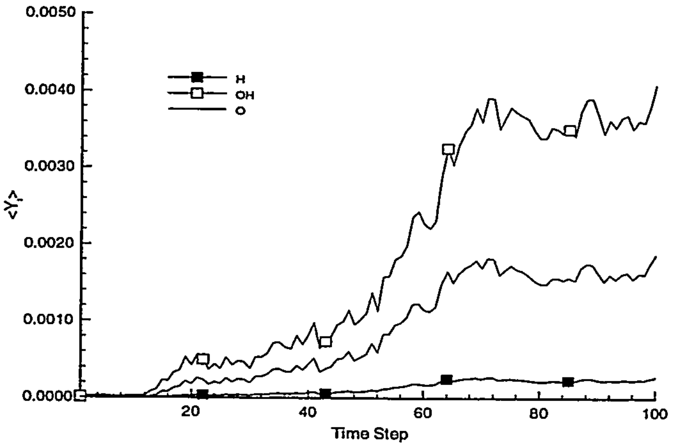

Figure 4. Average Mass Fraction of H, OH, O as Functions of Time

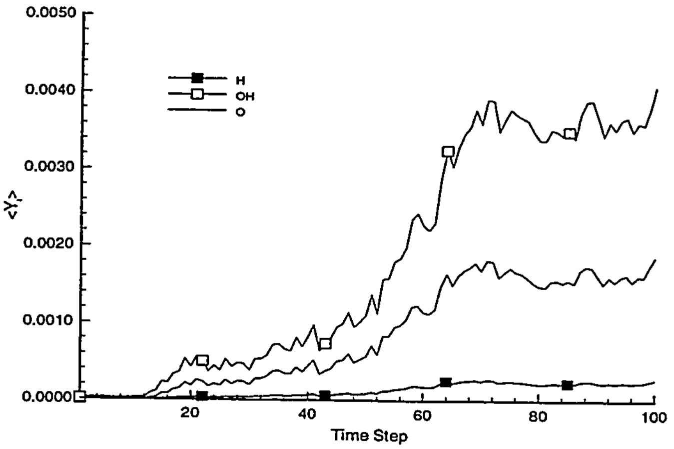

Figure 5. Average Mass Fractions of H_2, CH_3, HO_2, CH_2O as Functions of Time

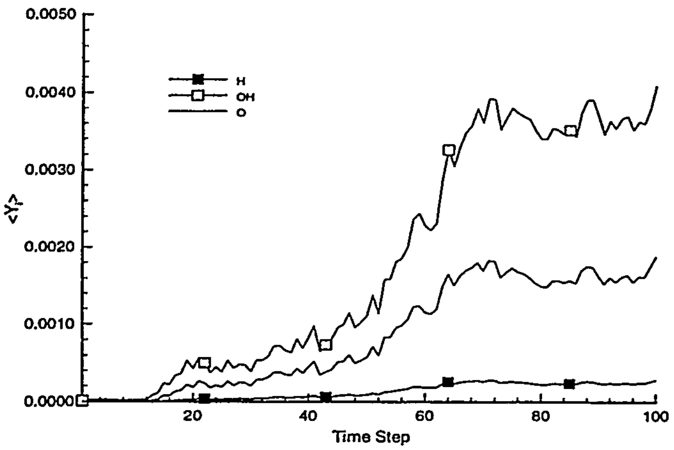

Figure 6. Average Mass Fractions of HCO, H_2O_2, CH_3O as Functions of Time

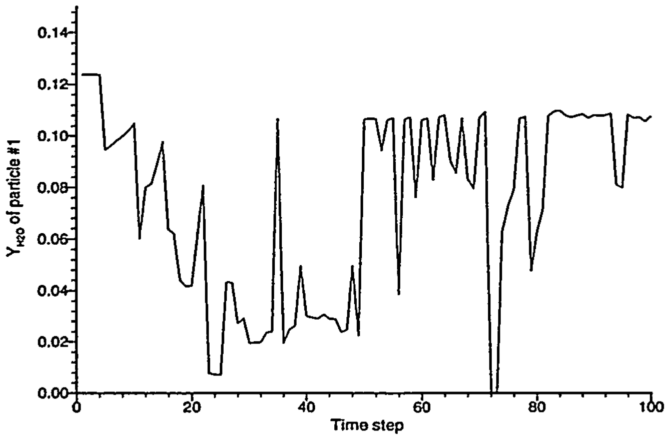

Figure 7. The Mass Fraction of H_2O of the First Particle as a Function of Time

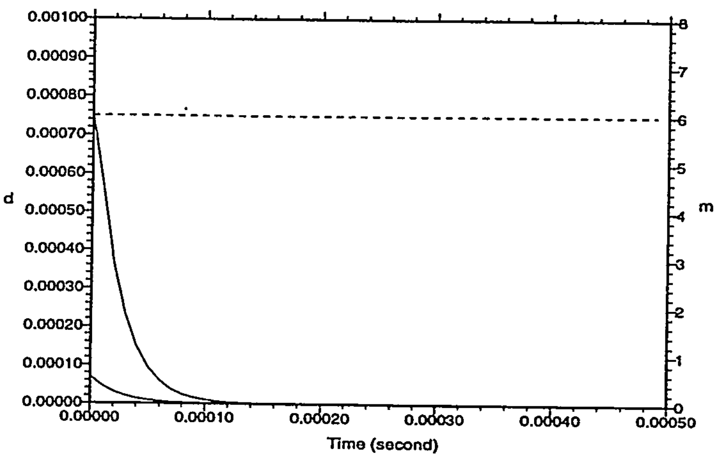

Figure 8. Changes of Distances of Particles from the Corresponding Manifold Points, d, Shown as Solid Lines, and the Dimension of the Manifolds, m, Shown as Dashed Lines, With Time. The Initial Dimensions are 6.

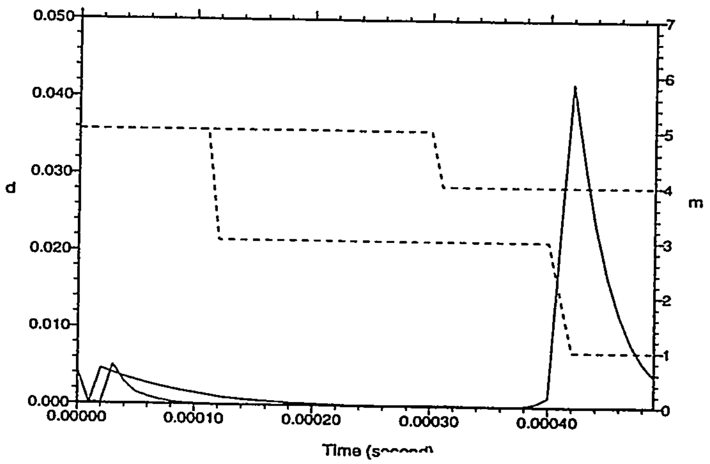

Figure 9. Changes of Distances of Particles from the Corresponding Manifold Points, d, Shown as Solid Lines, and the Dimension of the Manifolds, m, Shown as Dashed Lines, With Time. The Initial Dimensions are 5.

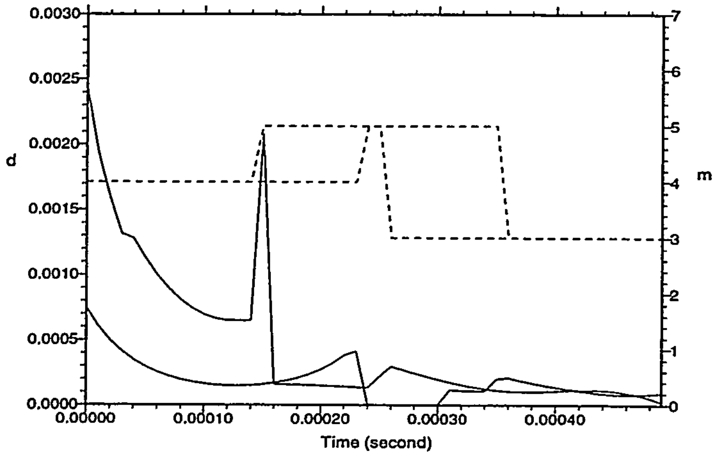

Figure 10. Changes of Distances of Particles from the Corresponding Manifold Points, d, Shown as Solid Lines, and the Dimension of the Manifolds, m, Shown as Dashed Lines, With Time. The Initial Dimensions are 4.

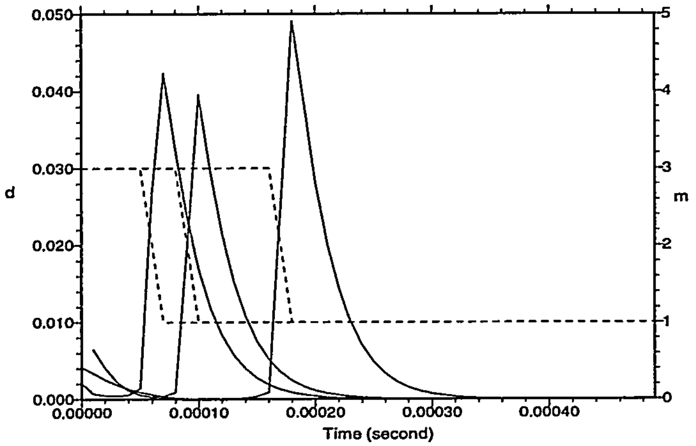

Figure 11. Changes of Distances of Particles from the Corresponding Manifold Points, d, Shown as Solid Lines, and the Dimension of the Manifolds, m, Shown as Dashed Lines, With Time. The Initial Dimensions are 3.

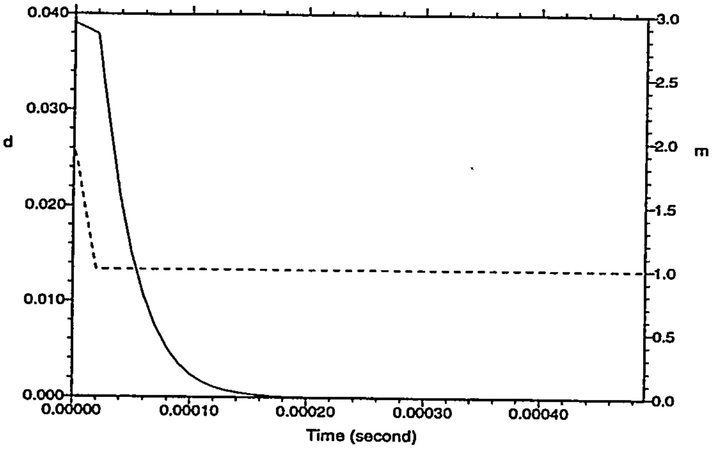

Figure 12. Changes of Distances of Particles from the Corresponding Manifold Points, d, Shown as Solid Lines, and the Dimension of the Manifolds, m, Shown as Dashed Lines, With Time. The Initial Dimensions are 2.

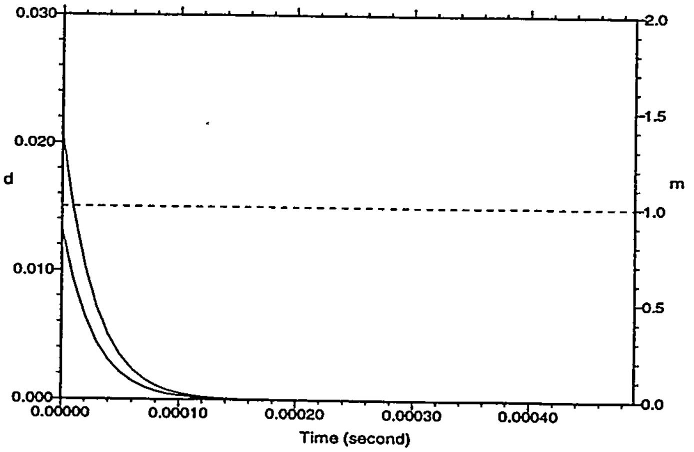

Figure 13. Changes of Distances of Particles from the Corresponding Manifold Points, d, Shown as Solid Lines, and the Dimension of the Manifolds, m, Shown as Dashed Lines, With Time. The Initial Dimensions are 1.

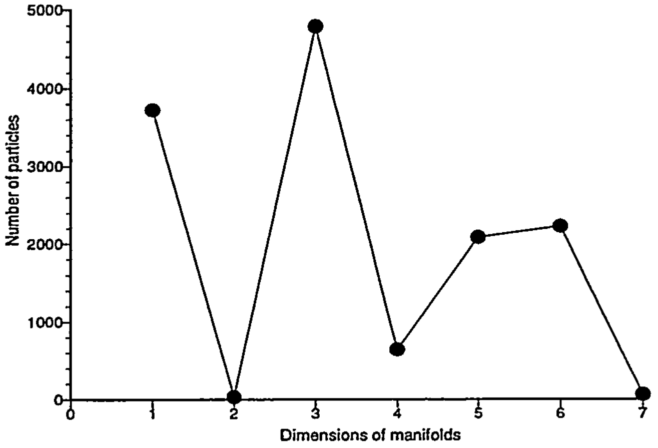

Figure 14. The Distribution of Particles as a Function of the Manifold Dimensions

P13 Advanced Multistage Turbine Blade Aerodynamics, Performance, Cooling, and Heat Transfer

Sanford Fleeter (fleeter@ecn.purdue.edu; 317-494-5622)
Patrick B. Lawless (lawless@ecn.purdue.edu; 317-494-7856)
Purdue University
School of Mechanical Engineering
West Lafayette, IN 47906

Background Information

The gas turbine has the potential for power production at the highest possible efficiency. The challenge is to ensure that gas turbines operate at the optimum efficiency so as to use the least fuel and produce minimum emissions. A key component to meeting this challenge is the turbine. Turbine performance, both aerodynamics and heat transfer, is one of the barrier advanced gas turbine development technologies. This is a result of the complex, highly three-dimensional and unsteady flow phenomena in the turbine.

Improved turbine aerodynamic performance has been achieved with three-dimensional highly-loaded airfoil designs, accomplished utilizing Euler or Navier-Stokes Computational Fluid Dynamics (CFD) codes. These design codes consider steady flow through isolated blade rows. Thus they do not account for unsteady flow effects. However, unsteady flow effects have a significant impact on performance. Also, CFD codes predict the complete flow field. The experimental verification of these codes has traditionally been accomplished with point data - not corresponding plane field measurements. Thus, although advanced CFD predictions of the highly complex and three-dimensional turbine flow fields are available, corresponding data are not.

To improve the design capability for high temperature turbines, a detailed understanding of the highly unsteady and three-dimensional flow through multi-stage turbines is necessary. Thus, unique data are required which quantify the unsteady three-dimensional flow through multi-stage turbine blade rows, including the effect of the film coolant flow. This requires experiments in appropriate research facilities in which complete flow field data, not only point measurements, are obtained and analyzed.

Also, as design CFD codes do not account for unsteady flow effects, the next logical challenge and the current thrust in CFD code development is multiple-stage analyses that account for the interactions between neighboring blade rows. Again, to verify and or direct the development of these advanced codes, appropriate experimental data, i.e., complete three-dimensional unsteady flow field data, not point measurements, in appropriate research facilities are needed. This will lead to experimentally verified advanced CFD multi-stage codes which can be used in the design process.

Objectives

The overall objective of this experimental research program is to improve the design capability for high temperature turbines by providing a thorough and detailed understanding and data base of the turbine flow field and its effect on heat transfer. In particular, the objective is to experimentally investigate the fundamental three-dimensional and unsteady flow and heat transfer phenomena which control the performance of advanced turbines. Specific experimental research objectives include an investigation to quantify the potential aerodynamic performance improvements associated with advanced design concept turbine blading designed with CFD codes. This will be accomplished in conjunction with the Allison Engine Company. In particular, advanced design

---

Research sponsored by the U.S. Department of Energy's Morgantown Energy Technology Center, under contract 94-01-SR019 with Purdue Research Foundation, Division of Sponsored Programs, West Lafayette, Indiana 47907; telefax 317-494-8323.

turbine airfoils will be designed by the Allison Engine Company specifically for these experiments. In addition, this research program will investigate and quantify the detailed three-dimensional and unsteady flow through the first stage, both stator and rotor, and second stage vane row of the multi-stage research turbine. The program will also investigate and quantify the detailed unsteady heat transfer due to vane-wake interaction.

Project Description

This project is directed at obtaining fundamental data, both steady and unsteady, to quantify the fundamental turbine flow and heat transfer phenomena inherent in high performance, high efficiency, multi-stage turbines.

A key requirement for these experiments is the facility itself. Experiments directed at the quantitative study of turbine aerodynamics, performance and heat transfer require that both the unsteady flow and the fundamental interactions of the unsteady flow with the inherently three-dimensional turbine flow field be experimentally simulated. Thus, the only valid facility for the experimental investigation of turbine aerodynamic performance and heat transfer is a research turbine facility. Thus, the experimental research will be performed in the Purdue Turbine Research Facility (Figure 1), a two stage, low speed turbine which produces the essential aspects of the steady and unsteady flow fields inherent in high speed multistage turbines. The current 50% reaction blading with A_3K_7 series airfoils will be used as a baseline for both the performance and heat transfer studies. The Allison Engine Company will design advanced concept turbine airfoils with one row of film cooling holes specifically for this program.

The unsteady three-dimensional flow through the multi-stage research turbine will be accomplished by means of Particle Image Velocimetry (PIV), a relatively new measurement technique which provides instantaneous whole field high resolution velocity field data. Taking advantage of the high frequency response of thin film sensors, the blade surface unsteady heat transfer measurements will be made using constant-temperature anemometry and platinum hot film surface sensors.

This series of experiments will improve the design capability for high temperature turbines by providing a thorough and detailed understanding and data base of the turbine flow field and its effect on heat transfer. With these data, the designer can increase turbine aerodynamic performance and optimize turbine cooling flow schemes.

Accomplishments

The program is progressing along two simultaneous paths. The first involves the experiments that will be performed in the baseline turbine facility to investigate and quantify the detailed three-dimensional unsteady aerodynamics and heat transfer through the first stage, both stator and rotor, and second stage vane row of the baseline multi-stage research turbine. Conventional steady aerodynamic performance instrumentation, i.e., blade surface static pressure taps, and advanced instrumentation including PIV and high frequency thin film sensors are being utilized in this effort.

Concurrently with this effort, the design and manufacture of advanced concept airfoils that will be used in the follow-on experiments is proceeding in conjunction with the Allison Engine Company.

Experiments With Baseline Blading

Flow field quantification on the baseline blading with the Particle Image Velocimetry System (PIV) is scheduled for this fall. The dual 400 mJ Nd:YAG lasers have been received and final qualification and tuning completed by the vendor. The remainder of the PIV system has been received and is operational, with some initial experiments performed in a low speed compressor to qualify the unit. The optical-path design for implementing the PIV system on the Purdue Research Turbine is shown in Figure 2. The first window has been installed and will allow characterization of the first vane flowfield.

The Purdue Research Turbine's current A_3G_7 free-vortex blading is being extensively instrumented with heat transfer gages and dynamic pressure transducers, as shown in Figure 3. Machining operations for the instrumentation for heat transfer and dynamic pressure measurements on the baseline blade are complete, and the blades are undergoing transducer installation at the vendor.

Advanced Airfoil Design, Fabrication & Instrumentation

The Allison Engine Company has finished the aerodynamic design for the advanced concept turbine blading, as shown in Figure 5. CFD code predictions for the three dimensional, steady blade loading has also been completed by Allison. The manufacture of the blades is now underway at Purdue. In addition, the geometry of the first vane film cooling holes are now being designed in cooperation with Allison. A new rotor drum and stator supports for this advanced blading has been designed and is also currently being fabricated.

Future Activities

As shown in the timeline given in Figure 5, the experiments on the Purdue/Allison AGT blading will commence early in 1996 after completion of the baseline experiments. In addition to the data obtained from the baseline blading, the AGT configuration will allow investigations of film cooling on the unsteady turbine flowfield.

Period of Performance: 8/15/94 to 8/14/97

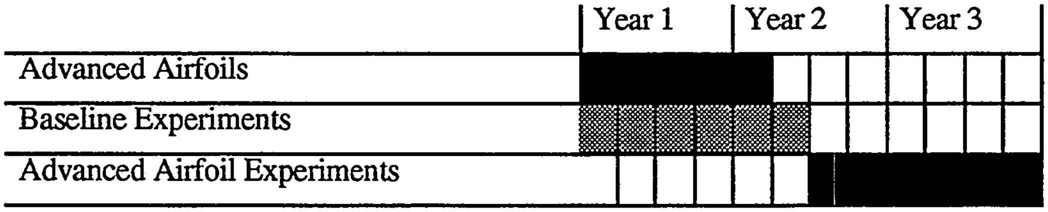

	Year 1				Year 2				Year 3			
Advanced Airfoils	■	■	■	■	■							
Baseline Experiments	▨	▨	▨	▨	▨	▨						
Advanced Airfoil Experiments							■	■	■	■	■	■

Table 1. Project Schedule.

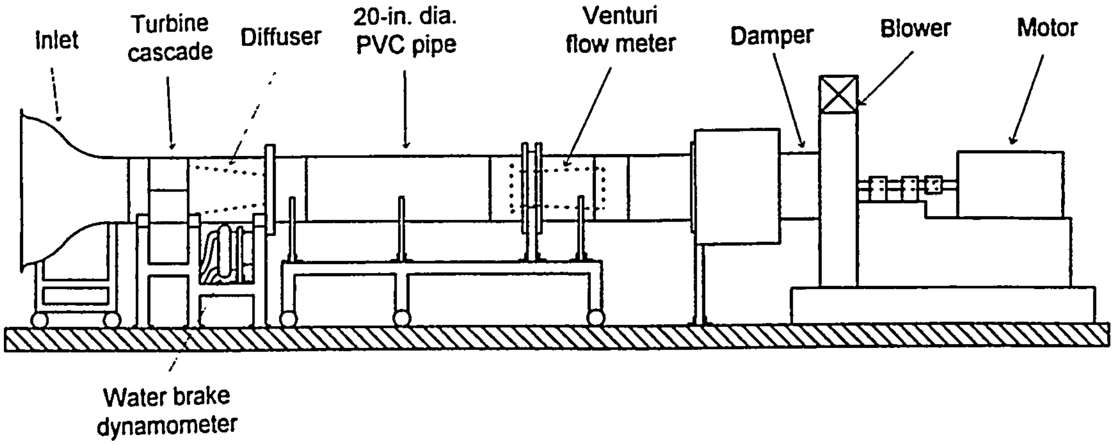

Figure 1. Purdue Turbine Research Facility

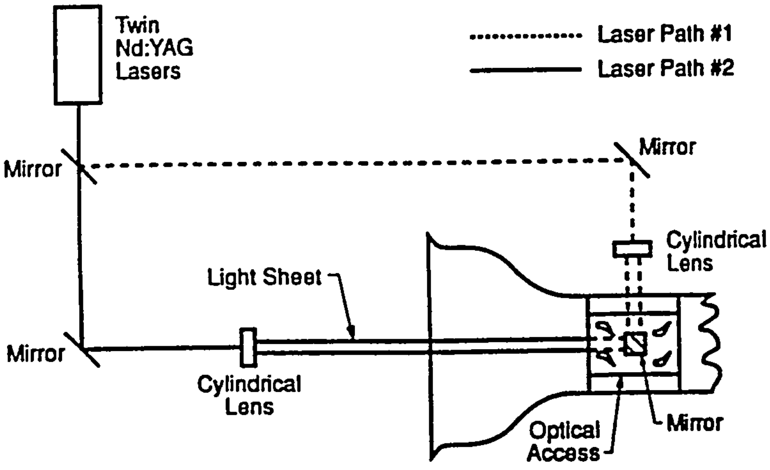

Figure 2. Optical Path For Particle Image Velocimetry.

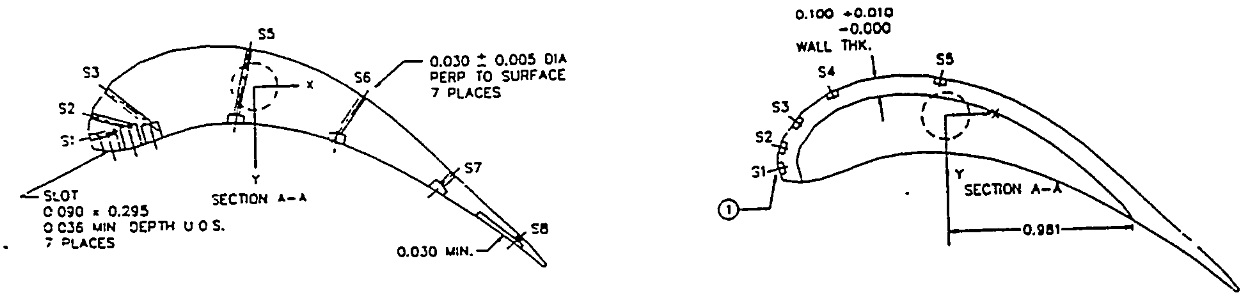

Pressure Transducers, Suction Side

Heat Transfer Gages, Suction Side

Figure 3. Instrumentation for A_3G_7 Blading.

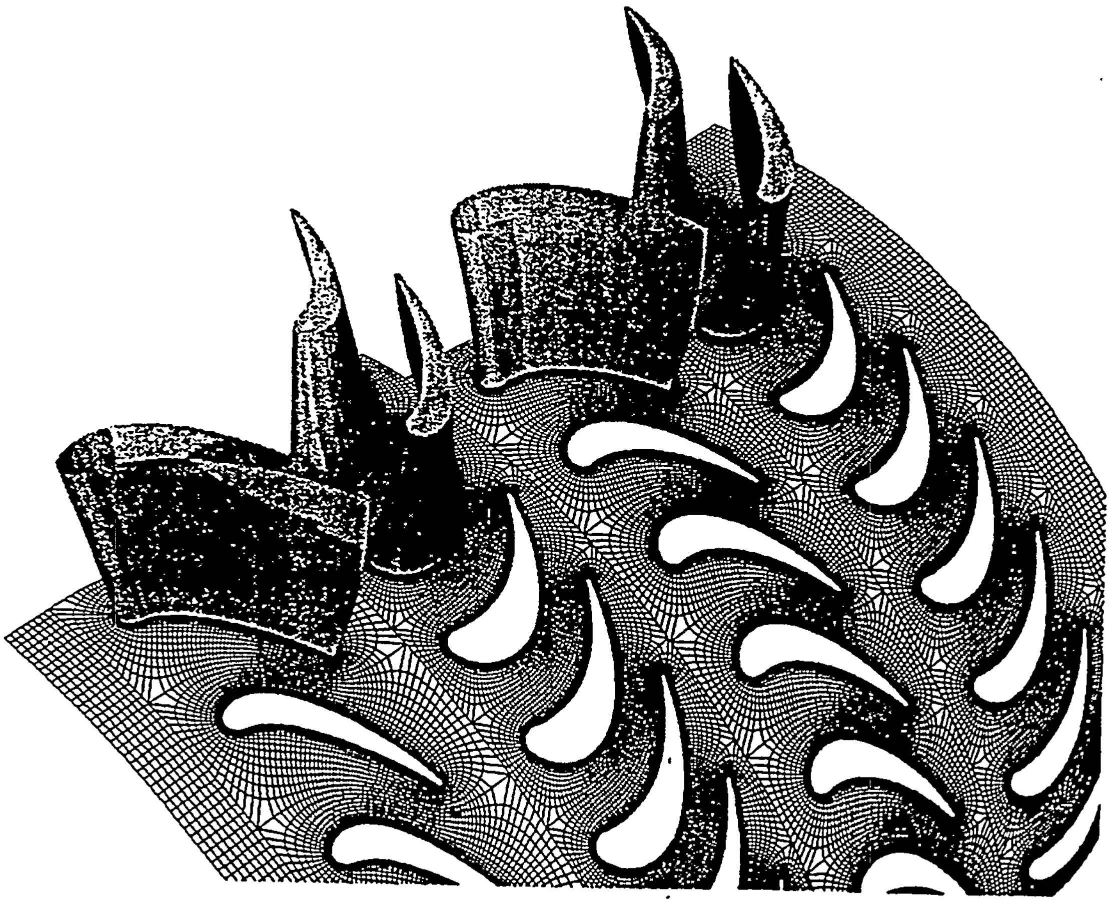

Figure 4. Purdue/Allison AGT Blading.

P14 The Role of Reactant Unmixedness, Strain Rate, and Length Scale on Premixed Combustor Performance

S. Samuelsen (gss@uci.edu; 714-824-5468)
J. LaRue (jlarue@maemaster.eng.uci.edu; 714-824-6724)
S. Vilayanur (srv@ucicl.eng.uci.edu; 714-824-5950)
D. Guillaume (dguillau@maemaster.eng.uci.edu; 714-824-4995)
UCI Combustion Lab
University of California, Irvine
Irvine, CA 92717-3550

Introduction

Lean premixed combustion provides a means to reduce pollutant formation and increase combustion efficiency (Sattelmayer et. al., 1990). However, fuel-air mixing is rarely uniform in space and time. This nonuniformity in concentration will lead to relative increases in pollutant formation and decreases in combustion efficiency. The nonuniformity of the concentration at the exit of the premixer has been defined by Lyons (1981) as the "unmixedness." Although turbulence properties such as length scales and strain rate are known to effect unmixedness, the exact relationship is unknown. Evaluating this relationship and the effect of unmixedness in premixed combustion on pollutant formation and combustion efficiency are an important part of the overall goal of US Department of Energy's Advanced Turbine Systems (ATS) program and are among the goals of the program described herein. The information obtained from ATS is intended to help to develop and commercialize gas turbines which have (1) a wide range of operation/stability, (2) a minimal amount of pollutant formation, and (3) high combustion efficiency. Specifically, with regard to pollutants, the goals are to reduce the NO_x emissions by at least 10%, obtain less than 20 PPM of both CO and UHC, and increase the combustion efficiency by 5%.

Objectives

The contributions to the program which the University of California (Irvine) Combustion Lab (UCICL) will provide are: (1) establish the relationship of inlet unmixedness, length scales, and mean strain rate to performance, (2) determine the optimal levels of inlet unmixedness, length scales, and mean strain rates to maximize combustor performance, and (3) identify efficient premixing methods for achieving the necessary inlet conditions.

To understand unmixedness, the initial part of the program addresses the definition and measurement of unmixedness. The heart of the program is anchored on three experiments -- one to study premixing strategies; a second controlled study to address the effect of unmixedness, turbulent length scale, and turbulent strain rate on mixing and pollutant formation; and a third to

---

Research sponsored by the U.S. Department of Energy's Morgantown Energy Technology Center, (contract DE-FC21-92MC29061), and the Southern California Gas Company, (contract SCG-19596).

study the effect of premixing strategies on combustor performance.

Background

Oxides of nitrogen (NO_x) refer to nitric oxide (NO) and nitrogen dioxide (NO_2). Air quality is significantly impacted by NO_x emissions since they directly or indirectly affect concentrations of nitrogen dioxide (NO_2), inhalable particulate (PM10) and photochemical oxidant (including ozone and peroxyacylnitrates). Furthermore, the NO_2 and PM10 formed from the emission of NO_x decrease visibility and lead to nitric acid deposition. Concerns have been expressed about the potential adverse health effects of other nitrogen compounds, such as nitrosamines, and nitrous oxide (N_20).

Several strategies are available for reducing NO_x emissions from gas turbines. Most notable are selective catalytic reduction (SCR), exhaust gas recirculation (EGR), steam injection, and retrofitting with low-NO_x combustors (LNC). The key to these low-NO_x combustors is either a combination of staged combustion air and staged fuel or partially premixing the fuel and air. The level or degree of premixing required to effectively manage a low-NO_x combustor is still to be determined. Specifically, the local fuel-air unmixedness inside the premixer and inside the combustor will affect the combustor's performance and, therefore, the effectiveness.

In a practical gas turbine, the fuel-air mixing is rarely uniform in time or space. Consequently, large deviations (i.e., fluctuations) about the mean local temperature can occur as packets of various mixtures of fuel and air pass through a point in space inside the combustor. These variations are not only observable as fluctuations in the flame luminosity; they also play a significant role in the generation of NO_x. Decreasing the amplitude of the temperature has been shown in simulations to have a significant effect on NO_x production. Understanding how to control the local turbulence to optimize the local unmixedness will aid in the design of more effective and less bulky fuel-air premixers.

Unmixedness is a quantity which is used to indicate, in a statistical sense, the degree of mixing of fuel and air at the molecular level. In a given system in which two or more streams of miscible fluids are mixing, a specific level of molecular unmixedness (grain size of fuel-and-rich parcels of fluid) depends on initial length scales, initial distribution of fuel-rich and air-rich parcels of fluid, the mean strain rate field, and the characteristics of the turbulent field (e.g., the intensity, the large structure, the degree of anisotropy, etc.). Two means are most frequently used to determine the statistical measure of unmixedness. Lyons (1981) introduces one which also requires the definition of the area averaged equivalence ratio, $\overline{\Phi}$, across the profile of the flow which in her case is a pipe of radius r. Thus:

$$\overline{\Phi} = \frac{\int_0^{r_{max}} \Phi_l r dr}{\int_0^{r_{max}} r dr}$$

where, Φ_l is the equivalence ratio at a particular radial location. Using this value for the area averaged equivalence ratio, an area averaged measure of unmixedness, S, can be defined as the area averaged standard deviation. This standard deviation can be expressed as follows:

$$S = \left(\frac{\int_0^{r_{max}} (\Phi_l - \overline{\Phi})^2 r dr}{\int_0^{r_{max}} r dr} \right)^{\frac{1}{2}}$$

The second measure of unmixedness (cited by Fric, 1992) is developed by considering temporal fluctuations in the fuel concentration. The level of unmixedness, U, at a particular position in the flow can be defined as a function of the mean fuel concentration, $\overline{C}$, at a location and the variance fluctuation about the mean, c^2, as:

$$U = \frac{\overline{c^2}}{\overline{C}(1-\overline{C})}$$

This equation provides a statistical measure of the unmixedness due to temporal fluctuations while the preceding equation provides a measure of the unmixedness due to spatial variation. Both of these equations are representative of the unmixedness in a statistical sense. However, neither of these equations indicate the flow structure that leads to a particular value of unmixedness. For example, the same unmixedness could be obtained with a small number of large fuel- and air- rich eddies or a large number of smaller fuel- and air- rich eddies. Thus a complete determination of the unmixedness requires nor only a statistical measure of the unmixedness but also a structural measure of the unmixedness, i.e., a measure of the statistical distribution of the length scales of fuel rich and air rich regions.

The structural measure of unmixedness can be obtained by first, forming indicator functions from the concentration signal and second determining the distribution of the length scales of fuel-rich and air-rich fluid parcels from those indicator functions. (Indicator functions are signals that have either zero or unity values depending on whether the concentration signals are, respectively, above or below a selected threshold.

Project Description

Although lean premixed combustion does lead to reduced production of NO_x, and increased efficiency of gas turbine combustors, the minimal unmixedness required to achieve adequate combustor performance, or the point at which further mixing is ineffective are unknown. Thus, a relationship that describes combustor emissions and efficiency as a function of unmixedness is required. Specifically, since turbulence properties such as length scales, mean strain rate and other turbulent properties are known to effect unmixedness, the goals of this study are to determine this relationship and then use the results of this study to optimize the performance of gas turbine combustors.

Mixing devices and turbulence measurement techniques will be used to obtain spatial and temporal unmixedness, as defined in the background section, for a wide range of initial fuel and air length scales and mean strain rates and intensities. With unmixedness quantified with respect to the turbulence properties, these properties can be used within premixed systems to control unmixedness. The data obtained from experiments within these reacting systems will be used to determine a relationship between unmixedness and combustor performance (efficiency, pollutant formation, stability, lean blow-out).

Approach

The program has three objectives:

- Establish the relationship of inlet unmixedness (spatial and temporal), length scales, turbulent intensity, and mean strain rate to combustor performance (i.e. emissions and combustor efficiency).

- Determine the optimal levels of inlet unmixedness, length scales, turbulent intensity, and mean strain rates to maximize combustor performance.

- Identify efficient premixing methods for achieving the necessary inlet conditions.

These three objectives are directly related.

Previous Work

During the last reporting period, the UCI program focused on obtaining industrial input, constructing mixing and combustion test fixtures and obtaining stabilized reactions. Controllable premixers were designed for both reacting and non-reacting studies that allow adjustment in mixedness, length scales, turbulent intensity and mean strain rate. Test protocols and time lines were established to assure that the main goals of the project were met. Fundamental experiments were developed that provide basic isolated information on the mixing process. These experiments will act as "bridges" between the research oriented premixer and combustor tests and practical industrial designs.

Present Work

The program during this reporting period is focused on developing a means to measure and qualify different degrees of temporal and spatial unmixedness. Laser diagnostic methods for planer unmixedness measurements are being developed and preliminary results are presented herein. These results will be used to 1), aid in the design of experimental premixers, and 2), determine the unmixedness which will be correlated with the emissions of the combustor. This measure of unmixedness coupled with length scale, strain rate and intensity information is required to attain the UCI goals.

Premixer Description

For this development period, a single premixer design has been the focus. Its basic structure is a jet-grid tube array. Figure 1. shows the location of the premixer in the axial can combustor used in the present sturdy. The premixer consists of 33 individually adjustable fuel tubes which are 0.085 in. and are positioned circumferentially on three different diameters. The air passes through 33 0.219 inch holes which are placed between the fuel tubes.

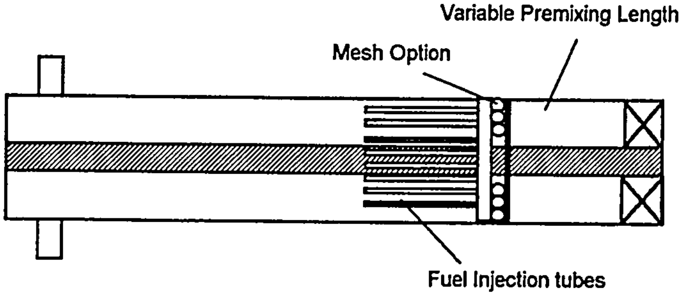

Figure 1. Schematic of premixer

Mixedness, with this premixer can be controlled by adjusting the length, and therefore time, between the point of gas injection and the point of measurement. Likewise, length scale can be changed by either adding nozzles of various sizes to the independent fuel jets or by added grid meshes to the outlet plane of the air flow passages. Finally, mean strain rate can be controlled by adjusting the fuel flow rate out of the jets to produce velocity gradients. In this manner, either strain rate in the radial direction or strain rate in a azimuthal direction can be induced. Figure 2 is a photograph of the premixer.

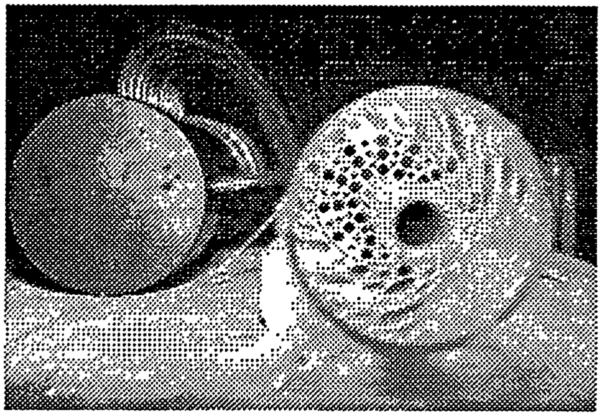

Figure 2. Photograph of premixer

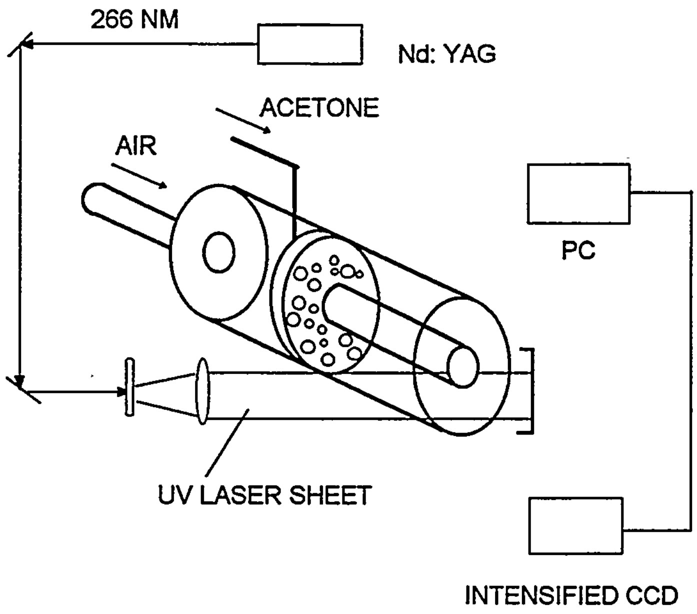

Figure 3. Schematic of PLIF System

Diagnostic Development

As mentioned in the background section, a measure of mixedness is key to this project. The inherent non-intrusive nature of laser diagnostics coupled with the ability to obtain planer information makes Planer Laser Induced Fluorescence (PLIF) the most attractive candidate at this time. During this reporting period, UCI has been developing a PLIF capability. For these initial non-reacting studies, acetone was selected as the fluorescing seed. A schematic of the setup can be seen in Fig. 3. The laser used is a frequency quadrupled YAG that generates the required 266 nm wavelength necessary for acetone to fluoresce.

For the tests presented in this paper, a 200 µm by 20 mm laser sheet was generated using a cylindrical lens and placed at the exit of the premixer, just prior to the swirl vane location. The photograph shown in Fig. 4 shows the PLIF system in operation.

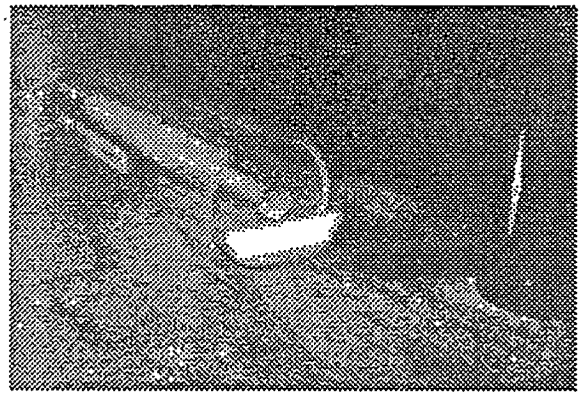

Figure 4. Photograph of PLIF System

A CCD camera was used to collect the data images. For these initial mixing tests, the sheet was purposely sized to not cover the entire output plane so that the laser power would remain fairly high. Figure 5 is an example image. The fluorescing portion of the image shows a relatively uniform output from the premixer. The laser sheet will be expanded for further tests such that overall fluid structures can be visualized and studied.

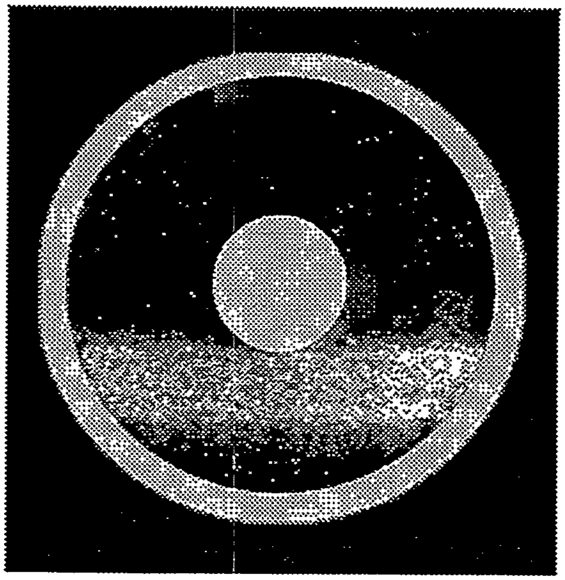

Figure 5. CCD Image of the PLIF Output

Fundamental Experiment

The purpose of this experiment was to access the strain effect of swirl vanes. To simplify the test conditions and to isolate the strain effects, straight vanes (plates) were used. A test facility was constructed to generate an initially low level of turbulence (RMS). A grid was then added to the system to generate a fixed, controlled RMS level at a specific test location. At this location, parallel plates were placed (Fig. 6).

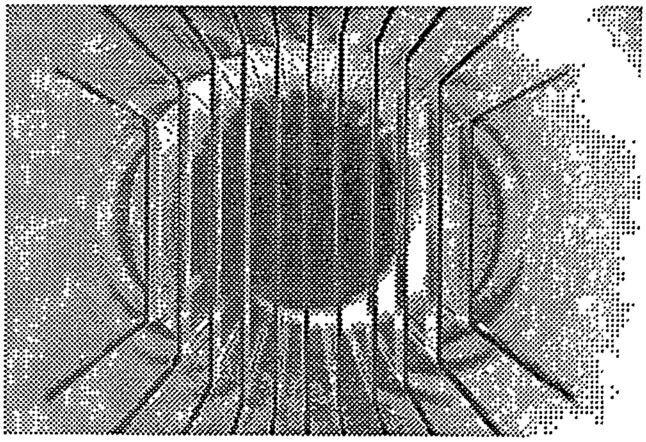

Figure 6. Photograph of Parallel Vanes

Velocity and RMS profiles were measured at the exit of the vanes. The finding are shown in Fig. 7. As expected, the RMS levels are high near the plate boundaries. One key finding is the decrease in RMS in the center region of the flow. This shows that the structure of the flow is altered by these vanes even though no swirl has been added and even though they are very short in length (0.5 inches). The significant observation is that the swirl vanes have an influence on the entire flow.

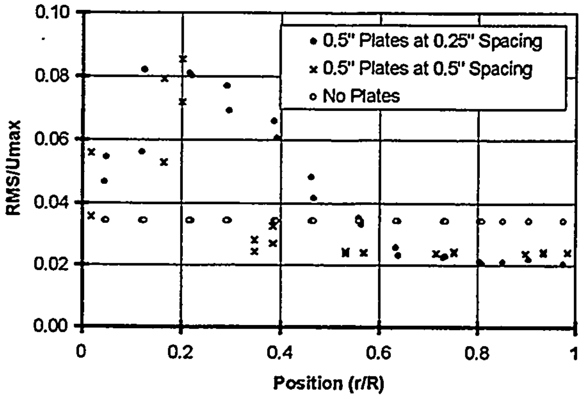

Figure 7. Results of the Plate Experiment

Future Activities

Below is a brief description of the plans for the immediate future plans for the program.

Facility Design and Development

Premixer and Combustor Hardware will be fabricated as needed. Emphasis will be placed on the design of the model combustor hardware for the elevated pressure, and elevated temperature experiments.

Experimental Studies

For the premixer studies, experiments will be conducted using temperature as a scalar indicator and thermocouples/cold-wires as the measurement sensors. In addition, a specially designed concentration probe will be used as a measurement technique for mixedness. Substantial emphasis will be placed on the already initiated PLIF diagnostics (described in this report) for non-intrusive mixedness measurements. Overall, attention will address the effect of premixing mixedness length scale, and on the control of premixing to establish specified mixedness and length scale characteristics at the premixer exit plane. The effort will continue to "hand-shake" with the model combustor studies.

The model combustor studies will focus on the effect of inlet conditions (mixedness and length scale) on combustor performance. Air preheat will be provided in the atmospheric test facility to more effectively simulate the practical environment for NOx production. In-situ measurements of composition and temperature using physical probes will be complemented with laser anemometry measurements for velocity, CARS measurements for temperature and PLIF measurements for mixedness.

Data Analysis

A major diagnostic to be added will be FLUENT modeling of both the premixer and the combustor. This will complement the experimental measurements, and facilitate the development of the mechanistic understanding required to reach the goals of the project. Design of Experiments will be extensively employed to provide both direction in the design of the experiments, as well as to serve as a tool for the interpretation of results.

Industrial Interaction

The first stage this task was completed and an industrial questionnaire was generated. Further progress was made through visits to Allison, GE and Westinghouse. These groups were specifically chosen given their background in industrial gas turbines. Industrial interaction was stressed during these visits by presenting the groups with UCICL's progress and inviting comments or suggestions to the work. Also a questionnaire was distributed for feedback to determine practical issues or concerns that the groups might have. This enabled further design and development of the program to be involved with immediate issues that the industrial gas turbine groups face today. The trips proved to be very productive and also helped establish a rapport with the groups, that will help in contributing to research.

Individual contacts made with each of these industrial participants provide good opportunity to maintain technical exchange and receive industrial input. At Allison contact was established with Dr. Mohan Razdan, Chief of Combustion Research. UCICL's point contact was identified to be Dr. Rahul Puri. At Westinghouse Corporation contact was established with the research group headed by Rick Antos. Our point contact was established to be Graydon

Whidden. At GE we established contact with Dr. Hukum Mongia, head of advanced combustion technology. Dr. Narendra Joshi will serve as our point contact. Current goals are to maintain a rapport with these individuals, keep them apprised of our progress, acquire and utilize input and comments.

The ATS internship program provided the opportunity for more industrial interaction.. Three students from the UCI Combustion Laboratory were placed at Allied Signal, Solar Turbines and Pratt & Whitney, respectively and provided the experience and opportunity to be involved with current state of the art work being conducted in industry.

Acknowledgments

This report was prepared with the support of the US Department of Energy, Morgantown Energy Technology Center under subcontract 94-01-SR020. This financial support is administered through the South Carolina Energy Research and Development Center (Dr. Dan Fant, Program Director, and Dr. Lawrence P. Golan, SCERDC Director). Significant and essential co-funding support is provided by the Southern California Gas Company (Cherif Youssef). The students and investigators are especially indebted to the following industrial liaisons for their continuing guidance and evaluation of the project's results: Allison (Mohan Razdan and Rahul Puri), GE (Hukum Mongia and Narendra Joshi), Westinghouse (Rick Antos and Graydon Whidden), and Solar (David J. White).

References

Fric, T. F., Effect of Fuel-Air Unmixedness on NOx Emissions, AIAA Paper No. 92-3345, (1992).

Kostiuk, L. W., Bray, K. N. C., and Cheng, R. K., Experimental Study of Premixed Turbulent Combustion in Opposed Streams. Part I -- Non-reacting Flow Field, Combustion and Flame, Vol. 92, pp. 377-395 (1993).

Kostiuk, L. W., Bray, K. N. C., and Cheng, R. K., Experimental Study of Premixed Turbulent Combustion in Opposed Steams. Part II -- Reacting Flow Field and Extinction, Vol. 92, pp. 396-409 (1993).

Lyons, V. J., Effect of Fuel-Air-Ratio Nonuniformity on Emissions of Nitrogen Oxides, NASA Technical Paper No. 1798, (1981).

Sattelmayer, Th., Felchlin, M. P., Haumann, J., Hellat, J., and Styner, D., Second Generation Low-Emission Combustor for ABB Gas Turbines: Burner Development and Test at Atmospheric Pressure, AIAA Paper No. 90-GT-162 (1990).

P15 Experimental and Computational Studies of Film Cooling With Compound Angle Injection

R.J. Goldstein (goldstei@mailbox.mail.umn.edu; 612-625-5552)
E.R.G. Eckert (612-625-8010)
S.V. Patankar (patan001@maroon.tc.umn.edu; 612-625-6302)
T.W. Simon (tsimon@me.umn.edu; 612-625-5831)
Heat Transfer Laboratory, Department of Mechanical Engineering
University of Minnesota
111 Church Street SE
Minneapolis, MN 55455

Introduction and Objectives

The thermal efficiency of gas turbine systems depends largely on the turbine inlet temperature. Recent decades have seen a steady rise in the inlet temperature and a resulting reduction in fuel consumption. At the same time, it has been necessary to employ intensive cooling of the hot components. Among various cooling methods, film cooling has become a standard method for cooling of the turbine airfoils and combustion chamber walls. The University of Minnesota program is a combined experimental and computational study of various film-cooling configurations. Whereas a large number of parameters influence film cooling processes, this research focuses on compound angle injection through a single row and through two rows of holes. Later work will investigate the values of contoured hole designs. An appreciation of the advantages of compound angle injection has risen recently with the demand for more effective cooling and with improved understanding of the flow; this project should continue to further this understanding.

Approaches being applied include: (1) a new measurement system that extends the mass/heat transfer analogy to obtain both local film cooling and local mass (heat) transfer results in a single system, (2) direct measurement of three-dimensional turbulent transport in a highly-disturbed flow, (3) the use of compound angle and shaped holes to optimize film cooling performance, and (4) an exploration of anisotropy corrections to turbulence modeling of film cooling jets.

The outcome of this research will be threefold. First, it will provide fundamental scientific information in the form of detailed measurements, computational results, and turbulence model validation. Second, the results of the experiments and computations will be presented in a generalized form so that they will be directly usable by design engineers in industry. And finally, the experimental and computational activities will be used to familiarize graduate and undergraduate students with the gas turbine industry. In the previous year, research on the turbulence generation has been conducted, test facilities for the experiments have been designed and constructed,

---

Research sponsored by the U.S. Department of Energy's Morgantown Energy Technology Center, under Contract 94-01-SR021 with University of Minnesota, Mechanical Engineering Department, 111 Church St., SE., Minneapolis, MN 55455; fax: 612-624-1398

and modeling of film cooling has begun. A discussion of these activities is presented. The high-turbulence facility is a modified version of one developed at Allision which simulates turbulence levels and scales which are representative of the combustor exit flow. The film-cooled test section simulates the cooling arrangement of modern, multi-row turbine cooling schemes. The surface mass transfer measurement facility is being modified for the new method of measurement to be employed in this study. The computational activity has begun with a study of the relative merits of parabolic and elliptic calculation procedures for film cooling flows. Also, modeling of the flow delivery plenum has begun. Finally, an analysis has been conducted to determine the magnitude of thermal gradients imposed by film cooling.

Project Description and Results

Flow Measurements

Complementary to surface measurements and in support of the turbulence model development and qualification of the numerical predictions, turbulence measurements are taken in the flow approaching the film cooling region and at several stations downstream of the film cooling injection zone. After tests with in-line injection, an experimental flow will be established which has compound angle injection of the film cooling flow from one or two rows of holes. This cooling flow merges with the high-disturbance level, primary flow field. After initial tests on a flat plate, streamwise pressure gradients which match those of the film cooling zones of modern gas turbine engines will be imposed. This flow then simulates those elements of the real gas turbine airfoil boundary layer and film coolant flows which are considered to be of major importance and which are not captured well by the present engine design models. The first configuration, already constructed, will be on a flat wall with one row of streamwise injection holes angled 35° to the surface but without cross-stream injection. The holes will be spaced laterally three diameters. Cases with lateral injection will follow this first sequence of cases. The flow will be established in a blown-type wind tunnel. Upstream of the film cooling zone, the primary air will pass either through a turbulence settling section (0.5 percent T.I.) or a turbulence generator (~10 percent T.I.). Both primary and secondary air streams will be at the same temperature; thus, the density ratio will be unity. Testing will be performed over various blowing rates or mass flux ratios. Velocity measurements will be taken with single-wire and triple-wire, hot-wire anemometry. The latter measurements will allow documenting the 3-D mean flow field and the six components of the Reynolds stress tensor. Turbulence kinetic energy needed for k-ε modeling will be documented. Measurement of the individual components of the Reynolds stress tensor will also allow documentation of the anisotropy of the flow, a characteristic that cannot be completely captured by the k-ε model. This is considered to be a weakness of present models. It may be necessary that the turbulence modeling incorporates relationships for anisotropy; examples include the Reynolds stress model, the algebraic stress model, or large-eddy simulation. These flow measurements, in conjunction with the detailed surface measurements, will indicate weaknesses in the modeling.

It is common for the turbulence intensity of the approach flow in a gas turbine mainstream to be as high as 15 to 20 percent (Bicen and Jones, 1986, and Young et al., 1992). Over the suction surface, this is reduced. Consequently, for a proper gas turbine study, a turbulence generator yielding about 10 percent turbulence intensity is required. High-disturbance turbulence generators create high levels of turbulence via the production of large-scale vortices. Several schemes for doing so are shown in Table 1. One important requirement of a turbulence generator for use in simulating the high-pressure turbine stage is that it produce a flow structure which is similar to that found in a gas turbine combustor. Recently, the combustor simulator shown in Figure 1 was designed and fabricated. It was fashioned after that of Ames and Moffat (1990). Air flow is directed from the inlet plenum through the rear and side panels of the simulator liner. Flow through the rear slots together with flow through the first row of holes in the side panel combine to create a recirculation zone inside the simulator and, consequently, high turbulence. Flow through a second row of holes in the side panel simulates dilution of the gas turbine combustor air. Ames and Moffat (1990) and Ames (1994) obtained turbulence intensity values of 15 to 17 percent at the exit of their turbulence generator and 7.5 percent at their test section 208 cm downstream of their nozzle.

The turbulence generator facility (Figures 1, 2, and 3) consists of primary fans, settling chamber, turbulence generator, secondary fan, air plenum, nozzle, and test section. The mainstream air flow supplied by primary fans passes through the settling chamber to the back panel and to the first row of jets. The flow supplied by the secondary fan is ducted to the second row of jets. The nozzle, located downstream of the turbulence generator, provides a high-turbulence, uniform-velocity wall jet to the test section. A wall jet configuration is different from the geometry of most previous studies but is similar to a series of studies which were recently completed at the Wright Laboratories (MacMullin, et al., 1989, and Bons, et al., 1994). It provides some simplicity to the test, but requires careful measurement to verify that engine boundary conditions, like flow conditions at the edge of the boundary layer, are met.

The test section consists of an upstream plate, the test plate, a downstream plate, and the injecting supply system (Figure 4). The design is such that it permits various plates to be removed and inserted with ease, thus favoring a large realm of testing possibilities. Three side walls and the first 12.5 cm (5 in.) of the upstream plate form a box-like channel at the exit of the turbulence generator nozzle. The side walls are fabricated with sharp trailing edges to minimize entrainment of flow from the surroundings. The downstream plate is 0.9 m (36 in.) in length. It is attached directly to the test plate and permits flow measurements at locations of up to x/D=40 downstream of the first row of injection. The injecting supply is provided by a plenum located behind the test plate. The plenum is partially constructed of clear Plexiglas® so as to permit flow visualization. Test plates will be attached in a fashion that allows exchanging one type of plate with another. All of the plates will be machined to the same major dimensions and will be constructed of 25 mm (1 in.) thick phenolic laminate plate material. Phenolic laminate is characterized by low thermal conductivity and is resistant to exposure to a temperature which is continuously in excess of 250 °C. Since hot-wire anemometry techniques will be employed for measurements, these properties will help eliminate errors associated with the near-wall measurements. Fully-developed flow is provided within the delivery tubes, which have a length-to-diameter ratio of 7. The facility will allow variations of the supply plenum geometry, a flexibility which will be employed in a complementary, but separate, series of tests. The initial film cooling configuration that will be studied will utilize a test plate with a single row of 11 film cooling holes. The film cooling is to be injected at an angle of 35 degrees in the streamwise direction and 0 degrees in the lateral direction. The holes will be drilled to a diameter of 19 mm (3/4 in.) and positioned three diameters apart, center-to-center.

Since measurements will be made with hot-wire anemometry, significant effort has been dedicated to the study and qualification of such measurements. Over the past year, experience and confidence was gained using single-wire, cross-wire, and triple-wire measurements in fully-developed pipe flow (Laufer, 1953). This appendix is not going to be attached. In addition, a suitable probe traversing system has been designed and is now available for use.

Qualification of the primary flow from the turbulence generator/combustor simulator has been a major activity over the last year. These qualification activities include documenting flow uniformity, turbulence intensity, and turbulent length scales. The turbulence generator facility is capable of delivering a variety of flows by adjusting fan controls. For this investigation, however, delivery flow with a mean velocity of 10 m/s and corresponding turbulence intensity of ~10 percent has been selected as the reference primary flow. Via velocity profile measurements at several locations in the proximity of the injection zone, the turbulence generator has been shown to generate a fairly uniform and symmetric flow field. The average variation in the mean velocity and turbulence intensity at any location was found to be on the order of 5 percent or less. Figures 5, 6, and 7 depict the flow variations normal to the wall along the spanwise centerline. Figures 8, 9, and 10 show the spanwise variations along the wall normal centerline.

The research group has utilized several different techniques to document the length scale associated with the turbulence generator exit flow, including auto-correlation, the frequency power spectra, and the two-point correlation. The auto-correlation (Figure 11) has yielded an integral length scale of 2.5 cm based upon the streamwise velocity fluctuation. Computation of length scales via power spectra for u', v', and w' taken with a triple-wire probe and the integral scale from a two-point technique is currently in progress.

A prime objective of this program to investigate the details and anisotropy of the three-dimensional flow field inherent to various film-cooling configurations within a range of blowing rates. To properly characterize these blowing rates, a flow metering system for the secondary flow has been designed and fabricated. The flow metering system consists of two parallel flow sections with a single flow meter in each. Each flow meter is composed of two banks of honeycomb with pressure taps located upstream and downstream of the banks. The honeycomb is comprised of approximately 500 tubes that are 3 mm in diameter and 133 mm in length. The flow meters have been calibrated against a Meriam laminar flow element. They yield a nearly linear relationship between the volumetric flow rate (SCFM) and the pressure drop (inches water) between the taps but a quadratic relation with a weak second-order term provides a better calibration fit. The meters will permit monitoring the film cooling flow. In addition, the variable frequency motor controller for the film cooling supply fan will facilitate adjusting to the desired blowing rates.

Presently, all items constituting the test assembly, except for the initial phenolic laminate test plate and the various inserts, have been fabricated. These items will be assembled into the facility and qualification measurements will be taken in early August. The current plans are to test streamwise injection configurations with low and high free-stream turbulence and then proceed with lateral injection studies.

Surface Measurements

A variation of the mass transfer analogy by which one can obtain effectiveness and heat transfer parameters for film cooling was described by Cho and Goldstein (1993). The surface of a blade is covered by a layer of naphthalene and its sublimation rate provides the required information. This method has a number of advantages; one experimental setup can produce effectiveness and heat transfer with great detail, the effect of variable properties can be studied, and mass transfer experiments exclude conduction in the solid wall. The experiments will utilize this technique. The flat plate with injection holes is covered with a thin layer of naphthalene and the local sublimation rate of the naphthalene is measured after the test plate has been exposed to the main and secondary film cooling airflows in the wind tunnel. In this way, the mass flow rate into the boundary layer is known for the given boundary conditions which, through the analogy, can be converted to the heat flow rate for the analogous thermal boundary conditions of the film cooling process.

Two sets of experiments are necessary to determine both the heat transfer coefficient and the adiabatic film cooling effectiveness. In the first experiment, pure air is injected as the film cooling flow. This is equivalent to a heat transfer case where the temperature of the cooling air is equal to the main stream temperature. In the second set, the injected (coolant) air is saturated with naphthalene vapor. This is equivalent to having the film cooling air temperature equal to the wall temperature. The film cooling effectiveness and the heat transfer coefficient for the film cooling process can be calculated from the results of the two data sets. As an application of this method, both mass (heat) transfer coefficient and cooling effectiveness distributions on test surfaces are determined for normal injection through perforated holes into a cross-flow (Figure 12). These results provide the information required to analyze temperature distributions and overall heat fluxes around injection holes. This detailed information will also aid the development of the numerical models for flow and mass/heat transfer around film cooling holes. To verify results from the naphthalene sublimation method for obtaining film cooling effectiveness, they are checked against measurements from the foreign gas sampling method which is presently used on the same test apparatus. The naphthalene test plate with an injection hole is replaced with a metal plate with an injection hole and 65 sampling taps near the injection hole. Helium is used as a tracer gas to produce mixture density ratios near unity. The local variations in the temperature field caused by the variations of effectiveness and heat transfer over the blade surface are partially smoothed by heat conduction in the solid material of the turbine blade. A knowledge of this effect is important to the designer in the evaluation of the cooling achieved by the film cooling arrangement. Once the distributions of local heat transfer and effectiveness are known, the influence of conduction is calculated numerically using the heat conduction equation. A temperature distribution in the film cooled wall is provided for the results obtained from the mass transfer measurements (Figure 13). The advantages of compound angle injection are only recently being understood.

Under many conditions, jets from discrete holes can penetrate into the mainstream and hot mainstream gases flow under the injected jet close to the surface to be protected, diminishing the film cooling performance. The purpose of the study is to investigate possible means for improving film cooling performance with injection through compound angled holes. Higher and more uniform film cooling effectiveness is expected with the compound angle injection due to the reduced axial momentum and the enhanced lateral momentum of the secondary flow at the larger lateral injection angles. The lower axial momentum and higher lateral momentum cause the jets to spread more widely in the lateral direction, rather than penetrate into the mainstream; this accounts for the higher film cooling effectiveness, particularly at high blowing rates. Another advantage of compound angle injection is that a more uniform effectiveness on the surface results for a wider range of blowing rates. This can reduce blade thermal stresses.

An experimental apparatus has been constructed to determine the combined film cooling effectiveness and heat (mass) transfer coefficient on a flat plate for angled injections. A schematic of the film cooling plate and naphthalene test surface is shown in Figure 14. Adjustable false walls are used to ensure a constant velocity within the test section and to contain the lateral spread of the injectant from the film cooling holes for 0^{O} lateral injection, shown from above in Figure 15. The arrangement for lateral injection is shown from above in Figure 16. Figure 17 shows the coordinate system and angle definitions for the compound injection case. A schematic representation of the injection system is shown in Figure 18. The key feature of this system is the use of naphthalene powder packs to saturate the secondary (film cooling) fluid with naphthalene vapor for some tests.

The downstream plate is cast with a thin layer of naphthalene and the local mass transfer rate is determined by measuring the surface elevation of the naphthalene both before and after exposing the plate to the main stream and secondary air flow in the wind tunnel. Two sets of experiments will be conducted (with and without the naphthalene powder packs in Figure 18) for each flow situation to determine the heat transfer coefficient and film cooling effectiveness distributions on the surface. In the first case, pure air is injected as the secondary flow ($\rho_{\gamma,2} = \rho_{\gamma,w}$ $\rho_{\gamma,2} = \rho_{\gamma,0}$ or $T_2 = T_0$). In the secondary case, air saturated with naphthalene vapor is injected as the secondary flow ($\rho_{\gamma,2} = \rho_{\gamma,w}$ or $T_2 = T_W$). Two angle orientations of film cooling holes will be investigated in this study ($\Phi = 35°$, $\beta = 0°$ and $45°$).

In the future, similar film cooling studies could be conducted in a turbine blade cascade. In this case, the flow situation is much more complex than that in a flat walled wind tunnel test section. Local mass transfer measurements have been conducted on the pressure and suction surface of a blade cascade. Figures 19 and 20 show the contour plots and surface flow visualization for comparison on the pressure and suction surface near the endwall of a linear cascade. The endwall surface flow visualization on the same cascade is also carried out and shown in Figure 21 for flow clarification.

Temperature distributions near film cooling holes have been obtained for different wall thermal conductivities (Figure 22). The conductivity of the material has been changed in a range of 1 to 100 w/m °C and the results show that temperature variation in a wall for $k \geq 20$ w/m °C is less than 15 percent of the overall temperature difference between the mainstream and coolant. The blade wall boundary condition is close to a constant temperature wall boundary condition. Thus, the data obtained from a naphthalene sublimation method, which corresponds to an isothermal boundary condition, can apply to the case in an actual gas turbine. Thermal stress near the film cooling hole occurs due to temperature gradients. The highest von-Mises stress (yield stress) is distributed near the front part of film cooling holes for a normal injection (Figure 23). The temperature and thermal stress distributions will give a limit of the gas temperature for a given film cooling hole geometry and blowing rate. This analysis can also be used to help design film cooling holes to reduce thermal stress.

Computation

Over the years, we have developed the capability to calculate three-dimensional flow fields and the associated heat transfer. Turbulence models of different complexity have been developed for the prediction of complex turbulent flows. In this research, computational activities directed at prediction of film cooling are performed. The computational work is coordinated with the corresponding experimental work. Wherever possible, computational results are compared with experimental data available in the literature and generated in the present project.

The computer programs for the prediction of turbulent flow and heat transfer in film-cooling situations have been tested. A large number of film-cooling situations have been calculated to determine the sensitivity to various numerical and physical parameters. One numerical issue examined is the suitability of a *parabolic* solution procedure over an *elliptic* procedure. Since most film cooling situations have a predominant flow direction, the flow can be treated as parabolic, at least for small angles of injection. The parabolic treatment turns out to be sufficiently accurate for a range of film-cooling situations.

So far, several benchmark solutions have been obtained for some film cooling situations by using the parabolic method. We subsequently plan to obtain elliptic solutions for the same problems and evaluate the applicability of the parabolic procedure. Relevant experimental data for comparison with the benchmark runs are being collected and analyzed.

Another activity which involves the inclusion of the upstream plenum in the calculation domain is in progress. Thus, the boundary condition for the injected fluid is not specified at the injection hole. These calculations that include the upstream plenum are being done as fully elliptic problems, since no predominant flow direction is identifiable in the domain of interest. These calculations will ultimately enable us to examine the effect of different hole geometries, upstream separation, and other complexities of the flow.

Two other issues that are being considered are the anisotropy of turbulence and modeling of transition. Advanced turbulence models are currently being examined for the prediction of these effects. The chosen models will subsequently be applied to the film-cooling situation.

Analysis

Conduction:

A system-level analysis was applied to the film cooling external and internal flow and blade surface. This analysis continued from that documented in the Appendix of Eckert (1992).

The temperature of a turbine blade is determined by the combined effects of the heat transfer from the cooling air as it approaches the film cooling holes, the heat transfer from the walls of the holes, the film cooling, and the heat conduction in the blade wall. The heat transfer coefficients vary strongly, locally, which causes temperature variations within the wall. An order of magnitude analysis resulted in a simple and quite general equation. The analysis considers the temperature variation parallel to the blade surface in a plane normal to the gas flow and downstream from the row of holes. The heat flux into the blade surface has a minimum in the region of the cooling air streaks and a maximum in between. The equation describes the effect as the ratio of the temperature difference in the blade wall, including the effect of conduction in the wall, to the temperature difference without wall conduction (for zero wall-conductivity). For a blade of normal dimensions manufactured out of alloyed steel and with measured heat transfer coefficients, this temperature difference ratio is 0.04. This means that the temperature differences are strongly reduced by wall heat conduction.

$$\frac{\Delta T_{w,o}}{\Delta T_w} = 4\pi^2 \frac{k}{(h_o + h_i)s} \left(\frac{s}{b}\right)^2 + 1 \qquad (1)$$

ΔT_w	temperature variation in the wall
$\Delta T_{w,o}$	temperature variation in the wall for $k = 0$
k	thermal conductivity of wall
h_o, h_2	heat transfer coefficients for gas to wall and on suction side of cooling air flow
s	wall thickness
b	spacing of film cooling holes

A computer calculation studied the effect of wall conduction and heat transfer from all parts of the blade surface (suction side, wall of cooling holes, film cooled surface) on the temperature distribution in the wall close to the cooling holes. Heat transfer coefficients were taken from measurements at this laboratory by Goldstein and Cho. A normal gas turbine blade and temperature conditions in a present-day gas turbine were considered. The calculation was performed as a check on the influence of the simplifying assumptions in the preceding analysis. The computed wall temperature varied in the average by 90 °C (162 °F) in a direction parallel to the blade surface and 60 °C (108 °F) normal to the surface. The resultant temperature gradients were 100 °C/cm (450 °F/in.) and 80 °C/cm (360 °F/in.), respectively, numbers which are of interest for thermal stress calculations. The agreement with the result of the described analysis is satisfactory.

Convection:

Streaks in the heat transfer coefficient are also generated on the surface of connectively cooled turbine blades by secondary flows. Figure 20 (Wang, 1995) presents a field of local Sherwood numbers, Sh, on the suction surface of a present-day turbine blade measured in a cascade tunnel by the naphthalene sublimation method at a chord Reynolds number of 500,000.

The heat-mass transfer analogy - exact for constant properties - states that local Nusselt numbers, Nu, are equal to the Sherwood numbers, Sh, at the same Reynolds numbers when the Prandtl number, Pr, of the heat transfer process is equal to the Schmidt number, Sc, for the mass transfer process. An empirical correction has to be applied where the ratio Sc/Pr is different from 1.0 (Goldstein and Cho, 1995). This leads to the expression

$$Sh = Nu\left(\frac{Su}{Pr}\right)^{1/3} \qquad (2)$$

from which the definition

$$Nu = \frac{h\ C}{k} \qquad (3)$$

(h, heat transfer coefficient; C, the characteristic length, which, in this instance, is the chord length; k, thermal conductivity). The following relation for the heat transfer coefficient can be obtained.

$$h = \frac{k}{C}\left(\frac{Sc}{Pr}\right)^{1/3} Sh \qquad (4)$$

This relation will later be used to obtain local heat transfer coefficients from Figure 19 in which the abscissa presents the ratio of the coordinate, s, measured along the blade surface in mainstream direction to the chord length, C. The ordinate z along the blade height is also made dimensionless with the chord length. The figure presents approximately one third of the blade height. The ratio z/C=0 is the location of the end wall.

Figure 20 shows that large local variations of the Sherwood number and, therefore, of the heat transfer coefficient occur at the stagnation line of the blade (near s/C=0) and along an inclined line starting at s/C ~ 0.3. This ridge is caused by the secondary flow through the blade passage.

For the design of the turbine, one has to know the temperature field of the turbine blade. This will be done by a numerical solution of Fourier's steady-state, two-dimensional heat conduction equation. It is expected that heat conduction in the blade wall flattens the temperature field as compared to the field of the heat transfer coefficient, especially at the location of the two ridges in Fig. and that a fairly coarse grid system can be used for the calculation. The required grid size will be estimated in the following section.

The dashed lines in Figure 24 sketch the expected shapes of the heat transfer coefficient and of the wall temperature across one of the ridges. They are approximated by the full lines. The direction z points across the ridge axis. The parameter H_o is the maximum variation of the heat transfer coefficient and h_o denotes here the base heat transfer coefficient in the neighborhood of the ridge. The parameter b is the location of z at which the heat transfer coefficient, H, has the value 0.5 H_o. Corresponding terms are used for the temperature profile.

The local heat transfer coefficient, h_o, approximated by an error-function is represented as

$$h_o = \bar{h}_o + H = \bar{h}_o + H_o e^{-\left(\frac{z}{k}\right)^2} \qquad (5)$$

The heat conduction equation for the blade wall is

$$-ks\frac{d^2\vartheta_w}{dz^2} = h_o\left(T_o - \bar{T}_w\right) - h_i\left(\bar{T}_w - T_i\right) \qquad (6)$$

The heat transfer coefficients are defined using the wall temperature averaged over the width, B, which is permissible as long as the wall temperature variation is small compared with the temperature differences in Equation (6).

Integrated over the width of the ridge, the equation takes the form

$$\bar{h}_o (T_o - \bar{T}_w) = h_i (\bar{T}_w - T_i) \qquad (7)$$

subtracting Equation (6) from Equation (7) one obtains

$$-ks \frac{d^2 \vartheta_w}{dz^2} = H_o e^{-\left(\frac{z}{b}\right)^2} \left(T_o - \bar{T}_w\right) \qquad (8)$$

or

$$\frac{d^2 (\vartheta_w / (T_o - \bar{T}_w))}{d(z/b)^2} = \frac{H_o s}{k} \left(\frac{b}{s}\right)^2 e^{-\left(\frac{z}{b}\right)^2} \qquad (9)$$

The solution will have the form

$$\vartheta_w / (T_o - \bar{T}_w) = f\left(\frac{H_o s}{k}\left(\frac{b}{s}\right)^2, \frac{z}{b}\right) \qquad (10)$$

and the half-width of the streaks will be described by a relation of the form

$$\frac{B}{b} = f\left(\frac{Hs}{k}\left(\frac{b}{s}\right)^2\right) \qquad (11)$$

Figure 25 presents the temperature field, B, the half width of the streak, with a similar definition to that of b. Boundary conditions are required along the rim of the field. For the turbine blade, one requires that the temperature field around the blade be continuous. For a sample calculation, this will be approximated by prescribing zero heat flux in the s direction of Figure 20 at s/C=0 and s/C=1.4. Further, $\vartheta_o = T_w$ will be postulated at the base. The boundary condition at the top will be zero heat flux in z/C direction which should approximate the actual condition because the temperature field T_w is essentially two dimensional away from the endwall.

References

Ames, F.E., and Moffat, R.J., 1990, "Heat Transfer With High Intensity, Large Scale Turbulence: The Flat Plate Turbulent Boundary Layer and The Cylindrical Stagnation Point." Report No. HMT-44.

Ames, F.E., 1994, "Experimental Study of Vane Heat Transfer and Aerodynamics At Elevated Level of Turbulence," NASA contractor report 4633.

Bicen, A.F., and Jones, W.P., 1986, "Velocity Characteristics of Isothermal and Combusting Flows in a Model Combustor," *Combust. Sci. and Technology*, Vol. 49, p. 1.

Bons, J.P., MacArthur, C.D., and Rivir, R.B., 1994, "The Effect of High Freestream Turbulence on Film Cooling Effectiveness," ASME Paper No. 94-GT-51.

Cho, H.H., and Goldstein, R.J., 1993, "Heat (Mass) Transfer and Film Cooling Effectiveness With Injection through Discrete Holes - Part I: Within Holes and on the Back Surface," *ASME Paper 93-WA/HT-58.*

Cho, H.H., and Goldstein, R.J., 1993, "Heat (Mass) Transfer and Film Cooling Effectiveness with Injection through Discrete Holes - Part II: on the Exposed Surface," *ASME Paper 93-WA/HT-59.*

Eckert, E.R.G., 1992, "Similarity Analysis of Model Experiments for Film Cooling in Gas Turbine," Wärme-und Stoffübertragung 27, 217-223.

Goldstein, R.J., and Cho, H.H., 1995, "A Review of Mass Transfer Measurements Using Naphthalene Sublimation," *Experimental Thermal and Fluid Science*, Vol. 10, pp. 416-434.

Jumper, G.W., Elrod, W.C., and Rivir, R.B., 1991, "Film Cooling Effectiveness in High-Turbulence Flow," *ASME Journal of Turbomachinery*, Vol. 113, pp. 479-483.

Laufer J., 1953, "The Structure of Turbulence in Fully Developed Pipe Flow," *NACA TN2954.*

MacMullin, R., Elrod, W.C., and Rivir, R.B., 1989, "Free Stream Turbulence From a Circular Wall Jet on a Flat Heat Transfer and Boundary Layer Flow," *ASME Journal of Turbomachinery*, Vol. 111, pp. 78-86.

Sahm, M.K., and Moffat, R.J., 1992, "Turbulent Boundary Layers With High Turbulence: Experimental Heat Transfer And Structure On Flat And Convex Walls." Report No. HMT-45.

Thole, K.A., Bogard, D.G., and Whan-Tong, 1994, "Simultaneous Temperature and Velocity Measurements," Meas. Sci. Technical Vol. 5 pp. 435-439.

Wang, H.P., Olsen, S.J., and Goldstein, R.J., "Secondary Flows in the Blade/Endwall Region of a Turbine Cascade," Proceedings of the Symposium on Thermal Science and Engineering in Honor of Chancellor Chang-Lin Tien, November 14, 1995, Berkeley, California.

Whan-Tong, J., and Bogard, D.G., 1991, "The Development of a Very High Free-stream Turbulence Generator For Use In Gas Turbine," University of Texas. Report TTCRL91-1.

Young, C.D., Han, J.C., and Rivir, R.B., 1992, "Influence Of Jet-Grid Turbulence On Flat Plate Turbulent Boundary Layer Flow and Heat Transfer," *Journal of Heat Transfer*, Vol. 114, pp. 65-72.

Table 1: Schemes for Generating Turbulence

Picture	Tu	Length Scale	Reference
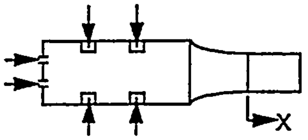	X=208cm Tu=7.5%	X=208cm Lx=5.4	Ames, 1994
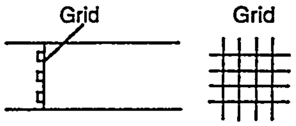	X=172cm Tu=4.5%		Sahm / Moffat, 1992
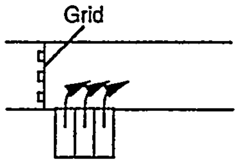			Sahm / Moffat, 1992
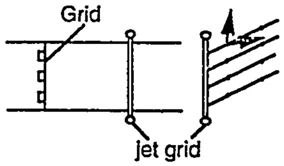	Tu=21%		Sahm / Moffat, 1992
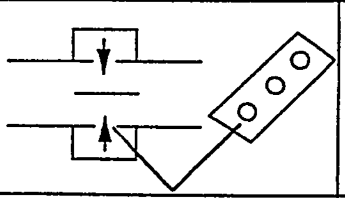	X/D=100 Tu=15%	Lx/D=7	Thole, Bogard and Whan-Tong, 1994
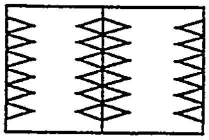	Compared with Bar-grid, Tu is much higher for delta-wing grid and the decay rate is slower		Whan-Tong and Bogard, 1991

Table 2: Operating Ranges of Parameters

Blowing rate	**$1 < M < 4$**
Hole-to-hole spacing	**$s = 3D$**
Inclined angles from surface	**$\Phi = 35$**
Lateral angles from mainstream	**$\beta = 0, 30, 45, \& 60$**

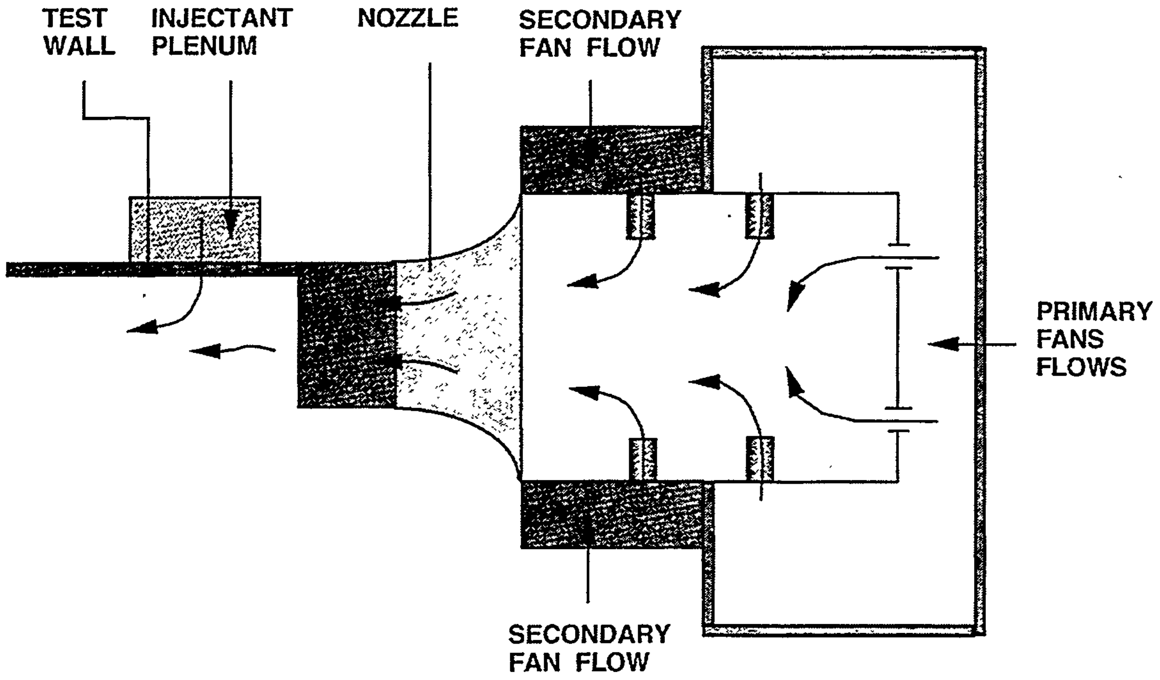

Figure 1. High Turbulence Facility

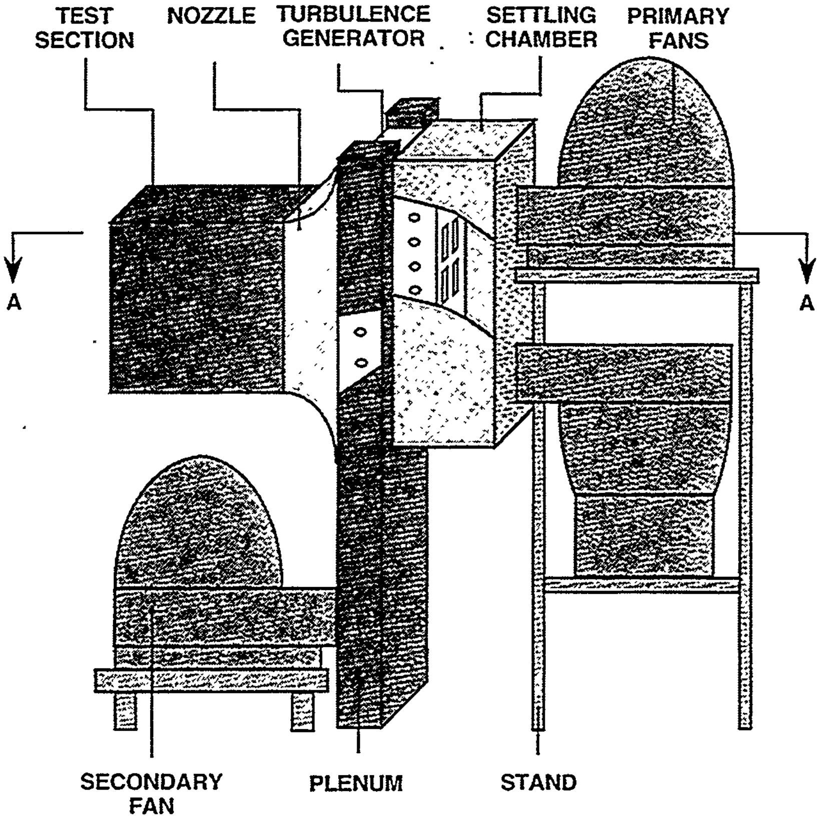

Figure 2. High Turbulence Facility

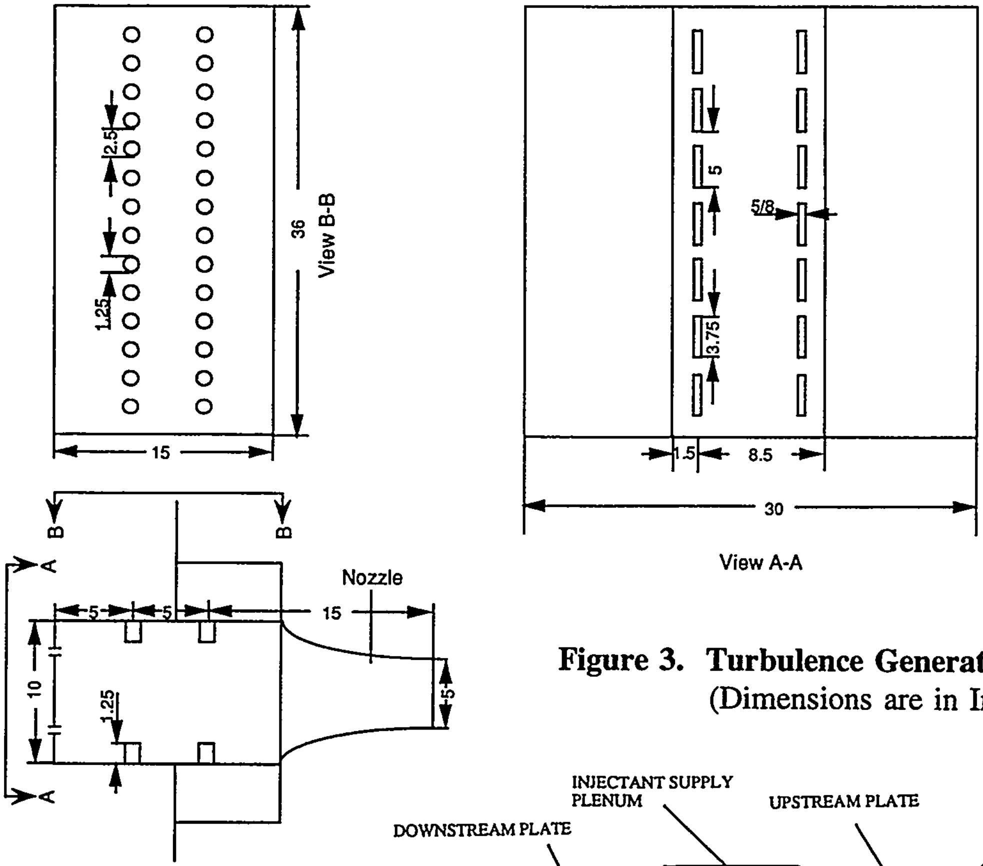

Figure 3. Turbulence Generator Panels
(Dimensions are in Inches)

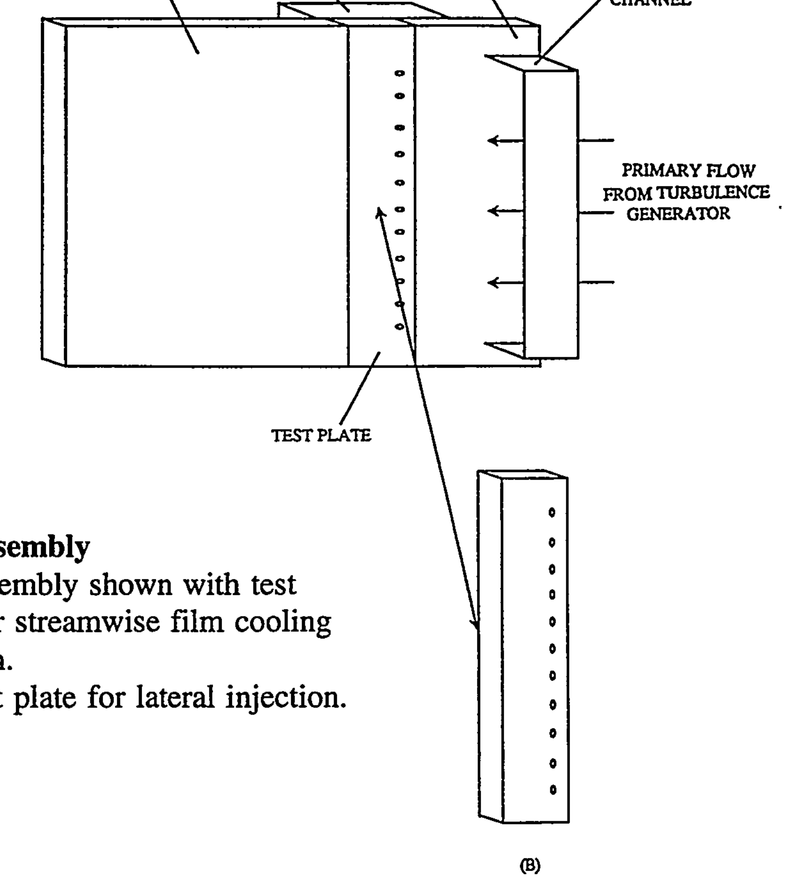

Figure 4. Test Assembly
(A) Assembly shown with test plate for streamwise film cooling injection.
(B) Test plate for lateral injection.

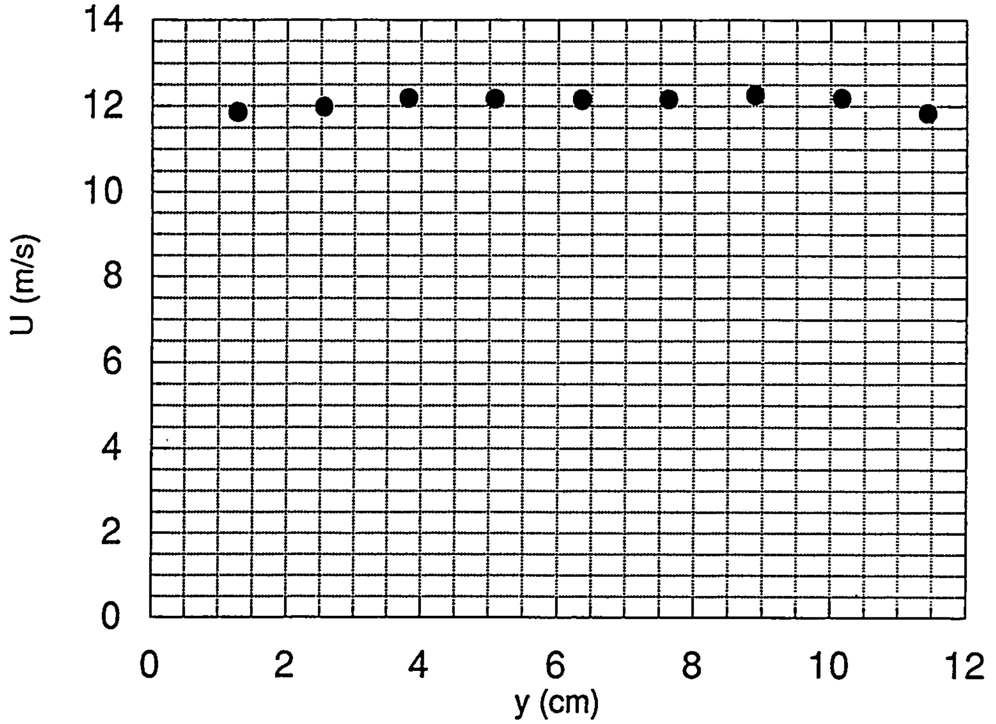

Figure 5. Streamwise Velocity Distribution at Spanwise Centerline (z = 13.5" and y = wall normal distance)

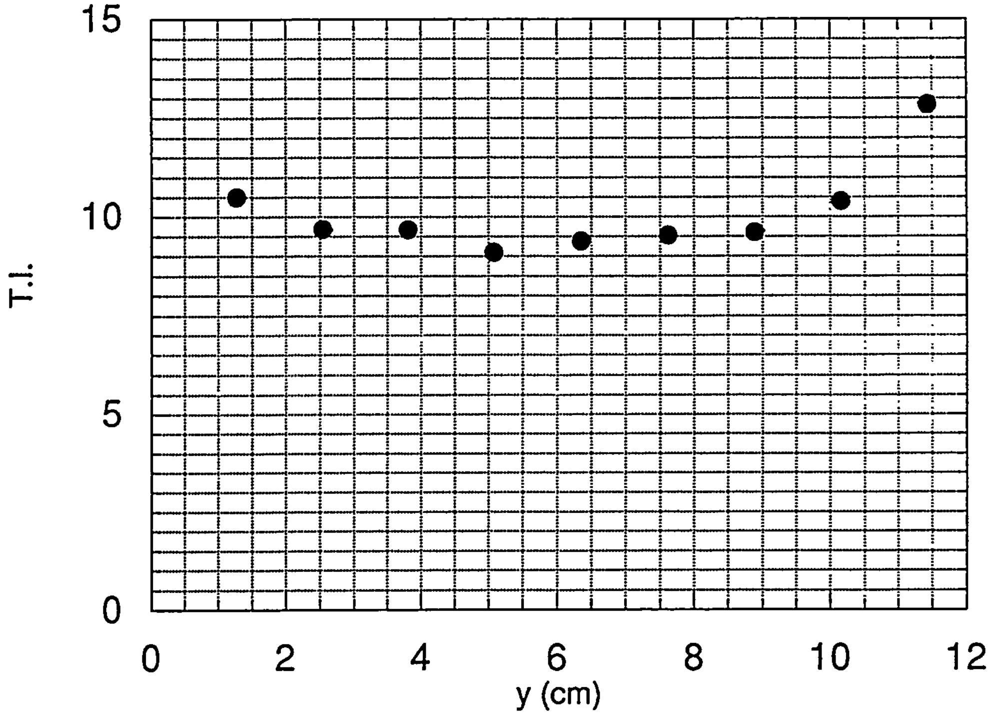

Figure 6. Streamwise Turbulence Intensity Distribution at Spanwise Centerline (z = 13.5" and y = wall normal distance)

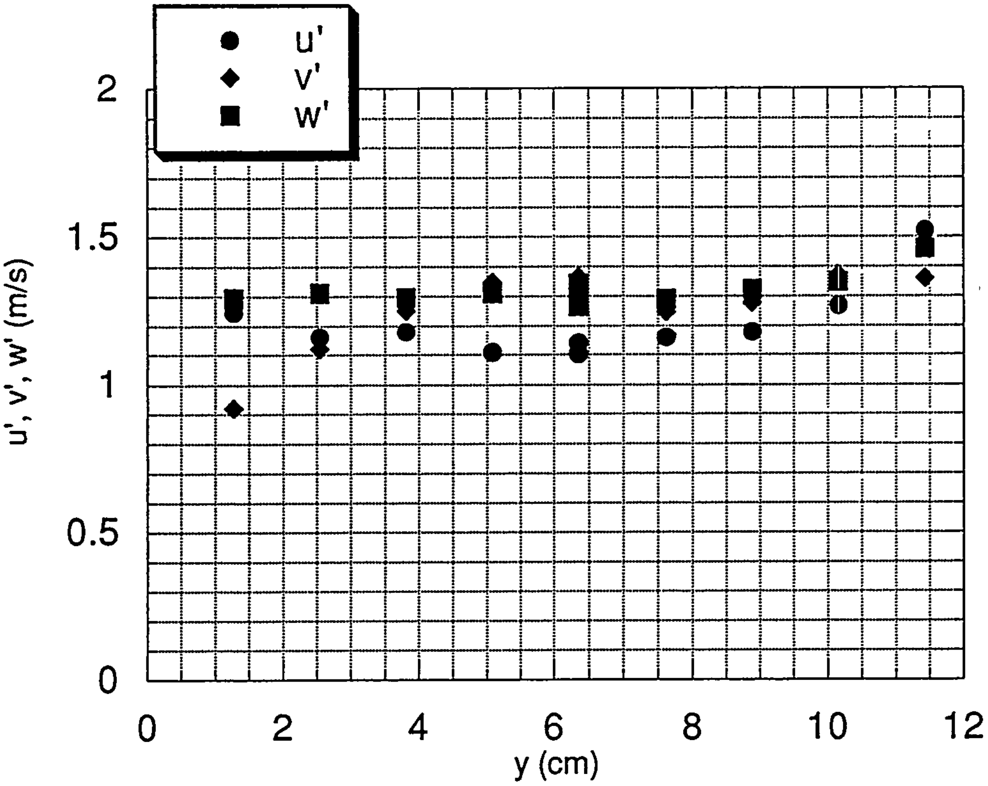

Figure 7. Velocity Fluctuation Distributions at Spanwise Centerline (z = 13.5" and y = wall normal distance)

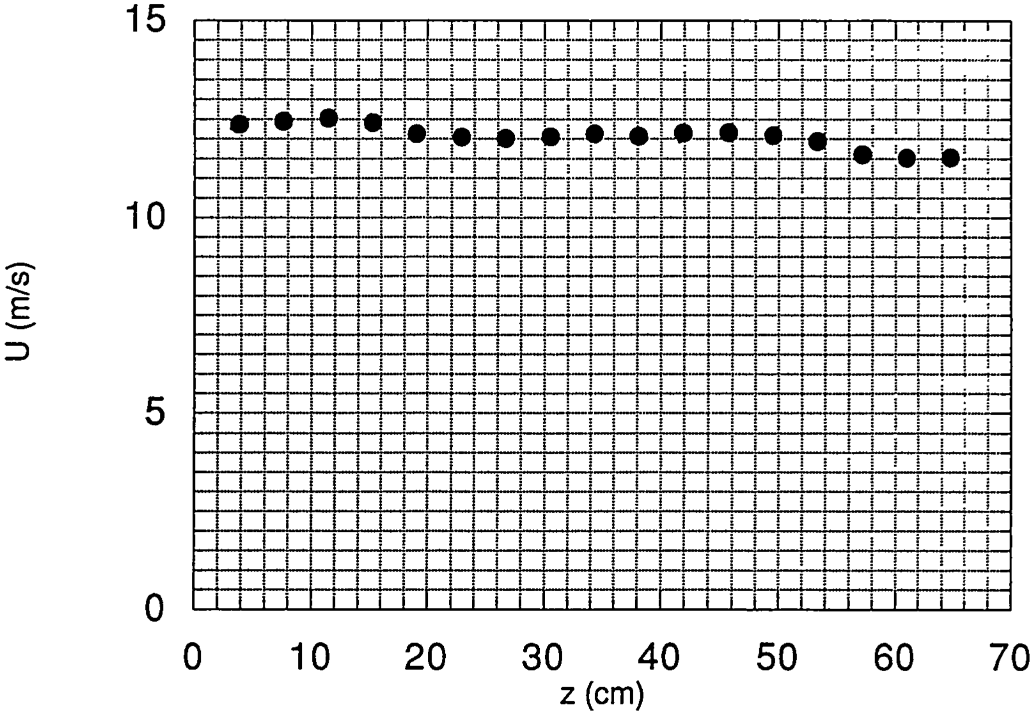

Figure 8. Streamwise Velocity Distribution at Wall Normal Centerline Centerline (y = 2.5" and z = spanwise distance)

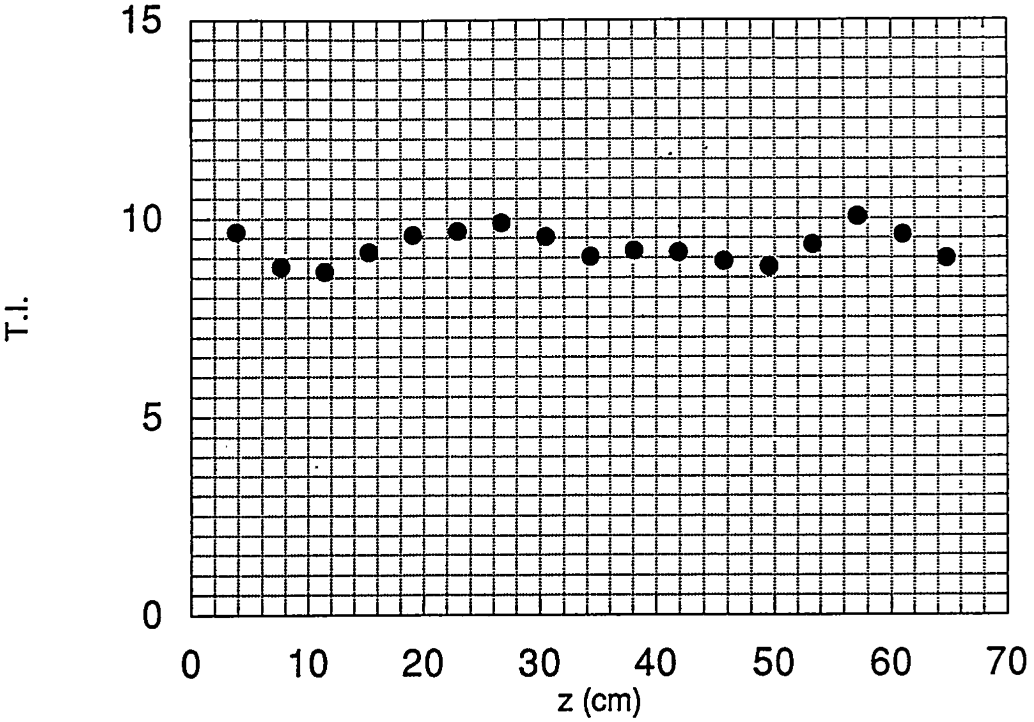

Figure 9. Streamwise Turbulence Intensity Distribution at Wall Normal Centerline
(y = 2.5" and z = spanwise distance)

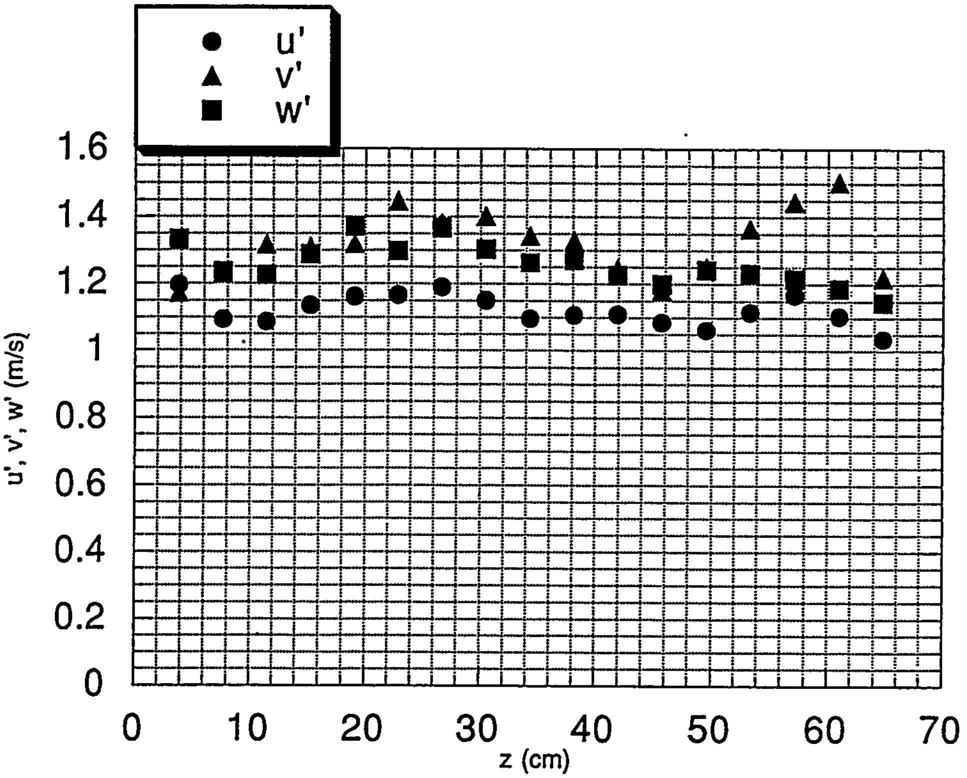

Figure 10. Velocity Fluctuation Distributions at Wall Normal Centerline
(y = 2.5" and z = spanwise distance)

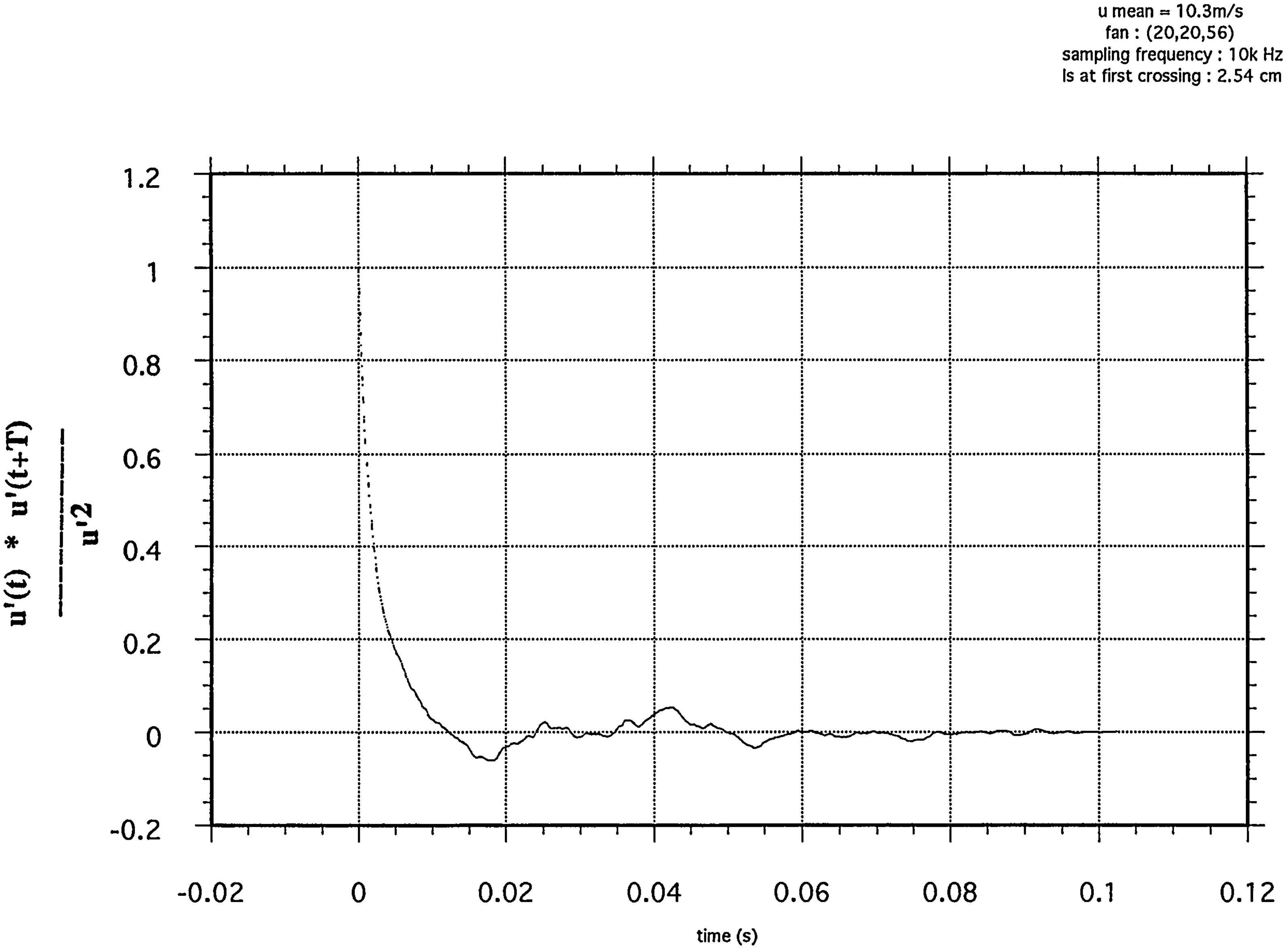

Figure 11. Autocorrelation Based on Streamwise Velocity

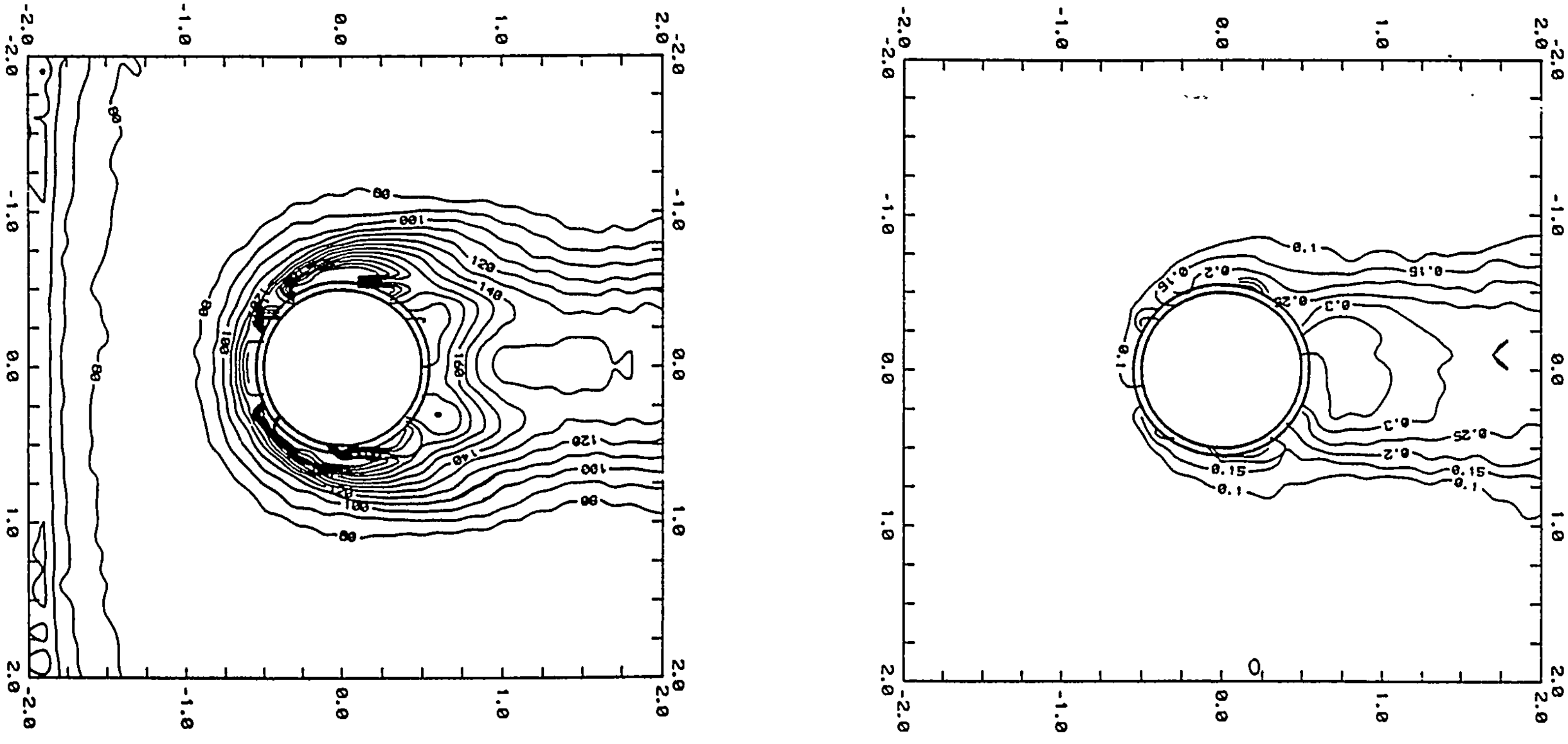

(a) Sherwood number

(b) Film cooling effectiveness

Figure 12. Sherwood Number and Film Cooling Effectiveness Contours for a Normal Injection at M = 1.0.

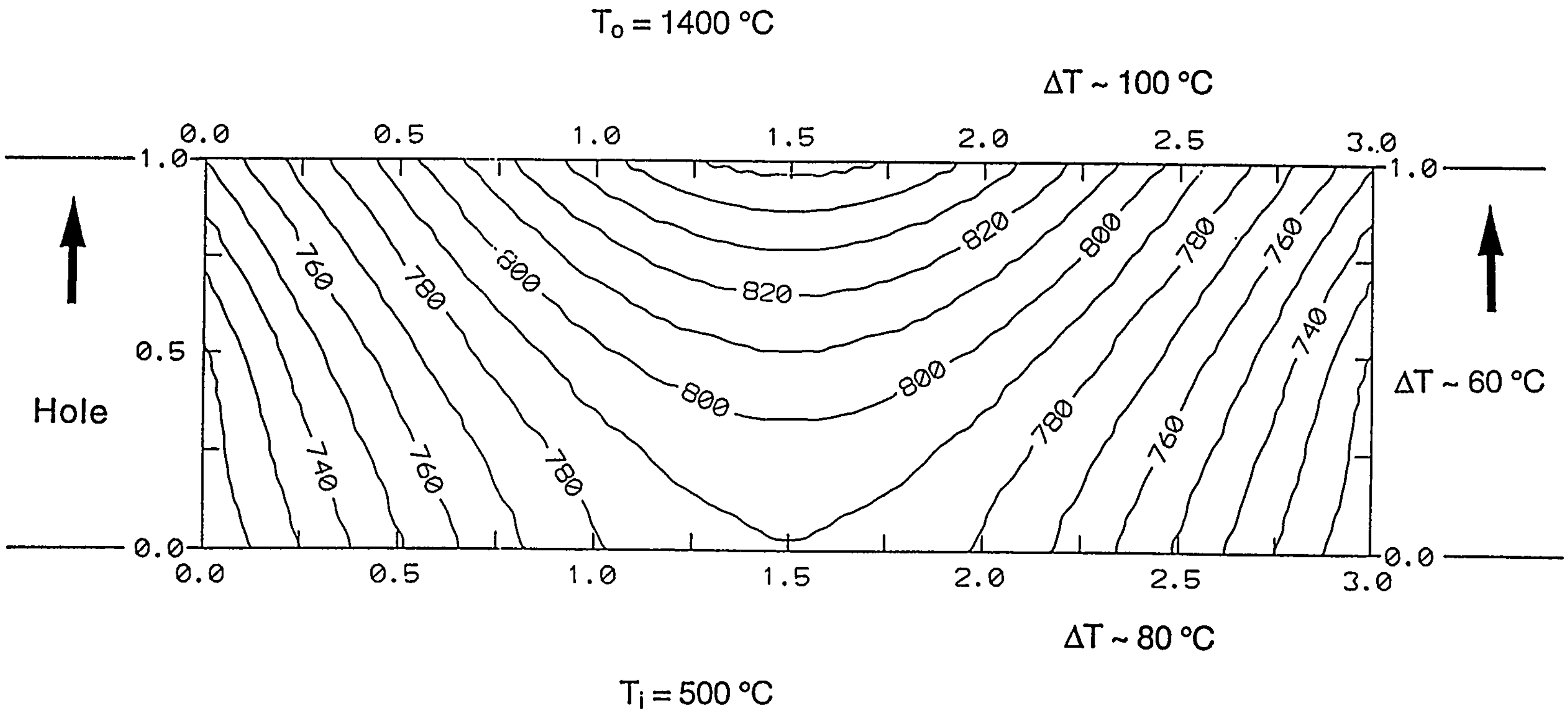

Figure 13. Temperature Field in Film Cooled Wall (k = 20 W/m °C)

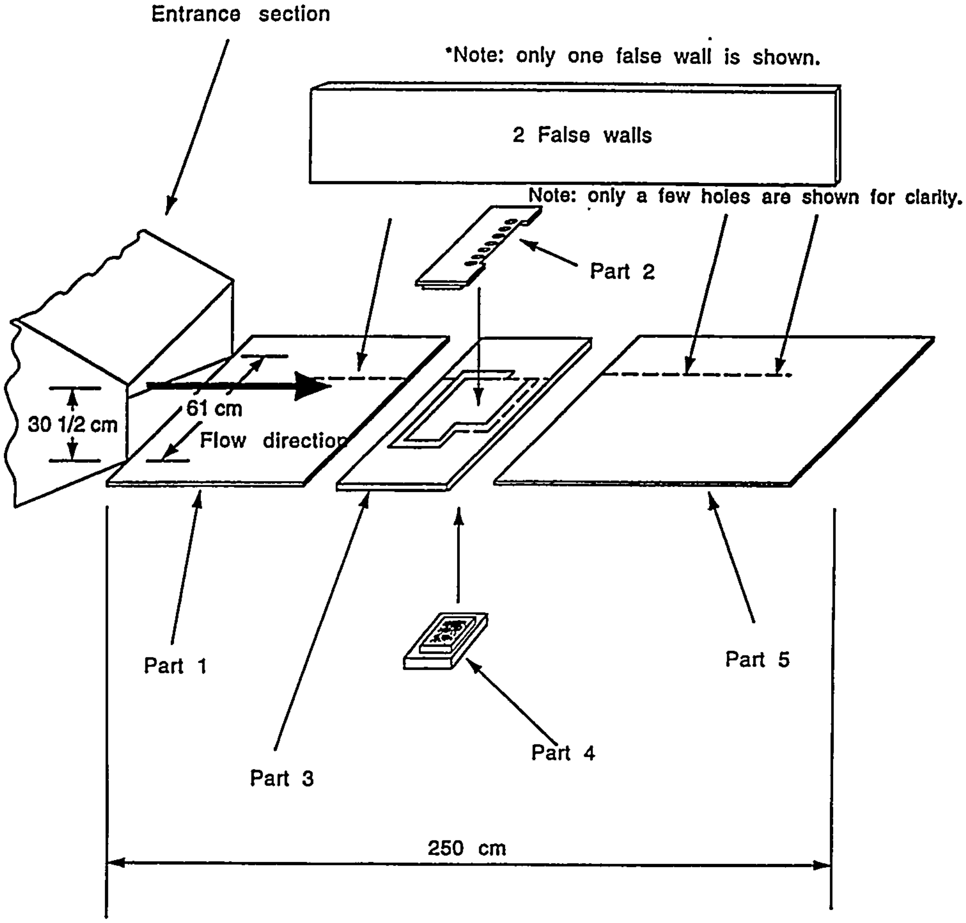

Figure 14.

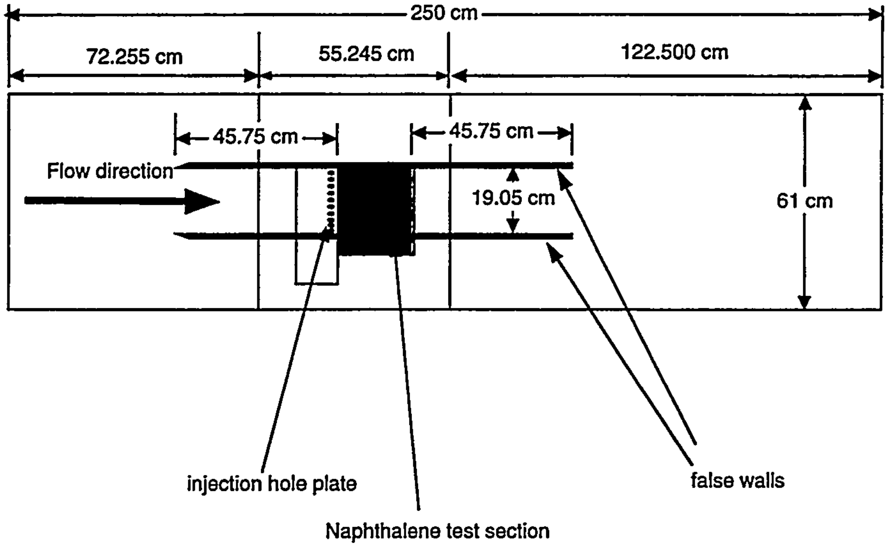

Figure 15.

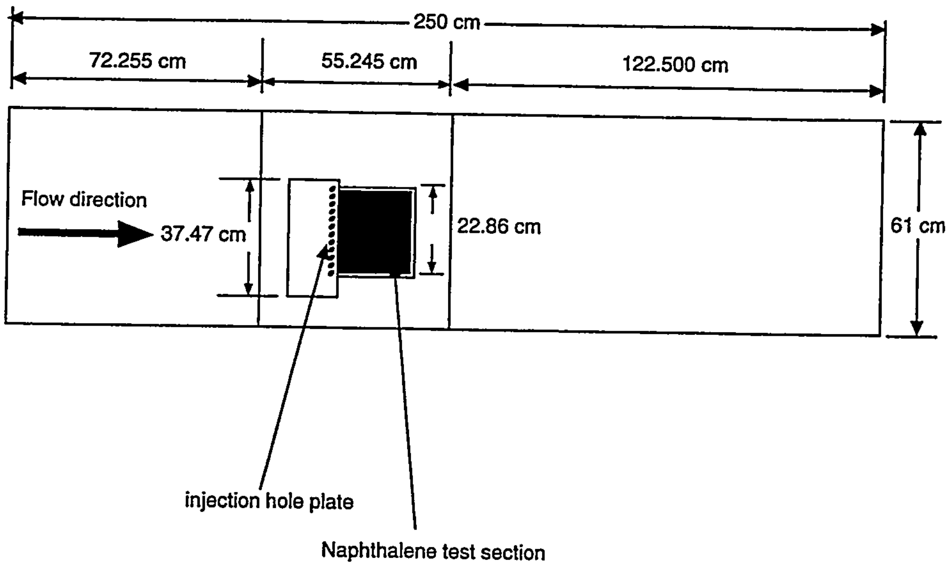

Figure 16.

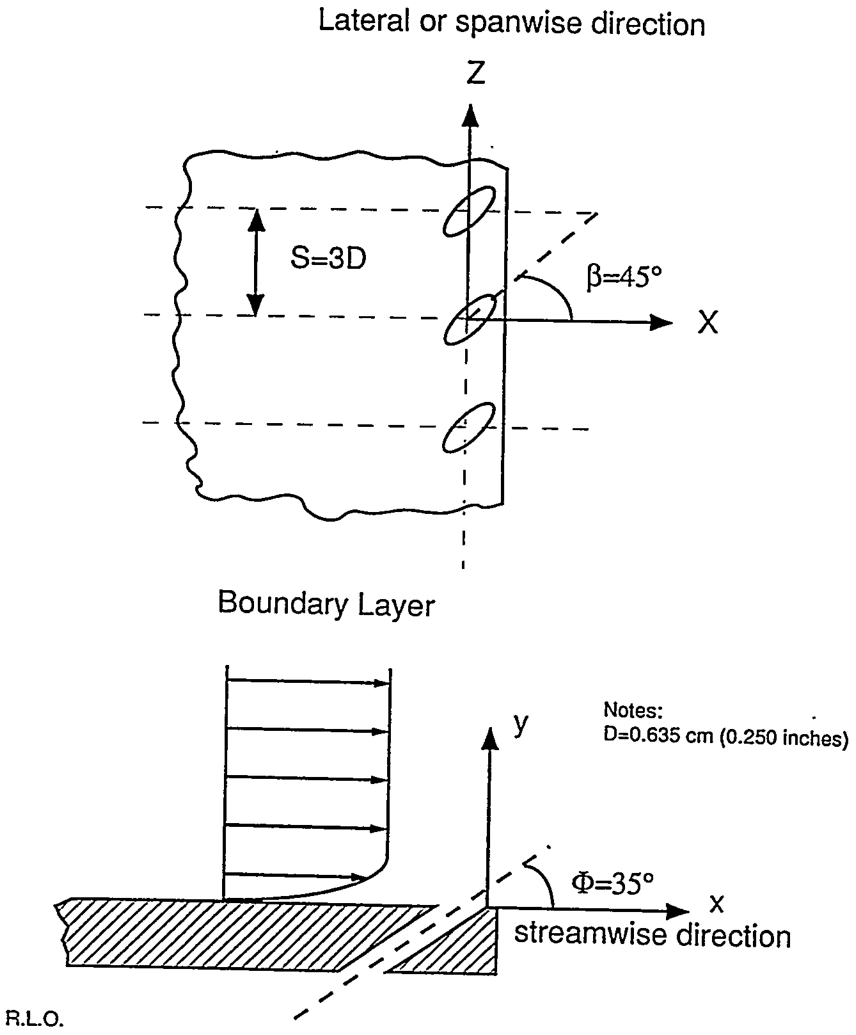

Figure 17.

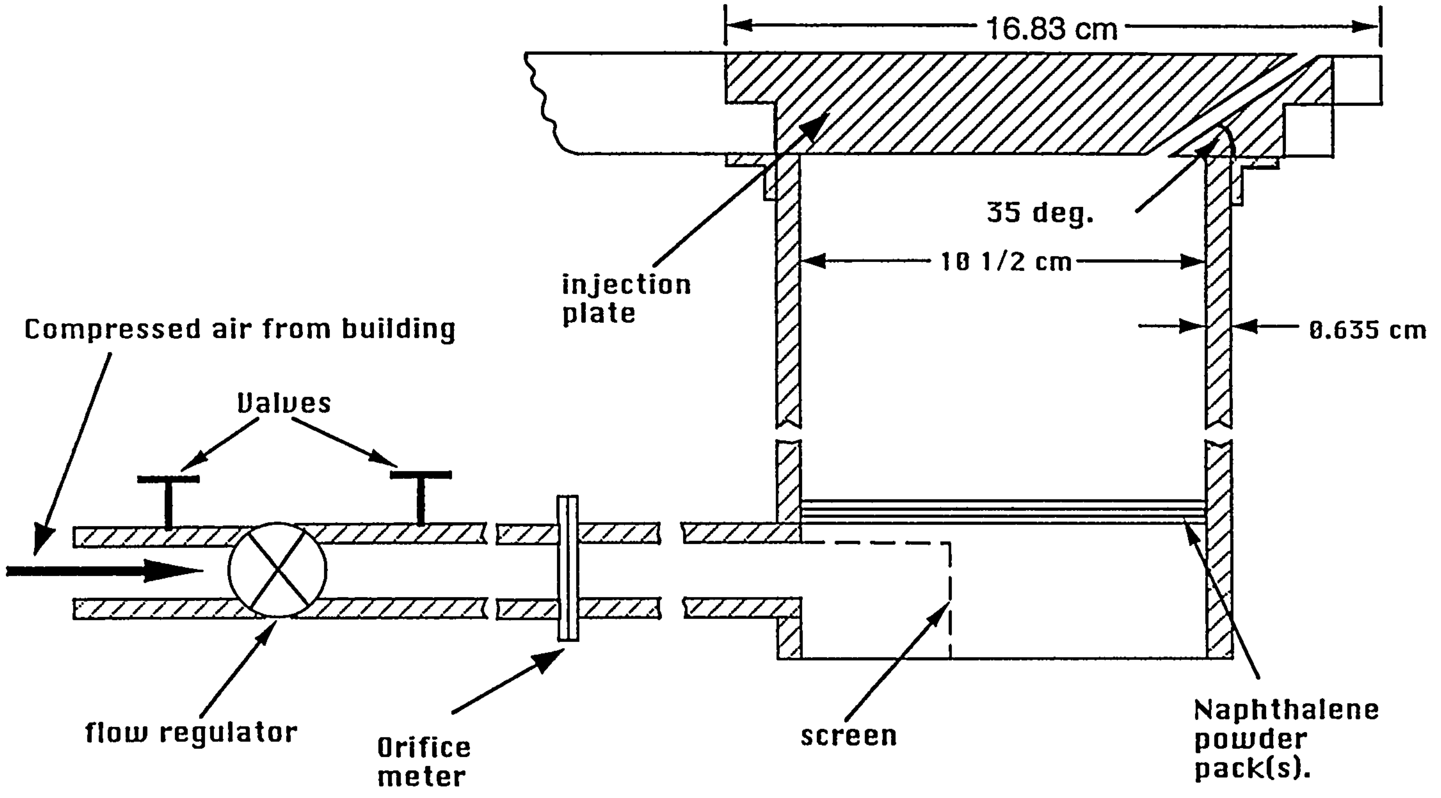

Figure 18. Cut Away Side View of Injection System

Notes:
1 D = 0.25 inches
main stream velocity: 10-15 m/s
blowing rate: 0.5-2.0
35 degree injection angle

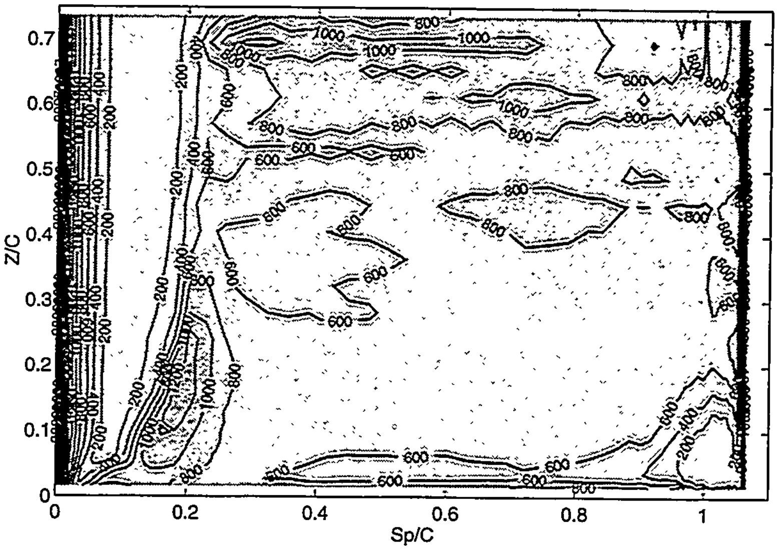

(a) Mass Transfer (Sh Contours)

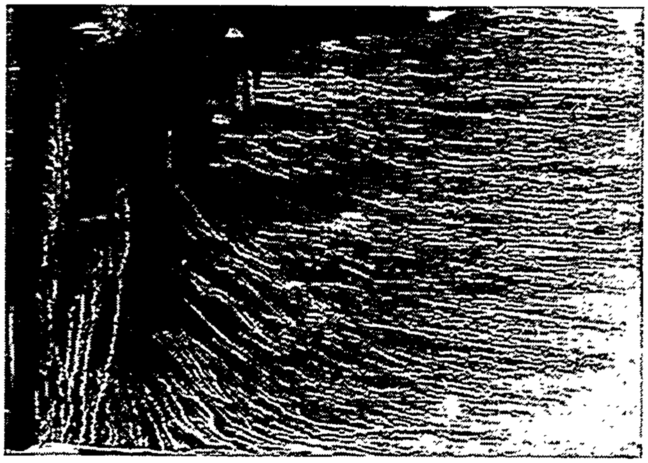

(b) Oil and Paint Pigment

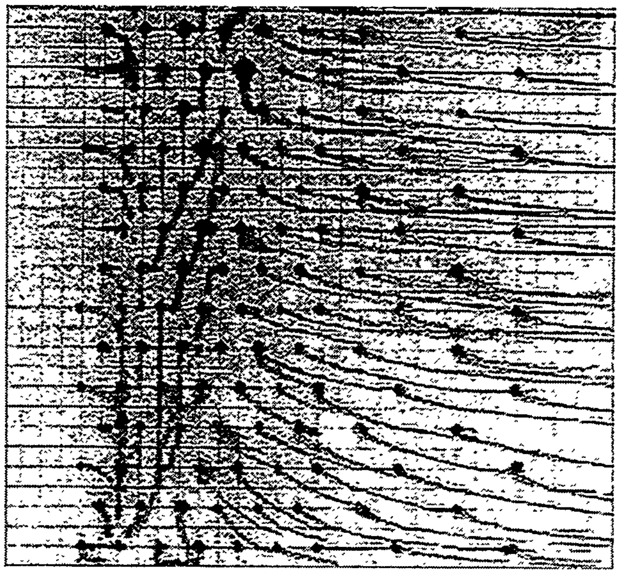

(c) Discrete Oil and Paint Pigment

Figure 19. Flow Visulization and Mass Transfer on the Pressure Surface of the Blade

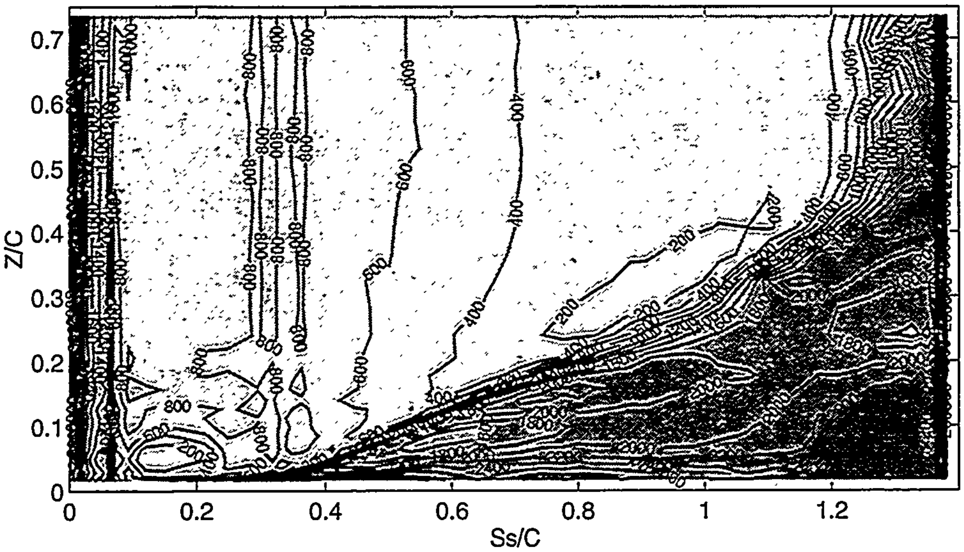

(a) Mass Transfer (Sh Contours)

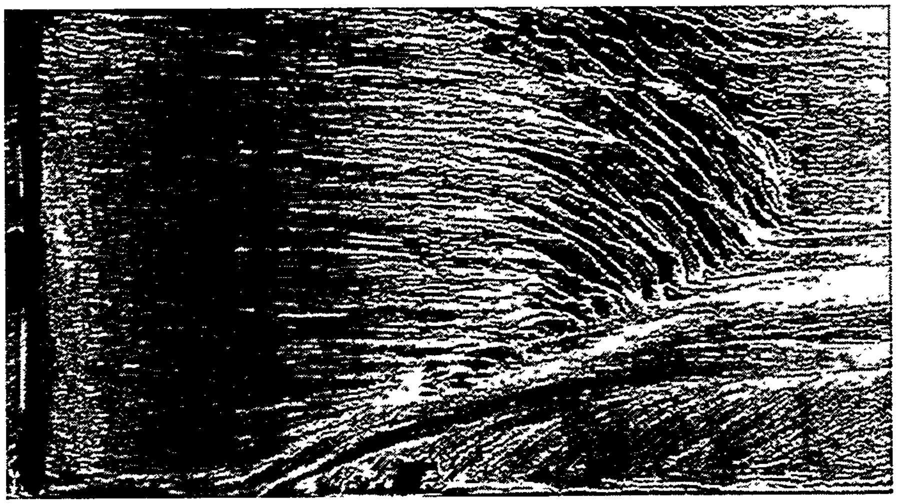

(b) Oil and Paint Pigment

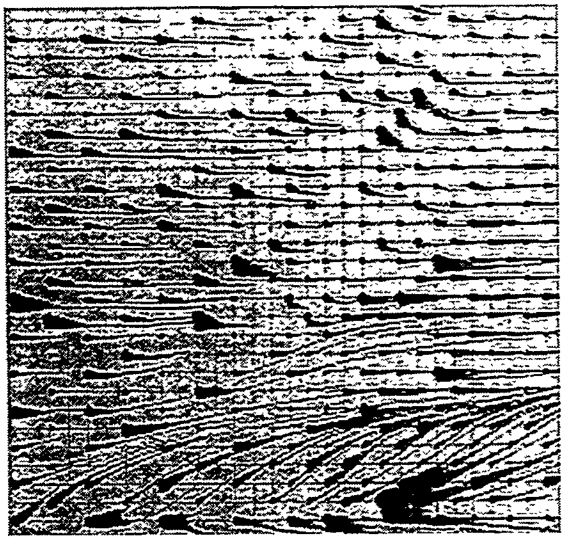

(c) Discrete Oil and Paint Pigment

Figure 20. Flow Visulization and Mass Transfer on the Suction Surface of the Blade

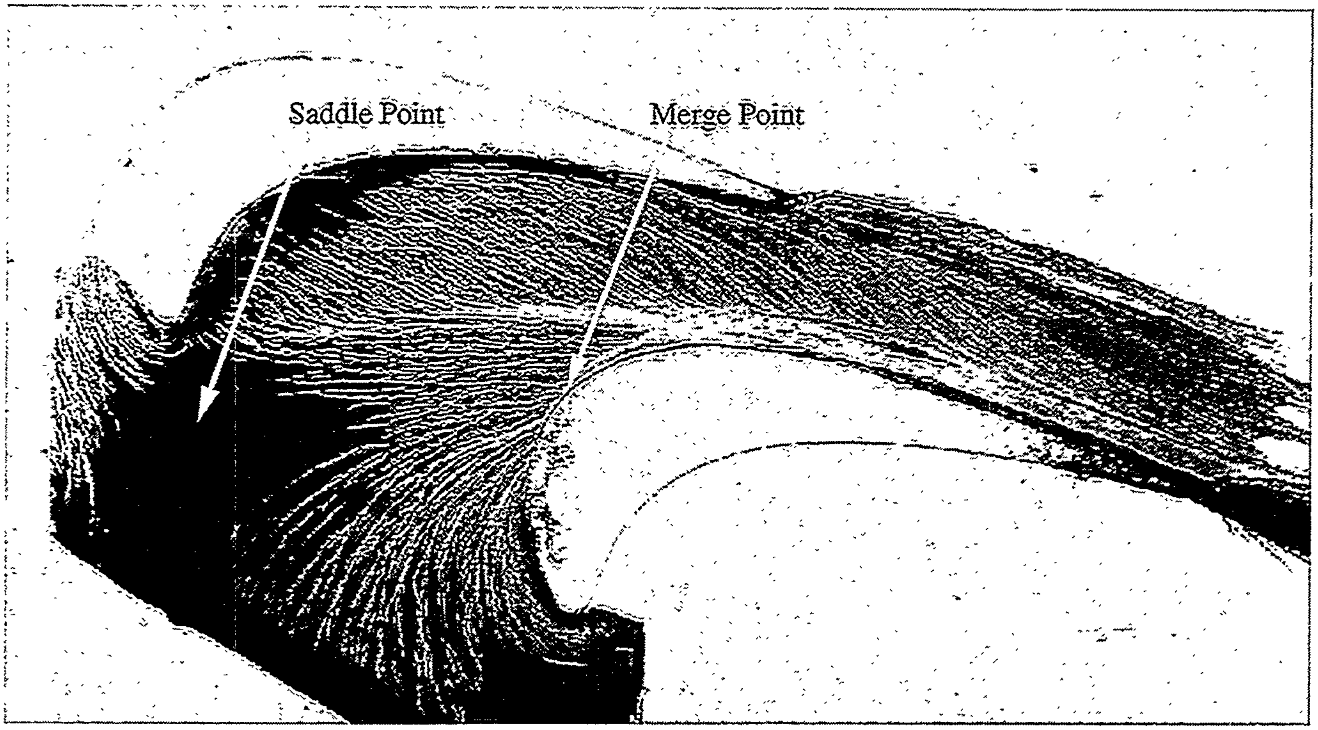

(a) Oil lampblack

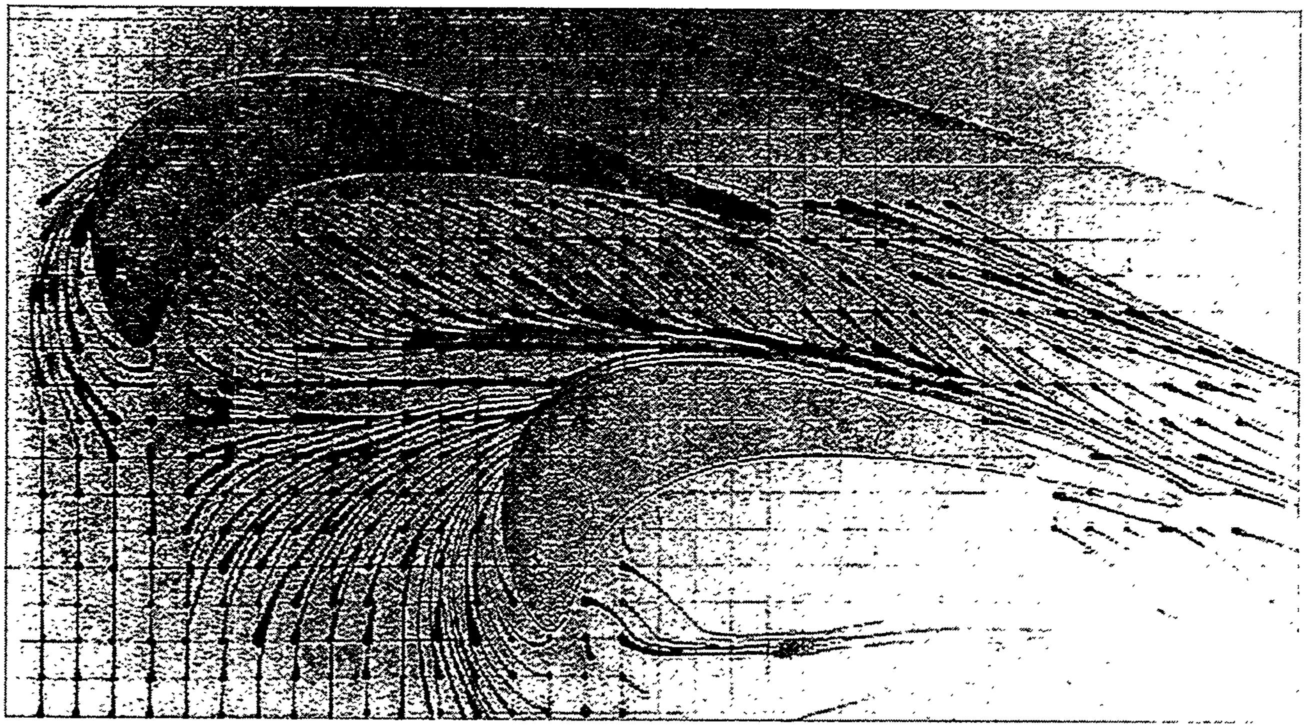

(b) Oil wintergreen

Figure 21. Endwall Flow Visualization

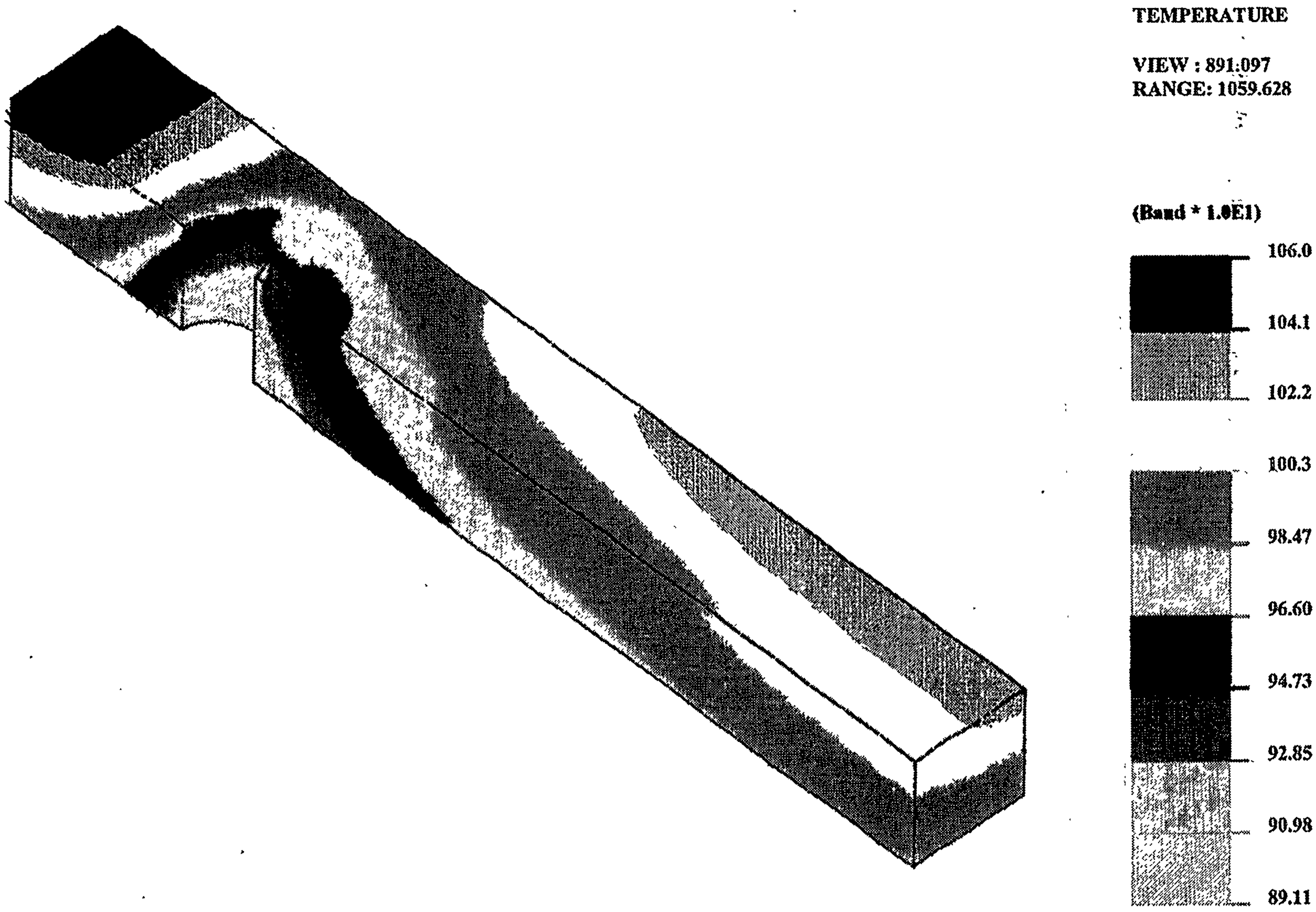

Figure 22. Temperature Distribution Near a Film Cooling Hole (Spacing s = 3d, Plate Thickness t = 1.5d; T_∞ = 1400 °C, T_i = 500 °C; M = 0.57, k = 21 W/m °C)

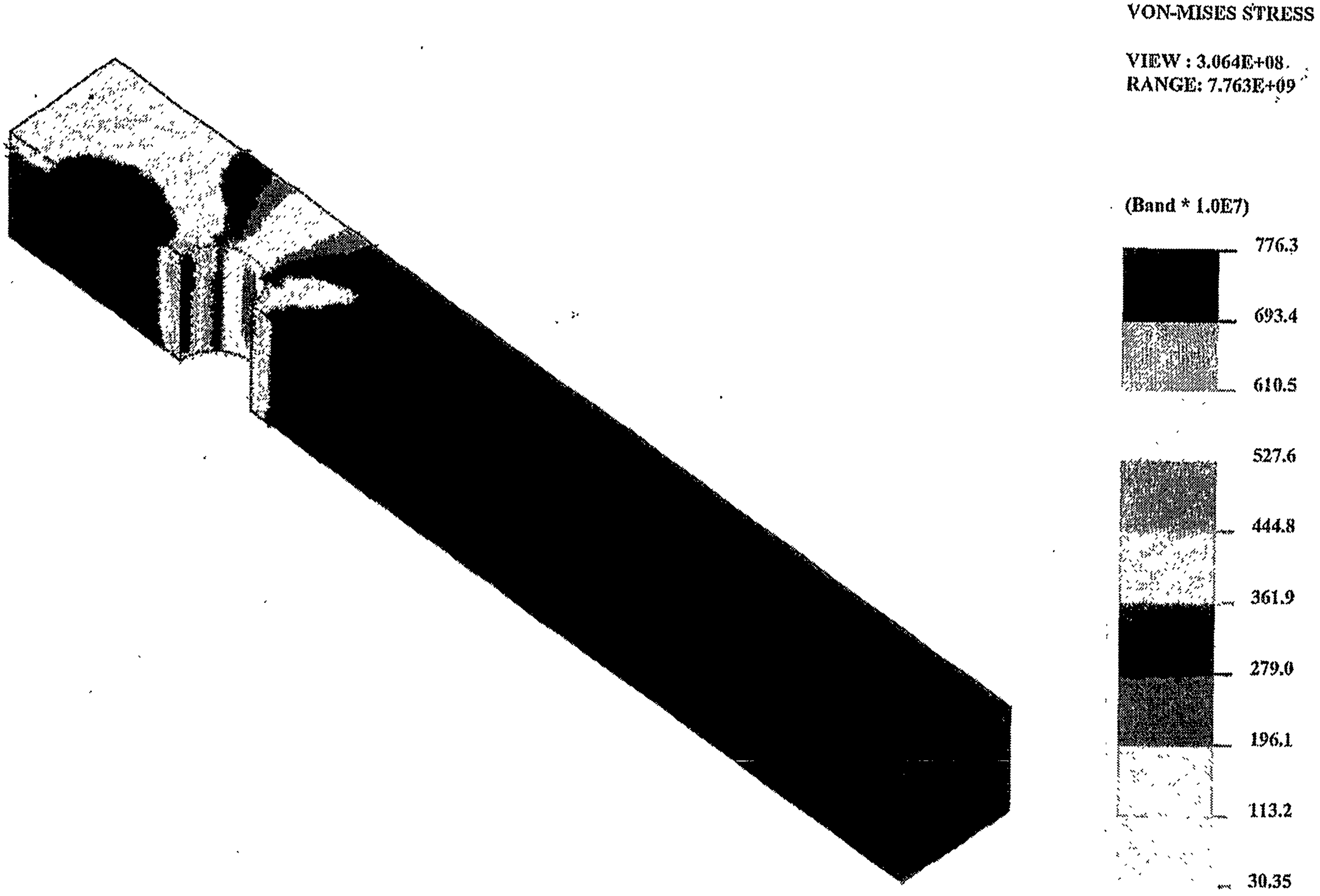

Figure 23. Von-Mises Stress Distribution Near a Film Cooling Hole due to Temperature Gradients (s = 3d, t = 1.5d; T_∞ = 1400 °C, T_i = 500 °C; M = 0.57, k = 21 W/m °C; $\alpha E = 3.5 \times 10^6$ N/m² °C, ν = 0.31)

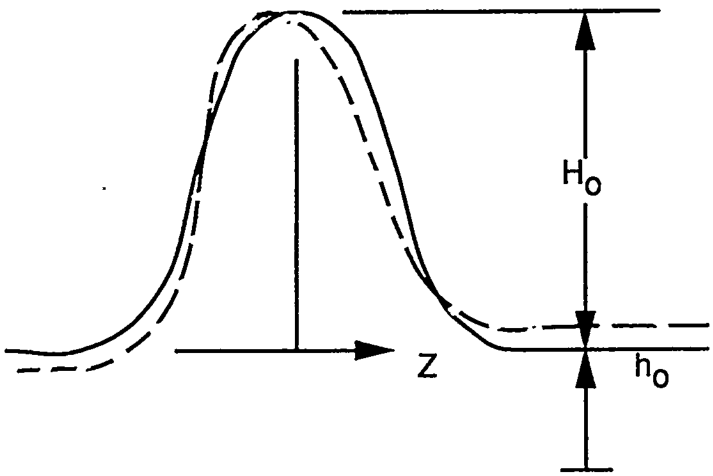

Figure 24. Measured and Assumed Shapes of the Convective Heat Transfer Coefficients

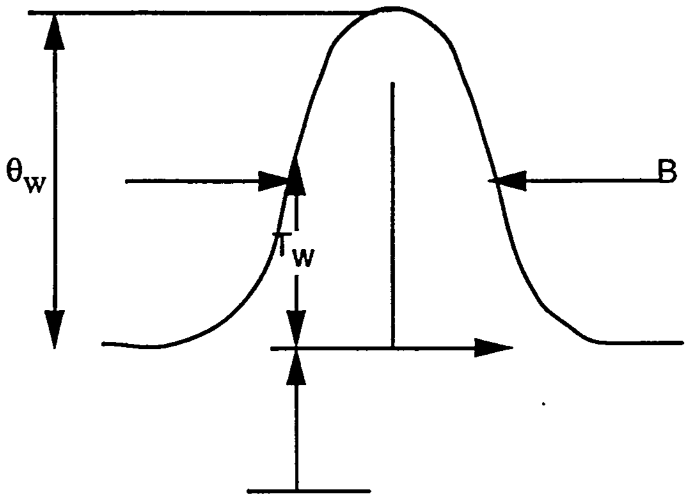

Figure 25. Computed Temperature Distribution

P16 Compatibility of Gas Turbine Materials With Steam Cooling

V. Desai (desai@mae.engr.ucf.edu; 407-823-5777)
D. Tamboli (dct@turbu.engr.ucf.edu; 407-823-5650)
Y. Patel (ypa@turbu.engr.ucf.edu; 407-823-5650)
Mechanical & Aerospace Engineering Department
University of Central Florida
Orlando, FL 38216

Introduction

Gas turbines had been traditionally used for peak load plants and remote locations as they offer advantage of low installation costs and quick start up time. Their use as a base load generator had not been feasible owing to their poor efficiency. However, with the advent of gas turbines based combined cycle plants (CCPs), continued advances in efficiency are being made. Coupled with ultra low NO_x emissions, coal compatibility and higher unit output, gas turbines are now competing with conventional power plants for base load power generation. Currently, the turbines are designed with TIT of 2300^0 F and metal temperatures are maintained around 1700^0 F by using air cooling. New higher efficiency ATS turbines will have TIT as high as 2700^0 F. To withstand this high temperature improved materials, coatings, and advances in cooling system and design are warranted. Development of advanced materials with better capabilities specifically for land base applications are time consuming and may not be available by ATS time frame or may prove costly for the first generation ATS gas turbines. Therefore improvement in the cooling system of hot components, which can take place in a relatively shorter time frame, is important. One way to improve cooling efficiency is to use better cooling agent. Steam as an alternate cooling agent offers attractive advantages because of its higher specific heat (almost twice that of air) and lower viscosity.

Steam cooling can lead to several materials related problems that warrant attention prior to its introduction in ATS. The most deleterious effect steam can have on the gas turbine materials is the hot corrosion aided by deposition of impurity salts from the steam. The solubility of salts in steam generally increase with increasing temperature and increasing pressure of the steam. As the steam flows through cooling passages, the steam pressure will be dropping which may lead to salt deposition from steam. The salt deposits can lead to enhanced corrosion and oxidation problems. Number of cases of hot corrosion by Na_2SO_4 deposits in gas turbines have been reported. The problem can be worse in the case of steam cooling because of presence of the chloride ions in the steam. The other major problem associated is the heavy internal oxidation of Al containing alloys. The extent of internal penetration of oxides and the large γ' depleted zone associated with it may cause severe degradation in mechanical properties. This in combination with hydrogen damage due to dissociation of steam at high temperatures, may pose severe problem.

Research sponsored by the U.S. Department of Energy's Morgantown Energy Technology Center (METC), under cooperative agreement DE-FC21-92MC29061 with South Carolina Energy Research and Development Center, 386-2 College Ave., Clemson, SC 29634-5181; phone: 803-656-2267; Subcontract no. 94-01-SR022.

Objectives

Information on steam/materials interaction is mainly available for materials relevant to steam turbines, boilers and heat exchanger tubes. The effect of steam on superalloys is little known. For the continuous reliable operation of gas turbines this information is very vital, so that alternatives can be considered and allowances can be made. The objective of this research program is to investigate performance of gas turbine materials in steam environment and evaluate remedial measures for alleviating the severity of the problem.

During the first year of this AGTSR funded project the emphasis was on the investigation of the nature and the extent of the problem that may be encountered, if any. This study demonstrated that hot corrosion can be a severe problem in case of steam cooling. In the next two years following issues will be studied.

A. Long terms effects of low impurity level steam environments.

B. Studying the effect of variables such as temperature, pressure and stress on the mode and kinetics of attack.

C Effectiveness of different techniques such as use of protective coatings and inhibitors for mitigating the material degradation in steam environment..

Apart from these technical objectives, important goals from the academic point of view are to educate students about issues relevant to gas turbine industry and to establish a close university-industry relationship.

Project Description:

For the first year of research, the emphasis was on investigating the nature and extent of material degradation and its relation with steam chemistry. For this three superalloys commonly used in gas turbines were exposed to three steam environments containing different impurity levels for periods ranging from two to six months. In this paper, the results of this research has been summarized. In the next phase of the research programs following tasks will be accomplished.

A. Long Term Testing in Low Impurity Steam Environment

Land based gas turbines are designed for long uninterrupted trouble-free operation. Therefore, for the reliable life prediction, long term kinetics data at low impurity levels are required. The typical steam pressures likely to be present in the cooling holes is about 140 psi[1]. The high steam pressure may have a significant effect on deposition of salts as well as on oxide scale morphology. Therefore steam pressure in the planned experiment will be maintained at levels closer to the actual industrial environment. The duration of the tests will be 12 months. this test will be carried out on both aluminide coated and un-coated superalloy specimens.

B. Measures to reduce the severity of problem:

1. **Coatings**: One possible solution for mitigating the severity of material degradation in cooling hole channels is the use of protective coatings. The two types of protective coatings used in gas turbine industry are MCrAlY and aluminide diffusion coatings. MCrAlY coatings tend to be more hot corrosion resistant than aluminide coatings whereas aluminide coatings tend to provide better resistance to high temperature oxidation. Since aluminide coatings can be formed with a relative ease in the internal cooling holes using CVD, aluminide coatings are likely candidate as internal cooling hole coating material. Therefore, the exposure studies will be

carried out with aluminide coated superalloy specimens to evaluate their effectiveness in retarding the hot corrosion problems in steam environment.

2. **Inhibitors:** Some studies[3] have indicated the beneficial effects of alkaline earth metals particularly Ba on inhibition of hot corrosion of superalloys. Ammonium dichromate is also known to alleviate hot corrosion by providing extra chromium needed for hot corrosion resistance. These water soluble compounds will be added to feedwater and the effect on the steam induced hot corrosion will be evaluated.

C. Effect of other variables

1. **Temperature:** Temperature significantly influences both the kinetics and the morphology of hot corrosion. It is important to investigate the possibility of type II hot corrosion in superalloys in the presence of steam. The existence of type I or II hot corrosion depends on temperature. In this study therefore, depth and morphology of attack will be monitored as a function of time at four different temperatures in the range 1500-1700^0 F.

2. **Stress**: For the turbine blade application, the effect of stress is likely to be critical. The proposed study will aim at understanding whether there is any synergetic effect between stress and salt deposit induced hot corrosion. Five different stress levels will be used at a chosen temperature and the specimens will then be examined metallographically to determine the severity of attack.

3. **Pressure:** The steam pressure can significantly influence the salt deposition process thus affecting the hot corrosion behavior. Also pressure may have some effect on oxide morphology and growth. These effects will be studied by carrying out the experiments at different pressure levels.

Experimental Techniques

The alloys chosen for the study are IN 738, X-45 and IN 617 which are commonly used for blade, vane and transition piece, respectively. The specimen geometry is cylindrical with a 1/4" diameter central bore through which steam is passed. Steam is made to pass through three different samples arranged in a series.

In order to study the effect of impurity contents, three different steam environments are used namely "aggressive", "mild" and "pure". A multiple steam generator was specially designed and fabricated to accomplish this task. Steam is generated by passing water through IN-600 heat exchanger pipes housed in a 5000 Watts radiative furnace. For "aggressive" steam environment, Na_2SO_4 and NaCl salts are added to water. The concentration of each salt is kept at 50 ppm in the water used for "aggressive" steam and 5 ppm each for "mild" steam generation.

In all cases, two types of tests are performed: simple exposure tests and ex-situ EIS. In the latter case, the progress of corrosion/oxidation is monitored as it occurs. All the specimens are housed in two furnaces; one for the Electrochemical Impedance Spectroscopy (EIS) tests and other for the exposure tests. The furnace housing test specimens for EIS studies are opened periodically (biweekly) for performing ex-situ EIS studies on the specimens, following which they are returned to the furnace. The material damage is identified using Scanning Electron Microscopy (SEM), Energy Dispersive X-ray Spectroscopy (EDS) and conventional metallography at the end of the test period for exposure tests.

For EIS testing, outer surface of the specimen is soldered to an electrically conducting wire. Since in this case the surface of interest is the inside surface, the outer surface is masked with MICCROSTOP^R polymer paint. The cylindrical specimens are immersed in an aqueous electrolyte containing a highly reversible redox $[Fe(CN)_6]^{3-}$ /$[Fe(CN)_6]^{4-}$ system at ambient temperatures. The specimen is held horizontal. The potential of the specimen is measured with respect to a Saturated Calomel Electrode (SCE) which was kept at the bore of the specimen. Graphite rods are used as counter electrodes. A sinusoidal voltage perturbation of about 10mV amplitude was applied and the response of the system is measured. The impedance spectrum was measured over a wide frequency range (1 mHz to 100 KHz) using a lock-in amplifier.

Results and Discussion

Microstructural Evaluation

Figure 1a shows scale thickness measurements taken at the end of the test periods. These values are averages of thirty measurements. The figure shows that the oxide thickness observed after two months exposure period in "aggressive" environment is comparable to the thickness observed after four months exposure in "mild" environment for IN 617 and IN 738. The internal penetration depth in the case of "mild" steam environment however is larger than "aggressive" steam environment for all the three alloys. The "mild" steam exposure was four months compared to two months in "aggressive" steam. Thus the results may indicate incubation time for the attack during which salt deposition and protective oxide brekdown are occurring. For IN 617 and X-45 the oxide scale thickness observed for "clean" steam environment is less or similar to what was observed for "aggressive" and "mild" environment even though the exposure time in "clean" steam environment was longest at six months. IN 738 however shows a contrary trend showing very high oxide scale thickness and internal penetration depth of oxides after six months exposure in "clean" steam environment (Figures 1a and 1b). This data may indicate that IN 738 is more susceptible to oxidation damage in steam environment, whereas IN 617 is more susceptible to hot corrosion attack in the presence of impurities in steam environment.

Figure 2a shows the micrograph of IN 738 cross-section after 6 months exposure in "clean" steam environment. Figure 2b is the x-ray dot map of the area shown in figure 2a broken into six elemental surveys. It shows top oxide layer to be rich in Cr and Ti while beneath the oxide scale there is a severe penetration of Al rich tentacles, indicating heavy internal oxidation of aluminum. As evident from figure 2c, there is a severe depletion of γ' because of this attack. IN 617 also showed similar type of attack. However, the extent of internal penetration of Al rich oxides was much smaller. In X-45, the oxidation damage is smallest for all environments compared to IN617 and IN738. The oxide layer in X-45 was observed to be Cr rich and internal penetration damage was mainly restricted to interdendritic boundaries.

Figure 3 is the electron micrograph indicating the microstructural damage of IN 617 observed in the "mild" steam environment. Locations of compositional microanalysis are labelled on the micrograph. The results from this semi-quantitative micro-analysis are depicted in figure 3. Results show the oxide layer to be Cr rich. Some nickel and aluminum rich sulfur containing particles were also observed. This type of morphology was observed in IN 738 and IN 617 in "mild" as well as "aggressive" steam environments.

Mechanism of Degradation

Oxidation of superalloys in air/oxygen is a well studied phenomenon[4,5]. The growth rates of NiO and CoO are too rapid to permit their presence at steady state in the oxidation of a practical alloy. In superalloys, Al_2O_3 and Cr_2O_3 rich oxide films formed on the surface are responsible for high temperature oxidation resistance. For a nickel base alloy to form a Cr_2O_3 rich scale in air, it must contain 15% or more chromium and less than about 5% aluminum. Whereas alloys with more than about 5% aluminum form Al_2O_3 scale. It has been suggested that the critical value of Cr/Al ratio seperating Al_2O_3 formers from Cr_2O_3 formers is 4. For Cr/Al ratio higher than 10, there is tendency for a preferential attack on alloy grain boundaries largely because of grain boundary carbide network there. Conventional cobalt base alloys generally do not contain aluminum and are consequently Cr_2O_3 formers. Al_2O_3 formers have scale morphology characterized by a thin continuous layer of Al_2O_3 adjacent to the metal substrate. The Al_2O_3 may be covered by an external layer of another oxide or other oxides may be dissolved in it, depending upon composition. Generally internal oxidation is absent behind the continuous scale. The scale morphology in Cr_2O_3 formers containing considerable aluminum is characterized by a predominantly Cr_2O_3 layer with internal oxidation of aluminum just beneath, resulting in tentacles of Al_2O_3 directed into the alloy as the Al activity is not sufficiently large to form a continuous scale. Other oxides may be dissolved in the Cr_2O_3 layer or may exist below or above of it. Generally higher Al content alloys show better resistance to oxidation owing to better protective properties of the Al_2O_3 scales.

However, the trend observed in steam environment is quite the opposite. IN 738 which has higher Al content and should have shown higher reistance to oxidation shows more oxidation damage than IN 617 in steam environment. To explain this abnormal behavior following mechanism is proposed.

Oxidation in steam environment may take place in two steps

$$H_2O \text{ -----> } H_2 + 1/2\ O_2 \qquad (1)$$

$$M + 1/2\ O_2 \text{ -----> } MO \qquad (2)$$

The overall reaction being

$$M + H_2O \text{ -------> } MO + H_2 \qquad (3)$$

Figure 4 plots equilibrium partial pressure of oxygen in H_2O-O-H system as a function of temperature using thermodynamic data for equation 1[6]. For most of the elements used in superalloys, free energy change for reaction 3 is negative which indicates that at equilibrium, reaction 3 may go to near completion. In fast flowing steam, conditions are far from equilibrium. Because of low residence time of steam with the alloys, extent of reaction 3 will be limited and oxygen potential in the environment may well be decided by equation 1. As a result, oxidation rates of pure metals in steam would be much lower than in air because of reduced Po_2 levels in steam environment. Aluminum has the most negative free energy of oxide formation and hence can form oxide at lower oxygen partial pressures comapred to other elements such as Ni, Co, Cr and Ti. Therefore it is prone to internal oxidation as the oxygen diffusing into the lattice may be sufficient to selectively oxidize Al. Higher the aluminum content higher will be the severity of internal attack. However at sufficiently large aluminum level, continuous Al_2O_3 scales may form which will provide oxidation resistance.

The compositions of the alloys used in this research program are listed in table 1 . All the three alloys are Cr_2O_3 formers. However these alloys have differing amounts of Ti and Al which make their oxidation response different. IN 738 has higher Al and Ti levels and though they are not sufficient for continuous scale formation, it is high enough to cause damage by internal penetration of Al-rich oxide stringers. IN 617 has lower levels of these elements leading to a lower internal penetration attack. X-45 which has a very large Cr content and no compositional Al shows the lowest damage.

The low Po_2 in steam environment may have also significant effect on hot corrosion. The lower stability of oxides in this case may lead to increased sulfidation as well. However, this could not be proven conclusively from these experiments because of the uncertainties involved in the onset of salt deposition. The actual time of the onset of salt deposition may affect the kinetics of sulfidation. Therefore hot corrosion in steam environment will be investigated by first coating the superalloy pins with salt and then exposing them to steam.

Electrochemical Testing

The electrochemical impedance behavior of an alloy with an oxide layer over it can be modelled using an electrical analog model (transmission line model) as shown in figure 5a. For a perfect oxide layer the oxide/metal interface will not play any role. The electrochemical impedance spectrum in this case , represented by the Nyquist plot will be perfectly semicircular completely dominated by oxide layer characteristics. However in these studies, the oxide layer is far from perfect. Because of discontinuities or defects present in the oxide film, ionically conducting low resistance paths perpendicular to the coated surface may penetrate to the metallic substrate. As a result, the double layer at the metal/electrolyte interface will also play an important role. Therefore, for an oxide layer with a number of defects, there will be an overlap of the double layer and oxide film characteristics. The equivalent circuit in this case could be represented as shown in figure 5b. This results in flattening of the impedance spectrum. Also, the presence of these defects lead to the depression of the semicircle below the real axis[7]. As the number of defects increases, the spectrum will become more and more complex. This type of behavior is apparent in the case of X-45 and IN 617 alloys shown here after exposure to "clean" steam environment (figures 6a and 6b). In the case of IN 738, the diameter of semicircle in Nyquist plot appears to be increasing with exposure time till 6 weeks reflecting the increase in thickness of the oxide film with time, without introduction of many defects. After 6 weeks however the trend reverses reflecting the degradation of the oxide film (fig. 5c). Even though "clean" steam exposure studies showed IN 738 to be most susceptible to degradation after six month exposure, at shorter times the oxide film was observed to be thin and uniform. This is reflected in the EIS short term (6-8 weeks) data which indicates IN 738 to be less susceptible than IN 617 or X-45. Thus again the results seem to indicate that the susceptibility of low Al content IN 738 is time dependant and that the internal penetration attack on this alloy become more pronounced with time. In all the three alloys, after long exposure times, the complexities because of heterogeneities induced by a large number of defects have made the estimation of numerical values from the results rather difficult.

Applications

This study has been helpful to understand the steam-superalloy interaction at high temperatures. A mechanism was proposed to explain the oxide morphology of these superalloys in steam environment. Following inferences can be drawn about the oxidation and hot corrosion behavior of nickel and cobalt based alloys in steam environment

1. Cr_2O_3 forming alloys containing considerable amount (1-4 wt. %) of aluminum such as IN 738 are susceptible to heavy internal oxidation of aluminum.

2. High Al (>5 wt%) alloys in which case continuous Al_2O_3 scale can be formed may not be susceptible to such attack.

3. Deposition of salts from steam will

accentuate hot corrosion problems. Alloys with higher Cr content such as X-45 are generally less prone to hot corrosion. The greater damage observed in IN 617 make this alloy less attractive for gas turbine applications with steam cooling.

4. Electrochemical impedance spectroscopy was found to be a good non-destructive technique to evaluate microstructural damage especially in the early stages of the attack. The technique has the potential of proving very useful in understanding the kinetics and mechanism of attack.

Future Activities

As mentioned earlier in the objectives section, the future rresearch will focus on the following aspects:

1. Long term effects of steam exposure
2. Evaluation of the efffect of pressure, mechanical stree and temperature on the kinetics of the attack.
3. Understanding the mechanism of the attack and identifying the species responsible for the degeadation.
4. Evaluate the efficacy of protection techniques such as protective coatings and inhibitors.

References

1. Rice I.G., "Steam Cooled Gas Turbine Casings, Struts and Disks in a Reheat Gas Turbine Combined Cycle", Transactions of ASME, Journal of Engineering for Power", Vol. 105, October 1983, pp. 844-858.

2. Arsen'ev L.V., Corsov Yu.G., Khodak E.A., Romankhova G.A., Bazhonov G.V., "A hHighly Efficient Combined Cycle Plant with Steam-Cooled Gas Turbine", ASME Cogen-Turbo, IGTI-Vol.6, 1991, pp. 31-41

3. Saunders S.R.J., "Effect of trace elements and Environmental Impurities on Oxidation and Hot Corrosion Characteristics of Superalloys", Metals Technology, 11(10), 1984, pp. 465-473.

4. Smialek J.L. and Meir G.H., "High Temperature Oxidation" in C.T. Sims, Stoloff N.S. and Hagel W.C. (eds), Superalloys II, Wiley, New York, 1987, pp. 291-326.

5. Whittle D.P., "High Temperature Oxidation", in "High Temperature Alloys for Gas Turbines", proceedings of COST-501 meeting in Liege, Belgium, Sept. 1878, Applied Science Publishers, pp. 109-124.

6. Barin I., Thermochemical Data for Pure Substances, VCH Publications, Germany, 1989.

7. Compere C, Frechette L. and Ghali E., "The Corrosion Evaluation of Painted and Artificially Damaged Painted Steel Panels by A.C. Impedance Measurements", Corrosion Science, Vol. 34, August 1993, pp. 1259-1274.

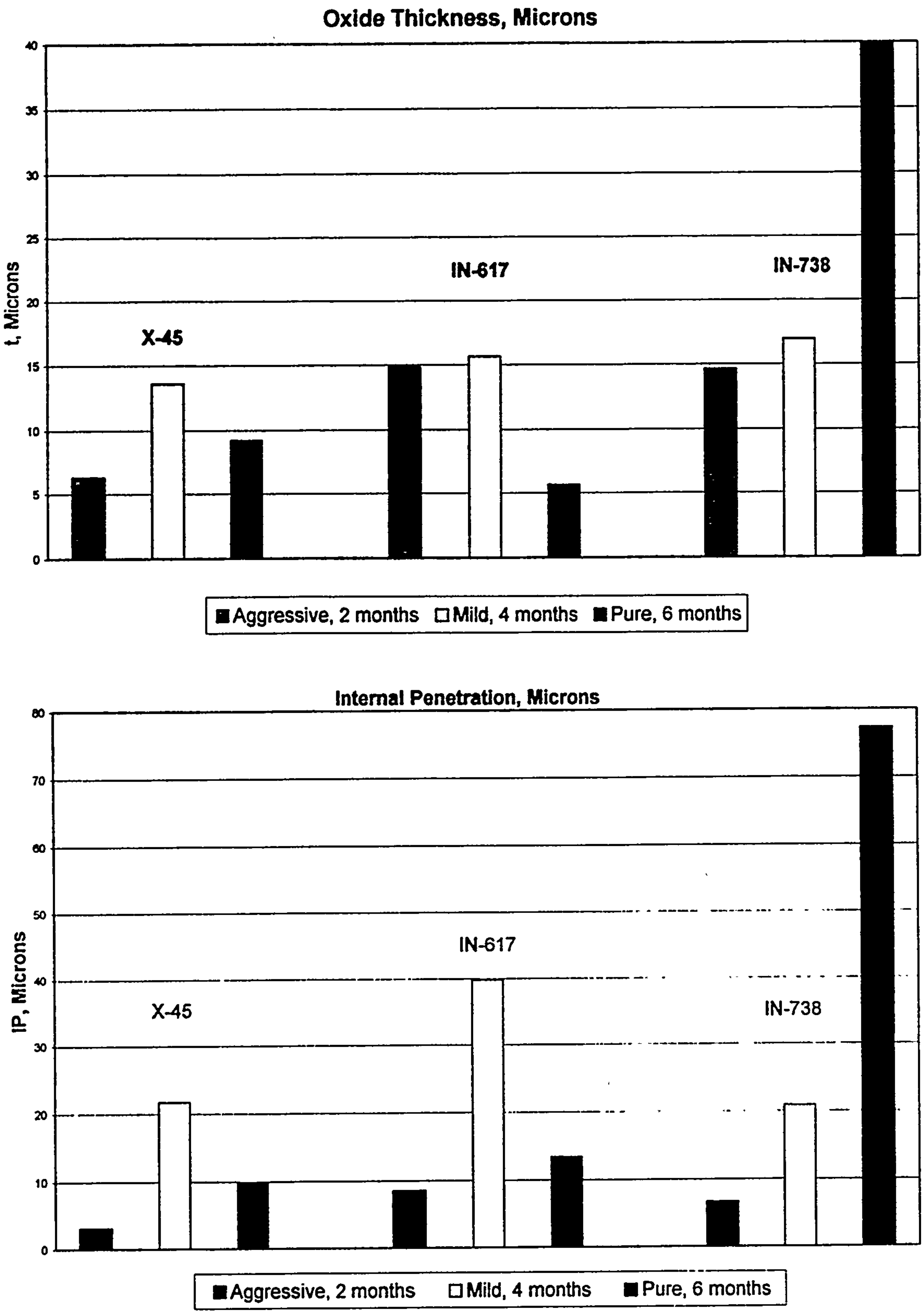

Figure 1: Oxide scale thickeness and internal penetration depths at the end of test periods in "aggressive", "mild" and "clean" environemnts at 1600^{0}F.

(a) Oxide scale thickness

(b) Internal penetration depth of oxidation or corrosion products.

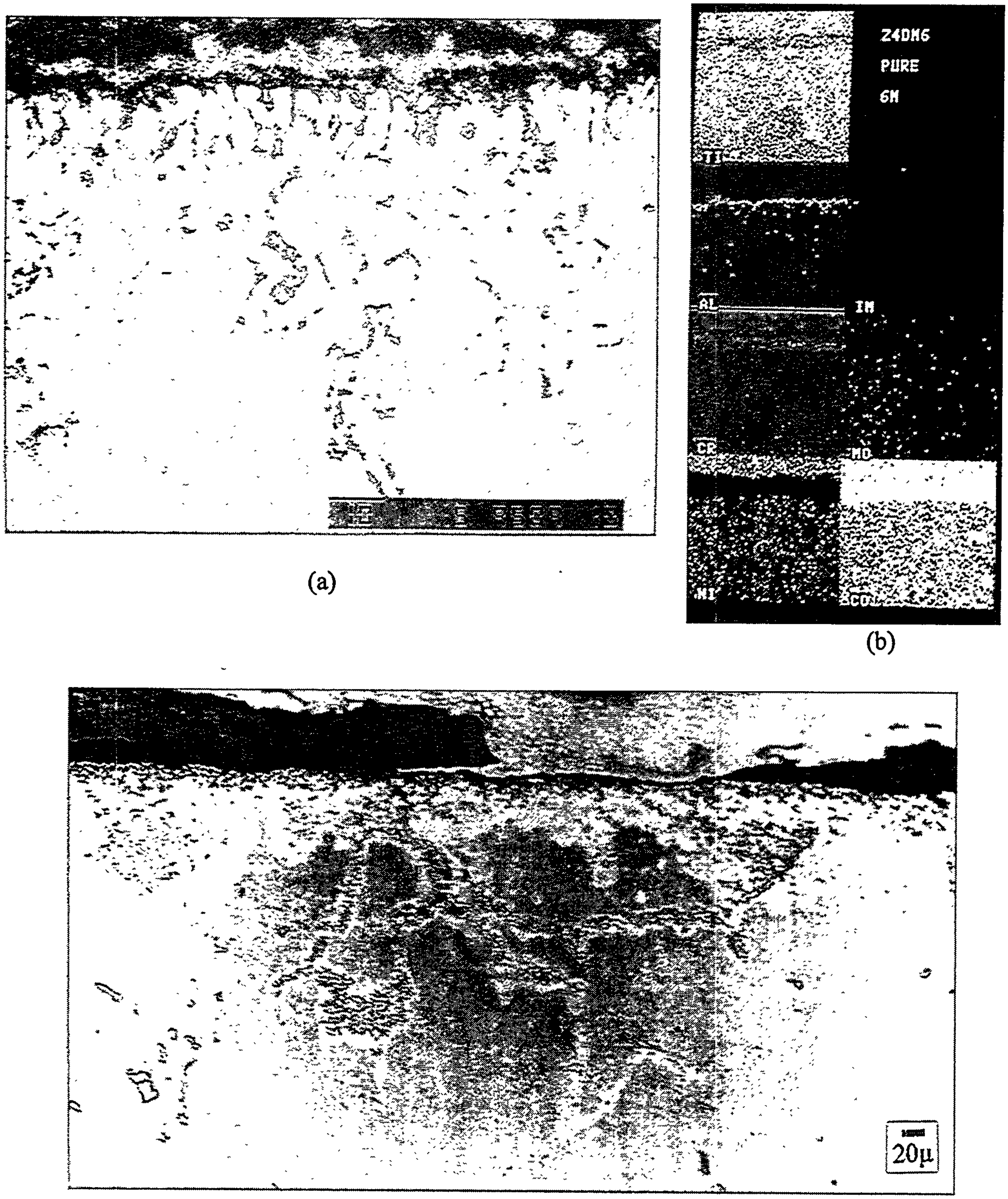

(a)

(b)

(c)

Figure 2: Microstructural degradation of IN 738 in "clean" steam environment after six months exposure.

(a) SEM micrograph showing heavy internal oxidation.
(b) X-ray dot-map of the area shown in figure 2a. It reveals that while oxide scales are mainly composed of Cr and Ti, the internal oxidation products are mostly Al rich.
(c) γ' depleted zone near the oxidation products revealed by using etchant.

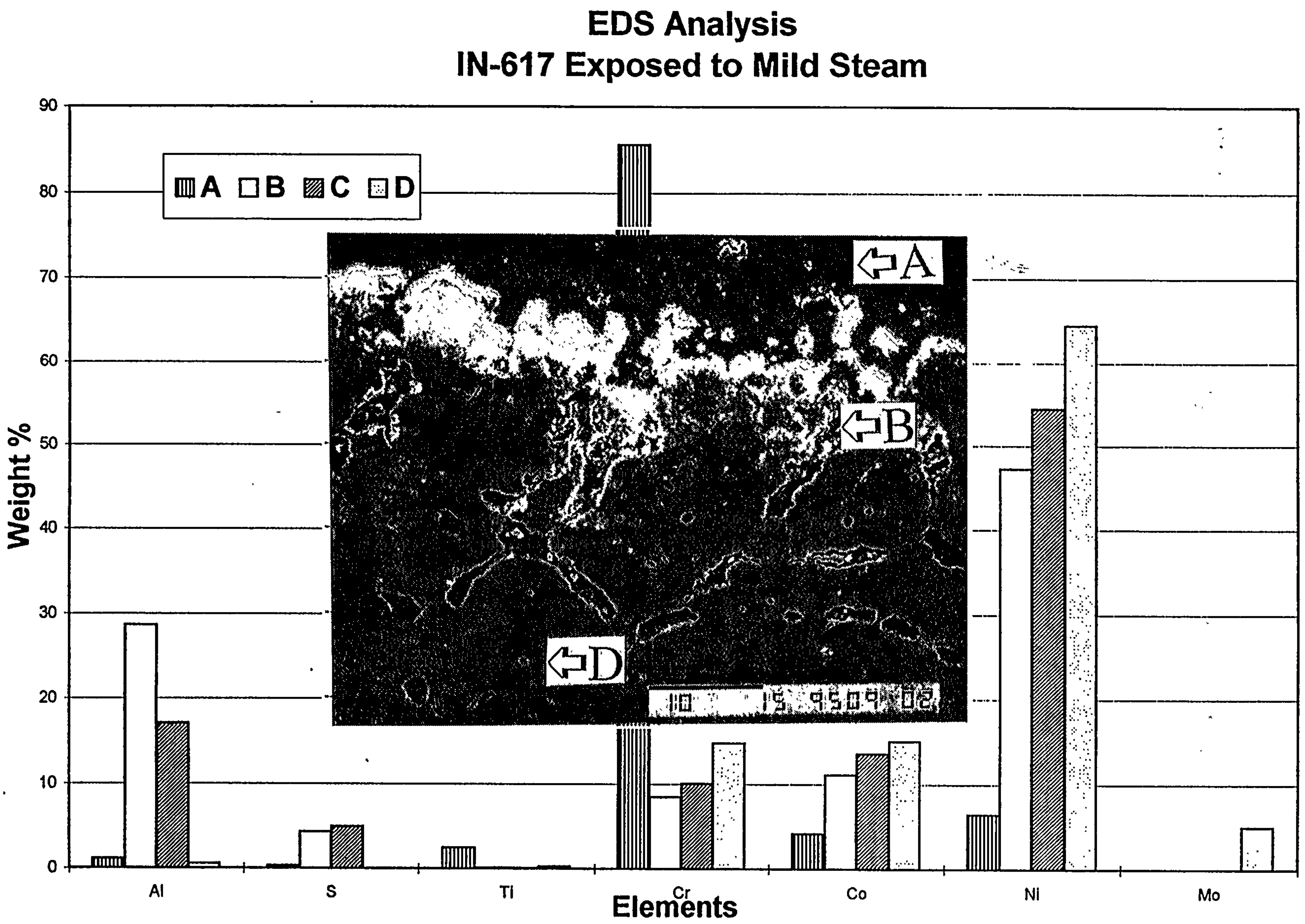

Figure 3: Microstructural damage in IN 617 after four month exposure to "clean" steam environment.SEM micrograph and EDS semi-quantitative analysis performed at different locations labelled in the micrograph are shown.

	C	Mn	Si	Cr	Ni	Co	Mo	W	Ta	Nb	Ti	Al	B	Zr
Inconel 617	0.07	0.5	0.5	22	bal.	12.5	9.0	--	--	--	0.3	1.0	--	--
IN-738	0.11	--	--	16	bal.	8.5	1.7	2.6	1.7	0.9	3.4	3.4	0.01	0.05
X-45	0.5	0.7	0.7	25.5	10	bal.	--	7.5	--	--	--	--	--	--

Table 1: Nominal Chemistry of the alloys

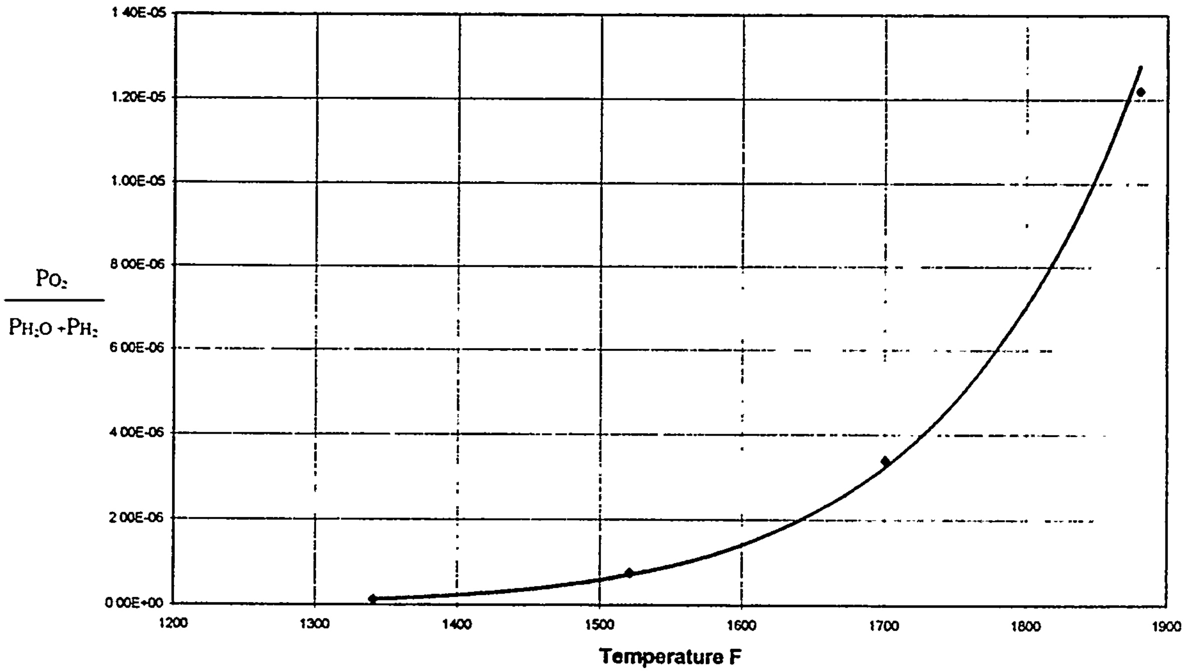

Figure 4: Equilibrium partial pressure of oxygen in H_2O-O-H system at different temperatures. It shows that oxygen partial pressure is very small in steam environment at temperature of interest. However at higher temperatures the dissociation of steam becomes easier.

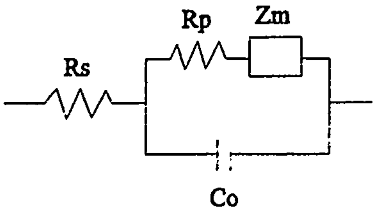

Rs = Solution Resistance
Rp = Oxide Resistance Perpendicular to Surface
Zm = General Impedance Characterizing Electrochemical Reactions at Metal / Oxide Interface
Co = Oxide Capacitance

(a)

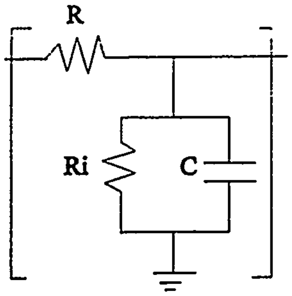

R = Interfacial Reistance Tangential to Surface
Ri = Interfacial Resistance

(b)

Figure 5: (a) General electric equivalent circuit model for coated metal system. For an ideal oxide layer the value of Zm will be zero.
(b) For the nonideal case where there are a number of short circuit paths are available for ionic conduction through defective oxide layer, Zm can be replaced by n unit cells in series. The unit cell can be represented by the equivalent circuit diagram as shown in figure 9b.

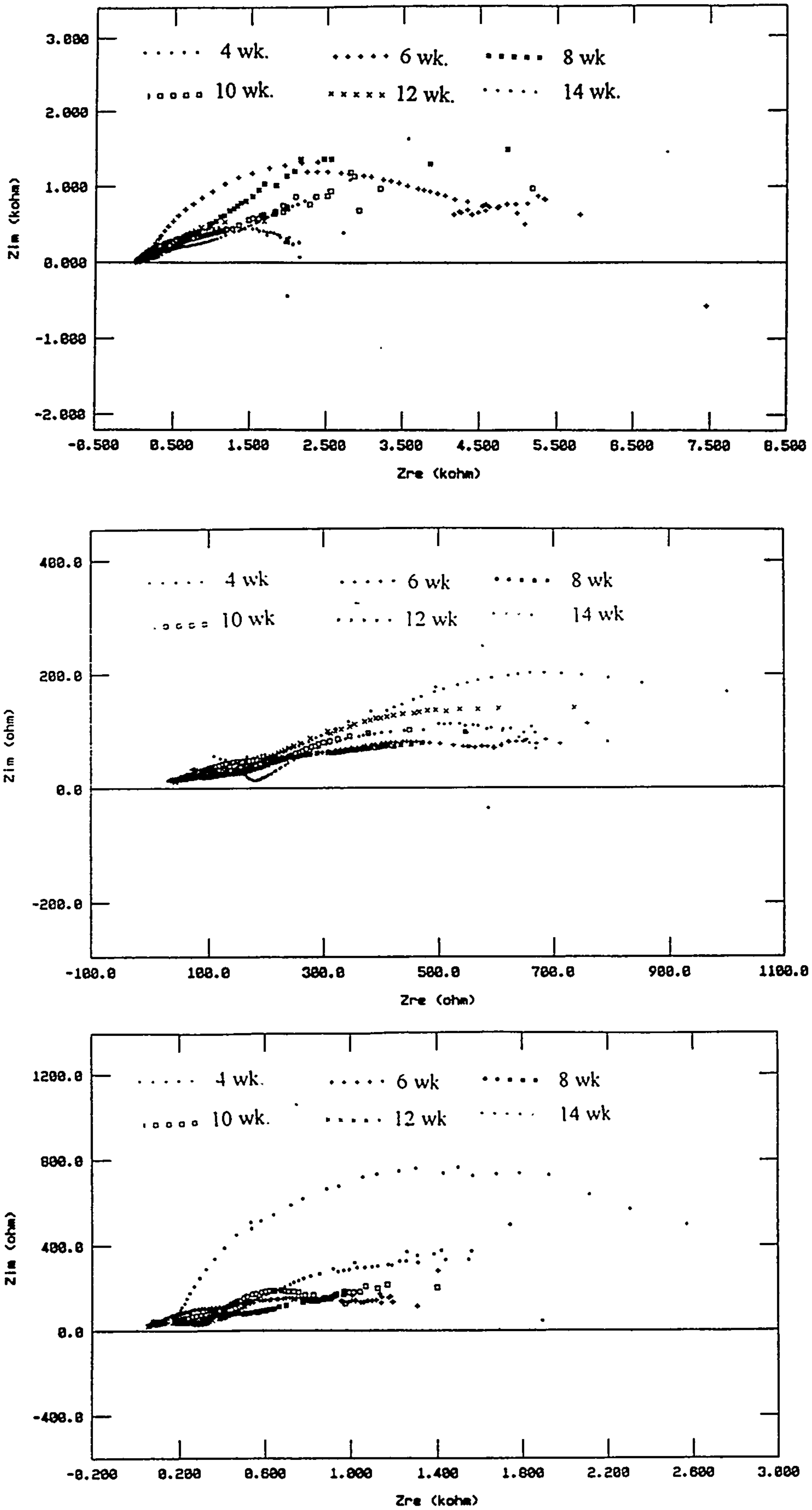

(a) X-45

(b) IN 617

(c) IN 738

Figure 6: Electrochemical impedance behavior as a function of exposure time in "clean" steam environment.

P17

Use of a Laser-Induced Fluorescence Thermal Imaging System for Film Cooling Heat Transfer Measurement

M. K. Chyu (mc47@andrew.cmu.edu; [412] 268-3658)
Department of Mechanical Engineering
Carnegie Mellon University
Pittsburgh, PA 15213

Abstract

This paper describes a novel approach based on fluorescence imaging of thermographic phosphor that enables the simultaneous determination of both local film effectiveness and local heat transfer on a film-cooled surface. The film cooling model demonstrated consists of a single row of three discrete holes on a flat plate. The transient temperature measurement relies on the temperature-sensitive fluorescent properties of europium-doped lanthanum oxysulfide ($La_2O_2S:Eu^{+3}$) thermographic phosphor. A series of full-field surface temperatures, mainstream temperatures, and coolant film temperatures were acquired during the heating of a test surface. These temperatures are used to calculate the heat transfer coefficients and the film effectiveness simultaneously. Because of the superior spatial resolution capability for the heat transfer data reduced from these temperature frames, the laser-induced fluorescence (LIF) imaging system, the present study observes the detailed heat transfer characteristics over a film-protected surface. The trend of the results agrees with those obtained using other conventional thermal methods, as well as the liquid crystal imaging technique. One major advantage of this technique is the capability to record a large number of temperature frames over a given testing period. This offers multiple-sample consistency.

Nomenclature

d	Injection hole diameter.
G	Mass velocity = ρ V.
h	Heat transfer coefficient in $q = h(T_r - T_w)$.
h_m	Heat transfer coefficient in $q = h_m(T_m - T_w)$.
h_0	Heat transfer coefficient without injection.
k	Thermal conductivity.
M	Blowing ratio = $\rho_f V_f / \rho_m V_m$.
Nu	Nusselt number.
Pr	Prandtl number.
q	Heat flux.
Re	Reynolds number.
t	Time.

Research sponsored by the U.S. Department of Energy's Morgantown Energy Technology Center, under Contract DE-FC21-92MC29061 with Carnegie Mellon University, 5000 Forbes Ave., Pittsburgh, PA 15213; telefax: [412] 268-3348.

T_i	Initial temperature.
T_f	Coolant temperature.
T_m	Mainstream temperature.
T_r	Reference temperature.
$T_w(t)$	Wall temperature at time t.
V_f	Coolant velocity.
V_m	Mainstream velocity.
α	Thermal diffusivity.
η	Effectiveness = $(T_r-T_m)/(T_f-T_m)$.
ρ_f	Density of mainstream.
ρ_m	Density of cooling film.
τ_j	Time step.
θ	Dimensionless temperature = $(T_f-T_m)/ T_w-T_m)$.

Introduction

This study examines the heat transfer characteristics of film cooling through a single row of discrete injection holes on flat surface, using a laser-induced fluorescence (LIF) thermal imaging system based on a thermographic phosphor. Film cooling is one of the most effective means for thermal control of gas turbine components subjected to intensive heat load. While research concerning film cooling has been very active for several decades, most of the studies were performed under near room temperature conditions. This is largely attributable to the limited thermal measurement capabilities in a high-temperature environment. As a result, many important effects pertaining to large temperature differential in the system, such as the coolant-to-gas thermal property variations, are unable to be explored effectively. With a proper choice of the phosphor material, the measurement approach present in this paper can be extended to high temperature applications.

Certain thermographic phosphors whose fluorescence intensity and/or lifetime are temperature sensitive have been successfully used for surface temperature measurement. Goss and Smith (1986) determined local surface temperatures during the combustion of the test specimen using the ratio of two emission lines of dysprosium-doped yttrium aluminum garnet ($YAG:Dy^{+3}$) crystals embedded in a thermal-setting plastic. Lutz et. al. (1988) and Noel et. al. (1990) used the approach based on the fluorescence lifetime sensitivity of certain rare-earth phosphors for temperature measurements on a heated turbine disk and on a first-stage stator vane in an operating turbine engine, respectively. While previous studies involved primarily discrete-point measurements, Chyu and Bizzak (1993, 1994) recently reported a detailed two-dimensional surface temperature measurement using an approach combining the thermal sensitivity of emission intensity and decay time. The particular thermographic phosphor they used is europium-doped lanthanum oxysulfide ($La_2O_2S:Eu^{+3}$).

The present study was based on the approach by Chyu and Bizzak (1993, 1994), in conjunction with a transient measurement technique, to simultaneously determine the film effectiveness and heat transfer coefficient. The particular LIF system used here exploits the temperature sensitivity of both the fluorescence intensity and the lifetime of certain emission lines. Fluorescent images of the temperature sensitive 512-nm triplet, along with that of the relatively temperature-insensitive 620-nm emission line, are acquired.

The ratio of the integrated intensities of these two emissions, which can be accurately correlated to temperature and intensity data from a reference isothermal surface image, permits the determination of temperatures at several discrete locations on the test surface.

To evaluate the capability of the LIF system in measuring the transient characters of three-temperature heat convection case, film cooling through a single row of injection holes is selected for the demonstration. Both the local film effectiveness, η, and local heat transfer coefficients, h, are determined simultaneously using the temperature measurements of a single test. The results are then compared with those obtained from other methods to allow assessment of the measurement capabilities of the LIF thermal imaging system.

Three-Temperature System

In case of general two-temperature force convection situation, the local surface heat flux is expressed as

$$q = h_0(T_m - T_w) \tag{1}$$

where T_w and T_m are the wall temperature and the mainstream temperature, respectively, and h is the convective heat transfer coefficient. The heat transfer coefficient, h_0, is usually considered as a function of primarily aerodynamic character of the flowfield. For a given flowfield, h is, therefore, a constant locally and can be determined by measuring q together with T_w and T_m.

In a film cooling system, temperature of the coolant injected from a cooling hole or a slot emerges as a third temperature that also control the heat transfer process in the system. Hence a system as such is termed three-temperature problem. One way to relate the surface heat transfer (q) and a heat coefficient, h_m, is

$$q = h_m(T_m - T_w) \tag{2}$$

Although the expression is somewhat convenient in nature and bears great similarity to Equation (1), h_m is not a constant quantity as h_0 is, since the temperature difference between the mainstream and the wall, T_m-T_w, is not a true driving potential of heat transfer. An alternative way to express the surface heat flux is

$$q = h\,(T_r - T_w) \tag{3}$$

where T_r is the reference temperature, and T_r-T_w represents the true driving potential for maintaining h_0 as a constant, and is actually an unknown. It can be considered as the mixing temperature of two interacting streams just above the surface. To find the unknown T_r in terms of known quantities T_m and T_f (the temperature of mainstream and coolant film, respectively), a dimensionless temperature is defined as film cooling effectiveness (η)

$$\eta = (T_r - T_m)/(T_f - T_m) \tag{4}$$

Thus,

$$T_r = \eta T_f + (1-\eta) T_m \tag{5}$$

Applying the analytical result of a semi-infinite solid whose surface is suddenly subjected to a step change in ambient temperature, that is

$$\frac{T_w - T_i}{T_r - T_i} = 1 - \exp\left(\frac{h^2 \alpha \cdot t}{k^2}\right) \operatorname{erfc}\left(\frac{h\sqrt{\alpha \cdot t}}{k}\right) \tag{6}$$

Replacing T_r in Equation (5) by Equation (4), the relationship of T_w, T_i, T_m, and T_f can be expressed as the following equation, with two unknowns, h and η.

$$T_w - T_i = [1 - \exp(\frac{h^2\alpha\cdot t}{k^2})\,\mathrm{erfc}(\frac{h\sqrt{\alpha\cdot t}}{k})] * \qquad (7)$$

$$[\eta T_f + (1-\eta)T_m - T_i]$$

In a real experiment, either T_m or T_f may not be a true step function, hence, by Duhamel's theorem, the temperatures are represented as a series of superimposed time step changes. Equation (7) can be written as

$$T_w - T_i = \sum_{j=1}^{N} U(t-\tau_j)[(1-\eta)\Delta T_m + \Delta T_f] \qquad (8)$$

where:

$$U(t-\tau_j) = 1 - \exp[\frac{h^2}{k^2}\alpha(t-\tau_j)]\,\mathrm{erfc}[\frac{h}{k}\sqrt{\alpha(t-\tau_j)}] \qquad (9)$$

To evaluate h and η, it is necessary to obtain two equations involving those two unknowns. The wall temperature data monitored by the laser-induced fluorescence (LIF) imaging system, in conjunction with the temperature history data of both coolant film and mainstream measured by thermocouples, yields several equation sets which allow simultaneous determination of h and η. One unique feature of the present LIF-based measurement approach is the capability of acquiring multiple solution sets (with different elapse-times) under a single transient test. These multiple solution sets can minimize the uncertainty of the calculated h and η.

Laser-Induced Fluorescence Imaging System

The LIF imaging system employed for the present study is shown schematically in Figure 1. The major elements of the system include (1) phosphor excitation laser, (2) fluorescence image detector, (3) image processing and control subsystem. While detailed description of the system has been given in earlier studies (Bizzak and Chyu, 1995 * use the scientific instrumentation paper), a brief discussion is given below.

Ultraviolet (UV) excitation of the phosphor coating of the test surface is provided by the tripled output (355 nm) of a ND:YAG pulsed laser. The tripled output from the laser is generated by passing the 1064-nm primary output through a harmonic generator, to obtain a beam of 355 nm wavelength light, along with residual components of the primary and first harmonic (532 nm). These undesired portions of the laser beam are then effectively separated and eliminated by a beam splitter assembly. The energy of the 355 nm output beam from the splitter, which is delivered over a 5 to 6 ns pulse, is approximately 75 mJ.

The critical element of the LEF thermal imaging system is the thin layer of europium-doped lanthanum oxysulfide ($La_2O_2S:Eu^{+3}$) phosphor that is applied to the test surface. When subjected to UV excitation, this phosphor fluoresces in the visible spectrum. The emission spectrum of this phosphor (as for other rare-earth doped phosphors) consists of a number of sharp emission lines, and certain of these lines exhibit a temperature sensitivity that is manifested in changes to both the fluorescence intensity and decay time. For

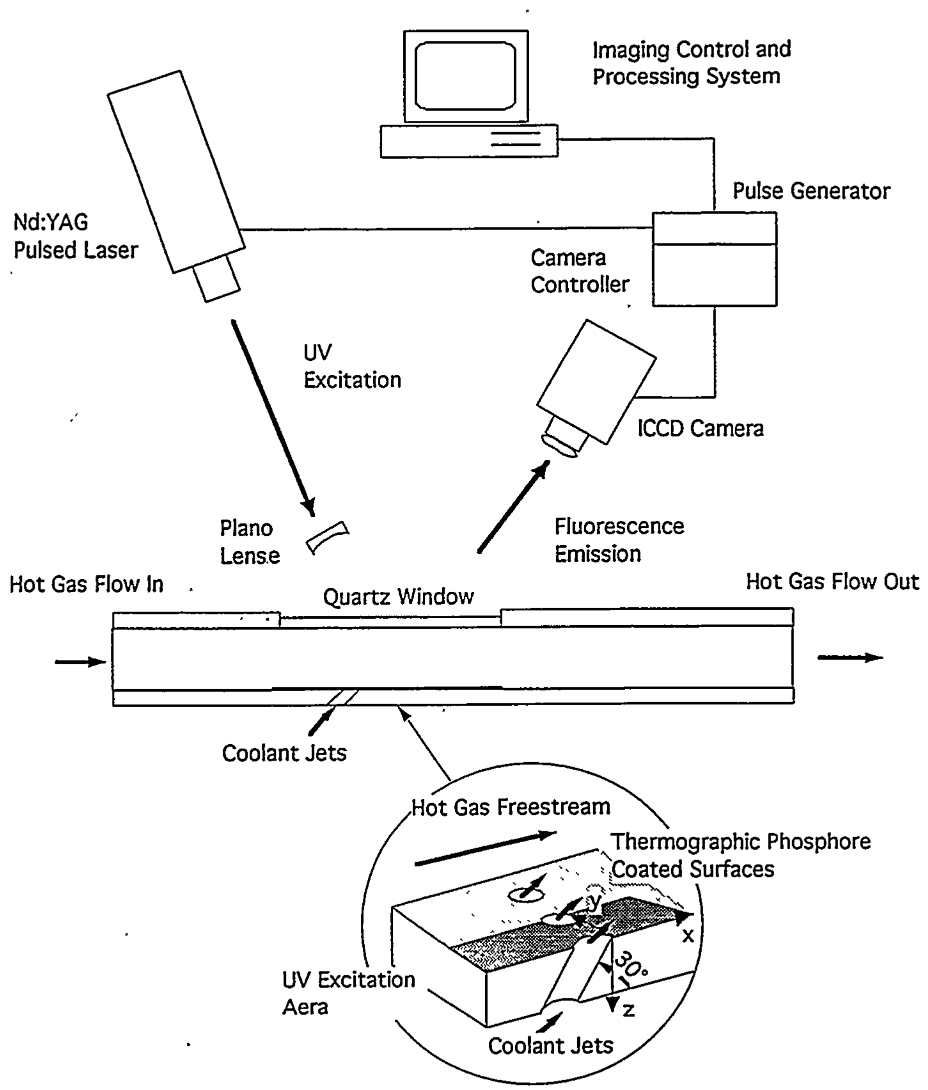

Figure 1. Apparatus Schematic

La$_2$O$_2$S:Eu^{+3}, the steady-state intensity of the 512 nm emission triplet decreases by a factor of 2.5 as temperature is increased from 20 to 60 C, while the lifetime of this temperature range decreases by an order of magnitude. Collection of the fluorescence signal during its decay permits a precise determination of temperature based on both of these sensitivities. However, since the initial fluorescence amplitude at a given surface location is dependent on both the excitation energy and phosphor coating density, use of the 512 nm fluorescence signal alone may be unable to yield accurate two-dimensional thermometry. To compensate for these spatial variations in the signal, the intensity of the 512 nm emission triplet is ratioed to that of the 620 nm emission. The intensity of the latter emission (which is relatively immune to temperature) provides a reference signal whose intensity variation, due to spatial nonuniformity in excitation energy or phosphor density, is identical to that of the 512 nm emission. As a result, this intensity ratio can be accurately correlated to temperature regardless of the absolute magnitude of the local emissions.

The fluorescent image of both 512-nm and 610-nm lines over the test surface following excitation is collected by a 150 mm enlarger lens and split into equal length optical paths that are focused side-by-side onto an image intensified-CCD detector. One optical path passes through a 510 nm narrow bandpass filter, while the other is directed through a 620 nm bandpass and a neutral density filter. The neutral density filter is required to reduce the intensity of the 620 nm fluorescence signal to a level comparable to that of the 510 nm signal, because the intensity and lifetime of the 620 nm emission is considerably greater than that of the temperature sensitive 510 nm emission.

The major components of the imaging subsystem include a gate pulse generator, a detector controller, and a microcomputer for overall system control. Concurrent with laser excitation, the detector simultaneously records images of the surface at the emission-line wavelengths of interest. The timing and duration of image acquisition are controlled by the gate pulse generator, which issues a square-wave pulse that enables the image intensifier. The duration of this pulse defines the fluorescence signal integration period. The pulse generator in this study is set to issue a 40-µs pulse approximately 280 ns in advance of laser firing. To prevent exposure of the detector during readout following image capture, the controller disables the pulse generator until image data have been read and stored to disk. Finally, a 80486 processor based computer provides overall system control and is used in image post-processing to calculate emission intensity ratio values which are then used in conjunction with the phosphor calibration to determine local surface temperatures.

Experimental Setup and Procedure

The apparatus for the film cooling tests is shown schematically in Figure 1. The test surface is part of the duct wall, with a constant area of rectangular cross-section; secondary flow is injected through a single row of three circular tubes with 30 degrees inclined angle ending flush to the test surface. Near the injection holes, a thin layer -- about 25 µm -- of $La_2O_2S{:}Eu^{+3}$ is coated on top of the test surface. Since this layer is so thin and presents virtually no thermal resistance, the material properties of the test section (Plexiglas) are used to calculate the local heat transfer coefficient and film effectiveness, based on Equations (7) and (8). During the test run the laser beam is expanded using a cylindrical concave lense to excite the phosphor on the test surface emitting fluorescence. The shone area is about 10 mm in width over all the test surface, as shown in Figure 2.

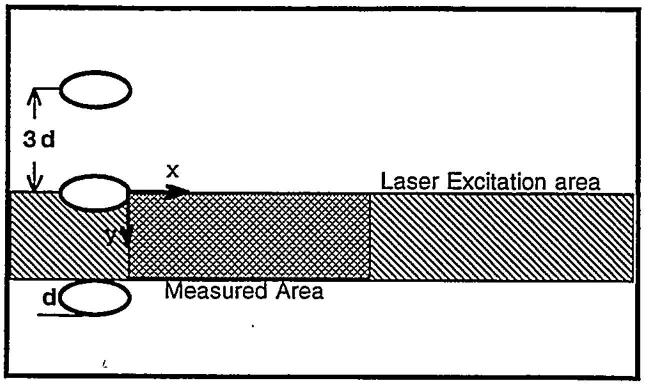

Figure 2. Laser Excitation Area

The air supply is divided into two paths, mainstream and secondary injection. The desired volumetric flow rate is set using a regulator in conjunction with a Pitot tube in the mainstream, and using a rotameter in the coolant film path. Metered flows are then heated using tubular heaters, with their temperatures monitored by thermocouples. The coolant-to-mainstream mass flux ratio is set to 0.2. The mainstream temperature in the range of 45 to 50 °C is reached within 40 seconds; the coolant temperature is kept at room temperature.

Prior to conducting the test, an isothermal fluorescent image (that is the fluorescent image of the test surface maintained in ambient air temperature) must be taken as a reference image for later use in data processing. A transient test is initiated by switching on the gate valve and routing the flow pass through the path of mainstream and coolant film. A PC-based data acquisition system is initiated at the same time to record the temperature history of both the mainstream and coolant film. Each fluorescent image is acquired after the initiation of flow, but before 100 seconds have elapsed. Each image frame represents the integrated fluorescent signal accumulation over 11 laser pulse -- or 1 second -- with the signal integration period following each pulse being 40 μs. The time from the initiation of test to collection of the first image, and the time between the collection of each image is clocked using a stop watch.

Following acquisition of the raw fluorescent image data, the PC starts to execute an image processing program and calculate both the film effectiveness and heat transfer coefficient for 174 locations on the test surface. For each surface location, intensity data from a 5 x 5 pixel array (which corresponds to an area of 0.8 mm by 0.8 mm viewed from 1 m distance) are used to calculate local surface emission-line intensity ratios. These intensity ratios are then divided by the value of intensity ratio at the same surface location obtained from the isothermal reference image. These "corrected" intensity ratios may be converted to temperature using a phosphor calibration curve. To permit direct determination of temperature however, the generic phosphor calibration data must be normalized by the value of the emission intensity ratio at the reference temperature. The temperature data for two different frames then serves as input to a software routine that implicitly solves Equations (7) and (8) for obtaining local heat transfer and local film effectiveness simultaneously. Since there are 11 data sets for different timeframes, the solution of h and η can use up to 55 combinations and produces much accurate results than those based on only single combination.

Results

Figures 3 and 4 give the contour plots of film effectiveness and heat transfer coefficient for the case of $M = 0.2$, respectively. The results shown here are those in the near wall region; i.e., $x/d < 5.2$. Due mainly to experimental difficulty, data of such nature have little been reported in the literature. As a typical case of film cooling with a low blowing ratio, both film effectiveness and heat transfer coefficient generally decrease toward downstream. Their magnitudes are higher along the injection axis directly behind the coolant holes and lower in the region between holes. There is no indication of the coolant liftoff that is often encountered in the cases with larger blowing ratios.

Figures 5 and 6 shows the distributions of the spanwise averaged film effectiveness and heat transfer coefficients, respectively. Reflecting the same phenomena shown in the contour plots, both figures reveal decreasing trend along the streamwise direction. Also present in the figures are some corresponding data available in the literature using different, while more conventional, measurement

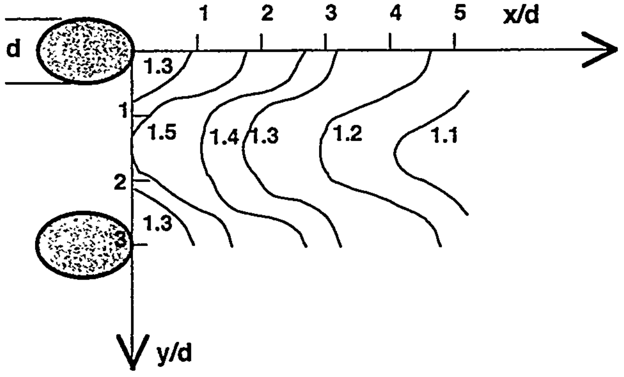

Figure 3. Full Field h/h_0 Distribution

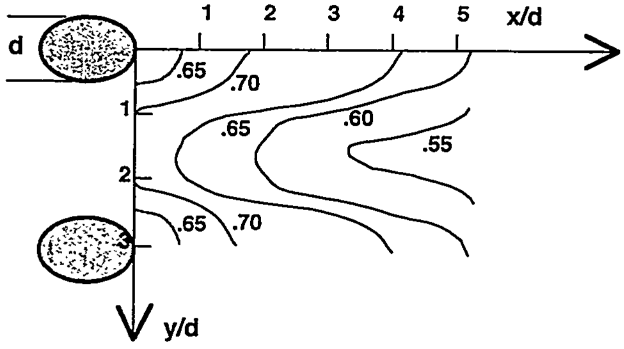

Figure 4. Full Field η Distribution

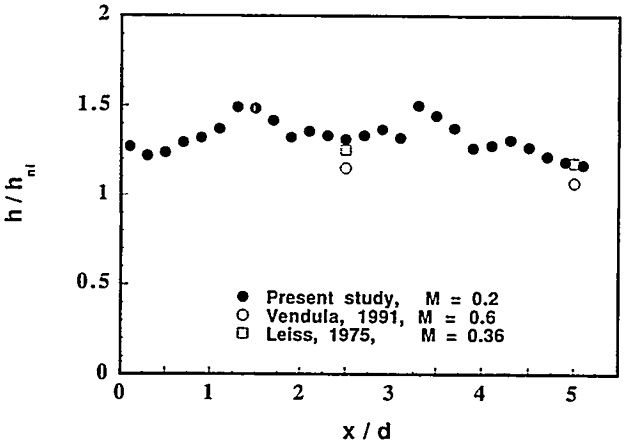

Figure 5. Center-Line Local Heat Transfer Distribution

techniques. The present results compare very favorably with those of earlier studies.

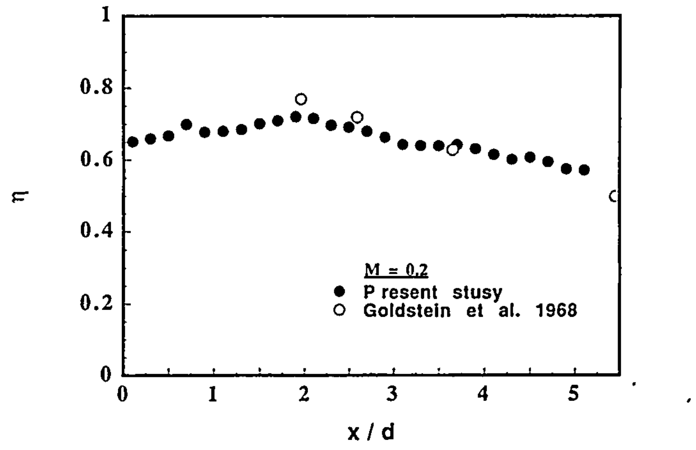

Figure 6. Center-Line Film Effectiveness Distribution

The uncertainties of the present data, based on the transient method suggested by Moffat (1985), are 0.76 percent for local heat transfer, and 2.2 percent for film effectiveness. This estimate encompasses the uncertainty in the calculation of these two parameters due to the measurement errors of initial temperature, wall temperature and mainstream temperature, the error in timing the initiation of working fluid and LIF system, and that of the thermal and mass properties for test surface. As for repeatability, the maximum deviation of heat transfer is 10 percent, the deviation of film effectiveness is 7 percent, occurring at the edges; the h and η value there is 28 and 0.59 respectively. Therefore this deviation represents an error of ±2.8 in h and ±0.04 in η.

Conclusions

Through the examination of the local heat transfer and effectiveness of cooling film injected from a single row of injection holes on flat surface, this study has demonstrated the efficacy of the LIF thermal imaging technique for transient two-dimensional surface temperature measurement, suitable for calculating h and η simultaneously for a three-temperature heat convection situation. Based on these results, and the inherent advantages in temperature measurement, such as nonintrusive measurement and high spatial resolution capabilities, etc., the present system promises to be a powerful optical technique suitable for use in the studies of gas turbine heat transfer. The operational principle of the three-temperature system approach is readily applicable for high-temperature applications.

References

1. Arts, T., 1991, "Convective Heat Transfer With Film Cooling Around Rotor Blade," Modern Research Topics in Aerospace Propulsion: in Honor of Carrado Casci," Springer-Verlag, New York, pp. 253-273.

2. Bizzak, D.J., 1993, "A Laser-Induced Fluorescence Thermal Imaging System for the Study of Local Convective Heat Transfer," Ph.D. Thesis, Carnegie Mellon University, Pittsburgh, Pennsylvania.

3. Chyu, M.K., and Bizzak, D.J., 1994, "Surface Temperature Measurement Using a Laser-Induced Fluorescence Thermal Imaging System," J. Heat Transfer, 116, pp. 263-266.

4. Fonger, W.H., and Struck, C.W., 1970, "Eu^{+35} D Resonance Quenching to the Charge-Transfer States in Y_2O_2S, La_2O_2S, and LaOC1," J. Chemical Physics, 52, pp. 6364-6372.

5. Goldstein, R.J., 1971, "Film Cooling," Advance in Heat Transfer, Vol. 7, Academic Press, New York and London, pp. 321-379.

6. Goss, L.P., and Smith, A.A., 1986, "Surface Thermometry by Laser-Induced Fluorescence," Rev. Sci. Instrument, 60, pp. 3702-3706.

7. Ito, S., Goldstein, R.J., and Eckert, E.R.G., 1978, "Film Cooling for a Gas Turbine Blade," J. Engrg for Power, 100, 3, pp. 476-489.

8. Lutz, S.S., Turley, W.D., Borella, H.M., Noel, B.W., Cates, M.R., and Probert, M.R., 1988, "Remote Temperature Measurement Instrumentation for Heated Rotating Turbine Disk," Los Alamos National Laboratory Technical Report, LA-UR-88-599.

9. Moffat, R.J., 1985, "Using Uncertainty Analysis in the Planning on an Experiment," J. Fluids Engineering, 75, June, pp. 173-178.

10. Noel, B.W., Borella, H.M., Lewis, W., Turley, W.D., Beshears, D.L., Capps, G.J., Cates, M.R., Muhs, J.D., and Tobin, K.W., 1990, "Evaluating Thermographic Phosphors in an Operating Turbine Engine," ASME Paper 90-GT-266.

11. Vedula, R.J., and Metzger, D.E., 1991, "A Method for the Simultaneous Determination of Local Effectiveness and Heat Transfer Distributions in Three-Temperature Convection Situations," ASME Paper 91-GT-345.

P18

Effects of Geometry on Slot-Jet Film Cooling Performance

Daniel G. Hyams
Kevin T. McGovern
James H. Leylek (jim.leylek@clemson.edu;803-656-5604)
Department of Mechanical Engineering
Clemson University
P.O. Box 340921
Clemson, SC 29634-0921

Abstract

The physics of the film cooling process for shaped, inclined slot-jets with realistic slot-length-to-width ratios (L/s) is studied for a range of blowing ratio (M) and density ratio (DR) parameters typical of gas turbine operations. For the first time in the open literature, the effect of inlet and exit shaping of the slot-jet on both flow and thermal field characteristics is isolated, and the dominant mechanisms responsible for differences in these characteristics are documented. A previously documented computational methodology was applied for the study of four distinct configurations: (1) slot with straight edges and sharp corners (reference case); (2) slot with shaped inlet region; (3) slot with shaped exit region; and (4) slot with both shaped inlet and exit regions. Detailed field results as well as surface phenomena involving adiabatic film effectiveness (η) and heat transfer coefficient (h) are presented. It is demonstrated that both η and h results are vital in the proper assessment of film cooling performance. All simulations were carried out using a multi-block, unstructured/adaptive grid, fully explicit, time-marching solver with multi-grid, local time stepping, and residual smoothing type acceleration techniques. Special attention was paid to and full documentation provided for: (1) proper modeling of the physical phenomena; (2) exact geometry and high quality grid generation techniques; (3) discretization schemes; and (4) turbulence modeling issues. The key parameters M and DR were varied from 1.0 to 2.0 and 1.5 to 2.0, respectively, to show their influence. Simulations were repeated for slot length-to-width ratio (L/s) of 3.0 and 4.5 in order to explain the effects of this important parameter. Additionally, the performance of two popular turbulence models, standard k-ε and RNG k-ε, were studied to establish their ability to handle highly elliptic jet/crossflow interaction type processes. The computational simulations showed exceptionally strong internal consistency. Moreover, the ability of using a state-of-the-art computational methodology to sort the relative performance of different slot-jet film cooling configurations was clearly established.

Nomenclature

DR	Density ratio = $\rho j/\rho\infty$
ES	Slot-jet with exit shaping
h	Heat transfer coefficient, (W/m^{2}K)

Research sponsored by the U.S. Department of Energy's Morgantown Energy Technology Center, under contract DE-FC21-92MC29601 with Clemson University, P.O. Box 340921, Clemson, SC 29634-0921, Telefax: 803-656-4435.

IS	Slot-jet with inlet shaping
IES	Slot-jet with inlet and exit shaping
L	Length of slot-jet
L/s	Slot-length-to-width ratio of slot-jet
M	Blowing (or mass flux) ratio = $(\rho V)j/(\rho V)\infty$
Re	Reynolds number
REF	Reference slot-jet case
s	Slot width
tke	Turbulent kinetic energy
TI	Turbulence intensity
y^+	Nondimensional distance away from wall
η	Adiabatic effectiveness = $(T\infty-T_{aw})/(T\infty-Tj)$

Subscripts

∞	Mainstream conditions at crossflow inlet plane
j	Conditions at coolant supply plenum inlet plane
w	Conditions at wall
aw	Adiabatic wall

1. Introduction

An understanding of jet-in-crossflow interaction is crucial in the design of hot section components in modern gas turbine engines. The temperature of the gases entering the turbine section is typically near the melting point of the alloys used in the turbine airfoils and endwalls. To prevent these components from failing at such elevated temperatures, they are commonly film cooled to isolate the metal from the hot gases. In addition, film cooling holes are often shaped in some manner to improve cooling performance, thus allowing for better metal protection and/or a decreased coolant supply; however, these configurations are often implemented with weak understanding of flow and heat transfer characteristics in and near the film hole. Although most film cooling is accomplished via discrete holes in the metal surface, slot-jets are used in gas turbine combustor liners, exhaust liners, and on the trailing edge of turbine blades. This study focuses on slot-jet film cooling physics and the effect of geometry on both flow and thermal field characteristics. Detailed field data, the adiabatic effectiveness, and the surface heat transfer coefficient are used to evaluate the advantages and/or disadvantages of slot shaping. Emphasis is placed on determining the dominant physical mechanisms responsible for the differences in film cooling performance of the various slot configurations.

2. Literature Review

A number of studies are available in the open literature that examine jet-in-crossflow interactions both experimentally and computationally. Butkiewicz et al. (1995) provides a thorough overview of these studies and their ramifications. Although a large number of studies exist, only the ones closely related to 2-D inclined slot-jets studied in the present paper will be discussed here.

Several recent studies have focused on geometry effects on heat transfer downstream of discrete jets. Compound angle injection was studied by Ekkad et al. (1995), Ligrani et al. (1994), Sen et al. (1994), and Schmidt et al. (1994). Also, film hole shaping was reviewed by Sen et al. (1994) and Schmidt et al. (1994). Each of these studies focus on the difference between film cooling configurations in terms of the resulting downstream behavior; the physical mechanisms that cause these differences were not explained. To effectively extrapolate from the database provided in these papers, it is crucial to understand the flow mechanisms responsible for the documented effects.

Metzger et al. (1968) examined slot-jets with various injection angles ranging from 20° to 60°. This work studied the changes in the surface heat transfer for various injection angles, blowing ratios, temperature ratios, and L/s ratios. Realistic L/s ratios were used for some of the test conditions; however, the inlet geometry was atypical of gas turbines and therefore has limited applicability. Also, no thorough documentation of the dominant physical mechanisms was offered.

A more recent computational study by Irmisch (1995) examined a turbine blade airfoil with leading edge slots. Some notable highlights of this work were the use of an unstructured grid to accurately capture the complex airfoil shape and the use of a realistic film cooling geometry. However, grid independence and grid quality were not addressed thoroughly, although comparison between computed and experimental pressure coefficient was favorable. No investigation into the blade surface heat transfer characteristics was attempted.

Garg and Gaugler (1995) studied the effect of exit velocity and temperature distribution on the film cooling performance. A 1/7th law and a parabolic velocity profile were assumed at the film hole exit to demonstrate this effect. They document that the distribution of coolant velocity and temperature at the hole exit can cause a change in the heat transfer coefficient of as much as 50% to 60%. This evidence supports the choice of computational model used in this paper; namely, that the computational domain must include the plenum, slot, and crossflow to accurately model the complex flow physics.

In two companion papers by Butkiewicz et al. (1995) and Walters et al. (1995), a 2-D normal slot-jet was studied to develop and validate a consistently accurate computational methodology using experimental data of Scherer and Wittig (1991). In these studies, four key issues of obtaining consistently accurate computational results in the context of a jet-in-crossflow interaction were emphasized: (1) proper computational modeling of flow physics, (2) exact geometry representation and high grid quality, (3) use of higher-order discretization schemes, and (4) selection of appropriate turbulence models.

3. Present Contributions

The primary goals of this study are to implement an established computational methodology to:

- Conduct careful comparison of results between a sharp-edged reference case (REF), and three distinct configurations with inlet shaping (IS), exit shaping, (ES), and combined inlet and exit shaping (IES).

- Explain and document all of the crucial physical mechanisms which determine downstream heat transfer characteristics in inclined slot-jets, and determine the effect of geometry on these mechanisms.

- Provide complete results for both the adiabatic effectiveness and heat transfer coefficient downstream of the slot-jet for various slot geometries and operating parameters.

- Objectively evaluate the performance of the standard k-ε and RNG k-ε turbulence models.

- Demonstrate that computational fluid dynamics (CFD) can be used to dependably capture complex flow physics so that the relative performance of various film cooling configurations can be accurately established.

4. Problem Description

A 35° inclined slot-jet is studied in this paper because of its common use in gas turbines. To investigate geometry effects on film cooling performance, four distinct geometric configurations are presented: (1) slot with straight edges and sharp corners [REF]; (2) slot with shaped inlet region [IS]; (3) slot with shaped exit region [ES]; and (4) slot with both shaped inlet and exit regions [IES]. Figure 1 shows these different geometric arrangements. Note that the geometry of the slot is changed systematically so that their individual influences can be isolated. For each of the distinct geometries, the length-to-slot-width ratio was varied from $L/s=4.5$ to $L/s=3.0$ (realistic and applicable lengths to the gas turbine industry) to examine the effect of this important parameter. The slot width was specified as 5 mm, and the length of the slot was varied to obtain the documented L/s ratios. Air was used as the working fluid in both the crossflow and coolant jet, with the temperature of the coolant jet adjusted to achieve the desired density ratio (DR).

5. Computational Methodology

The computational methodology implemented in this study is documented in Butkiewicz et al. (1995) and Walters et al. (1995). Application of this methodology is outlined below.

5.1 Computational Model

Due to the strong coupling of the crossflow, slot, and plenum (Garg and Gaugler, 1995; Leylek and Zerkle, 1993), each of these three regions are modeled simultaneously in the computational domain. This allows boundary conditions to be applied where they are certain, and also allows the complex interactions within the jet itself and between the jet and crossflow at the exit plane to be computed rather than applied in this highly elliptic region. Figure 2 graphically depicts the computational model used in the present study. Velocity inlet boundary conditions are specified for both the crossflow and plenum inlets. The crossflow velocity and temperature are set at 10 m/s and 25.15°C, respectively. The density ratio was set to the desired value by decreasing the temperature of the coolant entering through the plenum. The coolant inlet velocity was then calculated so that the correct blowing ratio was attained. Turbulence quantities at the velocity inlets are determined using a turbulence intensity of 0.7%, which matches planned experiments to complement the simulations presented in this paper. In order to decrease the size of the computational domain, a zero normal gradient condition is imposed at the top of the domain at 20 slot widths away from the test surface, and a flow outlet boundary condition is applied 30 slot widths downstream. The domain extends 40 slot widths upstream of the leading edge of the slot.

5.2 Geometry and Grid Generation

The I-DEAS solid modeling system was used to precisely capture the slot geometries and to fill the domain with the highest quality grid possible. Figure 3 shows a sample of one of these grids in the slot region. Grid quality was quantitatively evaluated by the cell skewness; a skewness of zero represents a perfect equilateral cell, and a skewness of unity denotes a degenerate cell. Each grid used in these simulations averaged a cell skewness of approximately 0.05, with 99.5% or more of the cells having a skewness under

0.2. Grid independence issues were addressed by performing test cases with coarse grids until grid independence was reached at approximately 30,000 cells. Grid y^+ along the upstream and downstream walls and inside of the slot was maintained between 20 and 30.

5.3 Discretization Scheme

The second order discretization scheme implemented in RAMPANT was used to reduce numerical viscosity in the flowfield. This scheme is a 2nd order linear reconstructive scheme and has been shown to perform extremely well in the jet-in-crossflow class of problems by Walters et al. (1995) and Newman (1995).

5.4 Turbulence Modeling

Experimental studies by Andreopoulos and Rodi (1984) and Pietrzyk et al. (1989, 1990) examined the correlation between the mean velocity gradients and the turbulent shear stresses on the centerline plane in jet-in-crossflow interactions. These works verify that eddy-viscosity models are applicable to the class of problems involving 2-D slot-jets in the present study. In addition, a study by Chekhlov et al. (1994) compares direct numerical simulation (DNS) results to those obtained via two k-ε turbulence models. Their results show good agreement between the two eddy-viscosity models and DNS in computing the time averaged Reynolds stresses, thus providing further evidence that eddy viscosity models are adequate in 2-D situations. Based on these conclusions and comparisons made in the present study (see Section 6.7), the standard k-ε model with generalized wall functions is selected for these computational simulations.

5.5 Convergence

A fully explicit, time-marching, unstructured/adaptive grid code was used to perform all processing of the computational simulations. Preprocessing and post-processing were performed on Sun workstations, while computations were performed on a 64 CPU Intel Paragon supercomputer. Simulations were typically run using 4 CPUs, which required approximately 6 hours per 1000 iterations. Convergence was accelerated using 4 multigrid levels, residual smoothing, a CFL number of 3.5 to 4.5, and local time stepping. The convergence of the simulations improved with M, and the total number of iterations to reach a fully converged state ranged from 3000 to 8000 iterations. In this study, convergence was established when the mass and energy imbalance in the entire computational domain was less than 0.1% and normalized residuals had fallen at least three orders of magnitude. The convergence and results of the simulations were insensitive to various initialization strategies.

6. Results and Discussion

6.1 Validation of Computational Methodology

Much in-house work has been undertaken to validate the computational methodology documented in Butkiewicz et al. (1995) and Walters et al. (1995) for a wide variety of problems. Among these are a laminar flow over a cylinder problem (Newman, 1995), a normal slot-jet-in-crossflow interaction, and an inclined discrete jet-in-crossflow interaction. Each case documents excellent agreement with experimental results.

The first case examined a laminar flow over a cylinder for various Reynolds numbers.

This challenging, benchmark test case was performed to verify the effectiveness of this methodology without the factor of turbulence modeling. Four key parameters were examined in this case: the distance between the vortex centers (b), the distance from the trailing edge of the cylinder to the vortex centers (a), the wake length (L), and the separation angle (θ_s), as shown in Figure 4. Predicted results for these parameters demonstrated excellent agreement with experimental measurements provided by Coutanceau and Bouard (1977), as shown in Table 1.

A normal slot-jet-in-crossflow problem was also examined, which is an extremely complex flow situation involving jet liftoff, separation, and reattachment. Reattachment length, the downstream pressure coefficient, and the downstream Nusselt number were investigated and compared to experimental results (Scherer and Witting, 1991). Figure 5 shows the agreement between computed and experimental results for the pressure coefficient, and the reattachment length was overpredicted by 17%. Note that extraneous blockage effects due to sidewall boundary layers and corner vortices documented in the experimental counterpart is expected to shorten the reattachment length, while the computations were purely two dimensional and did not suffer from these blockage effects; therefore, an overprediction of experimental results is expected.

A 3-D discrete inclined jet-in-crossflow was studied by Walters and Leylek (1996) as additional verification of the computational methodology used in this paper. Computations of adiabatic effectiveness were compared to experiments by Sinha et al. (1990), and field data were compared to results from Pietrzyk et al. (1989). The computations overpredicted η along the centerline as shown in Figure 6, but these simulations more effectively captured the spreading of the jet than any simulation found in the open literature. Differences between experimental and computational results were attributed to experimental discrepancies and turbulence modeling effects.

Some inclined slot-jet experimental results for the adiabatic effectiveness were available in-house and were compared to the simulations performed in this study. Experimental results are given for DR=1.55, L/s=2.79, and M=1.2. The predicted results were compared to experimental measurements for the same flow parameters and L/s=3.0 in Figure 7. Note that the computations slightly overpredict η; however, this behavior is expected due to the shorter L/s of the experimental study.

The excellent agreement obtained between predicted and measured data for all of the cases described above gives confidence in the computational methodology and provides validation that the computations will closely predict the flowfield and surface heat transfer results in the series of simulations conducted in the present study.

6.2 Reference Case — 35° Inclined Slot-Jet

First, reference cases are established for L/s=3.0 and L/s=4.5 for use in subsequent comparison of geometry effects at blowing ratios ranging from M=1.0 to M=2.0. The comparisons following in the next three sections are made using the L/s=4.5 reference case. Using this reference, the dominant features of the slot-jet-in-crossflow interaction are identified.

The flow features in the slot region which most significantly influence the downstream film cooling performance are highlighted in Figures 8, 9, and 10. The dominant

Table 1. Comparison of Experimental and Computational Results for Laminar Flow Over a Cylinder Case, Re=30. Experimental Data Provided by Coutanceau and Bouard (1977).

Parameters	Experiment	Computation	% Difference
L (mm)	78.08	81.25	4.06
a (mm)	28.05	27.69	1.30
b (mm)	27.54	26.40	4.32
θ_s (Degrees)	50.1	49.16	1.91

features of the flowfield are: (1) the separation region at the slot inlet, (2) the jetting region along the upstream wall within the slot, and (3) the high pressure gradient/velocity gradient region at the trailing edge of the slot exit. Figure 8 shows the velocity vectors in the vicinity of the slot, indicating a separation and reattachment region along the downstream wall of the slot. This separation occurs due to the sharp corner which must be negotiated by the incoming fluid. As a consequence, the fluid along the upstream wall is accelerated in a "jetting" effect. The resulting shear layer within the slot itself is a significant source of turbulent kinetic energy, as seen in Figure 10. The turbulence generated in the slot is convected into the crossflow and downstream along the test surface, decreasing the film cooling performance. The other key source of turbulence production is at the trailing edge of the slot jet exit plane. The turbulence generated at this location is augmented by a severe adverse pressure gradient, which is highlighted in Figure 9. This source of turbulence is particularly damaging to film-cooling performance due to its proximity to the test surface.

Each of the detrimental flow features discussed above can and will be avoided by rounding of the slot inlet and/or exit. In so doing, the film cooling performance, in terms of η and h, can be improved.

6.3 Inlet Shaping

As mentioned in Section 6.2, two of the dominant flowfield features of the inclined slot-jet in crossflow interaction are the inlet separation region and jetting region along the upstream side of the slot. Because of the shaping of the inlet (as shown in Figure 1b), the flow is able to smoothly negotiate the turn into the slot; therefore, much less turbulence is generated at the entrance of the slot when compared to the reference case. Since the exit geometry is common with the reference case, a severe pressure gradient is still present at the slot breakout which fuels turbulence that is injected into the film adjacent to the wall.

Shaping the inlet has a positive effect on both the adiabatic effectiveness and heat transfer coefficient. For each M, shaping the inlet consistently increased η and decreased h; however, these changes were not significant. At best, inlet shaping has the ability to increase η by up to 1 percentage point and decrease h by up to 10% (M=2.0). Plots of η and h for M=1.0 and M=2.0 are shown in Figures 11 and 12; note that since h exhibits asymptotic behavior far downstream, data is only shown for the near field, $0<x/s<10$. Moreover, as M decreases, the added performance benefit of inlet shaping also decreases, even becoming negligible at M=1.0. This gives preliminary indication that the separation region at low M does not significantly affect η and h.

As shown in Figure 13, the velocity profiles on the test surface downstream of the exit plane agree perfectly between the reference case and the inlet shaped case, except for the slight amount of upstream jetting that is still apparent in the near-field velocity profiles. However, this slight peak in velocity is quickly smoothed by the high amount of mixing in the film. The similarity of these profiles shows that any difference in heat transfer characteristics is primarily due to the difference in turbulence content in the film, especially close to the downstream wall. Also, these similarities indicate the internal consistency of this set of computational simulations.

Profiles of tke, shown in Figure 14, also show the consistency of these simulations. The overall level of turbulence convecting downstream is lower for the inlet-shaped case due to the decreased amount of turbulence generated within the slot. This decrease leads to a higher quality film with less turbulent mixing, and therefore better film cooling performance. Note that the maxima in the tke profiles are in the same nearwall y/s location, which corresponds to the generation of turbulence at the slot exit. It is important to note that as M decreases, the separation region becomes much smaller, which decreases both the amount of turbulence generation at the inlet and the magnitude of jetting along the upstream wall. This mechanism explains the behavior of the surface results as M decreases; eliminating an already insignificant separation region by shaping the slot inlet does not gain much benefit at low M.

Note that for the inlet shaped case, the adverse pressure gradient is slightly more severe than for the reference case. Velocity profiles inside of the slot show that the elimination of jetting actually has a negative effect on the film cooling performance of the inlet shaped case. Because of the jetting effect along the upstream wall, fluid velocity along the downstream wall is lower (due to continuity), whereas the inlet shaped case affords an approximate 1/7th law profile inside of the slot as shown in Figure 15. This means that, if the inlet is shaped, higher velocity fluid must turn the sharp exit corner, which results in a higher adverse pressure gradient at the slot breakout. Because of this mechanism, the advantage gained by eliminating the turbulence generation at the slot inlet is counteracted strongly by the extra turbulence generated at the slot breakout. So, although one would expect to see a large advantage in η and h because of the decreased turbulence levels exiting the slot, the mechanism described above counteracts this possibility.

6.4 Exit Shaping

Although the separation region and jetting region at the slot inlet still exists, shaping of the slot exit (as shown in Figure 1c) alleviates the severe adverse pressure gradient at the trailing edge of the exit plane in the reference and inlet shaped cases. Removal of this particularly detrimental turbulence source is expected to improve film cooling performance. Figure 16 demonstrates the structure of this turbulence generated at the slot exit in the reference and exit shaped cases.

For each M studied, shaping the slot exit consistently increases η and decreases h, both improving by a magnitude greater than that offered by inlet shaping. Exit shaping alone afforded an η increase of up to 2 percentage points and an h decrease of 20%. Unlike the varying amount of advantage given by inlet shaping, this additional benefit is approximately the same regardless of M.

The turbulence intensity profiles at various streamwise locations on the test surface, shown in Figure 17, demonstrate the removal of turbulence generation at the slot exit. There is an extremely large difference in the turbulence intensity at the wall -- at x/s=2, a 7% difference for M=2.0, and 4.5% at M=1.0. This large advantage makes its way downstream as a history effect. This point demonstrates the value of shaping the exit region, as well as the fact that the turbulence generated at the inlet region of the slot is quickly attenuated because of the lack of a source as the fluid nears the slot exit plane. Far downstream, the TI profiles meet near the wall, although the overall level throughout the film is lower than the reference case. This explains why h is constant far downstream of the slot, but η continues to show a benefit because the decreased level of turbulence offers less diffusion of the hot crossflow across the film.

Competing mechanisms force the advantage gained in the film cooling performance to remain constant regardless of M. At high M, extremely high levels of turbulence are generated at the slot inlet due to the separation region, but the need for exit shaping is not as great due to the upstream skewed velocity profile of the jetting fluid. On the other hand, not as much turbulence is generated at the inlet at low M, but the small size of the separation region forces a nearly uniform velocity profile in the slot which generates a larger amount of turbulence at the slot breakout. This combination of the jetting effect and the turbulence generation at the inlet allow shaping of the slot exit to offer a nearly constant advantage in the film cooling performance which is not a function of the range of M studied in this paper.

For each M (for L/s=4.5), shaping of the slot exit has a more dramatic impact on film cooling performance than shaping of the inlet. This result is consistent for each type of surface data examined (η and h). This greater effect is gained by the elimination of a particularly detrimental pocket of turbulence generation at the slot exit. As stated previously, the increase in film cooling performance over the reference case is constant regardless of the blowing ratio.

6.5 Combining the Effects of Inlet and Exit Shaping

Obviously, better film cooling performance should be attained by combining the benefits of inlet and exit shaping (Figure 1d). Based on the effects of geometry variations isolated in the previous two sections, each of the detrimental flow features discussed in Section 6.2 can be eliminated by the shaping of both the inlet and the exit of the slot-jet. As a consequence, the competing flow mechanisms discussed in the previous section are eliminated so that shaping the exit can increase the advantage in performance as M increases, rather than simply offering a constant advantage in film cooling performance regardless of the blowing ratio.

For each M studied, shaping both slot exit and inlet consistently increases η and decreases h to a greater magnitude than offered by either inlet or exit shaping alone. This configuration improves η by over 3 percentage points, and decreases h by over 30% compared to the reference geometry.

As shown by Figures 11 and 12, the trends in η and h can be interpreted as superposition of the separate results of the inlet shaped and exit shaped cases. Even so, this superposition does not account for all of the increased film cooling performance given by shaping the inlet and exit of the slot. As discussed in the previous section, extra film cooling performance is gained due to the elimination of competing flow mechanisms apparent in the exit-shaped case. For each M and L/s studied, shaping of both inlet and exit provides the best benefit in terms of film cooling performance.

6.6 Effects of Slot Length-to-Width Ratio (L/s)

Overall, film cooling performance is much poorer as L/s is decreased. Turbulence generated at the inlet is not given a chance to attenuate, so a more diffusive film is ejected from the slot. The same trends in the film cooling performance as a function of slot geometry are observed for these short L/s cases, for the same reasons as discussed above for the longer L/s. As the L/s is decreased, the need for inlet shaping increases accordingly; this characteristic is reflected in η and h. Indeed, for the L/s=3.0 cases, the benefit derived from shaping the inlet becomes greater when compared to the L/s=4.5 cases, but the benefit given by shaping the exit remains constant.

6.7 Effects of Density Ratio

To isolate the effect of DR on the film cooling performance, the density ratio was varied from DR=1.5 to DR=2.0 using the reference geometry and a blowing ratio of M=2.0. Results show that as DR increases, film cooling performance also increases. The simulations performed here are found to be fully consistent with the trends documented in the open literature regarding DR; therefore, no further explanation of these results will be offered. Note, however, that the dominant flow features identified in Section 6.2 do not change with DR.

6.8 Evaluation of Standard k-ε and RNG k-ε Turbulence Models

The standard k-ε model with generalized wall functions is used in this paper to investigate the geometry effects on inclined slot-jet-in-crossflow problems. However, the RNG k-ε model is another feasible choice of eddy-viscosity model. To compare the performance of these two models, the RNG k-ε model is employed in the reference case and inlet/exit shaped simulations, and the field and surface results are compared to the results obtained via the standard k-ε model.

The comparison of η confirms studies of the RNG model conducted by Walters et al. (1995) and Butkiewicz et al. (1995); it is found that η is unrealistically exaggerated. For M=2.0, η does not fall below 0.9 at any distance downstream using the RNG model. The calculated tke generated in the slot is confined strictly to the separation region and has a significantly lower level, resulting in unrealistically low diffusion effects in and across the film. Also, the relative absence of turbulent mixing in the slot causes the jetting region to remain extremely well defined at the exit of the slot. Profiles of all transport quantities remain well defined even at the exit of the domain at x/s=30 because of the lack of diffusive action. Coupled with the overprediction (using RNG k-ε) of a normal jet reattachment length presented in the companion papers of Butkiewicz et al. (1995) and Walters et al. (1995), the RNG model was judged to be unsatisfactory for the simulations presented in this paper.

It should be stressed that these simulations are strictly 2-D; therefore, conclusions regarding turbulence models may or may not be applicable to 3-D simulations. In the context of 2-D slot-jet problems, the RNG model was judged to be incapable of providing reasonable turbulence closure.

6.9 Review of Computational Simulations

Overall, surface results and flowfield details are exceptionally consistent between *all* computational simulations performed. Even the minute details (location of peaks in tke, velocity, velocity profiles, etc.) are in perfect agreement between simulations. When CFD is used properly, it is clear that trends can be accurately captured, which is often the gas turbine heat transfer designer's primary concern. Also, CFD gives access to all information in a flowfield so that complete understanding of the crucial flow mechanisms may be obtained. For example, this set of computational simulations contain evidence that shaping of the slot has a dramatic effect on the discharge coefficient. All of these conclusions support that CFD may be successfully and practically applied as a design tool in modem gas turbine design.

7. Conclusions

- Shaping of the slot-jet inlet dramatically decreases the amount of turbulence generated at the slot inlet; however, the expected gain in film cooling performance is lost due to the turbulence generation at the trailing edge of the slot breakout.
- Shaping of the slot exit consistently increases film cooling performance by eliminating turbulence generation at the slot breakout, which would otherwise immediately contaminate the film.
- As the blowing ratio (M) decreases, the effect of shaping the slot inlet declines rapidly, becoming negligible at low M. However, shaping of the slot exit significantly improves film cooling performance at any M, for the range of M investigated in the present study.
- Combining inlet and exit shaping superimposes the advantages displayed by both, and results in the best film cooling performance of the test cases for any blowing ratio. However, shaping inlet and exit does not provide significant advantage over shaping the exit only for low blowing ratios.
- To accurately estimate film cooling performance, information on both adiabatic effectiveness and the heat transfer coefficient must be obtained.
- The k-ε model was judged to give accurate turbulence closure; the RNG k-ε model produced unrealistic results in this 2-D slot jet study.
- The ability of CFD to accurately and dependably capture the flow physics and correct trends in 2-D slot-jet film cooling has been clearly established. The CFD model of 2-D slot-jet film cooling presented in this paper may be used as an effective preliminary design tool to screen alternative configurations.

Acknowledgments

This paper was prepared with the support of the U.S. Department of Energy, Morgantown Energy Technology Center, Cooperative Agreement No. DE-FC21-92MC29061. The authors would like to thank Mr. Dewitt Latimer, Mr. Gary Berger, and Mr. Richard Baldwin of the Engineering Computer Operations at Clemson University for their assistance in all computer related matters. Also, Dr. Pat Fay provided first-rate support for the Intel Paragon supercomputer used for the crunching of the many simulations. We are also deeply indebted to Dr. Rick Lounsbury at Fluent, Inc. for his invaluable support with RAMPANT. Lastly, special thanks to Mr. Robert Brittingham, who provided assistance with the simulations, and Mr. Andreas Zeisberger, who provided valuable experimental data.

References

Andreopoulos, J., 1982, "Measurements in a Jet-Pipe Flow Issuing Perpendicularly Into a Cross Stream," Journal of Fluids Engineering, Vol. 104, pp. 493-499.

Butkiewicz, J., Walters, D., McGovern, K., and Leylek, J., 1995, "A Systematic Computational Methodology Applied to a Jet-in-Crossflow Part 1: Structured Grid Approach," Accepted for Presentation at the ASME Winter Annual Meeting, San Francisco, CA.

Chekhlov, A., Orszag, S.A., Sukoriansky, S., Galperin, B., and Staroselsky, L., 1994, "Direct Numerical Simulation Tests of Eddy Viscosity in Two Dimensions," Phys. Fluids, Vol. 6, No. 7, pp. 2548-2550.

Coutanceau, M., and Bouard, R., 1977, "Experimental Determination of the Main Features of the Viscous Flow in the Wake of a Circular Cylinder in Uniform Translation, Part 1: Steady Flow," Journal of Fluid Mechanics, Vol. 79, Part 2, pp. 231-256.

Ekkad, S., Zapata, D., and Han, J., 1995, "Film Effectiveness Over a Flat Surface With Air and CO2 Injection Through Compound Angle Holes Using a Transient Liquid Crystal Image Method," ASME Paper No. 95-GT-11.

Ekkad, S., Zapata, D., and Han, J., 1995, "Heat Transfer Coefficients Over a Flat Surface With Air and CO2 Injection Through Compound Angle Holes Using a Transient Liquid Crystal Image Method," ASME Paper No. 95-GT-10.

Garg, V., and Gaugler, R., 1995, "Effect of Velocity and Temperature Distribution at the Hole Exit on Film Cooling of Turbine Blades," Presented at the International Gas Turbine and Aeroengine Congress and Exposition, Houston, TX.

Irmisch, S., "Simulation of Film-Cooling Aerodynamics With a 2D Navier-Stokes Solver Using Unstructured Meshes," Presented at the International Gas Turbine and Aeroengine Congress and Exposition, Houston, TX.

Ligrani, P., Wigle, J., Ciriello, S., and Jackson, S., 1994, "Film Cooling from Holes With Compound Angle Orientations, Part I: Results Downstream of Two Staggered Rows of Holes With 3D Spanwise Spacing," ASME Journal of Heat Transfer, Vol. 116, pp. 341-352.

Metzger, D., Carper, H., and Swank, L., 1968, "Heat Transfer With Film Cooling Near Nontangential Slots," Journal of Engineering for Power, Vol., pp. 157-163.

Newman, O., 1995, "The Development of an Effective Computational Methodology for Complex Flows," Senior Honors Thesis, Dept. of Mechanical Engineering, Clemson University, Clemson, SC.

Pietrzyk, J., Bogard, D., and Crawford, M., 1989, "Hydrodynamic Measurements of Jets in Crossflow for Gas Turbine Film Cooling Applications," ASME Paper No. 88-GT-194.

Schmidt, D., Sen, B., and Bogard, D., 1994, "Film Cooling With Compound Angle Holes: Adiabatic Effectiveness," ASME Paper No. 94-GT-312.

Sen, B., Schmidt, D., and Bogard, D., 1994, "Film Cooling With Compound Angle Holes: Heat Transfer," ASME Paper No. 94-GT-311.

Walters, D., McGovern, K., Butkiewicz, J., and Leylek, J., 1995, "A Systematic Computational Methodology Applied to a Jet-in-Crossflow Part 2: Unstructured/Adaptive Grid Approach," Accepted for Presentation at the ASME Winter Annual Meeting, San Francisco, CA.

Walters, D., and Leylek, J., "A Consistently Accurate Computational Methodology Applied to a Three Dimensional Film Cooling Flowfield," Abstract Accepted to the ASME/IGTI '96 Turbo Expo, Birmingham, England, June 1996.

Zeisberger, Andreas, 1994, "Experimental Investigation of Film Cooling Effectiveness With Slot Injection on a Flat Plate," Clemson University M.S. Thesis.

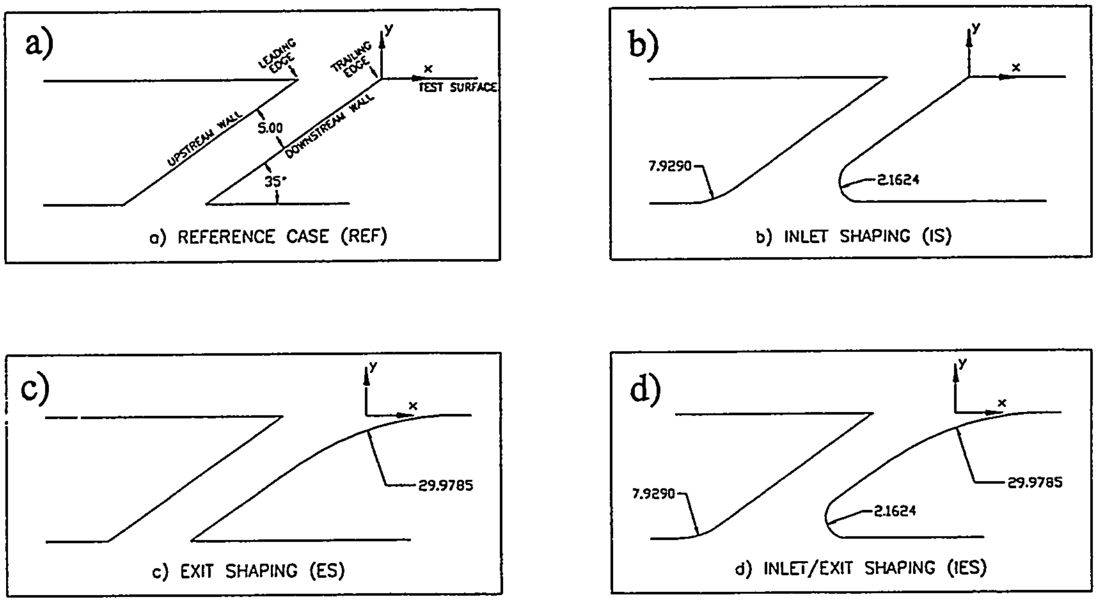

a) REFERENCE CASE (REF)

b) INLET SHAPING (IS)

c) EXIT SHAPING (ES)

d) INLET/EXIT SHAPING (IES)

Figure 1. Four Basic Configurations were Investigated: (a) Reference Case [REF], (b) Inlet Shaping [IS], (c) Exit Shaping [ES], and (d) Inlet/Exit Shaping [IES].

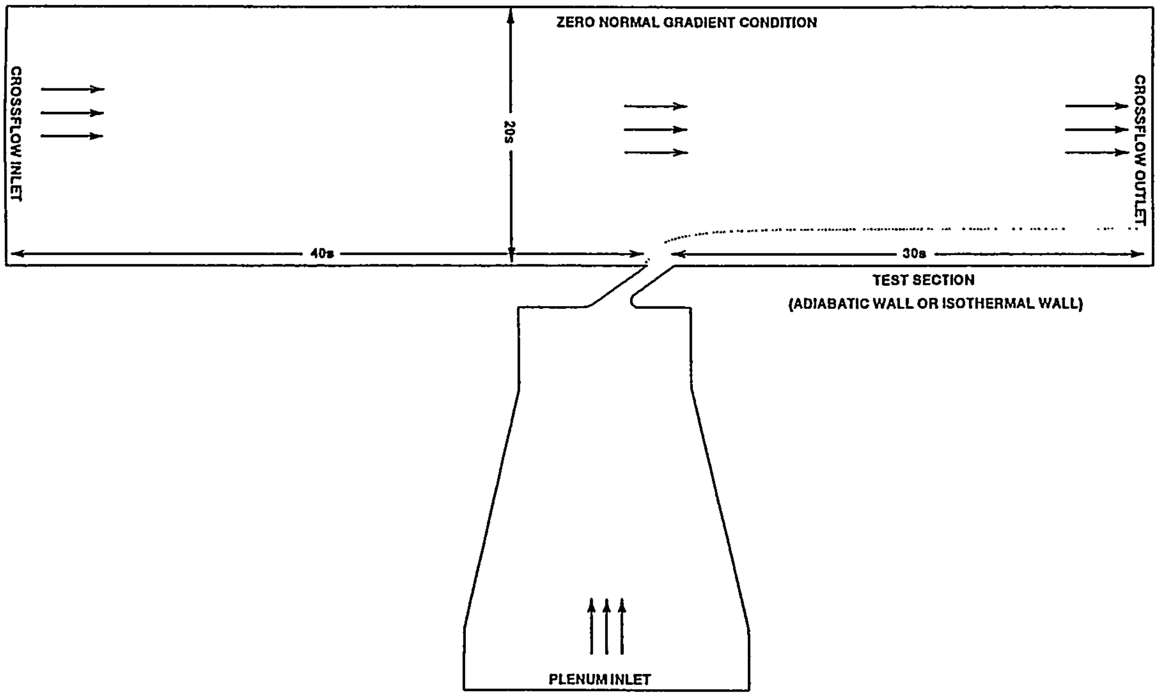

Figure 2. A Sketch of the Computational Model Shows the Domain With Boundary Conditions. All Thermal Boundary Conditions are Adiabatic Unless Stated Otherwise.

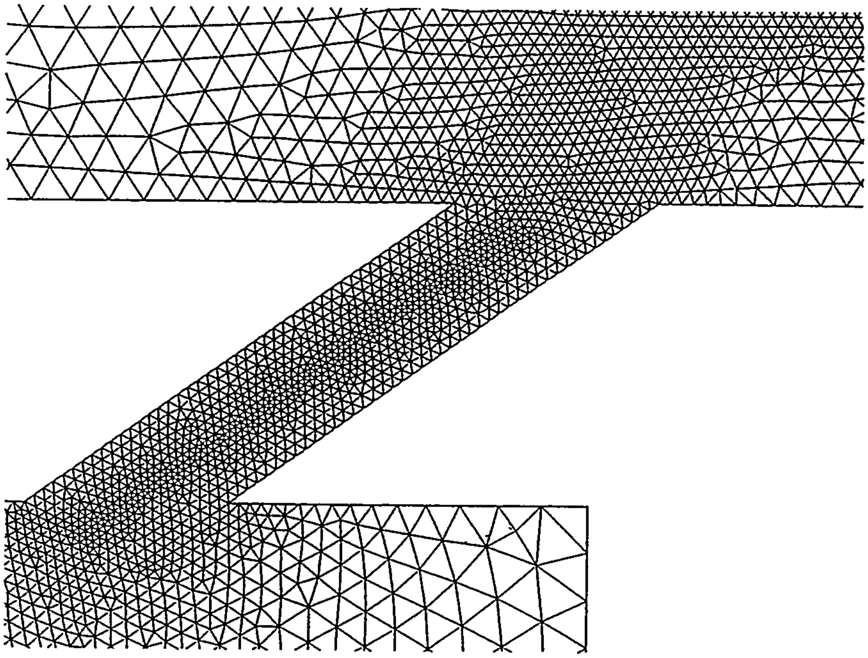

Figure 3. An Enlarged View of the Grid in the Slot Region Demonstrates the Quality and Resolution of the Unstructured/Adaptive Mesh.

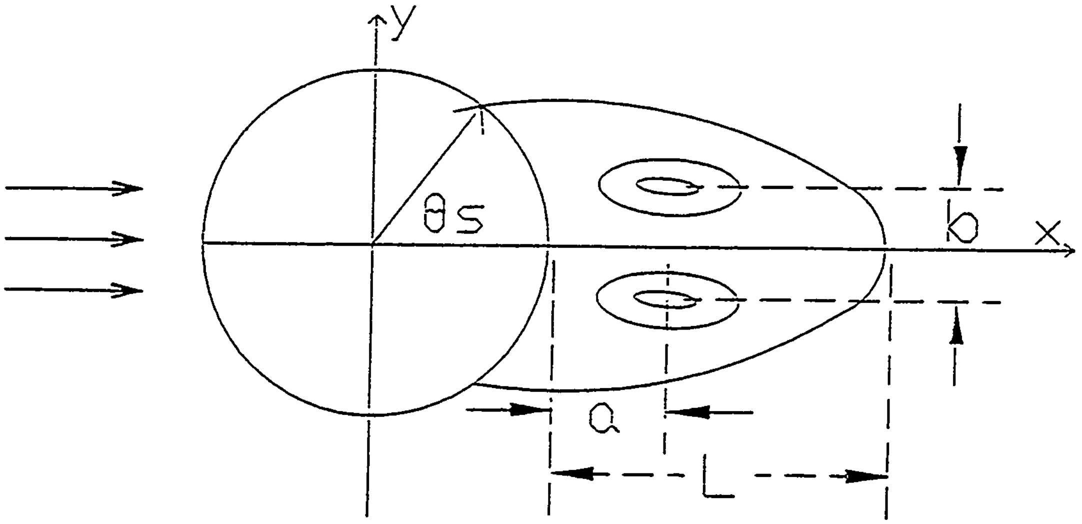

Figure 4. The Key Parameters of the Vortex Region Shown Above Were Investigated in the Laminar Flow Over a Cylinder Study. These Parameters are the Wake Length (L), the Distance Between the Vortex Centers (b), the Distance from the Trailing Edge of the Cylinder to the Vortex Centers (a), and the Separation Angle (Θ_s).

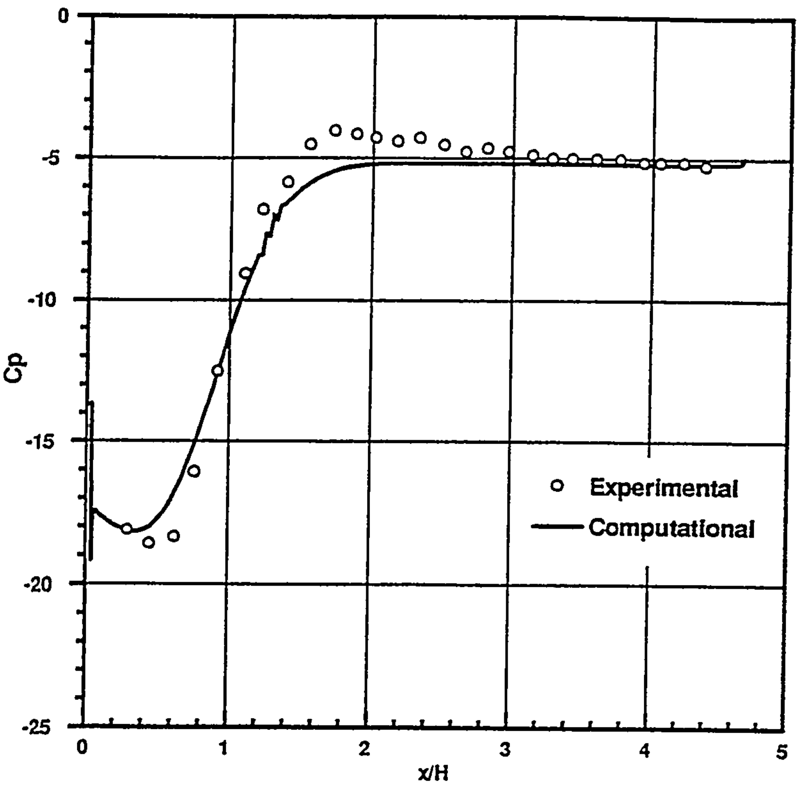

Figure 5. Plot of the Pressure Coefficient Shows the Excellent Agreement Between Computed Results and Experimental Measurements (Scherer and Wittig, 1990). H Denotes the Channel Height of 95 mm.

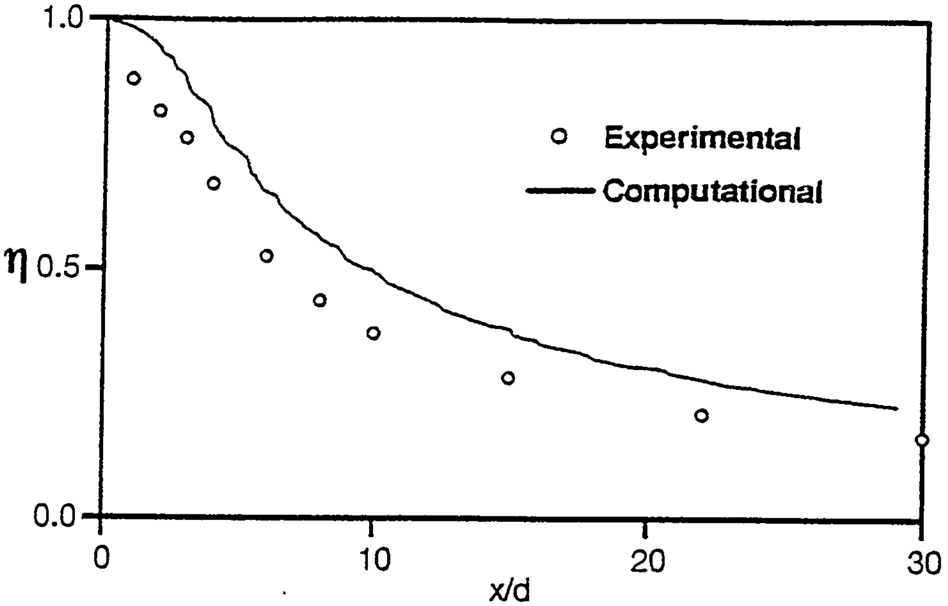

Figure 6. Plot of the Computed Adiabatic Effectiveness for the Discrete Inclined Jet Demonstrates Good Agreement With Data Provided by Sinha et al. (1990).

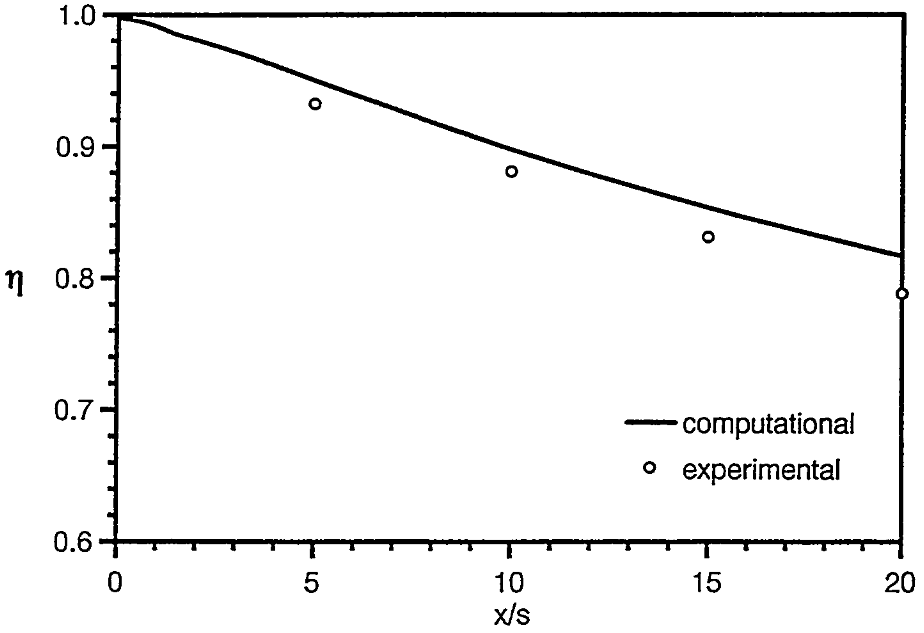

Figure 7. Plot of the Adiabatic Effectiveness for an Inclined Slot Jet Demonstrates the Excellent Agreement Between Computed Results and Experimental Measurements (Zeisberger, 1994).

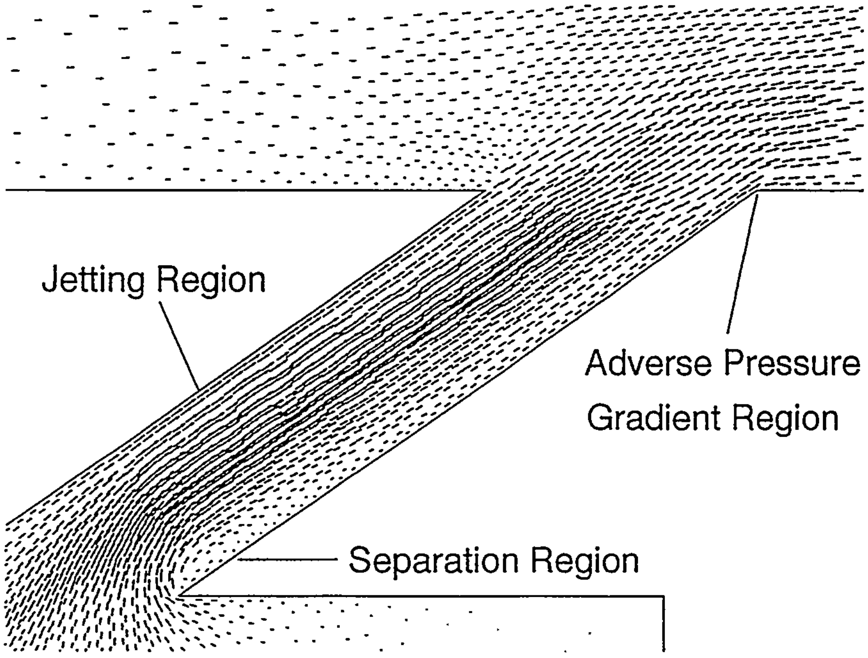

Figure 8. Velocity Vectors Provide an Overview of the Flowfield In and Near the Slot, Highlighting the Main Flowfield Features.

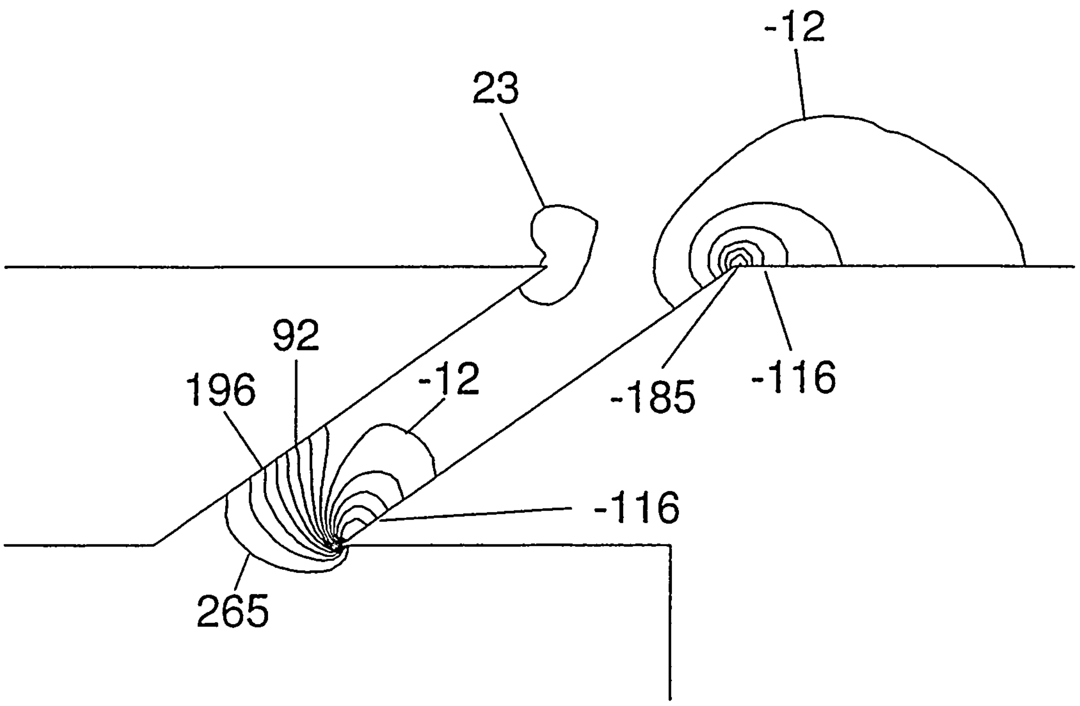

Figure 9. **Pressure Contours Demonstrate the Severe Adverse Pressure Gradient at the Trailing Edge of the Slot Exit.**

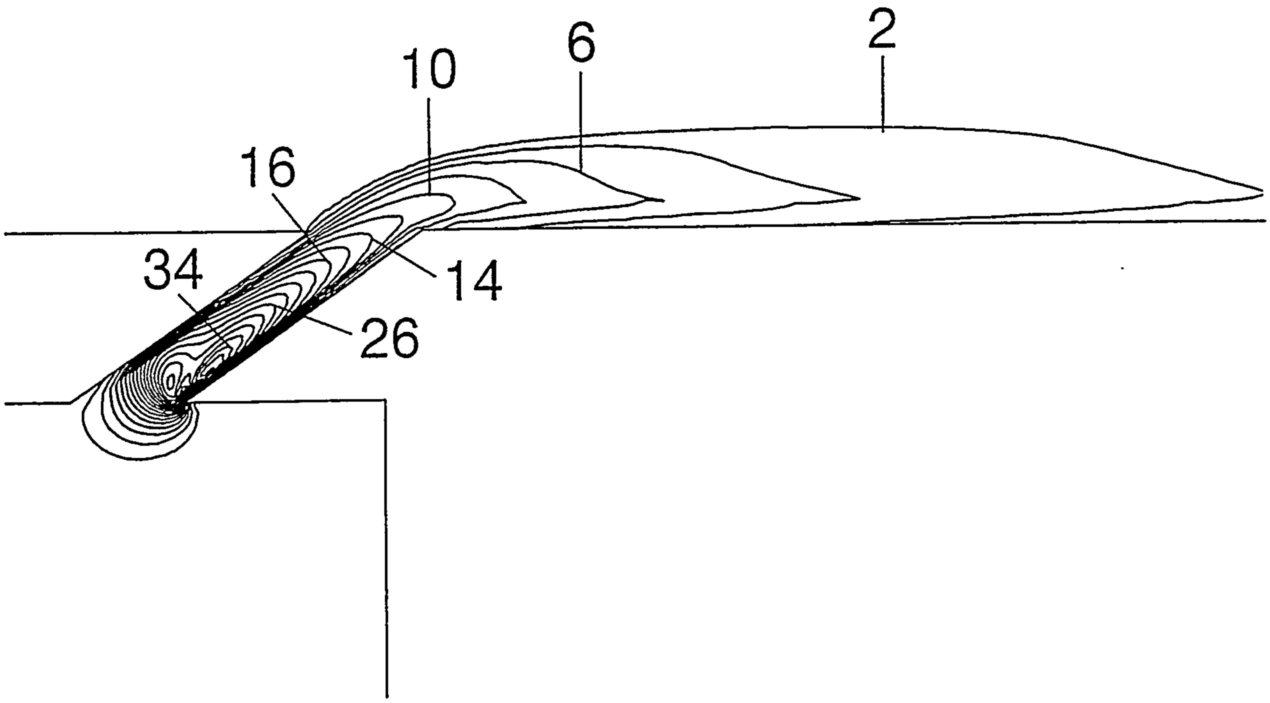

Figure 10. **Turbulent Kinetic Energy Contours Indicate the Crucial Areas of Turbulence Generation Within the Slot for the Reference Case [REF].**

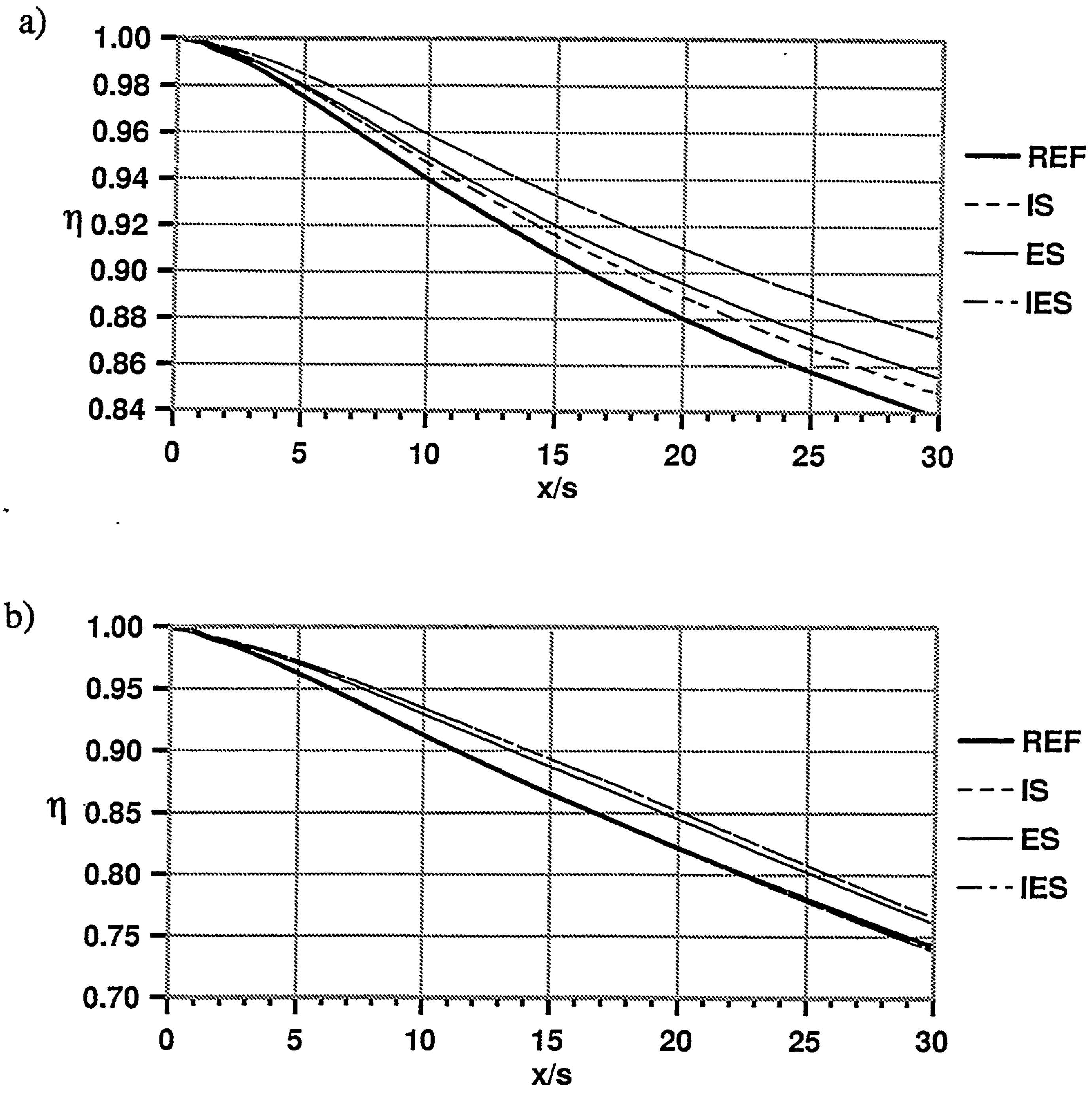

Figure 11. A Comparison of Adiabatic Effectiveness for (a) M=1.0, DR=1.5, and (b) M=2.0, DR=1.5 Demonstrates the Advantages of Slot Shaping and the Effect of M on Each Configuration.

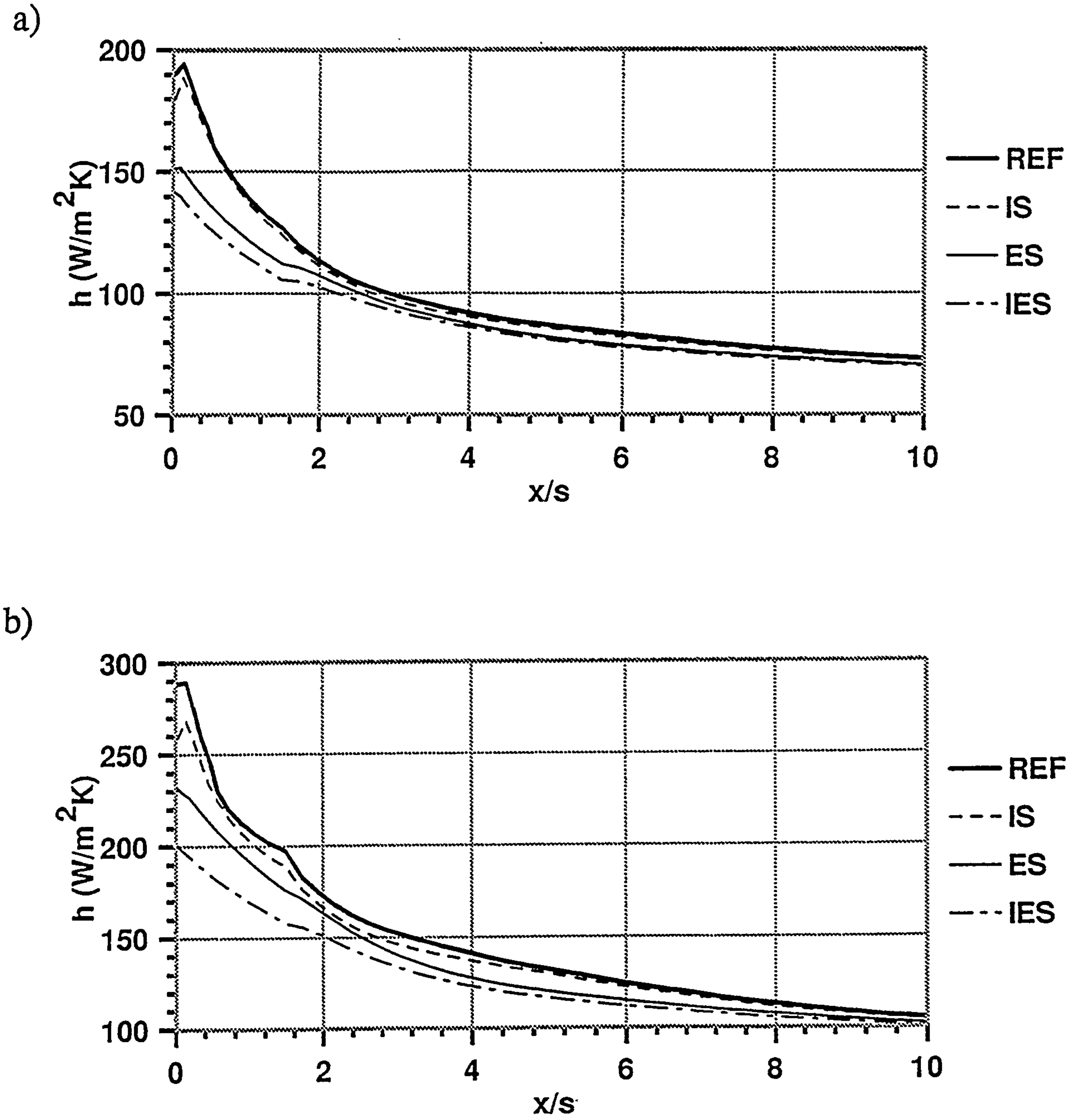

Figure 12. A Comparison of the Heat Transfer Coefficient for (a) M=1.0, DR=1.5 and (b) M=2.0, DR=1.5 Illustrates the Large Benefit in the Near Field Gained From Slot Shaping and the Effect of Blowing Ratio for Each Configuration. Since the Data Collapses for x/s > 10, h is Only Shown for 0 < x/s < 10.

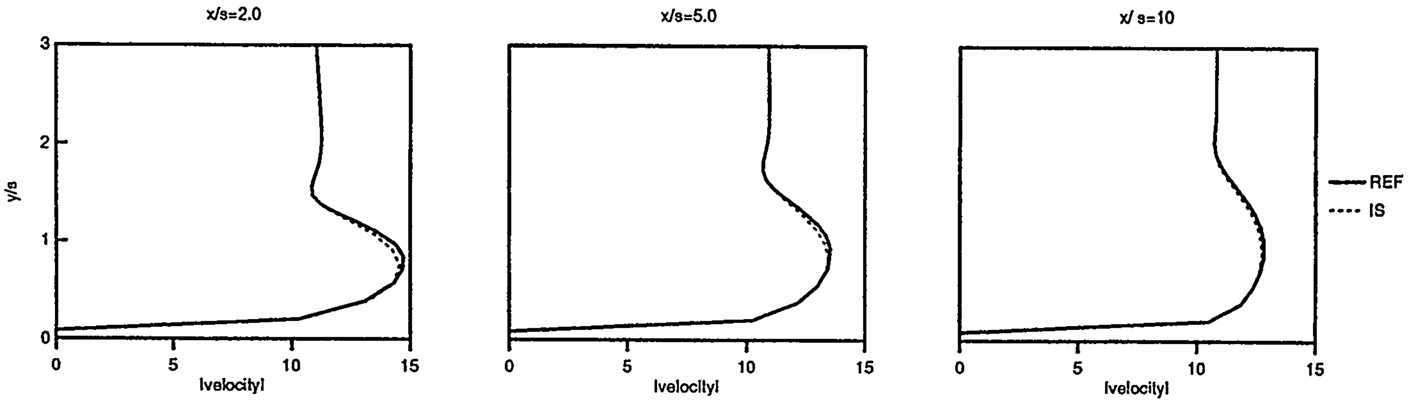

Figure 13. A Comparison of REF vs. IS Velocity Profiles at x/s=2, 5, and 10 Show the Internal Consistency of the Computational Simulations.

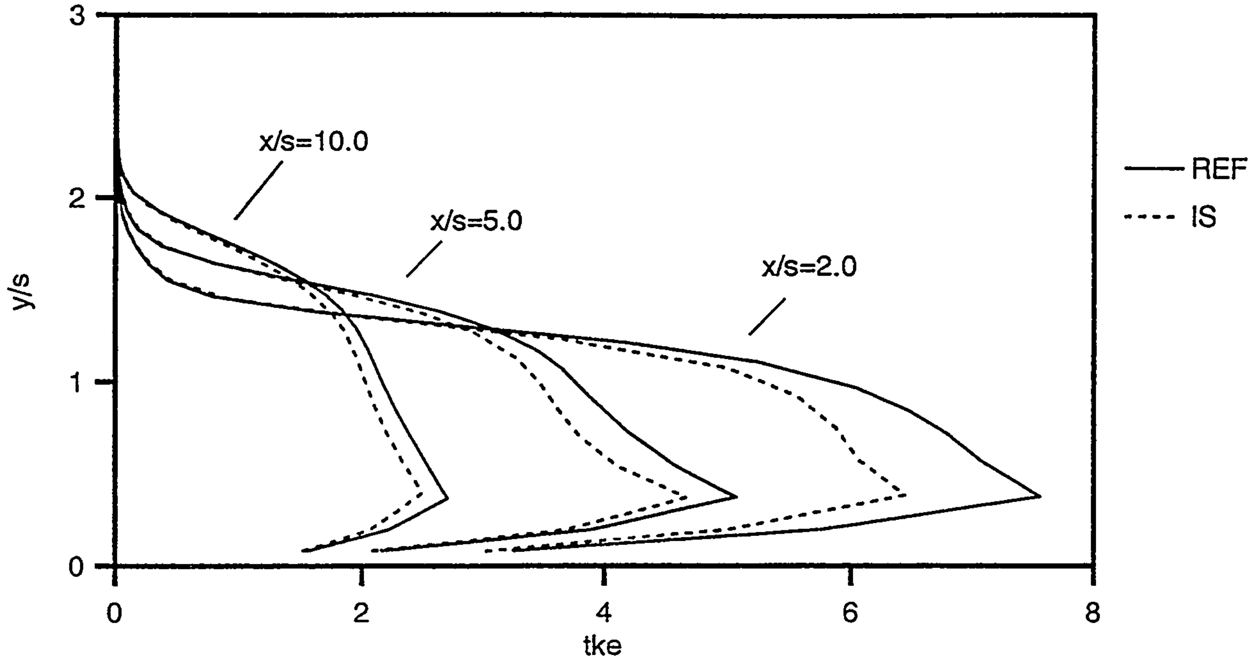

Figure 14. Turbulent Kinetic Energy Profiles at x/s=2, 5, and 10 Demonstrate the Benefit of Inlet Shaping in Terms of a Less Turbulent/Diffusive Film

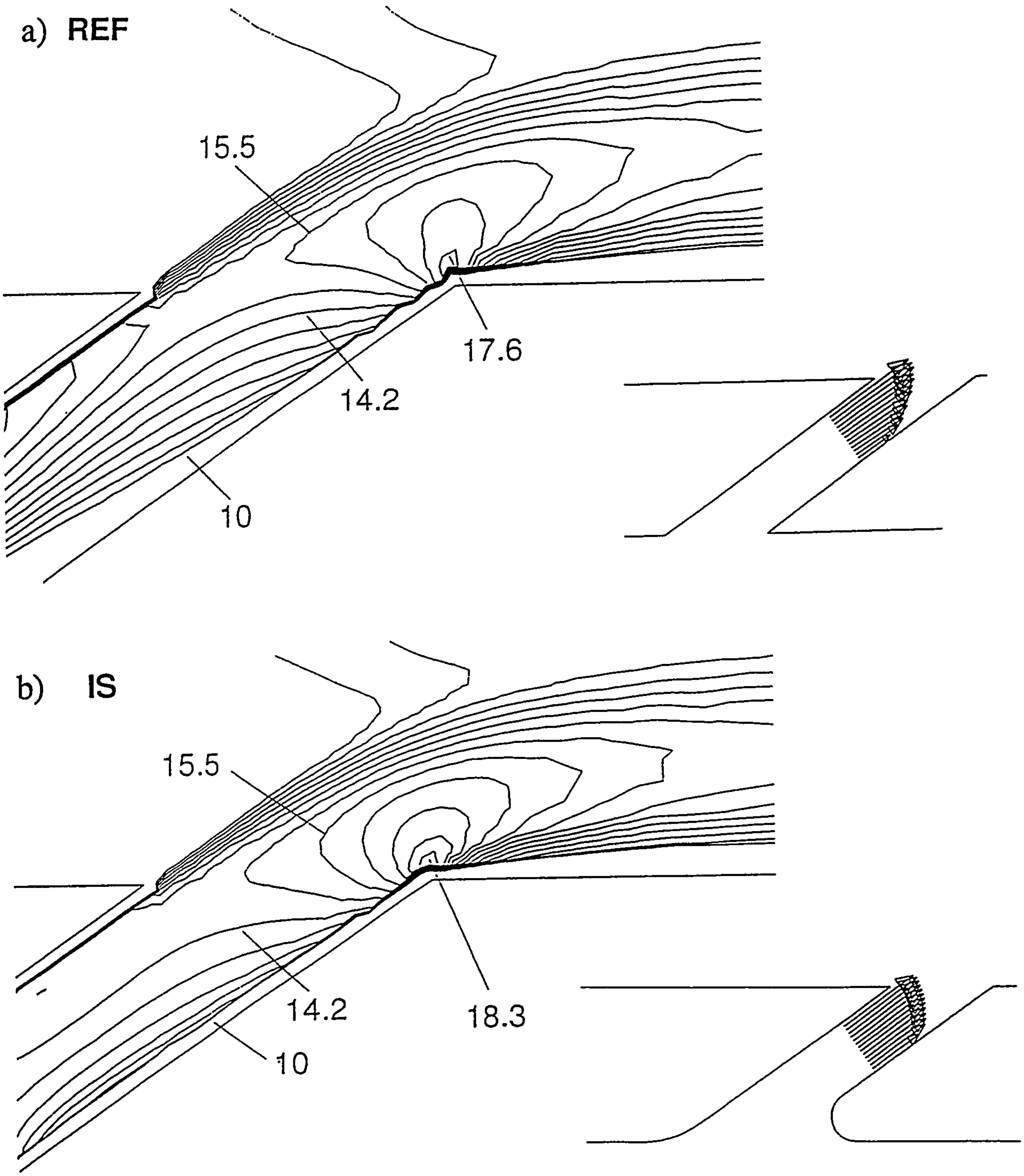

Figure 15. Velocity Contours and Velocity Profiles Demonstrate the Jetting Effect Inside the Slot, (a) Reference Case [REF] vs. (b) Inlet Shaped Case [IS]. Note the Lower Velocity Region for the Reference Case Along the Downstream Wall.

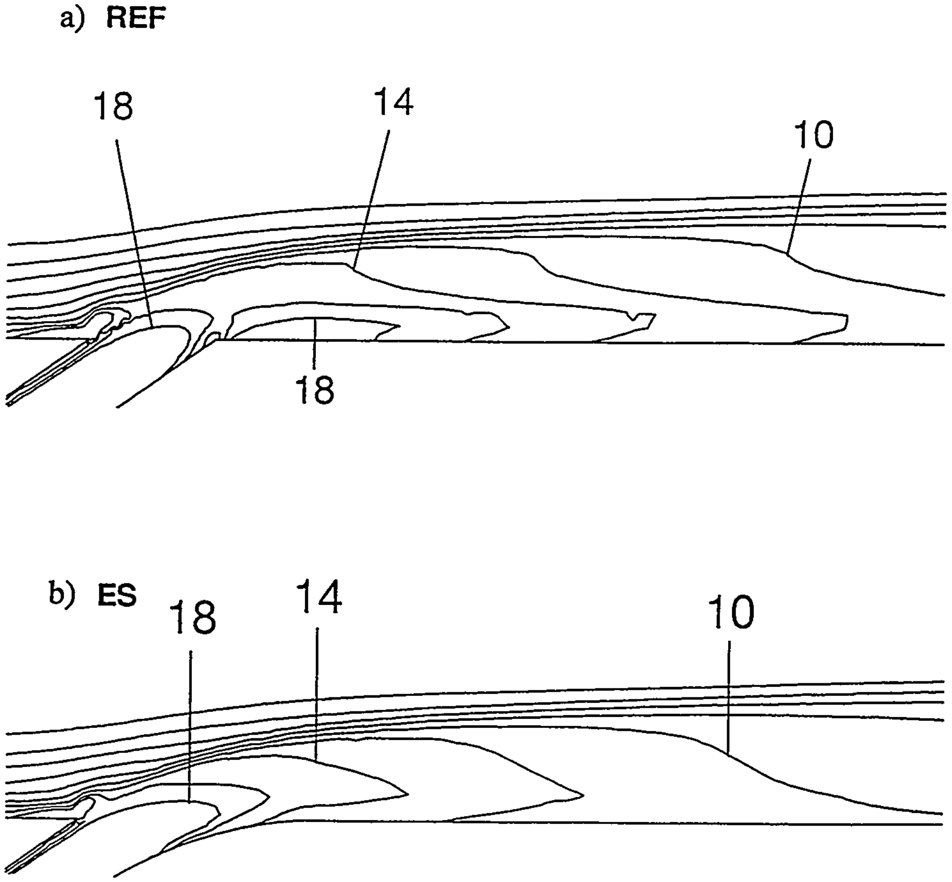

Figure 16. Turbulence Intensity Contours at the Slot Exit for (a) the Reference Case [REF] and (b) the Exit-Shaped Case [ES] Show That Exit-Generated Turbulence Can Be Effectively Eliminated by Exit Shaping.

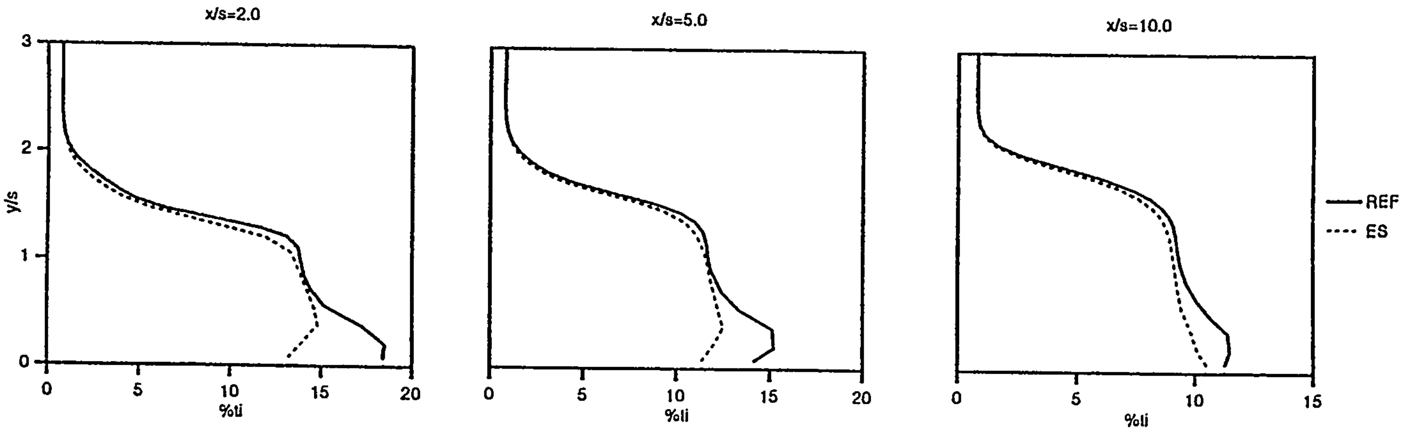

Figure 17. Turbulence Intensity Profiles at x/s=2, 5, and 10 (REF vs. ES) Show The Elimination of Turbulence Generated at the Downstream Slot Exit by Exit Shaping.

P19

Steam as Turbine Blade Coolant: Experimental Data Generation

Bernd Wilmsen (e-mail: wilmsenb@egr.msu.edu; pho.: 517-432 1102)
Abraham Engeda (e-mail: engeda@me.msu.edu; pho.: 517-432 1834)
John R. Lloyd (e-mail: lloyd@me.msu.edu; pho.: 517-355 9717)
A231 Engineering Building
Mechanical Engineering Department
Michigan State University
East Lansing, MI 48823

Abstract

Steam as a coolant is a possible option to cool blades in high temperature gas turbines. However, to quantify steam as a coolant, there exists practically no experimental data. This work deals with an attempt to generate such data and with the design of an experimental setup used for the purpose. Initially, in order to guide the direction of experiments, a preliminary theoretical and empirical prediction of the expected experimental data is performed and is presented here. This initial analysis also compares the coolant properties of steam and air.

Nomenclature

c_p	Avg. specific heat at const. press.
C, l, m, n, o	Condition dependent constants
D_i	Inside tube diameter
h	Avg. convective heat trans. coeff.
k	Avg. conductivity of fluid in tube
L	Length of tube
Nu	Nusselt Number
Pr	Prandtl Number
Re	Reynolds Number
T_b	Avg. bulk temperature of fluid
T_f	Avg. film temperature
v	Avg. velocity of fluid
ρ	Avg. density of fluid
μ	Avg. absolute fluid viscosity

Introduction

Maximizing power output from gas turbines requires engine operation at the highest possible temperature. However, the material limitations of the first turbine stages limit operating temperature: either strength deteriorates markedly at elevated temperatures or the material approaches its melting temperature. To allow for higher operating temperatures in gas turbines, under current know-how, blade cooling is the obvious solution.

Several methods, with differing merits, have been developed over the years to keep turbine blade temperatures below critical levels. In all cases, the main objective in turbine blade cooling has been to achieve maximum heat transfer coefficients while minimizing the coolant flow rate.

Even though steam as a thermodynamic working fluid is a common occurrence in the superheaters of steam power plants, general heat transfer data related to steam is not available. In particular there is a great lack of information on:

- The effect of steam flow passage geometry on the heat transfer and pressure drop, both for laminar and turbulent flows.
- Experimental data related to wall heat transfer and friction characteristics for fully developed turbulent steam flow.

Research sponsored by the U.S. DOE's METC, under Contract # 94-01-SR026 & 95-01-SR040 with Michigan State University

- Any work based on steam flow that studied, pumping work, and heat transfer coefficients, both with constant heat flux and constant surface temperature conditions.

The experimental set up

A compact stand alone steam unit with a controllable and measurable steam source has been developed as shown in figure 1 and 2.

As opposed to a real cooling situation where the 'coolant-steam' is heated by the turbine flow air, the heat transfer in this work is in the reverse direction where the air is heated by the steam.

The steam unit consists of a Chromalox 10KW steam generator followed by a superheater. The steam leaves the superheater and enters the test section. The steam entering the test section will have enough superheat to remain superheated as it leaves the test section for each test condition. Finally the steam is condensed and rejected.

The controllable superheater adds heat the steam. The associated instrumentation will measure the electrical input and steam mass flow in addition to all thermal properties of the steam, both in the radial and axial direction. The conduit inside wall temperature will also be measured.

The air loop is driven by a 15 KW FUGI Blower. The air loop is an open loop with flow control and flow measurements at the suction side. The pressure side is connected to the test section where the air exchanges heat with the steam.

A blade being cooled acts basically as a heat exchanger. The design and analysis of any heat exchanger requires a knowledge of the heat transfer coefficient between the wall of the conduit and the fluid flowing inside it. The sizes of the heat exchanger depend largely on the heat transfer coefficient between the inner surface of the tubes and the fluid. Once the heat transfer coefficient for a given geometry and specified flow condition is known, the rate of heat transfer at the prevailing temperature difference can be calculated. Also to determine the area required to transfer heat at a specified rate for a given temperature difference potential, the fluid temperature, which varies along the conduit and at any cross section, must be defined with care and precision.

Thermodynamic Design of the Steam Unit

The thermodynamic design of the steam and air flow cycles was carried out on an EXCEL spread sheet, which allowed instant component sizing and overall optimization. The design sheet used is summarized in Table I.

Major measured quantities

- temperatures
  - T_u, free stream air temperature
  - Tw, air side wall temperature
  - $T_{st,\ i\text{-}o}$, temperature of steam in and out
- pressures
  - $p_{surf.}$, st. pressure distrib. of test surface
  - $p_{st,\ i\text{-}o}$, steam pressure, in and out
- free stream air velocity, u_u
- turbulence intensity before test section
- steam and air flow rates

Major derived quantities

- h_a, heat transfer coeff. of air, local and avg.
- h_{st}, heat tran. coeff. of steam, local and avg.
- turbulence intensity of the air
- Re_a, the Reynolds number of air
- Re_{st}, the Reynolds number of steam
- temperature ratio
- M_a, the air Mach number
- q, heat flux from steam
- Δh_{st}, enthalpy fall of steam

Expected Results

First a simple tube geometry and next a simplified blade, both shown in figure 3 will be experimentally investigated.

Based on the works of Dittus-Boelter, Sieder-Tate, Kays-London, Petukhov-Popov, and Sleicher-Rouse extensive data and correlation for turbulent gas and liquid flow through tubes and ducts have been presented through the years. The correlation for the heat transfer, resulting from these works, takes the general form:

$$\frac{h\,D_i}{k} = C\left[\frac{\rho v D_i}{\mu}\right]^{l}\left[\frac{c_p \mu}{k}\right]^{m}\left[\frac{\mu_b}{\mu_f}\right]^{n}\left[\frac{D_i}{L}\right]^{o} \qquad (1)$$

The number of parameters have been shown to be reduced by introducing the following dimensionless numbers:

- Reynolds number (Re):

$$Re = \frac{\rho v D_i}{\mu} \qquad (2)$$

- Prandtl number (Pr):

$$Pr = \frac{c_p \mu}{k} \qquad (3)$$

- Nusselt number (Nu):

$$Nu = \frac{h\,D_i}{k} \qquad (4)$$

Equation 1 can then be expressed as

$$Nu = C[Re]^{l}[Pr]^{m}\left[\frac{\mu_b}{\mu_f}\right]^{n}\left[\frac{D_i}{L}\right]^{o} \qquad (5)$$

Colburn /1/ showed that the influence of the pipe length on the Nusselt number is negligible if the Reynolds number is larger than $5X10^3$. The Reynolds number in the present test section are expected to be higher than $1X10^4$ in all test cases.

The temperature difference between the pipe surface and pipe center may lead to variable fluid properties. This influence will be accounted for by the relationship between bulk dynamic viscosity and wall dynamic viscosity.

Properties of steam

The Reynolds and Prandtl numbers are calculated with averaged properties. In figure 4, the Prandtl number for various pressures is shown. The properties for steam are calculated using the 1967 IFC relationships for industrial use. Figure 5 shows, that for a given mass flow, steam can transport nearly twice the energy that air can. The density of steam is lower than the density of air, but despite that, steam can transport more energy per unit volume than air as can be seen in figure 6.

Calculation of Heat transfer

The Nusselt number has been calculated with equation (5) using the following constant values:

$C = 0.027$
$l = 0.8$
$m = 1/3$
$n = 0.14$

These constant values were suggested by Colburn /1/ and Sieder and Tate /2/ for flow conditions similar to the present planned test. The Nusselt number and the heat transfer coefficient have been calculated based on:

Pipe inner Diameter:	[1/2] inch
Test section length:	12.7 cm
Inlet pressure:	5 bar
Mass flow:	0.0035 kg/s
Inner wall temperature:	900 K for heating 300 K for cooling

For cooled steam, the Nusselt number is larger than for heated steam because of the smaller boundary layer. This is a result of the lower dynamic viscosity at lower temperatures. The same effect is visible for air. In figure 7, it is shown that the Nusselt number for steam is larger than for air at the same mass flow and the same thermodynamic conditions. The heat transfer in figure 8 shows the same trend.

Reynolds Number

In figure 9, it can be seen that the Reynolds number for steam flow is larger than for air flow. This means, the loss coefficient is lower in steam flow than in air flow.

The influence of the mass flow on the heat transfer coefficient can be seen in figure 10. The heat transfer coefficient increases nearly linearly with the mass flow. The slope of the curve for steam is much higher than air.

Conclusions

A preliminary simple theoretical evaluation has been performed, to test the coolant potential of steam and to seek justification for the planned experiments. The results confirm that the experimental data are essential and will be applicable and useful for actual blade cooling design.

References

[1] Colburn, A.P.. Engg. Bull. Purdue University, Vol. 26, No. 1 (Engineering Experiment Station, Res. Series No. 84); January 1942

[2] Sieder, E.N., and Tate G.E., Ind. Engg. Chem. 28, 1429; 1936

Part One: Steam Cycle			
Inlet conditions:			
Operating pressure [Pa]:	5.00E+05	Inl. temperature [K]:	313.00
Inlet enthalpy [kJ/kg]:	167.60		
Exit steam generator:			
hg [kJ/kg]:	2747.54	Enthalpy difference[kJ/kg]:	2579.94
Exit temperature [K]:	425.00		
Power steam generator [kW]:	9.00	max. Massflow [kg/s]:	0.00348845
Exit superheater:			
Steam temperature [K]:	773.00	Steam enthalpy [kJ/kg]:	3483.77
Enthapie difference [kJ/kg]:	736.23	Power superheater [kW]:	2.57
Test section:			
Pipe diameter [m]:	0.01270	Cross section [m2]:	0.00012668
Steam density [kg/m^3]:	1.407	Steam abs. viscosity [Pa s]:	2.86E-05
Avg. Velocity [m/s]:	19.572	Avg. Reynolds number:	12237.07
Part Two: Air Cycle			
Inlet conditions:			
Surrounding pressure [Pa]:	1.01E+05	Surrounding temperature [K]:	298.00
Exit blower:			
Exit total pressure [Pa]:	1.11E+05	Volume flow [m^3/s]:	0.24072
Exit total temperature [K]:	308.00		
Power blower [kW]:	15.00	max. Massflow [kg/s]:	0.28511723
Test section:			
Heigth [m]:	0.1143	Width [m]:	0.1143
Crossection [m2]:	1.16E-02		
Air density [kg/m^3]:	1.244	Air abs. viscosity [Pa s]:	1.90E-05
Avg. Velocity [m/s]:	19.730	Avg. Reynolds number:	16411
static pressure [Pa]:	1.10E+05	Machnumber:	0.06

Table I : Thermodynamic design of the Steam Unit

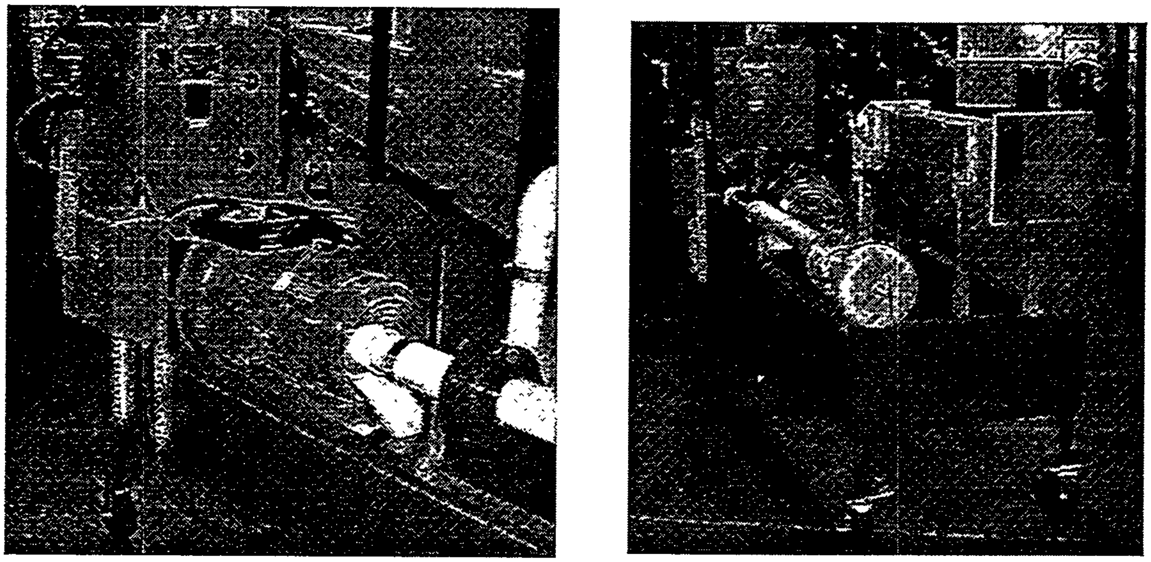

Figure 1: The Stand Alone Steam Unit

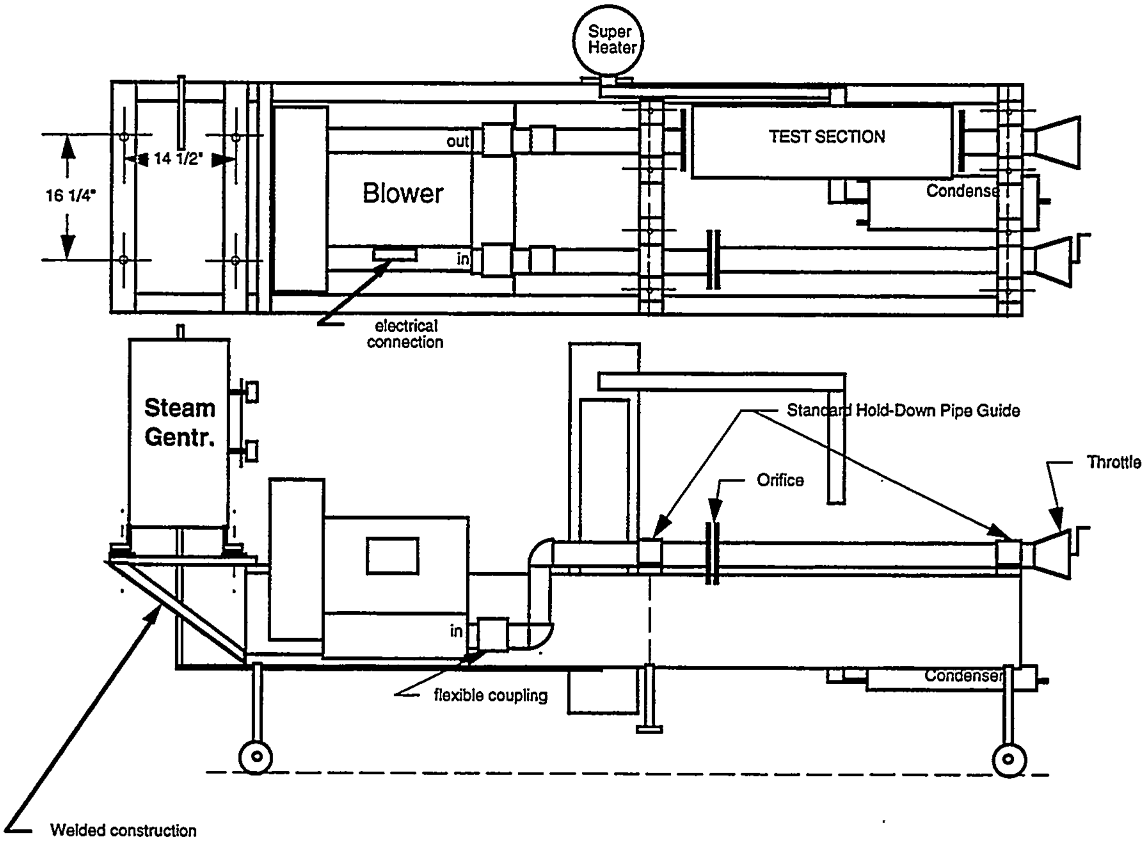

Figure 2.: The Stand Alone Steam Unit

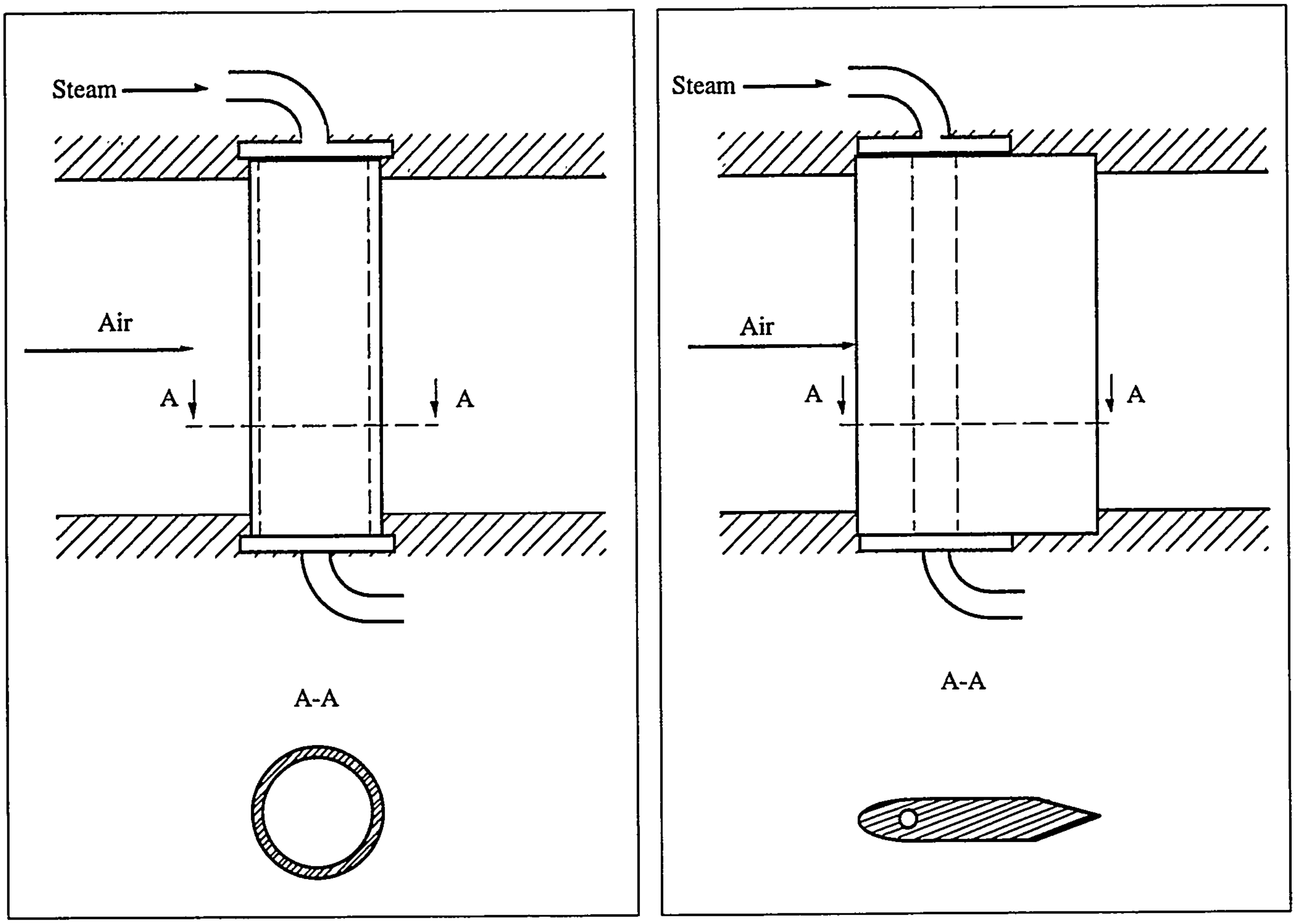

Figure 3 : Schematic representation of two blades to be investigated

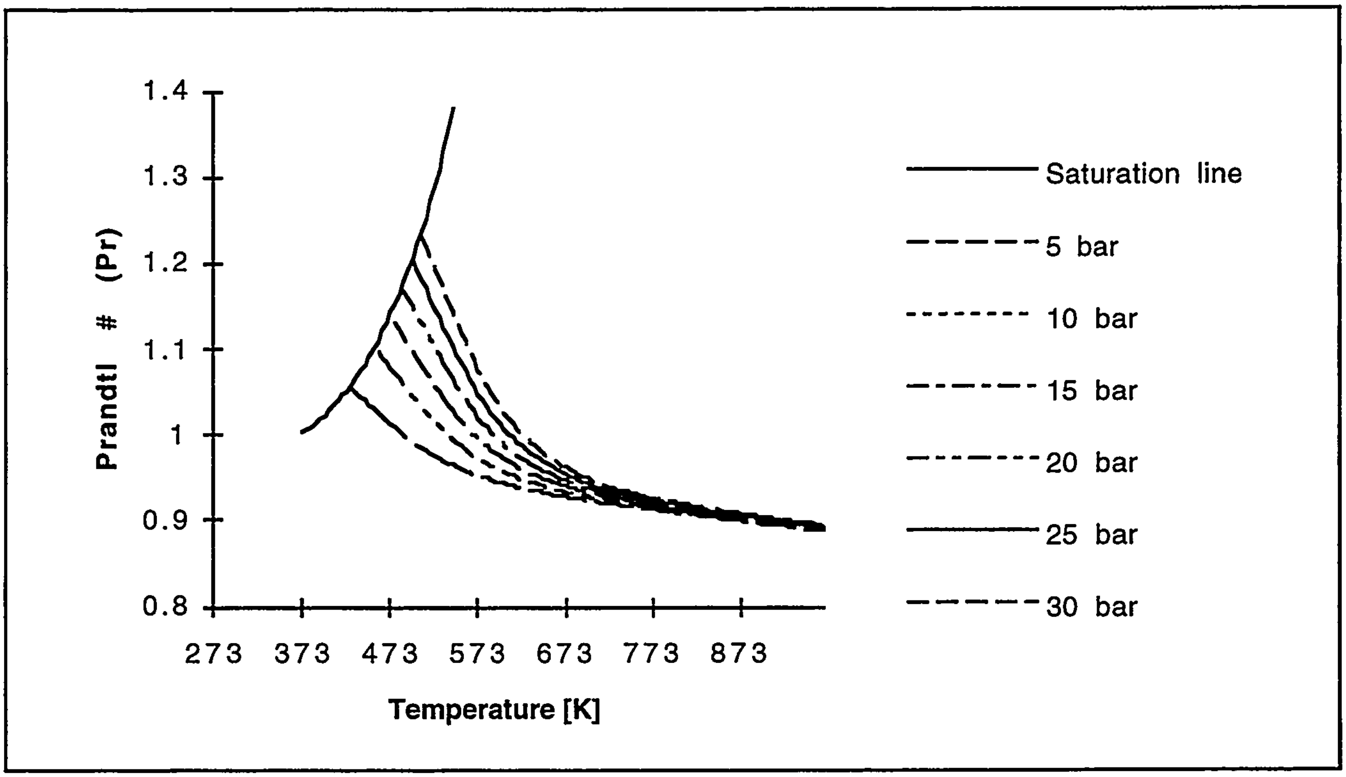

Figure 4 : Prandtl # vs. Temperature for steam

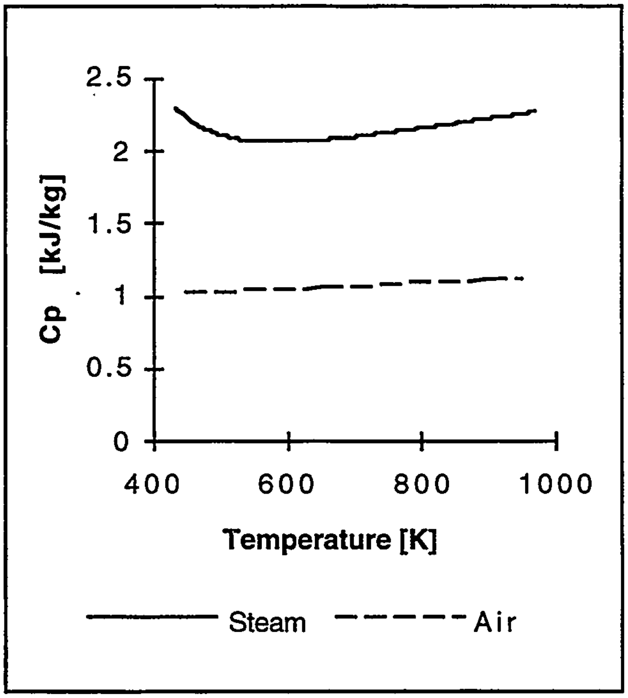

Figure 5 : Cp vs. Temperature

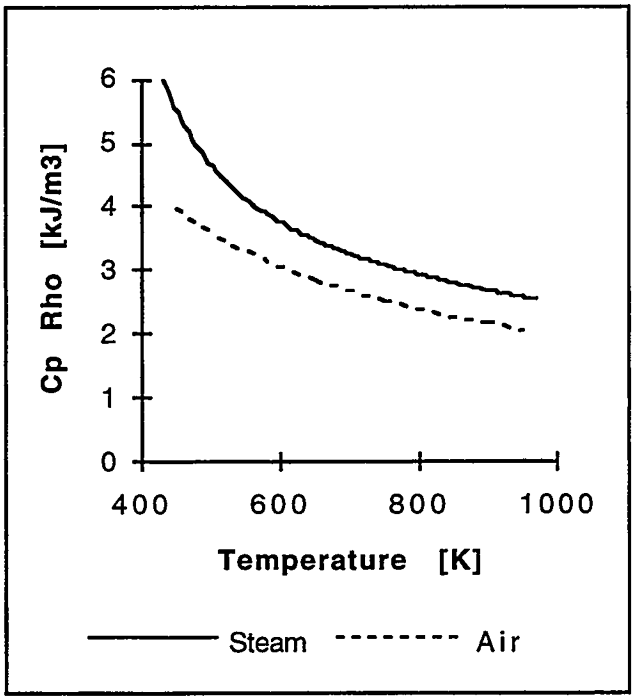

Figure 6 : Cp ρ vs. Temperature

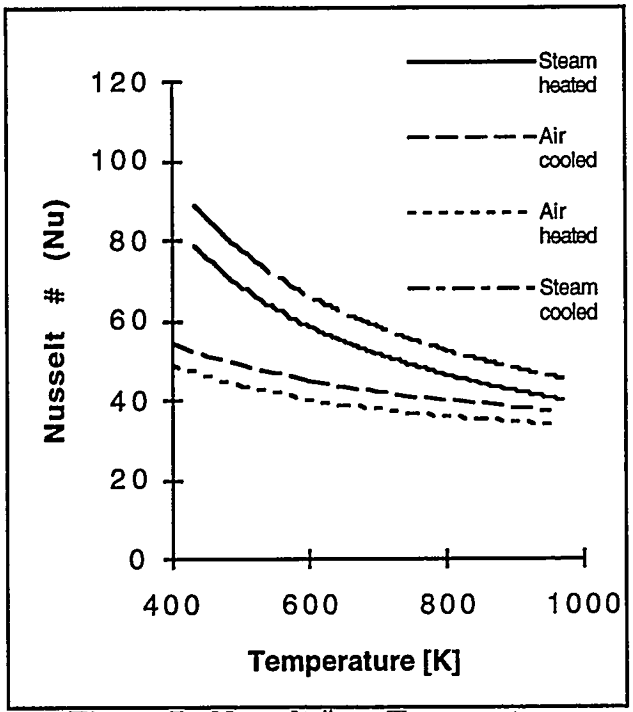

Figure 7 : Nusselt # vs. Temperature

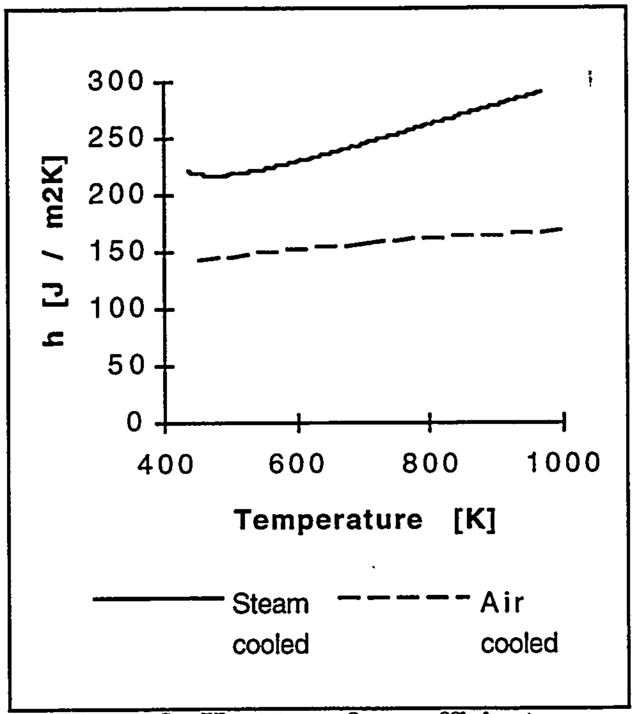

Figure 8 : Heat transfer coefficient vs. Temperature

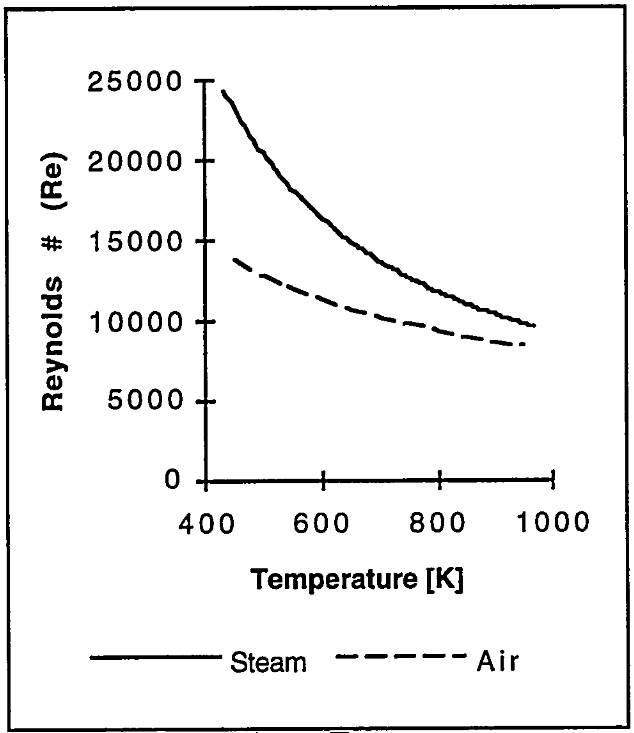

Figure 9 : Reynolds vs. Temperature

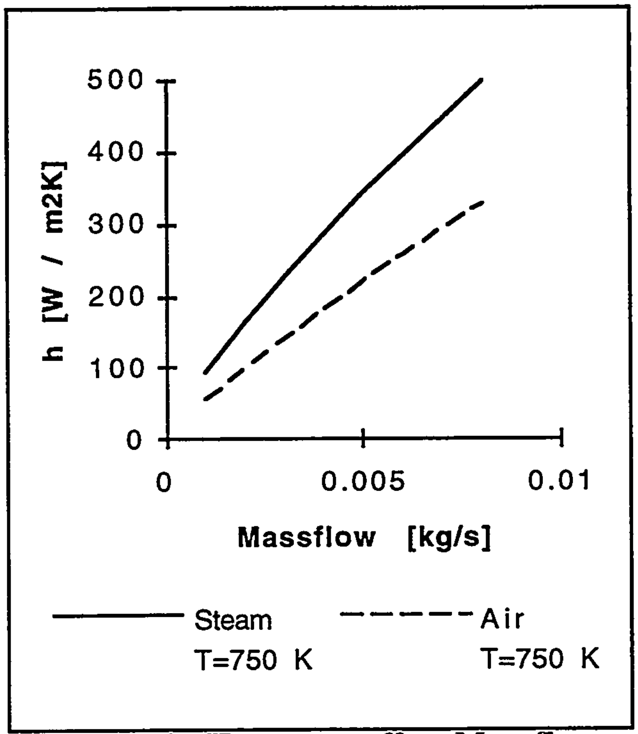

Figure 10 : Heat tra. coeff. vs Mass flow

P20 Combustion Chemical Vapor Desposited Coatings for Thermal Barrier Coating Systems

Janet M. Hampikian (janet.hampikian@mse.gatech.edu; 404-894-2845)
William B. Carter (brent.carter@mse.gatech.edu; 404-894-6762)
School of Materials Science and Engineering
Georgia Institute of Technology
Atlanta, GA 30332-0245

Introduction

The new deposition process, combustion chemical vapor deposition, shows a great deal of promise in the area of thermal barrier coating systems.[1] This technique produces dense, adherent coatings, and does not require a reaction chamber.[2] Coatings can therefore be applied in the open atmosphere. The process is potentially suitable for producing high quality CVD coatings for use as interlayers between the bond coat and thermal barrier coating, and/or as overlayers, on top of thermal barrier coatings.

Objectives

There were two principal objectives: first, to make depositions at reproducible temperatures below 1850°F (~1000°C), so as to form high quality coatings without compromising the final heat treatment of the substrate alloy. Second, to explore the deposition parameters of alumina and ceria coatings, and to begin the evaluation of the high temperature performance of these coatings.

Approach

The approach taken to achieve reproducible temperatures during deposition was to design and fabricate a holder which also serves as a heat reservoir. The holder assembly is depicted in Figure 1, and consists of a water-cooled copper sample holder which may be adjusted to achieve various degrees of cooling. Two thermocouples are employed during deposition, one which is pressed against the upper surface of the sample, and one which is beneath the sample, in the holder assembly, see Figure 1.

A novel approach was taken to the objective of minimizing deposition temperature. This was to employ a newly invented nozzle assembly, termed the oscillating capillary nebulizer (OCN), which was developed by Wang for sample introduction for ICP-AES and ICP-MS.[3] The OCN allows control over the droplet size distribution produced. This approach is predicated on the hypothesis that droplet size is critical in forming high quality coatings. This was based on the observation that when using a simple perfume sprayer type nebulizer, higher deposition temperatures usually produce dense, adherent coatings whereas lower deposition temperatures often produce powdery deposits when the solution

---

Research sponsored by the U.S. Department of Energy's Morgantown Energy Technology Center, under contract DE-FC21-92MC29061 with the South Carolina Energy Research and Development Center, Clemson University, 386-2 College Avenue, Clemson, SC 29634-5180.

concentration and other deposition parameters are left unchanged.

Alumina and ceria deposition conditions were explored through systematic variation of temperature, solvent, solute, oxidant and sample placement. Coatings were assessed through a variety of experimental techniques which included scanning electron microscopy (SEM), x-ray diffraction (XRD), transmission electron microscopy (TEM), optical microscopy and others.

Results

Deposition Temperature Minimization

For the liquid fuel combustion chemical vapor deposition of CeO_2, it was found that a smaller droplet size distribution allowed the deposition of higher quality coatings at lower temperatures than did a large droplet size distribution. Different droplet size distributions are obtained with the OCN, which consists of two concentric silica capillary tubes. Liquid is fed through the inner capillary and oxidizing gas through the outer capillary. By varying the diameters of the inner and outer capillaries, the pressure of the oxidizer, and the liquid feed rate, the droplet size distributions can be varied.

Various easily obtained configurations of the OCN were characterized with the use of toluene and oxygen. Droplet size determinations were made with laser light scattering. The Sauter mean diameter of the aerosols varied from 2.3 μm to 25 μm. Since the volume of a droplet goes as the third power of its diameter, average droplet volumes can be varied over a large range. In addition to allowing a degree of control over the droplet size distribution, the OCN produces a narrower droplet size distribution than does the simple pneumatic (perfume sprayer type) nebulizer used for depositing alumina. Figure 2 displays the results of the aerosol size determinations for two sets of capillary configurations and flow parameters.

Ceria and Alumina Coatings

Ceria (CeO_2) deposition conditions were explored on alumina substrates, using cerium 2-ethylhexanoate dissolved in toluene at 0.001 M concentration. Oxygen was used as the oxidizer. Figure 3 displays SEM micrographs of CeO_2 coatings deposited with different OCN configurations and flow rates. The coating shown in the top micrograph was produced with a larger size aerosol and higher temperature than the coating shown in the bottom micrograph (11 μm Sauter mean diameter vs. 2.3 μm, 1,250-1,300°C vs. 1,100-1,150°C). The coating produced with the larger size aerosol is powdery and non-adherent. The coating produced with the smaller size aerosol is dense, nodular, and adherent. This finding shows that through use of the OCN, droplet size can be reduced which results in high quality coatings at lower temperatures possible than can be obtained with the standard nebulizer.

Alumina coatings were deposited using a simple perfume sprayer type pneumatic nebulizer. Flat specimens of Ni-20 wt% Cr were rotated in the flame and thereby coated on both sides with alumina. Pertinent deposition parameters are listed in Table 1.

Bright and dark field TEM micrographs taken from abraded coating supported on a carbon film indicate that the coating is Θ-alumina with a grain size of 10 - 20 nm, see Figure 4. The inset diffraction pattern shows the diffracted beams which were selected to

Table 1. Alumina Deposition Parameters

Solvent	Ethanol
Reagent	Aluminum Acetylacetonate
Solution Concentration	0.00135 M
Solution Flow Rate	4 ml/min
Oxidizer	Oxygen
Oxidizer Flow Rate	3 l/min
Temperature*	850 ± 25°C
Substrate Rotation Rate	4 RPM
Deposition Time	40 min

* Measured with a thermocouple in the vicinity of the substrate surface.

form the dark field image. EDS analysis of the coating showed the presence of Al and O. The presence of aluminum and oxygen in the coating was confirmed by x-ray photoelectron spectroscopy (XPS).

A control sample was oxidized in a pure ethanol flame under similar conditions to those that were coated. Coated samples visually appear to be less oxidized in comparison with the control sample. This is confirmed by mass change measurements of the samples before and after coating. Coated samples show a mass change/area which is less than half that exhibited by flame treated samples. Thus, protection of the substrate metal from oxidation occurs during the deposition process.

Isothermal oxidation tests were performed for 48 hours on the alumina coatings using thermogravimetric analysis (TGA) in high purity air at three temperatures: 900, 1,000 and 1,100°C. Figure 5 displays the TGA results for an alumina coated and an uncoated substrate oxidized at 900°C. Results at 1,000 and 1,100°C were qualitatively similar. The coating results in a significant decrease in the weight gained at short times compared with non-coated specimens. For the uncoated sample, this initial rapid weight gain is due to the oxidation of Ni which commences at the onset of oxidation and proceeds until a continuous protective layer of Cr_2O_3 is formed adjacent to the metal.

The observed decrease in the transient stage of oxidation from the alumina coatings was accompanied by a significant decrease in the parabolic oxidation constant, K_p, measured between 20 and 40 hours of oxidation. Figure 6 displays K_p as a function of $1/T$ for coated and uncoated samples. At 1,000°C, the alumina coating resulted in an 80% reduction of the long-time parabolic rate constant.

Figure 7 displays SEM micrographs at low and higher magnifications of an uncoated sample after oxidation at 1,000°C for 48 hours. EDS analysis indicates a strong Ni signal from the uncoated sample, confirming that the oxide formed on the substrate is predominantly NiO. An alumina-coated sample, oxidized under the same conditions displays a different morphology, see Figure 8. The small protrusions yield a strong Ni signal, while the material in between the protrusions is rich in Cr. Thus, the alumina coating decreased the amount of surface NiO formed, consistent with the kinetic observations.

Summary and Future Activities

The ability to produce higher quality coatings at lower temperatures is a distinct advantage of the OCN over the simpler type nebulizer. This ability will enable deposition temperature to be kept low. Alumina coatings have been shown to decrease the isothermal kinetic oxidation response of a prototype alloy, Ni-20Cr, and to provide protection during the oxidizing conditions of the deposition process itself. The next phase of research for ceria and alumina coatings includes furnace cycle testing with ceria and alumina as interlayers and overlayers, in a thermal barrier coating system.

Acknowledgements

The authors would like to gratefully acknowledge the contributions made by M. Hendrick and G. Book. This research was performed at the Georgia Institute of Technology and was sponsored by the U.S. Department of Energy, Morgantown under cooperative Agreement DE-FC21-92MC29061 with the South Carolina Energy Research and Development Center, subcontract 94-01-SR027. The period of performance of the subcontract is 1 July 1994 - 30 June 1997. We would like to acknowledge the Advanced Gas Turbine Systems Research manager, Daniel B. Fant and the Morgantown Energy Technology Center Contracting Officer's Representative, Norman Holcomb.

References

1. W. B. Carter and J.M. Hampikian, "Combustion Chemical Vapor Deposited Coatings for Thermal Barrier Coating Systems," U.S. DOE Advanced Gas Turbine Systems Research Program Annual Review, Arlington, VA, Nov. 9-11, 1994.

2. A.T. Hunt, W.B. Carter and J.K. Cochran Jr., "Combustion Chemical Vapor Deposition: A Novel Thin Film Deposition Technique," Applied Physics Letters, **63** (2) (1993), 266-268.

3. L. Wang, Ph.D. Dissertation, School of Chemistry and Biochemistry, Georgia Institute of Technology, 1995.

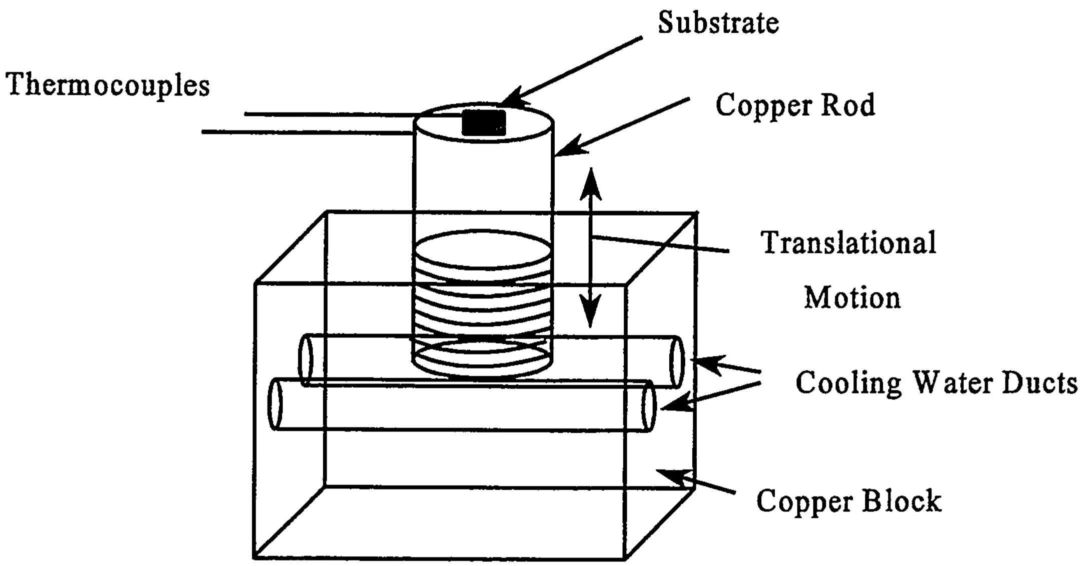

Figure 1 - Schematic of Sample Holder Used to Control Substrate Temperature.

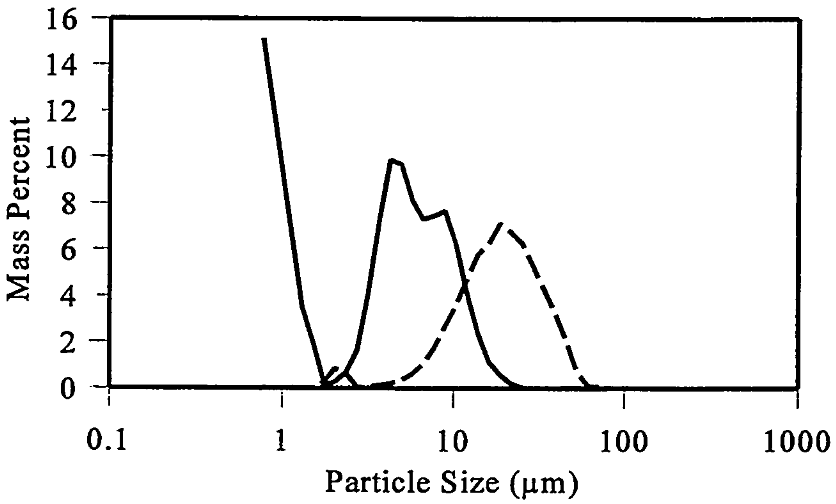

Figure 2 - Results of Aerosol Size Distribution Determination for Two OCN Configurations Producing Sauter Mean Diameters of 2.3 μm (Solid) and 11 μm (Dashed). Small Size Solid Tail Is an Artifact.

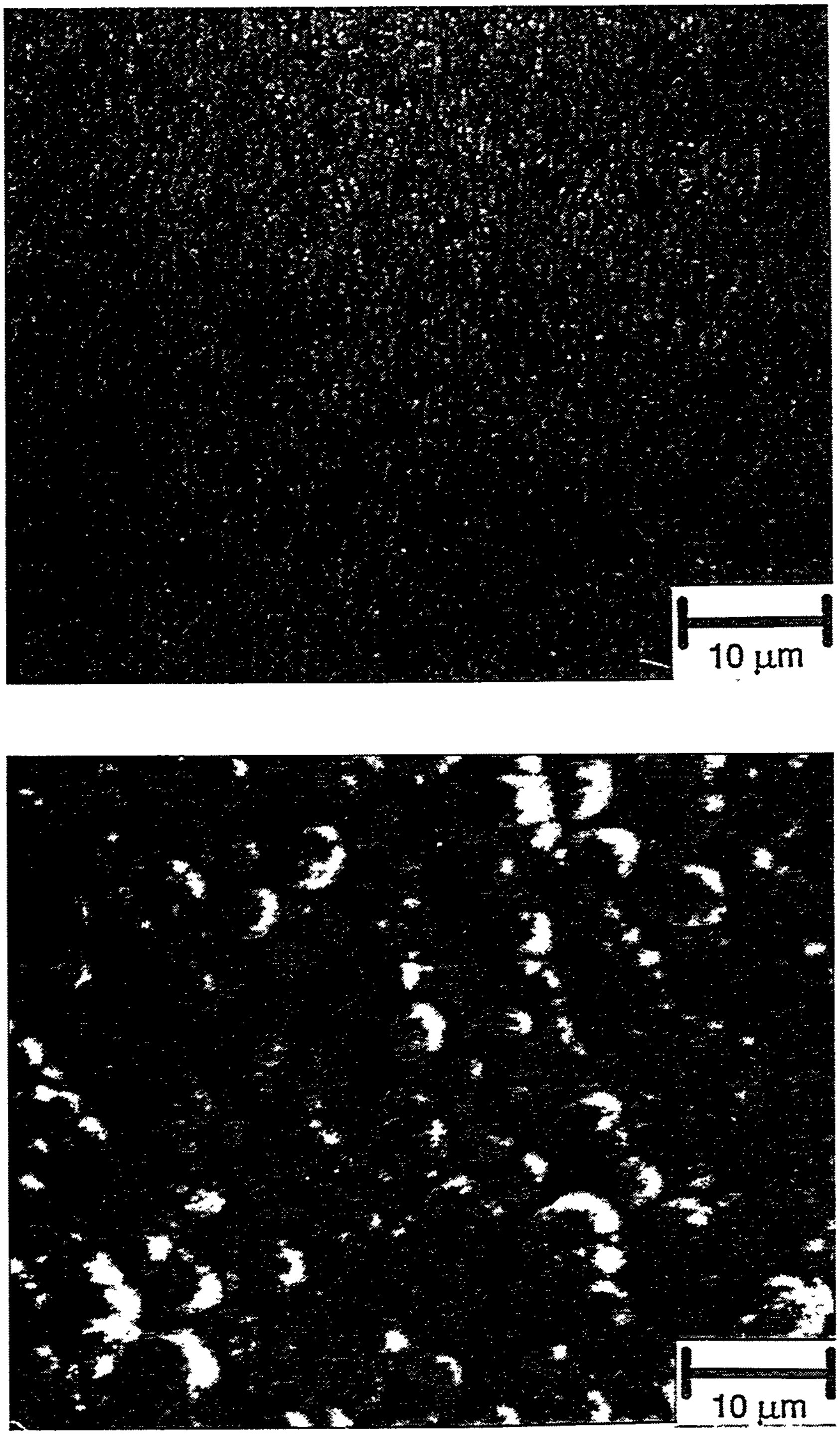

Figure 3 - SEM Micrographs of CeO$_2$ Coatings Deposited on Alumina Substrates with Different OCN Configurations and Flow Rates Using Ce 2-ethylhexanoate Precursor in Toluene at 0.001 M Concentration. Top: 11 um Aerosol Sauter Mean Diameter. Bottom: 2.3 um Aerosol Sauter Mean Diameter.

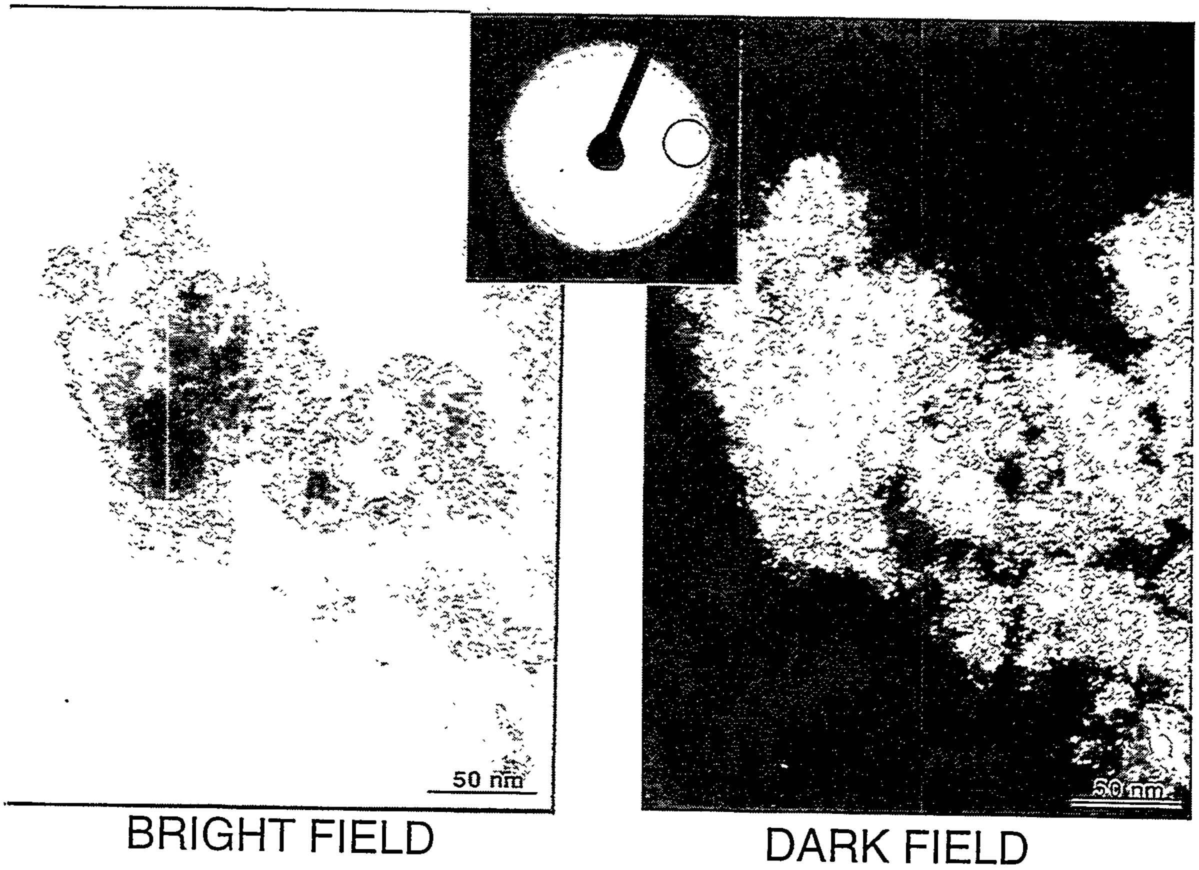

Figure 4 - Bright and Dark Field Transmission Electron Micrographs of Θ-alumina Coating with Inset Diffraction Pattern. Sample Prepared by Abrading Coating onto a Carbon Support Film.

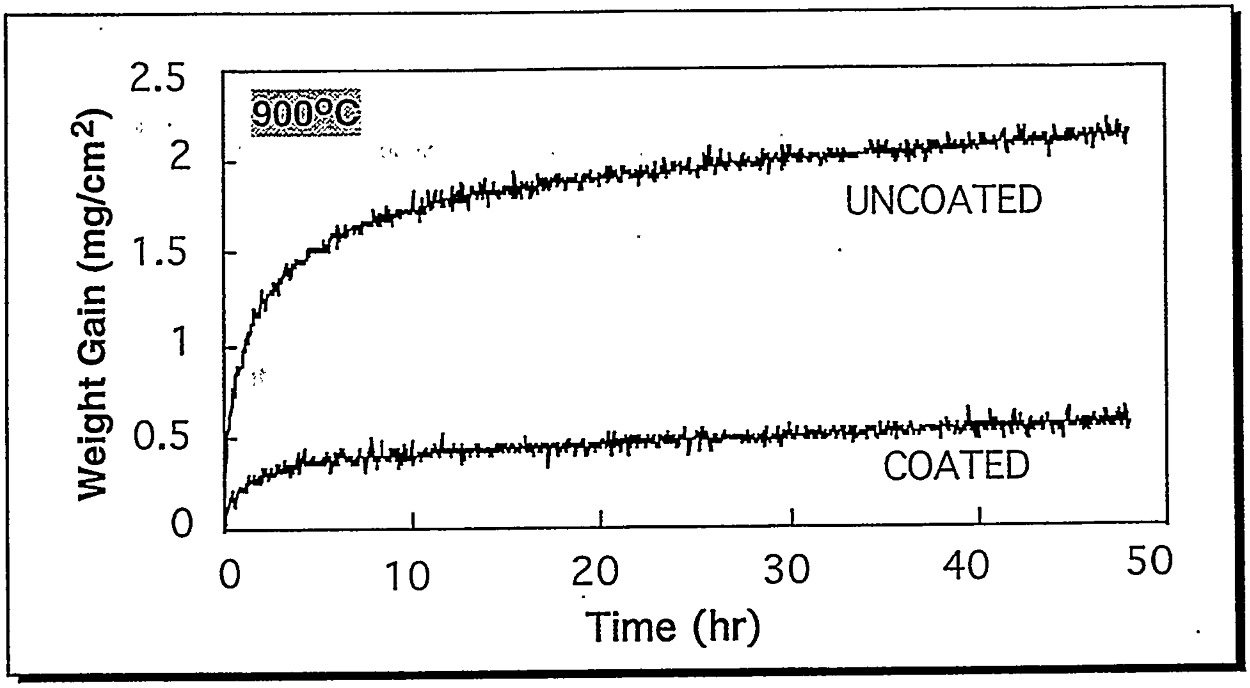

Figure 5 - TGA Results for Uncoated and Alumina Coated Substrates Isothermally Oxidized in High Purity Air at 900°C.

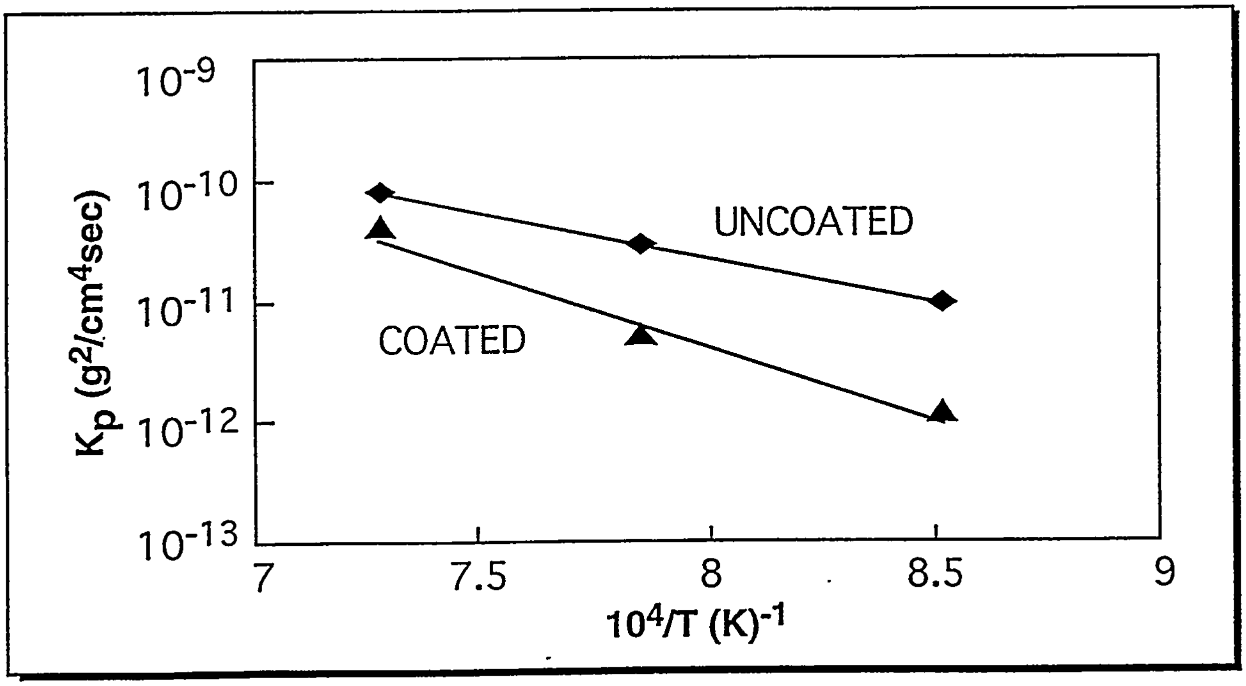

Figure 6 - Long-time Parabolic Rate Constant, K_p, as a Function of 1/T for Coated and Uncoated Samples.

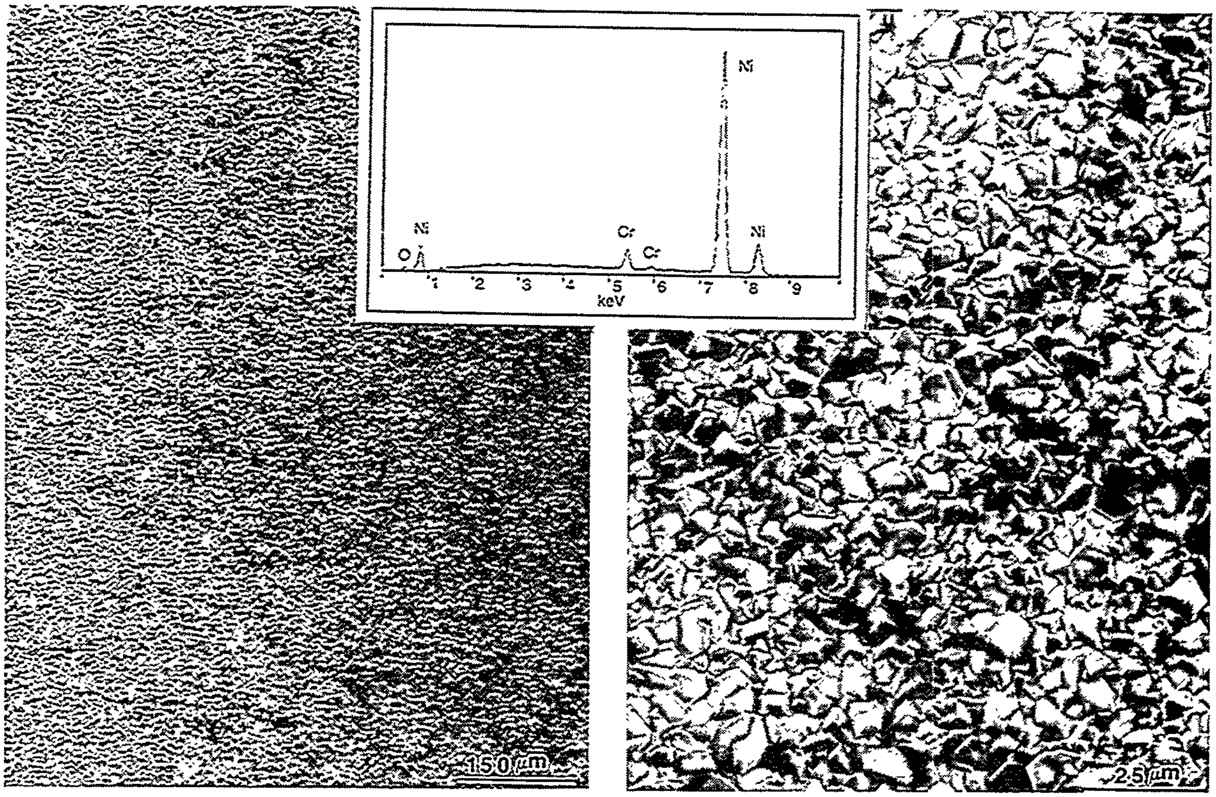

Figure 7 - SEM Micrographs at Two Magnifications of Uncoated Ni-20Cr Sample After Exposure to High Purity Air at 1,000°C for 48 Hours. EDS Indicates that the Surface Oxide is Predominantly NiO.

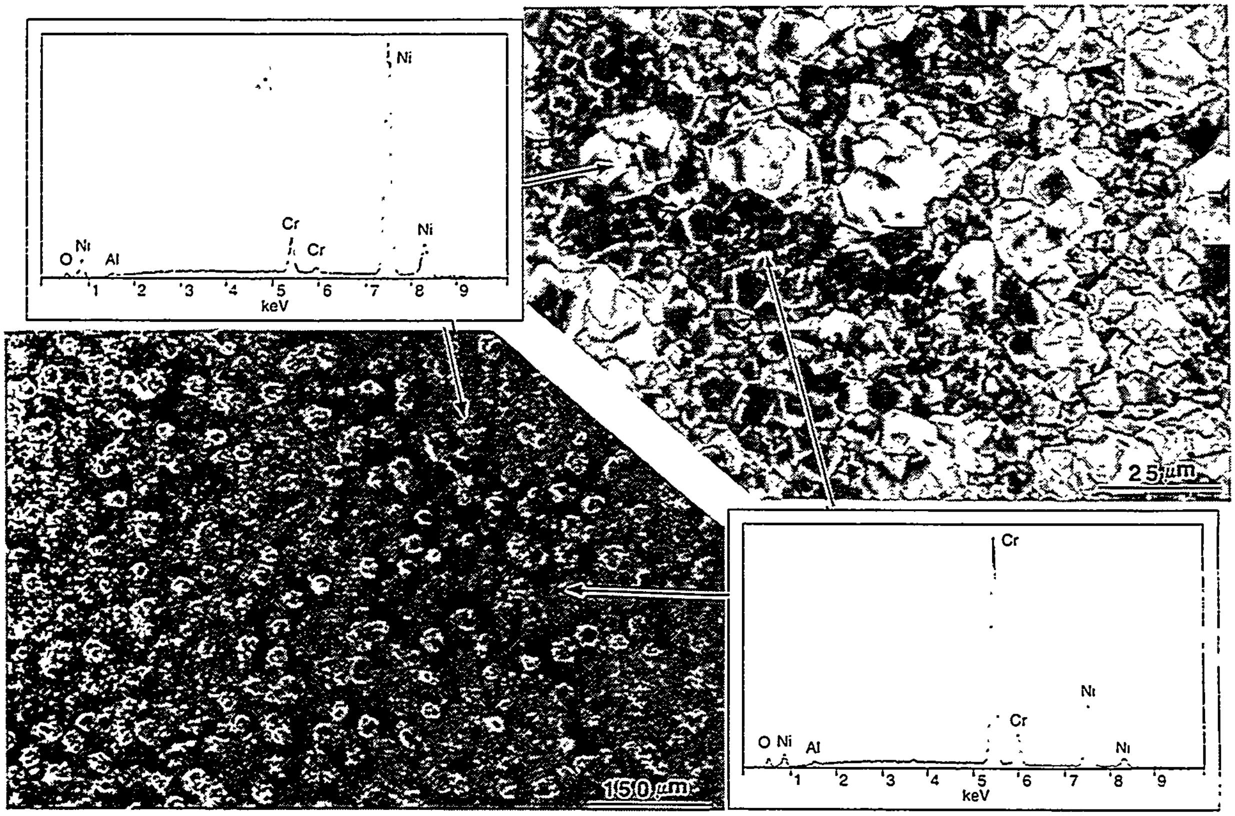

Figure 8 - SEM Micrographs at Two Magnifications of Alumina-coated Ni-20Cr Sample After Exposure to High Purity Air at 1,000°C for 48 Hours. EDS Indicates Surface Protrusions Predominantly NiO; Other Areas are Rich in Cr Signal.

P21

Premixed Burner Experiments: Geometry, Mixing, and Flame Structure Issues

Ashwani K. Gupta (akgupta@eng.umd.edu; 301-405-5276)
Mark J. Lewis (lewis@eng.umd.edu; 301-405-1133)
Maneesh Gupta (mgupta1@eng.umd.edu; 301-405-1151)
University of Maryland
Department of Mechanical Engineering
College Park, MD 20742

Adeboyejo A. Oni (oni@bach.eng.morgan.edu; 410-319-3106)
Qua Brown (qbrown@eng.morgan.edu; 410-319-3249)
Morgan State University
School of Engineering
Baltimore, MD 21239

Abstract

This research program is exploring techniques for improved fuel-air mixing, with the aim of achieving combustor operations up to stoichiometric conditions with minimal NO_X and maximum efficiency. The experimental studies involve the use of a double-concentric natural gas burner that is operable in either premixed or non-premixed modes, and the system allows systematic variation of equivalence ratio, swirl strength shear length region and flow momentum in each annulus.

Flame structures formed with various combinations of swirl strengths, flow throughput and equivalence ratios in premixed mode show the significant impact of swirl flow distribution on flame structure emanating from the mixedness. This impact on flame structure is expected to have a pronounced effect on the heat release rate and the emission of NO_X. Thus, swirler design and configuration remains a key factor in the quest for completely optimized combustion.

Parallel numerical studies of the flow and combustion phenomena were carried out, using the RSM and the k-ε turbulence models. These results have not only indicated the strengths and limitations of CFD in performance and pollutants emission predictions, but have provided guidelines on the size and strength of the recirculation produced and the spatio-temporal structure of the combustion flowfield.

The first stage of parametric studies on geometry and operational parameters at Morgan State University have culminated in the completion of a one-dimensional flow code that is integrated with a solid, virtual model of the existing premixed burner. This coupling will provide the unique opportunity to study the impact of geometry on the flowfield and vice-versa, with particular emphasis on concurrent design optimization.

Introduction

Current worldwide emphasis on environmental pollution reduction has resulted in more stringent NO_X emission

---

Research sponsored by the U.S. Department of Energy's Morgantown Energy Technology Center, under contract 94-01-SR028, with the University of Maryland, College Park, MD, 20742. Fax: 301-314-9477 and Morgan State University, Baltimore, MD 21239. Fax: 410-319-3843.

standards for stationary gas turbine combustion systems in addition to aircraft gas turbines[1]. Lean premixed combustion is receiving wide acceptance since this approach provides the lowest NO_X for combustor operations at any equivalence ratio and power setting. In addition, lean premixed combustion of gaseous fuel provides the most promising technology for CO emission control.

The key in premixed combustion is that the mixture must be adequately mixed at the microscopic level. In addition, constraints that must be met by a realistic mixer include: (1) geometry of the premixer in the fuel preparation tube (i.e., must design for minimum size and pressure drop, in order to avoid back flow during transient operation); (2) efficient method of fuel injection and mixing with the air so that gas residence time exceeds fuel ignition delay time[2] for autoignition; and (3) flame stabilization device (i.e., swirlers) effects on thermal non-uniformity of the flowfield and associated instabilities.

In industrial combustors, the fuel may not burn completely, and may mix and react with the air injected into the primary zone. This situation can lead to the formation of a diffusion flame[3] between the incoming air and the excess fuel or between the excess air in lean zones and excess fuel in rich zones. In this case the temperature of the burned gases is sufficiently high to allow ignition of the mixture. In order to address the above issues, one must examine the isolated effects of each parameter so that the subsequent controlling parameters may be determined for optimal design of combustor operation.

This research program is aimed at developing an understanding of techniques for improved fuel-air mixing, with the aim of achieving combustor operations over a wide range of stoichiometry (up to the limit of stoichiometric conditions) with minimal NO_X and maximum efficiency.

The experimental studies involve the use of a double concentric burner which allows systematic variation of equivalence ratio, swirl strength and flow momentum in each annulus as well as variation of shear between the two annuli. The facility permits combustor operations in both non-premixed and premixed modes. This flexibility allows for the comparison of results obtained in our previous systematic studies on non-premixed flames.

Results have been obtained on the structure of flames formed with various combinations of swirl strengths, flow throughput and equivalence ratios. Specifically, the dynamics of flow field, mean and temporal thermal signature, gas species concentration, mixture fraction distribution and global flame behavior have been examined for the purpose of determining their effects on combustion efficiency and pollutants emission.

The results show that swirl and flow distribution have a significant effect on the size and shape of flames produced, which in turn have a pronounced effect on the heat release rate and the emission of pollutants. The flame structure is controlled, in part, by flow disturbances associated with the swirlers; once these disturbances propagate downstream of the swirler, results show that there is a circumferential non-uniformity of the flame, with attendant consequences on pollutant emissions. Thus, swirler design and configuration remains a key factor in the quest for the fully optimized premixed combustor.

Direct comparisons of the premixed flame data results with the non-premixed flame data showed the compactness of the premixed flames. Furthermore, the flame dimension provided an indication on the quality of mixing. Correlations of flame temperatures indicated a 30% reduction in peak temperatures with premixed flames in comparison to the non -premixed flames. Uniform and lower overall temperatures obtained in premixed flames reveal reduction in the thermal NO_X formation.

The first stage of parametric studies on geometry and operational parameters at Morgan State University have focused on the development and refinement of a one-dimensional flow code that is integrated with a solid, virtual model of the existing premixed burner experimental facility. This one - dimensional flow code development activity has been completed. Driving the geometric design process concurrently with this code will ultimately provide the capability to study the impact of geometry on the flowfield and vice-versa, with particular emphasis on concurrent design optimization whose objective function is tied closely to emissions abatement.

Experimental Studies

Description of the Burner

A schematic diagram of the experimental premixed burner and flow schematic is shown in Figure 1. Methane was used as the fuel. The facility permits various concentrations of fuel and air to be mixed and introduced into the central jet, annulus 1 and annulus 2. The fuel -air mixture ratio in each of these three annuli can thus be varied independently of each other. This provides the required operational flexibility. Before entering the annulus 1 and annulus 2 the incoming fuel-air mixtures are split into four streams. Flame arrestors made of sintered stainless steel (porous plates) are placed inside each jet of the burner. This prevents the pre-mixed flame from propagating upstream of the burner in addition to facilitating the mixing of the reactants. The swirlers create a angular momentum that enhances mixing and creates a stabilizing recirculation zone for the flame. Swirlers are provided for both outer annuli 1 and 2 . The shear layer length between annuli 1 and 2 are changed by using quartz tubes placed at downstream exit of the burner. This also provided optical access to within the flame, inside the burner.

No swirl is used in the central jet. Swirl of any desired strength can be introduced into annulus 1 and 2 by using a pre-fabricated swirler assembly. This allows for investigation with any combination on the radial distribution of swirl in the burner. Eighteen flat vanes made of sheet metal are used for each swirler. This large number of vanes increases the swirler efficiency. The annulus 1 swirler blades are shorter than the annulus 2 due to vane angle manufacturing constraints. Both swirlers are at the same height in the burner.

A traversing mechanism is used to obtain temperature measurements at different spatial locations in the flame. The experimental data presented here is for a premixed case having no swirl in central jet, a swirler vane angle of 30^o in annulus 1, and 55^o in annulus 2, and equivalence ratio of 0.6 in each annulus. Flow rates in annulus 1 and 2 were 11 and 22 scfm, respectively.

Experimental Diagnostics

Information on the global size and shape of the flames obtained with various input and operational parameters were obtained using direct photography. A narrow depth of field and short exposure times were used to obtain tomographic information on the structure of the flame at any desired cross-section of the flow field.

Flow visualization experiments provide information on global instantaneous flame structure. Submicron-sized particles of aluminum oxide were used to enhance the scattered light intensity signal. An averaging technique was used to determine the parameter profiles, which in turn characterizes the mean structure of the flow. Here, information on global turbulence fluctuation of the flow as well as the distribution of the fuel within the flow field was obtained using a laser sheet beam photographic technique.

A CCD camera coupled directly to a PC via an image grabber was used to record the scattered light signal from within the test section. This technique allows for the determination of time mean and standard deviation of fuel fraction distribution within the flow field. The necessary software required for this analysis was developed in our laboratory[4]. This flow visualization experiment provides semi-quantitative information on mixing and concentration of fuel fraction in the flow under both non-burning and burning conditions.

Mean and time-dependent temperature measurements were determined using a 50 μm wire diameter type R thermocouple (Pt-13% Rh). The size of the thermocouple was chosen based on considerations of frequency response, mechanical strength, sensitivity and survivability. This arrangement allows temperature measurement up to the melting point of the thermocouple (1768° C).

Time mean information on temperature was obtained using 300,000 samples over a sampling duration of 30 seconds. This provided a mean data repeatability of better than one percent. However, time-dependent temperature information requires corrections for the thermal inertia associated with the large-size bead thermocouple junction. This in turn requires determination of the time constant of the thermocouple under local prevailing conditions of temperature and flow velocity. This time constant determines the response time to high-frequency changes in the thermal environment. A specially designed electronic circuit was used to determine the time constant of the thermocouple.

In the experiments reported here, temporal and spatial information on the thermal signatures within the premixed flames were obtained to quantify the degree of mixing in flames. Specifically, rms temperature fluctuations, power spectral density, probability density distribution, autocorrelation coefficient, and time scales of microscopic and large-scale turbulence fluctuations were obtained in both premixed and non-premixed flames. The area under the power spectral density - frequency curve is a measure of the variance in the fluctuations of temperature.

The temperature probability density curves are a measure of how closely the temperature data is packed around the mean value. They also give information regarding the nature of the temperature distribution about the mean. The temperature correlation plots give an idea about the microscopic and integral time scales involved in the reaction process. Premixed data show relatively higher values of the microscopic time than the diffusion cases, in certain regions of the flame. This is indicative of large scale eddy mixing of the fuel - air mixtures.

Experimental Results

Global Flame Structure

Results shown in Figure 2(a-c) show significant effects of fuel-air mixture ratio as well as the distribution of reactants within the three annuli on the flame structure. All three flames were obtained with swirl angle in annulus 1 and annulus 2 of 45° and 55°, respectively.

The flame shown in Figure 2(a) was obtained at an equivalence ratio of 0.5 in all three jets. The flame shown in Figure 2(b) was obtained with an equivalence ratio of about 1.0 in all three jets. It is important to note the presence, at this stoichiometry, of large scale structures in the flame that are believed to be caused by the swirlers in the upstream locations of the flame.

Flame photographs shown in Figure 2(c) was obtained with an equivalence ratio of 1.23 in the central jet and 0.52 in annulus 1 and 0.71 in annulus 2. The structure of this flame reveals the presence of a large size central toroidal recirculation zone (in contrast to that obtained for Figures 2(a) and 2(b) despite the identical swirl strength distribution in the combustor. The physical structure of the flame shown in Figure 2(c) appears to be very similar to that obtained from a non-premixed burner in which the fuel is supplied via the central jet.

Temperature Data

Temperature data were obtained with the burner having swirl angle in annulus 1 and annulus 2 of 30° and 55°, respectively. Data were obtained at several spatial locations from within the flame reflecting the central recirculation zone, the shear layer region, outer edge of the flame and the post-flame region, at an equivalence ratio of 0.6, in all three annuli. Sample data are presented in Figure 3, corresponding to spatial locations of r=0; z=1.5, and Figure 4 corresponding to a spatial position of r=1.5; z=1.5.

The results show a gaussian-shaped probability density distribution for temperature measurements in the central region of the flame (see Figure 3). In contrast, a bimodal distribution was obtained for the measurements in the outer shear layer region (see Figure 4). It is important to note that at these two probe volume locations, significant differences have been observed in the integral and microscopic turbulence time scales, and standard deviation of temperature.

The flame behavior in the central core region appears to be dominated by the large scale structures, as evidenced by the large temperature auto-correlation microscopic time scales of about 7.7 ms (Figure 3), as compared to 2.1 ms shown in Figure 4 for the shear layer region.

The integral time scales at these two positions were found to be 130 ms and 2 ms, respectively. The characteristic power spectral density for the shear layer and central core region was found to be several hundred to several kilo- hertz frequency, respectively. This suggests that in the shear layer region, the fuel-air mixture is better-mixed, while in the central core region large scale structures prevail. In an attempt to examine the structure of the flame under non-premixed condition with the same swirl distribution, temperature data were obtained at r=1.5, z=1.5 (see Figure 5).

The non-premixed data, obtained with fuel in the central jet at an overall equivalence ratio of 0.5, shows significant skewness of the temperature probability distribution (see Figure 5). The temperature auto-correlation microscopic time scales as well as the integral time scales were found to be comparable to that of premixed flame (compare auto-correlation coefficients in Figure 4 with those in Figure 5).

Computational Studies

CFD Code and Turbulence Models

The CFD code being used is a general purpose program for modeling fluid flow, heat transfer and chemical reaction. The code can model a wide range of physical phenomena including :

1. 2D/3D geometries in Cartesian, cylindrical or general curvilinear coordinates
2. Turbulent combusting flows
3. Mixing and reaction of chemical species
4. Temperature- and composition - dependent fluid/material properties
5. Incorporation of velocity, heat transfer and non-axisymmetric boundary conditions.

These physical phenomena are modeled by solving the conservation equations for mass, momentum, energy and chemical species using a control volume based, finite difference method. The governing equations are discretized on a curvilinear grid to enable computations in complex, irregular geometries.

A non-staggered system is used for storage of discrete velocities and pressures. Interpolation is accomplished via a first order power law scheme, or optionally, via the higher order QUICK scheme. The equations are solved using the SIMPLEC algorithm with an iterative line-by-line matrix solver and multi-grid acceleration, or with a GMRES full field iterative solver. Numerical solution of turbulent flows without direct simulation requires appropriate modeling procedures to describe the effects of turbulent fluctuations of velocity and scalar quantities in the basic conservation equations. The code used here makes use of either the k-ε or the Reynolds Stress turbulence models.

The major limitations of the k-ε model is that υ_t is assumed to be isotropic. This implies that the velocity and length scales are the same in all the directions. In complex swirling flows velocity and length scales can vary significantly with direction. For such flows, the k-ε model is inadequate and can produce physically incorrect results.

The RSM model computes the individual Reynolds stresses by solving the transport equations for the individual stresses. These transport equations can be derived from the momentum equations and contain triple order velocity correlations and pressure velocity correlations that must be modeled to obtain closure. This involves the modeling of the stress production rate, pressure-strain correlation, and viscous dissipation amongst other parameters.

Performance Prediction

To compare the experimental and computational results, a base line non-premixed case was considered which allowed direct comparison of the experimental and computational profiles. The flames considered are given in Table 1. Case 1 was chosen due to the availability of comprehensive experimental data from our own laboratory.

As seen from the experimental temperature profiles in Figure 6 and the computational temperature profiles in Figure 7, qualitative agreement is obtained. The computational software overpredicts the temperatures throughout the domain by about 100 deg. A two-step reaction scheme and activation of the radiation model may further improve the computational results.

Case 2 is similar to case 1 except that case 2 is a premixed flame. Some of the observations that could be made from the results from case 1 and 2 are as follows:

1. Non-premixed flames (Fig. 8) provide stronger recirculation and lower maximum positive axial velocities near to the burner exit than the premixed flame (see Figures 8 and 9).
2. Azimuthal velocities were almost identical for the two cases
3. On an average, a temperature reduction of 30% is obtained over the entire flow field for the premixed case. The temperature profile for the premixed are more non-uniform at the burner exit
4. Temperature profiles exhibit a different behavior in the expansion zone of the burner for the premixed and non-premixed cases. The temperature profile for the premixed case shows bimodal distribution having distinct peaks away from the burner centerline and a trough at the centerline (see Fig. 10). The profiles develop into a monomod form at an axial station located approximately at z/D=0.27, where z is the axial distance measured from the control inlet jet.

The results obtained for the non -premixed case, case 1, have a monomodal appearance throughout the entire combustor length. The bimodal peaks are probably due to the premixed nature of the fuel introduction in the outer two annuli and this effect is observed downstream until the fuel-air mixture attains a more homogenous composition.

The flame in case 3 is a premixed flame having conditions similar to that given for Figure 9 except that an equivalence ratio of 1.0 was used. A comparison between cases 1 and 3 data revealed the following:

1. The recirculation zone is almost non-existent for the premixed case 3 as shown in Figure 11. The maximum positive axial velocities are considerably higher than the non - premixed and the lean premixed cases 1 and 2. The velocity decay is higher for the stoichiometric premixed case 3 as compared to the other non-premixed and premixed cases. The higher axial velocity for case 3 inhibits the growth of a recirculation zone.
2. Maximum temperatures at higher equivalence ratio for the premixed case 3 are comparable to those obtained at lower equivalence ratio for the non-premixed case 1 (compare Figure 12 with Figure 7). Temperatures with the stoichiometric premixed case 3 are about 30% higher than lean premixed case 2 (compare Figure 12 with Figure 10).
3. The bimodal nature of the temperature profiles for the stoichiometric premixed case 3 diminish as compared to the lean premixed case 2 (compare temperature profiles near burner exit in Figures 10 and 12.
4. Significantly higher turbulent transport values are obtained for the stoichiometric

premixed case 3. The exact location and amplitude of these turbulent transport are responsible for improved mixing of the fuel - air mixture.

Analysis of Test Results

Comparison of the computational results for the premixed flames obtained with a systematic variation in the swirl, angular momentum ratio and equivalence ratio is now discussed. The following test matrix was considered:

- Flame Type: Premixed flame
- Total equivalence ratio : 0.5 and 1.0
- $[Q_{\mathrm{ann}1}/Q_{\mathrm{ann}2}]$: 0.5 , 1.0
- Swirl vane angle in annulus 1/annulus 2: 00/55, 45/55, 60/00, 60/35 degrees.

Impact of Swirl Flow Distribution

1. For all premixed cases the swirl vane angle in annulus 1 and annulus 2 had only a small effect on the size and strength of the recirculation zone.
2. The bimodal nature of the temperature profiles is most pronounced for the case with no swirl in annulus 1. With an increase in the swirl angle in annulus 1, this effect subsides. The temperature field was, in general, insensitive to the strength and distribution of swirl. This information requires verification
3. Turbulent kinetic energy levels increase with an increase in swirl vane angles in annulus 1 (compare Figure 13 with Figure 14 corresponding to cases 4 and 5, respectively).

Impact of Angular Momentum Ratio

The following observations were made when the flow ratios in the two annuli, $[Q_{\mathrm{ann}1}/Q_{\mathrm{ann}2}]$, were varied from 0.5 to 1:

1. A small increase in strength of the recirculation zone for equal flow in the two annuli as compared to the condition with higher flow in annulus 2.
2. Temperature field is insensitive to the variations in flow rates in the two annuli.
3. Figures 14 and 15 show that the turbulence kinetic energy increases by almost 100 % as the flow ratio is varied from 0.5 to 1. This finding may serve as a valuable aid to develop new mixing strategies.

Implications of Equivalence Ratio Variations

The following observations can be made from the studies carried out by varying the equivalence ratio from 0.5 to 1 :

1. Decreased size of the recirculation zone at higher equivalence ratios
2. Figures 16 and 17 show that higher values of azimuthal velocities are obtained at the higher equivalence ratios. Theoretically, this should lead to a well defined recirculation zone. The k-ε model is well known for underpredicting the strength of the recirculation zone. The RSM model may assist to capture this effect.
3. Mean temperatures decrease by almost 30% when the equivalence ratio is decreased from 1 to 0.5. Also the temperature profiles no longer have a monomodal appearance for the case of an equivalence ratio equal to 0.5.

Summary

The results presented here have shown a significant effect of the radial distribution of swirl on the degree of mixing and structure of premixed flames. Experimental data reveals that premixed flames can have large time integral scales in certain regions of the flame. The degree of mixing and flame structure are significantly affected by the presence of swirlers in the flow. The nonuniformity of thermal field is different in different regions of the flow field. Premixed flames at higher equivalence ratios yielded decreased size and strength of the central toroidal recirculation zone. Premixed flames yielded uniform and lower overall flame temperatures so that carefully mixed (premixed) flames have the most potential for reduced pollutants emission from flames. These results are of direct benefit in the design and development of gas turbine combustors, particularly for achieving higher efficiencies and low pollution.

Future Activities

Our future activities will focus on a closer examination of the regions that contribute to NO_X by examining in detail, the structure of the flames, non-intrusively, complimented with numerical calculations. Our immediate goal will be to provide a comprehensive mapping of these specific flames, with a view to correlating time scales with the propensity for NO_X generation.

Acknowledgments

The research support provided here is gratefully acknowledged. Technical support, assistance and collaboration provided by Pratt & Whitney, East Hartford, CT is deeply appreciated. We also acknowledge the assistance of DOE Project Managers Dr. Paul Micheli and Dr. Norm Holcombe, and also the ATS Research Manager, Dr. Daniel Fant. Technical assistance on this project was provided by Messrs Andre' Marshall, Song Qi, Robert Aftel and Harald Kafitz.

References

1. Gupta, A.K. and D.G. Lilley: Combustion and Environmental Challenges for Gas Turbines in the 1990s. AIAA Paper 91-1964.
2. Spadaccini, L.J. and J.A TeVelde: Autoignition Characteristics of Aircraft-Type Fuels, Combustion and Flame, Vol. 46, 1982, pp 283-300.
3. Libby, P.A. and F.A. Williams: *Turbulent Reaction Flows*, Academic Press, 1994.
4. Marshall, A : Ph.D Thesis (in progress), Department of Mechanical Engineering, University of Maryland, 1996.

Table 1. Test Matrix for the Presented Data

Case No	Flame Type	Swirl Vane Angle (deg.) Annulus 1	Swirl Vane Angle (deg.) Annulus 2	Flow Rates (SCFM) Annulus 1	Flow Rates (SCFM) Annulus 2	Equivalence Ratio
1	Non-premixed	45	55	11	22	0.5
2	Premixed	45	55	11	22	0.5
3	Premixed	45	55	11	22	1.0
4	Premixed	45	55	16.5	16.5	1.0
5	Premixed	60	35	16.5	16.5	1.0
6	Premixed	60	35	11	22	1.0
7	Premixed	60	35	11	22	0.5

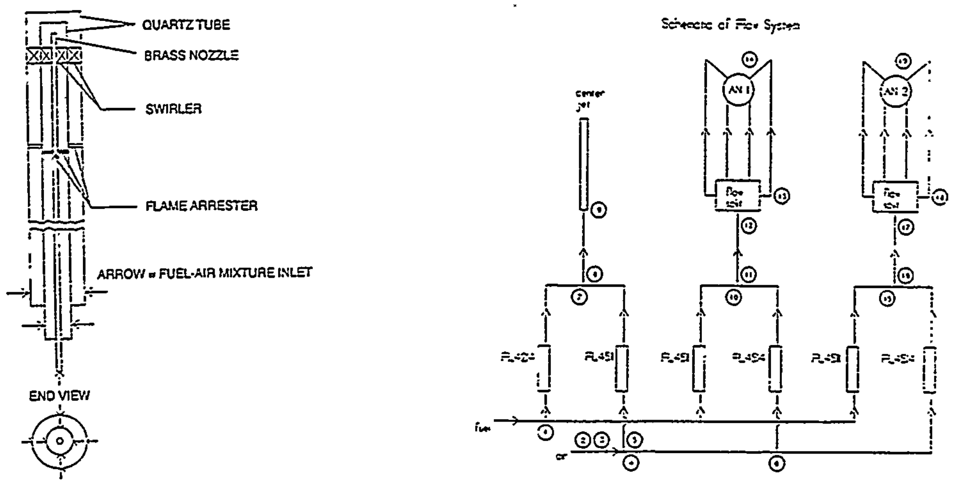

Fig. 1 Diagram of burner and flow delivery system.

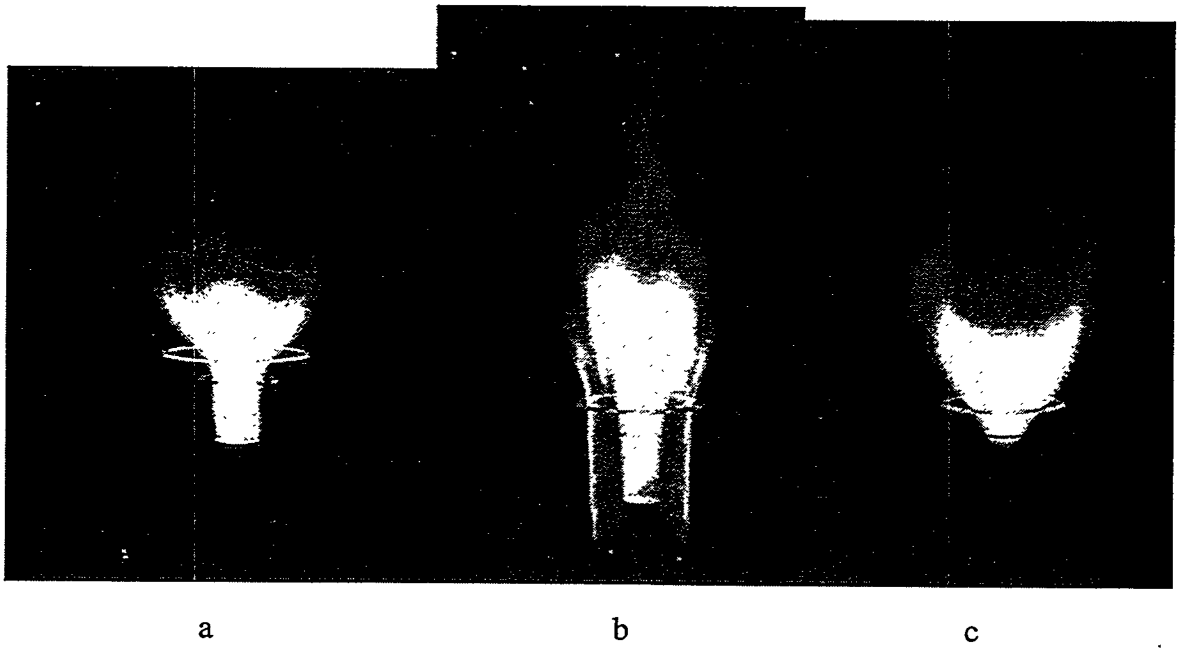

Fig. 2 (a) Flame photograph with ø = 0.5 in all three jets; (b) Flame photograph with ø = 0.98, 0.94 and 1.06 in central jet, annulus 1 and annulus 2, respectively (overall ø = 1.0); (c) Flame photograph with ø = 1.23, 0.52 and 0.71 in central jet, annulus 1 and annulus 2, respectively (overall ø = 0.65).

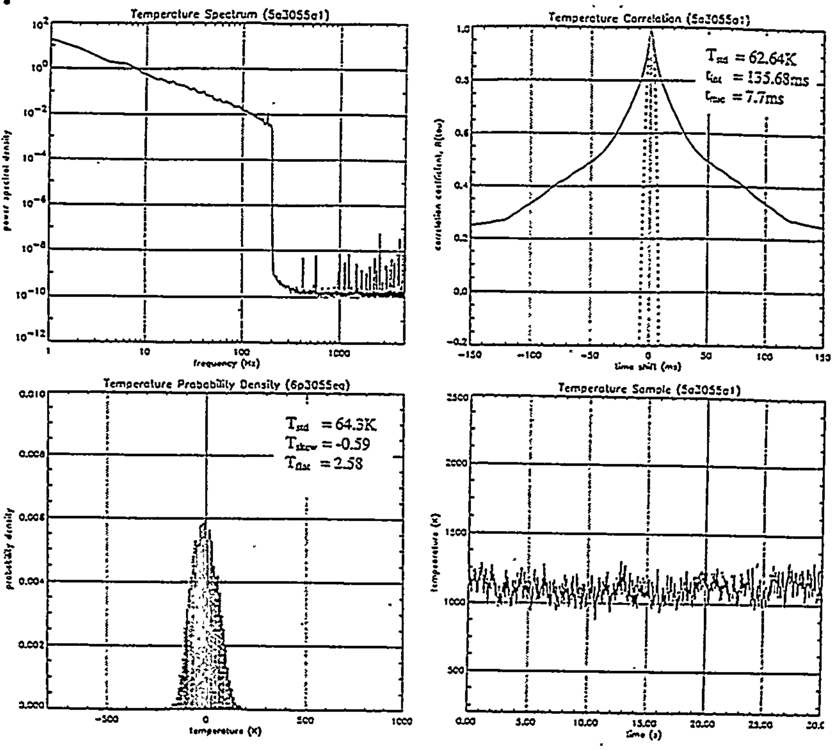

Fig. 3 Power spectral density, autocorrelation coefficient, probability density and temporal variation of temperature in premixed flame at r = 0 and z = 1.5 inches with S1 = 30^0 in annulus 1 and S2 = 55^0 in annulus 2. Flow in annulus 2 was twice that in annulus 1.

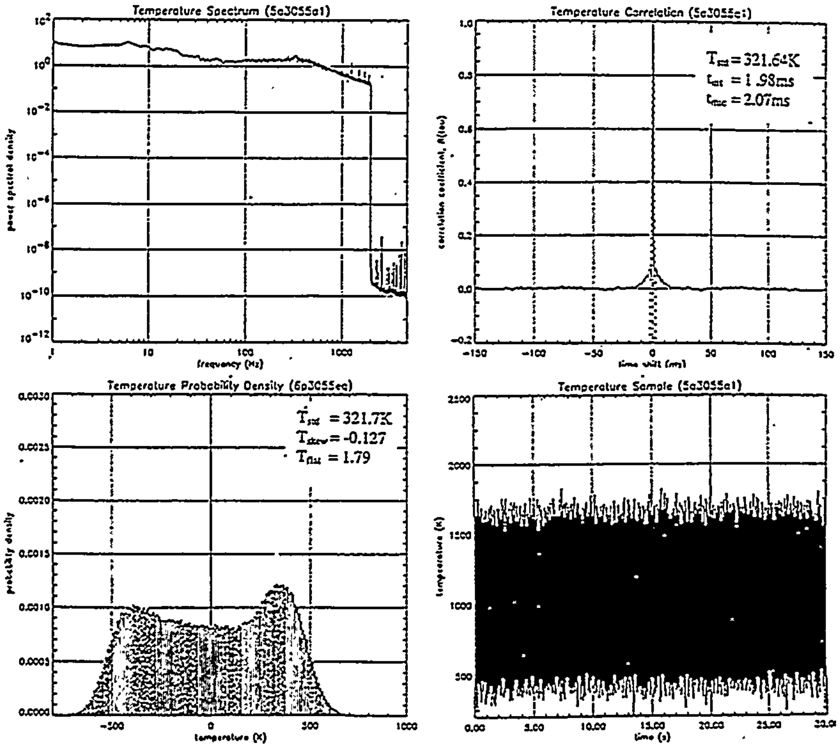

Fig. 4 Power spectral density, autocorrelation coefficient, probability density and temporal variation of temperature in premixed flame at r = 1.5 and z = 1.5 inches. Other conditions are the same as those given for Fig. 3.

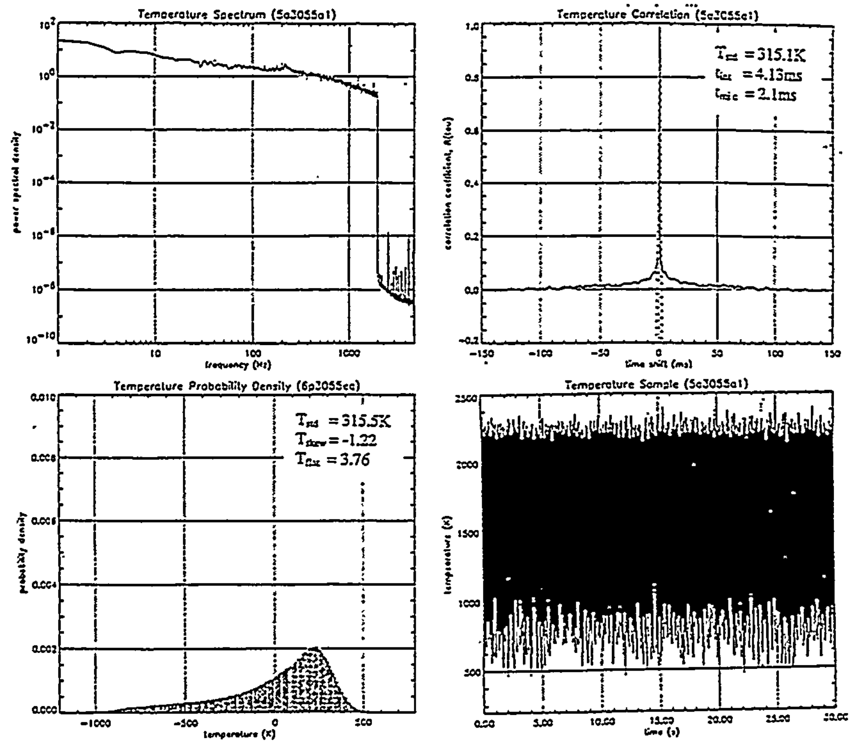

Fig. 5 Power spectral density, autocorrelation coefficient, probability density and temporal variation of temperature in non-premixed flame at r = 1.5 and z = 1.5 inches with S1 = 30°, S2 = 55°. Flow in annulus 1 was the same as that in annulus 2.

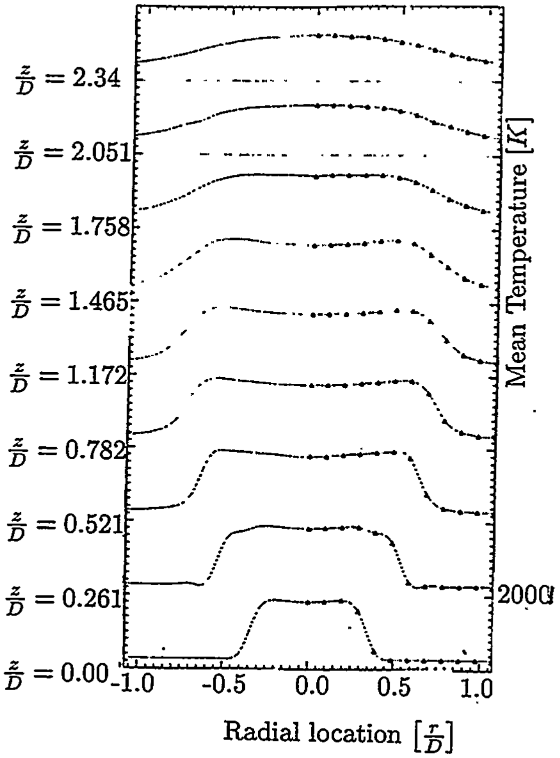

Fig.6. Experimental temperature profiles in non - premixed flame.

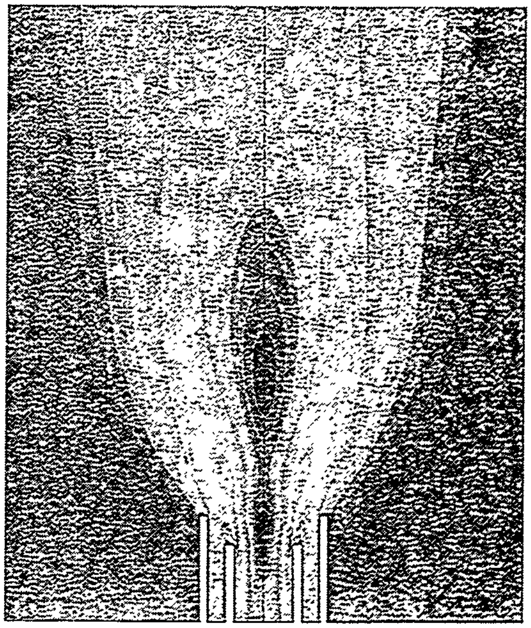

Fig.8. Computational U-velocity profiles for case 1 flame. Scale is 1 unit=3.63 m/sec.

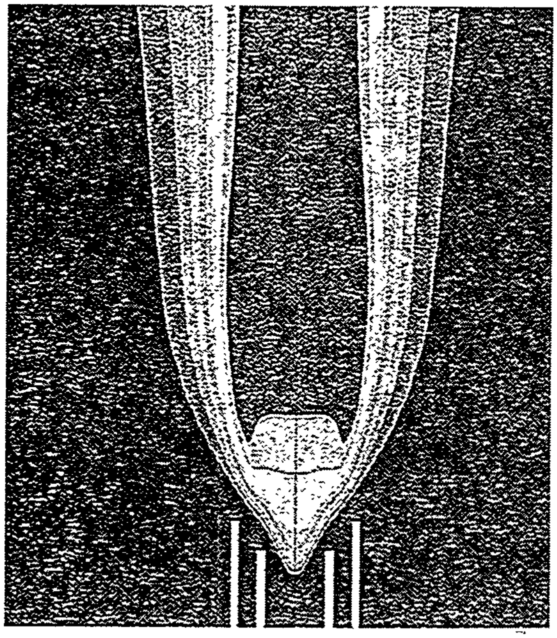

Fig.7. Computational temperature profiles for case 1 flame. Scale is 1 unit=400 K

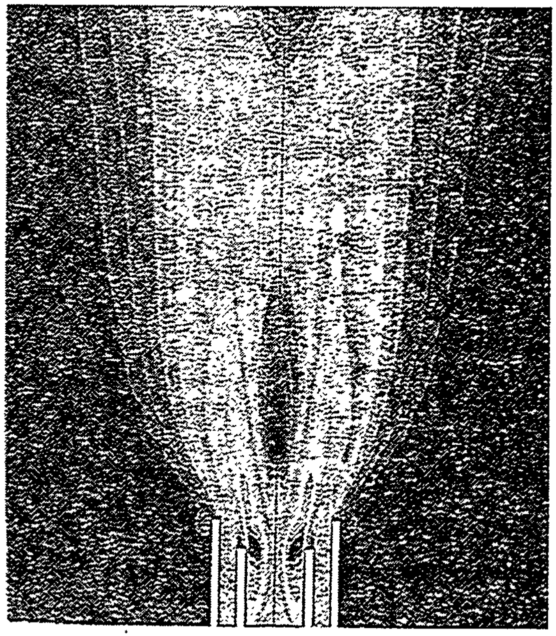

Fig.9. Computational U-velocity profiles for case 2 flame. Scale is 1 unit=3.725 m/sec

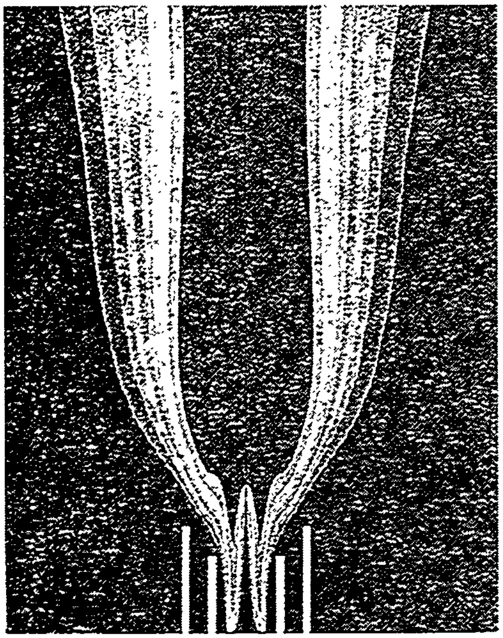

Fig.10. Computational temperature profiles for case 2 flame. Scale is 1 unit= 254 K.

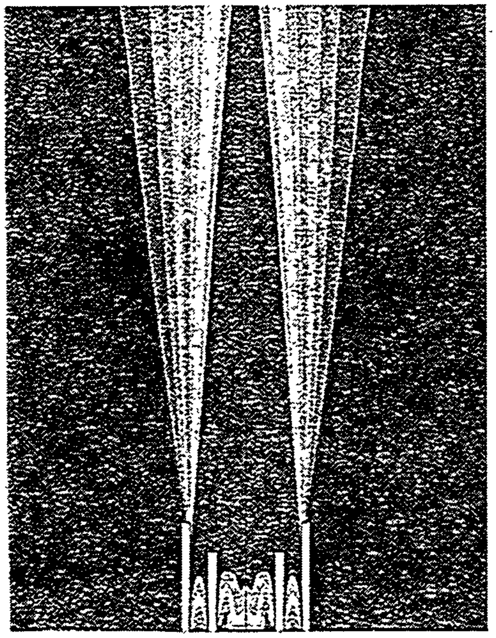

Fig.12. Computational temperature profiles for case 3 flame. Scale is 1 unit = 402 K.

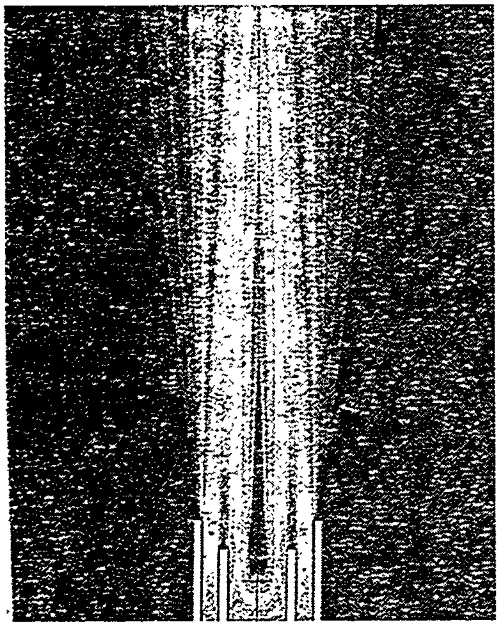

Fig.11. Computational U-velocity profiles for case 3 flame. Scale is 1 unit= 13.9 m/s

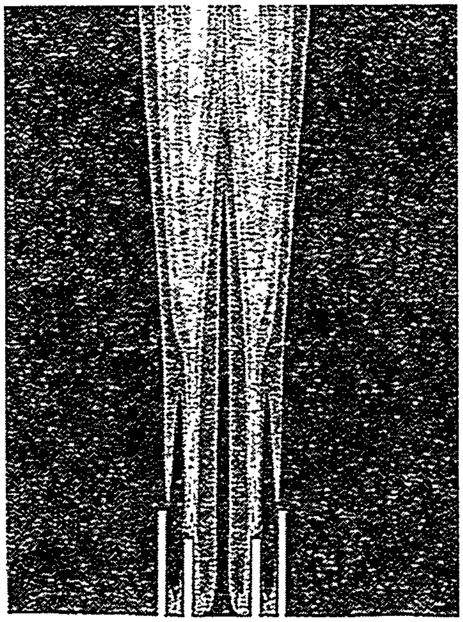

Fig.13. Computational turbulent kinetic energy profiles for case 4 flame. Scale is 1 unit = 67.5 m/s.

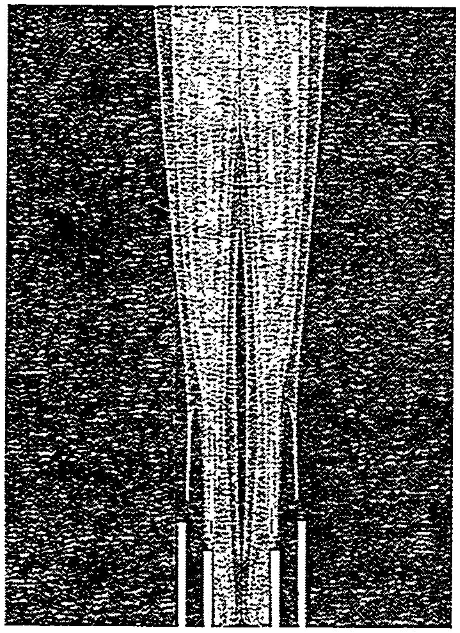

Fig.14. Computational turbulent kinetic energy profiles for case 5 flame. Scale is 1 unit = 89.5 m/s

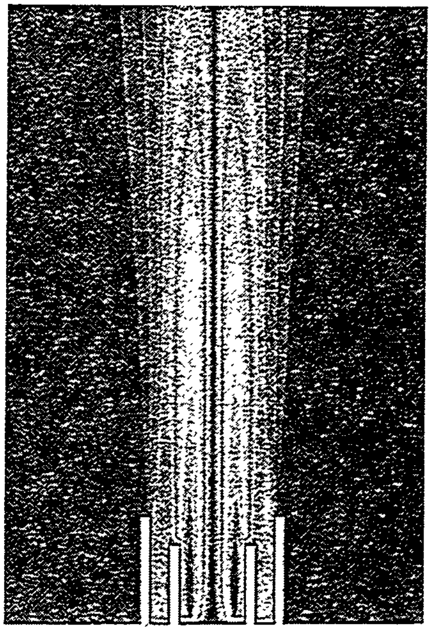

Fig.16. Computational azimuthal velocity plots for case 6 flame. Scale is 1 unit = 4.4 m/s

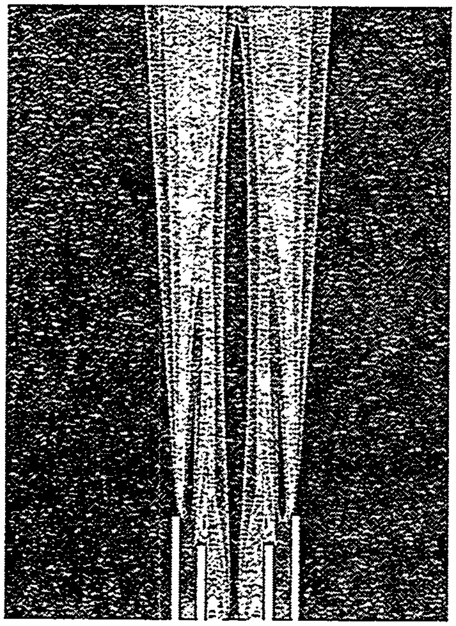

Fig.15. Computational turbulent kinetic energy profiles for case 6 flame. Scale is 1 unit = 42.75 m/s

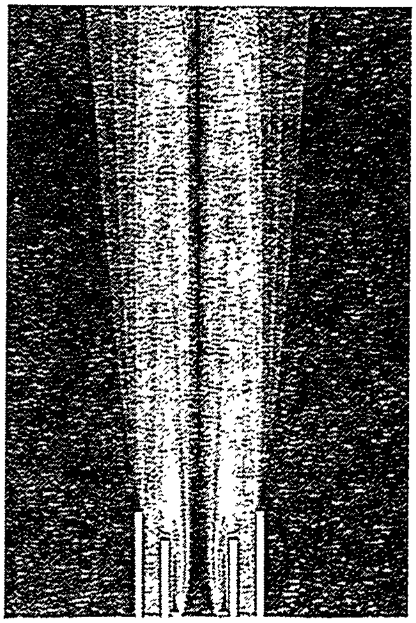

Fig.17. Computational azimuthal velocity plots for case 7 flame. Scale is 1 unit = 4.45 m/s

P22

Intercooler Flow Path for Gas Turbines: CFD Design and Experiments

Ajay K Agrawal (agrawal@mailhost.ecn.uoknor.edu, 405-325-1754)
Subramanyam R. Gollahalli (gollahal@mailhost.ecn.uoknor.edu, 405-325-5011)
Frank L. Carter (fcarter@mailhost.ecn.uoknor.edu, 405-325-0837)
John E. Allen (jeallen@mailhost.ecn.uoknor.edu, 405-325-0837)
University of Oklahoma
865 Asp Avenue, Room 212
Norman, OK 73019

Introduction

The Advanced Turbine Systems (ATS) program was created by the U.S. Department of Energy to develop ultra-high efficiency, environmentally superior, and cost competitive gas turbine systems for generating electricity. Intercooling or cooling of air between compressor stages is a feature under consideration in advanced cycles for the ATS. Intercooling entails cooling of air between the low pressure (LP) and high pressure (HP) compressor sections of the gas turbine. Lower air temperature entering the HP compressor decreases the air volume flow rate and hence, the compression work. Intercooling also lowers temperature at the HP discharge, thus allowing for more effective use of cooling air in the hot gas flow path.

The thermodynamic analyses of gas turbine cycles with modifications such as intercooling, recuperating, and reheating have shown that intercooling is important to achieving high efficiency gas turbines (Cook and Nourse, 1993; Wikes et al, 1993; Cohn, A., 1993). The gas turbine industry has considerable interest in adopting intercooling to advanced gas turbines of different capacities. This observation is reinforced by the US Navy's Intercooled-Recuperative (ICR) gas turbine development program to power the surface ships (Crisalli and Parker, 1993; Shepard et al., 1994; Valenti, M., 1995).

In an intercooler system, the air exiting the LP compressor must be decelerated to provide the necessary residence time in the heat exchanger. The cooler air must subsequently be accelerated towards the inlet of the HP compressor. The circumferential flow nonuniformities inevitably introduced by the heat exchanger, if not isolated, could lead to rotating stall in the compressors, and reduce the overall system performance and efficiency. Also, the pressure losses in the intercooler flow path adversely affect the system efficiency and hence, must be minimized. Thus, implementing intercooling requires fluid dynamically efficient flow path with minimum flow nonuniformities and consequent pressure losses.

Objectives

The objective of this research is to provide analytical tools and experimental data to help in the design of an effective intercooler flow path. Although the primary emphasis of the study is on

---

[1] Research sponsored by the U.S. Department of Energy's Morgantown Energy Technology Center, under subcontract 94-01-SR029 with the University of Oklahoma, 1000 Asp Avenue, Suite 314, Norman, OK 73019; telefax: 405-325-6029.

the intercooler, the information obtained could be applicable to other similar flow systems such as a recuperator and/or an aftercooler.

Approach

This study involves three phases. In the first phase, computational fluid dynamics (CFD) analysis is employed to design the flow passages. The second phase involves fabrication and flow experiments in a scaled model of the intercooler flow path to characterize the flow field and frictional losses in different regions. The third phase involves validation of the analytical predictions, refinement of the analysis, and development of the design guidelines.

Project Description

Configuration of the intercooler flow path between the LP and HP compressors consisting of a diffuser, an intercooler or heat exchanger, and a contraction is shown in Figure 1. The diffuser decelerates the LP compressor discharge air while recovering the flow kinetic energy, isolates the LP compressor from the intercooler by turning air away from the turbine axis, and improves the heat transfer effectiveness by uniformly supplying low speed air to the intercooler. Downstream of the intercooler, the contraction isolates the HP compressor from the heat exchanger while minimizing the compressor inlet flow losses by gradually accelerating the cooler air.

The intercooler may be located on-axis (as shown in Figure 1) or off-axis. A water-cooled intercooler, because of its smaller size, could be on-axis while an air-cooled intercooler might be located off-axis. An off-axis intercooler would be easy to install and access; however it would require asymmetric interconnecting passages. The on-axis configuration shown in Figure 1, intended to establish the baseline information, uses a shell-and-tube heat exchanger with air flowing axially inside finned tubes. This arrangement is typical of the multi-stage centrifugal compressors and it differs from the Navy's ICR design (Shepard et al, 1994) where the space constraints led to a compact plate and fin heat exchanger with airflow normal to the turbine axis.

The current emphasis of this study is on flow nonuniformities and pressure losses in the intercooler flow path. Thus, the airflow is considered without heat transfer in the intercooler. The following is a description of the computational and experimental components of the project.

Computational

The computational part of the project is to first develop configuration(s) providing the desired flow characteristics in the intercooler flow path. Subsequently, the analysis could be used to interpret the experimental data and be refined to develop the design guidelines. Because of the complex geometry, the design of the intercooler flow path is not amenable to simple analytical procedures. Thus, the computational fluid dynamics (CFD) was used for detailed modeling and analysis.

The goal of the CFD analysis was to generate optimum diffuser and contraction wall geometries, within the specified constraints, using an iterative approach. In this procedure, the fully elliptic Navier-Stokes equations for turbulent flow are solved repeatedly on a body-fitted coordinate system. A set of parameters was developed to describe the geometry of the contoured passage. These parameters were varied systematically to yield a configuration with the desired flow characteristics. Following are some of the details of the design procedure.

Diffuser. The diffuser was required to direct airflow away from the turbine axis with minimum frictional loss, thereby, demanding a high area in a small length. An area ratio of 5.4 in a length equals 10 times the inlet annulus height was chosen. Because a straight wall diffuser with such an area ratio would be long, a contoured wall design was sought. The overall diffuser was divided into a moderately diffusing pre-diffuser and a sudden expansion. Such a design is typical of the compressor-combustor diffusers used in gas turbines (Fishenden and Stevens, 1977). The pre-diffuser recovers majority of the flow kinetic energy while the sudden expansion ensures uniformity of flow at the diffuser exit. The sudden expansion could also attenuate fluctuations caused by flow non-uniformities.

Walls of the pre-diffuser were generated from the prescribed passage axis (updated iteratively) and the passage expansion rate based on the annular Cp* diffusers (Adkins, 1983). A sinusoidal distribution was used as the initial guess for the passage axis. This guess distribution was updated iteratively using the computed flow field such that the flow decelerated uniformly at the inner and outer diffuser walls. A similar procedure was used for the sudden expansion, except that the expansion rate was also prescribed to avoid flow separation and to ensure uniform flow at the diffuser exit. Further details of the analysis are given by Agrawal et al. (1996).

Contraction. The overall area ratio of the contraction was the same as that for the diffuser. Walls of the contraction were determined from two curves; one defining the passage axis and the other prescribing distribution of the passage area. Each of these two curves was formed by two contours joining together smoothly at the inflection point. The shape of the curves was varied to yield uniform flow acceleration at the inner and outer walls of the contraction. This criterion ensured a uniform velocity profile at the contraction exit.

Experimental

The goal of the experimental work was to obtain quantitative data in a scale model of the intercooler flow path. The scale model would correctly simulate flow in the prototype if the velocity profiles at its inlet matched those at the LP compressor discharge. This matching was achieved by inducing controlled airflow through the test model by a suction type wind-tunnel. The following are the details of the test model, wind tunnel, instrumentation and data acquisition system.

Test Model. The test section consists of a diffuser, an intercooler, and a contraction. The contoured outer passages of the diffuser and contraction were designed to provide optical access, high degree of dimensional accuracy, facilities for introducing probes and pressure taps, and a reasonable cost and time for fabrication. Clear plexiglas was the material of choice. However, forming plexiglas to yield a complex contoured diffuser or contraction was not feasible. Thus, a process was devised where the plexiglas panels representing a sector of the diffuser or contraction were pressure formed. The manufacturing process consisted of the following steps: (i) machining a pair of laminated, hard mahogany wood block on a milling machine/rotary table facility to conform to the shape determined by the CFD analysis, (ii) heating and conditioning 19mm thick plexiglas sheets at 175 °C in a programmable autoclave, (iii) forming panels by sandwiching heated plexiglass between molds on a hydraulic press, (iv) assembling the segments to form the circular expansion, and (v) machining to the precise dimensions, and polishing to recover the optical quality. Figure 2 shows a photograph of a pair of molds and a formed plexiglass panel in the hydraulic press.

The contoured inner passages of the diffuser and contraction were designed to provide structural rigidity with a contrasting background. Hard Mahogany wood was the material of choice. The wood was laminated to form rectangular blocks of the desired dimensions and then machined to yield the exact profile on the exterior. Figure 3 shows a photograph of the machined inner diffuser passage.

Two co-axial rolled metal pipes were used to simulate the intercooler. This system could subsequently be replaced by a shell-and-tube heat exchanger with a square-pitch tube design to more accurately represent the test conditions.

Flow System. An open circuit wind-tunnel, shown schematically in Figure 4, provides the desired airflow through the test section. The air entering this low-turbulence wind-tunnel passes through a honeycomb, a set of screens, and a 9:1 area ratio contraction which guides the airflow to the annular flow conditioning sections.

The flow conditioning sections were designed with the following objectives: (i) ability to control the velocity profile at the inlet of the test-section, (ii) ability to characterize flow at the exit of the test-section, (iii) optical access with a clear exterior wall and contrasting interior wall, (iv) high degree of dimensional accuracy, and (v) facilities for introducing pitot-static, hot-wire anemometer and other probes. Further requirements were the interchangeability of components, resistance to wear damage due to the prolonged use, and the ability to align and traverse probes while maintaining an airtight seal.

The outer walls of the annulus were made of clear plexiglas and the interior walls were made of polished aluminum. The aluminum pipes forming the inner wall were sealed at both ends to prevent air flow inside of it. Two aircraft propeller spinners were mounted at the ends to seal as well as to streamline the flow past them. Inner tube was mounted to the wall of the wind tunnel using three airfoil shaped struts located at 120° intervals on the circumference.

Because the large plexiglas pipes of the dimensions required were not available in the market, they were formed from commercially available flat stock. The process consisted of heat rolling the plane acrylic to provide the cylindrical shape, machining to obtain the required dimensions, and polishing to yield the optical quality. Figure 5 shows a photograph of the flow conditioning sections assembled to the wind-tunnel.

The axial velocity profile at the exit of a gas turbine compressor could be nominal, OD-peaked or ID-peaked. Circular rings mounted on the inner or outer pipes of the upstream flow developing section were used to simulate the desired levels of flow nonuniformities at the inlet of the test-section.

Instrumentation. The experiments involve hot-wire anemometer, pitot-static probe, 5-hole probe, and wall pressure taps. A computer controlled scanning system is used to simultaneously scan 4 pressure input ports from a total of up to 96 ports. The hot-wire system provides voltage output which is calibrated within the velocity range using a calibration wind-tunnel. The voltage signals from the pressure sensor and the hot-wire sensor are converted to pressure and velocities using high and low-speed data acquisition boards (Mini-16 and Frash 12) and accompanying software (Quicklog and Workbench for Windows) from Straberry Tree. This icon-based data acquisition software operated in DOS and Windows environments on a Pentium microprocessor and it allowed complete control of the experiments. A system to traverse probes was also designed, fabricated and interfaced with the microcomputer. An underlying feature of the instrumentation was that the different operations such as probe traversing, scanning pressure channels, measuring pressure, temperature and velocities, and storing data on hard disk were integrated and automated within an interactive software environment. The data are stored in ASCII files on the computer hard disk. These files were accessed and processed using commercial software.

Results

Computational

The analysis was used to design annular diffuser and contraction passages. Figure 6 shows velocity vectors in the optimized diffuser with fully developed flow at its inlet. The diffuser provided uniform flow at its exit without flow separation. This diffuser had an annulus height of 0.052m (2.063") at its inlet, an area ratio of 5.4 and a length of 0.533m (21"). The exit diameters of the inner and outer walls were 0.51m (20") and 0.84m (33"), respectively.

The velocity vectors in the optimized contraction are shown in Figure 7, which indicates uniform flow at the exit. The contraction dimensions were the same as those for the diffuser except that the contraction length was 0.46m (18").

Experimental

A series of experiments involving hot-wire anemometer, pitot-static probes, and wall pressure taps were conducted to characterize the wind-tunnel and to adjust the velocity profile at the test-section inlet. These experiments indicated that the flow in the annuli was axisymmetric.

Figure 8 shows velocity profiles at 4 axial locations (72, 76, 80, and 84 inches from the entrance of the flow conditioning section) for a circumferential positions 'A' indicating fully developed flow at the exit of the upstream conditioning section. Figure 9 shows velocity profiles at an axial location 80" from the entrance of the flow conditioning section, when a circular ring was placed on either the inner or the outer pipe of the annulus. An inner ring resulted in an OD-peaked profile while an outer ring caused an ID-peaked profile. The desired velocity profile at the inlet of the test-section could be obtained by placing the ring at a proper axial location.

Future Activities

The future activities include detailed mapping of the flow field in the diffuser and contraction sections. Then, the experimental data in conjunction with the CFD design will be used to develop guidelines for the annular diffuser and contraction design.

Acknowledgements

This work is sponsored by the U.S. Department of Energy's Morgantown Energy Technology Center under contract DE-FC21-92MC29061 with the Clemson University, subcontract 94-01-SR029 with the University of Oklahoma for the period from July 1994 to June 1996. The METC Contracting Officer's Representative is Dr. Norm Holcombe. Dr. Dan Fant was the program manager of the Advanced Gas Turbine Systems Research at Clemson University.

References

Adkins, R.C., 1983, "A Simple Method for Designing Optimum Annular Diffusers," *ASME Paper 83-GT-42*.

Agrawal, A.K, Carter, F.L., and Gollahalli, S.R., 1996, "Analysis of Annular Diffusers for a Gas Turbine Intercooler," submitted to the *ASME International Gas Turbine Conference*, Birmingham, U.K.

Cohn, A., 1993, "Collaborative Advanced Gas Turbine Program," *Proc. of the Joint Contractor's Meeting*, D.W. Geiling (ed.), DOE/METC-93/6132, pp 103-108.

Cook, C.S., and Nourse, J.G., 1993, "GE Power Generation Technology for Advanced Gas Turbines," *Proc. of the Joint Contractor's Meeting*, D.W. Geiling (ed.), DOE/METC-93/6132, pp 16-25.

Crisalli, A.J., and Parker, M.L., 1993, "Overview of the WR-21 Intercooled Recuperated Gas Turbine Engine System: A Modern Engine for a Modern Fleet," *ASME Paper 93-GT-231*.

Fishenden, C.R., and Stevens, S.J., 1977, "Performance of Annular Combustor-Dump Diffusers," *Journal of Aircraft*, vol 14, pp. 60-67.

Mikhail, M.N., 1979, "Optimum Design of Wind Tunnel Contractions," *AIAA Journal*, vol. 17, pp. 471-477.

Shepard, S.B., Bowen, R.L., and Chiprich, J.H., 1994, "Design and development of the WR-21 Intercooled Recuperated (ICR) Marine Gas Turbine," *ASME Paper 94-GT-79*.

Valenti, M., 1995, " A Turbine for Tomorrow's Navy," *Mechanical Engineering*, pp 70-73.

Wikes, C., Mukavetz, D.W., Knickerbocker, T.K., and Ali, S.A., 1993, "Advanced Turbine Systems Program," *Proc. of the Joint Contractor's Meeting*, D.W. Geiling (ed.), DOE/METC-93/6132, pp 33-41.

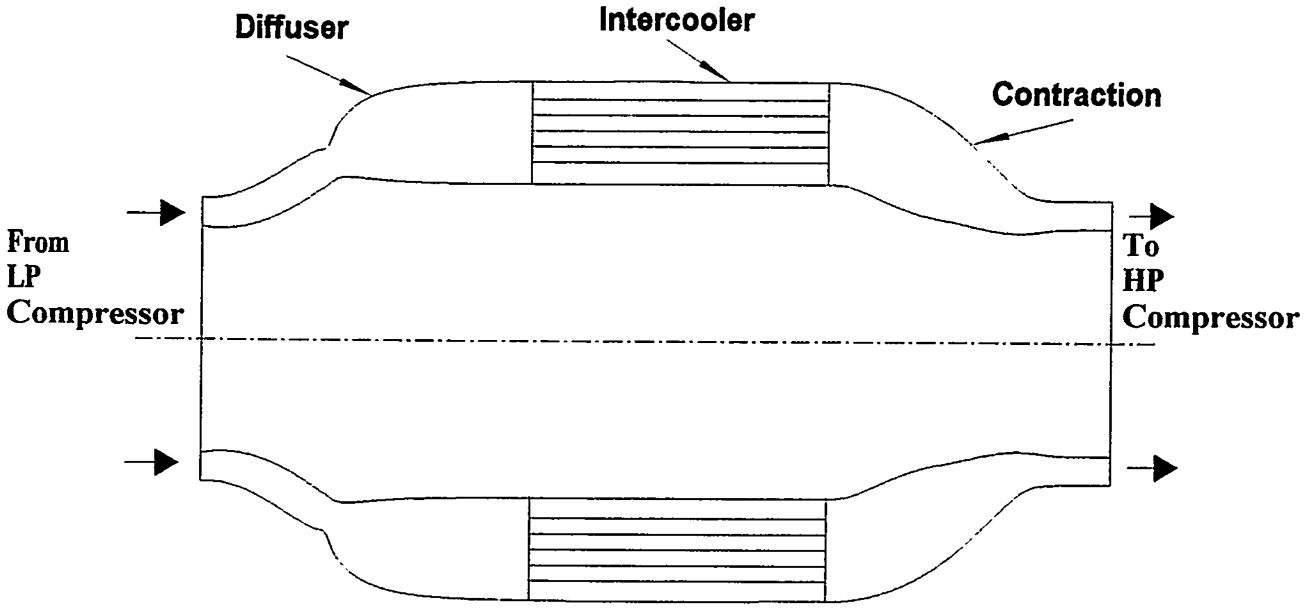

Figure 1. Schematic of the Intercooler Flow Path

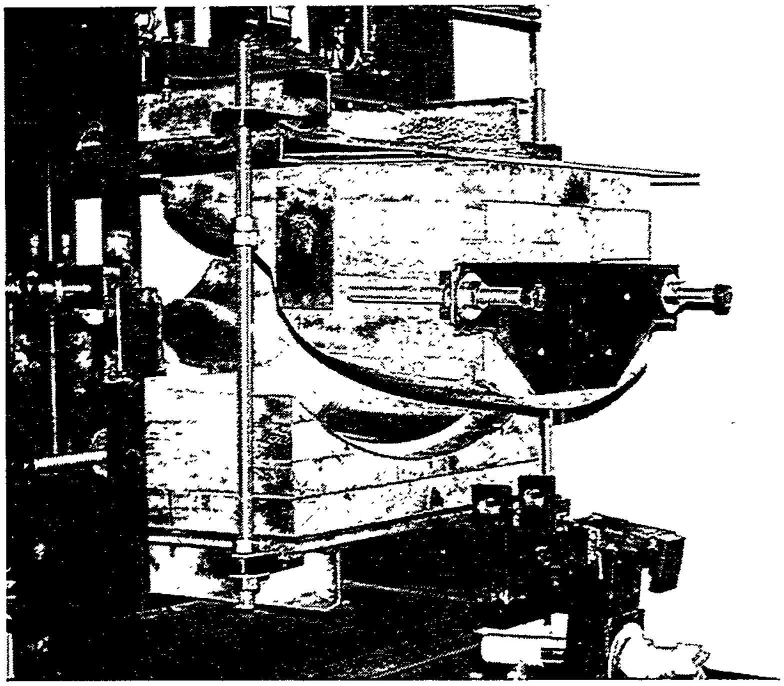

Figure 2. Molds, Plexiglass Panel and the Hydraulic Press

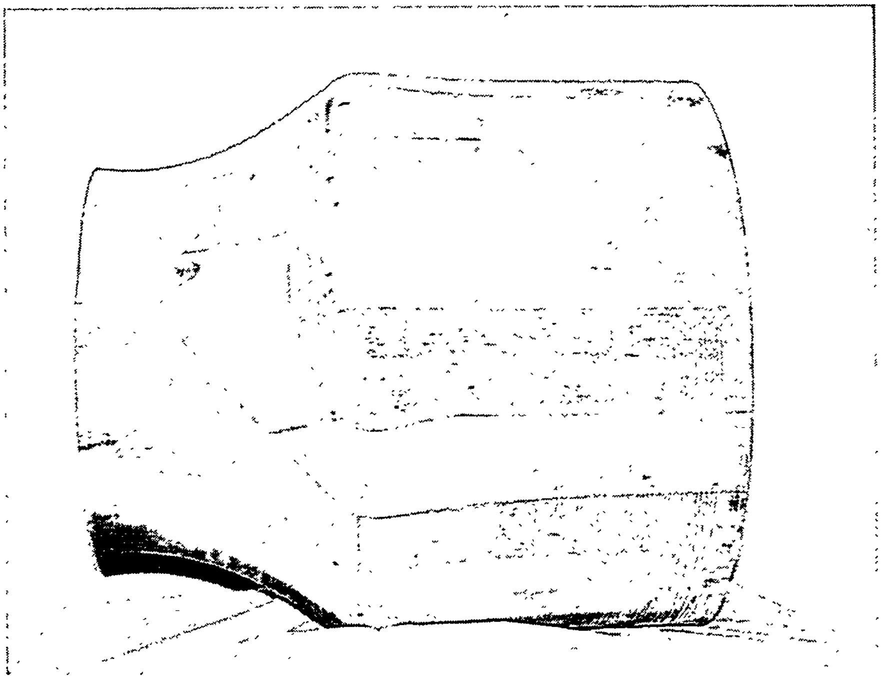

Figure 3. Machined Inner Diffuser Passage

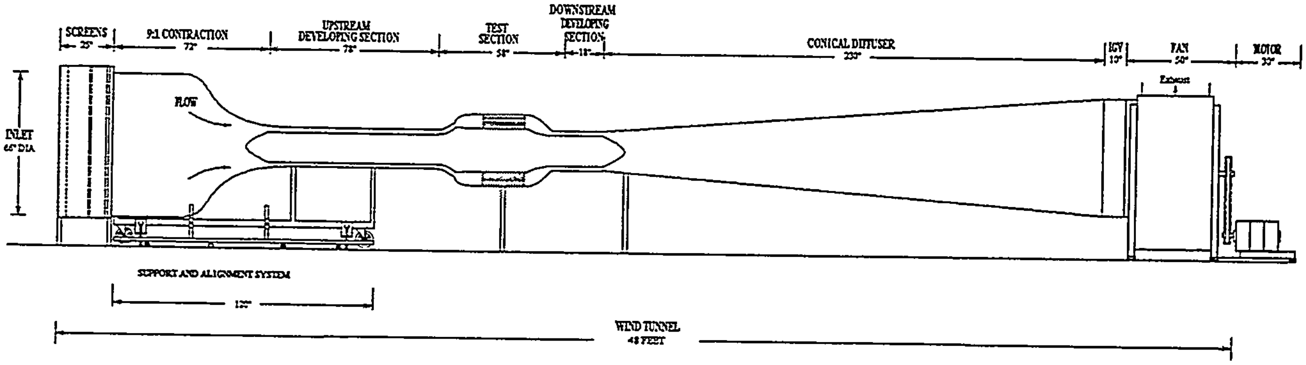

Figure 4. Schematic of the Wind-Tunnel

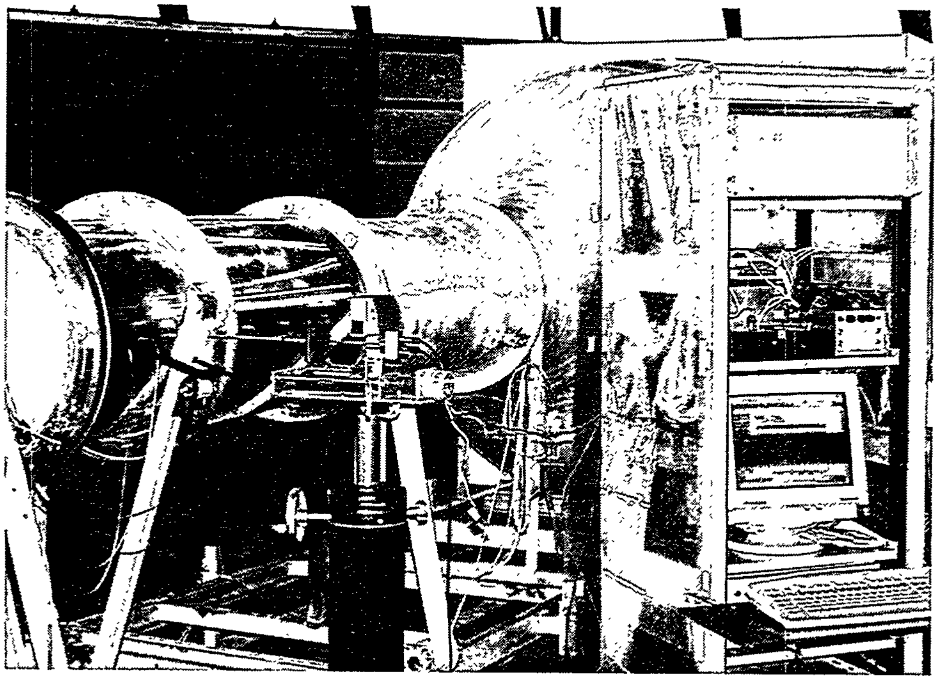

Figure 5. Wind-tunnel with the Flow Conditioning Sections

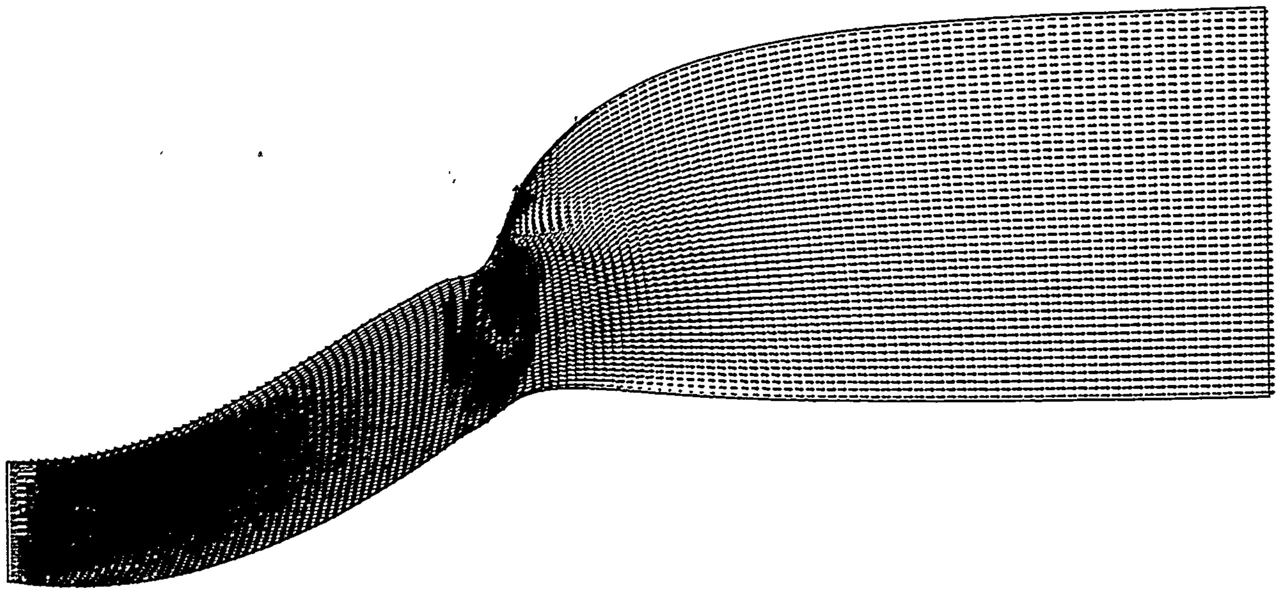

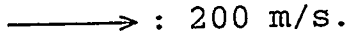

Figure 6. Velocity Vectors in the Optimized Diffuser

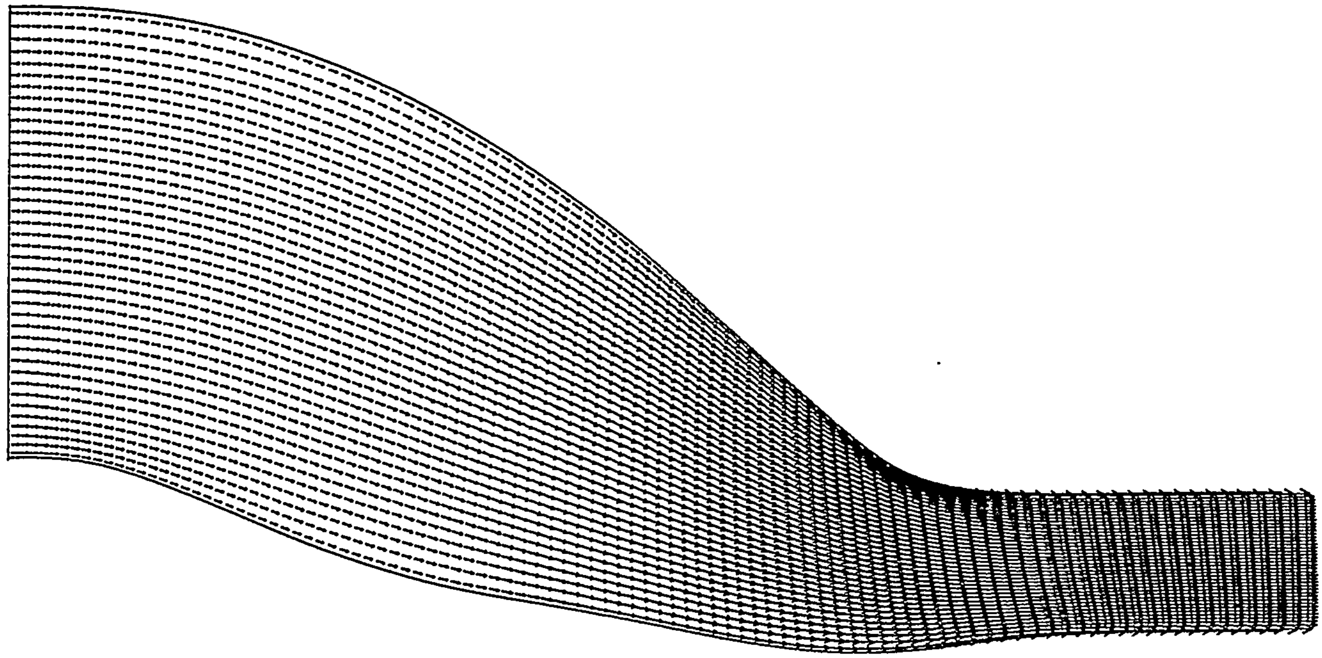

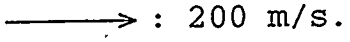

Figure 7. Velocity Vectors in the Optimized Contraction

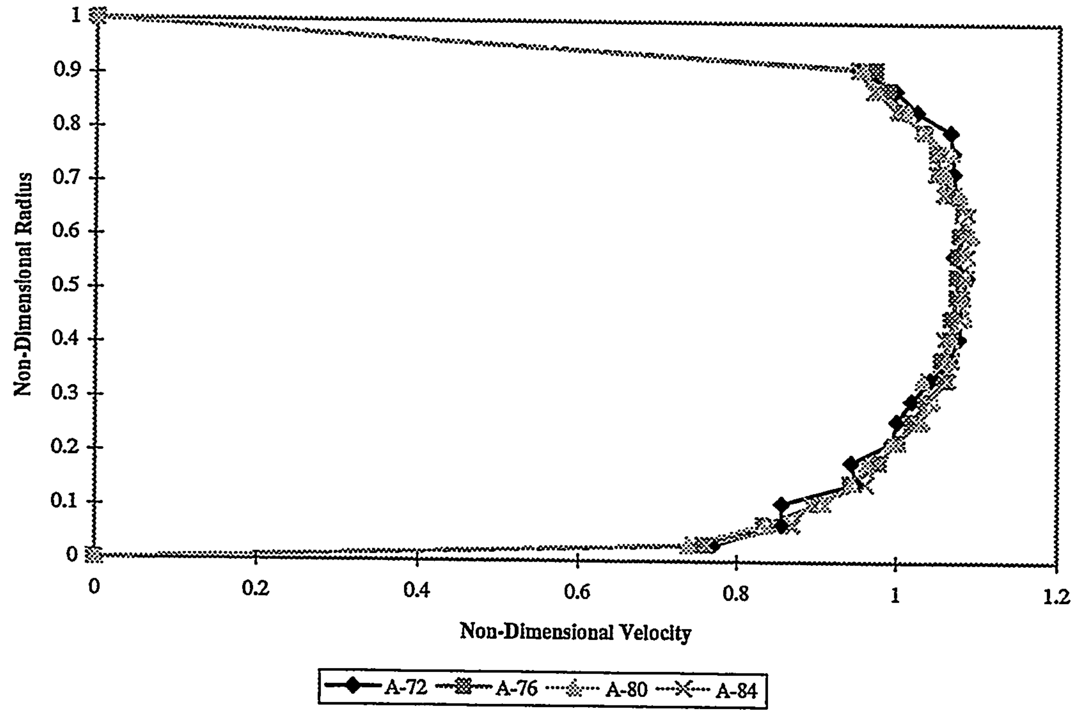

Figure 8. Axial Velocity Profiles in the Flow Developing Section (the Number after A indicates Distance, in inches, from the Entrance)

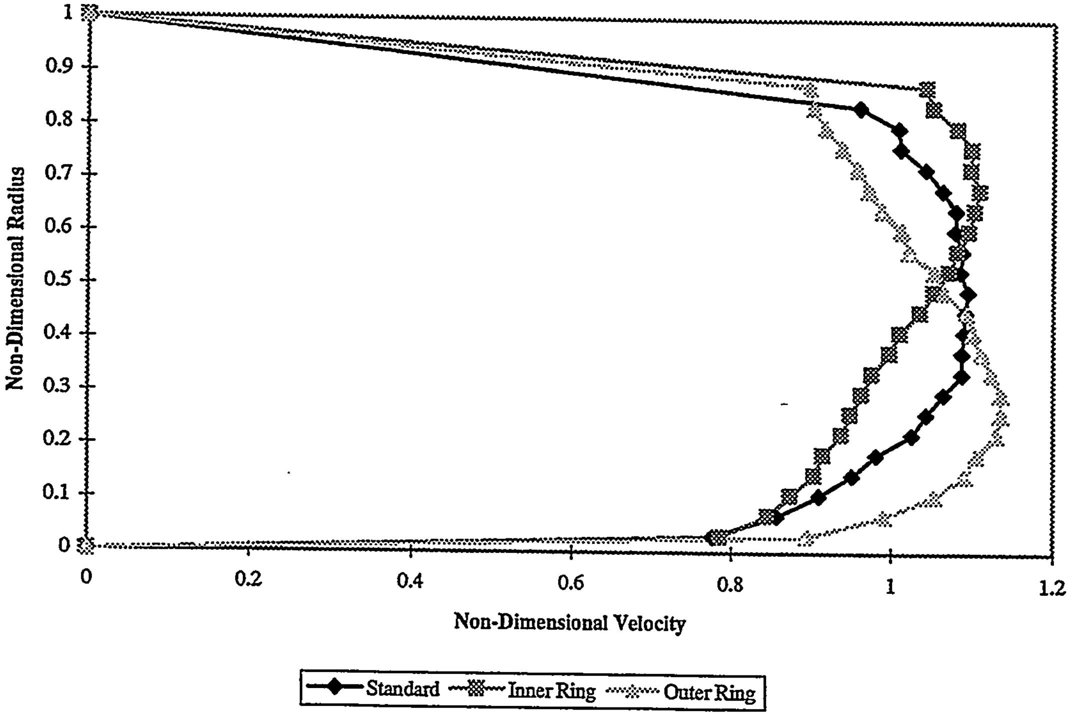

Figure 9. Axial Velocity Profiles in the Flow Developing Section at 80 inches from the Entrance (With and Without Circular Rings)

P23

Bond Strength and Stress Measurements in Thermal Barrier Coatings

Maurice Gell (860-486-3514)
Dept. of Metallurgical Engineering and Institute of Materials Science
Eric Jordan (jordan@eng2.uconn.edu; 860-486-2371)
Dept. of Mechanical Engineering
University of Connecticut
Storrs, CT 06269

Introduction

Thermal barrier coatings have been used extensively in aircraft gas turbines for more than 15 years to insulate combustors and turbine vanes from the hot gas stream. Plasma sprayed thermal barrier coatings (TBCs) provide metal temperature reductions as much as 300°F, with improvements in durability of two times or more being achieved. The introduction of TBCs deposited by electron beam physical vapor deposition (EB-PVD) processes in the last five years has provided a major improvement in durability and also enabled TBCs to be applied to turbine blades for improved engine performance. To meet the aggressive Advanced Turbine Systems goals for efficiency, durability and the environment, it will be necessary to employ thermal barrier coatings on turbine airfoils and other hot section components. For the successful application of TBCs to ATS engines with 2600°F turbine inlet temperatures and required component lives 10 times greater than those for aircraft gas turbine engines, it is necessary to develop quantitative assessment techniques for TBC coating integrity with time and cycles in ATS engines.

Thermal barrier coatings in production today consist of a metallic bond coat, such as an MCrAlY overlay coating or a platinum aluminide (Pt-Al) diffusion coating. During heat treatment, both these coatings form a thin, tightly adherent alumina (Al_2O_3) film. The ceramic layer, usually 5 to 10 mils of yttria stabilized zirconia, is applied over the alumina film by plasma spray or EB-PVD processes.

Failure of TBC coatings in engine service occurs by spallation of the ceramic coating at or near the bond coat to alumina or the alumina to zirconia bonds. Thus, it is the initial strength of these bonds and the stresses at the bond plane, and their changes with engine exposure, that determines coating durability.

The purpose of this program is to provide, for the first time, a quantitative assessment of TBC bond strength and bond plane stresses as a function of engine time and cycles. This information is needed by coating suppliers to provide coatings with higher and more consistent quality. It is also needed by engine manufacturers to determine life remaining in service, as well as to refine fracture mechanics analyses and lifetime prediction models.

Objectives

The objectives of this program are:

1. To develop fundamental understanding of the role of residual stress and bond strength in the failure of TBC's and to use that

---

Research sponsored by U. S. Department of Energy's Morgantown Energy Technology Center, under Contract # 95-01-SR030 with University of Connecticut, Storrs, Connecticut - 06269.

understanding to guide lifetime prediction modeling and coating development.

2. To use new, innovative techniques to obtain quantitative measurements of bond strength and bond stress.
3. To make the data generated as relevant as possible by obtaining representative production coatings tested under simulated ATS conditions in furnace, rig and engine tests from coating suppliers, ATS engine developers, and national laboratories.
4. To coordinate this research with the internal TBC programs at NASA-Lewis Research Center and Oak Ridge National Laboratory; thereby enhancing the scope and depth of this work.
5. To work with ATS engine developers, so this data can be utilized in their fracture mechanics analyses and lifetime prediction models.
6. To place major research emphasis on those bond strength and stress measurement techniques that have the potential for development into non-destructive inspection techniques (NDI) for initial coating quality, and for residual life remaining on service engine components.
7. To transfer NDI techniques to coating suppliers and to ATS engine developers for determination of initial coating quality and for residual life remaining for engine components.

Approach

Based on the extensive research conducted on thermal barrier coatings (TBCs) over the last ten years [1-6], it is possible to describe three essential features to the successful performance of thermal barrier coatings. First, partially stabilized zirconia thermal barrier coatings, that have good thermal stability to 2600°F and good thermal expansion matching with superalloys, are intentionally processed with microstructural defects such as porosity and microcracks to reduce the through-thickness thermal conductivity of the material compared to fully dense zirconia. The lower the thermal conductivity the more effective the coating is as a thermal barrier.

Second, the partially stabilized zirconia must be bonded to the superalloy. This is accomplished with the use of a metallic bond coat, such as an MCrAlY overlay coating or a platinum aluminide diffusion coating. During heat treatment, both these coatings form a thin, tightly adherent alumina (Al_2O_3) film (Figure 1). For plasma deposited TBCs, the bond coat surface is processed to be rough, so as to provide mechanical bonding between the bond coat and the ceramic. For EB-PVD deposited TBCs, the bond coat surface is processed to be smooth, so as to maximize chemical atomic bonding between the alumina and the zirconia. It is the strength of the bonds between the alumina and the superalloy, between the alumina and zirconia, and in the zirconia near the bond line that determines the durability of the coating in engine service.

Since the failure mechanism of thermal barrier coatings in engine service is spallation of the ceramic at or near the bond coat-zirconia interface (Figure 1), the third essential feature of thermal barrier coatings is maintaining low stresses at the bond plane. There are a number of contributors to keeping bond stresses low that include: (1) selection of a bond coat and ceramic that have a moderate thermal expansion mismatch, (2) the creation and maintenance of a microstructure with a low elastic modulus in the plane of the coating, (3) retarding the growth of the alumina film with its attendant volume expansion and increase in stress, and (4) avoiding cyclic creep rumpling of the bond coat with the creation of stress concentrations and additional surface area for oxide growth.

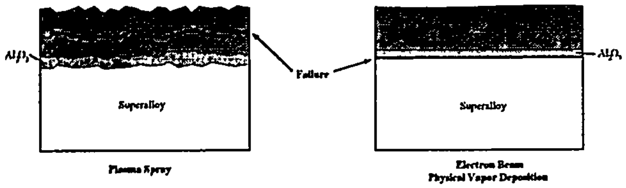

Figure 1:The layered structure and spallation location for plasma sprayed and electron beam physical vapor deposited thermal barrier coatings.

Bond Strength And Stress Changes

In plasma sprayed and EB-PVD deposited TBCs, the bond strengths in the as-coated and heat treated condition are relatively high. The relevant bonds are those that result in spallation in engine service and consist of the superalloy to alumina, the alumina to zirconia, and in the case of plasma deposited TBCs, the zirconia to zirconia bonds in the vicinity of the alumina to zirconia bond plane (Figure 1). With time and cycles in the engine, bond strength tends to degrade as a result of thermal activated interdiffusion between the various layers of the TBC coating. For example, superalloy and bond coat elements have been found on the spalled fracture surfaces of plasma and EB-PVD TBCs [4], and it is known that sulfur diffusion can markedly reduce alumina scale adhesion to superalloys [7].

In contrast, bond plane stresses are relatively low in the as-coated and heat treated condition as a result of bond coats and ceramics selected for moderate thermal expansion mismatch and because of high component temperatures during coating deposition. With time and cycles in the engine, bond plane stresses increase (Figure 2) as a result of (1) sintering of the ceramic, which increases the elastic modulus, (2) growth of the alumina film which involves a volume expansion and increased stress, and (3) "rumpling" of the bond coated resulting from cyclic plastic deformation, resulting in increased surface roughness, stress concentrations, and accelerated oxidation.

Coating Spallation Model

Thus, this state-of--the-art TBC spallation assessment indicates that bond strengths deteriorate and bond stresses increase with increased engine time and cycles. Local coating spallation occurs when the bond stress equals the bond strength (Figure 2). There are two views as to the important processes leading to that failure condition (1) coating failure is a fatigue process enhanced by residual stress effects and bond weakening or (2) failure is an overload, single cycle process. Crack propagation in ceramics is know to be an extremely sensitive function of stress intensity factor, depending for example, on the 20th power of the stress intensity factor [8]. For such behavior, once a cracks begins growing, failure will rapidly occur. Accordingly it may be that most of the life is spent in bond strength degradation and residual stress increase. The observation of prefailure damage at 20-30 percent of the coating life consisted of linking smaller cracks [9]. It may be that the accumulating residual strain is relieved by microcracking until there is so much crack linking that spallation occurs. In this study, we will obtain sufficient information on residual stress evolution and bond strength degradation to begin to distinguish between these two hypotheses.

In summary, the three essential features of successful thermal barrier coatings are: low thermal conductivity, high bond strength, and low bond plane stresses. For a given thermal barrier coating operating in a specific thermal environment, the durability of the coating is determined by the changes in bond strength and bond stress with time and cycles in the engine, as illustrated in Figure 2.

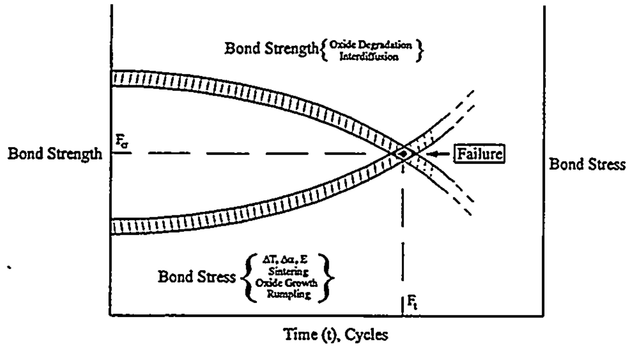

Figure 2: Coating spallation failure model based on the changes in bond strength and stress with engine cycles and time.

Project Description

In this program a number of analytical instrumental techniques, that are illustrated below, will be evaluated to quantitatively measure:

(I) TBC bond plane stresses as a function of time by (a) enhanced laboratory x-ray diffraction, (b) enhanced synchrotron x-ray diffraction, (c) laser fluorescence, (d) neutron diffraction, and (e) AC potential drop measurements and

(II) TBC bond strength by using: (a) a modified ASTM direct pull test, (b) laser-induced ultrasonics, (c) a cyclic Hertzian ball indentation test, and (d) a bend toughness test.

These tests will be conducted on current production TBC coatings, including plasma sprayed and EB-PVD deposited yttria stabilized zirconia thermal barrier coatings with both MCrAlY and Pt-Al bond coats. The specimens will be tested in a severe thermal cyclic environment, approximating ATS engine conditions.

I a. Enhanced Laboratory X-ray Diffraction

In measuring stress by x-ray diffraction, a single wave length x-ray beam is directed at a surface of interest and the diffracted intensity is measured as a function of scanning angle. Here the purpose is to measure the residual stress on the surface of the bond coat which is beneath the ceramic coating (Figure 3). Since the illuminating beam and the diffracted beam passing through the ceramic will suffer some attenuation, the following method is adopted: The wavelength of the illuminating beam is to be chosen to have a wavelength corresponding to local absorption minimum, which should be just below the zirconia absorption edge (≈17 KeV photon energy). Also the intensity of the illuminating beam will be maximized by use of a Johanssen ground and bent single crystal (Figure 4). to yield a beam of > 10^8 counts/sec. [10]

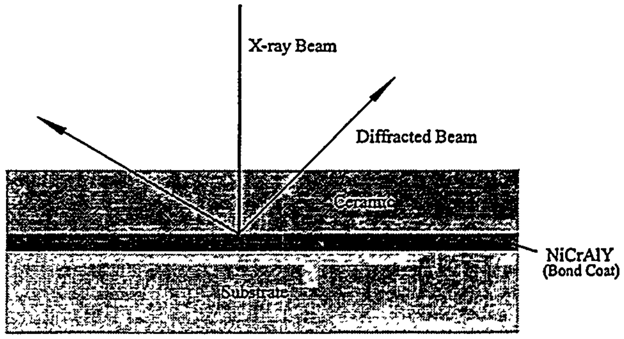

Figure 3: Schematic of a X-ray diffraction experiment on a TBC.

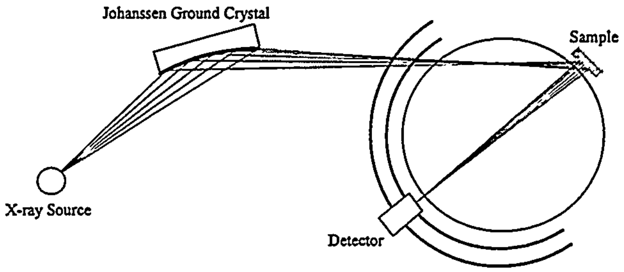

Figure 4: Enhancement of an incident X-ray beam using a Johanessen bent crystal.

I b Enhanced Synchrotron X-ray Diffraction

In the proposed experiments, an annular blocking slit with a large area detector behind it will be used to detect the entire diffraction cone, (Figure 5) mounted on a precision translator is to be used so that different diffraction lines may be selected. An increase of about 100X in the diffracted intensities compared to the usual configuration, is estimated.

The incident sagitally focused (pencil) beam with an intensity $>10^9$ counts/sec and having a beam size of only 1 mm x 1 mm will allow one to probe point by point and explore spatial variation in the residual stress [11]

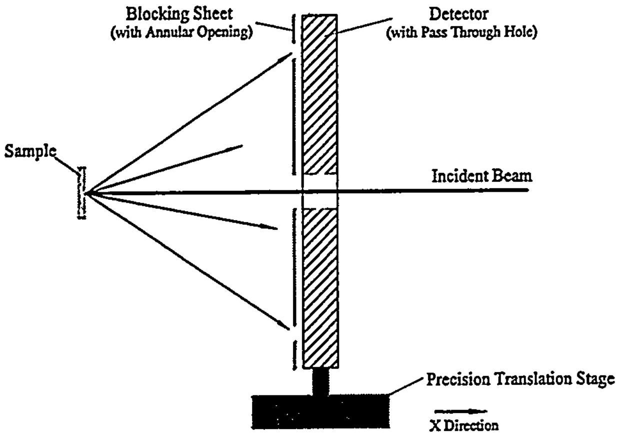

Figure 5: Schematic showing the collection of diffracted beam through an annular blocking slit.

I c Laser Fluorescence

The frequency shift in the fluorescence spectra of the alumina layer, characteristic of chromium-doped alumina, provides a means of non-destructively measuring the stress in alumina scales using the piezo-spectroscopic effect [12]. Furthermore, the broadening of the lines can be used to measure of the stress gradient. Zirconia based thermal barrier coatings (TBC) being optically translucent at certain wavelengths will be examined for the stress in the oxide scale formed on the bond coat underneath the TBC. (Figure 6 & 7)

The laser fluorescence work will be performed by Prof. David Clarke of University of California, Santa Barbara.

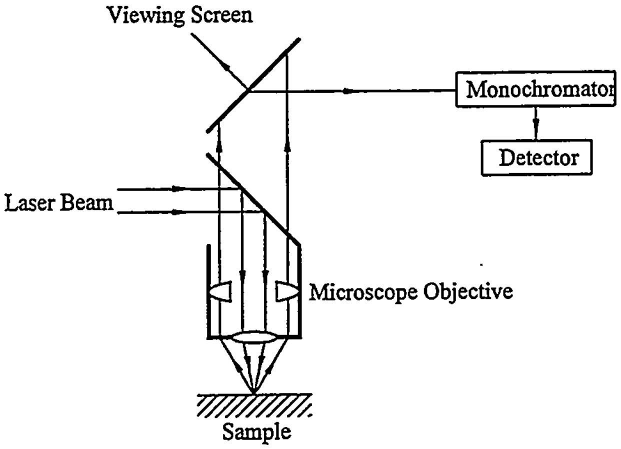

Figure 6: Experimental setup for performing laser fluoroscence[12].

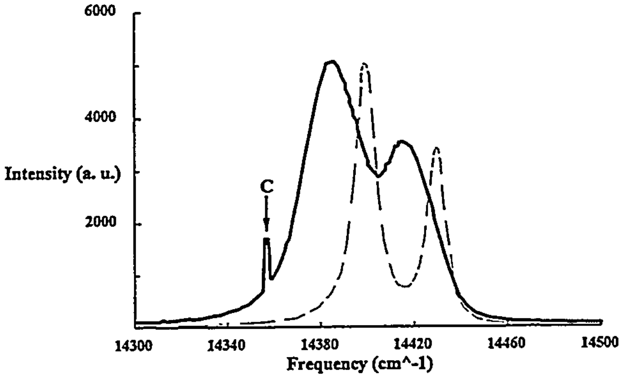

Figure 7: Spectra shows the shift in the frequency number for alumina scale under residual stress[12].

I d Neutron Diffraction

Neutrons are highly penetrating and diffract according to Braggs law, based on their DeBroglie wave lengths, in a manner directly analogous to x-rays. In the proposed work, a diffractometry setup called the Intense Pulsed Neutron Source (IPNS) (Figure 8) used for examining residual stress in subsurface fiber in composites, is to be utilized [13]. Here, the average residual stress developed at the crystallographically distinct bond coat and the alumina layer that forms at the bond coat to ceramic interface, is to be measured. The primary challenge in carrying out this technique is the relative small volume of the phases of interest (bond coat and alumina), which leads to relative few diffracted neutrons.

Neutron diffraction measurements will be conducted at Argonne National Labs and/or at Oak Ridge National Lab.

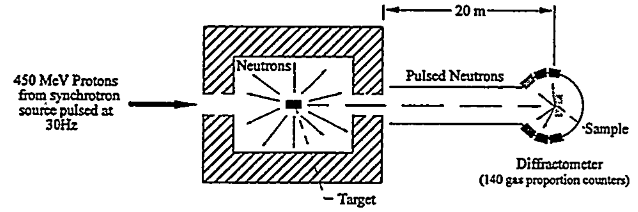

Figure 8: Schematic of the neutron diffraction facility

I e AC Potential Drop

In this technique, an alternating current is induced in the sample and a patented method is used to confine the current flow to a narrow line on the surface of the sample [14] (Figure 9). In addition to current confinement, the sensitivity of the method has been enhanced by the use of lock-in detection methods. Information is obtained as a function of depth by scanning in frequency, with the higher frequency current confined to the near surface location by the skin effect. This method has been successfully used to reliably detect small cracks in fatigue crack "initiation" experiments [15].

This work will be done by Dr. Norman Marchand of AMRA Inc.

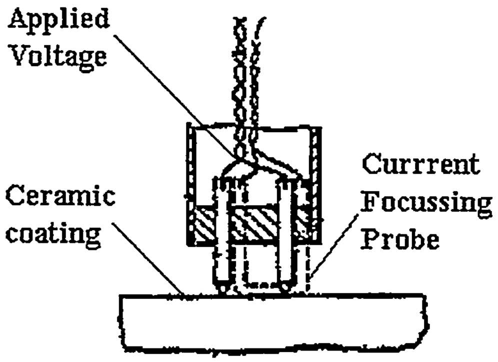

Figure 9 Schematic of AC potential drop measurement technique[15].

II a Modified ASTM Direct Pull Tests

Most thermal barrier bond strength testing to date has been done using methods similar to the ASTM Standard C633-79 "Standard Test Method for Adhesion or Cohesive Strength of Flame-Sprayed Coatings" in which a coating is applied to the end of a cylindrical bar and another bar is bonded to the top surface using a polymer adhesive. The assembly is then tested in tension to fail the ceramic metal interface (Figure 10). This type of test is unfortunately not suitable for unaged coatings, because the adhesive fails first and coating interface values are not obtained [16]. However successful tests using this method were done on thermally aged samples in which the TBC bond strength was reduced. The stress state in these direct pull tests is quite complex due to mismatch in mechanical properties and due to the non uniform stress distribution caused by attachment holes [16]. A recent design improvement will be incorporated into the test system design to produce dramatically more uniform stress distribution [17]. In addition improved adhesives and adhesive processing will be employed to provide higher failure stresses.

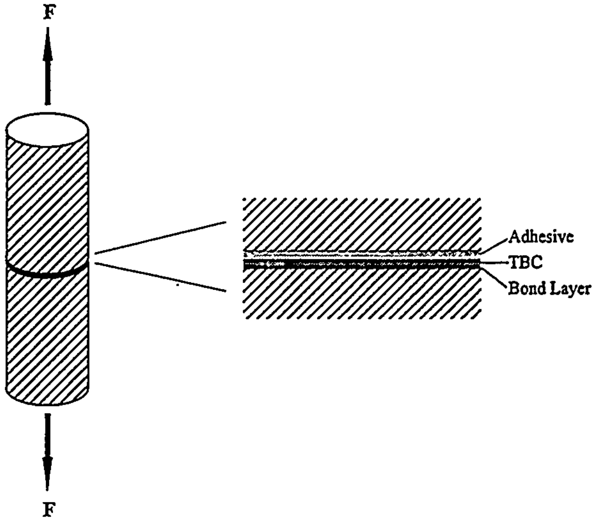

Figure 10: Blow-up of the specimen to be used for pull tests.

II b Laser Induced Ultrasonic Testing

In this recently developed method of testing, a laser induced sonic pulse is used to produce coating spallation [18,19]. In this method a very short duration laser pulse is made to fall on a gold foil behind a quartz window (Figure. 11). The sudden heating produces an intense acoustic pulse that reflects off the free surface of the coating, producing a tensile pulse that fails the coating. The stress at the coating interface is calculated from the measured acoustic pulse. This method produces a stress state free of the undesirable effects of bending and constraint present in most other test including the ASTM test.

This work will be done by Prof. Vijay Gupta of University of California, Los Angeles.

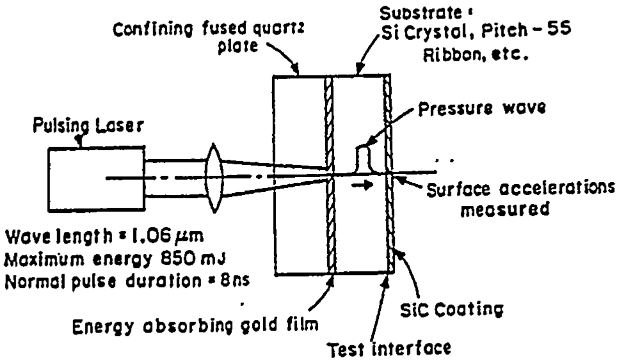

Figure 11: Illustration of coating spallation through LASER induced ultrasonic wave.[19].

II c Hertzian Ball Indentation Test

The Hertzian indentation test is chosen because of its ability to replicate the actual mode of failure of coatings in actual situations. Preliminary experiments have revealed that a common mode of coating failure exists between the specimens tested using the Hertzian indentation test and specimens subjected to simulated ATS engine conditions in both cases the coating failed within the ceramic but near the ceramic–bond coat interface [20]

Preliminary experiments on plasma sprayed coatings have suggested that during loading both coating and substrate deform elastically and plastically (Fig. 12). During unloading, due to a large amount of plasticity in the substrate and the bond coat relative to the ceramic coating, there is differential elastic recovery in the system.

This elastic recovery mismatch results in tensile stresses normal to the coating-substrate interface, and drive the delamination crack within the ceramic but near the ceramic bond coat interface (Fig. 13).

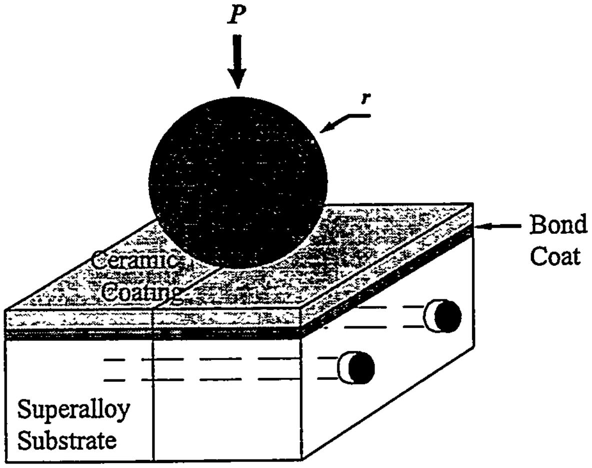

Figure 12: The Ball indendation test

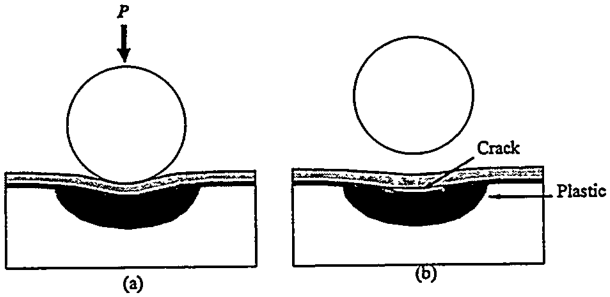

Figure 13: Plastic zone formation due to difference in the recovery rate.

II d Delamination Toughness Test

For brittle materials, the fracture strength, is directly related to their crack propagation resistance according to the well-known Griffith formula. According to the Griffith equation, measurement on the fracture energy of the interfacial region between the PSZ coating and the superalloy substrate reflects the strength of this interfacial region because of the brittle nature of the PSZ and PSZ/bond-coat interface. A sandwich-type chevron-notched specimen proposed by Shaw, *et al.* [21-23] is most attractive for our current applications. This specimen geometry can be modified to measure the bond strength between the thermal barrier coating and the superalloy substrate. The specimen consists of a thin layer (bond coat and PSZ coat) within an otherwise elastically homogeneous specimen with a chevron notch along the bond coat plane. The bonding between a superalloy block and a coated superalloy is formed through epoxy.

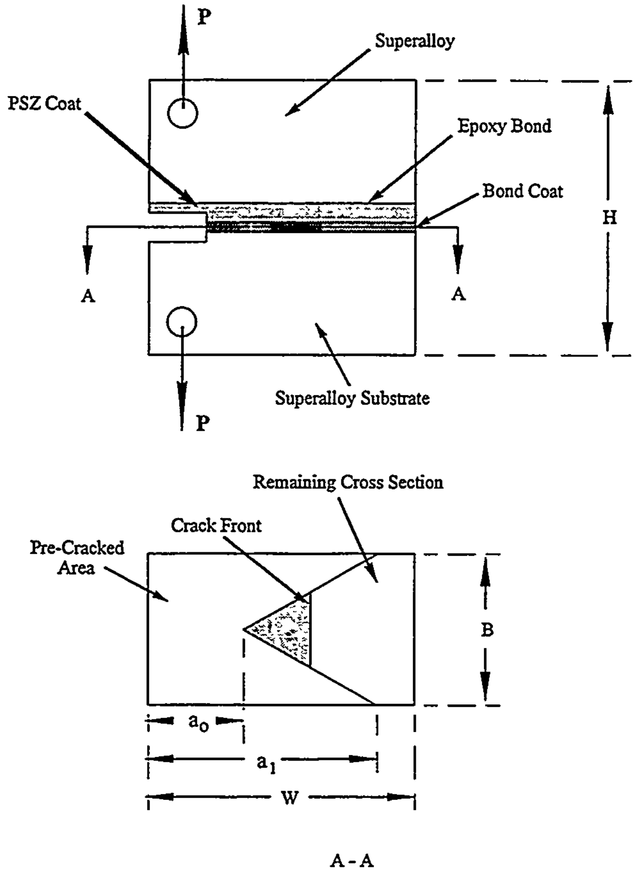

Figure 14: Sketch of the sample for delamination toughness measurements.

The chevron notch introduced only faces the PSZ/bond-coat and bond-coat/superalloy interfaces, as shown in Figure 14, to insure that the initiation and propagation of the crack is at the weakest position between the PSZ and superalloy substrate.

Benefits

The benefits of this program are to advance the state-of-the art of TBCs by providing a quantitative measurement of bond strength and bond plane stresses. These studies will be closely coordinated with ATS engine developers and coating suppliers, so that TBCs can be successfully implemented in support of ATS durability and performance goals. The results of this program will help to ensure that thermal barrier coatings in ATS will demonstrate "prime reliability;" i.e., they will be deposited and used in a way that will provide protection for the entire life of the component. This program also seeks to identify non-destructive inspection techniques that can be used to verify initial coating quality and to determine residual life remaining on engine service components.

Future Activity

The University of Connecticut has assembled a strong, knowledgeable team with a wealth of gas turbine engine and thermal barrier coating experience to conduct this program. The team consists of University investigators (University of Connecticut, University of California-Santa Barbara, University of California - Los Angeles, Ecole Polytechnique (Montreal), ATS engine developers (Allison Engine, General Electric, Solar Turbines, TurboPower and Marine, and Westinghouse Electric), coating manufacturers (Howmet Corporation and Pratt & Whitney), National Laboratories conducting TBC research (Oak Ridge National Laboratory, NASA-Lewis Research Center, and Argonne National Laboratory) and AGTSR member universities performing TBC research (Georgia Tech, Lehigh, Penn State). In addition, this program is structured to strongly contribute to the educational goals of ATS by providing industrial engine and TBC research experience to a number of graduate students.

The program was initiated September, 1995. Figure 15 shows the program schedule. The nine techniques for evaluating bond strength and stress will be evaluated in the first year. The best methods will be selected. In the second and third year the selected measurement techniques will be optimized and quantitative measurements of bond stress and strength will be obtained as a function of simulated engine cycles.

Acknowledgments

This research is sponsored under a subcontract from the South Carolina Energy Research and Development Center. We appreciate the interest and guidance of Dr. Daniel Fant, the AGTSR Program Manager.

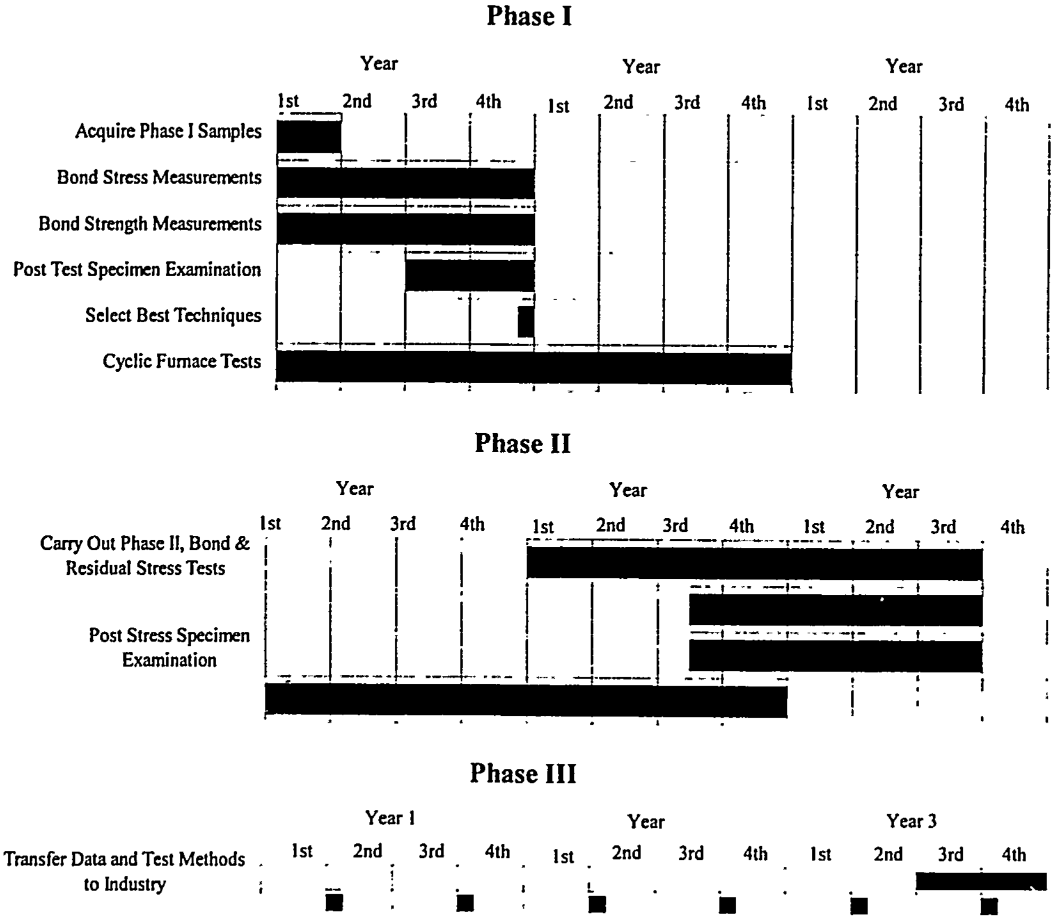

Figure 15 : Program Schedule

References

1. Meier, S. Manning, D. K. Gupta and K.D. Sheffler, "Ceramic Thermal Barrier Coatings for Commercial Gas Turbine Engines," JOM, 50-53, March 1991.
2. Hillery, R. V., and B. H. Pilsner, "Thermal Barrier Coating Life Prediction: Second Annual Report," NASA CR-179504, General Electric Company, 1986.
3. Strangman, T. E., J. Neumann and A. Liu, "Thermal Barrier Coating Life-Prediction Model Development Second Annual Report," NASA CR-179507, Garrett Turbine Engine Company, 1986.
4. Meier, S. M., D. M. Nissley and K.D. Sheffler, "Thermal Barrier Coating Life Prediction Model Development: Phase II-Final Report," NASA CR-189111, Pratt & Whitney, 1991.
5. Miller, R. A., and C. E. Lowell, "Failure Mechanisms of Thermal Barrier Coatings Exposed To Elevated Temperatures," Thin Solid Films, 99, p.265, 1982.
6. Gell, M., D. N. Duhl, D. K. Gupta and K.D. Sheffler, "Advanced Superalloy Airfoils," JOM, p. 11, July 1987.
7. Smialek, J. L., D. T. Jayne, J. C. Schaeffer and W. H. Murphy, "Effects of Hydrogen Annealing, Sulfur Segregation, and Diffusion on the Cyclic Oxidation Resistance of Superalloys: A Review," Thin Solid Films, 253, p. 285, 1994.
8. Ritter, J. E., "Crack Propagation in Ceramics", in Engineering Materials Handbook, vol. 4, Ceramics and Glasses, ASM International, p 694, 1991.
9. DeMasi, J. T., Sheffler, K. D. and Ortiz, M., "Thermal Barrier Coating Life Prediction Model Development," NASA CR 182230, 1989.
10. Canistraro, H. A., Jordan,E. H. , and Pease, D. M. 1992. "X-ray Based Displacement Measurement For Hostile Environments," Experimental Mechanics, 32, vol 4, p 289.
11. Geogopoulos, P. and Cohen, J. B., "Residual Stress Measurement of a Plasma Sprayed Coating Using Synchrotron X-ray Radiation," Materials Science and Engineering, 80, p L41, 1986.
12. Ma, Qing and Clarke, D. R. , "Stress Measurement in Single-Crystal and Polycrystalline Ceramics using their Optical Flourescence" J. of Am. Ceram. Soc. , Vol 76, p 1433, 1993.
13. Kupperman, D.S., Majumdar, J.P., and Singh, J.P., "Neutron Diffraction NDE for Advanced Composites," J. Eng. Mat. and Tech., 112, p 198, 1990.
14. Dai, Y. Marchand, N. J. and Hongoh, M., "Study Of Fatigue Crack Initiation and Growth In Titanium Alloys Using ACPD technique," Canadian Aeronautics and Space Journal, n.1, vol 39, p 35, March 1993.
15. Marchand, N. J. Dorner, W. and Ilschner, B., "A Novel Procedure to Study Crack Initiation and Growth in Thermal Fatigue Testing," ASTM STP 1060, p. 237,1990.
16. DeMasi, J. T., Sheffler, K. D. and Ortiz, M., "Thermal Barrier Coating Life Prediction Model Development," NASA CR 182230 1989.
17. Han, W. Rybicki, E. F. and Shadley, J. R. , "Bond Strength Testing of Thermal Spray Coatings Using ASTM C633-79: Effect of Specimen Size on Test Results," Thermal Spray: International Advances in Coatings Technology, Proceedings of the International Thermal Spray Conference, ASM International, p.911, 1992.
18. Gupta, V. Argon, A. S. , Cornie, and Parks, D. M., Mater. Sci. Eng. A 126, p.105.(1990)

19. Cornie, J. A. Argon, A. S. , Gupta, V "Designing Interfaces in Inorganic Matrix Composites," MRS Bulletin, p 32 April 1991.
20. Guiberteau, F., Padture, N. P. and Lawn, R., "Effect of Grain Size on Hertzian Contact Damage in Alumina," J. of Am. Cer. Soc. Vol. 77, p. 1825, 1994.
21. Shaw, L. and R. Abbaschian, "A Test Specimen for Characterizing the Fracture Energy of Interfaces in Composites", in Control of Interfaces in Metal and Ceramics Composites, edited by R. Y. Lin and S. G. Fishman, A Publication of TMS, p 211, 1994.
22. Shaw, L., D. Miracle and R. Abbaschian, "Microstructure and Mechanical Properties of Metal/Oxide and Metal/Silicide Interfaces", Acta Metall. Mater., in press 1995.
23. Suo, Z. and J. W. Hutchinson, "Sandwich Test Specimens for Measuring Interface Crack Toughness," Mater. Sci. Eng., A107, p 135, 1989.

P24

Active Control of Combustion Instabilities in Low No_x Gas Turbines

B. T. Zinn (404-853-9159)
Y. Neumeier (404-853-9159)
School of Aerospace Engineering
Georgia Institute of Technology
Atlanta, GA 30332-0150

Abstract

This 3-year research program was initiated in September, 1995, to investigate active control of detrimental combustion instabilities in low NO_x gas turbines (LNGT), which burn natural gas in a lean premixed mode to reduce NO_x emissions. The program will investigate the mechanisms that drive these instabilities. Furthermore, it will study active control systems (ACS) that can effectively prevent the onset of such instabilities and/or reduce their amplitudes to acceptable levels. An understanding of the driving mechanisms will not only guide the development of effective ACS for LNGT but may also lead to combustor design changes (i.e., passive control) that will fully or partially resolve the problem. While passive control of combustion instabilities would be preferable due to its simplicity, experience to date indicates that it does not provide satisfactory solutions. Consequently, alternate approaches for preventing LNGT instabilities, such as active control, will have to be developed.

Initial attempts to stabilize combustors (i.e., chemical rockets) by ACS were reported more than 40 years ago, but were unsuccessful due to lack of adequate sensors, electronics, and actuators for performing the needed control actions. Progress made in recent years in sensor and actuator technology, electronics, and control theory has rekindled interest in developing ACS for unstable combustors. While initial efforts in this area, which focused on active control of instabilities in air breathing combustors, have demonstrated the considerable potential of active control, they have also indicated that more effective observers, controllers, and actuators are needed for practical applications. Considerable progress has been made in the observer and actuator areas by the principal investigators of this program during the past 2 years under an AFOSR program. The developed observer is based upon wavelets theory, and can identify the amplitudes, frequencies, and phases of the five most dominant combustor modes in (virtually) real time. The developed actuator is a fuel injector that uses a novel magneto-strictive material to modulate the fuel flow rate into the combustor. The latter damps instabilities by interfering with the instability driving mechanisms and/or generating pressure oscillations that destructively interfere with the unstable combustor oscillations. The developed fuel actuator produces fuel flow rate oscillations with significant amplitudes and frequencies up to 1500 Hz, which is considerably higher than the maximum frequency of any known fuel injector. These observer and fuel injector will

---

Research supported by the U.S. Department of Energy Morgantown Energy Technology Center, under Contract DE-FC21-92MC29061 with Georgia Institute of Technology, Atlanta, GA;
Fax: 404-894-2760

be modified for LNGT applications and incorporated into an ACS whose effectiveness in controlling LNGT instabilities will be investigated under the proposed program.

The proposed research will consist of parallel experimental and theoretical studies. The theoretical efforts will develop models of the LNGT that will be used as a platform for the development and testing of ACS for LNGT. A simplified solution obtained with the Galerkin method, developed by one of the principal investigators of this program (Zinn), will provide a simplified analytical model that is needed for the development of the control approach. In view of the approximate nature of the Galerkin method, a numerical model for investigating active control will be also developed. It incorporates a numerical solution of ID Euler equations with a heuristic model of the combustor mixing processes and a global, Arrhenius type, description of the reaction rate. Such a model has been developed by the principal investigators under the AFOSR program and will be modified in the proposed studies to accommodate specific features of LNGT. The validity of the developed models will be checked by comparing their predictions with one another and measured data. Once validated, they will be used to investigate the effectiveness of various ACS and determine the configurations (e.g., location of the fuel actuator) that optimize their performance.

The experimental efforts will develop a small scale LNGT simulator that will be used to investigate the mechanisms that drive LNGT instabilities and the effectiveness of various ACS. This facility will simulate the salient features of LNGT combustors, and consist of variable lengths air inlet, mixing, and combustor sections. It will also utilize swirlers and gaseous fuel injectors similar to those in practical LNGTs. The setup will also include a rotary valve that will periodically interrupt all or a fraction of the exhaust flow and, thus, drive oscillations of desired amplitudes and frequencies within the setup. This capability will be used to study active control of instabilities over a wide range of LNGT operating conditions. The setup will be equipped with optical windows to permit high-speed flow and combustion process visualizations, and possess capabilities for measuring the spatial and temporal variations of acoustic pressure, temperature, and reaction rate, and exhaust flow concentrations of NO_X, CO_2, CO, and O_2. These data will be used to determine the mechanisms that drive LNGT instabilities, the manner in which a periodic, secondary, combustion process driven by a fuel injector actuator affects these instabilities and combustor operation, and the effectiveness of investigated ACS.

P25 Combustion Instability Modeling and Analysis

Robert J. Santoro (RJS@ECL.PSU.EDU; 814-863-1285)
Vigor Yang (VIGOR@ARTHUR.PSU.EDU; 814-863-1502)
Domenic A. Santavicca (VMS1@OAS.PSU.EDU; 814-863-1863)
The Pennsylvania State University
Research Building East, Bigler Road
University Park, PA 16802

Eric J. Sheppard (SHEPPARD@TUSK.EDU; 205-727-8851)
Tuskegee University
Dept. of Aerospace Engineering
Tuskegee, AL 36088

Abstract

It is well known that the two key elements for achieving low emissions and high performance in a gas turbine combustor are to simultaneously establish (1) a lean combustion zone for maintaining low NO_x emissions and (2) rapid mixing for good ignition and flame stability. However, these requirements, when coupled with the short combustor lengths used to limit the residence time for NO formation typical of advanced gas turbine combustors, can lead to problems regarding unburned hydrocarbons (UHC) and carbon monoxide (CO) emissions, as well as the occurrence of combustion instabilities. Clearly, the key to successful gas turbine development is based on understanding the effects of geometry and operating conditions on combustion instability, emissions (including UHC, CO and NO_x) and performance. The concurrent development of suitable analytical and numerical models that are validated with experimental studies is important for achieving this objective. A major benefit of the present research will be to provide for the first time an experimentally verified model of emissions and performance of gas turbine combustors.

The present study represents a coordinated effort between industry, government and academia to investigate gas turbine combustion dynamics. Specific study areas include development of advanced diagnostics, definition of controlling phenomena, advancement of analytical and numerical modeling capabilities, and assessment of the current status of our ability to apply these tools to practical gas turbine combustors. The present work involves four tasks which address, respectively, (1) the development of a fiber-optic probe for fuel-air ratio measurements, (2) the study of combustion instability using laser-based diagnostics in a high pressure, high temperature flow reactor, (3) the development of analytical and numerical modeling capabilities for describing combustion instability which will be validated against experimental data, and (4) the preparation of a literature survey and establishment of a data base on practical experience with combustion instability. This last task is intended to provide a mechanism for scaling the results of the laboratory and sub-scale studies to actual gas turbine engine applications.

Research sponsored by the U.S. Department of Energy's Morgantown Energy Technology Center, under contract DE-FC21-92MC29061 with Penn State University, University Park, PA 16802; telefax (814)865-3389.

The assembled team includes both theorists and experimentalists from The Pennsylvania State University and Tuskegee University. Specific arrangements have also been made with Morgantown Energy Technology Center participation in both the experimental and analytical aspects of the work. Practical application of the fiber-optic probe developed during the research effort is planned in collaboration with the Westinghouse Power Generation Business Unit and General Electric Power Generation.

Background

The key to achieving low emissions and high performance in gas turbine combustors involves achieving rapid mixing under conditions which assure good ignition and combustion stability characteristics while rapidly establishing a lean combustion zone to maintain low NO_x emissions. These requirements, when coupled with the short combustor lengths to limit the residence time for NO formation typical of advanced gas turbine combustors, can lead to problems regarding unburned hydrocarbons (UHC) and carbon monoxide (CO) emissions as well as the occurrence of combustion instabilities. Thus, issues related to combustion instability, low emissions and suitable performance are intimately linked for advanced gas turbine combustors, and must be addressed concurrently in any study. The present research effort involves experiments and analysis of combustion dynamics under conditions that examine the relationship between mixing, emissions and combustion stability which properly address a gas turbine combustor environment.

Combustion instabilities are observed in a wide variety of combustors including liquid and solid propellant rockets, ramjets, afterburners, gas turbines and furnaces [see Refs. 1-7]. The occurrence of combustion instability is accompanied by large periodic pressure oscillations, increased heat transfer, and resulting structural vibration. The most troublesome instabilities are associated with high energy density environments and typically correspond to the acoustic modes of the combustion chamber. The onset of the instability is sensitive to combustor design and fuel/oxidizer ratio, and results from the coupling between the gas dynamic flow field and the combustion distribution in the combustor [2-4]. Initiation of combustion instability requires only a small fraction of the available energy and is often observed to be self-exciting. The general mechanism leading to amplification of pressure waves in the chamber is given by Rayleigh's criterion which states that the energy from combustion must be released in-phase with the pressure oscillation being excited in the chamber [8]. The growth of the instability is a result of the net amplification of the pressure wave which requires that any attenuation or losses in the chamber are overcome by the amplification process. Since most combustors act as nearly closed chambers, they weakly attenuate unsteady motions. In summary, the spatial and temporal characteristics of combustion, the chamber geometry, the associated mean gas flow, and the boundary conditions associated with the inlet and exit flows must all be considered in a comprehensive study of combustion instability.

With regard to gas turbine combustors, combustion dynamics are often associated with two general processes: (1) self-excited instabilities occurring spontaneously as a result of the combustor response and (2) flow dynamics associated with the compressor. In the present study, both of these processes will be examined. The first will be studied explicitly by experimentation and analyses of a high pressure model combustor, and the second will be addressed by experimentally investigating the effects of inlet air conditions on combustion dynamics. When one discusses mechanisms by which combustion instability is initiated and sustained, a number of fundamental phenomena can be identified which potentially can drive the combustion dynamics. These processes are listed in Table 1. Many of these processes involve atomization and droplet phenomena that are not of direct relevance to the land-based, natural gas fueled combustors which are of interest for the present study. Consequently, the focus here is on mechanisms related to injector coupling, combustion zone distribution, fluid dynamic interactions and chemical kinetic effects.

The present study represents a coordinated effort to investigate combustion dynamics in terms of the diagnostic needs, phenomena controlling its occurrence, advancing analytical and numerical modeling capabilities, and assessing the current status of our ability to apply these tools to practical gas turbine combustors.

Table 1. Mechanisms For Driving Combustion Instabilities

Mechanism	Description
Atomization	Periodic perturbation of spray formation
Droplet-droplet Interaction	Secondary atomization or coalescence
Droplet Vaporization	Unsteady vaporization
Injector Coupling	Periodic variations in fuel and oxidizer flows
Combustion Zone Distribution	Coupling with acoustic modes
Fluid Dynamic Interactions	Vortex shedding
Chemical Kinetic Mechanisms	Finite chemistry
Nozzle Effects	Admittance effects
Turbulence Effects	Mixing and droplet turbulence interactions

Objectives

The objectives of the current research parallel the emphasis of the study to provide a basic understanding of the mechanisms that control the initiation and sustenance of combustion instabilities under conditions typifying low emission, high performance gas turbine combustors. Three specific objectives are being addressed by tasks described in the next section.

The key objective is to develop the basis for a predictive capability for gas turbine combustion stability, emissions, and performance. A major benefit of this research will be to provide <u>for the first time</u> an experimentally verified modeling capability to understand the conditions under which combustion instabilities occur in gas turbine combustors, specifically under conditions that also relate to low emissions and high performance operation. A cohesive understanding of the effects of combustor design and operating conditions on combustion instability, emissions (including UHC, CO and NO_x) and performance is critical to future gas turbine development. The concurrent development of suitable analytic and numerical models that are validated with the results of these experimental studies is also being pursued.
The experimental results and analytical tools developed for this program can then be used by designers for optimal gas turbine systems.

The second objective of the study is to develop and extend to practical gas turbine combustor environments, a novel fiber optic probe to measure the degree of fuel-air mixing *in-situ*.
The availability of such diagnostics is critical to the practical realization of the understanding gained from the experimental and modeling aspects of the current research program.

The final objective of the current effort is to address the issue of scaling of the results obtained in laboratory and sub-scale studies to actual land-based gas turbine hardware. This objective will be achieved through appropriate model comparisons with existing data documenting practical experience with combustion instability problems encountered in actual applications. An important part of this objective will be met by a comprehensive literature survey and establishment of the necessary data base through interaction with the gas turbine manufacturers to identify the appropriate practical experience base.

Fiber Optic Probe for Fuel-Air Ratio Measurements

The goal of the AGTSR Program is to increase the efficiency of land-based gas turbines by operating at higher combustion temperatures while decreasing NO_x emissions. In order to accomplish this objective, gas turbine manufacturers are attempting to develop various lean prevaporized premixed (LPP) and direct injection (DI) combustor concepts. An important consideration in both types of combustors is the degree to which the fuel and air are mixed immediately upstream of the flame stabilization zone, since both temporal and spatial non-uniformities can result in a significant increase in NO production as compared to the perfectly mixed case [9].

The uniformity of the fuel/air distribution is also important in terms of achieving a uniform pattern factor at the turbine inlet. This is particularly true when attempting to increase the average turbine inlet temperature to near the maximum temperature limit of the turbine blades. In addition, the degree of fuel-air mixing can affect the stability of the combustor, both in terms of lean blowout and combustion oscillations [9].

One concludes, therefore, that in order to increase efficiency by operating at higher combustion temperatures, it is essential to understand the limits imposed by fuel-air mixing on NO_x emissions, the pattern factor, lean blowout and combustion oscillations. This requires that diagnostics be available for characterizing the fuel-air distribution, where the measurement must be both spatially and temporally resolved. Considerable success has been achieved in our laboratory in the use of acetone laser-induced fluorescence (LIF) for making such measurements in laboratory scale combustors [9]. This technique yields the spatial distribution of both the mean and the rms fluctuation of the fuel-air equivalence ratio.

The objective of the present research is to develop fiber optic probes based on the laser-induced fluorescence technique which can be used to make spatially and temporally resolved equivalence ratio measurements in full-scale industrial combustors. Such a measurement capability is essential in determining the fuel-air mixing characteristics of full-scale industrial combustors in order to assess the effect of the fuel-air distribution on combustor performance, i.e., NO_x emissions, pattern factor, lean blowout and combustion oscillations. Clearly, our understanding of the effects of fuel-air mixing on combustor performance will be of most value in the development of full-scale industrial combustors with a more complete knowledge of the fuel-air distribution in such combustors.

The development of the fiber optic fuel-to-air ratio measurement probe is being carried out in collaboration with an on-going project supported by Westinghouse, and previously supported by General Electric Power Generation. The probe, as it is currently configured, is 5/8 inch in diameter, water cooled, and is comprised of two quartz fibers, one for transmitting the laser beam to the measurement point and the other for transmitting the collected fluorescence signal to the photomultiplier tube. The current probe is based on the acetone LIF technique and employs the 266 nm output of a pulsed frequency quadrupled Nd:YAG laser. The spatial resolution of the current probe is approximately 2 mm x 2 mm x 5 mm and the measurement rate is 10 Hz.

The specific objectives of the current research are three-fold. The probe will be redesigned to make it more compact and to improve its spatial and temporal resolution. The probe optics will be redesigned to increase the spatial resolution by at least a factor of two. Secondly, the probe will be tested in combustor facilities at Westinghouse (Orlando, FL), General Electric (Schenectady, NY), and METC (Morgantown, WV). It will also be evaluated and improved as required. And lastly, a modified version of the fiber optic fuel-to-air ratio measurement probe will be developed for use in liquid fueled combustors. This probe will be extensively tested at Penn State followed by preliminary tests at a yet to be selected industrial or government site.

Experimental Studies of Combustion Dynamics

Previous studies of combustion dynamics in rockets and ramjets [1-3] have clearly established the importance of combustion distribution and chamber geometry in the initiation and sustenance of instabilities. As previously mentioned, the growth of pressure oscillations is closely coupled to in-phase energy addition as described by Rayleigh's criterion [8]. Since energy release in gas turbine combustors is controlled by fuel-air ratio, mixing and inlet flow conditions, the effects of these parameters on combustion distribution have been selected for detailed study.

An extensive set of measurements will be obtained to determine the combustion distribution in the reactor under conditions corresponding to unstable and stable combustion conditions. In all experiments CO_2, NO_x and CO emissions will be monitored simultaneously at the reactor exit to relate combustion dynamics to actual emission and performance characteristics of the reactor. This is a critical requirement since it is always possible to operate at conditions which assure either high performance <u>or</u> low emissions <u>or</u> stable operation. However, the challenge for current gas turbine combustors is to achieve all three conditions simultaneously.

The combustion distribution is a key quantity to be determined in order to establish the combustion response function which controls the initiation and sustenance of the pressure oscillations which accompany combustion dynamics. These measurements and the resulting map of operating conditions that discriminates stable and unstable operation will be combined with modeling studies to yield an experimentally validated model of combustion dynamics appropriate for gas turbine combustor design.

To develop the empirical map, a series of investigations using the high pressure, high temperature turbulent flow reactor have been initiated with air temperatures up to 1000 K with methane as the fuel species. Facilities at Penn State currently exist to provide operation at 1000 K and 10 atm at air flow rates up to 0.5 lb/s.

Experiments are being conducted over a range of fuel-air ratios to map out the parameter space over which stable and unstable operation is observed. Lean premixed and direct injection combustor conditions will be investigated by varying the degree of premixing of the air and methane as in previous studies [9]. Combustion dynamics related to the inlet effects will be investigated through variations in the inlet air temperature, velocity and swirl level.

Measurements will be obtained *in-situ* for the pressure, velocity, fuel distribution, NO_x, CO_2, CO, O_2, soot, and flame structure as a function of operating conditions. Table 2 lists the measurement parameters and techniques to be applied in these studies which include laser Doppler velocimetry (LDV), laser-induced fluorescence (LIF), laser-induced incandescence (LII) and gas sampling. It should be especially noted that these measurements will be made synchronously with any pressure oscillations which occur due to combustion instability. The mode of the combustion stability will be determined from the dynamic pressure distribution in the reactor and will be related to the fundamental driving mechanism as determined from the *in-situ* measurements.

Table 2. Measurement Parameters and Techniques

Parameter	Technique
Pressure	Transducers
Velocity ($\bar{u}$, u')	LDV
Fuel Distribution (gas)	LIF, Raman
NO_x	LIF, gas sampling
CO	gas sampling
Soot	LII (2-D)
Flame Structure	OH LIF (2-D)

Modeling of Combustion Instability Mechanisms

A theoretical framework will be established with which to interpret empirical observations and within which various mechanisms for driving combustion instabilities in gas-turbine engine environments can be addressed. The theoretical model will also be used as a vehicle to transfer the results obtained in the laboratory combustor to predictions of stability in full-scale combustors. Because the relevant phenomena are extremely complicated, involving turbulent mixing, flame holding and spreading, combustion response, and acoustic oscillations, the development of the theory must be guided by empirical observations. For practical purposes, achievements of the theory will consist mainly in the ability to analyze, understand, and predict trends of behavior in the full-scale combustor. The influences of geometrical characteristics and combustion processes can be assessed, but in any event some experimental data are required to provide quantitative results. With judicious melding of theory, measurements and empirical observations, a framework which provides the basis both for understanding the general behavior and for formulating semi-empirical laws can be constructed.

Two sorts of theoretical approaches, approximate analytical and comprehensive numerical, will be undertaken. The approximate analytical approach will extend the existing analyses developed at Penn State for liquid-rocket and ramjet-engine combustion instabilities and accommodate the unique features of gas turbine combustion. Emphasis will be placed on the (i) interactions between compressor and combustor flows, (ii) effects of fuel injection and ensuing flame development on combustion chamber response, and (iii) influence of operating conditions (measured by inlet flow rates and fuel/air mixture ratio) on stability characteristics. The analysis will be established in three steps. First, a nonlinear wave equation for pressure will be derived from the set of conservation equations. This equation will accommodates various linear and nonlinear influences of mean flow, combustion processes, and acoustic oscillations. Although our current understanding of many fundamental processes remains limited, it is important to construct a general stability analysis so that the effects of each individual process on the stability behavior can be addressed in a formal and systematic manner. Second, with the aid of a procedure equivalent to spatial averaging, the wave equation governing the oscillatory flow field will be reduced to a system of ordinary differential equations for the time varying amplitude of each acoustic mode. Finally, this set of equations will be solved analytically using perturbation techniques. Within this task, the influences of various important design considerations on the engine stability behavior will be studied in detail. Specific parameters to be investigated include: injector characteristics, engine operating conditions, chamber geometry, thermochemical properties of fuels, and damping mechanisms.

In parallel to the analytical approach, a numerical investigation into the detailed physicochemical processes in gas-turbine combustion chambers will be conducted. The focus here is on understanding the coupling between combustion dynamics and acoustic oscillations. The model will be based on a finite difference approximation of the complete conservation equations with finite-rate chemical kinetics. Turbulence closure will be achieved using Large-Eddy-Simulation (LES) techniques in conjunction with dynamic sub-grid modeling [10].

A simplified combustor geometry with stipulated inlet conditions will be modeled. Implementation of the model will consist of algorithm development and validation making use of current and projected computational fluid dynamics (CFD) techniques and high-performance computer architecture. A unified solution technique will be used which accommodates the transient behavior of the modeled system through preconditioning of the conservation equations and implementation of the dual time-stepping integration technique. Combined, this methodology offers an algorithm which is robust at all Mach numbers ranging from molecular diffusion velocities to supersonic speeds. Further efficiency will be acquired through implementation of synchronous and asynchronous multi-grid strategies in a multiple processor environment. Massively parallel machines will also be used if possible. The model will be fashioned so that full advantage can be taken of current and future advancements in the state-of-the-art and projected computational power.

Throughout this program, efforts will be continuously made to survey relevant literature and to establish a data base for combustion instabilities in gas-turbine engines. The motivation of this task is to gain further insight into the mechanisms associated with combustion instability by providing detailed accounts and analyses of the design attributes that lead to unsteady motions in gas-turbine combustion chambers. Specific objectives are (i) to preserve the experience gained through development of stable gas turbine engines; (ii) to merge component engine and test results with corresponding theories and experiments; (iii) to analyze the effects of proposed solutions, and (iv) to establish scaling laws for bridging the gap between laboratory research results and full-scale engine data.

Several major sources comprise the core of the literature survey, including the data bases at NASA and CPIA, pertinent DOE and Air Force reports and a search of the Scientific and Technical Aerospace Reports (STAR) index for relevant reports and papers from AIAA, ASME and other journals. In addition, a great deal of information has been obtained from interactions with METC and gas turbine engine manufacturers regarding critical operating data and design requirements for practical gas turbine engines. To facilitate analysis, all available laboratory and full-scale component and engine test data will be combined into a single data base. The approach will follow the technique previously used for analyzing liquid rocket combustion instability data [11]. This compilation will provide a genealogy of various developmental injector design configurations and engine operating conditions, and will contain all available measured and observed test results.

The materials collected and compiled will shed substantial light on the previous studies of gas turbine combustion instabilities, and will provide an invaluable library for continued future reference. Throughout this program, our literature survey will be continuously updated to examine the effects of key mechanisms and controlling parameters on instabilities in various systems.

Acknowledgements

This research is supported by the Department of Energy's Office of Fossil Energy and Office of Energy Efficiency and Renewable Energy under subcontract number 95-01-SR032 for the period from May 1, 1995 through April 30, 1996. The METC Contracting Officer's Representative is N. Holcombe. The research on the fiber-optic probe is also supported by the ATS Program through a subcontract from Westinghouse.

References

1. Harrje, D. T. and Reardon, F. H., Liquid Propellant Rocket Combustion Instability, NASA SP-194, 1972.

2. Anderson, W. E., Ryan, H. M. and Santoro, R. J., "Combustion Instability Phenomena of Importance to Liquid Bi-Propellant Rocket Engines," 28th JANNAF Combustion Subcommittee Meeting, *CPIA Publication 573*, Vol. II, 1991, pp. 99-112.

3. Culick, F. E. C., "Combustion Instabilities in Liquid Fueled Propulsion Systems - An Overview," *AGARD Conference Proceedings No. 450*, 1989, pp. 1-1 - 1-73.

4. Kenworthy, M. J., Bahr, D. W., Burrus, D. L. and Mehta, J. M., "Dynamic Instability Characteristics of Aircraft Turbine Engine Combustors," *AGARD Conference Proceedings No. 450*, 1989, pp. 4-1 - 4-13.

5. Mickelsen, W. R., "An Analysis of Fuel-Oxidant Mixing in Screaming Combustors," *Jet Propulsion*, March 1958, pp. 172-177.

6. Samaniego, J. M., Yip, B., Poinsot, T. and Candel, S., "Low-Frequency Combustion Instability Mechanisms in a Side-Dump Combustor," *Combustion and Flame*, 94, 1993, pp. 363-380.

7. Richards, G. A., Morris, G. J. Shaw, D. W., Keely, S. A. and Welter, M. J., "Thermal Pulse Combustion," *Combust. Sci. and Tech.*, 94, 1993, pp. 57-85.

8. Lord Rayleigh, Theory of Sound, Vol. II, Dover Publications, 1945.

9. Shih, W-P, Lee, J. and Santavicca, D. A., "The Effect of Incomplete Fuel-Air Mixing on the Lean Blowout Limit, Lean Stability Limit and NO_x Emissions of Lean Premixed Gas Turbine Combustors," 1994 Fall Technical Meeting, The Eastern States Section of the Combustion Institute, Dec. 5-7, Clearwater Beach, FL.

10. Oefelein, J. C. and Yang, V., "The Micro-/Macro Scale Coupling of Spray Combustion Processes in Turbulent Reacting Environments," AIAA 94-0683, 32nd Aerospace Sciences Meeting and Exhibit, January 10-13, 1994, Reno, NV.

11. Oefelein, J. C. and Yang V., "A Comprehensive Review of Liquid-Propellant Combustion Instabilities in F-1 Engines," *Journal of Propulsion and Power*, 9, September-October 1993, pp. 657-677.

P26 Flow and Heat Transfer in Gas Turbine Disk Cavities Subject to Nonuniform External Pressure Field

Ramandra P. Roy (roy@asu.edu; 602-965-1482)
Yong W. Kim (602-965-3291)
Timothy W. Tong (tong@asu.edu; 602-965-1483)
Department of Mechanical and Aerospace Engineering
Arizona State University
Tempe, AZ 85287-6106

Introduction

Injestion of hot gas from the mainstream gas path into turbine disk cavities, particularly the first-stage disk cavity, has become a serious concern for the next-generation industrial gas turbines featuring high rotor inlet temperature [1,2]. Fluid temperature in the cavities increases further due to windage generated by fluid drag at the rotating and stationary surfaces. The resulting problem of rotor disk heat-up is exacerbated by the high disk rim temperature due to adverse (relatively flat) temperature profile of the mainstream gas in the annular flow passage of the turbine.

A designer is concerned about the level of stresses in the turbine rotor disk and its durability, both of which are affected significantly by the disk temperature distribution. This distribution also plays a major role in the radial position of the blade tip and thus, in establishing the clearance between the tip and the shroud.

To counteract mainstream gas ingestion as well as to cool the rotor and the stator disks, it is necessary to inject cooling air (bled from the compressor discharge) into the wheel space. Since this bleeding of compressor air imposes a penalty on the engine cycle performance, the designers of disk cavity cooling and sealing systems need to accomplish these tasks with the minimum possible amount of bleed air without risking disk failure. This requires detailed knowledge of the flow characteristics and convective heat transfer in the cavity.

The flow in the wheel space between the rotor and stator disks is quite complex. It is usually turbulent and contains recirculation regions. Instabilities such as vortices oscillating in space have been observed in the flow. It becomes necessary to obtain both a qualitative understanding of the general pattern of the fluid motion as well as a quantitative map of the velocity and pressure fields. These information are indispensable in the development and validation of a computational model of the flow, such a model being a useful design tool. Hence the need for careful and comprehensive experiments.

Research sponsored by the U.S. Department of Energy's Morgantown Energy Technology Center, under subcontract No. 95-01-SR033 from South Carolina Energy Research and Development Center.

Industrial gas turbines must be designed for long hours of continuous operation with little maintenance. This requires, that, in addition to cooling air injection into the wheel space, the designers incorporate a durable rim seal capable of protecting the disk cavity from hot mainstream gas injestion. An effective rim seal configuration coupled with optimum coolant air injection may eliminate ingress of hot mainstream gas into the cavity for all practical purposes, at the same time maintaining efficient engine performance.

Objectives

Our study has four objectives.

I. *Local convective heat transfer coefficient and cooling effectiveness distributions on the rotor disk.* Measurements are to be performed, by the thermochromic liquid crystal (TLC) technique, of radially local (and circumferentially-averaged) convective heat transfer coefficient and cooling effectiveness on the rotor disk surface facing the cavity. A nozzle vane-rotor disk combination, which would impart circumferential periodicity in the pressure field in the space between the vane and the blade external to the disk cavity, is to be used in the experiments. Two rim seal configurations are to be studied.

II. *Flow field in the disk cavity.* Velocity and pressure fields in the cavity are to be measured. The flow is expected to be turbulent and unsteady with recirculation regions. Particle image velocimetry [3] has been chosen as the technique for velocity interrogation and spatially distributed pressure taps communicating with a pressure transducer via scanivalve for pressure measurement.

III. *Computation of flow field and heat transfer in the disk cavity.* Computational fluid dynamic (CFD) modeling of the velocity, pressure, and temperature fields in the cavity are to be carried out. The modeling is to be performed in synergy with the experiments.

IV. *Mainstream gas injestion and rotor disk cooling effectiveness by mass transfer analogy.* The cooling air flow is to be seeded with CO_2 gas (tracer gas) and isothermal experiments conducted. The distribution of CO_2 concentration in the cavity will be measured and radially local cooling effectiveness at the rotor disk surface win be determined via heatmass transfer analogy. Injestion of mainstream air into the cavity is to be studied also by gas concentration measurement.

Experimental Rig

Major parts of the disk cavity rig are shown schematically in Figure 1 (one-eighth scale drawing). All hardware components have been procured and the rig is presently under construction. The main blower is capable of maintaining a flow rate of approximately 4000 cfm (at standard temperature and pressure) through the rig. The auxiliary blower which supplies the cooling air can deliver about 380 cfm at standard temperature and pressure. The maximum rotational speed of the rotor disk is 5000 rpm.

Preliminary Results - TLC Technique

We plan to use a relatively new TLC technique for measurement of the convective heat transfer coefficient at the rotor disk surface and the disk cooling effectiveness. This technique is referred to as the *quasi-steady state TLC technique.*

The technique has been validated very recently in our laboratory. Simple experiments were conducted in which a main airflow was established over a heated flat aluminum place of 12.4 mm thickness. Four equally spaced air injection holes (at an angle of 30° degrees to the surface) 10 mm in diameter were located 6 mm upstream of a 29.2 cm x 12.7 cm area of the plate surface. This area was first provided with a 1 mm epoxy layer and then with a TLC coating.

Figure 2(a) is a plot of the transverse (y)-averaged axially (x)-local convective heat transfer coefficient $\left(\bar{h}^y\right)$ versus the axial distance from the upstream edge of the TLC-coated surface nondimensionalized by the hole diameter (x/d). Figure 2(b) shows a plot of the axially-averaged transversely-local convective heat transfer coefficient $\left(\bar{h}^x\right)$ versus y/d, y being measured from one side edge of the TLC-centered surface. Both plots exhibit correct characteristics.

Figure 3(a) contains a plot of the y-averaged plate cooling effectiveness $\left(\bar{\eta}^y\right)$ versus x/d. Figure 3(b) shows a plot of the x-averaged plate cooling effectiveness $\left(\bar{\eta}^x\right)$ versus y/d. The cooling effectiveness is defined here as

$$\eta \equiv \frac{T_{\text{adiabatic wall}} - T_{\text{main air}}}{T_{\text{cooling air}} - T_{\text{main air}}} \qquad (1)$$

Future Activities

We are addressing Objectives I and II during the first year of this project. Work will soon be initiated on Objective III as well, in cooperation with Allied Signal Engines.

Objectives I-III will be the focus of our work during the second year of this project also. Objective IV will be addressed during the third and final year.

References

1. Abe, T., Kikuchi, J., and Takeuchi, H., 1979, "An Investigation of Turbine Disk Cooling (Experimental Investigation and Observation of Hot Gas Flow Into a Wheel Space)," Thirteenth International Congress on Combustion Engines (CIMAC), Vienna, Paper GT-30.

2. Owen, J.M., 1984, "Fluid Flow and Heat Transfer in Rotating Disk Systems," Heat and Mass Transfer in Rotating Machinery, D.E. Metzger and N. Afgan, Ed., Hemisphere, pp. 81-103.

3. Adrian, R.J., 1991, "Particle-Imaging Techniques for Experimental Fluid Mechanics," *Annual Review of Fluid Mechanics*, Vol. 23, pp. 261-304.

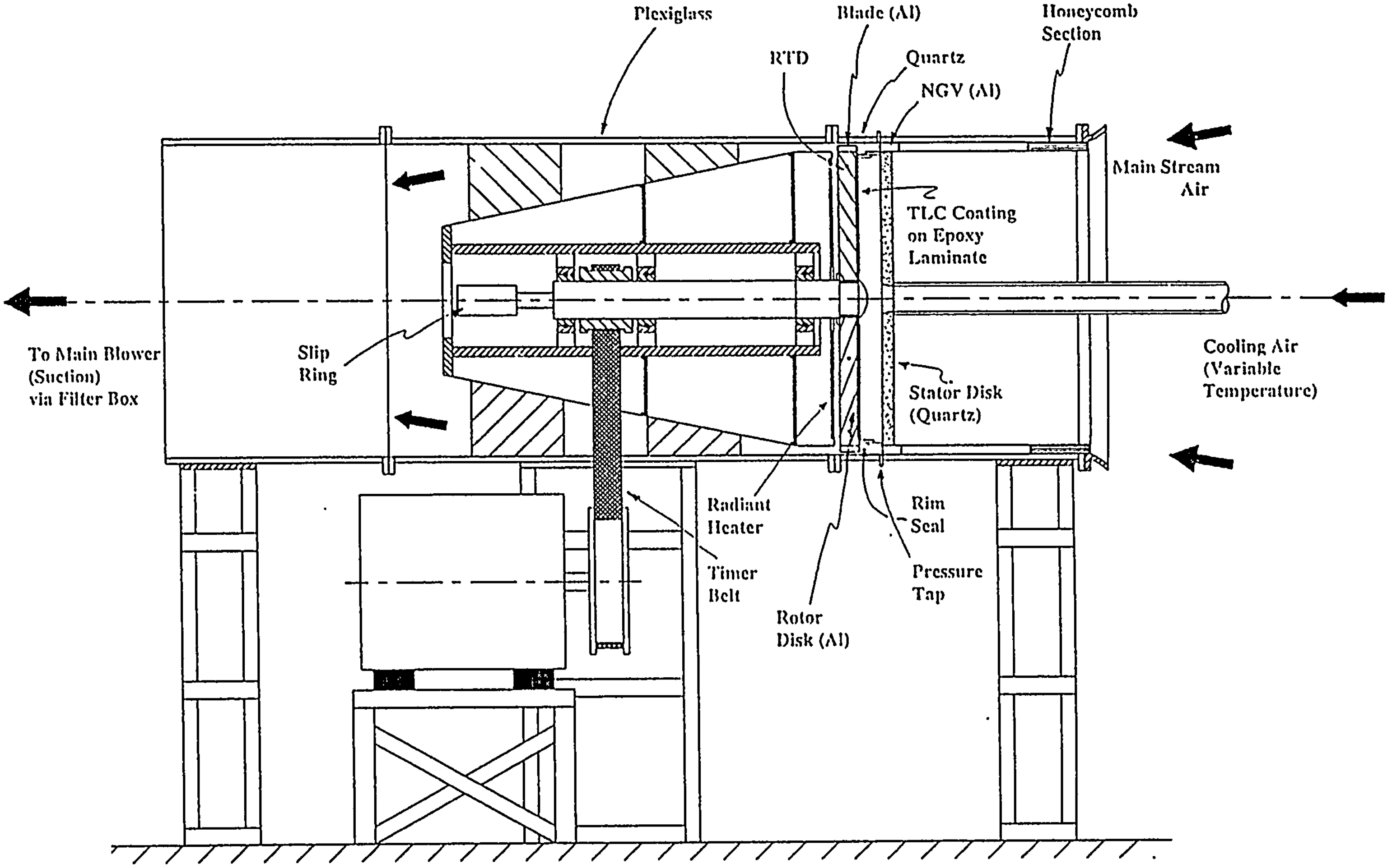

Figure 1. The Disk Cavity Experimental Rig

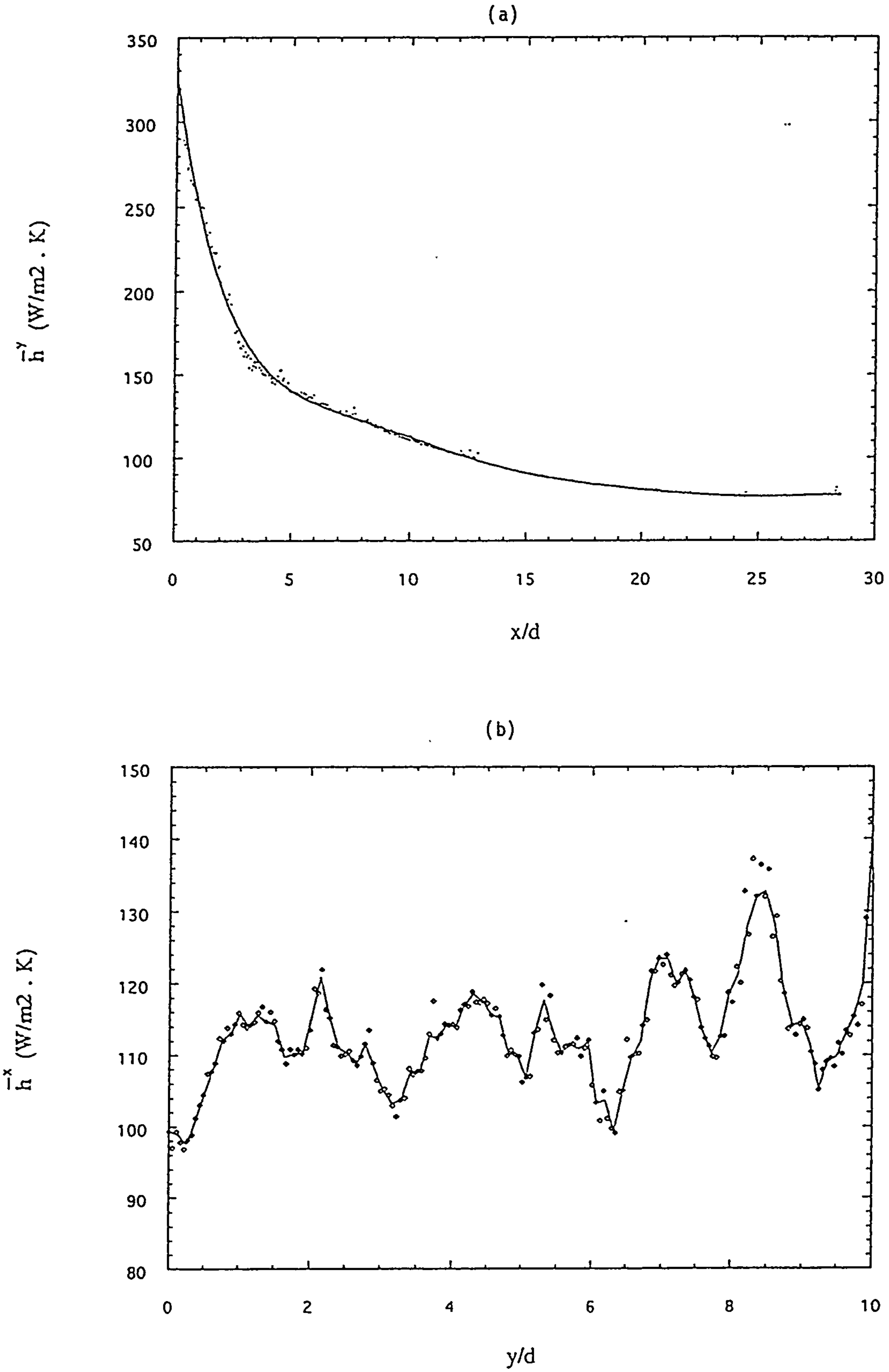

Figure 2. Convective Heat Transfer Coefficient by Quasisteady State TLC Technique

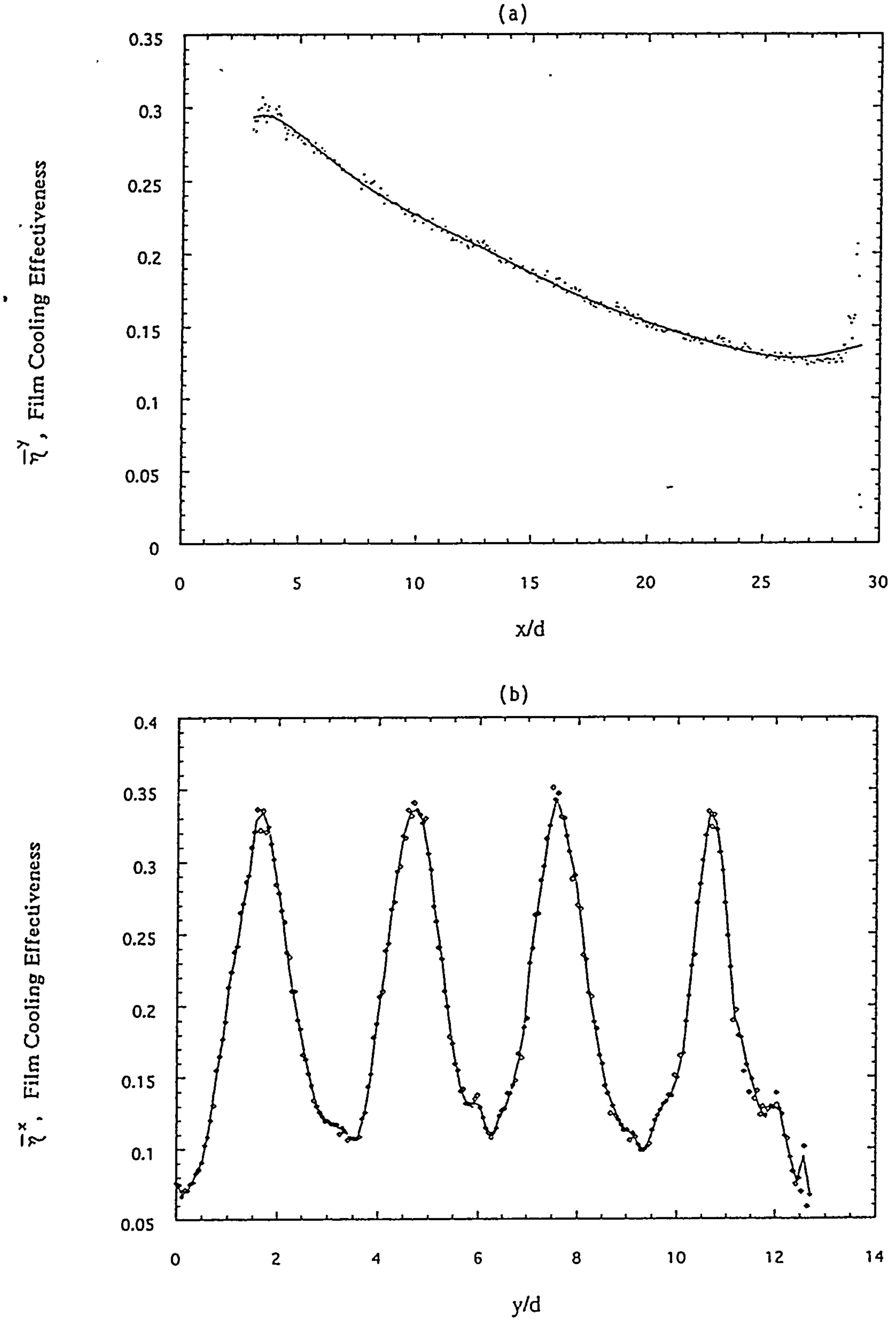

Figure 3. Film Cooling Effectiveness by Quasisteady State TLC Technique

P28 Heat Pipe Turbine Vane Cooling

L. Langston (203-486-5088; Fax: 203-486-4884)
A. Faghri (faghri@eng2.uconn.edu; 203-486-0419)
University of Connecticut
Department of Mechanical Engineering
191 Auditorium Road, U-139
Storrs, CT 06269-3139

Abstract

The applicability of using heat pipe principles to cool gas turbine vanes is addressed in this beginning program. This innovative concept involves fitting out the vane interior as a heat pipe and extending the vane into an adjacent heat sink, thus transferring the vane incident heat transfer through the heat pipe to heat sink. This design provides an extremely high heat transfer rate and an uniform temperature along the vane due to the internal change of phase of the heat pipe working fluid. Furthermore, this technology can also eliminate hot spots at the vane leading and trailing edges and increase the vane life by preventing thermal fatigue cracking. There is also the possibility of requiring no bleed air from the compressor, and therefore eliminating engine performance losses resulting from the diversion of compressor discharge air. Significant improvement in gas turbine performance can be achieved by using heat pipe technology in place of conventional air cooled vanes. A detailed numerical analysis of a heat pipe vane will be made and an experimental model will be designed in the first year of this new program.

Introduction

The heat pipe itself was first formally proposed for use in thermionic applications by George Grover of Los Alamos in 1963. Since then it has been shown that it is a heat transfer device that can exhibit an extremely high effective thermal conductivity, much greater in fact than any known homogenous material. A typical heat pipe (Faghri, 1995) is shown in Figure 1. In operation it is essentially a constant temperature device. It consists of a closed container in which vaporization and condensation of a fluid take place. The choice of a fluid depends on the temperature range in which the heat pipe will be used; e.g. for gas turbine application, sodium or lithium could be used. Heat added at one end of the container causes evaporation of liquid into vapor. Condensation of the vapor along the cooled end (condenser) of the

---

Research sponsored by the U.S. Department of Energy's Morgantown Energy Technology Center, under contract 95-01-SR035 with the University of Connecticut, Research Foundation, 438 Whitney Ext, Storrs, CT 06269-1133; Fax: (203) 486-5381

container maintains the container surface at a nearly constant temperature. The resulting condensate is returned to the heated end (evaporator) of the container by the action of capillary forces in the liquid layer which is contained in a wick lining the inside of the cavity. A typical wick might consist of layers of metal screen or some porous metallic structure.

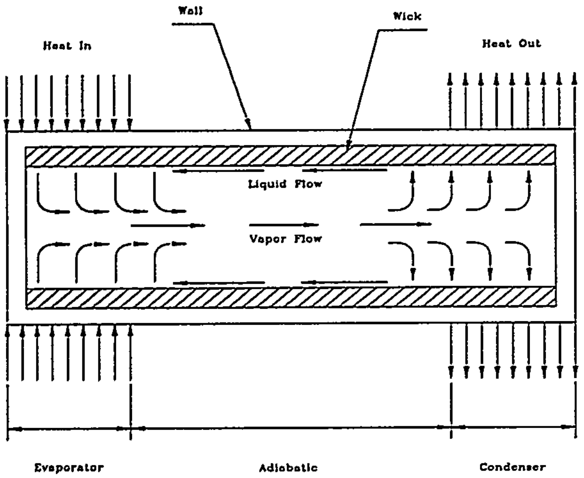

Figure1 :Heat pipe operation

Two heat pipe characteristics , its near constant temperature operation and its tremendous heat transfer ability (Faghri, 1995), make the heat pipe, if configured as a turbine airfoil, very attractive for high temperature gas turbine use. The idea of using it as a vane or stator (the 20,000 - 30,000 g acceleration fields typically generated in a rotating turbine blade limit it to stator use) in a turbine has been considered by some gas turbine specialists over the years. For instance one of the authors (Langston) proposed its use as a stator in 1964 and did a study of its use in a military jet engine (Langston, 1968), using the results of some preliminary 1967 liquid sodium heat pipe vane experiments done by SNECMA, the French jet engine manufacturer. Also, Silverstein (1992) did a preliminary analysis as part of a first phase investigation in conjunction with the United States Air Force and the Allison Gas Turbine Division of General Motors.

These, two rather limited heat pipe vane studies we are aware of have dealt with military or other high performance jet engines, (i.e. aviation gas turbines). Military engines have high turbine temperatures suitable for heat pipe applications, but they must operate with high maneuver loads (a 10 g dive or turn might adversely affect capillary pumping in a heat pipe vane) and a minimum of weight (heat pipe vanes could add some small amount of weight). The feasibility studies done to date have shown promising results, but not promising enough for jet engine manufacturers to make use of heat pipe vanes in a production engine. This is mainly due to the lack of experimental simulation and detailed design analysis.

Land based gas turbines are stationary (no maneuver loads) and therefore weight is not a major consideration. Thus our program differs from those of the past in its application to stationary shaft-power gas turbines rather than to maneuvering, thrust-power aviation gas turbines. Furthermore, a detailed experimental and numerical/analytical program including actual testing of a heat pipe vane will be started in this one-year contract and proposed for completion in the next year.

Problem

All modern high temperature turbines are cooled for the most part by bleeding relatively cool compressor air from the gas path and then reintroducing it in the turbine in such a way as to cool turbine airfoils (blades and vanes) that are in the hottest regions of the turbine. There are two general types of turbine vane cooling: 1) Internal convective cooling and 2) film cooling.

Internal convective cooling is used to cool the inside surfaces of a turbine vane. The cooling air usually exits at the vanes trailing edge. This leads to a thick trailing edge, which increases the turbine aerodynamic losses.

Film cooling is used for the highest turbine temperatures, especially for gas temperatures that significantly exceed the melting point of the nickel based alloys used to make vanes. Cooling air from the compressor is injected onto the gas path surface of the vanes, to form a protective layer of cool gas, shielding the vane from the hot gas path flow. Film cooling leads to aerodynamic losses in the turbine because of the disruption it causes in the gas path. There are many overall disadvantages of air cooling of turbine vanes and a few are as follows:

- There is an added cost of producing the turbine vanes in the machining of the internal passages and/or surface conditions.

- Turbine vane reliability is significantly reduced with the machining of the internal passages which can lead to mechanical stress concentrations.

- Turbine vanes have high losses associated with the thicker geometric design associated with internal passages.

- The injection of cooling air (especially for film cooling) into the gas path leads to aerodynamic losses through disruption of the gas path flow and through the mechanisms of mixing.

- Air cooled vanes are not isothermal and the resulting metal temperature gradients lead to thermal fatigue and cracking.

Approach

Use of heat pipe vane cooling for a turbine promises improvements in overall gas turbine durability and performance by at least one of three ways:

1) The isothermalization of vanes thereby minimizing thermal stresses.

2) Reduction of the amount of turbine cooling air required, thereby improving turbine efficiency or increasing the amount of cooling air available for NO_x control.

3) Removing turbine cooling air injection gas path sites, thereby reducing turbine aerodynamic losses.

For example, consider the simplest case of isothermalization of a vane. Suppose a turbine vane is operating under temperature conditions such that it needs no net cooling, but the designer has used convection cooling because of burner "hot spots" (earlier versions of the first vane of the JT8D fits this description.) By making such a vane into a heat pipe (no net cooling air required), it will be "isothermalized" with the hot spots cooled by heat pipe action with the heat being transferred to the colder parts of the vane. The vane surface acts as both evaporator and condenser for the heat pipe.

For the case of an existing <u>cooled</u> vane, we will consider three methods of fitting the turbine vane with a heat pipe. Other designs may result from the work proposed here. Option #1 is a conventional heat pipe turbine vane (Figure 2), Option #2 is a double-walled heat pipe turbine vane (Figure 3) and Option #3 is an annular heat pipe turbine vane (Figure 4). All three options will have the same overall characteristics in the operation of the heat pipe. First, the evaporator section of the heat pipe fitted turbine vane will be the section that is in direct contact with the combustion gas while the condenser section is actually an extension of the turbine vane into a passage that contains a stream of cooler air flow that acts as a heat sink. All three heat pipes will consist of a wicking material such as layered screens or a sintered porous material. The working fluid can be a high temperature substance such as liquid sodium or lithium.

The reader will possibly recall that the use of a liquid metal in a power plant is not new. Liquid sodium has been used in exhaust valves of high performance internal combustion engines for years. The differences of the three options are in the variety of heat pipe types and materials that are fitted into the turbine vane. These differences and correct procedure for the selection of working materials and fluids will be carefully considered.

Option #1, conventional heat pipe, is the simplest in theory and application. The turbine vane is fitted with a wick structure that covers the entire interior surface of the vane. The wick structure is saturated with the working fluid, i.e., sodium or lithium at ambient conditions. The turbine vane corresponds to the evaporator section of the heat pipe. During operation, the turbine vane is exposed to the combustion gas stream which vaporizes the working fluid in the wick. The vapor will then flow towards the condenser section where the fluid will condense back to its liquid form releasing the latent heat of vaporization energy into the heat sink.

The choice of the heat sink for the heat pipe vane is dependent on the particular application, and will be one of the things to be studied in the work proposed here. As an example, consider the case of the first vane (the nozzle). One can design the heat pipe evaporator section to extend into a cavity below the first vane ID platform (and forward of the first disk), into which cooling air from the compressor is introduced. The cooling air flows into the cavity, cools the heat pipe evaporator, and then could be reintroduced into the gas path at the first vane's platform leading edge. Another possibility is to exhaust the heated cooling air directly onto the first blade, in such a way as to attempt to control secondary endwall flow effects from the first vane. Other possible heat sinks include an air or stream closed loop system, where the vane heat removed from the gas path is returned to the cycle in a regenerator. Certainly other possibilities exist for effective heat pipe vane heat sinks in other gas turbine configurations such as the HAT cycle.

Option #1 is attractive since the interior of the vane does not have a cooling flow of air that is diverted from the compressor discharge directly into the gas path. This option allows uniform temperature along the turbine blade surface during and would allow the hot spots such as the leading and trailing edges to be sufficiently cooled. The temperature gradients along the surface would be reduced significantly, reducing the chances of thermal stress induced cracking. Overall, the heat pipe would still remove a much higher amount of heat then would a one phase flow of air as in existing conventional methods.

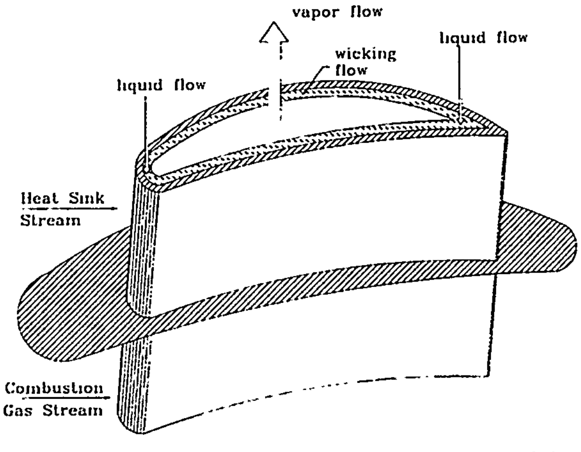

Figure 2: Conventional heat pipe turbine vane design (Option #1)

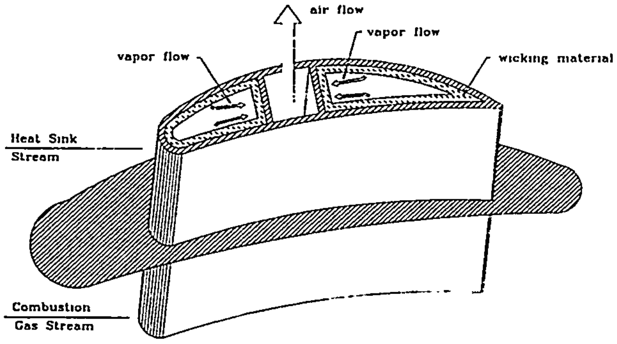

Figure 3: Double wall heat pipe vane cooled by heat pipe effect and internal air stream (Option #2)

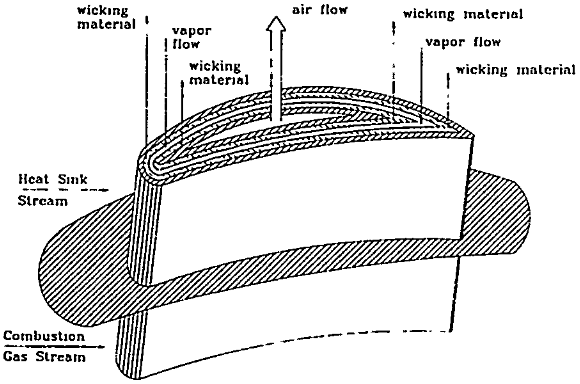

Figure 4: Annular heat pipe turbine vane cooled by heat pipe effect and internal air stream (Option #3)

Option #2, the double-walled heat pipe turbine vane, would also help reduce the hot spot temperatures at the leading and trailing edges and allow the surface of the blade to maintain a more uniform temperature at extremely high heat flux designs. Figure 3 shows the operating principle behind this option. Two separate heat pipes would be fitted into the turbine vane at theleading and trailing edges. The heat generated at the leading and trailing edges would conduct through the turbine and into the wick structure, where the working fluid would be vaporized. The vapor would then be transported to the heat adjacent heat sink as in Option #1. The difference in this option comes from the internal air flow passage in the turbine vane. This air flow is diverted from the compressor as in existing cooling methods. Overall, the high conductive heat pipes are positioned to concentrate on the removal of heat from the leading and trailing edge hot spots while the internal air flow is positioned to remove heat from the surface where the temperatures are lower. This would allow for a more uniform blade surface temperature, leading to a less likelihood of a surface temperature gradient which could result in thermal stresses. Option #2 may be useful, but as can be seen, the controlling heat transfer resistance is in the air flow passage.

Option #3, the annular heat pipe turbine, is another promising method of removing heat from the turbine blade surface and also will help the liquid to be returned to the evaporator. The operating principle behind the annular heat pipe turbine blade is very similar to Option #1 but allows for more surface area for the removal of heat. As shown in Figure 4, this annular heat pipe geometry consists of an internal air flow passage. The wick structure is placed on both the inner wall of the turbine vane and the outer wall of the air passage. The evaporator section of the turbine vane would remove heat from the combustion gas stream and vaporize the working fluid. However, with this option the vapor starts to condense close to the evaporator end of the turbine vane. This allows the evaporator section to absorb more energy from the surface. As the remainder of the vapor travels along the length of the vane it is continuously condensing into the wick structure and finally at the condenser end both wall surfaces act as a heat sink. This option allows the condensate to be returned to the evaporator end at a higher and more efficient rate then any of the other methods. Also, the capillary limit of this annular heat pipe is greater then a conventional heat pipe. A slight disadvantage exists in the fitting of the complex annular heat pipe geometry.

There are significant advantages of these proposed heat pipe turbine vanes over ones using conventional cooling techniques. Some of these are:

- The extremely high heat transfer rate of the heat pipe operating principle due to the change of phase. The removal of heat by latent heat of vaporization of a liquid metal is many order of magnitudes higher then that of conventional convective or conductive methods.

- Uniform temperature along the vane surface is accomplished by fitting the turbine vane with a heat pipe. With existing, conventional techniques of cooling turbine vanes the temperature distribution along the surface of the vanes is not uniform due to the difficulty, or impossibility, of running air cooling passages through the thinner parts of the turbine vane. With heat pipe fitting of the turbine vanes, this is not a concern.

- Elimination of hot spots at vane leading and trailing edges due to the very high effective heat transfer coefficients.

- There are no aerodynamic losses due to the injection of cooling air into the gas path. This in itself could increase the efficiency of an existing high temperature turbine by 2-4 percentage points (e.g. an 88% turbine going to 92% efficiency).

The one disadvantage that is foreseen at this time is the added weight of the turbine vane due to the greater length. However, this is of concern in aviation applications. A feasibility study done on an advanced military fighter turbine engine, showed an increase in engine weight of only 1% (Silverstein and et al, 1994).

One other possible disadvantage is the heat (energy) the heat pipe vane may remove from the gas path and hence the cycle, as discussed in Option #1. There are ways that this heat could be reintroduced back into the cycle, depending on the location of the vane and on the particular cycle under consideration.

Project Description

The time has come to do an in depth study and evaluation of the heat pipe vane for land based shaft power producing gas turbines, for the following reasons:

1) The turbine inlet temperatures of modern land based gas turbines are now approaching those of high performance jet engines. The application of an advanced cooling scheme such as the heat pipe vane would be ideally suited to the stationary installation of such machines. Performance gains beyond the standards set by jet engines might be possible with the elimination of compressor cooling air in the hot turbine gas path.

2) Over thirty years of research and development have vastly improved heat pipe performance and manufacturing. One of the authors, Dr. Faghri, is a noted heat pipe researcher and has just published a text on the latest developments in the field of heat pipe science and technology (Faghri, 1995).

Thus we are strongly convinced the time is right to seriously consider the use of heat pipe vanes for land based shaft power producing gas turbines. In this one year contract we will set out on a three part program whose objectives are as follows:

1) Numerical/Analytical Simulation Study.
   To develop a detailed numerical/ analytical simulation model to predict the performance characteristics of heat pipe vanes under various heat load distributions. What is the predicted transient performance of a heat pipe vane? What happens during engine startup and shut down? What are the heat transport limitations? No detailed transient numerical simulation accounting for the nonconventional geometry of the turbine vane has been done in the past.

2) Experimental Study:
   To develop an operating map for a heat pipe vane subjected to engine temperatures and heat loads. This will answer such questions as which geometries and materials are the most promising, what are performance limits and how isothermal is the heat pipe vane. No such experimental results are presently available in the open literature.

3) Gas Turbine Manufacturer Design System Study:
   Given the overall characteristics of a heat pipe vane and the results of 1) and 2) above, what does the design system used by a gas turbine manufacturer predict for performance gains in a modern gas turbine using heat pipe vanes? What stages in a turbine are best suited to heat pipe applications?

Efforts on all three of these objectives will be carried out during this one year contract. A proposal for a future contract will then be submitted, based on the first year results.

Acknowledgements

The Research Manager of this contract is Daniel B. Fant. The period of performance is for one year. Preparation of this paper has been done by Theresa L. Roy who is a University of Connecticut graduate student working on this contract.

References

Faghri, A., Heat Pipe Science and Technology, Taylor & Francis, Chapter 1, 1995.

Langston, L.S., Preliminary Study of the Heat Pipe Vane, *Internal Memo to Dr. M. Suo,* Pratt & Whitney Aircraft, East Hartford, CT., December 5, 1968.

Silverstein, C., Gottschlich, J., and Meininger, M., The Feasibility of Heat Pipe Turbine Vane Cooling, *Gas Turbine and AeroEngine Congress and Exposition,* The Hague, Netherlands, June 13-16, 1994.

P29

Improved Modeling Techniques for Turbomachinery Flow Fields

B. Lakshminarayana (B1laer@engr.psu.edu; 814-865-5551)
Dept. of Aerospace Engineering
The Pennsylvania State University
University Park, PA 16802

J. R. Fagan, Jr. (fagan_bob/agt-openmail@dms2agt.gmeds.com; 317-230-5304)
Allison Engine Company
Indianapolis, IN 46206

Abstract

This program has the objective of developing an improved methodology for modeling turbomachinery flow fields, including the prediction of losses and efficiency. Specifically, the program addresses the treatment of the mixing stress tensor terms attributed to deterministic flow field mechanisms required in steady-state Computational Fluid Dynamic (CFD) models for turbomachinery flow fields. These mixing stress tensors arise due to spatial and temporal fluctuations (in an absolute frame of reference) caused by rotor-stator interaction due to various blade rows and by blade-to-blade variation of flow properties. This will be accomplished in a cooperative program by Penn State University and the Allison Engine Company. These tasks include the acquisition of previously unavailable experimental data in a high-speed turbomachinery environment, the use of advanced techniques to analyze the data, and the development of a methodology to treat the deterministic component of the mixing stress tensor. Penn State will lead the effort to make direct measurements of the momentum and thermal mixing stress tensors in high-speed multistage compressor flow field in the turbomachinery laboratory at Penn State. They will also process the data by both conventional and conditional spectrum analysis to derive momentum and thermal mixing stress tensors due to blade-to-blade periodic and aperiodic components, revolution periodic and aperiodic components arising from various blade rows and non-deterministic (which includes random components) correlations. Allison Engine Co. will lead the modeling effort to synthesize this data into improved flow field models. The modeling results from this program will be publicly available and generally applicable to steady-state Navier-Stokes solvers used for turbomachinery component (compressor or turbine) flow field predictions. These models will lead to improved methodology, including loss and efficiency prediction, for the design of high-efficiency turbomachinery and drastically reduce the time required for the design and development cycle of turbomachinery.

Research sponsored by the U.S. Department of Energy's Morgantown Energy Technology Center, under contract DE-FC21-92MC29061 with South Carolina Energy R&D Center, Clemson University, Clemson. This program was initiated in September 1995; hence, this paper represents a summary of the proposed program.

Introduction

Until recent years, the aerodynamic modeling tools (including losses) used in turbomachinery component design systems were primarily based upon empirical correlations and had limited capability to model the actual flow field physics. With the development of adequate empirical databases, these models have served the gas turbine industry well, however, their limitations become evident as the designer tries to develop a component with characteristics sufficiently different from the empirical design base. The other obvious limitation is the inability of these tools to model the detailed structure of the flow field and the aerodynamic losses associated with viscous layers, secondary and leakage flow. The conflicting demands upon the gas turbine industry to drive to higher component performance while reducing the acquisition and operating cost to our customers through a more efficient design and development process required a new generation of aerodynamic modeling tools.

There have been tremendous advances over the past decade in the capabilities of digital computers together with parallel developments in numerical algorithms to solve the steady-state Navier-Stokes (N-S) equations (the fundamental equations that govern viscous fluid flow) for subsonic and transonic flows. This gives the turbomachinery component designer new tools with the potential capability to accurately model the detailed structures of the flow field resulting in improved predictions of the component performance. More importantly, these models are based upon fundamental fluid mechanics allowing the designer to analytically investigate component design features outside his empirical database. As component design tools, these models have had a significant impact on the design of fan stages and the front stage of core compressors and turbines. However, they have had far less impact upon the design of embedded stages in compressors and turbines. This is primarily due to limitations in the treatment of the mixing stress tensors in these models.

Solution of the steady-state N-S equations requires special treatment of stress tensor terms that are due to the turbulent (random) fluctuations of the flow field and are introduced during time-averaging of the instantaneous equations of motion (this is referred to as closure of Reynolds stress tensors). The additional mixing stress terms required for modeling steady-state turbomachinery flow fields have identical structure to the Reynolds stress terms and have traditionally been modeled using conventional turbulence models. However, the physics associated with these terms is fundamentally different than the turbulent fluctuations that result in the Reynolds stress terms. These terms result from deterministic features of the flow field such as blade wakes and shed vortices which are known to be dominant features in turbomachinery flow fields. It is not surprising that the treatment of the mixing stress tensor for turbomachinery flow fields based solely upon the random processes of turbulence is not adequate to accurately model turbomachinery component flow fields.

Adequate data to support this modeling effort is not available, and the acquisition and analysis of unsteady temperature, pressure, and velocity measurements in a high-speed multistage compressor constitute a significant part of this program. Advanced data analysis techniques will be used to resolve the mixing stress tensor into the random and deterministic components. Important questions that need to be addressed include what is the relative contribution to the total mixing stress tensor of the random and the deterministic components and how do the deterministic features of the flow field in the rotor frame of reference affect the mixing processes in the stationary frame and vice-versa.

Minimal effort has been made to address closure of the deterministic terms in the mixing stress tensor. Adamczyk, Mulac, and Celestina (1986) proposed a model for the inviscid form of the average passage equation system, but it has not been extended to the viscous form of the equations. Currently, traditional turbulence models are used to address these terms, and this program will develop and evaluate alternatives for modeling the deterministic terms in the mixing stress tensor. Since this unsteadiness is associated with deterministic mechanisms observed in a different frame of reference, the primary approach will be to develop a model with the governing equations with an appropriate change in the frame of reference. The model equations can be formulated in physical space, with the stress terms expressed as convolution of Fourier or wavelet components. Analysis of the experimental data will be used to guide this or identify another modeling approach. The results of this modeling effort will be directly applicable and easily integrated into steady 3-D Navier-Stokes solvers which are used throughout the industry for component design.

Objectives

The objective of the program is to develop improved methodology for modeling turbomachinery flow fields. Specifically, it will address the deficiencies of the stress tensor models in steady-state 3-D Navier-Stokes models used for the design of turbomachinery components. Since the derivation of the average-passage equations (Adamczyk, 1985) clearly show that the deterministic features of the turbomachinery flow contribute to the mixing stress tensor and stress tensor modeling does not address these contributions, the approach is to directly measure the mixing stress tensor in a high-speed turbomachinery component. Advanced analysis tools will be used to resolve the random and the deterministic components of the mixing stress tensor and a model will be developed from the governing equations with an appropriate change in the frame of reference. These models will be tested in Navier-Stokes solvers available at Allison and Penn State.

The results of this program will be of broad interest to the gas turbine industry and has potential benefit in several manners. The experimental data which will include measurement of the momentum and thermal mixing stress tensors in a realistic turbomachinery environment is not previous available. This data will be valuable to the industry for the insight it will provide on the fundamental physics and can be used in the development of proprietary mixing stress tensor models. In wavelet processing, this program will introduce and exercise a new tool which has promise in significantly impacting analysis and modeling of turbomachinery flow fields. The results of this modeling effort will be directly applicable and easily integrated into the fundamental tools used throughout the industry for the design of compressors and turbines.

The overall objective is to provide models and tools for improved methodology for the design of high efficiency turbomachinery and drastically reduce the time required for the design and development cycle. This methodology will replace present day approach based on empiricism and extensive testing.

Benefits of the proposed program are (1) enhanced fuel economy and performance of turbomachinery in gas turbine systems, (2) drastic reduction of the time required for the design and development cycle of turbomachinery, and (3) improved and systematic methodology for modelling and prediction of the flow field, including losses and efficiency, and design techniques based on computational fluid dynamics.

Method of Approach

The proposed research consists of three tasks:

(1) Experimental investigation of three-dimensional steady and unsteady flow field in multistage turbomachinery, including analysis and processing the data required for modelling multi-stage turbomachinery flows. Statistical analysis of the data acquired will be carried out to identify flow events at various scales using conventional and wavelet technique. The wavelet analysis should lead to identification of sources not associated with blade or shaft frequency and involves decomposition of "unresolved unsteadiness" to derive random fluctuations and other sources of unsteadiness.

(2) Modelling of multistage flow field using the data acquired. The modelling will involve order-of-magnitude analysis of various sources associated with unsteady flow and its importance in the performance and design of turbomachinery.

(3) Incorporation of the model in Navier-Stokes code to predict flow field in multistage and single stage turbomachinery, including aerodynamic losses. Allison personnel will incorporate this in their proprietary code and Penn State will incorporate this in their three-dimensional Navier-Stokes Code.

The background material and the method of approach used in accomplishing these tasks are given below.

Experimental Investigation

The experimental investigation will be conducted in the multistage axial flow compressor available at Penn State. It should be emphasized here that the research proposed here is generic, even though the experimental program is carried out in a multistage compressor. The phenomena is similar in both compressors and turbines.

The test compressor is a three-stage axial flow compressor consisting of an inlet guide vane row and three stages of rotor and cantilevered stator blading with a rotating hub. The general specifications of the compressor are listed in Table 1. The compressor was donated to Penn State University by Pratt and Whitney Aircraft of United Technologies Corporation. The compressor located on the test stand consists of the following major components: drive assembly, compressor, inlet and exhaust ducting, and the control and data acquisition system. The drive assembly comprises of the 372 KW induction motor (with a frequency controlled inverter) coupled to the compressor via a 1:1.67 ratio speed increaser gear box and torque-meter. Filtered ambient air is ducted into the compressor inlet plenum via a silencer unit to reduce noise levels. The plenum (in the shape of a scroll) provides axisymmetric uniform flow and temperature distributions at the inlet to the compressor. The flow path consists of a honeycomb section with screens to assure a uniform flow distribution at inlet. A contraction section is also provided to accelerate the flow smoothly into the IGV section of the compressor. A throttle located downstream of the compressor is used to control the mass flow through the compressor. The throttle system includes a surge control device, which activates a quick release feature of the discharge throttle, for rapid stall recovery in the event of surge. The surge control system features a differential pressure transducer which senses the pressure difference between the exit of the compressor and the exit plenum. If this pressure difference is higher than a previously set set-point, the throttle is opened for rapid recovery. The flow is exhausted through a duct into an exhaust anechoic chamber to reduce noise levels. Details of the compressor and preliminary data can be found in Lakshminarayana et al. (1994).

Table 1
General Specifications of Pratt and Whitney Compressor 4N

Number of Stages	3
Design Corrected Rotor Speed	5410 rpm
Design Corrected Mass Flow	8.61 kg/s
Design Overall Total Pressure Ratio	1.354
Peak Efficiency at 100% Speed (torque based)	90.65%
Blade Tip Mach Number	0.5
Average Reynolds Number (based on Stator 3 chord and axial velocity)	2.45×10^5
Average Hub-Tip Ratio	0.843
Diffusion Factor (avg.)	0.438
Average Flow Coefficient (V_x/U_t) (Average for a stage)	0.509
Reaction (avg.)	0.570
Space-chord Ratio (avg.)	0.780
Aspect Ratio (avg.)	1.5
Average Rotor Tip Clearance (static)	1.328 mm
Average Rotor Tip Clearance (dynamic)	0.667 mm
Average Stator Hub Clearance (τ)	0.686 mm

The overall measurement and data analysis program proposed consists of the following:

1. (1) Unsteady stagnation temperature and pressure measurement (Aspirating Probe).
2. (2) Instantaneous velocity measurement (Hot Film).
3. (3) Data analysis for mixing coefficients.
4. (4) Data analysis to understand the unsteady effects.

In order to accomplish the objectives outlined in the previous section, an experimental investigation of the steady and unsteady flow in the embedded rotor and stator stage of a three-stage axial flow compressor will be undertaken. Two types of slow response probes and two types of fast response probes will be used in this investigation. The slow response probes used are the pneumatic five hole probe (pressure and velocity) and a thermocouple probe (temperature). The high response probes are a slanted single sensor hot-film probe (three dimensional time resolved velocity field) and an aspirating probe (time resolved total temperature and total pressure field). The principle of operation of the aspirating probe involves operating 2 coplanar hot-wires at different overheat ratios (different wire temperatures) in a 0.9 mm dia channel of a choked orifice. Detailed description of the working of the probe is given by Ng and Epstein (1983). Van Zante et al. (1993) have modified the design to eliminate the piggy back pressure transducer. This modified design will be used in this investigation. The frequency response of the aspirating probe is estimated to be 10-30 kHz (Ng and Epstein (1983)). The kulite total pressure transducer is of XB-062-25A type with a frequency response of typically 60 kHz. This transducer can be traversed in either a total pressure probe configuration or piggybacked to the aspirating probe. The single sensor slanted hot-film probe is a TSI 1263-10 hot-film slanted at 45 degrees to the axis of the probe. The hot-film is 25 μm in diameter and has a frequency response of approximately 50 kHz. A complete range of tests were conducted both in a high speed jet as well as in the compressor to assess the ability of the hot-film probe to measure both mean and the fluctuating velocity field.

Detailed area traverses in the radial (from hub to casing) and tangential locations (1.85 stator blade pitches) with clustering of measurement stations in the wake and endwall regions) of the high response probes will be carried out downstream of rotor 3, of the multistage compressor facility at both the peak efficiency and the peak pressure ratio operating conditions. Depending on the success of the program, attempts will be made to acquire the data at the exit of other embedded stages (e.g., rotor 2 and stator 1 exit). The two operating conditions chosen is typical of most compressor operations. The traverse would include approximately 15 to 20 radial and 15 to 20 tangential locations. An area traverse of the kulite total pressure probe was conducted downstream of stator 2 at the peak efficiency condition. The objective of this traverse is to provide an unsteady pressure field for comparison against the unsteady pressures derived from the aspirating probe and to test out the ensemble averaging and analysis software.

Ensemble averaging and conditional sampling techniques will be utilized to decompose the instantaneous pressures, temperatures, and velocities into time averaged, periodic, aperiodic, and unresolved unsteadiness components. Random data analysis procedures will be utilized to determine the various velocity-velocity and velocity-temperature correlations used to close the passage averaged equation set. The equations of motion will be suitably averaged and the relative magnitudes of each of the terms of the equations will be estimated based on the experimental data. Contour and vector plots of various quantities in both the rotor and the stator frames of reference will then be utilized to explain the transport phenomena as well as the rotor-rotor and the rotor-stator interaction phenomena. Then mechanisms for spanwise mixing will be postulated. Fourier decomposition of the periodic and aperiodic signals as well as spectral analysis of each of the instantaneous signals will also be conducted in order to determine the influence of the upstream and downstream rotors on the flow field as well as the effects of rotor-stator interaction. This data will be properly organized and made available to industry.

The conventional analysis will be supplemented by wavelet analysis to resolve events at frequencies other than the shaft frequencies. As much information as possible about the flow physics will be collected, by identifying scale-dependent events of different types (local maxima, gradients, etc.) in the various signals, by quantifying the correlations between these events, including filtered and conditional statistics, and by mapping the spectral content of the stress terms at different stations in the flow. Experimental data will be decomposed into time average, revolution aperiodic, blade periodic, blade aperiodic, and unresolved components. Stress maps will identify the velocity scale(s) and time scale(s) relevant to the dynamics of the corresponding stress terms.

Modeling Effort

There are several approaches to modeling a turbomachinery component with steady 3-D Navier-Stokes solvers. The simplest approach is for the designer to make predictions with a single blade solver using the exit conditions from one solution as the inlet conditions for the successive blade row. The thermodynamic and gas dynamic properties at the boundaries must be circumferentially averaged to account for the change in the frame of reference. With this approach only secondary effects of a blade row upon the upstream blade row such as blockage can be addressed. The next step in model complexity is to make a simultaneous solution of multiple blade rows using a mixing plane formulation. The same equations are solved and the circumferentially-averaged properties at the mixing plane are automatically updated as the solution progresses. In this procedure, the influence of a blade row on the upstream blade row is directly addressed. Models using these approaches are available to the gas turbine community.

Allison Engine Company has made a considerable effort evaluating steady-state models for turbomachinery component flow fields, and the results of those efforts have led to two conclusions. First, solution using a solver with a mixing plane formulation and a solver based upon the average-passage equations using similar gridding results in very similar results. This is not surprising because the average-passage solver uses a standard turbulence model (identical to the one used in the mixing plane calculation) to model both the random and deterministic terms in the mixing stress tensor. Second, the predictions for fans or the front stages of multistage compressor and turbines compare well with test data. However, the predictions get increasingly worse further back in the component for embedded stages in multistage compressors and turbines. The data indicates these models are not accurately predicting the component blockage, the endwall loss generation and the profiles of total pressure and temperature. These are all highly dependent on the treatment of the mixing stress tensors.

The aspirating probe and hot-film data will be analyzed and synthesized to derive a detailed understanding of the physics and correlations associated with mixing coefficients. This involves both the qualitative and quantitative interpretation of data.

The important controversy to be resolved is in regard to the physics associated with the mixing and the following points will be addressed:

(1) The contribution to the mixing from periodic time averaged mean flow: included in this are the radial motion within the wake, secondary and leakage flow in the endwall region.
(2) The contribution due to mixing from the random fluctuation (turbulence).

The modeling effort will involve the following steps:

a. The Allison developed Vane-Blade Interation (VBI) model (Rao and Delaney, 1992), based on unsteady 3-D Navier-Stokes solver, will be used to generate an analytical data set for validating the data processing methodologies.

b. An analytical mixing stress tensor model will be developed using results from the unsteady experimental data and unsteady analytical predictions. This work will be modified as required to generate the data required to develop and validate the model.

c. This model will be used in Allison proprietary 3-D Navier-Stokes solvers and compared to predictions using mixing stress tensor models. These predictions will be made to evaluate the progress of the modeling effort and to demonstrate the capabilities of the completed model.

Acknowledgment

This research is sponsored by METC through SCERDC, (through subcontract No. 95-01-SR036) with Dr. D. Fant as the contract monitor.

References

Adamczyk, J.J., 1985, "Model Equation for Simulating Flows in Multistage Turbomachinery," ASME paper 85-GT-226.

Adamczyk, J.J., Mulac, R.A., and Celestina, M.L., 1986, "A Model for Closing the Inviscid Form of the Average Passage Equation System," ASME paper 86-GT-227.

Lakshminarayana, B., Suryavamshi, N., Prato, J., and Moritz, R., 1994, "Experimental Investigation of the Flow Field in a Multistage Axial Flow Compressor," ASME paper 94-GT-455.

Ng, W.F., and Epstein, A.H., 1983, "High Frequency Temperature and Pressure Probe for Unsteady Compressible Flows," <u>Review of Scientific Instruments</u>, Vol. 54, No. 12, pp. 113-124.

Rao, K.V., Delaney, R.A., and Dunn, M.G., 1992, "Vane-Blade Interaction in a Transonic Turbine, Part I-Aerodynamics," AIAA Paper 92-3323.

Van Zante, D.E., Suder, K.L., Strazisar, A.J., and Okiishi, T.H., 1993, "An Improved Aspirating Prove for Total Temperature and Total Pressure Measurements in Compressor Flows," Private Communication.

P30

Advanced 3D Inverse Method for Designing Turbomachine Blades

T. Dang (tqdang@mailbox.syr.edu; 315-443-4311)
Department of Mechanical/Aerospace/Manufacturing Engineering
149 Link Hall
Syracuse University
Syracuse, NY 13244

Introduction

To meet the goal of 60% plant-cycle efficiency or better set in the ATS Program for baseload utility scale power generation, several critical technologies need to be developed. One such need is the improvement of component efficiencies. This work addresses the issue of improving the performance of turbomachine components in gas turbines through the development of an advanced three-dimensional and viscous blade design system. This technology is needed to replace some elements in current design systems that are based on outdated technology.

Objectives

In the design process of turbomachinery blading, there are two categories of Computational-Fluid-Dynamics tools available to the designers: the analysis method and the inverse method. The **analysis method** predicts the flowfield about a specified blade geometry. On the other hand, in an **inverse method**, the designers prescribe certain desired conditions for the flowfield, and the method generates the blade geometry. Although a large number of robust and well-established 3D Euler/Navier-Stokes computer codes have been developed in the analysis mode and are being used daily by designers, no such method appears to exist in the **inverse** mode for **fully three-dimensional** flows. The proposed work will produce a unique CFD capability for designers in the gas turbine industry.

Current state-of-the-art blade design systems consist of two primary stages. In the first stage, the combined throughflow and blade-to-blade methods (or the so-called quasi-3D methods) based on the general theory of Wu (1952) are used to design the blade profiles at several spanwise stations to produce some prescribed flow conditions. These 2D cascaded airfoils are then "stacked" together to form the initial design of the 3D blade profile. In many situations such as highly-loaded and low-aspect ratio blading, when the blade profile designed with a quasi-3D methods is built and tested, it will not produce the prescribed flow conditions. The primary reason for this deficiency is that the quasi-3D approach does not properly model the complex three-dimensional nature of the flowfield in turbomachines. Consequently, a second blade design iteration is required. In this second stage of the blade design cycle, advanced 3D Euler and/or Navier-Stokes analysis codes are used to assist the designers to "manually"

Research sponsored by the U.S. Department of Energy's Morgantown Energy Technology Center, under Contract DE-FC21-92MC29061 with Syracuse University, Syracuse, NY 13244; (315) 443-2807.

modify the 3D blade profile until the desired flowfield is obtained.

The objective of this research is to develop a robust fully three-dimensional and viscous inverse method for turbomachine blades. This method is developed to replace the quasi-3D inverse methods currently employed in industry. Blade profiles designed by a fully 3D and viscous inverse method will result in more efficient blade design and shorter blade design cycle. We also believe that the use of a 3D and viscous inverse method can result in great advancements in blade designs because it has the potential of inventing new or "revolutionary" blade designs. The current practice generally will only produce "evolutionary" changes in blade design.

Project Description

In this work, we will develop an inverse design method that has the following capabilities: (1) full three-dimensionality, and (2) prediction of three dimensional viscous effects. Two primary tasks are to be carried out in this proposed work. The first task consists of extending the 2D inviscid-flow inverse method of Dang (1995) to a fully 3D viscous-flow inverse method. The second task consists of the validation work for the proposed 3D inverse method.

The general three-dimensional equations of motion written in the blade-relative frame using cylindrical coordinates (r,θ,x) can be expressed in the vector form as

$$\frac{\partial U}{\partial t} + \frac{1}{r}\frac{\partial (rE_{inv})}{\partial r} + \frac{1}{r}\frac{\partial (F_{inv})}{\partial \theta} + \frac{\partial (G_{inv})}{\partial x} = \frac{1}{r}(S_{inv} + S_{visc} + S_{bl}) \qquad (1)$$

where $\mathbf{U}$ is the conservative-variable vector, $\{\mathbf{E}_{inv},\mathbf{F}_{inv},\mathbf{G}_{inv}\}$ are the conventional inviscid-flux vectors. The source vector $\mathbf{S}_{inv}$ accounts for (1) terms arising from the use of the cylindrical coordinate system, and (2) for the inertial forces in the case of a rotating blade row. The source vector $\mathbf{S}_{visc}$ contains the viscous stresses, while the additional source vector $\mathbf{S}_{bl}$ contains the blade body force field.

In Eq. (1), the source term denoted by $\mathbf{S}_{visc}$ models viscous effects as a distributed body-force field and can be represented as

$$S_{visc} \equiv \left\{ \begin{array}{c} 0 \\ \rho r F_{visc,r} \\ \rho r F_{visc,\theta} \\ \rho r F_{visc,x} \\ 0 \end{array} \right\} \qquad (2)$$

In this study, we propose to use the simple but effective 3D viscous-model of Denton (1992) to predict viscous losses. This method has been shown to give good agreements with the measured flowfields about many axial and radial turbomachines, and the method is being used by many design offices. In the viscous method of Denton (1992), by assuming that the grid points one element away from solid surfaces lie within the log-law region of a turbulent boundary layer, the surface shear stress is calculated using the well accepted relationship between the shear stress, velocity and distance in the log-law region. The method assumes that the surface streamlines lie on the edge of the viscous sublayer so that the velocity has slip at solid boundaries. Finally, away from the wall, the shear stresses are obtained from a simple mixing length model.

In theory, we modelled the presence of the blades with a discrete and periodic body-force field (Dang & Isgro, 1996). The blade body force represents entirely the reaction on the fluid as a result of pressure forces concentrated at the blade surfaces. Consequently, the blade body force is zero everywhere except at the blade surfaces (i.e. a discrete body-force field). In practice, by taking the "conventional" computational domain that comprises the flow passage between two consecutive blades and excluding the blade surfaces, the blade body-force term appearing in the equations of motion is replaced by a pressure-jump boundary condition.

By considering the θ-component of the momentum integral equation, one can readily show that the local pressure jump across the blade (or the blade loading) is

$$\begin{aligned} \Delta p(s,n) &\equiv p^{+} - p^{-} \\ &= \frac{\partial}{\partial s}\int_{gap} rV_\theta(\rho V_s d\theta) + \frac{\partial}{\partial n}\int_{gap} rV_\theta(\rho V_n d\theta) \end{aligned} \tag{3}$$

where s and n are distances measured along and across some quasi-meridional streamlines, respectively. These quasi-meridional streamlines can be the grid lines in the meridional plane.

From an order-of-magnitude consideration, the first term on the right-hand-side of Eq. (3) accounts for the streamwise change in the tangential momentum-flux, while the second term on the right-hand-side of Eq. (3) accounts for the change in the tangential momentum-flux across the quasi-meridional streamsurface. Consequently, we have

$$\frac{\partial}{\partial n}\int_{gap} rV_\theta(\rho V_n d\theta) < \frac{\partial}{\partial s}\int_{gap} rV_\theta(\rho V_s d\theta) \tag{4}$$

and we see that the blade loading is on the order of

$$\Delta p(s,n) \sim O\left(\frac{\partial}{\partial s}\int_{gap} rV_\theta(\rho V_s d\theta)\right) \tag{5}$$

Let us define the mass-averaged tangential velocity $r\hat{V}_\theta(s,n)$ as

$$r\hat{V}_\theta(s,n) \equiv \frac{1}{\dot{m}(s,n)}\int_{gap} rV_\theta(\rho V_s d\theta) \tag{6}$$

where $\dot{m}$ (s,n) is defined as the local pitch-averaged mass flow rate per unit area, i.e.

$$\dot{m}(s,n) \equiv \int_{gap} \rho V_s d\theta \tag{7}$$

On substituting the above definitions into Eq. (3), we obtain

$$\begin{aligned} \Delta p &= \frac{\partial}{\partial s}\int_{gap} rV_\theta(\rho V_s d\theta) + \frac{\partial}{\partial n}\int_{gap} rV_\theta(\rho V_n d\theta) \\ &= \frac{\partial}{\partial s}\left[\dot{m}\ r\hat{V}_\theta\right] + \frac{\partial}{\partial n}\int_{gap} rV_\theta(\rho V_n d\theta) \end{aligned} \tag{8}$$

From the order-of-magnitude discussed earlier (Eq. (4)), the first term on the right-hand-side of Eq. (8) is much larger than the second term, and we have

$$\Delta p \sim O\left(\frac{\partial}{\partial s}[\dot{m}\ r\hat{V}_\theta]\right) \tag{9}$$

Furthermore, we expect the mass flow rate to be relatively constant within the quasi-meridional streamtubes, i.e.

$$\Delta p \sim O\left(\frac{\partial}{\partial s}[\dot{m}\ r\hat{V}_\theta]\right) \sim O\left(\dot{m}\frac{\partial(r\hat{V}_\theta)}{\partial s}\right) \propto \frac{\partial(r\hat{V}_\theta)}{\partial s} \tag{10}$$

and we conclude that the blade loading is proportional to the rate of change of rV_θ along the quasi-meridional streamlines. In this proposed inverse method, the circumferential mass-averaged angular momentum per unit mass rV_θ (or approximately the blade loading) is the prescribed flow quantity. During the inverse calculation, the blade loading is iterated using Eq. (8). The other prescribed quantity is the blade thickness distribution.

The central philosophy behind the proposed inverse method is to use the slip boundary conditions along the blade surfaces to "trace out" the blade shape. In the inverse problem, the boundary conditions at the blade surfaces for Eq. (1) are different from those used in the analysis problem. The usual no-flux condition (or the slip boundary condition) along the blades surfaces is not enforced in solving Eq. (1). Instead, fluid is allowed to cross the blade surfaces during the iteration for the blade shape, and a pressure-jump condition is imposed along the blade surfaces. The slip boundary conditions along the blade surfaces are used to adjust the blade profile so that it aligns with the local flow. Finally, we will formulate the boundary conditions so that blade cooling can be accounted for.

The equations of motion given in Eq. (1) is solved using the well-known Jameson et al. (1981) four-stage Runge-Kutta time-stepping scheme. This algorithm, and its variations, are being used in many Euler and Navier-Stokes turbomachine analysis codes (Adamczyk, 1989; Dawes, 1992; Denton, 1992).

Accomplishments

This project started in September 1995. We are in the process of developing the 3D inviscid-flow version of the code.

Acknowledgements

This work is supported by the DOE Morgantown Energy Technology Center through the South Carolina Energy Research & Development Center. Dr. D. Fant is the contract monitor.

References

Adamczyk, J. J., Celestina, M. L., Beach, T. A., and Barnett, M., 1990, "Simulation of Three-Dimensional Viscous Flow within a Multistage Turbine," **Journal of Turbomachinery**, Vol. 112, pp. 370-376.

Dang, T., 1995, "Inverse Method for Turbomachine Blades Using Shock-Capturing Techniques," AIAA paper no. 95-2465.

Dang, T. and Isgro, V., 1996, "Inverse Method for Turbomachinery Blade Design Using Modern Shock Capturing Techniques: Part I - Two Dimensional Cascades," to appear in **AIAA Journal**.

Dawes, W. N., 1992, "Toward Improved Throughflow Capability: The Use of Three-Dimensional Viscous Flow Solvers in a Multistage Environment," **Journal of Turbomachinery**, Vol. 114, pp. 8-17.

Denton, J. D., 1992, "The Calculation of Three-Dimensional Viscous Flow Through Multistage Turbomachines," **Journal of Turbomachinery**, Vol. 114, pp. 18-26.

Jameson, A., Schmidt, W. and Turkel, E., 1981, "Numerical Solution of the Euler Equations by Finite Volume Methods using Runge-Kutta Time-Stepping Schemes," AIAA Paper No. 81-1259.

Wu, C. H., 1952, "A General Theory of Three-Dimensional Flow in Subsonic and Supersonic Turbomachines of Axial, Radial, and Mixed-Flow Types," NACA TN 2604.

Appendices

Agenda

Advanced Turbine Systems Annual Program Review Meeting
October 17-19, 1995

TUESDAY, OCTOBER 17, 1995

7:30 a.m. REGISTRATION/CONTINENTAL BREAKFAST

SESSION 1 — POLICY AND STRATEGIC ISSUES

Session Chair: Charles M. Zeh

8:15 a.m. *Opening Remarks*
Charles M. Zeh
Morgantown Energy Technology Center

8:25 a.m. 1.1 *Keynote Address — FE*
Thomas F. Bechtel
Morgantown Energy Technology Center

8:55 a.m. 1.2 *Keynote Address — EE*
Denise Swink
U.S. Department of Energy

9:25 a.m. 1.3 *Keynote Address — Government Roles*
Henry Kelly
White House Office of Science and Energy

9:55 a.m. 1.4 *Keynote Address — Industry*
The Role of Advanced Gas Turbines in the Power Generation Industry
Jim Scalf
Florida Power and Light Company

10:25 a.m. BREAK

SESSION 2A — ATS PROGRAM ELEMENT OVERVIEWS

Session Chair: Stan Blazewicz

10:45 a.m. 2.1 *Allison ATS Program Element Overview*
Sy A. Ali
Allison Engine Company

11:10 a.m. 2.2 *Advanced Turbine Systems Program Overview*
David W. Esbeck
Solar Turbines Incorporated

11:35 a.m. 2.3 *H Gas Turbine Combined Cycle*
James C. Corman
General Electric Company

12:00 p.m. 2.4 *Overview of Westinghouse's Advanced Turbine Systems Program*
Frank P. Bevc
Westinghouse Electric Corporation

12:25 p.m. LUNCH

SESSION 2B — ATS PROGRAM TECHNICAL REVIEWS

Session Chair: Stan Blazewicz

1:25 p.m. 2.5 *Allison Engine ATS Program Technical Review*
Dale W. Mukavetz
Allison Engine Company

1:50 p.m. 2.6 *Advanced Turbine Systems Program Technical Review*
Stephen Gates, Jr.
Solar Turbines Incorporated

2:15 p.m. 2.7 *Advanced Turbine System Program Phase 2 Cycle Selection*
John Latcovich
ABB Power Generation

2:40 p.m. 2.8 *General Electric ATS Program Technical Review Phase 2 Activities*
David P. Smith
General Electric Company

3:05 p.m. 2.9 *Technical Review of Westinghouse's Advanced Turbine Systems Program*
Ihor S. Diakunchak
Westinghouse Electric Corporation

3:30 p.m. BREAK

SESSION 3 — ATS RELATED ACTIVITIES

Session Chair: Edward L. Parsons

3:45 p.m. 3.1 *Advanced Combustion Turbines and Cycles: An EPRI Perspective*
George Touchton
Electric Power Research Institute

4:10 p.m. 3.2 *Advanced Turbine Systems Annual Program Review*
William E. Koop
Wright Patterson Air Force Base

4:35 p.m. 3.3 *TBD*
Steve Friedman
Gas Research Institute

5:00 p.m. Poster Session Setup

6:00 p.m. SOCIAL
6:30 p.m. DINNER
Lakeview Resort and Conference Center

WEDNESDAY, OCTOBER 18, 1995

7:30 a.m. REGISTRATION/CONTINENTAL BREAKFAST

8:00 a.m. POSTER SESSION

P1 *Lean Premixed Combustion Stabilized by Radiation Feedback and Heterogeneous Catalysis*
Robert W. Dibble
University of California

P2 *Rayleigh/Raman/LIF Measurements in a Turbulent Lean Premixed Combustor*
Robert W. Pitz
Vanderbilt University

P3 *Lean Premixed Flames for Low NOx Combustors*
Paul E. Sojka
Purdue University

P4 *Functionally Gradient Materials for Thermal Barrier Coatings in Advanced Gas Turbine Systems*
Martin P. Harmer
Lehigh University

P5 *Advanced Turbine Cooling, Heat Transfer, and Aerodynamic Studies*
Je-Chin Han
Texas A&M University

P6 *Life Prediction of Advanced Materials for Gas Turbine Application*
Sam Y. Zamrik
The Pennsylvania State University

P7 *Actuators for Combustion Control: New Approaches and Materials*
L. A. Roe
University of Arkansas

P8 *Combustion Modeling in Advanced Gas Turbine Systems*
L. Douglas Smoot
Brigham Young University

P9 *Heat Transfer in a Two-Pass Internally Ribbed Turbine Blade Coolant Channel with Cylindrical Vortex Generators*
Sumanta Acharya
Louisiana State University

P10 *Reduction of Turbine Endwall Total Pressure Loss and Heat Transfer Using the Iceformation Design Method*
Ronald S. LaFleur
Clarkson University

P11 *Rotational Effects on Turbine Blade Cooling*
G. R. Guenette
Massachusetts Institute of Technology

P12 *Manifold Methods for Methane Combustion*
S. B. Pope
Cornell University

P13 *Advanced Multistage Turbine Blade Aerodynamics, Performance, Cooling and Heat Transfer*
Patrick B. Lawless
Purdue University

P14 *The Role of Reactant Unmixedness, Strain Rate, and Length Scale on Premixed Combustor Performance*
S. Samuelsen
University of California, Irvine

P15 *Experimental and Computational Studies of Film Cooling with Compound Angle Injection*
R. J. Goldstein
University of Minnesota

P16 *Compatibility of Gas Turbine Materials with Steam Cooling*
V. H. Desai
University of Central Florida

P17 *Simultaneous Measurement of Film Cooling Effectiveness and Heat Transfer Using a UV-Induced Thermographic Phosphor Imaging System*
Mingking K. Chyu
Carnegie Mellon University

P18 *Advanced Design Methodology Using Combined Computational/ Experimental Techniques for Gas Turbine Film Cooling*
James Leylek
Clemson University

P19 *Steam as Turbine Blade Coolant*
Abraham Engeda
Michigan State University

P20 *Combustion Chemical Vapor Deposited Coatings for Thermal Barrier Coating Systems*
J. M. Hampikian
Georgia Institute of Technology

P21 *Premixed Burner Experiments: Burner Geometry, Mixing and Flame Structure Issues*
Ashwani K. Gupta
University of Maryland

P22 *Intercooler Flow Path for Gas Turbines: CFD Design and Experiments*
Ajay K. Agrawal
University of Oklahoma

P23 *Bond Strength and Stress Measurements in Thermal Barrier Coatings*
Maurice Gell and Eric Jordan
University of Connecticut

P24 *Active Control of Combustion Instabilities in Low NOx Gas Turbines*
Ben Zinn
Georgia Institute of Technology

P25 *Combustion Instability Modeling and Analysis*
Domenic A. Santavicca
The Pennsylvania State University

P26 *Flow and Heat Transfer in Gas Turbine Disk Cavities Subject to Non-Uniform External Pressure Field*
R. P. Roy
Arizona State University

P27 *Innovative Schemes for Closed-Loop Air/Stream Cooling for Advanced Gas Turbine Systems*
Ting Wang
Clemson University

P28 *Heat Pipe Turbine Vane Cooling*
Lee S. Langston
University of Connecticut

P29 *Improved Modeling Techniques for Turbomachinery Flow Fields*
Bud Lakshminarayana
The Pennsylvania State University
J. R. Fagan
Allison Engine Company

P30 *Advanced 3-D Inverse Method for Designing Turbomachine Blades*
Thong Dang
Syracuse University

SESSION 4 — UNIVERSITY/INDUSTRY CONSORTIUM INTERACTIONS

Session Chair: Norman T. Holcombe

9:30 a.m. 4.1 *The AGTSR Consortium: An Update*
Lawrence P. Golan
Clemson University

9:50 a.m. PANEL: University/Industry Consortium Interactions

Sy A. Ali
Allison Engine Company

Ihor Diakunchak
Westinghouse Power Corporation

Maurice Gell
University of Connecticut

Vimal Desai
University of Central Florida

11:00 a.m. BREAK

SESSION 5 — ATS SUPPORTIVE PROJECTS

Session Chair: Steve Waslo

11:20 a.m. 5.1 *Design Factors for Stable Lean Premix Combustion*
George A. Richards
Morgantown Energy Technology Center

11:40 a.m.	5.2	*Ceramic Stationary Gas Turbine* Mark van Roode Solar Turbines Incorporated
12:00 p.m.	5.3	*DOE/Allison Ceramic Vane Effort* Richard Wenglarz Allison Engine Company
12:20 p.m.		LUNCH
1:20 p.m.	5.4	*Materials/Manufacturing Element of the Advanced Turbine Systems Program* M. A. Karnitz Oak Ridge National Laboratory
1:40 a.m.	5.5	*Land Based Turbine Casting Initiative* Boyd A. Mueller Howmet Corporation
2:00 p.m.	5.6	*Turbine Airfoil Manufacturing Technology* Charles S. Kortovich PCC Airfoils, Inc.
2:20 p.m.		BREAK
2:40 p.m.	5.7	*Pratt & Whitney Thermal Barrier Coatings* Norman S. Bornstein United Technologies Research Center
3:00 p.m.	5.8	*Westinghouse Thermal Barrier Coatings Development* John Goedjen Westinghouse Electric Corporation
3:20 p.m.	5.9	*High Performance Steam Developments* Thomas E. Duffy Solar Turbines Incorporated
3:40 p.m.		CLOSING REMARKS
3:50 p.m.		Adjourn
4:00 p.m.		METC Site Tour

Meeting Participants

Kim Aasberg-Petersen
Chemical Engineer
Haldor Topsoe
Nymollevej 55
P.O. Box 213
Lyngby DK-2800
Denmark
454-527-2000; Fax: 454-527-2999
KAP@HTAS.DK

Jeff Abboud
Dir., Government Affairs
Gas Turbine Association
1600 Wilson Blvd., Suite 1008
Arlington, VA 22209
703-812-8740; Fax: 703-812-8743
IAISTAFF@INTERRAMP.COM

Sumanta Acharya
L.R. Daniel Professor
Louisiana State University
Mechanical Engineering Dept.
Baton Rouge, LA 70803
504-388-5809; Fax: 504-388-5924
ACHARYA@ME.LSU.EDU

Ajay K. Agrawal
Assistant Professor
University of Oklahoma
865 Asp Ave., Room 212
Norman, OK 73019
405-325-1754; Fax: 405-325-1088
AGRAWAL@MAILHOST.ECN.
UOKNOR.EDU

Sy A. Ali
Dir., Industrial Engine Tech.
Allison Engine Company
P.O. Box 420, W16
Indianapolis, IN 46206-0420
317-230-6864; Fax: 317-230-5600

John E. Allen
Undergraduate Research Asst.
University of Oklahoma
865 Asp Ave., Room 212
Norman, OK 73019
405-325-1754; Fax: 405-325-1088
JEALLEN@MAILHOST@ECN.
UOKNOR.EDU

R. P. Allen
Consulting Engineer
155 Kare Fre Blvd.
West Union, SC 29696
803-638-8575 Fax: 803-638-8575

Robert Allinson
Dir., Business Planning
Aerospace Alloys, Inc.
130-6 Utopia Road
Manchester, CT 06040
860-649-0092; Fax: 860-649-9069

Chuck Alsup
Project Manager
Morgantown Energy Tech. Center
U.S. Department of Energy
P.O. Box 880, MS D06
Morgantown, WV 26507-0880
304-285-5432; Fax: 304-285-4403
CALSUP@METC.DOE.GOV

Rodney Anderson
Program Manager, Tech. Transfer
Morgantown Energy Tech. Center
U.S. Department of Energy
P.O. Box 880, MS A03
Morgantown, WV 26507-0880
304-285-4709; Fax: 304-285-4403
RANDER@METC.DOE.GOV

Zenen Antoniak
Sr. Development Engineer
Battelle PNL, MS K7-15
Richland, WA 99352
509-375-3841; Fax: 509-375-3641

Juan Araujo
Research Assistant
Clarkson University
Box 5725, Dept. MAE
Potsdam, NY 13699
315-268-3887; Fax: 315-268-6438

David H. Archer
Adjunct Professor
Carnegie Mellon University
114 Kentzel Road
Pittsburgh, PA 15237-2816
412-268-6808; Fax: 412-268-3348

Andy Ayoob
Manager, C.T. Engineering
Westinghouse Electric Corporation
4400 Alafaya Trail
Orlando, FL 32826-2399
407-281-3365; Fax: 407-281-5014

Richard Bajura
Dir., NRCCE
West Virginia University
P.O. Box 6064
Morgantown, WV 26506-6064
304-293-2867; Fax: 304-293-3749

Rita A. Bajura
Associate Dir., OPTM
Morgantown Energy Tech. Center
U.S. Department of Energy
P.O. Box 880, MS B06
Morgantown, WV 26507-0880
304-285-4109; Fax: 304-285-4292
RBAJUR@METC.DOE.GOV

Stephen W. Banovic
Research Assistant
Lehigh University
Whitaker Laboratory
5 East Packer Ave.
Bethlehem, PA 18015
610-758-4270; Fax: 610-758-4244
SWB0@LEHIGH.EDU

Terry R. Barnett
Mgr., Experimental Mechanics
Southern Research Institute
757 Tom Mertig Drive
Birmingham, AL 35211
205-581-2378; Fax: 205-581-2414
BARNETT@SRI.ORG

Kevin P. Barr
Sr. Engineer Specialist
Allied Signal
2525 W. 190th Street
Torrance, CA 90504-6099
310-512-3350; Fax: 310-512-3075

Arun Basu
Senior Engineer
Amoco
Mail Code: E-1F
Amoco Research Center
Naperville, IL 60565
708-420-4602; Fax: 708-420-3848
ABASU@AMOCO.COM

Reda Bata
Associate Professor
West Virginia University
Dept. of Engineering
Morgantown, WV 26506
304-293-3111

Thomas F. Bechtel
Director
Morgantown Energy Tech. Center
U.S. Department of Energy
P.O. Box 880, MS C02
Morgantown, WV 26507-0880
304-285-4931; Fax: 304-285-4292
TBECHT@METC.DOE.GOV

David J. Bennett
Dir. Fed. Business Dev.
Dow Corning Corporation
1800 M. St. NW., Suite 325 S.
Washington, DC 20036
202-785-0585; Fax: 202-785-0421
USDCCB23@IBMMAU.COM

Frank Bevc
Mgr., Emerging Technologies
Westinghouse Electric Corporation
4400 Alafaya Trail, MS 381
Orlando, FL 32826-2399
407-281-3393; Fax: 407-281-5014

Stanley Blazewicz
Industrial ATS Program Manager
U.S. Department of Energy
1000 Independence Ave., S.W.
Washington, DC 20585
202-586-4679; Fax: 202-586-7114
STANLEY.BLAZEWICZ@HQ.DOE.GOV

Norman S. Bornstein
Research Scientist
United Technologies Research
411 Silver Lane
East Hartford, CT 06108
203-727-7487; Fax: 203-727-7879
BORNSTNS@UTRC.UTC.COM

Daniel Boss
Research Scientist
BIRL Northwestern University
1801 Maple Ave.
Evanston, IL 60201
708-491-3373; Fax: 708-467-1022
DBOSS@NWU.EDU

Richard S. Brent
Mgr., Communication ATS
Solar Turbines Incorporated
2200 Pacific Highway, P.O. Box 85376
San Diego, CA 92186-5376
619-544-5663; Fax: 619-544-2878

William D. Brentnall
Mgr., Material and Processes
Solar Turbines Incorporated
2200 Pacific Highway, P.O. Box 85376
San Diego, CA 92186-5376
619-544-5520; Fax: 619-544-2830

G. H. Bronnenberg
Dir., Indust. Gas Turbine Sales
Allison Engine Company
P.O. Box 420, Speed Code U-06
Indianapolis, IN 46206-0420
317-230-4151; Fax: 317-230-2900

James T. Bueche
Director
Power Data Group
1045 Newkirk Drive
La Jolla, CA 92037
619-454-6419; Fax: 619-454-6419

Virgil Bullington
Engineer
Oak Ridge National Laboratory
P.O. Box 2008
Oak Ridge, TN 37831-6066
423-675-6294; Fax: 423-574-6098

R. J. "Bob" Burgess
Principal Engineer
Florida Power and Light
P.O. Box 14000
Juno Beach, FL 33408
407-691-2212; Fax: 407-691-2695

Peter A. Carroll
V.P., Government Relations
Solar Turbines Incorporated
818 Connecticut Ave., N.W.
Suite 600
Washington, DC 20006-2702
202-293-4327; Fax: 202-293-4336

Frank L. Carter
Graduate Research Asst.
University of Oklahoma
865 Asp Avenue, Room 212
Norman, OK 73019
405-325-1754; Fax: 405-325-1088
FCARTER@MAILHOST.ECN.UOKNOR.
EDU

Kent Casleton
Research Chemist
Morgantown Energy Tech. Center
U.S. Department of Energy
P.O. Box 880, MS N05
Morgantown, WV 26507-0880
304-285-4573; Fax: 304-285-4403
KCASLE@METC.DOE.GOV

Thomas F. Chance
General Program Mgr., ATS Phase 2
GE Power Generation
1 River Road, Bldg. 53, Room 425
Schenectady, NY 12345
518-385-2868; Fax: 518-385-4314
CHANCETH@GEIPS00.SCH.GE.COM

Tan-Ping Chen
Mgr., Coal and Gas Conversion
Bechtel Group, Inc.
50 Beale Street
P.O. Box 193965
San Francisco, CA 94119-3965
415-768-1419; Fax: 415-768-3580

Shilong Chu
Post Doctoral Student
The Pennsylvania State University
Dept. of Aerospace Engineering
University Park, PA 16802
814-863-0156; Fax: 814-865-7092
CHU@TURBO3.PSU.EDU

Mingking K. Chyu
Professor
Carnegie Mellon University
Dept. of Mechanical Engineering
Pittsburgh, PA 15213-3890
412-268-3658; Fax: 412-268-3348
MC47@ANDREW.CMU.EDU

Joe R. Cleveland
Mgr., Operations Engineer
Rockwell/Rocketdyne
6633 Canoga Ave., T487
Canoga Park, CA 91303
818-586-6128; Fax: 818-586-5032

Arthur Cohn
Technical Manager
Electric Power Research Inst.
3412 Hillview Ave.
Palo Alto, CA 94304
415-855-2525; Fax: 415-855-8759
ACOHN@EPRINET.EPRI.COM

Nancy C. Cole
Mgr., Fossil Energy Program
Oak Ridge National Laboratory
P.O. Box 2008, MS-6067
HTML Room 209
Oak Ridge, TN 37831-6067
423-574-4824; Fax: 423-574-6098
COLENC@ORNL.GOV

Robert L. Coleman
Supervisory Auditor
U.S. General Accounting Office
5029 Corporate Road, Suite 300
Virginia Beach, VA 23462
804-552-8132; Fax: 804-552-8197

James C. Corman
General Manager
General Electric Company
1 River Road
Schenectady, NY 12345
518-385-7779; Fax: 518-385-2490
CORMANJA@PSEDMAIL.SCH.GE.COM

Sanjay M. Correa
Mgr., Combustion Program
GE Corporate R&D
P.O. Box 8, K1, ES 112
Schenectady, NY 12301
518-387-5853; Fax: 518-387-7258
CORREA@CRD.GE.COM

Kevin Craig
Sr. Chemical Process Engineer
National Renewable Energy Laboratory
1617 Cole Blvd.
Golden, CO 80401
303-275-2931; Fax: 303-275-2905
CRAIGK@TCPLINK.NREL.GOV

Mark H. Crawford
Reporter
New Technology Week
627 National Press Bldg.
Washington, DC 20045
202-662-9730
SCITECH@IX.NET.COM.

Thong Dang
Associate Professor
Syracuse University
149 Link Hall
Syracuse, NY 13244
315-443-4311; Fax: 315-443-9099
TGDANG@MAILBOX.SYR.EDU

Keith Davidson
Vice President
Onsite Energy Corporation
701 Palomar Airport Rd., Suite 200
Carlsbad, CA 92009
619-931-2400; Fax: 619-931-2405
ONSITE@ELECTRICITI.COM

Frank G. Davis
Mgr., Cleveland Office
Allied Signal Aerospace
7550 Lucerne Dr., Suite 203
Middleburg Heights, OH 44130
216-826-0330; Fax: 216-826-0333

William H. Day
Mgr., Advanced Indust. Prog.
Pratt & Whitney
400 Main Street, MS 165-22
East Hartford, CT 06108
860-565-0086; Fax: 860-565-0168

Vimal H. Desai
Associate Professor
University of Central Florida
Mech. and Aerospace Engrg. Dept.
Orlando, FL 32816
407-823-5777; Fax: 407-823-0208
DESAI@MAE.ENGR.UCF.EDU

Ihor Diakunchak
Advisory Engineer
Westinghouse Electric Corporation
4400 Alafaya Trail
Orlando, FL 32826-2399
407-281-5115; Fax: 407-281-5633

Robert W. Dibble
Professor, Mechanical Engrg.
Univ. of California, Berkeley
50-B Hesse Hall
Berkeley, CA 94720
510-642-4901; Fax: 510-642-1850
RDIBBLE@FIREBUG.ME.BERKELEY.
EDU

Clark Dohner
Project Manager
Electric Power Research Inst.
3412 Hillview Ave.
Palo Alto, CA 94303
415-855-2501; Fax: 415-835-8759

Thomas E. Duffy
Manager, Steam Programs
Solar Turbines Incorporated
2200 Pacific Highway, P.O. Box 85376
San Diego, CA 92185-5376
619-544-7429; Fax: 619-544-2878

George S. Dulikravich
Associate Professor
The Pennsylvania State University
233 Hammond Bldg.
Dept. of Aerospace Engineering
University Park, PA 16802
814-863-0134; Fax: 814-865-7092

Abraham Engeda
Assistant Professor
Michigan State University
Mechanical Engineering Dept.
A 231 EB
East Lansing, MI 48823
517-432-1834; Fax: 517-353-1750
ENGEDA@ME.MSU.EDU

David W. Esbeck
Vice President
Solar Turbines Incorporated
2200 Pacific Highway
P.O. Box 85376, M2 C1
San Diego, CA 92186-5376
619-544-5267; Fax: 619-595-7511

Daniel Fant
Research Manager
SC Energy R&D Center
386-2 College Avenue
Clemson, SC 29634-5180
803-656-2267; Fax: 803-656-0142
DFANT@MAIL.CLEMSON.EDU

William P. Fefferle
Chief Scientist
25 Science Park
New Haven, CT 06511-1968
203-786-5215; Fax: 203-786-5214

Richard Fleming
Consultant and Director
Catalytica
430 Ferguson Drive
Mountain View, CA 94043-5272
415-960-3000; Fax: 415-960-0127

Doug Freitag
Account Manager
DuPont Lanxide Company
17 Rocky Glen Ct.
Brookeville, MD 20833
301-570-3821; Fax: 301-570-3836
OFREITAG@DELPHI.COM

Albert Z. Fresco
Market Development Mgr.
DuPont Lanxide Composites
1300 Marrows Road
Newark, DE 19714
302-456-6241; Fax: 302-456-6480

Steve Friedman
Executive Tech. Manager
Gas Research Institute
8600 West Bryn Mawr Ave.
Chicago, IL 60631
312-399-8390; Fax: 312-399-8170

Christine M. Furstoss
Materials Program Manager
General Electric Company
1 River Road
Schenectady, NY 12345
518-385-4842; Fax: 518-385-3253

Stephen Gates
Director, ATS
Solar Turbines Incorporated
2200 Pacific Highway, P.O. Box 85376
San Diego, CA 92185-5376
619-544-5135; Fax: 619-544-2681

Maurice Gell
Professor in Residence
University of Connecticut
97 North Engleville Road, U-136
Storrs, CT 06269
203-486-3514; Fax: 203-486-4745

Daniel J. Gernhard
Engineer/Laboratory Supervisor
ABB/PPL
1000 Prospect Hill Road
Windsor, CT 06095
203-285-3397; Fax: 203-285-2513

Madhav R. Ghate
Director, TBM
Morgantown Energy Tech. Center
U.S. Department of Energy
P.O. Box 880, MS C05
Morgantown, WV 26507-0880
304-285-4135; Fax: 304-285-4403
MGHATE@METC.DOE.GOV

John Goedjen
Westinghouse Electric Corporation
4400 Alafaya Trail, MC 303
Orlando, FL 32826-2399
407-281-5372; Fax: 407-281-2334

Lawrence P. Golan
Director
SC Energy R&D Center
386-2 College Avenue
Clemson, SC 29634-5180
803-656-2267; Fax: 803-656-0142

H. Lawrence Goldstein
Sr. Engineering Analyst
National Renewable Energy Laboratory
409 12th Street, S.W., Suite 710
Washington, DC 20024-2125
202-651-7526; Fax: 202-651-7501

Richard Goldstein
Regents Professor
University of Minnesota
111 Church St., S.E.
Minneapolis, MN 55455
612-625-5552; Fax: 612-625-3434
GOLDSTEI@MAILBOX.MAIL.UMN.
EDU

S. R. Gollahalli
Professor
University of Oklahoma
865 Asp Ave., Room 212
Norman, OK 73019
405-325-5011; Fax: 405-325-1088
GOLLAHAL@MAILHOST.ECN.
UOKNOV.EDU

Jay P. Gore
Professor
Purdue University
1003 Chatee Hall
West Lafayette, IN 47907-1003
317-494-1452; Fax: 317-494-0530
GORE@ECN.PURDUE.EDU

Heinz A. Gorges
President
Vineta, Inc.
3705 Sleepy Hollow Road
Falls Church, VA 22041
703-941-7252; Fax: 703-941-7252

Jim Grabulis
Div. Director, AAD
Morgantown Energy Tech. Center
U.S. Department of Energy
P.O. Box 880, MS I07
Morgantown, WV 26507-0880
304-285-4435; Fax: 304-285-4403
JGRABU@METC.DOE.GOV

Charles B. Graves
Project Engineer
United Technologies
Pratt & Whitney
MS 715-89, P.O. Box 109600
West Palm Beach, FL 33410-9600
407-796-5289; Fax: 407-796-5825

George A. Graves
Senior Research Ceramist
Univ. of Dayton Research Inst.
300 College Park
Dayton, OH 45469-0172
513-229-4415; Fax: 513-229-2503

J. Gruszczynski
Consultant
Turbo Consultants, Inc.
211 Burning Bush Road
Greenville, SC 29607
803-288-4491; Fax: 803-675-5824

Gerald R. Guenette
Principal Research Engineer
MIT Gas Turbine Laboratory
77 Mass Ave., Room 31-214
Cambridge, MA 02139
617-253-3764; Fax: 617-258-6093

Tao Guo
Graduate Student
Clemson University
Dept. of Mechanical Engrg.
326 EIB
Clemson, SC 29634
803-656-7203; Fax: 803-656-4435
TGUO@ENG.CLEMSON.EDU

Ashwani K. Gupta
Professor
University of Maryland
Dept. of Mechanical Engrg.
College Park, MD 20742
301-405-5276; Fax: 301-314-9477
AKGUPTA@ENG.UMD.EDU

Edward J. Hall
Staff Research Scientist
Allison Engine Company
2001 S. Tibbs, T-14A
Indianapolis, IN 46206-0420
317-230-3722; Fax: 317-230-3691
EHALL@NAS.NASA.GOV

Michael Halter
Research Engineer
Clarkson University
Box 5725, Dept. MAE
Potsdam, NY 13699
315-268-3887; Fax: 315-268-6438

Awatef Hamed
Professor
University of Cincinnati
Dept. of Aerospace Engrg.
Cincinnati, OH 45221-0070
513-556-3553; Fax: 513-556-5038
AHAMED@UCENG.UC.EDU

Janet M. Hampikian
Asst. Professor
Georgia Inst. of Technology
Georgia Tech.
778 Atlantic Dr.
Atlanta, GA 30332-0245
404-636-7635; Fax: 404-853-9140
JANET.HAMPIKIAN@MSE.GATECH.EDU

Je-Chin Han
Professor
Texas A&M University
Mechanical Engrg. Dept.
College Station, TX 77843-3123
409-845-3738; Fax: 409-862-2418
JCH2187@ACS.TAMU.EDU

Fumihiko Hanayama
Chief of Branch
Babcock-Hitachi K.K.
6-9 Takara-Machi
Kure-Shi, 737
Japan

Martin P. Harmer
Professor
Lehigh University
S.E. Packer Ave.
Bethlehem, PA 18015
610-758-4227; Fax: 610-758-4244
MPH2@LEHIGH.EDU

Robert W. Harrison
Consultant, M&P Technology
Oak Ridge National Laboratory
414 Waterbury Circle
Cincinnati, OH 45231
513-771-3158
POPIE@CSO.CIN.IX.NET

George Hay
CAGT Program Planning
Collaborative Adv. Gas Turbine
42 Sunrise Lane
Lafayette, CA 94549
510-988-9792; Fax: 510-988-9792

K. Hemmes
Engineer
ECN
P.O. Box 1
Petten, 1755 2G
Netherlands
312-246-4729; Fax: 312-246-3489

Eugene E. Hoffman
Mgr., National Materials Prog.
U.S. Department of Energy - Oak Ridge
10504 Sandpiper Lane
Knoxville, TN 37922-5518
423-576-0735; Fax: 423-574-9275
HOFFMANEE@ORNL.GOV

Robert S. Holcomb
Dev. Engineer
Oak Ridge National Laboratory
P.O. Box 2008, Building 9108
Oak Ridge, TN 37831-6065
615-574-0273; Fax: 615-574-2102

Norman Holcombe
Project Manager
Morgantown Energy Tech. Center
U.S. Department of Energy
P.O. Box 880, MS C05
Morgantown, WV 26507-0880
304-285-4829; Fax: 304-285-4403
NHOLCO@METC.DOE.GOV

Gary M. Holloway
Senior Staff Engineer
GE Aircraft Engines
4187 Allenhurst Close
Cincinnati, OH 45241
513-552-4155; Fax: 513-552-5558

Diane Hooie
Project Manager
Morgantown Energy Tech. Center
U.S. Department of Energy
P.O. Box 880, MS D06
Morgantown, WV 26507-0880
304-285-4524; Fax: 304-285-4403
DHOOIE@METC.DOE.GOV

Ivan Howell
Principal Engineer
Westinghouse MTD
P.O. Box 18249
Large, PA 15236-0249
412-382-7584; Fax: 412-382-1965

David J. Huber
Project Engineer
Westinghouse Electric Corporation
4400 Alafaya Trail, MS 381
Orlando, FL 32826-2399
407-281-5597; Fax: 407-281-5014

Wendy Hughes
Princeton University
C.E.E.S. E-Quad Princeton Univ.
Princeton, NJ 08544
609-258-5276; Fax: 609-258-3661
WEHUGHES@PHOENIX.PRINCETON.
EDU

Michael Janus
Mechanical Engineer
Morgantown Energy Tech. Center
U.S. Department of Energy
P.O. Box 880, MS N05
Morgantown, WV 26507-0880
304-285-4912; Fax: 304-285-4403
MJANUS@METC.DOE.GOV

Andrew J. Jarabak
Manager, Program Development
Westinghouse Electric Corporation
1310 Beulah Road, 501-3028
Pittsburgh, PA 15235
412-256-2881; Fax: 412-256-1948
JARABAK.A.J@WEC.COM

Lisa Jarr
Patent Advisor
Morgantown Energy Tech. Center
U.S. Department of Energy
P.O. Box 880, MS A03
Morgantown, WV 26507-0880
304-285-4555; Fax: 304-285-4403
LJARR@METC.DOE.GOV

Eric K. Johnson
Professor
West Virginia University
P.O. Box 6106
Morgantown, WV 26506
304-293-3111; Fax: 304-293-6689

Richard A. Johnson
Project Manager
Morgantown Energy Tech. Center
U.S. Department of Energy
P.O. Box 880, MS D06
Morgantown, WV 26507-0880
304-285-4564; Fax: 304-285-4403
RJOHNS@METC.DOE.GOV

Eric H. Jordan
Professor
University of Connecticut
191 Auditorium Road
Storrs, CT 06269-3139
860-486-2371; Fax: 860-486-5088
JORDAN@ENG2.UCONN.EDU

Jay S. Kapat
Visiting Assist. Professor
Clemson University
244 EIB, Box 34-0921
Clemson, SC 29634-0921
803-656-5643; Fax: 803-656-1890
JMK@ENG.CLEMSON.EDU

Michael Karnitz
Mgr., Industrial Tech.
Oak Ridge National Laboratory
P.O. Box 2008, MS 6065
Oak Ridge, TN 37831-6065
423-574-5150; Fax: 423-574-6098
KARNITZMA@ORNL.GOV

Karl W. Karstensen
ATS Phase-2 Program Manager
Solar Turbines Incorporated
7691 Flag Lake Street
San Diego, CA 92119-2150
619-544-5490; Fax: 619-544-2878

George Kassianides
Director of Engineering
Westinghouse MTD
P.O. Box 18249
Pittsburgh, PA 15236-0249
412-382-7652; Fax: 412-382-1965

Ryan Katofsky
Consultant
Arthur D. Little, Inc.
20 Acorn Park
Cambridge, MA 02140-2390
617-498-5462; Fax: 617-498-7007
KATOFSKY.R@ADLITTLE.COM

Henry C. Kelly
Asst. Dir., Technology
Office of Science and Tech. Policy
White House
Washington, DC 20500
202-456-6034; Fax: 202-456-6023
HKELLY@OSTP.EOP.GOV

James Kimball
Principal Technology Mgr.
Gas Research Institute
8600 W. Bryn Mawr Ave.
Chicago, IL 60631
312-399-8178; Fax: 312-864-3530
JKIMBALL@GRI.ORG

Naokazu Kimura
Manager
EPDC
Gimza 6-15-1
Tokyo Chuo-Ku 104
Japan

Thomas J. King
U.S. Department of Energy
1064 Hayslope Dr.
Knoxville, TN 37919
615-241-4536; Fax: 615-574-6098

Carey A. Kinney
Program Manager
U.S. Department of Energy
5208 Grinnell Street
Fairfax, VA 22032
301-903-2827; Fax: 301-903-2406

David Knowles
Program Manager
Oak Ridge National Laboratory
600 Maryland Ave. S.W.
Suite 30
Washington, DC 20024
202-479-0254; Fax: 202-479-0575
DAVID.KNOWLES@HQ.DOE.GOV

Klod Kokini
Professor
Purdue University
1288 Mechanical Engrg. Bldg.
West Lafayette, IN 47907-1288
317-494-5727; Fax: 317-494-0539
KOKINI@ECN.PURDUE.EDU

William E. Koop
IHPTET
Wright Patterson Air Force Base
1950 5th
Wright Patterson AFB, OH 45433-7251
513-255-8211; Fax: 513-255-4100

Charles Kortovich
Mgr., Physical Metallurgy
PCC Airfoils, Inc.
25201 Chagrin Blvd., Suite 290
Beachwood, OH 44122
216-766-6202; Fax: 216-766-6217
BRANEM@HP750.PCCAIRFOILS.COM

Gil Kraemer
R&D Engineer
25 Science Park
New Haven, CT 06511-1968
203-786-5215; Fax: 203-786-5214

Michael Krumpelt
Mgr., Fuel Cell Technology
Argonne National Laboratory
9700 S. Cass Avenue
Argonne, IL 60439
708-252-8520; Fax: 708-252-4176

Roger Kuhl
Venture Development Manager
Thermo Technology Ventures
P.O. Box 1625, MS 3821
Idaho Falls, ID 83415-3821
208-526-7573; Fax: 208-526-4492
RDKUHL@INEL.GOV

Ronald S. Lafleur
Associate Professor
Clarkson University
Box 5725, Dept. MAE
Potsdam, NY 13699
315-268-3823; Fax: 315-268-6438

B. Lakshminarayana
Evanpugh Professor
The Pennsylvania State University
153 Hammond, Building 5
University Park, PA 16802
814-865-5551; Fax: 814-865-7092
B1LAER@ENGR.PSU.EDU

Lee Langston
Professor
University of Connecticut
Mechanical Engrg. Dept.
191 Auditorium Road, U-139
Storrs, CT 06269-3139
203-486-4884; Fax: 203-486-5088

Donald L. Larose
Program Manager, Marketing
General Electric Company
1 River Road, 2-724A
Schenectady, NY 12345
518-385-3149; Fax: 518-385-4374

John LaRue
Associate Professor
Univ. of California, Irvine
Mech. and Aerospace Engrg.
Irvine, CA 92717
714-824-6724; Fax: 714-824-8585
JLARUE@MAEMASTER.ENG.UCI.EDU

John A. Latcovich
Program Manager, ATS
ABB Power Generation, Inc.
5309 Commonwealth Ctr. Parkway
Midlothian, VA 23112
804-763-2353; Fax: 804-763-3070

Patrick B. Lawless
Assistant Professor
Purdue University
1003 Chappee Hall
W. Lafayette, IN 47907-1003
317-494-7856; Fax: 317-494-0530
LAWLESS@ECN.PURDUE.EDU

Abbie Layne
Project Manager
Morgantown Energy Tech. Center
U.S. Department of Energy
P.O. Box 880, MS D01
Morgantown, WV 26507-0880
304-285-4603; Fax: 304-285-4403
ALAYNE@METC.DOE.GOV

Hwes-Min Lee
Research Assistant Professor
West Virginia University
P.O. Box 6106
Dept. of MAE
Morgantown, WV 26506-6106
304-293-3111

Jongguen Lee
The Pennsylvania State University
13 Research Building, East
University Park, PA 16802
814-863-6278; Fax: 814-865-3389

David Lendon
Director of GTEC
European Gas Turbines, Ltd.
P.O. Box 1, Thorngate House
Lincoln
England
152-258-3202; Fax: 152-258-3594

Gerald R. Leverant
Director
Southwest Research Institute
4220 Culebra Road
San Antonio, TX 78238
210-522-2041; Fax: 210-522-6965
GLEVERANT@SWRI.EDU

Mark J. Lewis
Associate Professor
University of Maryland
Dept. of Aerospace Engineering
College Park, MD 20742
301-405-1133; Fax: 301-314-9001
LEWIS@ENG.UMD.EDU

James Leylek
Associate Professor
Clemson University
Dept. of Mechanical Engrg.
313-B Riggs Hall
Clemson, SC 29634-0921
803-656-5640; Fax: 803-656-4435

James N. Lingscheit
Group Mgr., Advanced Materials
BIRL Northwestern University
1801 Maple Avenue
Evanston, IL 60201
708-491-3284; Fax: 708-467-1022
JLINGSCHEIT@NWU.EDU

William G. Long
Consulting Engineer
Babcock & Wilcox
R&D Division
P.O. Box 11165
Lynchburg, VA 24506-1165
804-522-5716; Fax: 804-522-6196

John Loth
Professor
West Virginia University
Mechanical and Aerospace Engrg.
Morgantown, WV 26506-6106
304-293-4111; Fax: 304-293-6689

Wayne L. Lundberg
Principal Engineer
Westinghouse STC
1310 Beulah Road
Pittsburgh, PA 15235-5098
412-256-2418; Fax: 412-256-2002

Don Lyons
Chairman and Professor
West Virginia University
Mechanical and Aerospace Engrg.
Morgantown, WV 26506-6106
304-293-3111; Fax: 304-293-6689
LYONS@CEMR.WVU.EDU

Val F. Madden
Principal Research Engineer
New England Power Serv. Company
25 Research Dr.
Westborough, MA 01582
508-389-3054; Fax: 508-389-2107

Dan Maloney
Physical Scientist
Morgantown Energy Tech. Center
U.S. Department of Energy
P.O. Box 880, MS N05
Morgantown, WV 26507-0880
304-285-4629; Fax: 304-285-4403
DMALON@METC.DOE.GOV

Leo Marbun
Graduate Research Assistant
West Virginia University
600 Morgan Drive
Morgantown, WV 26505
304-598-7858
MARBUN@COE.WVU.EDU

Jeanine Marcin
Materials Engineering Mgr.
Pratt & Whitney Aircraft Company
400 Main Street
East Hartford, CT 06108
203-565-4784; Fax: 203-565-5635

Kenneth E. Markel, Jr.
Assoc. Director, OPM
Morgantown Energy Tech. Center
U.S. Department of Energy
P.O. Box 880, MS E02
Morgantown, WV 26507-0880
304-285-4364; Fax: 304-285-4403
KMARKE@METC.DOE.GOV

Hans C. Maru
Executive Vice President
Energy Research Corporation
3 Great Pasture Road
Danbury, CT 06813
203-792-1460; Fax: 203-798-2945

Junichiro Masada
Manager
Mitsubishi Heavy Industries
12124 High Tech. Avenue
Suite 170
Orlando, FL 32817-1245
407-281-3047; Fax: 407-275-1427

Marvin McKimpson
Program Manager
Michigan Technological Univ.
1400 Townsend Drive
Houghton, MI 49931-1295
906-487-2600; Fax: 906-487-2921
MMCKIMP@MTU.EDU

Harry T. Morehead
Mgr., New Program Dev.
Westinghouse Electric Corporation
4400 Alafaya Trail, MC 381
Orlando, FL 32826-2399
407-281-3322; Fax: 407-281-5014

Boyd A. Mueller
Manager, Process Science
Howmet Corporation
1500 S. Warner Street
Whitehall, MI 49461-1895
616-894-7216; Fax: 616-894-7826
BMUELLER@HOWMET.COM

Dale W. Mukavetz
Engineer
Allison Engine Company
P.O. Box 420
Indianapolis, IN 46206-0420
317-230-2575; Fax: 317-230-3691
IEDWM@AGT.GMEDS.COM

Kenneth Murphy
Senior Project Engineer
Howmet Corporation
1500 S. Warner St.
Whitehall, MI 49461-1895
616-894-7954; Fax: 616-894-7826

Ben Nagaraj
Senior Engineer
GE Aircraft Engines
MD-H85, Ineumann Way
Cincinnati, OH 45215
513-786-2287; Fax: 513-243-6511

Nobuo Nagasaki
Senior Engineer
Hitachi, Ltd.
1-1 Salwai-Cho 3-Chome
Hitachi, Ibaraki 317
Japan
029-423-5267; Fax: 029-423-6607

David Napoli
Mechanical Engineer
U.S. Department of Energy
1000 Independence Ave., S.W.
Washington, DC 20585
202-586-5377; Fax: 202-586-3237

Yedidia Neumeier
Research Engineer
Georgia Inst. of Technology
Georgia Tech.
Atlanta, GA 30332-0150
404-853-9159; Fax: 404-894-2760

Gary J. Neuner
ICR Gas Turbine Bus. Dev. Mgr.
Westinghouse Electric Corporation
401 East Hendy Ave., MS 71-37
Sunnyvale, CA 94088
408-735-2712; Fax: 408-735-4419

Richard A. Newby
Fellow Engineer
Westinghouse STC
1310 Beulah Road
Pittsburgh, PA 15235
412-256-2210; Fax: 412-256-2121

Dimitris Nikitopoulos
Associate Professor
Louisiana State University
2513B CEBA
Mechanical Engineering Dept.
Baton Rouge, LA 70803
504-388-5903; Fax: 504-388-5924

Paul F. Norton
Principal Design Engineer
Solar Turbines Incorporated
2200 Pacific Highway, P.O. Box 85376
San Diego, CA 92186-5376
619-544-5207; Fax: 619-544-2682

Thomas S. Norton
Mechanical Engineer
Morgantown Energy Tech. Center
U.S. Department of Energy
P.O. Box 880, MS N05
Morgantown, WV 26507-0880
304-285-4617; Fax: 304-285-4403
TNORTO@METC.DOE.GOV

Igor Ondryas
Technical Director
Fluor Daniel
3333 Michelson Drive
Irvine, CA 92677
714-975-4728; Fax: 714-975-3149

Adeboyejo A. Oni
Professor
Morgan State University
PI-ECSEL, 5200 Perring Parkway
Baltimore, MD 21239
410-319-3249; Fax: 410-319-3982

Nick Otter
Director of Technology
European Gas Turbines, Ltd.
EGT Whetstone
Cambridge Road
Whetstone, Leicester
England
116-275-0750; Fax: 116-275-0768

George Padgett
Mgr., Advanced Products
Solar Turbines Incorporated
2200 Pacific Highway, P.O. Box 85376
San Diego, CA 92186-5376
619-544-5708; Fax: 619-544-2682

Walter G. Parker
Manager, Applications Engrg.
Westinghouse Electric Corporation
1310 Beulah Road
Pittsburgh, PA 15235
412-256-2417; Fax: 412-256-2002

Bill Parks
Program Manager
U.S. Department of Energy
1000 Independence Ave., S.W.
Washington, DC 20585
202-586-2093

Edward L. Parsons
Div. Director, PST
Morgantown Energy Tech. Center
U.S. Department of Energy
P.O. Box 880, MS D06
Morgantown, WV 26507-0880
304-285-4533; Fax: 304-285-4403
EPARSO@METC.DOE.GOV

Mark Patterson
Tech. Assessment and Transfer
133 Defense Hyw.
Annapolis, MD 21401
301-261-8373; Fax: 410-224-4678
TATINC@AOL.COM

Leland E. Paulson
Project Manager
Morgantown Energy Tech. Center
U.S. Department of Energy
P.O. Box 880, MS D06
Morgantown, WV 26507-0880
304-285-4074; Fax: 304-285-4403
LPAULS@METC.DOE.GOV

Cindy M. Petronis
Research Assistant
Lehigh University
Whitaker Laboratory
5 E. Packer Avenue
Bethlehem, PA 18015
610-758-4701; Fax: 610-758-4244
CMP4@LEHIGH.EDU

Robert W. Pitz
Professor
Vanderbilt University
Mechanical Engrg. Dept.
P.O. Box 1592 - Station B
Nashville, TN 37235
615-322-0209; Fax: 615-343-8730

Stephen B. Pope
Professor
Cornell University
240 Upson Hall
Ithaca, NY 14853
607-255-4314; Fax: 607-255-6111
POPE@MAE.CORNELL.EDU

Douglas G. Puerta
Research Assistant
Lehigh University
Whitaker Laboratory
5 East Packer Ave.
Bethlehem, PA 18015
610-758-5000; Fax: 610-758-4244
DGP2@LEHIGH.EDU

Massood Ramezan
Principal Engineer
Burns & Roe
P.O. Box 18288
Pittsburgh, PA 15236
412-892-6451; Fax: 412-892-4664
RAMEZAN@PETC.DOE.GOV

Lawrence K. Rath
Div. Director, PPE
Morgantown Energy Tech. Center
U.S. Department of Energy
P.O. Box 880, MS E01
Morgantown, WV 26507-0880
304-285-4094; Fax: 304-285-4403
LRATH@METC.DOE.GOV

Geo Richards
General Engineer
Morgantown Energy Tech. Center
U.S. Department of Energy
P.O. Box 880, MS N05
Morgantown, WV 26507-0880
304-285-4458; Fax: 304-285-4403
GRICHA@METC.DOE.GOV

T. J. (Tom) Richards
Staff Engineer
Caterpillar, Inc.
P.O. Box 1875
Peoria, IL 61656-1875
309-578-8597; Fax: 309-578-6988

Tom Risley
Mgr., Turbomachinery
Westinghouse MTD
P.O. Box 18249
Large, PA 15236-0249
412-382-7676; Fax: 412-382-1965

Richard J. Roby
Dir., Combustion Research
Hughes Associates, Inc.
3610 Commerce Drive, Suite 817
Baltimore, MD 21227-1652
410-737-8677; Fax: 410-737-8688
RROBY@HAIFIRE.COM

Glenn Romanoski
Development Engineer
Oak Ridge National Laboratory
P.O. Box 2008, MS 6088
Oak Ridge, TN 37830
423-574-4838; Fax: 423-576-8424
ROMANOSKIGR@ORNL.GOV

Ramendra P. Roy
Professor
Arizona State University
Mechanical and Aerospace Engrg.
Tempe, AZ 85287-6106
602-965-1482; Fax: 602-965-1384
ROY@ASU.EDU

Hitoshi Sakai
Engineering Manager
NGK-LOCKE, Inc.
2900 Lakeside Dr., Suite 103
Santa Clara, CA 95054
408-986-9255; Fax: 408-986-9256
KINSAKAI@CERFNET.COM

Louis A. Salvador
Deputy Director
Morgantown Energy Tech. Center
U.S. Department of Energy
P.O. Box 880, MS A05
Morgantown, WV 26507-0880
304-285-4147; Fax: 304-285-4403
LSALVA@METC.DOE.GOV

Scott Samuelsen
Professor
Univ. of California, Irvine
VCI Combustion Laboratory
Irvine, CA 92717-3550
714-824-5468; Fax: 714-824-7423
GSS@UCI.EDU

David A. Sands
Engineering Manager
Florida Power Corporation
3201 34th Street S.
St. Petersburg, FL 33711
813-866-5386; Fax: 813-866-4938

Domenic A. Santavicca
Professor
The Pennsylvania State University
132 Research Bldg. East, Bigler Rd.
University Park, PA 16802
814-863-1863; Fax: 814-865-3389
MVS1@OAS.PSU.EDU

Jim Scalf
Vice President, Engineering
Florida Power and Light
700 Universe Blvd.
Juno Beach Office
Juno Beach, FL 33408
407-691-2600; Fax: 407-691-2606

M. T. Schobeiri
Associate Professor
Texas A&M University
Dept. of Mechanical Engrg.
College Station, TX 77843-3123
409-845-0819; Fax: 409-845-3081
TMS1885@ACS.TAMU.EDU

Dilip M. Shah
Materials Technologist
Pratt & Whitney Aircraft Company
400 Main St., MS 114-45
East Hartford, CT 06108
203-565-8499; Fax: 203-565-5635

Crystal Sharp
Contract Specialist
Morgantown Energy Tech. Center
U.S. Department of Energy
P.O. Box 880, MS I07
Morgantown, WV 26507-0880
304-285-4442; Fax: 304-285-4403
CSHARP@METC.DOE.GOV

Michelene Shepperd
Technical Marketing Rep.
Hope Gas, Inc.
P.O. Box 2868
Clarksburg, WV 26302-2868
304-623-8657; Fax: 304-623-8919

Naoki Shibukawa
Engineer
Toshiba Corporation
2-4 Suehiro-Cho, Tsurumi-Ku
Yokohama, Kanagawa 230
Japan
045-510-5925; Fax: 045-500-1973

Hajime Shiomi
Manager
Toshiba International Company
120 Erie Blvd.
Schenectady, NY 12305
518-469-9488; Fax: 518-382-5751

Terrence Simon
Professor
University of Minnesota
111 Church Street
Minneapolis, MN 55455
612-625-5831; Fax: 612-625-3434
TSIMON@ME.UMN.EDU

Mark Skowronski
Program Manager
Southern California Edison
6070 N. Irwindale Ave., No. 1
Irwindale, CA 91702-3271
818-812-7692; Fax: 818-812-7646

Daniel P. Smith
Mgr., Diag. and Heat Transfer
GE Corporate R&D Center
P.O. Box 8, Building K1-ES142
Schenectady, NY 12301
518-387-6413; Fax: 518-387-7258
SMITHDP@CRD.GE.COM

Jeffery S. Smith
Mgr., Surface Technology
Howmet Corporation
1500 S. Warner St.
Whitehall, MI 49461-1895
616-894-7573; Fax: 616-894-7826
JSSMITH@HOWMET.COM

William Cary Smith
Project Manager
Morgantown Energy Tech. Center
U.S. Department of Energy
P.O. Box 880, MS D06
Morgantown, WV 26507-0880
304-285-4260; Fax: 304-285-4403
WSMITH@METC.DOE.GOV

L. Douglas Smoot
Director, ACERC
Brigham Young University
265-L CTB
Chemical Engineering
Provo, UT 84602
801-378-8930; Fax: 801-378-6033
LDS@BYU.EDU

Inyoung Song
Senior Scientist
T/J Technologies, Inc.
P.O. Box 2150
Ann Arbor, MI 48106
313-213-1637; Fax: 313-761-7458

William Sowa
Research Engineer
United Technologies Research
411 Silver Lane
East Hartford, CT 06070
860-727-7958; Fax: 860-727-7669
SOWAWA@UTRC.UTC.COM

Robert Spicer
Project Engineer
Howmet Corporation
1500 S. Warner Street
Whitehall, MI 49461-1895
616-894-7933; Fax: 616-894-7826
RSPICER@HOWMET.COM

Raja Srivastava
Senior Planning Engineer
Northern States Power Company
414 Nicollet Mall
Minneapolis, MN 55401-1993
612-330-6515; Fax: 612-330-5913

E. A. (Ed) Steigerwald
Division Sales Manager
PCC Airfoils, Inc.
25201 Chagrin Blvd., No. 290
Beachwood, OH 44122
216-766-6202; Fax: 216-766-6205

George Steinfeld
Program Manager
Energy Research Corporation
3 Great Pasture Road
Danbury, CT 06813
203-792-1460; Fax: 203-743-6204

Ted Strickland
R&D Engineer
25 Science Park
New Haven, CT 06511-1968
203-786-5215; Fax: 203-786-5214

Fred Sudhoff
Project Manager
Morgantown Energy Tech. Center
U.S. Department of Energy
P.O. Box 880, MS E01
Morgantown, WV 26507-0880
304-285-4560; Fax: 304-285-4403
FSUDHO@METC.DOE.GOV

Denise F. Swink
Deputy Assistant Sec., OIT
U.S. Department of Energy
1000 Independence Avenue, SW
Washington, DC 20585
202-586-9232; Fax: 202-586-9234

W. Tabakoff
Professor
University of Cincinnati
Mechanical and Aerospace Engrg.
Cincinnati, OH 45221-0070
513-556-3226; Fax: 513-556-5038
WTABAKOFF@UCENG.UC.EDU

Dnyanesh Tamboli
Graduate Student
University of Central Florida
Mechanical and Aerospace Engrg.
Orlando, FL 32816
407-823-5650; Fax: 407-823-0208
DCT@TURBU.ENGR.UCF.EDU

Robert E. Taylor
Project Specialist
Tennessee Valley Authority
1101 Market St., WR 5H
Chattanooga, TN 37402
423-751-7453; Fax: 423-751-2463

George L. Touchton
Team Manager
Electric Power Research Inst.
3412 Hillview Ave.
Palo Alto, CA 94304-1395
415-855-8935; Fax: 415-855-8759
GTOUCHTO@MSM.EPRI.COM

Herman B. Urbach
Scientific Staff Assistant
Naval Surface Warfare Center
Carderock Division
3 A Leggett Circle
Annapolis, MD 21402-5067
410-293-2864; Fax: 410-293-3553

Mark van Roode
CSGT Project Manager
Solar Turbines Incorporated
2200 Pacific Highway, P.O. Box 85876
San Diego, CA 92186-5376
619-544-5549; Fax: 619-544-2830
USCATAJP@IBMMAIL.COM

Uri Vandsburger
Professor
Virginia Tech.
Dept. of Mechanical Engineering
Randolph Hall, 0238
Blacksburg, VA 24061
540-231-4459; Fax: 540-231-9100
URI@STNICK.ME.VT.EDU

John Vanosdol
Engineer
Morgantown Energy Tech. Center
U.S. Department of Energy
P.O. Box 880, MS A04
Morgantown, WV 26507-0880
304-285-5446; Fax: 304-285-4403
JVANOS@METC.DOE.GOV

Venkat Venkataraman
Project Manager
Morgantown Energy Tech. Center
U.S. Department of Energy
P.O. Box 880, MS C05
Morgantown, WV 26507-0880
304-285-4105; Fax: 304-285-4403
VVENKA@METC.DOE.GOV

H. J. Veringa
ECN
P.O. Box 1
Petten, 1755 2G
Netherlands
312-246-4729; Fax: 312-246-3489

Katsuo Wada
Chief Engineer
Hitachi, Ltd.
Gas Turbine R&D Center
1-1, Saiwai-Cho 3-Chome
Hitachi, Ibaraki 317
Japan
029-423-5310; Fax: 029-423-6716
WADA@CM.HITACHI.HITACHI.CO.JP

Tian Wan
West Virginia University
Mechanical and Aerospace Engrg.
Morgantown, WV 26506
304-293-3111

Ting Wang
Professor
Clemson University
Mechanical Engineering Dept.
P.O. Box 340921
Clemson, SC 29634-0921
803-656-5630; Fax: 803-656-4435
TING.WANG@CES.CLEMSON.EDU

Steve Waslo
ATS Industrial Program Mgr.
U.S. Department of Energy
9800 S. Cass Ave.
Argonne, IL 60439
708-252-2143; Fax: 708-252-8649

Richard E. Weinstein
Project Manager
Gilbert/Commonwealth
Parsons Power
2675 Morgantown Road
Reading, PA 19607
610-855-2699; Fax: 610-855-2384
GC!CHMAIL02!A929@GILCOM.
ATTMAIL.COM

Richard Wenglarz
Senior Staff Research Engineer
Allison Engine Company
P.O. Box 420
Speed Code T14
Indianapolis, IN 46206-0420
317-230-2185; Fax: 317-230-3619
IERAW@AGT.GMEDS.COM

Michael R. Wherley
Mechanical Engineer
Science Applications Int'l Corporation
11251 Roger Bacon Drive
Reston, VA 22090
703-318-4650; Fax: 703-709-1042
MICHAEL.R.WHERLEY@CPMX.SAIC.
COM

David J. White
Manager, Advanced Development
Solar Turbines Incorporated
2200 Pacific Highway, P.O. Box 85376
San Diego, CA 92186-5376
619-544-5542; Fax: 619-544-2681

Paul R. Wieber
Assoc. Director, OID
Morgantown Energy Tech. Center
U.S. Department of Energy
P.O. Box 880, MS A03
Morgantown, WV 26507-0880
304-285-4544; Fax: 304-285-4403
PWIEBE@METC.DOE.GOV

Laurence S. Wilken
Business Mgr., Adv. Turbine
Solar Turbines Incorporated
2200 Pacific Highway, P.O. Box 85376
San Diego, CA 92186-5376
619-544-5650; Fax: 619-544-2878

Mark Williams
Product Manager, Fuel Cells
Morgantown Energy Tech. Center
U.S. Department of Energy
P.O. Box 880, MS D01
Morgantown, WV 26507-0880
304-285-4747; Fax: 304-285-4403
MWILLI@METC.DOE.GOV

John Wills
Dir., Business Dev. IPG
Rolls-Royce, Inc.
11911 Freedom Drive
Reston, VA 22090
703-318-9008; Fax: 703-318-9009

Bernd Wilmsen
Graduate Student
Michigan State University
Mechanical Engineering Dept.
A 231 Engineering Bldg.
East Lansing, MI 48823
517-432-1834; Fax: 517-353-1750
WILMSENB@EGR.MSU.EDU

Ronald H. Wolk
Principal
Wolk Integrated Tech. Servs.
1056 Hyde Ave.
San Jose, CA 95129
408-996-7811; Fax: 408-996-2746
WOLKINTTS@AOL.COM

Steven D. Woodruff
Research Chemist
Morgantown Energy Tech. Center
U.S. Department of Energy
P.O. Box 880, MS A04
Morgantown, WV 26507-0880
304-285-4175; Fax: 304-285-4403
SWOODR@METC.DOE.GOV

Richard Root Woods
Executive Advisor
M-C Power Corporation
8040 S. Madison St.
Burr Ridge, IL 60521
708-986-8040; Fax: 708-986-8153

I. G. Wright
Staff Development Engineer
Oak Ridge National Laboratory
P.O. Box 2008, Bldg. 4500S
Oak Ridge, TN 37831-6065
615-574-4451; Fax: 615-574-5118
WRIGHTIG@ORNL.GOV

Katsuyuki Yamasaki
Sales Engineer
Hitachi, Ltd.
S. Kanda-Surugadai
4-Chome, Chiyoda-KU
Tokyo 101
Japan
035-295-5880; Fax: 033-258-5232

Ling Yang
West Virginia University
Mechanical and Aerospace Engrg.
Morgantown, WV 26506
304-293-3111

M. Joseph Yip
Mechanical Engineer
Morgantown Energy Tech. Center
U.S. Department of Energy
P.O. Box 880, MS N05
Morgantown, WV 26507-0880
304-285-5434; Fax: 304-285-4403
MYIP@METC.DOE.GOV

Sam Y. Zamrik
Professor
The Pennsylvania State University
121 Hammond Bldg.
University Park, PA 16802
814-865-5241; Fax: 814-865-5241
SYZESM@ENGR.PSU.EDU

Charles M. Zeh
Product Manager, Heat Engines
Morgantown Energy Tech. Center
U.S. Department of Energy
P.O. Box 880, MS D01
Morgantown, WV 26507-0880
304-285-4265; Fax: 304-285-4403
CZEH@METC.DOE.GOV

Dadong Zhou
Research Associate
Clemson University
Dept. of Mechanical Engrg.
Clemson, SC 29634-0921
803-656-0482; Fax: 803-656-4435

Author Index

Organization Index

☆ U. S. GOVERNMENT PRINTING OFFICE : 1996-709-196